Transactions of the ASME®

Transactions of the ASME, Journal of Turbomachinery (ISSN 0889-504X) is published quarterly (Jan., Apr., July, Oct.) for $130.00 per year by The American Society of Mechanical Engineers, 345 East 47th Street, New York, NY 10017. Second class postage paid at New York, NY and additional mailing offices. POSTMASTER: Send address change to Transactions of the ASME, Journal of Turbomachinery, c/o THE AMERICAN SOCIETY OF MECHANICAL ENGINEERS, 22 Law Drive, Box 2300, Fairfield, NJ 07007-2300.
CHANGES OF ADDRESS must be received at Society headquarters seven weeks before they are to be effective. Please send old label and new address.
PRICES: To members, $40.00, annually; to nonmembers, $130.00.
Add $24.00 for postage to countries outside the United States and Canada.
STATEMENT from By-Laws. The Society shall not be responsible for statements or opinions advanced in papers or ... printed in its publications (B7.1, Par. 3).

INDEXED by Applied Mechanics Reviews and Engineering Information, Inc.
Canadian Goods & Services Tax Registration #126148048

Journal of Turbomachinery

Published Quarterly by The American Society of Mechanical Engineers

VOLUME 116 • NUMBER 1 • JANUARY 1994

TECHNICAL PAPERS

1 An Experimental Study of Heat Transfer in a Large-Scale Turbine Rotor Passage (92-GT-195)
M. F. Blair

14 Time-Averaged Heat Transfer and Pressure Measurements and Comparison With Prediction for a Two-Stage Turbine (92-GT-194)
M. G. Dunn, J. Kim, K. C. Civinskas, and R. J. Boyle

23 The Effects of Incident Turbulence and Moving Wakes on Laminar Heat Transfer in Gas Turbines (92-GT-377)
K. Dullenkopf and R. E. Mayle

29 Wake-Induced Unsteady Stagnation-Region Heat Transfer Measurements (92-GT-196)
P. J. Magari and L. E. LaGraff

39 Tip Clearance Effect on Heat Transfer and Leakage Flows on the Shroud-Wall Surface in an Axial Flow Turbine (92-GT-200)
M. Kumada, S. Iwata, M. Obata, and O. Watanabe

46 The Effect of a Turbulent Wake on the Stagnation Point: Part II—Heat Transfer Results (92-GT-197)
A. J. Hanford and D. E. Wilson

57 Heat Transfer on a Flat Surface Under a Region of Turbulent Separation (92-GT-198)
R. B. Rivir, J. P. Johnston, and J. K. Eaton

63 An Experimental Study of Film Cooling in a Rotating Transonic Turbine (92-GT-201)
R. S. Abhari and A. H. Epstein

71 An Experimental Study of Film Cooling Effectiveness Near the Leading Edge of a Turbine Blade
M. Salcudean, I. Gartshore, K. Zhang, and I. McLean

80 Interactions Between Embedded Vortices and Injectant From Film Cooling Holes With Compound Angle Orientations in a Turbulent Boundary Layer (92-GT-199)
P. M. Ligrani and S. W. Mitchell

92 Discharge Coefficients of Holes Angled to the Flow Direction (92-GT-192)
N. Hay, S. E. Henshall, and A. Manning

97 Experimental Study on the Flow Characteristics of Streamwise Inclined Jets in Crossflow on Flat Plate (92-GT-181)
Sang Woo Lee, Joon Sik Lee, and Sung Tack Ro

106 Behavior of the Laterally Injected Jet in Film Cooling: Measurements of Surface Temperature and Velocity/Temperature Field Within the Jet (92-GT-180)
S. Honami, T. Shizawa, and A. Uchiyama

113 Heat Transfer in Rotating Serpentine Passages With Trips Skewed to the Flow (92-GT-191)
B. V. Johnson, J. H. Wagner, G. D. Steuber, and F. C. Yeh

124 Experimental Heat Transfer Investigation of Stationary and Orthogonally Rotating Asymmetric and Symmeteric Heated Smooth and Turbulated Channels (92-GT-189)
H. A. El-Husayni, H. E. Taslim, and D. M. Kercher

133 Heat Transfer in Serpentine Flow Passages With Rotation (92-GT-190)
S. Mochizuki, J. Takamura, S. Yamawaki, and Wen-Jei Yang

141 The Solution-Adaptive Numerical Simulation of the Three-Dimensional Viscous Flow in the Serpentine Coolant Passage of a Radial Inflow Turbine Blade (92-GT-193)
W. N. Dawes

(Contents Continued on p. 13)

(Contents Continued)

149 **Influence of Surface Heating Condition on Local Heat Transfer in a Rotating Square Channel With Smooth Walls and Radial Outward Flow** (92-GT-188)
J. C. Han, Y. M. Zhang, and C. P. Lee

159 **Effect of Trailing-Edge Ejection on Local Heat (Mass) Transfer in Pin Fin Cooling Channels in Turbine Blades** (92-GT-178)
R. D. McMillin and S. C. Lau

169 **Heat Transfer and Turbulence in a Turbulated Blade Cooling Circuit** (92-GT-187)
N. Abuaf and D. M. Kercher

ANNOUNCEMENTS

158 **Change of address form for subscribers**

178 **Information for authors**

An Experimental Study of Heat Transfer in a Large-Scale Turbine Rotor Passage

M. F. Blair
Manager, Heat Transfer Technology,
United Technologies Research Center,
East Hartford, CT 06108
Mem. ASME

An experimental study of the heat transfer distribution in a turbine rotor passage was conducted in a large-scale, ambient temperature, rotating turbine model. Heat transfer was measured for both the full-span suction and pressure surfaces of the airfoil and for the hub endwall surface. The objective of this program was to document the effects of flow three dimensionality on the heat transfer in a rotating blade row (versus a stationary cascade). Of particular interest were the effects of the hub and tip secondary flows, tip leakage, and the leading-edge horseshoe vortex system. The effect of surface roughness on the passage heat transfer was also investigated. Midspan results are compared with both smooth-wall and rough-wall finite-difference two-dimensional heat transfer predictions. Contour maps of Stanton number for both the rotor airfoil and endwall surfaces revealed numerous regions of high heat transfer produced by the three-dimensional flows within the rotor passage. Of particular importance are regions of local enhancement (as much as 100 percent over midspan values) produced on the airfoil suction surface by the secondary flows and tip-leakage vortices and on the hub endwall by the leading-edge horseshoe vortex system.

Introduction

It is well established that the aerodynamics and heat transfer occurring in turbine passages are strongly three dimensional in nature. These complex flows occur in both stator and rotor passages due to a variety of viscous and inviscid flow mechanisms. Viscous effects, in the form of boundary layers and wakes, produce flow three dimensionalities on all passage surfaces of both stators and rotors. Inviscid effects, though present for any three-dimensional airfoil geometry, are more important for rotor passages where the rotating frame of reference produces additional three dimensionalities in the flow.

To date, most of the experimental work aimed at understanding and documenting the effects of turbine passage three dimensionalities has been conducted in stationary cascades. These experiments have produced a large volume of high-quality aerodynamic and heat transfer data, which are available to the computational community for assessing turbine-passage predictions. For example, the complexities associated with cascade endwall boundary layers are discussed thoroughly by both Langston et al. (1977) and Sieverding (1985). An excellent compilation of up-to-date stator airfoil heat transfer data is given by Hylton et al. (1983) while Graziani et al. (1980) and Harvey et al. (1989) provide detailed information about three-dimensional heat transfer effects on both airfoil and endwall surfaces.

Due to the experimental difficulties involved, only a limited number of heat transfer studies have been conducted in rotor passages. The results presented by Lokay and Trushin (1970). Dunn and Hause (1982), Dunn (1986), Dunn et al. (1989), Guenette et al. (1989), and Blair et al. (1989) comprise, to the author's knowledge, all of the data containing rotation effects that are currently available in the open literature.

At least four important factors that influence turbine rotor passage heat transfer distributions are only present in full-stage (stator/rotor) turbine models with rotation: (1) The flow field entering the rotor passage is highly unsteady as it contains airfoil wakes, turbulence, and secondary flows generated in the upstream stator. This combination of periodic and random disturbances produces earlier boundary layer transition and significant enhancement to the overall level of heat transfer. (2) The secondary flows emerging from the upstream stator induce other secondary flow effects within the rotor passage. The data of Joslyn and Dring (1989, 1992) have established that stator-induced secondary flows move preferentially toward the hub endwall where they produce particularly strong effects. (3) The "relative eddy," an inviscid mechanism produced by the vorticity due to the rotating frame of reference, can create significant secondary flow effects on rotor pressure surfaces (see Dring and Joslyn, 1983). This phenomenon can only be produced in a rotating model. (4) Accurate simulation of tip-leakage-vortex effects requires rotation. Although some tip-leakage effects (e.g., heat transfer to the tip itself) can be very accurately modeled without rotation effects, the tip-leakage-induced enhancement of the suction surface heat transfer can only be properly simulated in a rotating passage.

Contributed by the International Gas Turbine Institute and presented at the 37th International Gas Turbine and Aeroengine Congress and Exposition, Cologne, Germany, June 1–4, 1992. Manuscript received by the International Gas Turbine Institute February 17, 1992. Paper No. 92-GT-195. Associate Technical Editor: L. S. Langston.

The primary objective of this program was to document the effects of flow three dimensionality on the heat transfer in a rotating blade row (versus a stationary cascade). Of particular interest were the effects of the hub and tip secondary flows, tip leakage, and the leading-edge horseshoe vortex system. The effect of surface roughness on the passage heat transfer was also investigated.

Modeling of turbine passage aerodynamics has progressed to the stage where prediction of the inviscid flow effects in multiple blade rows is well in hand. For example, both Ni and Bogoian (1989) and Denton (1992) have demonstrated the capability to predict accurately both airfoil pressure distributions and the effects of the relative stator/rotor motion. Development of prediction techniques that include the effects of viscosity, however, is less complete. As demonstrated recently by Dorney and Davis (1991), three-dimensional Navier–Stokes procedures can, at very high computational cost, accurately predict the flow through a single airfoil row. Restrictions in grid resolution and inadequacies in turbulence modeling, however, currently inhibit the prediction of local flow phenomenon (e.g., the endwall skin friction) for multiple blade row applications.

Accurate analytical models for turbulent heat transfer in the extremely hostile environment of the gas turbine airfoil, e.g., high levels of free-stream unsteadiness (both periodic and random), local separations, and strong surface curvature still need to be developed for two-dimensional flows. It is certain that even more turbulence-model-development problems will be encountered in the computation of the three-dimensional flows of the full-span turbine airfoil and endwall. A secondary objective of the present study was to provide a benchmark-quality data base for the assessment of such computational procedures.

A comprehensive discussion of this experiment is given by Blair (1991). This report contains detailed descriptions of the experimental apparatus, instrumentation, and techniques employed. In addition Blair (1991) presents both the turbine airfoil coordinates and the rotor-passage heat transfer data in tabulated form.

The results of this study have demonstrated that three-dimensional flows within the rotor passage produced local regions with significantly enhanced heat transfer rates (as much as 100 percent over midspan values). Increased surface roughness also significantly increased heat transfer rates for all locations on both the airfoil and endwall (as much as 100 percent relative to the smooth-wall data). Midspan heat transfer predictions of the STAN-5 boundary layer code with the van Driest (1956) "modified-mixing length" turbulence model produced excellent agreement with data over a factor-of-ten range in surface roughness.

Experimental Equipment

Turbine Model. All experimental work for this program was conducted in the United Technologies Research Center Large Scale Rotating Rig (LSRR), a facility designed for conducting high spatial-resolution investigations of flow within turbine and compressor blading. For the present program the turbine test section was arranged in the 1 1/2 stage (stator1/rotor/stator2) configuration. The turbine model has 22 first-stage stator airfoils. 28 first-stage rotor airfoils, and 28 second-stage stator airfoils. The turbine model simulates a relatively heavily loaded machine with a hub/tip radius ratio of 0.8. All three airfoil rows have solidities and aspect ratios very near unity. When operating at design conditions the turbine (at midspan) has a flow coefficient (Cx/U) of 0.78, a rotor relative inlet flow angle (β_1) of 40 deg, a stage loading coefficient ($c_p \Delta T/U^2$) of 2.8, and 34 percent static pressure reaction ($\Delta Ps_{rotor}/\Delta Ps_{stage}$). The axial spacing between the first stator and the rotor was 50 percent of the average of the first-stage stator and rotor axial chords (Bx). The axial spacing between the rotor and the second stator was 63 percent Bx. The rotor tip clearance was 0.060 inches or 1 percent span, which is typical for current aircraft engine design.

Rotor-Passage Heat Transfer Model. The rotor airfoil and the hub endwall test models were constructed of low-conductivity rigid foam covered by an electrically heated, stainless steel foil skin. The test models were designed so that a nearly uniform heat flux could be applied over the entire surface of a single rotor passage (rotor hub endwall and the pressure and suction surfaces of a pair of adjacent rotor airfoils). The techniques employed to construct the rotor passage test models were developed and thoroughly assessed as part of previous programs (Blair, 1983; Dring et al., 1986). Care was taken to assure that the heater power buss bar arrangement produced extremely uniform current density within the heater foil. Corrections for changes in local resistivity due to foil temperature were incorporated into the data reduction equations. Evaluation tests, conducted with simple two-dimensional flows, demonstrated that these techniques could be used to measure convective coefficients within 2 percent of predicted values (Blair, 1983).

The use of rigid urethane foam for the models' substrate ensured that conduction errors (back-losses and transverse smearing) were minimized. Calculations indicate that even in a region with a lateral gradient of heat transfer coefficient of 40 percent per cm, local coefficients could be measured within an accuracy of 5 percent (Graziani et al., 1980; Blair, 1983, 1985).

The hub-endwall heat transfer distributions were obtained using a foam/heated-foil model mounted in a relief cut into the rotor hub. The heated endwall surface extended axially from 3.8 cm. (0.24 Bx) upstream of the rotor leading edge to 3.3 cm. (0.21 Bx) downstream of the rotor trailing edge (total axial heated length of 23.2 cm). Circumferentially, the heated surface covered the entire endwall between the instrumented airfoils and extended to approximately midway across the endwalls of the two adjacent passages (total circumferential extent of approximately 2 rotor airfoil pitches).

With this arrangement the endwall heating foil passed beneath the bases of the two instrumented heat transfer airfoils. Since there would be no gap at the bases of the airfoils, and hence no airflow across the bases, there would be no exterior convective mechanism to remove the locally generated heat. To alleviate this problem cooled copper plates, shaped to conform to the airfoil profile at the hub, were incorporated into

Nomenclature

Bx = airfoil axial chord distance
C_f = skin friction coefficient
c_p = specific heat at constant pressure
Cx = axial flow speed
Pr = molecular Prandtl number
Ps = static pressure
Re = Reynolds number based on axial chord and exit flow conditions
Re_x = Reynolds number based on distance along surface and local velocity
Re_θ = Reynolds number based on momentum thickness
S = surface arc length
St = Stanton number
U = rotor velocity at midspan
U_τ = friction velocity
β_1 = relative flow angle from tangential at first stator exit
ν = kinematic viscosity

the endwall model. These cooled plates removed the heat generated by the endwall heating foil beneath the base of the heat transfer airfoils.

The heater foils for the airfoil models covered the airfoils entirely, from root to tip. Because the rotor airfoil geometry is three dimensional (airfoil contour is a function of radius), the heater foils were slightly nonrectangular in shape. These shapes resulted, in turn, in the production of nonuniform current density over the surfaces. Corrections for this nonuniformity of the current density were determined using a commercially available finite-difference, two-dimensional Laplace equation solver (ANSYS-PC/THERMAL4.3, Anon., 1988). Although the software was configured as a thermal conduction solution, the results could be applied to the present problem because the Laplace equation governs the potential flow of both heat and electrical current. The analysis was performed by imposing a voltage (temperature) potential difference between the buss bar attachment sites and solving for the current (heat) flux distribution over the foil surface. Current density, over the central 20 percent of the span, was determined to be within ± 3 percent of the mean. The largest deviations from the mean (± 10 percent) were found at 0 and 100 percent span near the airfoil leading edge.

Similar current density calculations were performed for the endwall foils. Here, local current nonuniformities were produced by instrumentation access holes cut through the foils. These holes were located beneath the airfoil root, away from the actual hub test surface, so their impact in the actual heat transfer measurement region was small (± 3 percent).

The results of these current distribution calculations were incorporated into the data reduction equations in the form of local current-density corrections. In this manner the local heat transfer coefficient computed for any site on the rotor passage surface was determined from the local surface heat flux and the associated locally measured surface temperature.

Measurement of Model Temperature Distributions. Local heat transfer coefficients were determined using thermocouples to measure the temperature difference between the heated wall and the free stream. Thermocouples on the rotor surface were located at the intersections of locii of constant percent span and constant percent surface distance (measured from the airfoil leading edge). The endwall thermocouples were arranged along loci running gapwise at fixed percent *Bx*. Arrays of 89, 124, and 101 thermocouples were installed on the pressure, suction, and endwall surfaces, respectively (a total of 314). Thermocouples instrumentation diagrams and descriptions of the thermocouple recording system and the methods used to correct for slipring induced signal errors can be found in Blair et al. (1991) and Blair (1991). It is estimated that surface temperatures on the rotating model were measured within $\pm 1/2$°C.

Liquid-crystal techniques were used in conjunction with the thermocouple data in order to obtain information with greater spatial resolution in regions of strong variations of the passage heat transfer distributions. Mixtures of encapsulated, chiral-nematic paints with different color-change temperatures were utilized in order to produce multiple color bands for a single model power setting. A complete description of the techniques employed to acquire these liquid-crystal measurements can be found in Blair et al. (1991).

Rotor Passage Surface Roughness. One objective of the present study was to determine the effects of surface roughness on the rotor-passage heat transfer. Data were obtained for identical flow conditions with surface conditions ranging from aerodynamically smooth to an extremely rough condition simulating current Space Shuttle Main Engine (SSME) turbopump hardware. All surface roughness data for this study were obtained using a Dektak Model 3030 profilometer with a 12.5 μm radius diamond stylus. This instrument provided measurements of both the rms and max-to-min heights of the roughness distributions for each test surface.

Table 1

Rotor-Model Surface Condition	RMS Roughness Height (Microns)	Max-to-Min Roughness Height (Microns)	Max-to-Min Chord %
Smooth (Liquid-Crystal)	0.33	7.6	0.0047
Near-Smooth (Flat-Black)	6.4	51	0.032
Rough (Grit)	Not Measured	660	0.41

The profilometer measurements for the liquid-crystal coating indicated rms and max-to-min roughness heights of 0.33 and 7.6 μm, respectively. For the range of Reynolds numbers involved in these present tests, this surface can be considered to have been aerodynamically smooth and will be referred to from here forward as "smooth."

Midspan rotor heat transfer data were obtained for this same turbine airfoil in a previous study (Blair et al., 1989). Profilometer measurements for the flat-black surface coating used for the airfoil model of this previous study indicated rms and max-to-min roughness heights of 6.4 and 51 μm, respectively. The flat-black coating, therefore, was approximately 10 times more rough than the liquid-crystal coating and will be referred to from here forward as "near-smooth."

Profilometer measurements for a sample SSME turbine rotor airfoil (provided by NASA-Marshall Space Flight Center) indicated rms and max-to-min roughness heights of 15.5 and 84 μm, respectively. Simulation of this extremely rough surface condition for the present large-scale tests was achieved by scaling the max-to-min roughness of the SSME airfoil by the ratio of the respective axial chords ($6.4/0.8 \times 84 = 660$). A screened grit of 660 micron-sized particles was applied uniformly over the entire rotor model test surface for these rough-wall tests. The "rough" surface, then, was approximately 10 times rougher than the flatback (near-smooth surface) and approximately 100 times rougher than the liquid-crystal coating (smooth surface). Grit distribution density (particles per unit area) on the model test surface was determined using close-up photographs of the completed roughened model. Photographs of nine sample regions of the model were enlarged so that the individual particles within prescribed unit cm^2 areas could be counted. The mean particle count over the nine sample areas was $95.8/cm^2$ with a standard deviation of $10.3/cm^2$.

The surface roughness heights for the various test models are listed in Table 1.

Flowpath Aerodynamic Documentation. The aerodynamic characteristics of the LSRR 1 1/2 stage turbine model have been thoroughly documented in previous investigations. All of these aerodynamic data are available either in the form of UTRC reports, Government Contract reports, or as open literature publications (see Blair, 1991, or Joslyn and Dring, 1992).

The highly three-dimensional nature of the flow through the rotor is demonstrated by the flow visualization results of Fig. 1. The suction surface results clearly show the flow convergence produced by the hub and tip secondary vortices (endwall cross-passage flow moving onto the suction surface). The suction surface view also shows how the path taken by the tip leakage flow varied along the chord. The dominant feature on the rotor pressure surface was the radial flow toward the tip due to the relative eddy. Its effect was strongest on the forward portion of the pressure surface because the surface flow speed

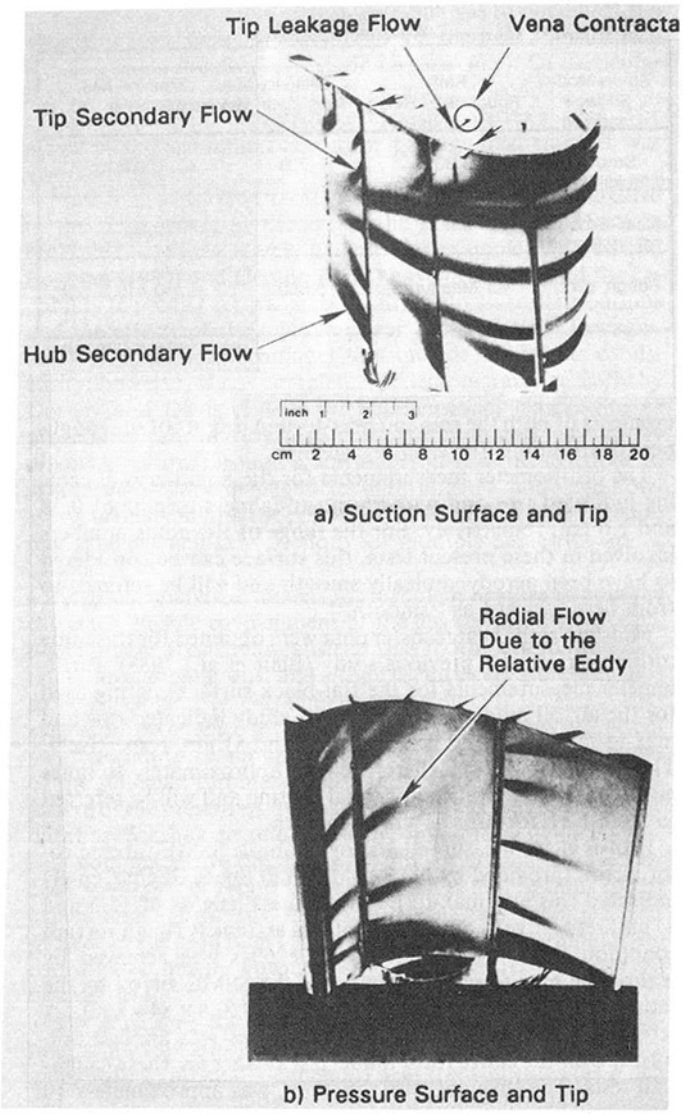

Fig. 1 Rotor surface flow visualization, showing hub and tip secondary flow, tip leakage, and effect of relative eddy

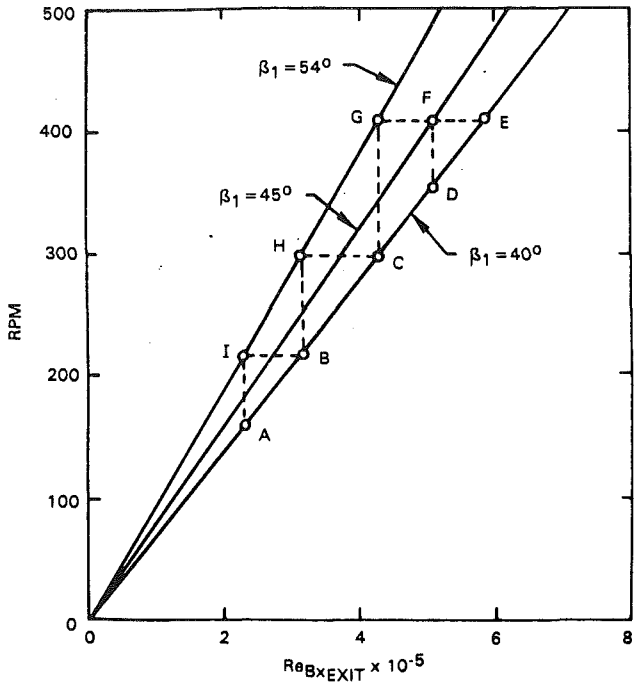

Fig. 2 Matrix of test data obtained for the present program

was lowest there. The surface streamlines turned away from the radial direction as the flow accelerated toward the trailing edge.

Test Matrix. Rotor passage heat transfer data were obtained over a range of Reynolds numbers and rotor inlet flow angles. The variations were produced by changing rotor rotational speed and turbine throughflow velocity. The airfoil exit Reynolds numbers were dependent only upon the throughflow velocity and not upon the rotational speed. A map of the operating conditions for which heat transfer data were obtained is presented in Fig. 2. Heat transfer data were obtained for all nine conditions with both the smooth-wall model and the rough-wall model for a total of eighteen (18) data sets. A similar set of data (midspan only) are available for the near-smooth model in Blair et al. (1989).

Experimental Results

The experimental results will be presented in two forms: First, the measured midspan Stanton number distributions are compared with predictions from various smooth-wall and rough-wall computational procedures. Next, contour maps showing the heat transfer distribution over the full-span airfoil and endwall surfaces are presented for various inlet flow angles and Reynolds numbers. These maps display highly localized heat transfer effects on the airfoil and endwall surfaces.

Midspan Heat Transfer Data for the Smooth-Wall Model. The midspan heat transfer distributions are presented as Stanton numbers based upon exit velocity and density. The Stanton numbers are plotted as a function of surface distance from the leading edge nondimensionalized by the axial chord.

Smooth-wall midspan heat transfer distributions measured at design inlet flow angle ($\beta_1 = 40$ deg) are presented in Fig. 3 for three Reynolds numbers ($Re = 5.80$, 4.40, and 2.30×10^5). Results for the intermediate test Reynolds numbers ($Re = 5.15$ and 3.20×10^5) were entirely consistent with the data presented but were excluded for the sake of brevity. Data obtained for the same flow conditions with the near-smooth wall (Blair et al., 1989) are also presented. Each of the data sets of Fig. 3 are shown compared to two-dimensional boundary layer predictions (Edwards et al., 1981; Carter et al., 1982) for that specific test condition. Predictions for laminar boundary layer flow on the suction surface are labeled *L*. Predictions for both suction and pressure surfaces for fully turbulent flow (labeled *T*) employed the algebraic turbulence model of Cebeci and Smith (1974).

An examination of the data and predictions for the suction surface reveals a continuous trend with increasing Reynolds number. At $Re = 2.30 \times 10^5$ the Stanton number distribution indicates that the heat transfer was laminar from the leading edge to approximately $S/Bx = 0.5$. Downstream of this location, the boundary layer passed through transition as indicated by the streamwise increase in the measured heat transfer. Boundary layer transition appears to near completion around $S/Bx = 1.2$ where the measured heat transfer and fully turbulent predictions agree. This same sequence can be observed for all three Reynolds numbers with the onset of transition moving upstream progressively with increasing Reynolds number. As the Reynolds number was increased the region of laminar flow in the forechord decreased. Simultaneously, in the aftchord region, the length of the fully turbulent zone is seen to increase progressively.

Comparisons between the smooth suction-surface data from

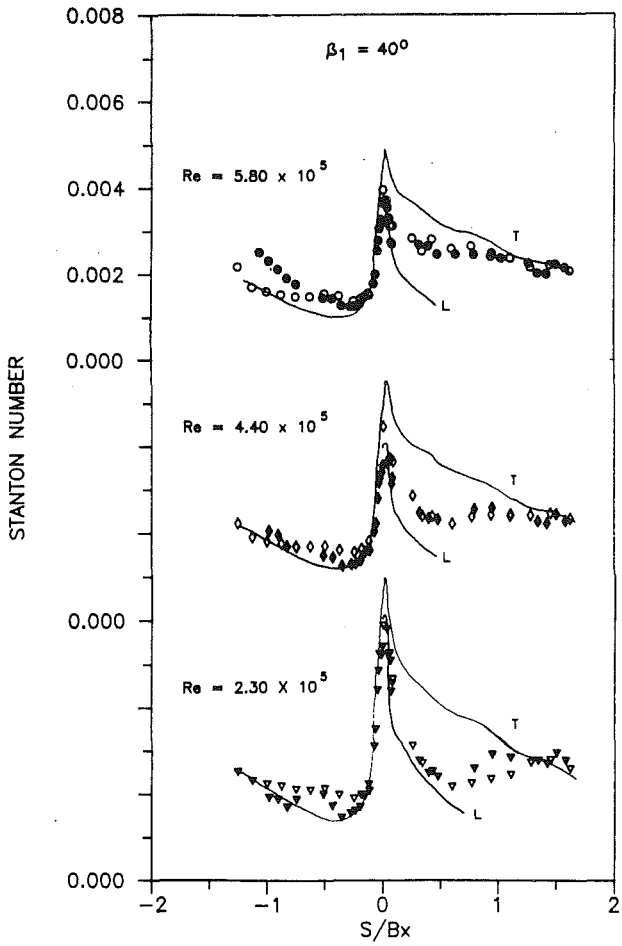

Fig. 3 Comparisons of midspan rotor airfoil heat transfer distributions obtained for various Reynolds numbers and $\beta_1 = 40$ deg, open symbols—smooth, solid symbols—near-smooth

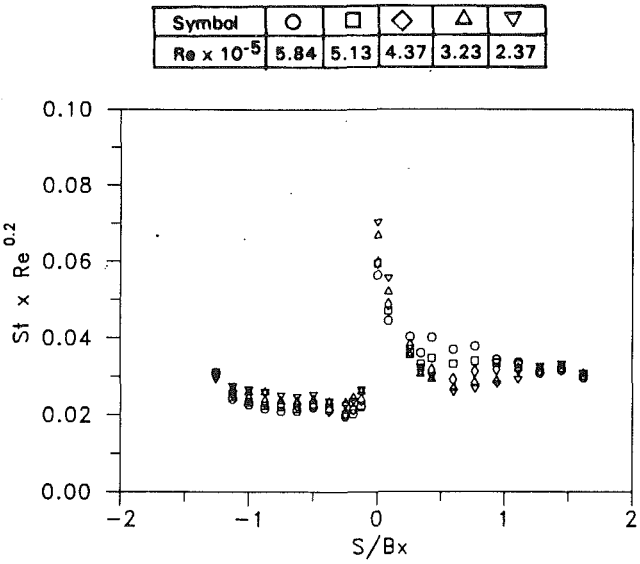

Fig. 4 Comparisons of midspan rotor airfoil heat transfer distributions obtained for various Reynolds numbers and $\beta_1 = 40$ deg for the smooth wall model

the present program and the near-smooth data of Blair et al. (1989) indicate close agreement. At the lowest Reynolds number, however, there is some evidence that transition of the suction surface boundary layer began somewhat later for the present study. At about $S/Bx = 0.5$ the heat transfer for the smooth-wall test increased toward the fully turbulent prediction at a reduced rate. This difference in transition location was probably caused by the difference in surface roughness between the smooth and near-smooth models. Recall that the max-to-min roughness for the smooth model was 7.6 μm while that of the near-smooth model was 51 μm.

An examination of the pressure surface results indicates that, for the two lower Reynolds numbers, there was quite good agreement between the two-dimensional predictions and both sets of experimental data. The largest difference between the two data sets resulted for the downstream half of the pressure surface at the highest Reynolds number. Here, the heat transfer rates for the smooth airfoil were as much as 25 percent less than those recorded for the near-smooth model. This difference is examined in a following section where, like the previously discussed suction surface transition shift, it is demonstrated to be a result of the difference in surface roughness of the smooth and near-smooth models.

There are two general conclusions that can be reached from the results shown in Fig. 3: first, that the data obtained at all three Reynolds numbers for both the smooth and near-smooth cases form an orderly, systematically behaved set; second, that the midspan, smooth wall data obtained in the present study are in good agreement with similar results measured for the earlier investigation of Blair et al. (1989).

The midspan (smooth) heat transfer distributions for all five design-incidence test Reynolds numbers are presented in Fig. 4 in the coordinates of surface distance versus the product $St \times Re^{0.2}$. This format demonstrates that the aftchord data on both the suction and pressure surfaces can be correlated within a narrow band when scaled by $Re^{0.2}$. This collapse indicates that the aftchord flows on both airfoil surfaces are behaving as classic equilibrium, fully turbulent, smooth-wall boundary layers. It is interesting that the stagnation-region heat transfer measurements also collapsed (not shown) when plotted as $St \times Re^{0.5}$ (Froessling scaling for a fixed Pr).

Midspan Heat Transfer Data for the Rough-Wall Model. Sample midspan Stanton number distributions for the rough-wall model are presented in Fig. 5 for two representative test Reynolds numbers. Data for the same test conditions are also shown for the smooth-wall and near-smooth-wall models. Also included in Fig. 5 are fully turbulent predictions from the two-dimensional, smooth-wall boundary layer computation procedure of Edwards et al. (1981) and Carter et al. (1982).

The most significant feature of Fig. 5 is the profound impact that the rough-wall condition had on the heat transfer rates relative to the smooth-wall and near-smooth-wall conditions. The effect of the surface roughness was to increase the heat transfer everywhere on the airfoil surface with the largest increase (approximately 100 percent) in the forechord region of the suction surface. Note that the farthest-downstream point on the (rough-wall) pressure surface registered a local decrease in Stanton number for both Reynolds numbers. This effect may be the result of one of the roughness grains being located directly over a thermocouple site and should probably be disregarded.

Midspan rough-wall heat transfer data for design inlet flow angle are presented in Fig. 6 for all five test Reynolds numbers. The rough-wall midspan Stanton number distributions were nearly identical for all Reynolds numbers (unlike the smooth-wall data of Fig. 4 where $Re^{0.2}$ scaling was required to collapse the various data sets). This result indicates that these rough-wall data are representative of "fully rough" conditions, i.e., surface roughness so extreme that the Stanton number (and skin friction coefficient) become independent of Reynolds number.

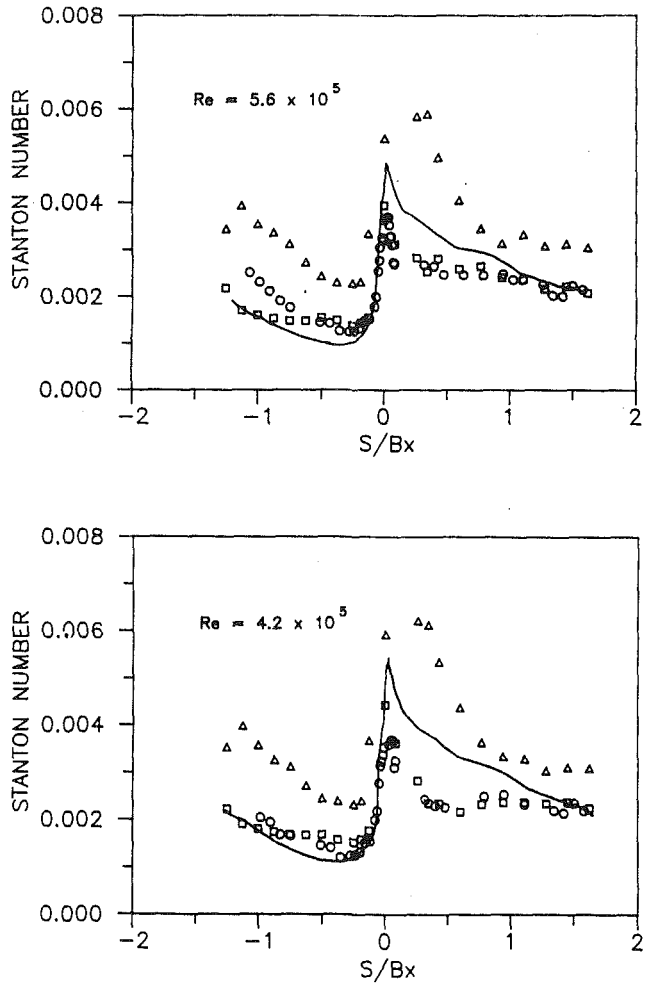

Fig. 5 Comparison of midspan rotor airfoil heat transfer distributions obtained for two Reynolds numbers at $\beta_1 = 40$ deg; □: smooth, ○: near-smooth, △: rough

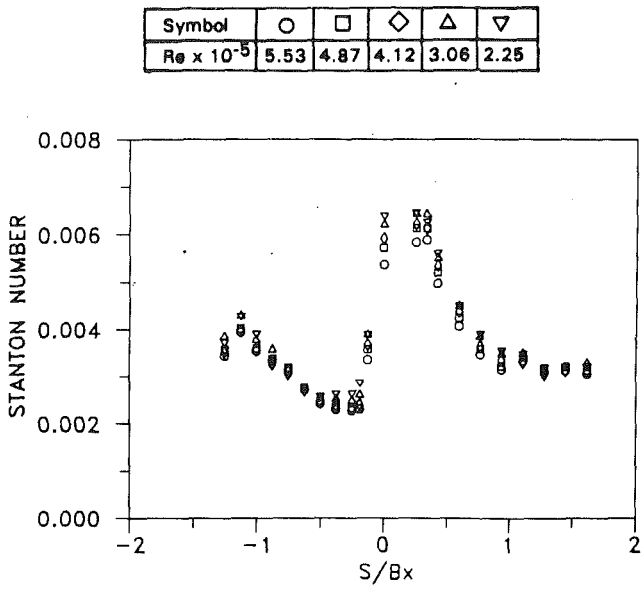

Fig. 6 Comparisons of midspan rotor airfoil heat transfer distributions obtained for various Reynolds numbers and $\beta_1 = 40$ deg for the rough wall model

Comparisons of Rough-Wall Data With Correlations. The parameter most commonly used to characterize the regimes of turbulent boundary layer flow over rough surfaces is the roughness Reynolds number $k^+ = kU_\tau/\nu$. Here U_τ is the friction velocity and k is some characteristic height of the roughness elements. Turbulent boundary layer flow can be grouped into three categories:

(1) hydraulically smooth $0 < k^+ < 5$

(2) transitionally rough $5 < k^+ < 55$–70

(3) fully rough $k^+ > 70$

A carefully constructed model for analysis and calculation of rough surface turbulent boundary layers is given by Han (1985). This analysis is based upon a modification of a mixing-length turbulence model in which the mixing length is multiplied by an appropriate amplification factor. Han conclusively demonstrated that his mathematical formulation satisfactorily reproduced numerous experimentally measured rough-wall turbulent boundary layer velocity profiles. Han also produced an empirical model to link the type and height of roughness with the amplification factor required for the mixing-length model. Results from Han's predictive model were presented in the form of charts of skin friction coefficient plotted as a function of Re_x and a "laboratory" roughness parameter $\mathrm{Re}_k = Uk/\nu$.

For the present program, Han's zero-pressure-gradient results were employed to estimate the skin friction distribution along the rotor midspan. The roughness parameter was computed from the local velocity and the grit size (660 μm) while Re_x was computed from the local velocity and the surface distance along the airfoil measured from the stagnation line. The skin friction coefficient distributions, in turn, were used to determine the k^+ distributions along the rotor midspan. These calculations indicated that for $\mathrm{Re}_{Bx} = 5.8 \times 10^5$ the entire suction surface and the downstream half of the pressure surface were in the fully rough regime. The upstream half of the pressure surface fell into the transitionally rough regime.

The impact of surface roughness on turbulent boundary layer heat transfer has been examined in numerous earlier investigations. These studies were mostly limited to zero-pressure-gradient flows but included examinations of a wide variety of types and size of surface roughness. All of these studies have proposed correlative equations to predict the heat transfer given the local Reynolds number, Prandtl number, some roughness parameter, and the skin friction coefficient. Comparisons will be presented here between four of these correlation-based predictions and the present rough-wall midspan data. The correlations were selected to represent results for an extremely wide range of turbulent convective circumstances including incompressible flow over flat plates, flow inside tubes, and supersonic exterior flows. The skin friction distribution computed by the method of Han was used as a common input to all the rough-surface heat transfer correlations to be described below.

The following heat transfer correlations for prediction of roughwall heat transfer were examined:

1 Dippery and Sabersky (1963)—based on flow through rough tubes

$$\mathrm{St} = \frac{C_f/2}{1 + [g(k^+) - 8.48]C_f/2}$$

where $g(k^+)$ is a function of the molecular Prandtl number and the roughness Reynolds number.

2 Kadar and Yaglom (1972)—based on flat-plate data

$$\mathrm{St} = \frac{\sqrt{C_f}\,\mathrm{Pr}^{-1}}{4.3\ \mathrm{In}\ (\mathrm{Re}_x C_f) + 3.8}$$

3 Seidman (1978)—based on the supersonic exterior flows

$$\mathrm{St} = C_f/2[1 + 0.52(C_f/2)^{0.725}(\mathrm{Re}_k)^{0.45}\mathrm{Pr}^{0.8}]^{-1} + 0.0002$$

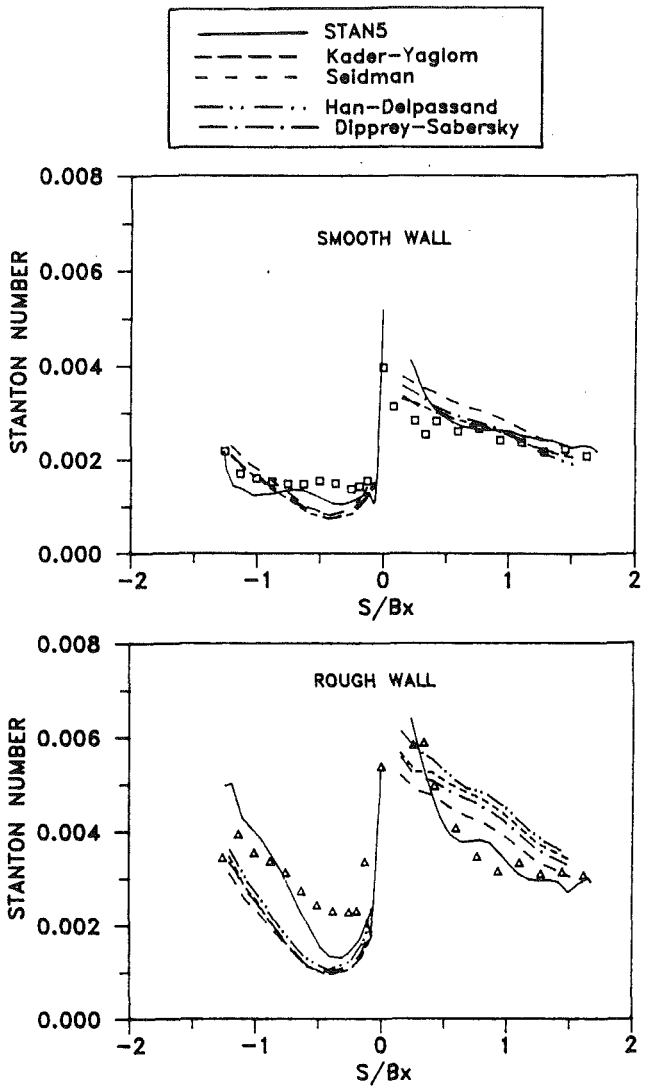

Fig. 7 Comparisons of midspan rotor airfoil heat transfer distributions obtained at $Re = 5.8 \times 10^5$ and $\beta_1 = 40$ deg with various analytical predictions

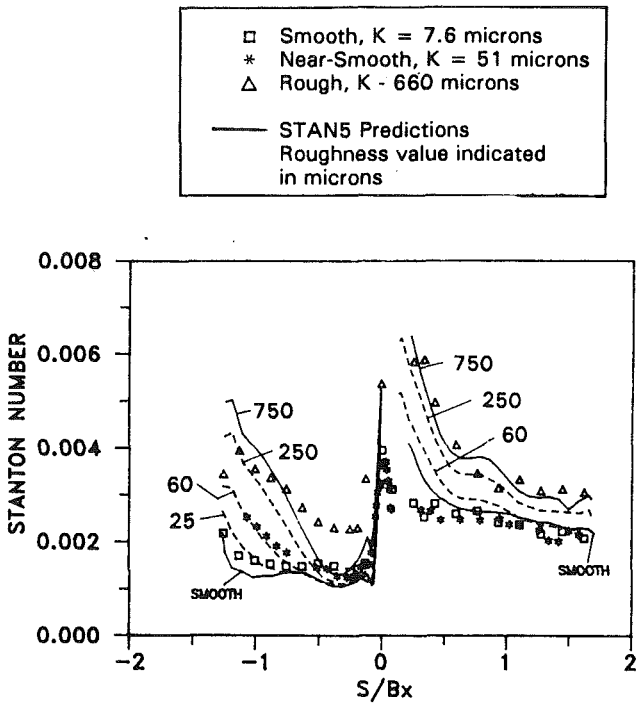

Fig. 8 Comparisons of midspan rotor airfoil heat transfer distributions obtained at $Re = 5.8 \times 10^5$ and $\beta_1 = 40$ deg with STAN-5 predictions for various wall roughness values

4 Han and Delpassand (1990)—an analytical model with empirically determined coefficients

St is determined from plotted computational results $St = St(Re_x, Re_k)$

The above four analyses were used to compute the heat transfer distributions for the rotor airfoil at midspan. The results of these computations are compared with the experimental data in Fig. 7 for both the smooth-wall ($k = 7.6$) and rough-wall ($k = 660$ μm) conditions for $Re = 5.8 \times 10^5$. An examination of Fig. 7 reveals that for the smooth-wall condition all four predicted distributions are in fairly good agreement with the measurements for both the suction and pressure surfaces. The degree of agreement is remarkable given the wide range of flows that produced these correlative equations. For the rough-wall condition, however, all of the methods overpredict the suction surface rates and seriously underpredict the pressure surface rates.

Comparisons of Rough-Wall Data With STAN-5 Predictions. Theoretical predictions (Sharma and Butler, 1991) were also conducted using the STAN-5 (Crawford and Kays, 1976) boundary layer code, modified to account for surface roughness through the van Driest (1956) model. According to this model, surface roughness erodes the effect of viscous damping near the wall causing an increase in mixing length in the inner part of the boundary layer. The modified damping function due to surface roughness is given as:

$$D = D_s + D_r$$

D = damping term for modifying mixing lengths
D_s = damping term for smooth surfaces
D_s = damping term for rough surfaces

$$D_r = -60y^+/k^+A^+$$

A^+ = const

Midspan rotor airfoil Stanton number distributions predicted with the Pratt and Whitney version of STAN-5 are given in Fig.7. Predictions are presented for both a smooth wall and for a wall roughness equal to the size of the grit on the rough-wall model. The STAN-5 predictions are significantly superior to any of the correlation based predictions, both for the smooth-wall and rough-wall cases. It is significant that the STAN-5 calculations predict both the absolute levels and the streamwise distributions of the measured heat transfer. The superiority of the finite-difference boundary layer flow solution, of course, lies in the fact that it reflects the impact of the flow history (velocity distribution) along the airfoil surface. The correlation-based equations, on the other hand, were based upon zero-pressure-gradient data and only represent a prediction of a local Stanton number at some point on a constant-velocity surface.

It should be pointed out that the STAN-5 predictions for the smooth-wall case are in very good agreement with the predictions from the Edwards et al. two-dimensional code for this same Reynolds number (see Fig. 3).

Results from a more detailed examination of predictions from the Pratt and Whitney version of STAN-5 are presented in Fig. 8. All of the predictions and data presented in Fig. 8 are for design inlet flow angle and $Re = 5.8 \times 10^5$. Measured heat transfer results are given for the smooth-wall, the near-smooth-wall, and the rough-wall cases. Predictions from the

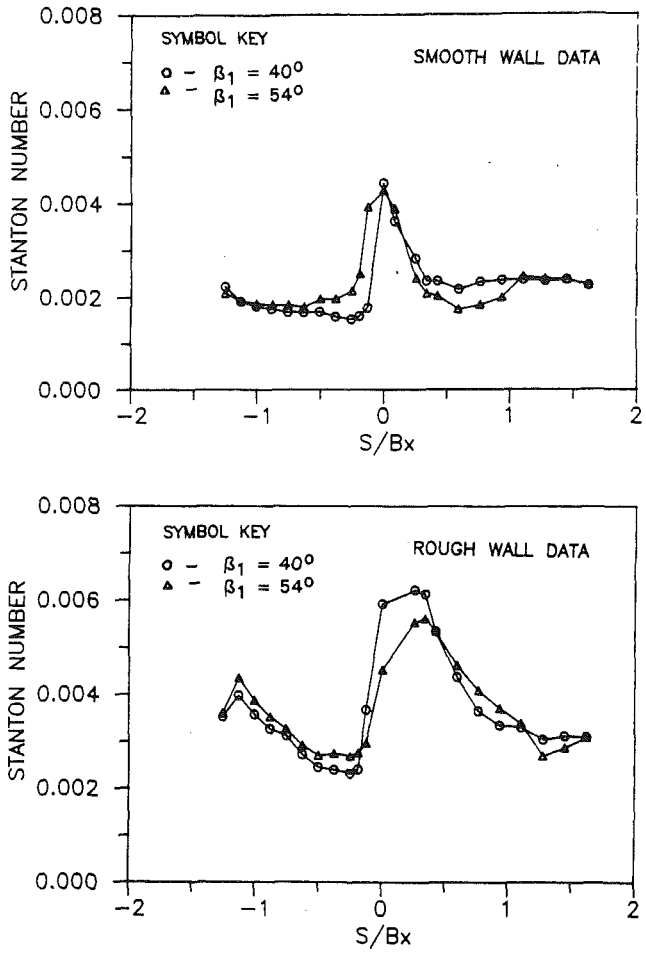

Fig. 9 Comparisons of midspan rotor airfoil heat transfer distributions obtained for two flow coefficients at Re = 4.2 x 10^5

STAN-5 code are given for surface roughness values ranging from 0 to 750 μm. As discussed for Fig. 7, the smooth-wall predictions are seen to agree very well with the smooth-wall data. Agreement is excellent for the entire pressure surface and for the post-transitional portion of the suction surface. The predictions for $k = 60$ μm and the near-smooth-wall data (measured max-to-min roughness = 51 μm) are also in excellent agreement. Finally, predictions for $k = 750$ μm and the rough-wall data (grit size = 660 μm) are excellent for the entire suction surface and reasonably good for the pressure surface. The conclusion reached from the results of Fig. 8 is that the van Driest roughness model produced quite accurate rough-surface heat transfer distribution predictions for a very wide range of surface roughness heights. It is important to note that successful predictions for the various surface conditions were produced using the max-to-min roughness values as input (k) to the van Driest model. This result suggests that the extremes of the roughness distribution may be much more important than the mean roughness height in determining the enhancement of heat transfer.

Effects of Inlet Flow Angle on the Midspan Heat Transfer Distributions. Figure 9 shows comparisons of the smooth-wall (upper figure) and rough-wall (lower figure) data obtained at the same Reynolds number Re = 4.2 x 10^5 but different inlet flow angles. The effects were well behaved for the smooth-wall cases. Increasing the inlet flow angle increased and decreased heat transfer in the forechord regions of the pressure and suction surfaces, respectively. Note that for the smooth-wall cases the trailing-edge-region heat transfer for the two inlet flow angles were equal for both the suction and pressure surfaces. This is the expected result because the passage exit velocity (Reynolds number) was nominally the same for these two cases.

Results for the rough wall cases were less clear. Inlet flow angle had little effect on either the pressure or suction surface heat transfer. This was probably because any leading-edge overspeed/separation-bubble effects associated with off-design operation were overwhelmed by the extreme surface roughness.

Heat Transfer Contour Maps. As previously discussed, rotor-passage heat transfer distribution data were obtained over the complete airfoil and endwall surfaces using arrays of thermocouples supplemented with liquid-crystal thermography techniques. Photographs of rotor-passage liquid-crystal temperature patterns were recorded for the smooth-wall model at all nine test conditions. Samples of these liquid-crystal patterns are reproduced in color in Blair (1991). These sample photographs revealed numerous local heat transfer effects and proved to be invaluable for interpretation of the rotor-passage distributions.

Contour maps of the rotor passage Stanton number distributions are presented for representative sample combinations of Reynolds number, inlet flow angle, and surface roughness. The contour maps were created from the thermocouple array data using a commercial topographical plotting routine (SURFER—Golden Software, Inc.). Liquid-crystal results (smooth wall only) were used to supplement the thermocouple data in regions where extremely localized effects were beyond the resolution of the thermocouple array, e.g., the leading-edge separation bubbles fell between the rows of thermocouples.

The airfoil contour maps are presented in rectilinear coordinates nondimensionalized by the airfoil span. The horizontal axis (percent span) corresponds to the radial distance from the hub divided by the total rotor span of 15.24 cm. The vertical axis is somewhat more complex because of the three dimensionality of the airfoil. The airfoil surface, when unwrapped and flattened on a plane, was not rectangular because the total surface-arc-length on both the suction and pressure surfaces was a function of span. Rectangular projections were achieved by plotting off-midspan data at surface distances proportionally scaled by the ratio of midspan/local arc length (%S^*).

$$\%S^* = \frac{S}{S_{\text{tot(r)}}} \frac{S_{\text{tot(midspan)}}}{\text{SPAN}}$$

Contour maps for all test conditions examined in this program are presented by Blair (1991). Also Blair (1991) gives expanded, separate views of the suction, pressure, and endwall surfaces with finer increments of Stanton number than could be clearly presented here.

Sample contour maps of the rotor passage heat transfer distributions (smooth-wall model) are presented in Fig. 10 for two Reynolds numbers and two inlet flow angles. Each data set is presented as a combined view of both the endwall and airfoil heat transfer distributions. The inlet flow angle (β_1) and the test Reynolds number (Re) are given for each of the contour maps. The solid contours were constructed from the thermocouple data while the dash-dot contours were inferred from the liquid-crystal photographs. The scales of the airfoil surface and hub endwall plots are identical for Fig. 10. That is, spanwise, surface-arc-length, and the chordwise and gapwise dimensions are all consistent.

The various data sets (see Fig. 2 for test condition designation system) of Fig. 10 are presented in the following order: upper-left (a)—set A; upper-right (b)—set I; lower-left (c)—set C; and lower-right (d)—set G. These particular sets were selected for discussion because the A–I and the C–G sets have approximately equal Reynolds numbers while the A–C and the I–G sets have equal rotor inlet flow angles.

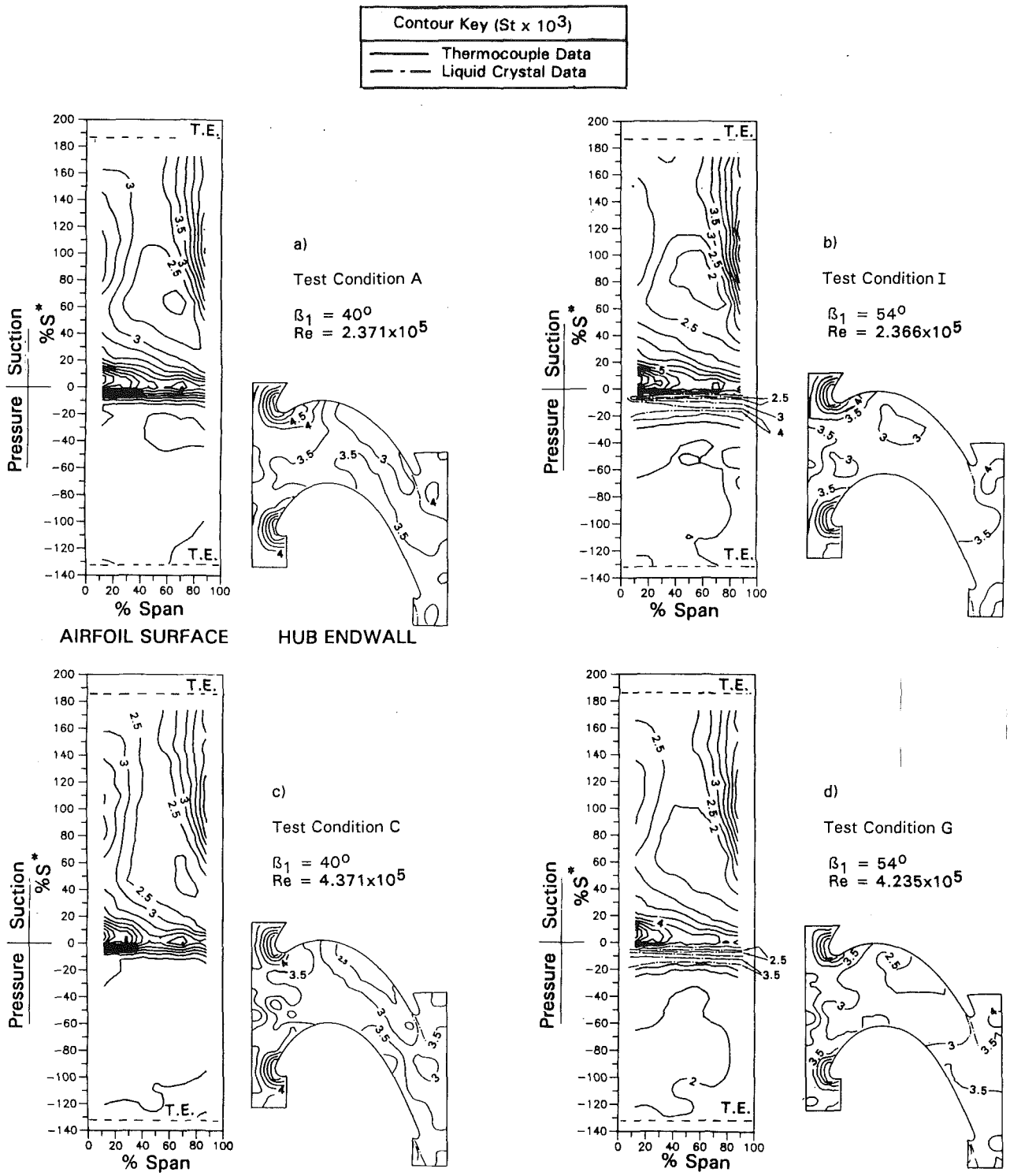

Fig. 10 Samples of Stanton number contours on airfoil and hub endwall surfaces for smooth wall model

General Discussion of Sample Data Set. The data set presented in Fig. 10(*a*) was obtained for $\beta_1 = 40$ deg and $\mathrm{Re} = 2.37 \times 10^5$. The airfoil surface contours indicate that three-dimensional flow effects had a much stronger influence on the suction surface than on the pressure surface. The endwall boundary layers, having been swept across the endwall toward the suction surface by the cross-passage static pressure gradient, roll up into a pair of vortices located near the suction-surface-tip/endwall and the suction-surface-hub/endwall corners. This pair of passage secondary flows has the effect of producing a streamwise-converging flow pattern in the suction-surface boundary layer. Flow visualization data of Langston et al. (1977) and Joslyn and Dring (1989) showed that this converging pattern corresponded to a pair of suction-surface separation lines. These separation lines divided the streamwise flow in the midspan region from the hub and tip regions, which are dominated by the secondary passage flows. The effect on the suction-surface heat transfer is to produce a pattern of enhanced local Stanton number, the shape of which corresponds directly with the shape of the lines of separation deduced from the flow visualization results presented in Fig. 1.

The absolute level of the Stanton number contours within

the zones dominated by secondary flow was higher than observed at any streamwise station at midspan (downstream of the immediate vicinity of the leading edge). Near the hub the maximum heat transfer was 60 percent greater than the midspan value. The highest heat transfer rates on the suction surface, more than 100 percent greater than the midspan value, were recorded near the tip for 70 percent $< S^* <$ 130 percent. This highly localized enhancement was produced by the tip-leakage flow, which rolls up into a tip-leakage vortex in that region.

Another region of locally enhanced heat transfer on the suction surface can be observed in the leading edge region (0 percent $< S^* <$ 20 percent) near the hub (from 0 to 40 percent span). A very similar heat transfer pattern was observed by Graziani et al. (1980) where full-span heat transfer data were acquired in a two-dimensional cascade having the midspan rotor airfoil geometry. No similar region of enhancement was evident near the tip at this location for the present rotating model tests. The fact that similar patterns were observed for the cascade tests and near the hub (but not the tip) of the rotating tests indicates that the phenomenon is related to leading-edge/endwall interaction effects (the horseshoe vortex system). The aerodynamic effects produced at the hub/leading-edge junction were similar to those produced in the stationary cascade at the endwall/leading-edge junction since, in both cases, there was no relative motion or gap between the airfoil and the endwall. At the tip leading edge, however, the tip leakage and the tip/casing relative motion must certainly produce an entirely different local secondary flow pattern. Unfortunately, at this time interpretation of the near-tip heat transfer patterns is limited by a lack of existing data for secondary flows generated near moving-tip/casing junctures. The results of the present program, however, do indicate that enhancement of the airfoil heat transfer by leading-edge/endwall interaction effects is limited to the hub region. This enhancement increased heat transfer by as much as 50 percent above midspan values.

The heat transfer variation over the pressure surface was much less than for the suction surface. Those readers specifically interested in details of the small variations in pressure-surface heat transfer should consult the liquid-crystal pictures and the fine-contour-interval plots of Blair (1991). Note that in the trailing-edge region the heat transfer rates were slightly higher (approximately 10 percent) near the tip than for the remainder of the span. This was probably a result of the tip-leakage flow. Because of the flow across the airfoil tip from the pressure surface to the suction surface, the pressure-surface boundary layer near the tip is thinned relative to the rest of the span. Somewhat higher heat transfer rates result for this near-tip region of reduced Re_θ boundary layers.

The hub endwall contour map of Fig. 10(*a*) clearly shows regions of intense heat transfer near the rotor-leading-edge/endwall junction. This effect, a product of the leading-edge horseshoe vortex system, was also visible in the liquid-crystal photographs of Blair (1991). The leading-edge horseshoe vortex system, then, enhanced the heat transfer both on the endwall and, as discussed above, on the airfoil surface near the hub. The heat transfer beneath these leading-edge vortices was the maximum observed anywhere on the endwall. Notice that the region of enhanced heat transfer near the leading edge is not symmetric about the stagnation line but extends considerably farther toward the suction surface. This result is almost certainly related to the previously discussed near-hub region of enhancement on the airfoil suction surface for 0 percent $< S^* <$ 20 percent. The lowest heat transfer on the endwall occurred near the pressure-surface corner.

Effects of Increasing Re for Design Inlet Flow Angle. The effects of increasing the Reynolds number for fixed design inlet flow angle can be seen by comparing Figs. 10(*a*) and 10(*c*). Recall that the midspan Stanton number distributions for the test cases with $\beta_1 = 40$ deg (Fig. 3) indicated that the suction-surface boundary layers started out laminar, passed through transition, and ended as fully turbulent near the trailing edge. These same midspan distributions indicated that the transition process moved upstream progressively with increasing Reynolds number. The suction-surface contour maps of Figs. 10(*a*) and 10(*c*) clearly show this boundary layer transition process with a region of minimum heat transfer centered at approximately $S^* = 50$ and 70 percent span. An examination of these regions of minimum Stanton number reveals that the transition process was highly three dimensional with transition beginning farther upstream for spanwise locations $<$ 50 percent span and farther downstream for locations $>$ 50 percent span.

In addition, an examination of the Stanton number contours in the near-midspan region of the suction surface from 140 percent $< S^* <$ 170 percent reveals a drop in the Stanton number with increasing Re. This trend reflects the fact that the boundary layers in this part of the airfoil are fully turbulent. As was demonstrated in Fig. 4, the aftchord/midspan heat transfer can be accurately described by $St \propto Re^{-0.2}$, the well-known equilibrium turbulent boundary layer relationship.

Consistent trends with increasing Re can also be observed in the regions of enchanced heat transfer near the suction surface tip and root in the midchord region. As at midspan, these enhanced zones show a continuous and progressive decrease in St with increasing Re for the full range of test Re.

Effects directly attributable to changes of Re were smaller on the endwall than on the airfoil surfaces. Slight decreases in St with increasing Re can be observed across the entire gap in the trailing-edge region and in the midchord region near the pressure surface.

Effects of Increasing Re for $\beta_1 = 54$ deg. An examination of the contour maps of Figs. 10(*b*) and 10(*d*) reveals the same trends observed at $\beta_1 = 40$ deg (Figs. 10*a* and 10*c*) on the suction, pressure, and endwall surfaces. The transitional behavior on the forechord suction surface is clearly evident (note sizes of St = 0.002 contours) while for all locations where the flow was fully turbulent St decreased progressively with increasing Re.

Effects of Increasing Inlet Flow Angle for Fixed Re. Changes to β_1 were achieved experimentally by operating the facility at a fixed throughflow velocity and altering the rotor rotation speed. An increased β_1 for a fixed exit Re corresponds to a decreased relative inlet velocity and a fixed exit velocity (reduced velocity in the forechord with stronger acceleration to reach the same exit velocity). The effect of increasing β_1 from the nominal design value of 40 deg (14 deg negative incidence) is to shift the stagnation line away from the pressure surface and towards the suction surface. This shift strengthens the overspeed at the leading-edge/pressure surface juncture and produces a relatively stronger favorable pressure gradient at the leading edge/suction surface juncture.

Comparisons between Figs. 10(*a*) and 10(*b*) and between Figs. 10(*c*) and 10(*d*) reveals that increases in β_1 produced decreased heat transfer in the forechord region of the suction surface (0 percent $< S^* <$ 100 percent). For the suction surface plots at increased β_1, the laminar-flow region in which St $<$ 0.002 (centered around 60 percent span) expanded considerably compared to the respective design inlet flow angle data. In addition, the turbulent-flow regions of the forechord (near the blade root) also show reduced heat transfer for increased β_1. This general reduction in forechord heat transfer is primarily the result of the reduction in relative inlet velocity associated with increased β_1. Since the suction surface boundary layer is still laminar in the midspan/forechord region, the increase in β_1 also reduces the heat transfer through a pressure gradient effect. The increased favorable pressure gradients in the fore-

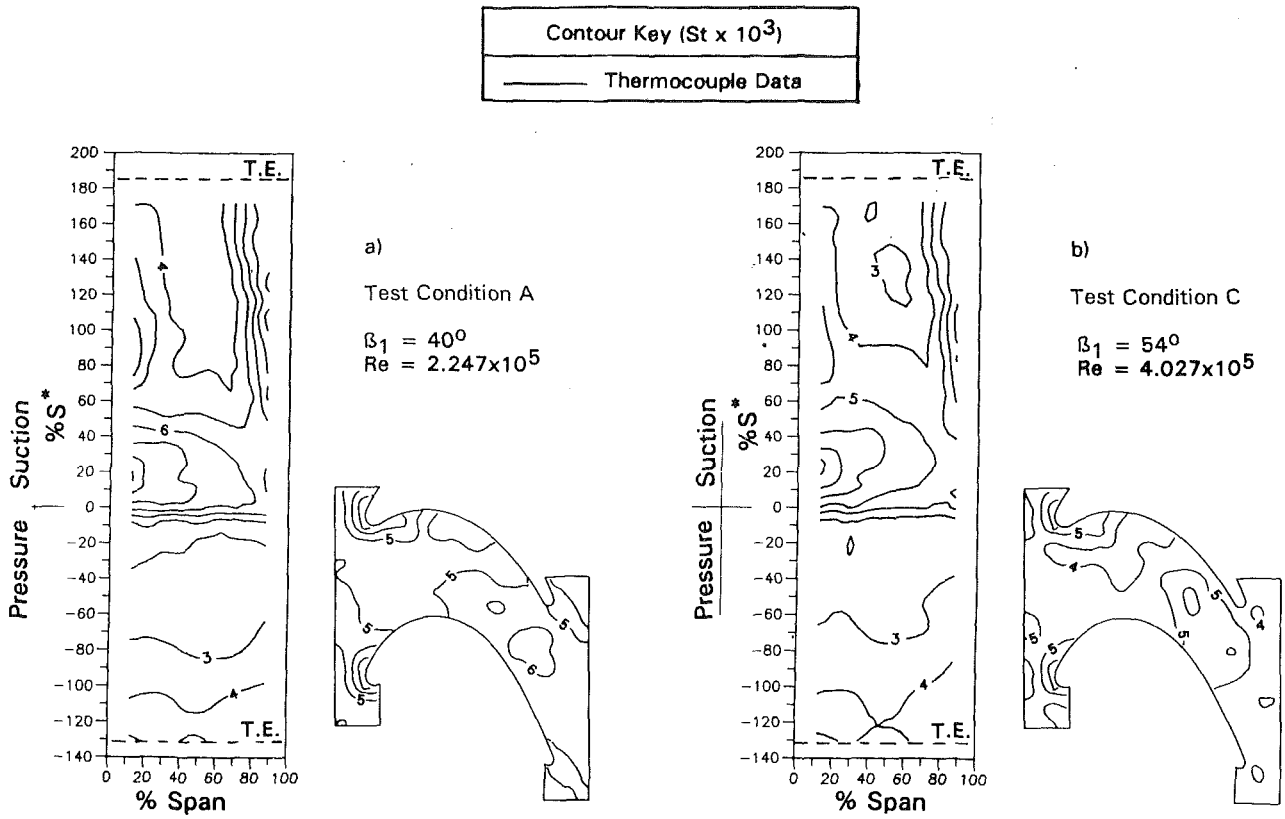

Fig. 11 Samples of Stanton number contours on airfoil and hub endwall surfaces for rough wall model

chord tend to inhibit boundary layer transition and permit the region of laminar flow to extend further onto the suction surface.

For both data sets obtained at increased inlet flow angle (Figs. 10*b* and 10*d*), a narrow band of reduced heat transfer (i.e., a minimum of St = 0.0025) can be seen at $S^* = -5$ percent. Downstream of this narrow band of low heat transfer, the Stanton number increased rapidly to a maximum (0.0035–0.0040) and then gradually decreased for $S^* > -20$ percent. This heat transfer pattern indicates that, for the cases with increased inlet flow angle, a short separation bubble resulted due to the pressure-surface leading-edge overspeed. The low heat transfer resulted directly beneath the bubble while the rapid rise to a much higher level was associated with reattachment (Stanton numbers approximately 60 percent greater than for that streamwise location with attached flow). The gradual decline of the Stanton number downstream of reattachment coincided with the streamwise growth of the pressure-surface boundary layer. A comparison of all four sets of increased-inlet-flow-angle data (Blair, 1991) reveals that the separation bubble was much weaker for the $\beta_1 = 45$ deg case (Fig. 2, Pt. *F*) than for the three cases at $\beta_1 = 54$ deg (Fig. 2, Pts. *G*, *H*, and *I*).

The most important effects of the change in inlet flow angle on the hub endwall heat transfer distribution were found in the forechord region. Comparisons between the sets of fixed exit Re data reveal that increased β_1 produced reductions in heat transfer both at midgap and beneath the horseshoe vortex patterns. As discussed above, these decreases in heat transfer almost certainly resulted from the decrease in relative inlet velocity.

Effects of increased inlet flow angle were very small for the mid and aftchord regions of the endwall. Slight decreases in heat transfer, relative to design inlet flow angle, were observed in the midchord region near the suction surface corner. Slight increases in heat transfer, again relative to design inlet flow angle, were recorded across the entire gap in the trailing edge region and in the midchord region near the pressure surface corner. All of these small adjustments to the endwall heat transfer probably resulted from the redistribution of the rotor-passage acceleration produced by the inlet angle change.

Heat Transfer Contours for the Rough Wall. Sample contour maps of the rotor passage heat transfer distributions for the rough-wall model are presented for two test conditions in Figs. 11(*a*) and 11(*b*). Comparison of any of the rough-wall and smooth wall data sets obtained at similar operating conditions reveals that the surface roughness significantly increased the heat transfer rates at all locations. The largest relative changes (>100 percent) occurred in the forechord, suction-surface region for all cases. For the smooth-wall tests the boundary layer in this region was laminar/transitional while for the rough-wall cases it was fully turbulent. The heat transfer data indicate that the surface roughness tripped the suction-surface boundary layer very near the stagnation line. This produced a low Re_θ turbulent boundary layer with very high levels of heat transfer.

It is interesting to note that the local regions of augmented heat transfer, e.g., the leading-edge/endwall junction and the midchord, near-hub, and near-tip regions of the suction surface, were still present on the rough-wall model. This result indicates that surface roughness had important (20–40 percent) augmentation effects even in regions with extremely thin, skewed, nonequilibrium boundary layers.

Examination of these data sets reveals that for both the airfoil and endwall surfaces local heat transfer rates were highly insensitive to changes in the Reynolds number. This result is not unexpected, considering the extremely coarse grit used for roughwall tests. It is well established that for "fully rough" surfaces both the skin friction coefficient and the heat transfer coefficient become independent of Reynolds number.

For the rough-wall test conditions, the effects of inlet flow

angle were almost exclusively confined to the forechord region of the rotor passage. Decreases in heat transfer, relative to design inlet flow angle operation, were observed in the forechord region of both the rotor airfoil and endwall surfaces. As discussed previously, this effect results from the decrease in relative inlet velocity associated with increased relative inlet flow angles.

Concluding Comments

An experimental program has been conducted to examine the heat transfer distributions over the airfoil and hub endwall surfaces of a rotor passage. The effects of Reynolds number, rotor inlet flow angle, and surface roughness were documented. Conclusions that were reached and observations that were made are summarized below:

Conclusions

1 The results of this program have demonstrated that three-dimensional flows within the rotor passage produced localized regions with significantly enhanced heat transfer rates.

A Hub and tip secondary flow effects—On the suction surface, the Stanton numbers observed within the zones dominated by the hub and tip secondary flows were as much as 60 percent higher than at midspan.

B Tip leakage effects—The highest heat transfer rates on the suction surface, more than 100 percent greater than the midspan value, were recorded near the tip for 70 percent $< S^* <$ 130 percent. This highly localized enhancement was produced by the tip-leakage flow, which rolls up into a vortex in that region. An associated effect was observed near the tip on the pressure surface where the heat transfer rates were slightly higher (approximately 10 percent) than for the remainder of the span.

C Leading-edge/horseshoe vortex system effects—The leading-edge/horseshoe vortex system produced enhanced heat transfer on the endwall near the rotor-leading-edge/endwall junction with local Stanton numbers 90 percent greater than at the leading-edge midgap. In addition, this same vortex system caused a local region of higher heat transfer on the suction-surface near the leading-edge/hub corner with local Stanton numbers as much as 50 percent higher than at midspan.

2 Increased surface roughness greatly increased heat transfer rates relative to the smooth-wall test cases for all locations on both the airfoil and endwall. The largest changes produced by the wall roughness (> 100 percent) occurred in the forechord region ($0 < S/Bx < 0.7$) of the suction surface. Local regions of augumented heat transfer that were observed for the smooth-wall test cases were also present for the rough-wall cases, e.g., the leading-edge/endwall junction and the tip-leakage vortex site.

3 Comparisons between the smooth-wall, near-smooth-wall, and rough-wall data and predictions of a modified version of the STAN-5 boundary layer code showed excellent agreement. Use of the van Driest "modified-mixing-length" turbulence model based on max-to-min surface roughness values produced excellent heat transfer predictions over a factor-of-ten range in surface roughness.

Observations—Design Inlet Flow Angle Test Cases

1 The heat transfer data indicate that at design inlet flow angle the flow was everywhere attached; there was no evidence of separation bubbles on either the airfoil or endwall surfaces.

2 Increasing the Reynolds number produced the expected reduction of local Stanton number for all locations in the rotor passage where the boundary layers were turbulent. Increasing the Reynolds number also hastened the transition process in regions where the boundary layer was laminar/transitional.

3 Comparisons of the present smooth-wall midspan heat transfer distributions with midspan data previously obtained for this same airfoil section (near-smooth wall) show very good agreement.

4 The minimum heat transfer on the hub endwall occurred in the midchord region near the endwall/pressure-surface corner.

Observations—Off-Design Inlet Flow Angle Test Cases

1 Increasing the rotor inlet flow angle from $\beta_1 = 40$ to 54 deg (14 deg negative incidence relative to design) produced a full-span separation bubble (approximate streamwise length of 2 percent S^*) near the streamwise location of the pressure-surface leading edge overspeed. Reattachment downstream of this bubble produced a narrow, full-span band of relatively high heat transfer with Stanton numbers approximately 60 percent greater than for that streamwise location for the design inlet flow angle, i.e., with no separation bubble.

2 Increasing the rotor inlet flow angle increased the heat transfer in the forechord region of the pressure surface and simultaneously decreased the heat transfer in the forechord region of the suction surface. Since the test Reynolds numbers (based on exit velocity) were held constant, trailing-edge-region heat transfer rates for both the pressure and suction surfaces were unchanged by changing incidence.

3 The forechord region of the endwall showed a decrease in heat transfer with increased inlet flow angle, an effect produced directly by the decrease in relative inlet velocity.

Acknowledgments

The work presented in this paper was sponsored by the National Aeronautics and Space Administration (NASA), George C. Marshall Space Flight Center under NASA Contracts NAS8-37351 and NAS8-38870. The technical monitors for the work were Dr. Helen V. McConnaughey and Ms. Lisa W. Griffin. The author gratefully acknowledges the contributions of Dr. Om Sharma (Pratt & Whitney, Commercial Engine Business) and Mr. Joel H. Wagner who provided the STAN-5 computations, of Mr. Richard Roback who performed the ANSYS-PC/THERMAL computations, and of Dr. Robert P. Dring who provided invaluable guidance throughout the project.

References

Anon., 1988, ANASYS-PC.Thermal 4.3 Reference Manual, Swanson Analysis Systems, Inc., Houston, PA.

Blair, M. F., 1983, "Influence of Free-Stream Turbulence on Turbulent Boundary Layer Heat Transfer and Mean Profile Development," ASME *Journal of Heat Transfer*, Vol. 105, pp. 33–47.

Blair, M. F., 1985, "Heat Transfer in the Vicinity of a Large Scale Obstruction in a Turbulent Boundary Layer," *AIAA Journal of Propulsion and Power*, Vol. 1, No. 2, pp. 158–160.

Blair, M. F., Dring, R. P., and Joslyn, H. D., 1989, "The Effects of Turbulence and Stator/Rotor Interactions on Turbine Heat Transfer: Parts I & II," ASME JOURNAL OF TURBOMACHINERY, Vol. 111, pp. 87–103.

Blair, M. F., Wagner, J. H., and Steuber, G. D., 1991, "New Applications of Liquid-Crystal Thermography in Rotating Turbomachinery Heat Transfer Research," ASME Paper No. 91-GT-354.

Blair, M. F., 1991, "The Effects of Reynolds Number, Rotor Incidence Angle and Surface Roughness on the Heat Transfer Distribution in a Large-Scale Turbine Rotor Passage," UTRC Report R91-970057-3, Final Technical Report NAS8-38870.

Carter, J. E., Edwards, D. E., and Werle, M. J., 1982, "Coordinate Transformation for Laminar and Turbulent Boundary Layers," *AIAA Journal*, Vol. 20, No. 2, pp. 282–284.

Cebeci, T., and Smith, A. M. O., 1974, *Analysis of Turbulent Boundary Layers*, Academic Press, New York.

Crawford, M. E., and Kays, W. M., 1976, "STAN-5 Program for Calculation of Two-Dimensional Internal and External Boundary Layer Flows," NASA CR-2742.

Denton, J. D., 1992, "The Calculation of Three-Dimensional Viscous Flow Through Multistage Turbomachines," ASME JOURNAL OF TURBOMACHINERY, Vol. 114, pp. 18–26.

Dippery, R. B., and Sabersky, R. H., 1963, "Heat and Mass Transfer in Smooth and Rough Tubes at Various Prandtl Numbers," *Int. J. Heat Mass Transfer*, Vol. 6, pp. 329–353.

Dorney, D. J., and Davis, R. L., 1991, "Navier-Stokes Analysis of Turbine Blade Heat Transfer and Performance," AGARD 77th Symposium on CFD Techniques for Propulsion Applications, San Antonio, TX.

Dring, R. P., and Joslyn, H. D., 1983, "The Relative Eddy in Axial Turbine Rotor Passages," ASME Paper No. 83-GT-22.

Dring, R. P., Blair, M. F., Joslyn, H. D., Power, G. D., and Verdon, J. M., 1986, "The Effects of Inlet Turbulence and Rotor/Stator Interactions on the Aerodynamics and Heat Transfer of a Large-Scale Rotating Turbine Model," Vol. 1, Final Report, NASA Contractor Report 4079.

Dunn, M. G., and Hause, A., 1982, "Measurements of Heat Flux and Pressure in a Turbine Stage," ASME *Journal of Engineering for Power*, Vol. 104, pp. 215–223.

Dunn, M. G., 1986, "Heat-Flux Measurements for the Rotor of a Full-Stage Turbine: Part I—Time-Averaged Results," ASME JOURNAL OF TURBOMACHINERY, Vol. 108, pp. 90–97.

Dunn, M. G., Seymour, P. J., Woodward, S. H., George, W. K., and Chupp, R. E., 1989, "Phase-Resolved Heat-Flux Measurements on the Blade of a Full-Scale Rotating Turbine," ASME JOURNAL OF TURBOMACHINERY, Vol. 111, pp. 8–19.

Edwards, D. E., Carter, J. E., and Werle, M. J., 1981, "Analysis of the Boundary Layer Equations Including a Coordinate Transformation," The ABLE Code, UTRC81-30.

Graziani, R. A., Blair, M. F., Taylor, J. R., and Mayle, R. E., 1980, "An Experimental Study of Endwall and Airfoil Surface Heat Transfer in a Large Scale Turbine Blade Cascade," ASME *Journal of Engineering for Power*, Vol. 102, pp. 257–267.

Guenette, G. R., Epstein, A. H., Giles, M. B., Haimes, R., and Norton, R. J. G., 1989, "Fully Scaled Transonic Turbine Rotor Heat Transfer Measurements," ASME JOURNAL OF TURBOMACHINERY, Vol. 111, pp. 1–7.

Han, L. S., 1985, "Turbulent Flow Over Rough Turbine Airfoils," AFWAL-TR-85-2056, Final Contractor Report, The Ohio State University.

Han, L. S., and Delpassand, M., 1990, "A Heat Transfer Analysis for Rough Turbine Airfoils," WRDC-TR-89-2135, Final Contractor Report, The Ohio State University.

Harvey, N. W., Wang, Z., Ireland, P. T., and Jones, T. V., 1989, "Detailed Heat Transfer Measurements in Nozzle Guide Vane Passages in Linear and Annular Cascades in the Presence of Secondary Flows," AGARD CCP-468/469.

Hylton, L. D., Mihelc, M. B., Turner, E. R., Nealey, D. A., and York, A., "Analytical and Experimental Evaluation of the Heat Transfer Distribution Over the Surfaces of Turbine Vanes," NASA CR 168015, Final Report for Contract No. NAS3-22761.

Joslyn, H. D., and Dring, R. P., 1989, "Three Dimensional Flow and Temperature Profile Attenuation in an Axial Flow Turbine," Final Report under AFOSR Contract F49620-86-C-0020, UTRC Report R89-957334-1.

Joslyn, H. D., and Dring, R. P., 1992, "Three-Dimensional Flow in an Axial Turbine," ASME JOURNAL OF TURBOMACHINERY, Vol. 114, pp. 61–78.

Kadar, B. A., and Yaglom, A. M., 1972, "Heat and Mass Transfer Laws for Fully Turbulent Wall Flows," *Int. J. Heat Mass Transfer*, Vol. 15, pp. 2329-2351.

Langston, L. S., Nice, M. S., and Hooper, R. M., 1977, "Three-Dimensional Flow Within a Turbine Cascade Passage," ASME *Journal of Engineering for Power*, Vol. 99, pp. 21–28.

Lokay, V. I., and Trushin, V. A., 1970, "Heat Transfer From the Gas and Flow-Passage Elements of a Rotating Gas Turbine," *Heat Transfer—Soviet Research*, Vol. 2, No. 4.

Ni, R. H., and Bogoian, J. C., 1989, "Prediction of Three-Dimensional Multistage Turbine Flow Field Using a Multiple Grid Euler Solver," AIAA Paper No. 89-0203.

Seidman, M. H., 1978, "Rough Wall Heat Transfer in a Compressible Turbulent Boundary Layer," AIAA Paper No. 78-163, presented at the AIAA 16th Aerospace Sciences Meeting, Huntsville, AL.

Sharma, O., and Butler, T., 1991, private communication.

Sieverding, C. H., 1985, "Recent Progress in the Understanding of Basic Aspects of Secondary Flows in Turbine Blade Passages," ASME *Journal of Engineering for Gas Turbines and Power*, Vol. 107, No. 2, pp. 248–257.

van Driest, E. R., 1956, "On Turbulent Flow Near a Wall," *J. Aeronautical Sci.*, Vol. 23, pp. 1007–1011.

Time-Averaged Heat Transfer and Pressure Measurements and Comparison With Prediction for a Two-Stage Turbine

M. G. Dunn

J. Kim

Calspan-UB Research Center,
Buffalo, NY 14225

K. C. Civinskas
U.S. Army Propulsion
Directorate—AVSCOM.

R. J. Boyle
NASA Lewis Research Center,
Cleveland, OH 44135

Time-averaged Stanton number and surface-pressure distributions are reported for the first-stage vane row and the first-stage blade row of the Rocketdyne Space Shuttle Main Engine two-stage fuel-side turbine. These measuremeents were made at 10, 50, and 90 percent span on both the pressure and suction surfaces of the component. Stanton-number distributions are also reported for the second-stage vane at 50 percent span. A shock tube is used as a short-duration source of heated and pressurized air to which the turbine is subjected. Platinum thin-film gages are used to obtain the heat-flux measurements and miniature silicone-diaphragm pressure transducers are used to obtain the surface pressure measurements. The first-stage vane Stanton number distributions are compared with predictions obtained using a quasi-three dimensional Navier-Stokes solution and a version of STAN5. This same N-S technique was also used to obtain predictions for the first blade and the second vane.

Introduction

The results described in this paper represent the initial step in an investigation designed to obtain detailed heat-flux and surface-pressure data for a multistage machine. The data obtained from this program are intended to serve two purposes: (*a*) to provide experimental information for code validation, and (*b*) to provide comparison data for a blowdown test rig at Marshall Space Flight Center, which uses the same multistage turbine. The program is structured so that time-averaged, time-resolved, and phase-averaged data have been obtained. However, only the time-averaged results and their comparison with predictions will be presented herein.

The results of several previous measurement programs that utilized the same diagnostic techniques as used here, but for different turbine stages, have been reported by Dunn and Stoddard (1979); Dunn and Hause (1982); Dunn et al. (1984); Dunn et al. (1986); Dunn and Chupp (1988, 1989); and Dunn et al., (1990). The short-duration facility used for the experiments reported here is the same one used to obtain the results reported by Dunn et al. (1990).

The flow and heat transfer that occur in a turbine stage (or stages) represent one of the most complicated environments seen in any practical machine: The flow is always unsteady, can be transonic, is generally three dimensional, and is subjected to strong body forces. Despite these problems, satisfactory designs have been achieved over the years due to advances in materials and manufacturing processes, as well as to the development of a sound analytical understanding of the flow and heat transfer mechanics that define performance. These analytical developments were made possible by a series of approximations, in which the level of detail retained in the modeling was sufficient to reveal important physical effects, while still allowing solutions to be found by available analytical/numerical methods.

The major milestones in the development of these methods have been the approximations that flow through each blade row is steady in coordinates fixed to the blades, that three dimensionality can be handled by treating a series of two-dimensional flows in hub-to-shroud and blade-to-blade surfaces, and that the effects of viscosity can be estimated by noninteracting boundary-layer calculations and by loss models to account for secondary flow.

This technology base is surrounded by many analyses and numerical codes, which can treat the flow on higher levels of approximation, and which are used from time to time to provide refined estimates of the flow field and heat transfer, typically near a design point. Three-dimensional and unsteady flow effects are two areas where recently developed computational tools can provide useful information on the flow conditions, at least for the first stage of a multistage turbine. However, in the second and subsequent stages, these effects become more pronounced. The current state-of-the-art analyses can predict reasonably well the second-stage vane pressure distribution, but the predicted heat-flux levels on the second vane are not as good as desired, as illustrated by Blair et al.

Civinskas et al. (1988) have previously presented an analysis of the first-stage blade of the turbine used here. The predictions presented here are a continuation of that work. The Navier-

Contributed by the International Gas Turbine Institute and presented at the 37th International Gas Turbine and Aeroengine Congress and Exposition, Cologne, Germany, June 1-4, 1992. Manuscript received by the International Gas Turbine Institute February 17, 1992. Paper No. 92-GT-194. Associate Technical Editor: L. S. Langston.

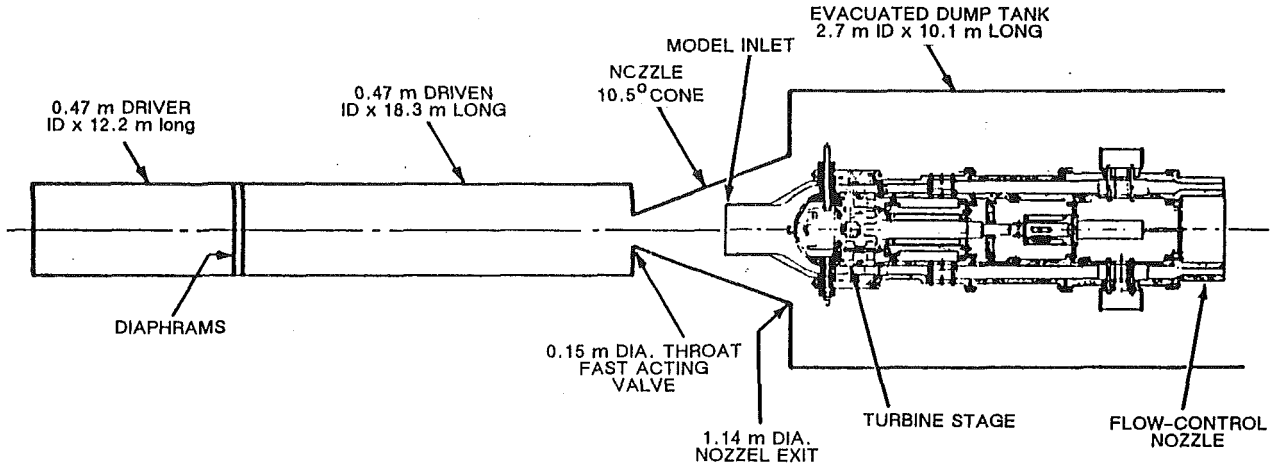

Fig. 1 Sketch of SSME turbine stage located in the shock tunnel

Stokes analysis of heat transfer was done using a modified version of the quasi-three-dimensional thin-layer code developed by Chima (1986). The modifications are explained by Boyle (1991). An additional change for the purposes of this paper has been to incorporate the transition model of Mayle (1991) for the first vane and the intermittency model of Mayle and Dullenkopf (1989, 1991) for the first blade and the second vane. In addition to the quasi-three-dimensional Navier–Stokes analysis, the STAN5 (Crawford and Kays, 1976) boundary layer analysis, as modified by Gaugler (1981), was used. Both the Navier–Stokes and boundary analyses used the MERIDL hub-to-shroud analysis of Katsanis and McNally (1977) to determine the streamtube variation at appropriate spanwise locations. The edge conditions for the STAN5 boundary layer analysis were obtained using the TSONIC analysis of Katsanis (1969).

The balance of the paper provides a brief summary of the experimental apparatus, the experimental conditions, a discussion of the experimental results, and a comparison of these results with the predictions. This paper is confined to a discussion of the vane and blade pressure and suction surface results. Other results for the blade platform, the blade tip, and the stationary shroud as well as off-design speed results are presented by Dunn and Kim (1992).

Description of the Experimental Technique, the Turbine Flow Path, and the Instrumentation

The Experimental Technique. The measurements are performed utilizing a shock tunnel to produce a short-duration source of heated and pressurized gas that passes through the turbine. Air has been selected as the test gas for these experiments. A schematic of the experimental apparatus illustrating the shock tube, an expansion nozzle, a large dump tank, and a device that houses the turbine stage and provides the flow path geometry is shown in Fig. 1. The shock tube has a 0.47-m (18.5-in.) diameter by 12.2-m (40 ft) long driver tube and 0.47-m (18.5-in.) diameter by 18.3-m (60 ft) long driven tube. The driver tube was designed to be sufficiently long so that the wave system reflected from the driver endwall (at the left-hand end of the sketch) would not terminate the test time prematurely. At the flow conditions to be run for these measurements, the test time is very long for a short-duration facility being on the order of 40 ms.

In order to initiate an experiment, the test section is evacuated while the driver, the double diaphragm section, and the driven tube are pressurized to predetermined values. Pressure values are selected to duplicate the design flow conditions. The flow function ($\dot{w}\sqrt{\theta}/\delta$), wall-to-total temperature ratio (T_w/T_o), stage pressure ratios, and corrected speed are duplicated. The shock-tunnel facility has the advantage that the value of T_o can be set at almost any desired value in the range of 800 R to 3500 R, and the test gas can be selected to duplicate the desired specific heat ratio. The design pressure ratio across the turbine is established by altering the throat diameter of the flow control nozzle located at the exit end of the device housing the turbine. Simple one-dimensional calculations provide a good first estimate of the necessary exit area. Another characteristic of this facility that was used here is that the total pressure (or the Reynolds number) at the entrance to the vane row can be changed by moving the inlet to the device housing the turbine axially in the expanding nozzle flow so as to intercept the flow at a different free stream Mach number. If moving the inlet isn't satisfactory, then the reflected-shock pressure can be increased, which was the approach taken in these tests, or the total temperature can be decreased in order to increase the Reynolds number.

The Turbine Flow Path. Figure 2 is a drawing of the turine stage illustrating the extent to which the flowpath of the SSME hardware has been reproduced. The first-stage vane row (41 vanes) and the first-stage rotor row (63 blades), as well as the second-stage vane row (39 vanes) and the second-stage rotor row (59 blades) are shown. The first-stage vane has a significant cutback (see photograph in Dunn and Kim, 1991) at the trailing edge, which extends from the hub to about 35 percent span. This cutback was modeled in the analysis presented herein. The preburner dome and bolt, the 13 struts upstream of the first-stage vane, the 12 flow straighteners, and 6 struts downstream of the second rotor have been included. Flowpath static pressure was measured on the outer wall at the inlet and exit to the turbine stages and between each blade row. The measured upstream static pressure was nearly equal to the upstream total pressure because the inlet Mach number was low. The inlet Mach number was calculated and the inlet total pressure was obtained from the isentropic flow relationship. Total pressure was measured in the passage downstream of the second rotor. The reader is referred to Dunn and Kim (1991) for details of the configuration.

Heat-Flux Instrumentation. The heat-flux measurements were performed using thin-film resistance thermometers. These devices represent an old and very well-established technology that was developed as part of the early hypersonics flow research work in the late 50s for measurement of heat flux in short-duration facilities. The thin-film gages are made of platinum (~100 Å thick) and are hand painted on an insulating Pyrex substrate in the form of a strip that is approximately 1.02×10^{-4} m (0.004 in.) wide by about 5.08×10^{-4} m (0.020 in.) long. The response time of the elements is on the order of 10^{-8} s. The substrate onto which the gage is painted can

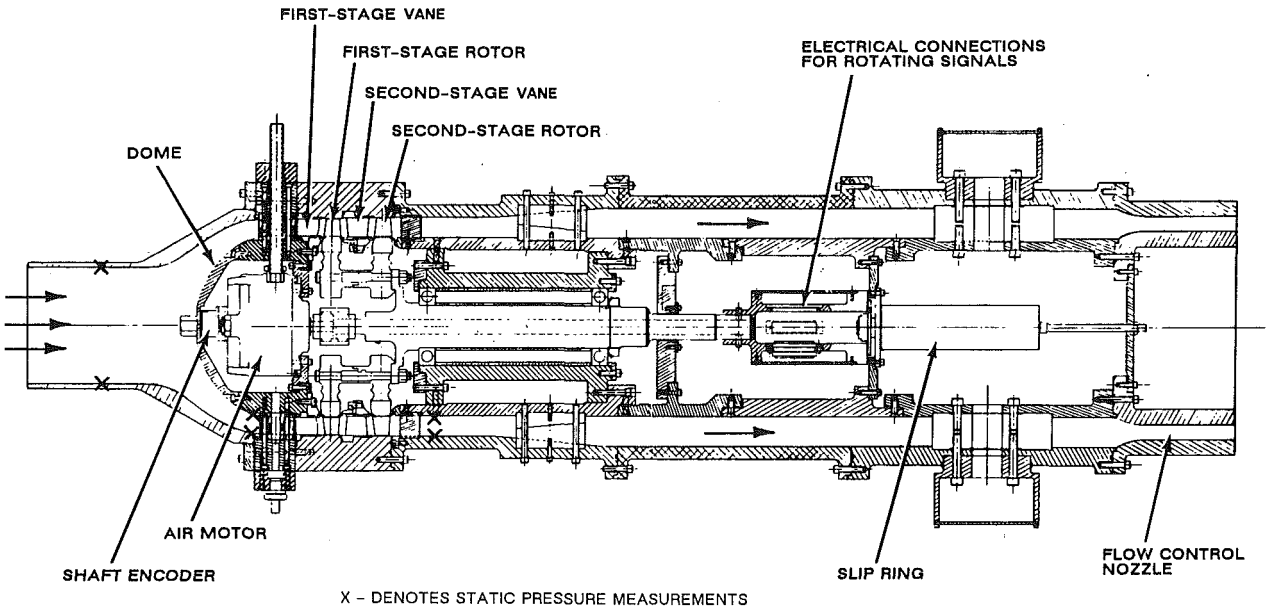

Fig. 2 Sketch of device housing SSME turbine stage

be made in many sizes and shapes. The substrates are Epoxied within the base metal throughout the turbine stage.

Both button-type gages and contoured leading-edge inserts were used for this work. Figure 3(*a*) is a photograph of a rotor blade that has been instrumented with button-types gages and Fig. 3(*b*) is a photograph of a blade containing a contoured leading-edge insert. A detailed listing of the gage locations is given by Dunn (1990*b*). Figure 4(*a*) is a blown-up photograph of the blade surface qualitatively illustrating the surface roughness. The surface roughness for this blade has been measured[1] and a typical profilometer scan of the blade surface is given in Fig. 4(*b*). The results shown in this figure suggest an rms roughness of about 150,000 Å, which was used in the analysis of the heat transfer data. Blair and Anderson (1989) used the rms value to provide a roughened surface and performed heat flux measurements for that blade in the UTRC large scale rotating rig. The results of that work are reported by Blair and Anderson (1989) and Blair (1994).

Surface-Pressure Instrumentation. Measurements were also obtained using miniature silicon diaphragm pressure transducers located on the first-stage vane and the first-stage blade. The particular gages being used are Kulite Model LQ-062-600A with an active pressure area of 0.64 mm by 0.64 mm and a frequency response of about 100 kHz in the installed configuration. Twenty-eight pressure transducers were installed on the vanes and twenty-four were installed on the blades. The pressure transducers were placed at 10, 50, and 90 percent span at the locations given by Dunn (1990) and were distributed over several different vanes and blades so as to not disturb the integrity of the surface.

Experimental Conditions

Table 1 provides a summary of the reflected-shock conditions, the flow conditions at the turbine inlet, and the turbine speed. Two shock-tube conditions were run for these experiments: the first at a reflected-shock pressure and temperature of approximately 6.2×10^3 kPa (900 psia) and 544 K (980 R), respectively, and the second at a reflected-shock pressure and temperature of approximately 10×10^3 kPa (1445 psia) and 602 K (1084 R), respectively. For a given test condition, the run-to-run variation in reflected-shock pressure was the result of attempting to increase the test time by changing the relative amount of helium in the driver gas which also influences the incident shock Mach number. These reflected-shock conditions result in first vane inlet Reynolds numbers (based on first vane axial chord) of approximately 1.40×10^5 and 2.50×10^5, respectively. The area of the downstream exit nozzle of the device housing the turbine (see Fig. 2) was changed so that data could be obtained at two values of stage pressure ratio, for each test condition. Measurements were obtained with the turbine speed set at 100 ± 1 percent of the design value or at approximately 103 percent of the design value. Limited data were obtained at off-design speed and are reported by Dunn and Kim (1991).

Experimental Results

Surface pressure and heat flux were measured at 10, 50, and 90 percent span on the first vane and the first rotor. Static pressure measurements were made along the flow path on the outer wall. Total pressure was measured in the flow path downstream of the second rotor. Table 2 gives the measured upstream total pressure along with the pressure ratios for each of the vane and blade rows. Heat flux was also measured on the first blade platform, the first blade tip, and at 50 percent span on the second vane. It is not possible to present all of the data collected during the measurement program in this paper. However, a complete compilation is presented by Dunn and Kim (1991), along with the vane and blade coordinates. This paper will concentrate on the surface pressure and heat transfer measurements for the first vane, the first blade, and the second vane.

The Stanton number results presented here for both the vane rows and the first blade row are based on conditions at the first vane inlet. The relationship used to evaluate the Stanton number was

$$\mathrm{St} = \frac{\dot{q}(t)}{(\dot{W}/A[H_o(T_o) - H_w(T)])}$$

The value of A used for this evaluation was 1.73×10^{-2} m^2 (0.186 ft^2), and corresponds to the annular area upstream of the first-stage vane. In this formulation, the heat flux and the wall enthalpy are both evaluated at the same temperature, T. If the cold-wall heat flux, $\dot{q}(T_w)$, is desired, then it can be obtained by multiplying the given Stanton number by $(\dot{W}/$

[1]Roughness measurements were performed at the United Technologies Research Center and supplied to CUBRC courtesy of M. Blair. Figure 4(*b*) has been reproduced here with permission of M. Blair.

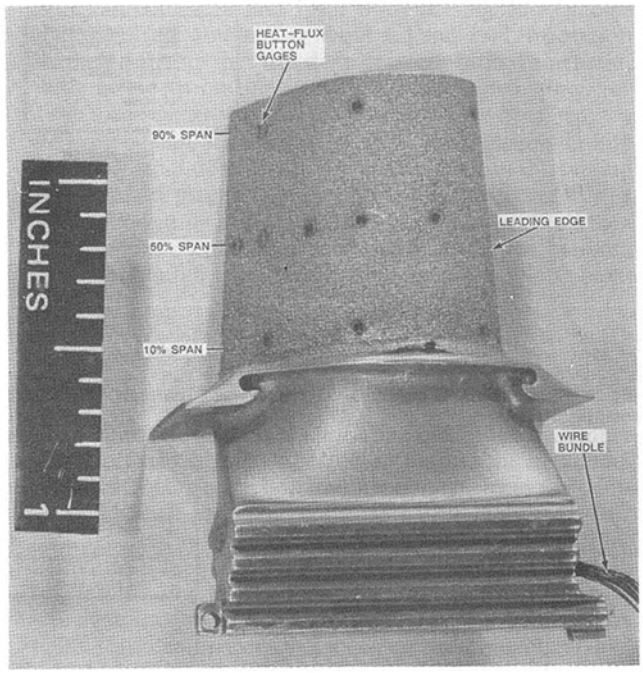

Fig. 3(*a*) Button-type heat-flux gages on first-stage blade suction surface

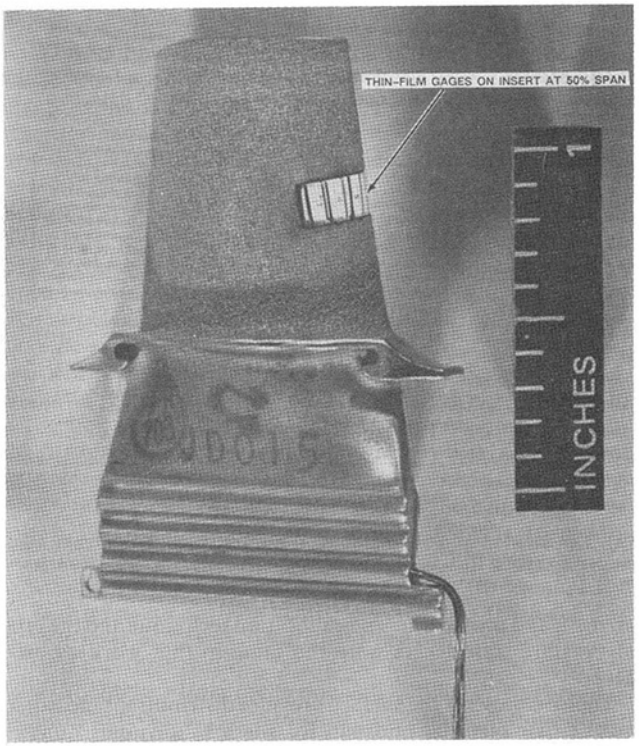

Fig. 3(*b*) Photograph of leading-edge insert heat-flux gages on first-stage blade

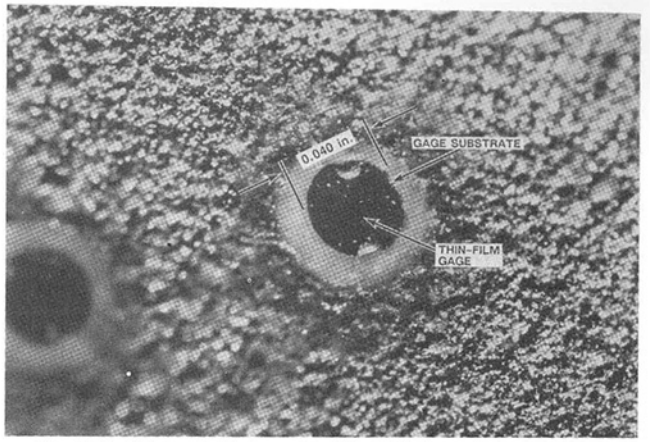

Fig. 4(*a*) Enlarged photograph of first blade surface roughness

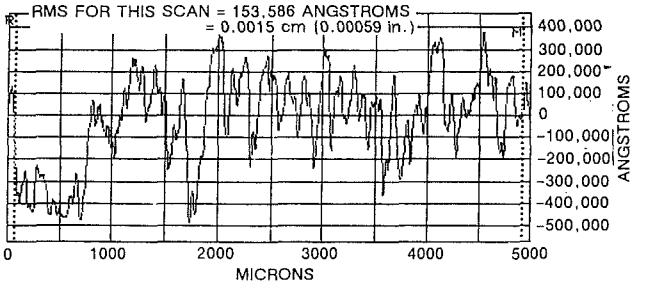

Fig. 4(*b*) Profilometer scan of blade surface

Table 1 Summary of flow parameters

Run	$\dot{W}$ [lbm/s]	$\left.\frac{P_{T,in}}{P_{s,out}}\right\|_{stage}$	$P_{s,in}$ [psia]	Reflected shock pressure [psia]	Reflected shock temp. [°R]	$Re\|_{vc}$ $(\times 10^{-5})$*	Actual speed [rpm]	% Design speed**
5	5.59	1.66	46.6	900	995	1.39	9075	99
6	5.81	1.65	48.3	929	990	1.44	9468	103
7	10.2	1.48	86	1519	1112	3.00	9612	99
8	9.74	1.38	89	1442	1084	2.69	9690	101
11	10.0	1.42	98	1369	1057	2.40	9585	101
12	5.83	1.54	48.3	925	981	1.45	9380	103
13	5.51	1.54	45.3	878	970	1.38	9365	103

*Reynolds number based on vane chord and vane inlet conditions.
** $N_{corr} = 291.4 \text{ rpm} / \sqrt{°R}$

Table 2 Component pressure ratios. Static pressures were measured at the outer shroud.

Run	P_t into 1st vane (psia)	First vane $\frac{P_{T,in}}{P_{s,out}}$	First stage $\frac{P_{T,in}}{P_{s,out}}$	Second vane $\frac{P_{s,in}}{P_{s,out}}$	Second rotor $\frac{P_{s,in}}{P_{s,out}}$	$\left.\frac{P_{T,in}}{P_{s,out}}\right\|_{stage}$	$\left.\frac{P_{T,in}}{P_{T,out}}\right\|_{stage}$
5	47.1	1.17	1.37	1.12	1.08	1.66	1.62
6	48.9	1.14	1.34	1.12	1.09	1.65	1.61
7	86	1.13	1.24	1.11	1.08	1.49	1.45
8	89	1.10	1.20	1.10	1.06	1.40	1.40
11	98	1.10	1.26	1.10	1.04	1.44	1.47
12	48.8	1.13	1.31	1.09	1.08	1.54	1.52
13	45.8	1.14	1.32	1.08	1.08	1.54	1.52

$A)[H_o(T_o) - H_w(T_w)]$. the greatest contributor to the uncertainty in the Stanton number is the uncertainty in the weight flow $\dot{w}$. For these experiments, the weight flow was found from an experimentally determined flow calibration curve supplied by NASA MSFC, which plotted the flow function as a function of the total to static pressure ratio across the first-stage nozzle. The uncertainty in the vane row pressure measurement translates into an uncertainty in the flow function and the weight flow. An error of approximately 10 percent in the weight flow was found. Assuming an uncertainty in the heat flux and temperature measurements to be 5 percent, the expected error in the Stanton numbers can be calculated using the methodology of Kline and McClintock (1953) to be 12 percent.

Vane and Blade Surface Pressure Results. The measured surface pressure distributions are presented on Fig. 5 for the first vane at 50 percent span for the low Reynolds number cases. These results are presented for two-stage pressure ratios, approximately 1.54 and 1.65. The predicted surface pressure distribution is also included on Fig. 5. The agreement between the data and the prediction is not particularly good. The cause of the disagreement is in large part attributable to the uncertainty in the pressure measurement. Prior to the initial exper-

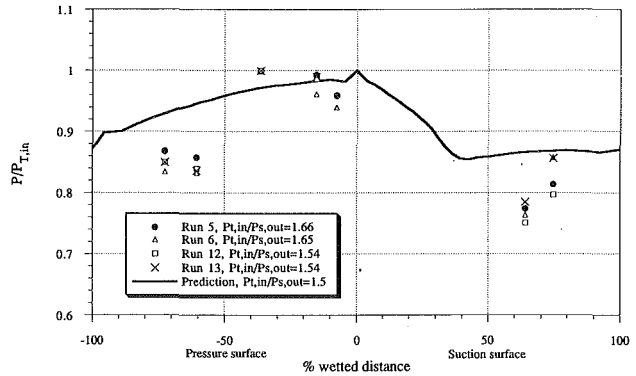

Fig. 5 Pressure distribution at 50 percent span on first vane, Re ~ 140,000, comparison with predictions

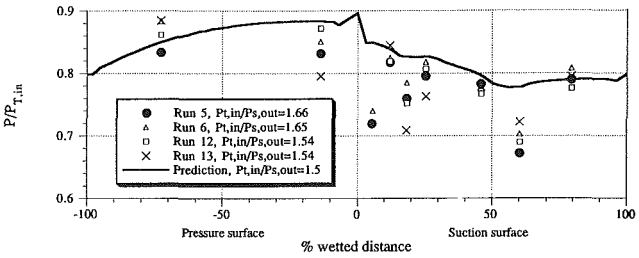

Fig. 6 Pressure distribution at 50 percent span on first blade, Re ~ 140,000

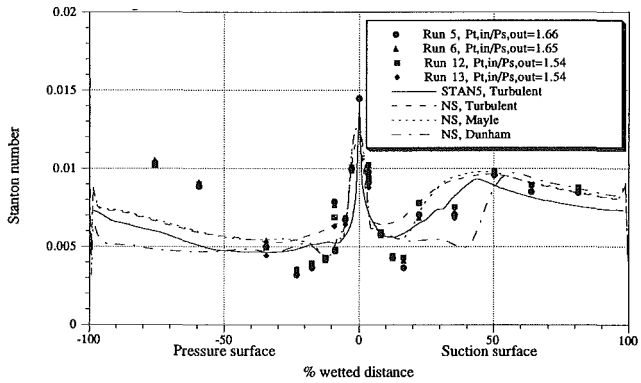

Fig. 7 Stanton number distribution on first vane, 50 percent, Re ~ 140,000

iment, the pressure transducers were calibrated over the range from vacuum to 1.48 MPa (215 psia). During and after the experiments, they were calibrated again from vacuum to 0.655 MPa (95 psia). These latter calibrations were done by pressurizing the dump tank housing the turbine stage (see Fig. 1). The pressure readings were recorded using the entire data recording system that is used during the experiment. A linear fit was obtained for each data set over the pressure range of these experiments. The slope of the calibrations for most of the transducers was reproducible to within 3 percent. For a few others, the slope varied by as much as 5 percent. The pressure drop across the first vane row and the first blade row is relatively small for this turbine, being on the order of 10 to 15 percent of the inlet total pressure, which makes the uncertainty in the slope of the transducer calibration an important consideration. If a pressure measurement uncertainty of 3 percent due to variations in the slope of the calibration equation is assumed, along with a 2 percent uncertainty due to shock tunnel reproducibility, the expected error in the normalized pressures (P/P_T) may be calculated, using the methodology of Kline and McClintock (1953), to be 4.7 percent. The difficulty encountered here with the pressure measurements was unanticipated. A previous measurement program reported by Dunn et al. (1990*a*) demonstrated much better agreement between measurement and prediction. The calibration technique and the type of pressure transducers were the same in that work as used here.

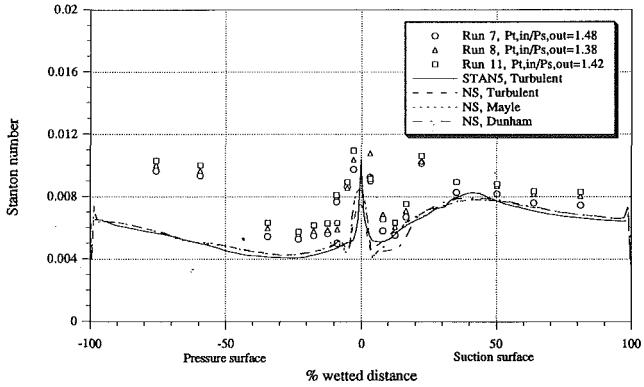

Fig. 8 Stanton number distribution on first vane, 50 percent, Re ~ 250,000 results

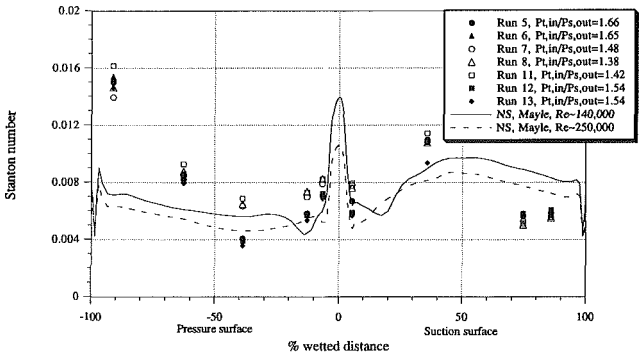

Fig. 9 Stanton number distribution on first vane, 10 percent span: closed symbols: Re ~ 140,000 data, open symbols: Re ~ 250,000 data

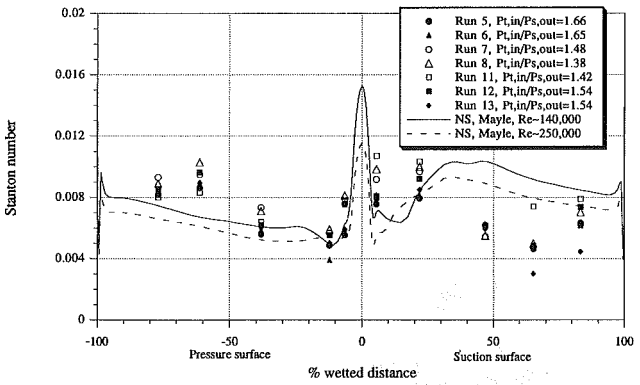

Fig. 10 Stanton number distribution on first vane, 90 percent span: closed symbols: Re ~ 140,000 data, open symbols: Re ~ 250,000 data

Figure 6 presents the surface pressure distributions measured on the first blade at midspan for the low Reynolds number case at both values of stage pressure ratio. The disagreement between the measurements and the prediction is largely similar to what was found on the vane. Again, the difficulty is felt to be due to inaccuracy in the pressure measurement for reasons described in the previous paragraph. Similar results were obtained at the 10 and 90 percent locations.

First Vane Stanton Number Results. Figures 7 and 8 present the measured Stanton number distributions for the vane at 50 percent span for Reynolds numbers of 140,000 and 250,000, respectively. Figure 9 presents the Stanton number data for both Reynolds numbers at 10 percent span and Fig. 10 represents the data for both Reynolds numbers at 90 percent span. The low Reynolds number data were obtained at stage

pressure ratios of 1.54 and 1.65, while the higher Reynolds number data were obtained at about 1.4 and 1.48. Inspection of the data suggests that the stage pressure ratio, in general, has little influence on the Stanton number distributions for the vane locations at which measurements were obtained.

The experimental results for the first vane presented in Fig. 7 illustrate a rapid decrease in Stanton number on the suction surface from the stagnation point to about 15 percent wetted distance followed by a sharp increase near this location, then a peak at about 50 percent wetted distance. On the pressure surface, the data fall sharply from the stagnation point, reaching a minimum at about 25 percent wetted distance, then increases steadily toward the trailing edge. This trend in the pressure surface data is consistent with that seen previously for the Garrett TFE731-2 HP turbine (Dunn et al., 1984), the Air Force LART (Dunn et al., 1986) and the Teledyne 702 turbine (Dunn and Chupp, 1988). The peak Stanton number is shown to occur at the stagnation point and the maximum values reached on the suction and pressure surfaces are comparable with each other and equal to a little more than half of the stagnation value. Similar trends are seen at high Reynolds numbers (Fig. 8) but with the minima occurring closer to the stagnation point. Furthermore, the maximum in the suction surface data also occurs closer to the stagnation point.

Figure 7 also compares vane midspan experimental results with four predictions. Two of the predictions are for fully turbulent flow. The third and fourth predictions incorporate transition models. The two fully turbulent predictions were done using the quasi-three-dimensional Navier–Stokes analysis described by Boyle (1991) and Gaugler's modified version of the STAN5 boundary layer analysis of Crawford and Kays (1976). The predictions including transition were obtained by incorporating the transition model of Mayle (1991) and the transition model due to Dunham (1972) into the just-noted Navier–Stokes analysis. Of the two fully turbulent predictions, the STAN5 prediction illustrates better overall agreement with the data. On the suction surface, the STAN5 prediction doesn't fall as low as the data in the vicinity of 15 percent wetted distance, and it doesn't climb as high as the data beyond 50 percent wetted distance. On the pressure surface, both of the fully turbulent predictions agree with the data reasonably well from the stagnation point to about 40 percent wetted distance. The data points at 60 and 80 percent wetted distance are significantly greater than the prediction. It was noted earlier in this section that this trend has been seen previously for full-stage turbines. This same trend was noted by Nealy et al. (1984) for a vane ring downstream of a combustor. However, the Navier–Stokes analysis used here was applied to those data (Boyle, 1991) and reasonably good agreement between data and prediction was obtained. It is felt that the relatively high upstream turbulence in itself is not sufficient to account for the high pressure surface heat transfer, since the local turbulence level decreases significantly as the flow accelerates through the vane passage. The good agreement between the STAN5 boundary layer prediction and the Navier–Stokes fully turbulent analyses suggests that the numerical solutions of the analyses are not the source of the disagreement with the experimental data.

For the calculation incorporating the Dunham (1972) transition model, transition occurs midway along the suction surface. However, the prediction is not in good agreement with the experimental data from about 7 percent wetted distance to 50 percent wetted distance. This analysis predicts Stanton numbers along the pressure surface that are generally in agreement with STAN5 over the initial 50 percent of that surface. Beyond 50 percent, the shape of the Dunham prediction deviates from the other two and falls below them and well below the data. This is because the flow never becomes fully turbulent with this model. Also included on Fig. 7 is the Navier–Stokes prediction with the Mayle (1991) transition model incorporated. This prediction is in much better agreement with the data than is the other prediction incorporating transition. Overall, the Navier–Stokes prediction that includes the Mayle transition model appears to be in better agreement with the data than any of the other predictions.

Figure 8 presents a comparison between the high Reynolds number data and the same four predictions described above. There is very little difference among the predictions at this higher Reynolds number except in the vicinity of the stagnation point and in the region of 5 to 20 percent on the suction surface. Both the N–S and the STAN5 solutions predict the stagnation region data reasonably well. The N–S solution with the Mayle transition model predicts the 5 to 20 percent wetted distance region better than the N–S solution with the Dunham model. On the pressure surface, all the predictions are in reasonably good agreement with each other and all fall below the data from the stagnation point to about 40 percent wetted distance. The experimental results at 60 and 80 percent wetted distance are underpredicted by a significant amount by all four solutions. In summary, the predictions shown in Figs. 7 and 8 show best agreement with the data when a fully turbulent analysis is used, even for the low Reynolds number cases. The transition models of both Mayle and Dunham are highly dependent on the forestream turbulence intensity. Previous measurements gave an intensity of about 6 percent at the turbine inlet. At the low Reynolds number Dunham's model predicts the start of transition too far downstream on the suction surface. Mayle's model agrees better with the data. At the high Reynolds number, transition occurs close to the leading edge, and there is little difference among the predictions.

Figures 9 and 10 present the first vane Stanton number results at 10 and 90 percent span, respectively. Both sets of Reynolds number data are included on these figures. The N–S prediction with the Mayle transition model has been selected for comparison with the experimental data. It would be anticipated that the high Reynolds number data set should be consistently lower than the low Reynolds number data by about 15 percent ($(2)^{0.2} = 1.15$). There is sufficient uncertainty in the Stanton number results as described in Section 4 that generally the data sets appear to overlap. The agreement between the suction surface prediction and the data is not as good as it was at midspan for either 10 or 90 percent span. In general, beyond 50 percent wetted distance, the prediction fell well above the data on the suction surface. The data point at 60 percent wetted distance is above the prediction, but no more so than the suction surface data points are below the prediction. The pressure surface data at 90 percent span are in as good agreement with the prediction as has been seen at any location on this vane.

First Blade Stanton Number Results

Discussion of Blade Data. Figures 11 and 12 present the measured Stanton number distributions for the first blade at midspan for Reynolds numbers of 140,000 and 250,000 respectively. The Reynolds number data sets are both given on the same figure for the 10 percent span (Fig. 13) and the 90 percent span (Fig. 14) locations. The heat-flux values in the vicinity of the leading-edge region are known to be sensitive to incidence angle. However, the rotor speed range over which data were taken in these experiments (99 to 103 percent of design) was sufficiently small that it is unlikely that incidence angle had a significant effect. Likewise, the local Stanton number is sensitive to stage pressure ratio because of the change in incidence angle associated with the higher axial velocity (increased weight flow) at the lower value of pressure ratio. From the weight flow data presented in Table 1 it was difficult to obtain an estimate of the incidence angle variation resulting from the difference in pressure ratio. The experimental data (runs 5, 6, 12, and 13) at the 10 and 90 percent spanwise

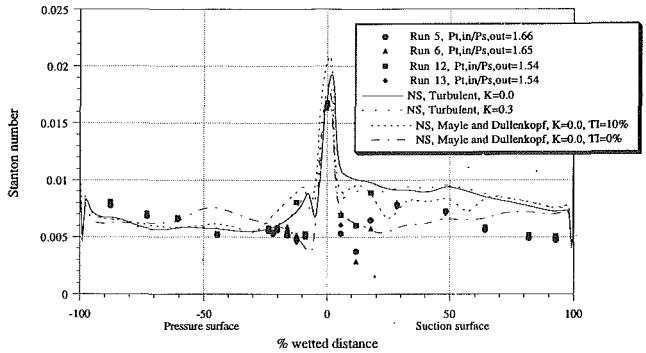

Fig. 11 Stanton number distribution on first blade, 50 percent span, Re ~ 140,000

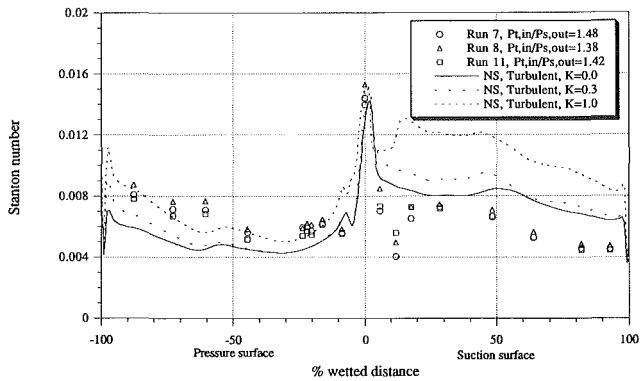

Fig. 12 Stanton number distribution on first blade, 50 percent span, Re ~ 250,000; comparison with predictions for various roughness heights

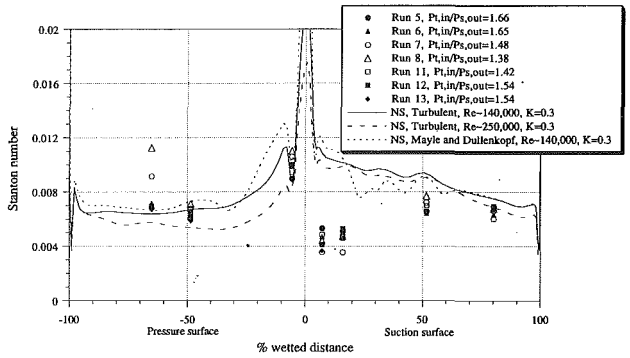

Fig. 13 Stanton number distribution on first blade, 10 percent span: closed symbols: Re ~ 140,000 data, open symbols: Re ~ 250,000 data

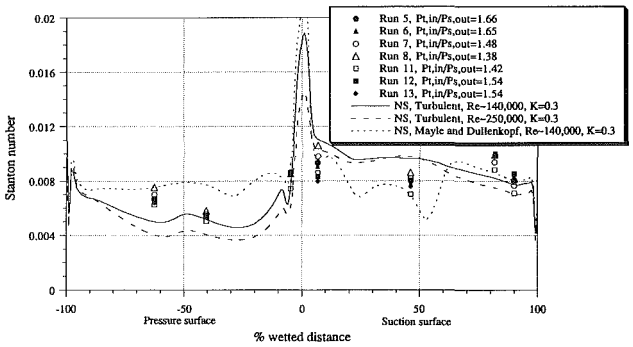

Fig. 14 Stanton number distribution on first blade, 90 blade span: closed symbols: Re ~ 140,000 data, open symbols: Re ~ 250,000 data

locations are consistent with each other near the leading edge in that the Stanton numbers for runs 5 and 6 are consistently greater than those for runs 12 and 13. However, the trend in the Stanton number results from the fact that these same runs at midspan are opposite to that observed at 10 and 90 percent, suggesting that if there was an influence, it didn't occur all along the leading edge. Another interpretation of the data would be that within the uncertainty of the data, no significant influence of pressure ratio or speed was observed for the range of conditions used here. Beyond 50 percent wetted distance, the results illustrate little influence on the Stanton number distribution for either the pressure or suction surface. Returning for a moment to the midspan results presented on Fig. 11, at the stagnation point the experimental results are in agreement with each other, but immediately thereafter (from 0 to 15 percent wetted distance) on the suction surface and in the vicinity of 12 percent wetted distance the data do not coalesce. Three of the runs (run 6, 12 and 13) shown on this figure were for nominally 103 percent of design speed, and the other (run 5) for 99 percent of design speed. Two of the runs at 103 percent of design speed were for a stage pressure ratio of 1.54 (runs 12 and 13) while the other two runs were at a pressure ratio of about 1.65 (runs 5 and 6). At the 12 percent wetted distance location, two of the 103 percent speed points (runs 12 and 13 for the same stage pressure ratio) are in good agreement while the other one (run 6, higher pressure ratio) is low. Also note that runs 5 and 6 which are for the same stage pressure ratio but different speeds, 99 and 103 percent, are in reasonably good agreement with each other, suggesting that for this speed variation the influence on Stanton number distribution is not large.

The experimental data presented on Fig. 11 show that the Stanton number fell rapidly from the stagnation point to about 10 percent wetted distance, followed by a rapid increase, reaching a maximum value for the suction surface at about 25 percent wetted distance. On the pressure surface, the Stanton number increases from a minimum value in the vicinity of 15 percent wetted distance to a maximum near 90 percent wetted distance. The maximum values occurring on these two surfaces are comparable and well below the stagnation point value. Included on Fig. 11 are two fully turbulent Navier–Stokes predictions, one for a rough airfoil and the other for a smooth airfoil, and a N-S prediction, with the Mayle and Dullenkopf (1989, 1991) intermittency model included, for a smooth airfoil. The STAN5 boundary layer analysis showed separation for the midspan pressure surface using the predicted inviscid flow field for a boundary condition and, therefore, the STAN5 prediction could not be obtained for the blade. The Navier–Stokes analyses do not indicate a significant increase in heat transfer due to blade surface roughness. On the pressure surface both of the fully turbulent analyses are in good agreement with the experimental data. However, on the suction surface these same predictions fall consistently above the data. The third prediction included on Fig. 11 is in essential agreement with the fully turbulent predictions on the pressure surface. On the suction surface, it also overpredicts the data, but is closer than the fully turbulent predictions. The predicted heat transfer at the leading edge is higher than the experimental data. The average augmentation of the heat transfer in the laminar region was calculated assuming a turbulence intensity of 10 percent. The transition model used a background turbulence intensity of 2 percent. The intermittency model overpredicted the heat transfer at the leading edge by about 33 percent. This indicates that the augmentation due to free-stream turbulence was excessive. The Froessling number at the stagnation region was calculated from the experimental results for this case, and using the cylinder in crossflow correlation of Traci and Wilcox (1975), a free-stream turbulence intensity of about 7 percent was estimated.

Along the entire pressure surface the fully turbulent predictions are nearly identical, and agree well with the experimental data. These predictions for the rotor are in contrast with those for the vane, where the pressure surface heat transfer

exceeded the fully turbulent prediction. The transitioning prediction, which includes the effect of free-stream turbulence, overpredicts the pressure surface heat transfer. The largest source of uncertainty in the heat transfer predictions is due to the uncertainty in the free-stream turbulence for the augmentation of the laminar viscosity due to this free-stream turbulence.

Blade Surface Roughness Considerations. The first-stage blade of this turbine appeared to be rough and there was concern that the roughness may enhance the heat transfer. Blair (1994) has illustrated that this enhancement can be significant. The influence of surface roughness on the blade data presented herein was therefore investigated.

Boyle and Civinskas (1991) investigated the influence of surface roughness on the predicted heat transfer to an airfoil surface. The effective roughness height was strongly dependent on both the roughness and the density. The roughness density can be found from the trace shown in Fig. 4(*b*). In this figure, the horizontal axis is compressed by more than a factor of ten over the vertical axis. Even though the blade shown in Figs. 3(*a*) and 3(*b*) is visibly rough, the peaks are not spaced closely together.

Comparing the two analyses shows that the effect of surface roughness is very small. This was not unexpected. The insensitivity to surface roughness is the result of both the low Reynolds number, and the effect of surface roughness density. In the Navier-Stokes analysis a reference y^+ was used for an a priori determination of the grid spacing. This reference value is given by

$$y^+_{\mathrm{REF}} = 0.17 y \mathrm{Re}^{0.9}/s^{0.1}$$

where y is the distance from the surface, Re is the exit Reynolds number per unit length, and s is a characteristic distance.

An analogous reference roughness height is

$$k^+_{\mathrm{REF}} = 0.17 k \mathrm{Re}^{0.9}/s^{0.1}$$

For the low Reynolds number case the exit unit Reynolds number was 1.28×10^7 m (3.9×10^6/ft).

The roughness height, k, in the above equations is not the actual roughness height, but rather the equivalent roughness height. The equivalent roughness height was estimated using the approach taken by Boyle and Civinskas (1991) to be less than 0.3 of the actual roughness height. Even though the actual roughness height was ~150,000 Å (590 min.), the value of k^+_{REF} was calculated to be only 2.7. This value of the reference roughness height is only approximate since it is based on a friction factor for a smooth flat plate. Nonetheless, the value of k^+ is less than the corresponding value of 5 for a hydraulically smooth surface. Consequently, the rough and smooth heat transfer predictions are nearly identical. It should be noted that blades with this surface roughness, when operated in the SSME environment, are no longer hydraulically smooth due to the much higher Reynolds number of the actual engine. Calculations showed an increase in heat transfer of up to 25 percent due to surface roughness at the SSME operating conditions for $K = 0.3$. The parameter K represents the ratio of the equivalent roughness height (k) to the actual roughness height.

Figure 12 presents the first blade midspan Stanton number data for the high Reynolds number case. Also included on this figure are three N-S predictions that were performed for different surface roughness heights. The N-S turbulent prediction with $K = 0$ is consistently above the N-S prediction with the Mayle and Dullenkopf intermittency model. The value of Stanton number at the stagnation point is predicted reasonably well by the N-S solution. On the suction surface, the N-S turbulent prediction for a smooth surface ($K = 0$) is consistently above the data. The prediction for $K = 0.3$ is about 12 percent higher over the initial 50 percent of the surface and then about the same over the remainder of the surface. The prediction for $K = 1.0$ represents a significant enhancement and is well above the data over the entire surface.

On the pressure surface of the blade, Fig. 12 illustrates that the shape of the predictions is consistent with the data. The predictions for $K = 0$ and $K = 0.3$ both fall below the data. The prediction for $K = 1.0$ is in reasonably good agreement with the data over the entire pressure surface.

Figures 13 and 14 present the experimental data and comparisons with predictions for the 10 percent span and the 90 percent span locations, respectively. Both sets of Reynolds number data are included on these figures. Figure 13 includes the fully turbulent N-S predictions for both Reynolds numbers and the N-S prediction with the Mayle and Dullenkopf intermittency model for the low Reynolds number. At the high Reynolds number, this prediction is essentially the same as the corresponding N-S fully turbulent prediction. For the suction surface there is very little difference among the three predictions. The data between 5 and 15 percent wetted distance are substantially below the predictions, while the data between 50 and 80 percent are below, but in reasonable agreement with the predictions. For the pressure surface, the fully turbulent prediction is generally below the data, while the intermittency model provides a reasonable representations of the data. The comparison presented in Fig. 14 for the 90 percent span location demonstrates reasonably good agreement between the data and the intermittency model prediction for the suction surface and correspondingly good agreement on the pressure surface for the N-S fully turbulent prediction.

Second Vane Stanton Number Results. The second vane Stanton number measurements are shown in Fig. 15 for both Reynolds number cases and both stage pressure ratios. For the second vane, only midspan heat-flux data were taken. Figure 15 also includes the predicted midspan Stanton number distributions. A fully turbulent and an intermittency model prediction are shown. The high Reynolds number intermittency prediction provides a good prediction at the stagnation point. On the suction surface, the fully turbulent and the low Reynolds number intermittency model predictions are conservative over the entire surface. The high Reynolds number intermittency model prediction is a better representation of the data. On the pressure surface, both the fully turbulent and the low Reynolds number intermittency models provide reasonable predictions of the data. The high Reynolds number intermittency model prediction on this surface is lower than the other two predictions by about 15 percent as would be anticipated.

Conclusions

Surface pressure and Stanton number distributions have been measured at selected locations on the first vane, first blade, and second vane of a full two-stage turbine. The first vane and first blade pressure measurements have been compared

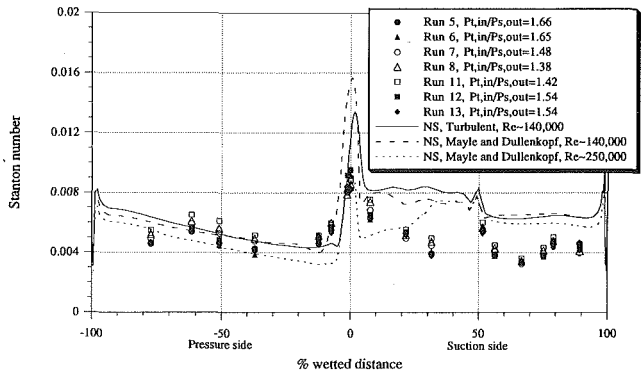

Fig. 15 Stanton number distribution on second vane, 50 percent span: closed symbols: Re ~ 140,000 data, open symbols: Re ~ 250,000 data

with the prediction, but the agreement was not particularly good because of difficulties with the measurement. The measured Stanton number distributions at midspan for the first vane and the first blade have been compared with predictions obtained using a quasi-three-dimensional N–S code and a modified STAN5 technique. For the first vane, comparisons were presented for the fully turbulent case and for the transition case using two transition models (Mayle, 1991; Dunham, 1972). At the low Reynolds number, the Mayle transition model and the fully turbulent prediction provided good agreement with the suction surface data. The fully turbulent, the Mayle transition model, and the Dunham transition model all provided good agreement with the suction surface data for the high Reynolds number case. The first vane pressure surface data were consistently underpredicted by all of the predictions. The sensitivity of the predictions to flow parameters such as turbulence intensity, coupled with the lack of agreement for the vane pressure surface heat transfer, illustrates the importance of correctly modeling the actual flow field in any heat transfer analysis.

The first blade data were compared to N–S turbulent and N–S with the Mayle and Dullenkopf (1989, 1991) intermittency model predictions. There is very little difference between the results of these two predictions. For the blade suction surface, the predictions were consistently above the data. The agreement between data and prediction for the pressure surface was reasonably good.

The surface of the blade used in these experiments appeared to be very rough. However, when the roughness density was accounted for, the analysis showed only a small increase in blade heat transfer due to surface roughness. The relatively good agreement between the measured and predicted blade heat transfer supports this conclusion. In the analysis the effect of surface roughness is strongly dependent on Reynolds number. Consequently, for the actual SSME engine operating conditions the analysis predicts a significant increase in blade heat transfer due to surface roughness.

The second vane data were compared with N–S fully turbulent calculations and with a N–S solution including the Mayle and Dullenkopf intermittency model. For the suction surface, both calculations were generally conservative. However, for the pressure surface, the predicted Stanton number distributions were in good agreement with the experimental data.

Acknowledgments

This research was supported under Grant No. NAG3-581 and monitored by Dr. R. Gaugler and Mr. K. Civinskas of the NASA Lewis Research Center, Cleveland, Ohio.

References

Blair, M. F., Dring, R. P., and Joslyn, H. D., 1989, "The Effects of Turbulence and Stator/Rotor Interactions on Turbine Heat Transfer: Part I: Design Operating Conditions," ASME JOURNAL OF TURBOMACHINERY, Vol. 111, pp. 87–96.

Blair, M. F., and Anderson, O. L., 1989, "The Effects of Reynolds Number, Rotor Incidence Angle and Surface Roughness on the Heat Transfer Distribution in a Large-Scale Turbine Rotor Passage," UTRC Report No. UTRC-R89-957852-24.

Blair, M. F., 1994, "An Experimental Study of Heat Transfer in a Large Scale Turbine Rotor Passage," ASME JOURNAL OF TURBOMACHINERY, Vol. 116, this issue, pp. 1–13.

Boyle, R. J., 1991, "Navier–Stokes Analysis of Turbine Blades Heat Transfer," ASME JOURNAL OF TURBOMACHINERY, Vol. 113, pp. 392–403.

Boyle, R. J., and Civinskas, K. C., 1991, "Two-Dimensional Navier–Stokes Heat Transfer Analysis for Rough Turbine Blades," AIAA/SAE/ASME 27th Joint Propulsion Conference, Paper No. AIAA-91-2129.

Chima, R. V., 1986, "Development of an Explicit Multigrid Algorithm for Quasi-Three-Dimensional Flows in Turbomachinery," AIAA Paper No. 86-0032; NASA TM-87128.

Civinskas, K. C., Boyle, R. J., and McConnaughey, H. V., 1988, "Impact of ETO Propellants on the Aerothermodynamic Analyses of Propulsion Components," AIAA/ASME/SAE/ASEE 24th Joint Propulsion Conference, Paper No. AIAA -88-3091.

Crawford, M. E., and Kays, W. M., 1976, "STAN5—A Program for Numerical Computation of Two-Dimensional Internal and External Boundary-Layer Flows," NASA CR-2742.

Dring, R. P., and Joslyn, H. D., 1986, "Through-Flow Analysis of a Multistage Compressor: Part 1—Aerodynamic Input," ASME JOURNAL OF TURBOMACHINERY, Vol. 108, pp. 17–22.

Dunham, J., 1972, "Predictions of Boundary Layer Transition on Turbomachinery Blades," AGARD-AG-164.

Dunn, M. G., and Stoddard, F. J., 1979, "Measurement of Heat Transfer Rate to a Gas Turbine Stator," ASME *Journal of Engineering for Power*, Vol. 101, pp. 275–280.

Dunn, M. G., and Hause, A., 1982, "Measurement of Heat Flux and Pressure in a Turbine Stage," ASME *Journal of Engineering for Power*, Vol. 104, pp. 215–223.

Dunn, M. G., Rae, W. J., and Holt, J. L., 1984, "Measurement and Analyses of Heat Flux Data in a Turbine Stage: Part II—Discussion of Results and Comparison With Predictions," ASME *Journal of Engineering for Gas Turbines and Power*, Vol. 106, pp. 234–240.

Dunn, M. G., Martin, H. L., and Stanek, M. J., 1986, "Heat-Flux and Pressure Measurements and Comparison With Prediction for a Low Aspect Ratio Turbine Stage," ASME JOURNAL OF TURBOMACHINERY, Vol. 108, pp. 108–115.

Dunn, M. G., 1986, "Heat-Flux Measurements for the Rotor of a Full-Stage Turbine: Part I—Time-Averaged Results," ASME JOURNAL OF TURBOMACHINERY, Vol. 108, pp. 90–97.

Dunn, M. G., and Chupp, R. E., 1988, "Time-Averaged Heat-Flux Distributions and Comparison With Prediction for the Teledyne 702 hp Turbine Stage," ASME JOURNAL OF TURBOMACHINERY, Vol. 110, pp. 51–56.

Dunn, M. G., and Chupp, R. E., 1989, "Influence of Vane/Blade Spacing and Injection on Stage Heat-Flux Distributions," AIAA *Journal of Propulsion and Power*, Vol. 5, No. 2, pp. 212–200.

Dunn, M. G., Bennett, W., Delaney, R., and Rao, K., 1990, "Investigation of Unsteady Flow Through a Transonic Turbine Stage: Part II—Data /Prediction Comparison for Time-Averaged and Phase-Resolved Pressure Data," AIAA/SAE/ASME/ASEE 26th Joint Propulsion Conference, Orlando, FL, AIAA Paper No. 90-2409.

Dunn, M. G., 1990, "Heat Transfer and Pressure Measurements for the SSME Fuel-Side Turbopump," *Proc. of the NASA 1990 Earth-to-Orbit Conference*, Marshall Space Flight Center, AL.

Dunn, M. G., and Kim, J., 1991, "Time Averaged and Phase-Resolved Heat-Transfer and Pressure Measurements for the Turbine of the SSME Fuel Side Turbopump," CUBRC Report No. 6401.

Gaugler, R. E., 1981, "Some Modifications to, and Operating Experiences With the Two-Dimensional Finite-Difference, Boundary-Layer Code STAN5," ASME Paper No. 81-GT-89.

Katsanis, T., 1969, "FORTRAN Program for Calculating Transonic Velocities on a Blade-to-Blade Stream Surface of a Turbomachine," NASA TN D-5427.

Katsanis, T., and McNally, W. D., 1977, "Revised FORTRAN Program for Calculating Velocities and Streamlines on the Hub-Shroud Mid-channel Stream Surface of an Axial-, Radial-, or Mixed-Flow Turbomachine or Annular Duct," Vol. I, User's Manual, Vol. II, Programmer's Manual, NASA TN D-8430, 8431.

Kline, S. J., and McClintock, F. A., 1953, "Describing Uncertainties in Single-Sample Experiments," *Mechanical Engineering*, Vol. 75, Jan. pp. 3–8.

Mayle, R. E., and Dullenkopf, K., 1989, "A Theory of Wake-Induced Transition," ASME JOURNAL OF TURBOMACHINERY, Vol. 112, pp. 188–195.

Mayle, R. E., 1991, "The Role of Laminar–Turbulent Transition in Gas Turbine Engines," ASME JOURNAL OF TURBOMACHINERY, Vol. 113, pp. 509–537.

Mayle, R. E., and Dullenkopf, K., 1991, "More on the Turbulent-Strip Theory for Wake-Induced Transition," ASME JOURNAL OF TURBOMACHINERY, Vol. 113, pp. 428–432.

Nealy, D. A., Mihele, M. S., Hylton, L. D., and Gladden, H. J., 1984, "Measurements of Heat Transfer Distribution Over the Surfaces of Highly Loaded Turbine Nozzle Guide Vanes," ASME *Journal of Engineering for Gas Turbines and Power*, Vol. 106, pp. 149–158.

Traci, R. M., and Wilcox, D. C., 1975, "Freestream Turbulence Effects on Stagnation Heat Transfer," *AIAA Journal*, Vol. 13, No. 7, pp. 890–896.

The Effects of Incident Turbulence and Moving Wakes on Laminar Heat Transfer in Gas Turbines

K. Dullenkopf

R. E. Mayle[1]

Institut für Thermische Strömungsmaschinen, Universität Karlsruhe, 76128 Karlsruhe, Germany

The effect of free-stream turbulence and moving wakes on augmenting heat transfer in accelerating laminar boundary layers is considered. First, the effect of free-stream turbulence is re-examined in terms of a Nusselt number and turbulence parameter, which correctly account for the free-stream acceleration and a correlation for both cylinders in crossflow and airfoils with regions of constant acceleration is obtained. This correlation is then used in a simple quasi-steady model to predict the effect of periodically passing wakes on airfoil laminar heat transfer. A comparison of the predictions with measurements shows good agreement.

Introduction

From a simple point of view, turbulence in the wakes from a preceding row of airfoils may be considered to be superposed on the free-stream or "background" turbulence such that the turbulence level incident to an airfoil row in a gas turbine varies something like that shown in Fig. 1. While this variation is accompanied by variations in the velocity, angle of attack, temperature, and the length scale of turbulence, only the effect of a temporal variation in free-stream turbulence will be considered in this paper. Neglecting the wakes from the airfoils two rows upstreams, the period of this variation will be $\tau = 2\pi/\omega$, where ω is the blade passing frequency of the upstream row of airfoils.

In general, designers always circumferentially mass average the flow and thermal energy leaving an airflow row, which in turn provides a "time-averaged" steady flow with a uniform turbulence level entering the next row. While this considerably simplifies the aerodynamic and heat transfer analysis through each row of airfoils, it generally leads to significant discrepancies when compared to time-averaged unsteady measurements. Comparisons of this type have only been made within the last decade. Most notable are those made by Dring et al. (1982, 1986), Hodson (1984), Dunn et al. (1986), and Dong and Cumpsty (1990a, b).

One difficulty in predicting the aerodynamic loss and heat transfer arises from the unsteady, wake-induced transition that occurs on the suction surface of most turbine airfoils. The wakes, passing with a period τ, induce a laminar-turbulent transition earlier than that which would occur for a steady, time-averaged incident flow. As a result, the time-averaged aerodynamic loss and heat load on the suction surface is usually underpredicted when the mass-averaged inlet flow conditions are used. Recently, Mayle and Dullenkopf (1990, 1991) showed how to incorporate this unsteady effect into a steady-flow analysis by introducing a time-averaged intermittency factor. In particular, they showed that the time-averaged Nusselt number distribution on the airfoil surface may be obtained from

$$\tilde{\mathrm{Nu}}(x) = [1 - \tilde{\gamma}(x)]\ \mathrm{Nu}_L(x) + \tilde{\gamma}(x)\mathrm{Nu}_T(x) \tag{1}$$

where $\tilde{\gamma}$ is the time-averaged intermittency factor, i.e., the average fraction of time that the boundary layer flow is turbulent, x is the streamwise coordinate along the airfoil's surface, and $\mathrm{Nu}_L(x)$ and $\mathrm{Nu}_T(x)$ are the laminar and turbulent Nusselt number distributions as calculated from a steady flow analysis. For transition through "multiple modes," they also showed that the intermittency factor $\tilde{\gamma}$ is given by

$$\tilde{\gamma} = [1 - \gamma_n(x)][1 - \tilde{\gamma}_w(x) \tag{2}$$

where γ_n and $\tilde{\gamma}_w$ are the intermittency factors for the steady, normal mode of transition (e.g., natural or bypass transition) and the unsteady, wake-induced mode, respectively. Equations and correlations for obtaining γ_n and $\tilde{\gamma}_w$ have since been provided by Mayle (1991).

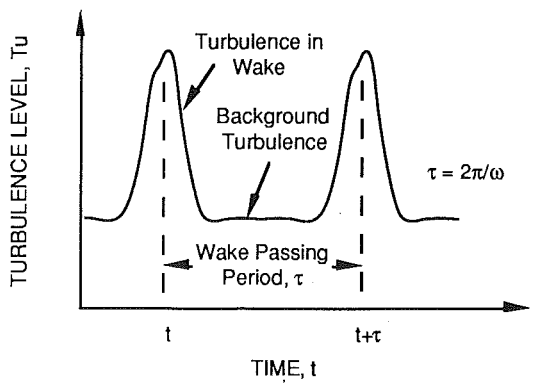

Fig. 1 Incident turbulence variation caused by passing wakes

[1]Present address: Department of Mechanical Engineering, Rensselaer Polytechnic Institute, Troy, NY 12180.

Contributed by the International Gas Turbine Institute and presented at the 37th International Gas Turbine and Aeroengine Congress and Exposition, Cologne, Germany, June 1-4, 1992. Manuscript received by the International Gas Turbine Institute February 17, 1992. Paper No. 92-GT-377. Associate Technical Editor: L. S. Langston.

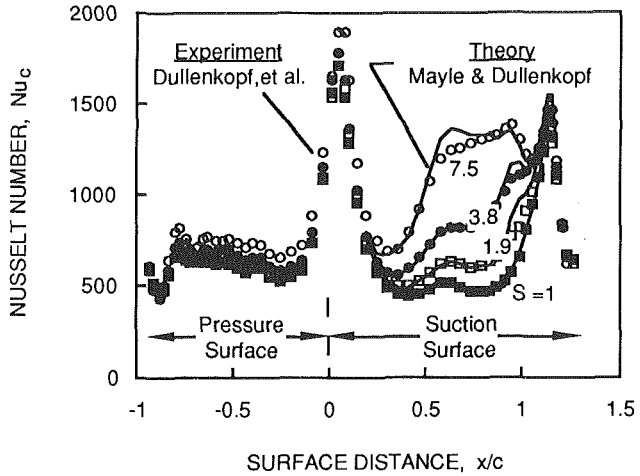

Fig. 2 Effect of passing wakes on airfoil Nusselt number distribution

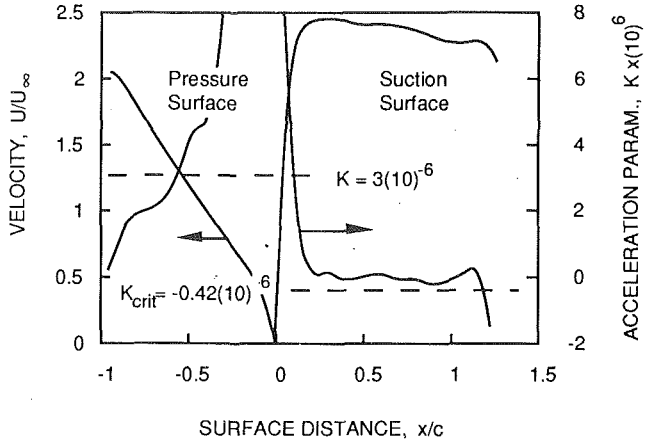

Fig. 3 Velocity and acceleration distributions for airfoil of Dullenkopf et al. (1991) with $Re_c = 380{,}000$

The effect of wake-induced transition on the time-averaged Nusselt number for the suction surface of a fore-loaded turbine airfoil is shown in Fig. 2. The measurements, obtained by Dullenkopf et al. (1991), are shown for both the pressure side, $x/c < 0$, and suction side, $x/c > 0$, of the airfoil for different wake passing frequencies expressed in the form of a Strouhal number, i.e., $S = \omega c/U_\infty$ where U_∞ is the incident velocity. A comparison between the transition theory just described and the measurements on the suction surface is also presented in the figure and is seen to be excellent.

While not so important when considering the aerodynamic loss of a turbine airfoil, the effect of incident turbulence and moving wakes on the laminar portions of the boundary layer when considering heat transfer, i.e., $Nu_L(x)$, is important. In these regions, it is not uncommon to find a 60 percent increase in the laminar heat transfer rate above that predicted. Here it is important to separate this increase, which results from the highly disturbed nature of the laminar boundary layer when a free-stream fluctuation, such as turbulence, is imposed on the flow, from that associated with laminar-turbulent transition. The increase in heat transfer resulting from free-stream turbulence is solely an unsteady effect within a completely, albeit highly disturbed, laminar boundary layer (see Paxson and Mayle, 1991). This response to free-stream turbulence is well known, particularly for steady flow around the forward portion of circular cylinders (see Schlichting, 1979), and is significant compared to that found for a turbulent boundary layer where the effect of free-stream turbulence on heat transfer is small (Blair, 1983). The effect is also small for laminar boundary-layer flow where, as will be seen, the free-stream acceleration is small. While this is the situation for most of the results shown in Fig. 2 on the suction surface, it is not the case for that on the pressure surface.

The free-stream velocity distribution and acceleration parameter of the airfoil used to obtain the data presented in Fig. 2 is shown in Fig. 3. The acceleration parameter, defined as $K = (\nu/U^2)(dU/dx)$ where ν is the kinematic viscosity and U is the free-stream velocity, has been plotted for a Reynolds number based on chord and incident velocity, i.e., $Re_c = U_\infty c/\nu$, of 380,000. Since $K \propto 1/Re_c$ for a given airfoil, incident angle, and cascade geometry, the acceleration parameter for smaller Reynolds numbers will be larger in magnitude. In addition, the value of K above which a laminar boundary will not transition, i.e., $K \approx 3(10)^{-6}$, and that below which it may separate before transition, i.e., $K < K_{crit} \approx -5.13(10)^{-7} Tu^{5/4}$ (see Mayle, 1991), are also shown. For the latter, the measured background turbulence of $Tu = 0.86$ (percent) was used. The velocity distribution is somewhat typical of a fore-loaded airfoil with a nearly constant acceleration on the pressure surface and a nearly constant velocity on the suction surface after a strong, initial acceleration. Over most of the suction surface, the acceleration parameter is slightly negative indicating a mild deceleration, but it is always greater than that which would cause separation to occur before transition. In fact, transition without wakes passing occurs via a bypass mode at $x/c = 0.95$ (see Mayle and Dullenkopf, 1990).

Since the acceleration parameter over most of the pressure surface is above $3(10)^{-6}$, the boundary layer there is mostly laminar and the measured increase in Nusselt number (Fig. 2 for $x/c < 0$) must be caused by the turbulence in the passing wakes. Since the free-stream strain rate $a = dU/dx$ is nearly constant on this surface, this flow must be similar to that found for stagnation flow or flow on the forward portion of a circular cylinder, except for magnitude. It follows, therefore, that the effect of free-stream turbulence and the turbulence within moving wakes on the heat transfer in the accelerating laminar boundary layer on this airfoil must be related to that for a

Nomenclature

a = strain rate $= dU/dx$
a_1 = dimensionless strain rate coefficient
b = blockage ratio
c = airfoil chord
d = cylinder diameter
h = heat transfer coefficient
k = thermal conductivity
K = acceleration parameter $= (\nu/U^2)(dU/dx)$
Nu = Nusselt number
P = wake or airfoil pitch
Pr = Prandtl number
Re = Reynolds number
S = Strouhal number
Tu = turbulence level
U = free-stream velocity
x = surface coordinate in streamwise direction
y = lateral distance, normal to flow
γ = intermittency
ν = kinematic viscosity
ρ = density
τ = wake-passing period
ω = blade passing frequency

Subscripts

a = quantity based on dU/dx
c = quantity based on chord
d = quantity based on diameter
L = laminar
n = normal transition mode
T = turbulent
w = wake induced transition mode
∞ = incident, or outside wake conditions

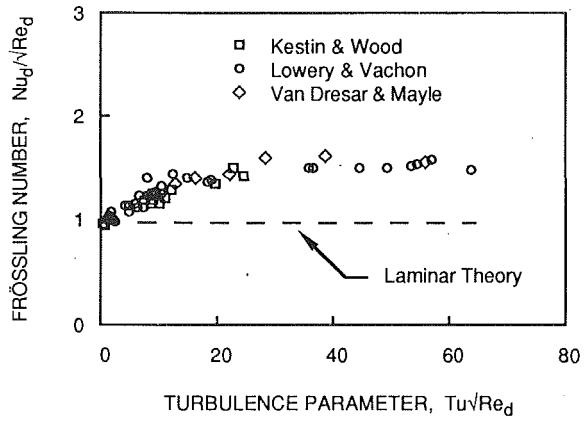

Fig. 4 Effect of incident turbulence level on the stagnation heat transfer from a cylinder in a crossflow

similar flow on the forward portion of a circular cylinder. The only problem appears to be one of finding the appropriate correlation parameters.

The present paper addresses this problem by first reviewing the literature regarding the effect of free-stream turbulence level on laminar heat transfer and coupling the results for stagnation flow on a cylinder to that for flow on an airfoil with constant acceleration. A simple theory is then presented for predicting the heat transfer augmentation as a result of a time-varing turbulence level. Finally, a comparison with the data shown in Fig. 2 is made and some conclusions drawn.

Effect of Turbulence on Laminar Heat Transfer

It is now recognized that the effect of free-stream turbulence on heat transfer in a laminar boundary layer is strongly coupled to the free-stream acceleration. In particular, Kestin et al. (1961) and Junkhan and Serovy (1967) showed that turbulence has no effect on heat transfer if the flow is nonaccelerating. For flows with acceleration, however, numerous experiments (Kestin et al., 1961; Junkhan and Serovy, 1967; Dyban and Epick, 1970; Kestin and Wood, 1971; Lowery and Vachon, 1975; Brown and Martin, 1979) have shown dramatic increases in heat transfer at relatively small free-stream turbulence levels.

Some results for a cylinder in a turbulent crossflow are presented in Fig. 4 where the Nusselt number at stagnation divided by the square root of the Reynolds number is plotted against the incident turbulence level times the square root of the Reynolds number. Both the Nusselt number and the Reynolds number are based on the diameter of the cylinder. Also, the Reynolds number and turbulence level are based on the incident velocity. For this plot, the absolute value of the turbulence level (not percent) is used. The data of Kestin and Wood and Van Dresar and Mayle (1989) were obtained using mass transfer techniques and the well-known heat/mass transfer analogy. Those of Lowery and Vachon are from heat transfer measurements. Despite the data scatter, an increase in heat transfer of 35 percent is found at a turbulence level of 5 percent for $Re_d = 100{,}000$, i.e., $Tu\sqrt{Re_d} \approx 16$.

In the past, although little has been done to determine the effect, the data scatter seen in Fig. 4 has been attributed to the length scale of turbulence (Yardi and Sukhatme, 1978). However, little attention has been paid to the effect of the free-stream strain rate $a = dU/dx$. Therefore, it is best to review the theory for heat transfer in a laminar boundary layer with a constant strain rate to ascertain the important parameters of this flow.

Frössling (1940) numerically evaluated the heat transfer in a laminar boundary with a variable free-stream acceleration and a Prandtl number of 0.7 using the series expansion technique. For stagnation flow, i.e., $U = ax$, he found $Nu_x\sqrt{Re_x} = h\sqrt{\nu/a}/k = \text{const}$, where h is the heat transfer coefficient and k is the thermal conductivity. The quantity $Nu_x/\sqrt{Re_x}$, where the Nusselt and Reynolds numbers are based on x and the Reynolds number is based on the local free-stream velocity U, is called the Frössling number. One may also call this quantity a Nusselt number based on the length scale $\sqrt{\nu/a}$. In order to avoid the confusion in the literature regarding Frössling numbers for flow around a cylinder, the latter outlook will be taken and a Nusselt number based on the length scale $\sqrt{\nu/a}$ will be defined, viz., $Nu_a \equiv h\sqrt{\nu/a}/k$. Later, Eckert (1942) obtained the solution for different Prandtl numbers, Pr, and provided a relatively simple expression for Nu_a, viz.,

$$Nu_a = 0.571\ Pr^{0.37}, \tag{3}$$

which for $Pr = 0.7$ yields $Nu_a = 0.5$.

When the incident flow is nonturbulent, heat transfer in laminar stagnation flow is determined by two characteristic length scales (one viscous, the other thermal) and one characteristic velocity scale. The characteristic viscous length scale is $\sqrt{\nu/a}$ and the characteristics velocity scale is $\sqrt{a\nu}$. The ratio between the viscous and thermal length scales is simply the Prandtl number. Hence, for a nonturbulent incident flow, the Nusselt number Nu_a can only be a function of the Prandtl number as seen in Eq. (3). When the incident flow is turbulent, however, one must also consider the characteristic turbulence intensity, say u', and length scale, say L. Hence, Nu_a for a turbulent incident flow can be a function of Pr, $u'/\sqrt{a\nu}$ and $L\sqrt{a/\nu}$, or a combination thereof. Although the scale of turbulence is known to have an effect (see Yardi and Sukhatme), measurements are scant and it will presently be considered that the main effect of turbulence may be characterized for the most part by

$$Nu_a \approx fnc(\text{Pr},\ Tu_a) \tag{4}$$

where the characteristic turbulence parameter has been defined as $Tu_a \equiv u'/\sqrt{a\nu}$.

For flow around a cylinder, the velocity near stagnation varies according to $U = a_1 U_\infty x/d$. Using $a = a_1 U_\infty/d$, the Nusselt number $Nu_a = h\sqrt{\nu/a}/k$ becomes

$$Nu_a = Nu_d/\sqrt{a_1 Re_d} \tag{5}$$

and the turbulence parameter Tu_a becomes

$$Tu_a = Tu\ \sqrt{Re_d/a_1} \tag{6}$$

In this case, the turbulence intensity has been defined as $u' \equiv TuU_\infty$. Hence, as they stand, the coordinates in Fig. 4 are not sufficient to characterize the effect of incident turbulence on laminar heat transfer for a cylinder since both $Nu_d/\sqrt{Re_d} = 0.571\sqrt{a_1}Pr^{-0.37}$ and $Tu\sqrt{Re_d} = Tu_a\sqrt{a_1}$ depend on the coefficient a_1.

For potential flow around a circulation cylinder $a_1 = 4$. Kwon et al. (1983) report $a_1 = 3.63$ as typical for flow around a circulation cylinder without blockage, while Van Dresar and Mayle measured values as low as 2.3. In general, the coefficient a_1 for a circular cylinder depends on Reynolds number, blockage, and incident turbulence level. A correlation that accounts for these effects was obtained by Dyban and Epick (1985) and is given by

$$a_1 = 4.0 - 1.15\ Re_d^{-0.01} + 2b/(1+b) - 2\ Tu$$

where b is the blockage ratio. For the values $Re_d = 10^5$, $b = 0.1$, and $Tu = 0.05$, this expression yields $a_1 = 3.09$.

The data presented in Fig. 4 were replotted using Eqs. (5) and (6) to obtain Nu_a and Tu_a for stagnation flow on a cylinder. For Van Desar and Mayle's data, the measured values of the acceleration coefficient were used. For the data of Kestin and Wood, and Lowery and Vachon, values of a_1 were obtained using Dyban and Epick's expression. The resulting plot is shown in Fig. 5. While only marginally successful in collapsing the data, plotting the data in this format does produce a noticeable

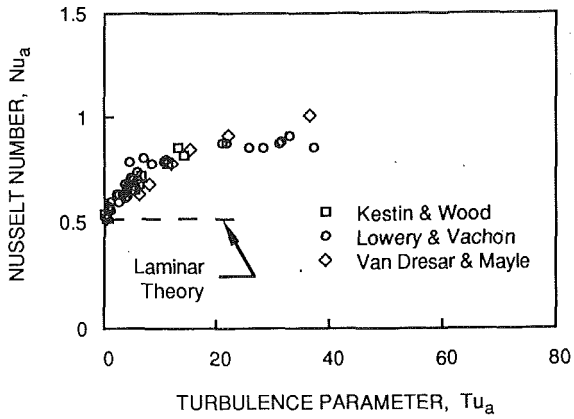

Fig. 5 Cylinder heat transfer results plotted in a format independent of diameter

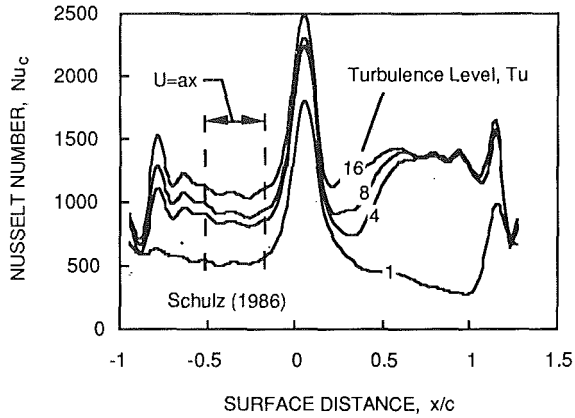

Fig. 6 Effect of incidence turbulence level on airfoil Nusselt numbers

realignment at the higher turbulence levels and, as will be seen shortly, allows a correlation of both cylinder and airfoil data.

For flow on an airfoil in a region where $U = ax$, the free-stream velocity may be expressed as $U = a_1 U_\infty x/c$ where U_∞ is the incident velocity. Using $a = a_1 U_\infty / c$, the Nusselt number $\sqrt{Nu_a} = h\sqrt{\nu/a}/k$ becomes

$$\mathrm{Nu}_a = \mathrm{Nu}_c / \sqrt{a_1 \mathrm{Re}_c} \tag{7}$$

where Nu_c is the local Nusselt number based on the chord length and Re_c is the Reynolds number based on the incident velocity and chord length. The turbulence parameter $Tu_a = u'/\sqrt{av}$ $(= TuU_\infty/\sqrt{av})$ becomes

$$Tu_a = Tu\sqrt{\mathrm{Re}_c/a_1} \tag{8}$$

In this case, of course, the value of a_1 depends on the airfoil's design. For the airfoil velocity distribution shown in Fig. 3, two regions of constant acceleration are found. One is near the leading edge on the suction surface at stagnation, where $a_1 \approx 32$, while the other is over the forward portion of the pressure surface where $a_1 \approx 1.9$. As discussed before, a laminar boundary layer is likely in both.

Heat transfer measurements for this airfoil at different incident turbulence levels were obtained by Schulz (1986) and are shown in Fig. 6. The highest values of Nusselt number are evident at stagnation near the leading edge where the acceleration is the largest (see Fig. 3). The results on the suction surface are typical in that they reflect an earlier transition with increasing turbulence. Transition here is via the bypass mode. On the pressure surface, the Nusselt number is nearly constant within the region having a constant strain rate a, but increases with increasing turbulence level in a manner similar to that on the forward portion of a cylinder. These data were used to calculate Nu_a and Tu_a according to Eqs. (7) and (8) for the region of constant acceleration on the pressure surface. A similar procedure was followed to evaluate Nu_a and Tu_a using Priddy and Bayley's (1988) and Turner's (1971) pressure side measurements. Both Priddy and Bayley, and Turner tested foreloaded airfoils, which had substantial regions where $U = ax$ on their pressure surfaces.

The results of these calculations are shown in Fig. 7 together with the data from Fig. 5 for cylinders. The airfoil data are presented using solid symbols, while the cylinder data are presented using open symbols. Both Kestin and Wood's, and Lowery and Vachon's data are shown using the same symbol to indicate that their data were obtained using calculated values of the acceleration coefficient. A previously pointed out, Van Dresar and Mayle's results were obtained using their measured values. The relevant Reynolds numbers for the data shown in this figure vary from 75,000 to 460,000, turbulence levels vary from 0.2 to 17 percent, and the coefficients a_1, vary from 1.1 to 4.4. The effect of the latter is well illustrated by comparing

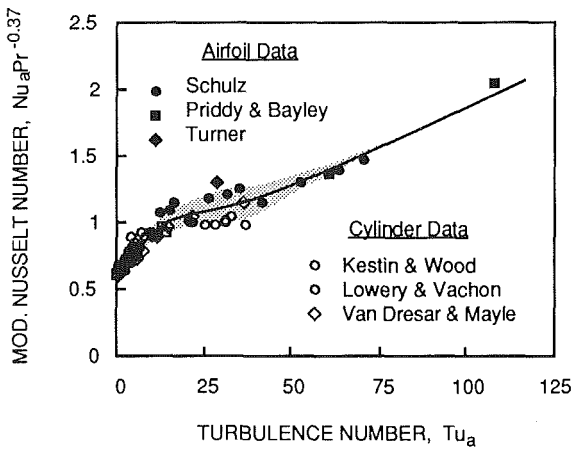

Fig. 7 Correlation of cylinder and airfoil Nusselt numbers for laminar flow with $U = ax$

the data of Priddy and Bayley's at $Tu_a = 108$ with that of Schulz at $Tu_a = 70$. Both data are for airfoils with an incident turbulence level of about 16 percent and nearly the same chord Reynolds numbers. The coefficients a_1, respectively 1.13 and 1.95, however, are substantially different.

The large data scatter at the low values of Tu_a (shaded area) are presently attributed to the effects of turbulent length scale. At these values, it is thought that the turbulent energy within the necessary range of length scales to cause an increase in heat transfer is highly dependent on both the turbulence level and the method of producing the turbulence (integral length scale). At higher turbulence levels, however, the energy necessary to produce the increase is probably always available, and independent of the level and the method used. A correlation of the results that best fits both the airfoil and cylinder data was found to be given by

$$\mathrm{Nu}_a \mathrm{Pr}^{-0.37} = 0.571 + 0.0125\ Tu_a \left\{ 1 + \frac{1.8}{[1 + (Tu_a/20)^3]} \right\} \tag{9}$$

where Tu_a is evaluated using the absolute incident turbulence level and not percent. This correlation is also shown in Fig. 7.

The correlation and data scatter band are reproduced in Fig. 8 together with the theory presented by Smith and Kuethe (1966). They solved the time-averaged equations of motion and energy for a laminar flow with free-stream turbulence by relating the turbulent viscosity to the turbulence in the free stream. In the present notation, their theory provides

$$\mathrm{Nu}_a \mathrm{Pr}^{-0.37} = 0.571 + 0.0316\ Tu_a$$

As seen in Fig. 8, this result is only good for low values of

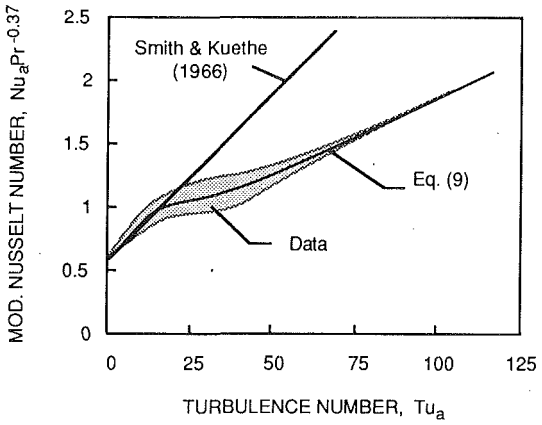

Fig. 8 Comparison of cylinder and airfoil data with theory

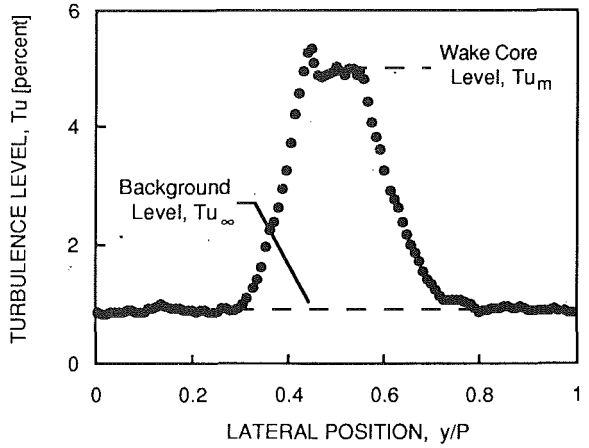

Fig. 9 Variation of incident turbulence in one pitch for the test results shown in Fig. 2 with S = 3.8

the free-stream turbulence parameter, i.e., $Tu_a \leq 10$. At higher values, the increase is about half that predicted by their theory. In fact, for $Tu_a \geq 50$, Eq. (9) yields

$$\mathrm{Nu}_a \mathrm{Pr}^{-0.37} \approx 0.571 + 0.0125\ Tu_a$$

These two expressions, diverging in behavior, may indicate that the effect of free-stream turbulence on laminar heat transfer involves two very different physical mechanisms: one at low levels and another at high levels. In fact, these two linear expressions may simply represent the upper and lower limits of data for all turbulence levels and length scales.

A Simple Theory

Recently, Van Dresar and Mayle (1989) presented two simple quasi-steady models to account for the effect of turbulence in moving wakes on the time-averaged laminar Nusselt number. One uses the wake turbulence distribution $Tu(y)$, while the other uses the wake intermittency distribution $\gamma(y)$ together with the maximum turbulence level in the wake. In these expressions, y is the coordinate measured across the wake. Both models assume that the boundary layer reacts immediately to the impressed free-stream turbulence. For gas turbine type flows, Paxson and Mayle showed this to be true. The expressions proposed by Van Dresar and Mayle for the time-averaged Nusselt number are:

Model using the wake turbulence distribution

$$\tilde{\mathrm{Nu}} = \frac{1}{\tau}\int_t^{t+\tau} \mathrm{Nu}[Tu(t)]dt = \int_0^1 \mathrm{Nu}[Tu(y)]d(y/P) \qquad (10)$$

where τ is the wake passing period and P is the pitch of the wakes, i.e., pitch of the upstream row of airfoils. Here, as in all of the following expressions, the subscript L on the Nusselt number has been dropped in order to make the subscripts less cumbersome, i.e., Nu_L (see Eq. (1)) is now being replaced by Nu.

Model using the wake intermittency distribution

$$\tilde{\mathrm{Nu}} = \frac{1}{\tau}\int_t^{t+\tau} \mathrm{Nu}dt = \mathrm{Nu}_\infty + (\mathrm{Nu}_m - \mathrm{Nu}_\infty)\int_0^1 \gamma(y)d(y/P)$$

where Nu_∞ and Nu_m are, respectively, the Nusselt numbers one obtains using the free-stream (background) turbulence level and maximum level of turbulence in the wake, i.e., $\mathrm{Nu}_\infty = \mathrm{Nu}(Tu_\infty)$ and $\mathrm{Nu}_m = \mathrm{Nu}(Tu_m)$.

They compared these models to experimental results and showed that the transfer rate on the forward portion of a cylinder within a wake caused by another upstream cylinder is best represented by the intermittency model. They also showed that the turbulence model overpredicts the time-averaged, wake-augmented increase by about 20 percent. Fortunately, since the intermittency distribution is generally not known nor measured, this discrepancy is small enough such that the turbulence model may be sufficient to predict the effect. In Fig. 2, the discrepancy between the two models amounts to an error equal to the size of the symbols used in the figure.

The time-varying turbulence level (streamwise and lateral components) of the incident flow entering the cascade was measured for the test with S = 3.8 whose results are shown in Fig. 2. The measurements are presented in Fig. 9 as a turbulence level versus the fractional distance between the wakes. Here, it appears that the wake is "buried" in a flow with a background turbulence level somewhat less than one percent. The maximum turbulence level in the wake is about 5 percent. If this distribution is used to determine the time-averaged Nusselt number on the pressure surface for the test results shown in Fig. 2 (using Eqs. (9) and (10) with $\mathrm{Nu} = \mathrm{Nu}_a\sqrt{a_1 \mathrm{Re}_c}$ and the measured value of $a_1 = 1.95$), the resulting predicted value is $(\tilde{\mathrm{Nu}})_{S=3.8} = 644$. The Nusselt number obtained from Eq. (9) using the background turbulence level is $\mathrm{Nu}_\infty = 542$. For a given a_1 and turbulence distribution, both Nu_S and Nu_∞ are independent of x.

Assuming that the wakes do not overlap to cause an increase in background turbulence, it is easy to show (using Eq. (10)) that the time-averaged Nusselt number at any wake passing frequency (for the test results shown in Fig. 2) is given by

$$\tilde{\mathrm{Nu}} = \mathrm{Nu}_\infty + \frac{S}{3.8}\left[(\tilde{\mathrm{Nu}})_{S=3.8} - \mathrm{Nu}_\infty\right] \qquad (11)$$

This expression was used to evaluate the time-averaged Nusselt number distributions for S = 3.8 and 7.5. The results are shown in Fig. 10. In this plot, however, the measured Nusselt number distribution for S = 0 (i.e., no wakes) was used for $\mathrm{Nu}_\infty(x)$. This was done to compensate partially for the slight variation in a_1 (see Fig. 3) over the pressure surface. If Nu_∞ were obtained from a boundary layer computational program, this would be unnecessary. In any event, the quasi-steady model using an augmented heat transfer as described by Eq. (9) is seen to predict the time-averaged effect of periodically passing wakes on heat transfer quite well.

Conclusions

Data for heat transfer on the forward portion of circular cylinders and on airfoils with a constant free-stream strain rate and different free-stream turbulence levels were found to correlate using a Nusselt number and turbulence parameter, which depend on the strain rate $a = U/x$. The correct Nusselt number

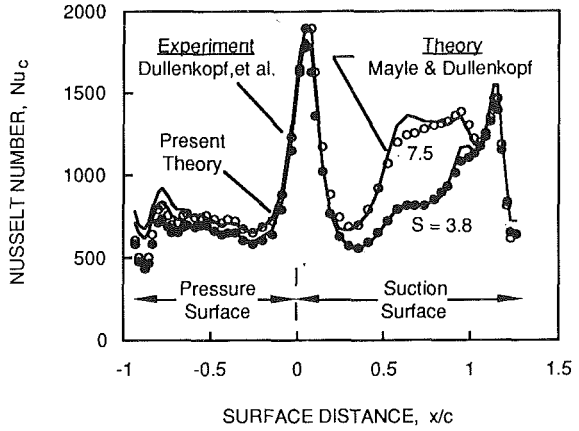

Fig. 10 Comparison of the quasi-steady model and new heat transfer correlation with data

for these flows is $\mathrm{Nu}_a = h\sqrt{\nu/a}/k$ and the correct turbulence parameter appears to be $Tu_a = u'/\sqrt{a\nu}$ where u' is the turbulence intensity. A correlation that best fits both the cylinder and airfoil data was found to be

$$\mathrm{Nu}_a \mathrm{Pr}^{-0.37} = 0.571 + 0.0125\ Tu_a \left\{ 1 + \frac{1.8}{[1 + (Tu_a/20)^3]} \right\}$$

Heat transfer data on the pressure side of an airfoil with wakes passing at various frequencies was compared to a simple quasi-steady model, viz.,

$$\tilde{\mathrm{Nu}} = \frac{1}{\tau} \int_t^{t+\tau} \mathrm{Nu}[Tu(t)]dt$$

where $\mathrm{Nu} = \mathrm{Nu}_a\sqrt{a_1 \mathrm{Re}_c}$ is the Nusselt number in the laminar portion of the flow. This model assumes that the laminar boundary layer reacts immediately to the impressed free-stream turbulence. When the correlation above was used to obtain Nu_a, the agreement was found to be very satisfactory for the present set of data.

References

Bayley, F. J., and Priddy, W. J., 1981, "Effects of Free-Stream Turbulence Intensity and Frequency on Heat Transfer to Turbine Blading," ASME JOURNAL OF ENGINEERING FOR POWER, Vol. 103, pp. 60–64.

Blair, M. F., 1983, "Influence of Free-Stream Turbulence on Turbulent Boundary Layer Heat Transfer and Mean Profile Development, Part I—Experimental Data," ASME *Journal of Heat Transfer*, Vol. 105, pp. 33–40.

Brown, A., and Martin, B. W., 1979, "Heat Transfer to Turbine Blades, With Special Reference to the Effects of Mainstream Turbulence," ASME Paper No. 79-GT-26.

Dong, Y., and Cumpsty, N. A., 1990a, "Compressor Blade Boundary Layers: Part 1—Test Facility and Measurements With No Incident Wakes," ASME JOURNAL OF TURBOMACHINERY, Vol. 112, pp. 220–230.

Dong, Y., and Cumpsty, N. A., 1990b, "Compressor Blade Boundary Layers: Part 2—Measurements With Incident Wakes," ASME JOURNAL OF TURBOMACHINERY, Vol. 112, pp. 231–240.

Dring, R. P., Joslyn, H. D., Hardin, L. W., and Wagner, J. H., 1982, "Turbine Rotor-Stator Interaction," ASME JOURNAL OF ENGINEERING FOR POWER, Vol. 104, pp. 729–742.

Dring, R. P., Blair, M. F., Joslyn, H. D., Power, G. D., and Verdon, J. M., 1986, "The Effects of Inlet Turbulence and Rotor/Stator Interactions on the Aerodynamics and Heat Transfer of a Large-Scale Rotating Turbine Model," NASA CR 4079.

Dunn, M. G., Martin, H. L., and Stanek, M. J., 1986, "Heat-Flux and Pressure Measurements and Comparison With Prediction for a Low-Aspect-Ratio Turbine Stage," ASME JOURNAL OF TURBOMACHINERY, Vol. 108, pp. 108–115.

Dullenkopf, K., Schultz, A., and Wittig, S., 1991, "The Effect of Incident Wake Conditions on the Mean Heat Transfer of an Airfoil," ASME JOURNAL OF TURBOMACHINERY, Vol. 113, pp. 412–418.

Dyban, E., and Epick, E., 1970, "Some Heat Transfer Features in the Air Flow of Intensified Turbulence," *Proc. 4th Int. Heat Transfer Conf.*, Paris.

Dyban, E., and Epick, E., 1985, *Thermal/Mass Transport and Hydrodynamics of Turbulent Flows*, Kiev [in Russian].

Eckert, E., 1942, "Die Berechnung des Wärmeübergangs in der laminar Grenzschicht umströmter Körper," *VDI-Forschungsheft* 416.

Frössling, N., 1940, "Verdunstung, Wärmeübertragung und Geschwindigkeitsverteilung bei zweidimensionaler und rotation-ssymetrischer Grenzschichtströmung," Lunds Universitets Arsskrift, N. F. Avd. 2, 36.

Hodson, H. P., 1984, "Boundary Layer and Loss Measurements on the Rotor of an Axial-Flow Turbine," ASME *Journal of Engineering for Gas Turbines and Power*, Vol. 106, pp. 391–399.

Junkhan, G. H., and Serovy, G. K., 1967, "Effects of Free-Stream Turbulence and Pressure Gradient on Flat-Plate Boundary-Layer Velocity Profiles and on Heat Transfer," ASME *Journal of Heat Transfer*, Vol. 89, pp. 169–176.

Kestin, J., Maeder, P. F., and Wang, H. E., 1961, "Influence of Turbulence on the Transfer of Heat From Plates With and Without a Pressure Gradient," *Int. J. Heat Mass Transfer*, Vol. 3, pp. 133–154.

Kestin, J., and Wood, R. T., 1971, "The Influence of Turbulence on Mass Transfer From Cylinders," ASME *Journal of Heat Transfer*, Vol. 93, pp. 321–327.

Kwon, O. K., Turner, E. R., and Kou, Y. M., 1983, "Prediction of Stagnation Flow Heat Transfer on Turbomachinery Airfoils," AIAA Paper No. 83-1173.

Lowery, G. W., and Vachon, R. L., 1975, "The Effect of Turbulence on Heat Transfer From Heated Cylinders," *Int. J. Heat Mass Transfer*, Vol. 18, pp. 1229–1242.

Mayle, R. E., and Dullenkopf, K., 1990, "A Theory for Wake-Induced Transition," ASME JOURNAL OF TURBOMACHINERY, Vol. 112, pp. 188–195.

Mayle, R. E., 1991, "The Role of Laminar-Turbulent Transition in Gas Turbine Engines," 1991 ASME International Gas Turbine Institute Scholar Award Paper, ASME JOURNAL OF TURBOMACHINERY, Vol. 113, pp. 509–537.

Mayle, R. E., and Dullenkopf, K., 1991, "More on the Turbulent-Strip Theory for Wake-Induced Transition," ASME JOURNAL OF TURBOMACHINERY, Vol. 113, pp. 428–432.

Paxson, D. E., and Mayle, R. E., 1991, "Laminar Boundary Layer Interaction With an Unsteady Passing Wake," ASME JOURNAL OF TURBOMACHINERY, Vol. 113, pp. 419–427.

Priddy, W. J., and Bayley, F. J., 1988, "Turbulence Measurements in Turbine Blade Passages and Implications for Heat Transfer," ASME JOURNAL OF TURBOMACHINERY, Vol. 110, pp. 73–79.

Schlichting, H., 1979, *Boundary-Layer Theory*, McGraw-Hill, New York.

Schultz, A., 1986, "Zum Einfluß hoher Freistromturbulenz, intensiver Kühlung und einer Nachlaufstömung auf den äußeren Wärmeübergang einer konvektiv gekülten Gasturbinenschaufel," Ph.D. Thesis, U. Karlsruhe, Karlsruhe, Federal Republic of Germany.

Smith, M., and Kuethe, A., 1966, "Effects of Turbulence on Laminar Skin Friction and Heat Transfer," *Physics of Fluids*, Vol. 9, pp. 2337–2344.

Turner, A. B., 1971, "Local Heat Transfer Measurements on a Gas Turbine Blade," *J. Mech. Engng. Science*, Vol. 13, pp. 1–12.

Van Dresar, N., and Mayle, R. E., 1989, "A Quasi-Steady Approach to Leading Edge Transfer Rates," ASME JOURNAL OF TURBOMACHINERY, Vol. 111, pp. 483–490.

Yardi, N. R., and Sukhatme, S. P., 1978, "Effect of Turbulence Intensity and Integral Length Scale of a Turbulent Free Stream on Forced Convection Heat Transfer From a Circular Cylinder in Crossflow," *Proceedings 6th International Heat Transfer Conference*, Toronto, Canada, Vol. 5, FC(b)-29, pp. 347–352.

Wittig, S., Schulz, A., Dullenkopf, K., and Fairbank, J., 1988, "Effects of Free-Stream Turbulence and Wake Characteristics on the Heat Transfer Along a Cooled Gas Turbine Blade," ASME Paper No. 88-GT-179.

Wake-Induced Unsteady Stagnation-Region Heat Transfer Measurements

P. J. Magari[1]

L. E. LaGraff

Department of Mechanical and Aerospace Engineering, Syracuse University, Syracuse, NY 13244

An experimental investigation of wake-induced unsteady heat transfer in the stagnation region of a cylinder was conducted. The objective of the study was to create a quasi-steady representation of the stator/rotor interaction in a gas turbine using two stationary cylinders in crossflow. In this simulation, a larger cylinder, representing the leading-edge region of a rotor blade, was immersed in the wake of a smaller cylinder, representing the trailing-edge region of a stator vane. Time-averaged and time-resolved heat transfer results were obtained over a wide range of Reynolds number at two Mach numbers: one incompressible and one transonic. The tests were conducted at Reynolds numbers, Mach numbers, and gas-to-wall temperature ratios characteristic of turbine engine conditions in an isentropic compression-heated transient wind tunnel (LICH tube). The augmentation of the heat transfer in the stagnation region due to wake unsteadiness was documented by comparison with isolated cylinder tests. It was found that the time-averaged heat transfer rate at the stagnation line, expressed in terms of the Frossling number ($Nu/\sqrt{Re}$), reached a maximum independent of the Reynolds number. The power spectra and cross-correlation of the heat transfer signals in the stagnation region revealed the importance of large vortical structures shed from the upstream wake generator. These structures caused large positive and negative excursions about the mean heat transfer rate in the stagnation region.

Introduction

The importance of wake passing to the heat transfer and aerodynamics of a downstream turbomachinery blade has inspired a great deal of research in recent years (e.g., Doorly and Oldfield, 1985; O'Brien et al., 1986; Ashworth et al., 1985; Wittig et al., 1988; Guenette et al., 1989). Because of the high degree of unsteadiness in the wake, premature boundary-layer transition and highly augmented stagnation-region heat transfer result from wake interaction. The stagnation region is of particular interest because this is usually the region of highest heat transfer rate, and the physical mechanism by which the heat transfer augmentation occurs in this region is not well understood at present. Consequently, accurate prediction of the wake-augmented heat transfer in this region has not been fully achieved as yet.

In the present experiment, a larger diameter cylinder (representing the leading edge of a rotor blade) was immersed in the wake of a smaller diameter cylinder (representing the trailing edge of a stator vane). The purpose of the study was to investigate the effect of wake interaction in the stagnation region of a simulated rotor blade and to determine how the wake and its internal structure influence the heat transfer in the stagnation region of a downstream blade. The intention was not to complicate the experiment by introducing relative motion between the two cylinders in the hope that some fundamental insight to the problem could be gained through a quasi-steady representation of the phenomenon, which might otherwise be difficult to extract from a wake-passing type experiment.

The literature relevant to stagnation-point heat transfer and the heat transfer to a cylinder is quite vast, but several significant studies stand out. The first analytical work presented on the subject was given by Frossling (1958) who provided a semi-analytical solution for the Frossling number, $Nu/\sqrt{Re}$, as a function of the angular position from the stagnation point (θ in radians):

$$\frac{Nu}{\sqrt{Re}} = 0.9449 - \frac{0.510}{4}\theta^2 - \frac{0.596}{16}\theta^4 \qquad (1)$$

This relation is valid for the laminar region on the front face of a cylinder ($\theta \leq 55$ deg) in a fluid with a Prandtl number of 0.7 and a wall temperature slightly lower than the free-stream temperature. The solution is semi-analytical in that it utilizes an experimentally measured pressure distribution at a relatively low Mach number and low Reynolds number.

Frossling's solution is only valid in an incompressible flow, and no similar result exists for compressible flow around a cylinder. White (1974), however, provided an analytical estimate of the stagnation-point heat transfer in a compressible flow. The relation shows that the stagnation-point heat transfer

[1]Present address: Creare Inc., Hanover, NH.

Contributed by the International Gas Turbine Institute and presented at the 37th International Gas Turbine and Aeroengine Congress and Exposition, Cologne, Germany, June 1-4 1992. Manuscript received by the International Gas Turbine Institute February, 17, 1992. Paper No. 92-GT-196. Associate Technical Editor: L. S. Langston.

decreases with Mach number in the subsonic regime and increases with gas-to-wall temperature ratio. No experimental studies on the heat transfer distribution on a cylinder are presented in the literature at transonic Mach numbers. However, Nagamatsu and Duffy (1984) measured the stagnation-point heat transfer on a cylinder at a Mach number of 0.45 and a gas-to-wall temperature ratio of 1.5 and found that Frossling's solution underpredicted the heat transfer rate there. The only other relevant measurements on a cylinder in transonic flow reported in the literature are the skin-friction measurements performed by Murthy and Rose (1978). They measured the skin-friction distribution in the laminar boundary-layer region of a cylinder and found that for supercritical Mach numbers, the skin-friction coefficient away from the stagnation line was considerably lower than at subcritical Mach numbers.

The effect of turbulence intensity and scale upon stagnation-region heat transfer has been the subject of much study for some time. One of the earliest studies was that by Smith and Kuethe (1986) who used an eddy-viscosity model to estimate the enhancement of the stagnation-point heat transfer by free-stream turbulence. Their model revealed the quantity $Tu\sqrt{\mathrm{Re}}$ as an important correlation parameter for stagnation-point heat transfer in the presence of elevated free-stream turbulence levels. Many of the correlation equations presented in the literature utilize this parameter exclusively, and consequently they do not take into account any effect due to the turbulence length scale. One such correlation is that provided by Lowery and Vachon (1975):

$$\frac{\mathrm{Nu}}{\mathrm{Re}^{1/2}} = 1.010 + 2.624\left[\frac{Tu\ \mathrm{Re}^{1/2}}{100}\right] - 3.070\left[\frac{Tu\ \mathrm{Re}^{1/2}}{100}\right]^2 \quad (2)$$

The above equation is valid in the range $0 < Tu\sqrt{\mathrm{Re}} < 64$ (where Tu is an absolute fraction here). The correlation indicates, as do the experimental data, that the stagnation-point Frossling number reaches an asymptotic value of approximately 1.6 for $Tu\sqrt{\mathrm{Re}} \approx 45$, beyond which further increases in the stagnation-region Frossling number were not observed with increases in either Tu or Re. The asymptotic value of approximately 1.6 has been observed by others, although some investigators (e.g., Zukaskas, 1985) report stagnation-point Frossling numbers above 2 for high values of $Tu\sqrt{\mathrm{Re}}$. More data are needed at high values of the parameter $Tu\sqrt{\mathrm{Re}}$ to make any definitive statements in this regard. The effect of turbulence length scale on stagnation-point heat transfer has been a subject of intensive study (e.g., Yardi and Sukhatme, 1978; VanFossen and Simoneau, 1985; Gorla, 1984), but few conclusions have been drawn. The only universal conclusion that can be drawn from these studies, which seems to be physically intuitive anyway, is that smaller scales are more effective at enhancing the heat transfer in the stagnation region than larger scales. It is also generally conjectured that eddies whose axes are aligned perpendicular to the mean flow and the axis of the cylinder are the most effective at augmenting the stagnation-region heat transfer. Eddies whose axes are aligned in this manner are stretched by streamline divergence in the stagnation region. Once these vortex filaments enter the boundary layer, they cause significant three-dimensional effects believed to be the mechanism responsible for augmenting the stagnation-region heat transfer in the presence of free-stream turbulence (see Sutera et al., 1963, for a discussion of this proposed mechanism).

Because of its geometric simplicity, the cylinder has been utilized by a host of investigators interested in fundamental studies of the heat transfer near the leading edge of a turbine blade (e.g., VanFossen and Simoneau, 1985; O'Brien and Capp, 1988; Van Dressar and Mayle, 1989). The simulation of the trailing edge of a stator blade by a cylinder was introduced by Doorly and Oldfield (1985) in a classic experiment, which utilized a rotating spoked-wheel wake generator to simulate wake-passing events in a two-dimensional cascade, and the simulation has been used extensively since (see, for example, O'Brien et al., 1986; Wittig et al., 1988; LaGraff et al., 1989; Van Dressar and Mayle, 1989). Doorly and Oldfield showed that the simulation was quite good in terms of producing the correct wake-defect profiles and relative velocity-vector diagram. Recent tests on a common blade profile by Guenette et al. (1989) and Ashworth et al. (1985) showed remarkable correspondence between the midspan time-resolved heat transfer in the real rotating stage and the passing bar-wake simulation in a fixed two-dimensional cascade. Actual turbine blade wakes and cylinder-simulated wakes have been compared by Pfeil and Herbst (1979), Doorly and Oldfield (1985), Wittig et al. (1988), and O'Brien and Capp (1988). Pfeil and Herbst found that the best simulation was obtained by choosing the cylinder diameter such that the profile drag between the particular airfoil and the cylinder are matched. However, Wittig et al. found that to achieve sufficient similarity between the profiles, it was necessary to move the cylinder axis somewhat upstream of the trailing-edge location in the actual stage. They also found good similarity between the turbulence intensity profiles in the streamwise direction, but the turbulence intensity in the cross-stream direction was significantly greater in the case of the airfoil. O'Brien and Capp found similar results.

Beyond the similarity in the velocity-defect and turbulence intensity profiles, Han and Cox (1983), among others, have observed that over a wide range of operating conditions, turbine airfoils shed vortex streets that are very similar to those shed by cylinders. It is believed that these large vortical structures may be responsible for large excursions in the instantaneous heat transfer observed in experiments during a wake-passing event, but little experimental evidence has been presented to support this conclusion.

To provide theoretical insight to this problem, Rigby and Rae (1989) examined the heat transfer at the stagnation point of an infinite flat plate as a vortex approached from above. Taking into account thermal boundary-layer thickness and unsteady temperature fluctuations due to the vortex, they were able to show that the vortex passage could indeed cause large fluctuations in heat transfer about the mean. The interesting thing to note is that these fluctuations can take place in both directions about the mean, potentially driving the heat transfer to nearly zero instantaneously.

Experimental evidence of the effect of such vortical structures was obtained by O'Brien (1988) who measured the bound-

Nomenclature

a = acoustic speed, m/s
D = instrumented cylinder diameter, m
d = wake-generating cylinder diameter, m
f = frequency, Hz
Fr = Frossling number = $\mathrm{Nu}/\sqrt{\mathrm{Re}}$
M = Mach number = U_∞/a_∞
Nu = Nusselt number = hD/k
Re = Reynolds number = $\rho_\infty U_\infty D/\mathrm{M}_\infty$, or $\rho_\infty U_\infty d/\mathrm{M}_\infty$
St = Strouhal number fd/U_∞
Tu = Turbulence intensity = $\sqrt{u'^2}/U_\infty$, percent or absolute fraction
U = velocity, m/s
θ = angular position from stagnation line, deg or radians
μ = viscosity, kg/(m s)
ρ = density, kg/m^3

Subscripts

∞ = free-stream quantity
D = based on instrumented-cylinder diameter
d = based on wake-generator diameter

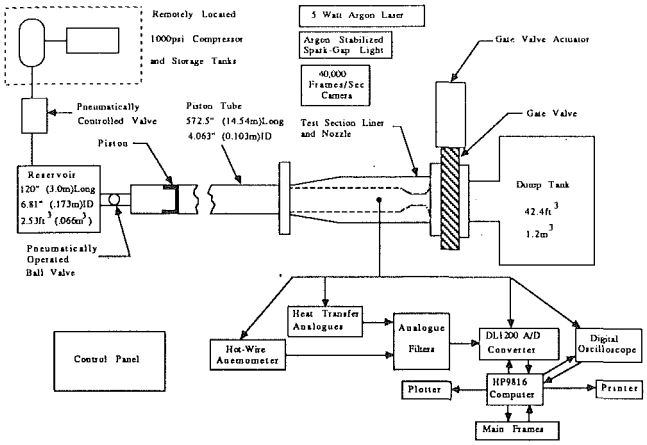

Fig. 1 Syracuse University LICH tube schematic

ary-layer velocity spectra with hot-film gages in the stagnation region of a cylinder. The experiment was conducted in an annular facility in which a rotating spoked-wheel wake generator was placed upstream of an annular cascade of stationary instrumented pins. In the experiment, O'Brien first positioned one of the wake-generator pins immediately in front of an instrumented cylinder and measured the velocity spectra at several circumferential locations about the stagnation point. He found that the shedding frequency of the upstream wake generator was most evident at 60 deg from the stagnation line. As the wake-generator passing frequency was increased from zero, the peak in the velocity spectra remained but became much more broadband and shifted to lower frequencies. The most interesting result was that the vortices did not seem to have much effect upon the boundary-layer velocity spectra at the stagnation line itself. A similar analysis of the heat transfer data obtained in the same facility was not performed, but heat transfer experiments in the same facility (O'Brien et al., 1986) clearly show the enhancement of the heat transfer rate in the stagnation region due to wake passing. O'Brien et al. quote a 10 percent increase in the time-averaged heat transfer rate due to wake passing and the appearance of transient heat transfer spikes that are 30 to 40 percent greater than the interwake heat transfer rate.

Facility and Instrumentation

Facility. The experiments presented herein were carried out in a piston-driven, short-duration wind tunnel facility (shown schematically in Fig. 1) known as a LICH tube (*L*udweig tube with *I*sentropic *C*ompression *H*eating). The operating principle of a LICH tube was first described by Oldfield et al. (1973). The device consists of a high-pressure reservoir, which can be vented rapidly via a fast-acting ball valve into a relatively low-pressure tube fitted with a lightweight piston. At the initiation of the run, the piston starts its stroke near the reservoir end of the tube and is propelled toward the test section by venting the reservoir into the region behind the piston. As the piston travels down the bore of the tube the gas ahead of it is compressed, and therefore heated, since the test section is sealed from the dump tank by a fast-acting gate valve. The compression process is relatively slow since the piston velocity is much less than the local acoustic speed. Therefore, if heat transfer from the hot test gas to the walls is neglected, the compression process can be considered to be essentially isentropic. When the desired operating conditions are achieved, the reservoir valve is opened, and the hot test gas washes through the test section.

The original conception of the facility by Oldfield et al. was mainly for the purpose of driving a hypersonic nozzle. However, the facility is also ideally suited for most applications that require the simulation of a compressible, high-Reynolds number, high-enthalpy flow. The facility is capable of producing the flow conditions necessary to simulate the gas turbine environment correctly (e.g., Reynolds number, Mach number, and gas-to-wall temperature ratio). A very distinct advantage to this type of facility is that Mach number, Reynolds number, and gas-to-wall temperature ratio can be controlled independently of one another. The test-section Mach number is controlled by the ratio of test-section area to nozzle area, and the gas-to-wall temperature ratio is determined by the ratio of final tube pressure to initial tube pressure. In turn, the Reynolds number is controlled by the initial tube pressure selected for a given temperature or pressure ratio. Heat transfer measurements in this type of facility are generally less complicated than in a steady-flow facility since the test gas is compression heated to a level significantly above that of a model placed in the test section, and heat transfer will take place naturally between the flow and the model during the running time of the facility.

A schematic representation of the present LICH facility is provided in Fig. 1 along with all relevant dimensions. The available run time of the facility is approximately 80 ms. The LICH mode of operation offers the advantage of approximately an order of magnitude increase in available testing time over similar sized shock-heated facilities. A complete description of this facility was given by Magari and LaGraff (1991). The operating map of such a facility is difficult to define in a concise manner because of the number of independent parameters that are easily controlled. In the present study, Mach numbers of 0.08 and 0.5 were utilized with Reynolds numbers, based on the diameter of the instrumented cylinder, in the range of 67,500–112,000 and 112,000–383,000 for each of the Mach numbers, respectively. All the experiments were conducted with a gas-to-wall temperature ratio of 1.35. Background turbulence levels were approximately 0.5 percent at $M_\infty = 0.08$ and 0.04 percent at $M_\infty = 0.5$. The free-stream turbulence level was enhanced with turbulence grids placed at the test-section entrance to produce turbulence levels of 4.5 and 1.75 percent at $M_\infty = 0.08$ and $M_\infty = 0.5$, respectively. The turbulence length scale was approximately 20 percent of the instrumented-cylinder diameter for both Mach numbers. The grids consisted of perforated plates with an open area significantly greater than that of the downstream throat to prevent choking at the grid. The openness ratio of the grids was 0.44 at $M_\infty = 0.08$ and 0.21 at $M_\infty = 0.5$. The grids were located 0.356 m upstream of the measurement location. The measurements of Baines and Peterson (1950) with similar grids indicate that there should be a high degree of isotropy and homogeneity of the turbulence at this downstream location, so extensive hot-wire studies were not conducted owing to the difficulties associated with these types of measurements in short-duration facilities.

Instrumentation. Instantaneous and time-averaged heat transfer measurements were acquired from a 12.7-mm-dia ceramic (Macor™) test cylinder instrumented with platinum thin-film heat transfer gages (see Schultz and Jones, 1973, for a complete description of the technique). Two cylinders were utilized in the study: one with heat transfer gages located at 20 deg circumferential increments about the stagnation line and the other with 22.5 deg spacing. The gages were located on the front and rear surfaces of the cylinder, but only results from the laminar boundary-layer region on the front surface of the cylinders are presented here. The gages were approximately 5.8 mm (0.230 in.) in spanwise extent and covered approximately 0.38 mm (0.015 in.) in the circumferential direction. The gages were deposited onto the surface of the Macor™ cylinders using a painting and firing technique, and films produced via this technique typically have a thickness of approximately 1 μm.

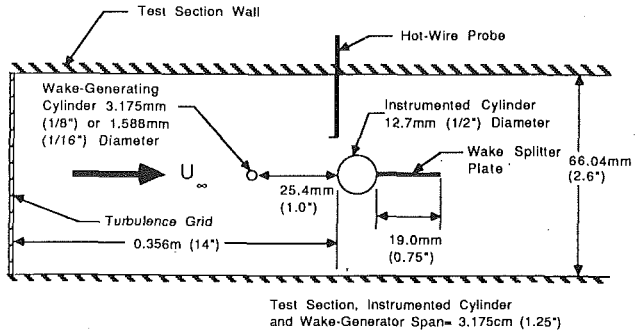

Fig. 2 Schematic of test setup

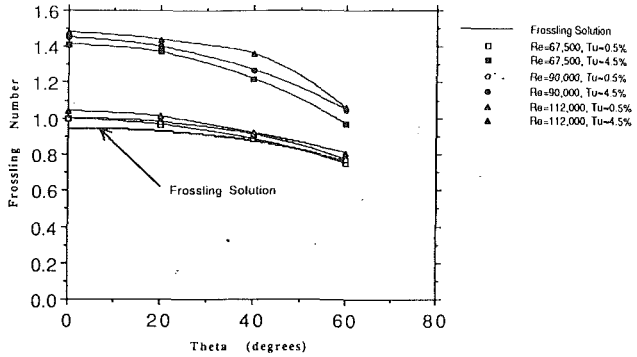

Fig. 3 Frossling number distribution for M = 0.08

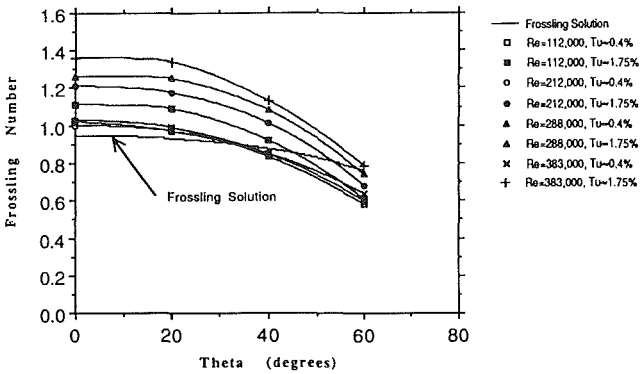

Fig. 4 Frossling number distribution for M = 0.5

The operating principle of the thin-film heat transfer gage is based upon the fact that the resistance of the gage is a function of its temperature. Therefore, by passing a constant current through the gage, a measure of surface temperature is obtained by monitoring the voltage across the film. The frequency response of the gages themselves is on the order of 2 MHz because of their extremely small thermal mass. Instantaneous heat transfer rates can be deduced from the surface-temperature signal by making the assumption that the heat transfer to the surface is essentially one-dimensional heat conduction to a semi-infinite solid. This assumption is well founded in the case of a thermally insulating substrate such as Macor™. The transformation from temperature to heat transfer can be performed digitally, or alternatively, the conversion can be performed in an analog fashion with an electrical analog to the one-dimensional heat-conduction equation (Oldfield et al., 1984). The latter method offers several advantages over the former and was utilized here. The bandwidth of the heat transfer analogs used was approximately 0.01 Hz to 100 kHz.

The heat transfer results were subjected to a detailed uncertainty analysis as outlined by Kline and McClintock (1953) for single-sample experiments. The analysis indicates that the uncertainty in the Frossling-number results obtained is approximately 6.8 percent with a 95 percent confidence limit.

Hot-wire anemometry was used to characterize the free-stream conditions and those existing behind the wake-generating cylinders. To obtain a sufficiently high overheat ratio, it was necessary that all hot-wire runs be performed under cold running conditions whereby the test gas was not compression heated prior to opening the test-section nozzle. Because of the relatively short run times of the facility, to obtain reasonable resolution in the spectral domain required that many runs (≈ 15) be ensemble averaged. A similar technique was utilized for the spectral analysis of the heat transfer signals.

Experimental Setup. A schematic diagram of the experimental setup used is presented in Fig. 2. The 12.7 mm (0.5 in.) instrumented cylinder had an exposed span of 31.7 mm (1.25 in.), yielding an aspect ratio of 2.5. The test section was 66.0 mm (2.6 in.) high, resulting in a projected tunnel blockage of 19 percent. No corrections were applied for either the effects of tunnel blockage or aspect ratio since the primary objective of the study was to provide a qualitative understanding of the wake-interaction phenomenon. The spacing between the leading edge of the instrumented cylinder and the centerline of the wake-generating cylinder was held constant at two instrumented-cylinder diameters for all tests. In terms of the wake-generator diameter, the spacings were 8 and 16 wake-generator diameters for the larger and smaller wake generators, respectively. The spacing was selected to be the same as that utilized by O'Brien et al. (1986) and O'Brien (1988) and in the range of that used by Bayley and Priddy (1987). Additionally, the spacing was chosen to be representative of the actual turbine stage utilized by Doorly and Oldfield (1985), LaGraff et al. (1989), and Guenette et al. (1989), which had an axial gap of approximately 10 trailing-edge diameters. The centers of the two cylinders were kept along the tunnel centerline for most of the experiments, but some testing was performed with the centerlines offset. A wake-splitter plate was employed on the rear of the instrumented cylinder to reduce the effect of wake shedding from the instrumented cylinder upon the stagnation-region heat transfer.

Experimental Results

Isolated Cylinder Heat Transfer. To establish a baseline for comparison and as a means of establishing a certain level of confidence in the system, a series of tests were conducted with the instrumented cylinder alone. The Frossling-number distribution for the $M_\infty = 0.08$ and 0.5 cases are presented in Figs. 3 and 4 along with the incompressible prediction of Frossling (Eq. (1)). For the $M_\infty = 0.08$ case, the experimental results are in excellent agreement with the prediction for the 0.5 percent free-stream turbulence level. There is a slight increase in the stagnation-line Frossling number with Reynolds number, as expected for a flow with nonzero free-stream turbulence intensity. At a free-stream turbulence intensity of 4.5 percent, the heat transfer is enhanced at all circumferential locations about the stagnation region. The level of enhancement at the stagnation line itself is consistent with the correlation results of Lowery and Vachon and is shown in Fig. 5 with the observed data. The correlation results of Lowery and Vachon (1975) tend to underpredict the Frossling number observed at the high free-stream turbulence level and overpredict it at the low free-stream turbulence level for the $M_\infty = 0.08$ case. The observed values are all within 10 percent of the correlation. The observed fluctuations in heat transfer at the low free-stream turbulence intensity were between 1 and 2 percent of the mean for all of the Reynolds numbers utilized throughout the laminar bound-

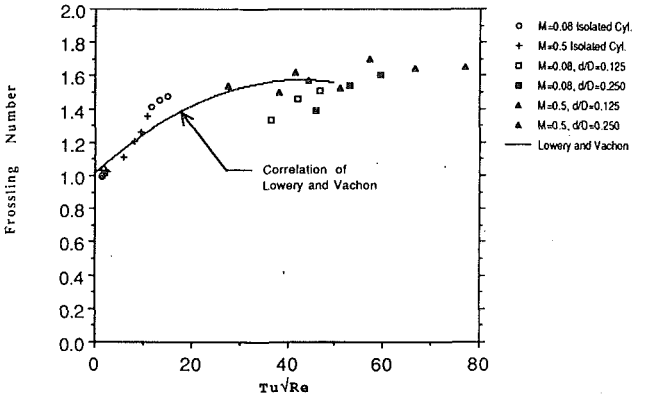

Fig. 5 Stagnation line Frossling number versus the parameter $Tu\sqrt{Re}$

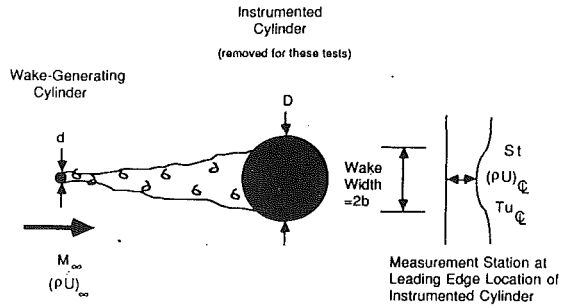

M_∞	D/d	Re_d	Wake Width/D	$(\rho U)_{\text{℄}}/(\rho U)_\infty$	$Tu_{\text{℄}}$(%)	St
0.08	0.125	6,000	0.75	0.767	16	0.23
0.08	0.250	12,000	1.0	0.712	21	0.23
0.5	0.125	37,500	0.75	0.845	9	0.19
0.5	0.250	75,000	1.0	0.788	14	0.19

Fig. 6 Wake development at leading edge location of instrumented cylinder

ary-layer region. These levels increased dramatically after 60 deg to about 20 percent at 80 deg from the stagnation line. At a free-stream turbulence intensity of 4.5 percent, the observed fluctuations were between 10 and 15 percent of the mean and quite constant throughout the laminar boundary-layer region. The behavior beyond the laminar boundary-layer region was similar to that observed in the low free-stream turbulence cases.

The Frossling number distribution results observed for the $M_\infty = 0.5$ cases are presented in Fig. 4. As with the low Mach number, the $1/\sqrt{Re}$ scaling collapses the low turbulence data well. The effects of compressibility on the stagnation-point heat transfer are not distinguishable for the range of conditions utilized here since the observed Frossling number is approximately the same as the incompressible prediction. However, the Frossling number drops off much faster with the angle from the stagnation line than the incompressible prediction. This is a result of the fact that at supercritical Mach numbers, the pressure distribution on the front face of the cylinder is markedly different from that observed in an incompressible flow, and as a result, the hydrodynamic and thermal boundary layers are also quite different. The fact that the heat transfer rate decreases faster with θ at supercritical Mach numbers is consistent with the results of Murthy and Rose (1978) who found a similar behavior with the skin friction. The effect of free-stream turbulence intensity at compressible Mach numbers upon the stagnation-region heat transfer is qualitatively similar to the results observed at incompressible Mach numbers. An insufficient range of $Tu\sqrt{Re}$ was investigated to make any firm conclusions as to the validity of Lowery and Vachon's stagnation-point Frossling-number correlation under these conditions, but it does appear that the correlation provides a reasonable estimate as illustrated in Fig. 5.

Wake Survey. To obtain both a qualitative and quantitative picture of the conditions existing in the wake of the wake-generating cylinders utilized, an experimental program was undertaken to measure the wake characteristics using hot-wire anemometry. The measurements were taken at a single downstream location, which corresponded to the leading edge of the instrumented cylinder which was removed for the present series of tests. The experiments involved both wake generators at both Mach numbers and all the free-stream turbulence intensities available.

At each of the Mach numbers, only a single unit Reynolds number was thoroughly investigated, but the qualitative nature of the results was checked at several Reynolds numbers for each of the two Mach numbers. It was felt that the effect of Reynolds number on the gross structure of the wake would be relatively small since all of the Reynolds numbers (based on the wake-generator diameter) were in the subcritical Reynolds number regime for all of the test conditions investigated. The effect of a supercritical Mach number on the nature of the wake was not known a priori, however.

The results of this investigation are summarized in Fig. 6 for the four test conditions thoroughly investigated. For both wake-generator diameters utilized, the wake width was sufficient to encompass the entire laminar boundary-layer region of the downstream cylinder. Additionally, the wake width appeared to be unaffected by Mach number. However, the mass-flux defect at the centerline decreased for the higher Mach number by approximately 10 percent for both wake generators. The range of mass flux observed at the centerline for all the cases tested was from 70 to 85 percent of the free-stream value. The wake profiles measured were all well correlated by a Gaussian-type profile (see White, 1974), which is, strictly speaking, only valid for the far wake, but worked well here.

The turbulence intensities observed in the wake at $M_\infty = 0.08$ were on the order of 16 percent for the $d/D = 0.125$ wake generator and 21 percent for the $d/D = 0.250$ wake generator. At the transonic Mach number, however, the turbulence intensities measured in the wake were considerably lower than those observed at the incompressible Mach number (9 and 14 percent for the smaller and larger wake generators, respectively). (The turbulence intensities were computed based upon the local mean velocity as opposed to the free-stream velocity.) This observation was most likely related to the appearance of shock waves at the shoulders of the wake generator at $M_\infty = 0.5$ and their attendant effect upon the wake flow. As with the defect profiles, the turbulence intensity profiles were also Gaussian in appearance and reached the free-stream turbulence level at a distance slightly greater than the mass-flux defect profiles, as one might expect. Free-stream turbulence intensity had no appreciable effect upon the turbulence intensities at the centerline or the turbulence intensity profiles except, of course, at the wake edges.

The spectra of the turbulence in the wake were broadband and revealed vortex-shedding frequencies with Strouhal numbers ($St = fd/U_\infty$) slightly less than 0.2 for both wake generators at $M_\infty = 0.5$ and approximately 0.22 for $M_\infty = 0.08$. The slight differences are easily attributed to the range of Reynolds numbers utilized. Naumman et al. (1966) showed that the wake-shedding frequency at supercritical Mach numbers was a function of the Reynolds number, and Strouhal number was not affected by the appearance of the shock waves at the shoulders of the cylinder. The shedding frequency was most dominant at the wake edges for all cases, but especially so for the larger wake generator at both Mach numbers investigated. The shedding frequencies and the spectra of the

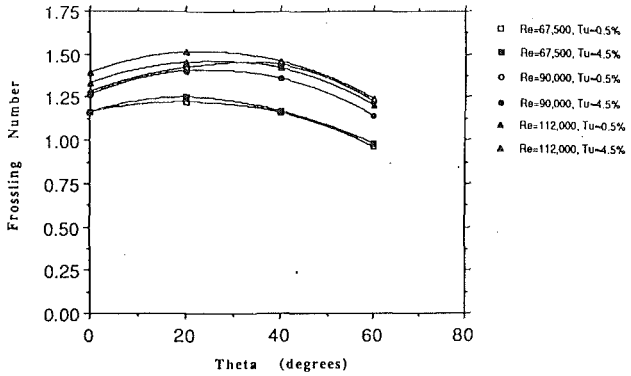

Fig. 7 Frossling number distribution for M = 0.08 with *d/D* = 0.250 wake generator

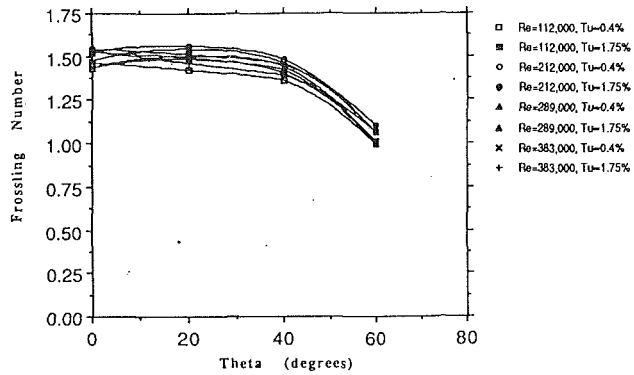

Fig. 8 Frossling Number distribution for M = 0.5 with *d/D* = 0.250 wake generator

mass flux in the wake seemed to be relatively unaffected by the free-stream turbulence level. The shedding frequencies were found to decrease somewhat with the insertion of the instrumented cylinder into the wake, as discussed in the following section. Unfortunately, it was not practical to estimate the turbulence length scale in the wakes because of the number of ensembles required to make the estimate and the short life expectancy of the probes under these conditions.

Wake-Induced Unsteady Heat Transfer. After obtaining the isolated cylinder results and documenting the conditions behind the wake generators, the instrumented cylinder and wake generator combination was placed in the flow. Primarily the results obtained with the $d/D = 0.250$ wake generator are presented here, but the results obtained with the smaller wake generator were qualitatively, and in many respects quantitatively similar, as discussed below.

The time-averaged heat transfer results for the $d/D = 0.250$ wake generator with $M_\infty = 0.08$ are presented in Fig. 7 in terms of the Frossling-number distribution over a Reynolds number range of 67,500 to 112,000 based on the instrumented-cylinder diameter. Because of the mass-flux defect at the centerline, the stagnation-point heat transfer is not maximum, but rather maximizes near 25 deg from the stagnation line. The effect of the ambient free-stream turbulence level appears to be minimal on all the results with the wake generator in place. As one might expect by analogy with a typical turbulent free-stream flow, an increase in Reynolds number tends to increase the heat transfer everywhere in the stagnation region. As the Reynolds number increases, the stagnation-line Frossling number appears to approach a maximum. The Frossling number distributions measured with the $d/D = 0.25$ wake generator in place at $M_\infty = 0.5$ are presented on Fig. 8 for $Re_D = 112{,}000$ to 383,000 (28,000 to 95,750 based on the large wake-generator diameter). For this case, the stagnation-line Frossling numbers are not significantly lower than the values observed at circumferential locations away from the stagnation line as noted at the lower Mach number. The curves collapse to essentially a single curve with the $1/\sqrt{\mathrm{Re}}$ scaling, indicating that the effect of the magnitude of $Tu\sqrt{\mathrm{Re}}$ had reached a limiting condition.

In Fig. 5 the observed stagnation-line Frossling numbers are plotted against the parameter $Tu\sqrt{\mathrm{Re}}$ for both wake-generator diameters and Mach numbers. The turbulence intensity utilized was that measured at the wake centerline in the hot-wire experiments. As a rough correction for the effect of the mass-flux defect at the centerline, the Reynolds number used in the calculation of $Tu\sqrt{\mathrm{Re}}$ and $\mathrm{Nu}/\sqrt{\mathrm{Re}}$ was calculated using the mass flux measured in the hot-wire experiments. Also plotted in this figure is the correlation equation of Lowery and Vachon, which shows reasonable agreement with the results obtained at $M_\infty = 0.08$ and excellent agreement with $M_\infty = 0.5$. The observed Frossling numbers (corrected for the mass-flux defect) at $M_\infty = 0.5$ reach a maximum of approximately 1.65, which is consistent with the observations of Lowery and Vachon (1975) for the enhancement of stagnation-point heat transfer by free-stream turbulence at incompressible Mach numbers. The fact that the observed stagnation-line Frossling numbers lie below the correlation for the incompressible Mach number is likely related to several factors, which include: the relative scale of the turbulence in the wake flow, the mass-flux-defect profile, and the fact that the bulk of the vortex filaments in the wake flow, have their axes aligned parallel to the instrumented cylinder axis since the wake is not fully developed for the separation distances utilized. As stated earlier, it is generally believed that vortex filaments with their axes aligned perpendicular to the cylinder axis and the free-stream directions are the most effective at augmenting the stagnation-region heat transfer. An additional consideration of significance is that the tunnel blockage used in the present study was relatively high and may also influence the comparison with Lowery and Vachon's correlation.

Figures 9 and 10 present simultaneous heat transfer traces obtained at the stagnation line and circumferential locations of −20, 20, 40, and 60 deg for the two Mach numbers with the $d/D = 0.250$ wake generator placed upstream. The high degree of correlation between the large excursions in the signals from adjacent gages is relatively evident. The level of unsteadiness observed in these signals is quite significant as illustrated in Figs. 11 and 12, which present the normalized rms distributions of the Nusselt number. For the low Mach number, the fluctuations are on the order of 16–19 percent of the mean throughout most of laminar boundary-layer region and decrease slightly with the angle from the stagnation line. At the higher Mach number, the fluctuations are greater and are on the order of 20–25 percent of the mean throughout the entire laminar boundary-layer region. This result is interesting because the turbulence intensity observed in the wake of the larger wake generator at the high Mach number was on the order of 14 percent and was significantly lower than that observed at the incompressible Mach number (≈21 percent).

The large peaks and valleys observed in the signals presented in Figs. 9 and 10 are not characteristic of the signals obtained with isotropic free-stream turbulence. The excursions in the unsteady heat transfer rate are as large as 65 percent of the mean in the positive direction and 50 percent of the mean in the negative direction for the higher Mach number. These large excursions are likely the result of structures in the wake flow, which are large compared to the instrumented cylinder and not present in isotropic free-stream turbulence. The periodicity of the large excursions is relatively evident at the higher Mach number, but not quite so evident at the lower Mach number. An interesting point to note is that the minima of the signals at both Mach numbers are generally much greater than the stagnation-region Frossling numbers expected in a low tur-

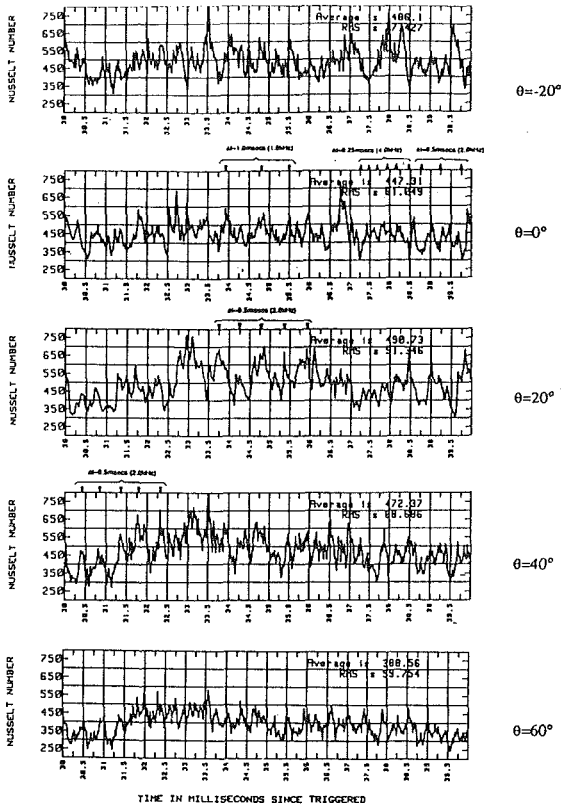

Fig. 9 Simultaneous heat transfer traces for M = 0.08, Re = 112,000, *Tu* = 0.5 percent, with *d/D* = 0.250 wake generator

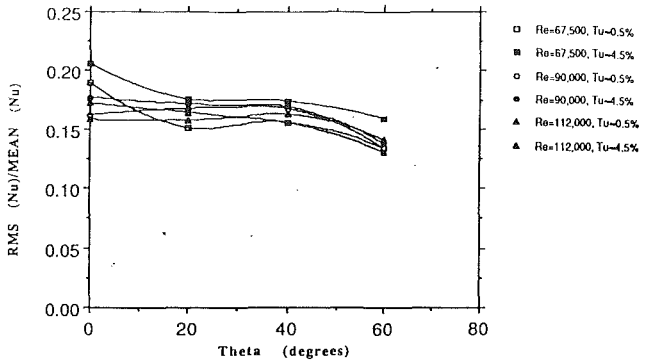

Fig. 11 Magnitude of unsteady component of heat transfer at M = 0.08, with *d/D* = 0.250 wake generator

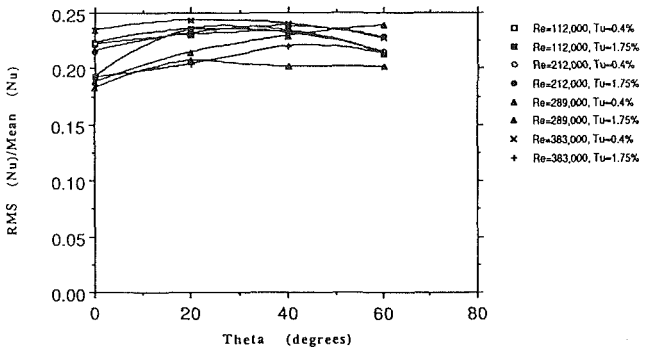

Fig. 12 Magnitude of unsteady component of heat transfer at M = 0.5, with *d/D* = 0.250 wake generator

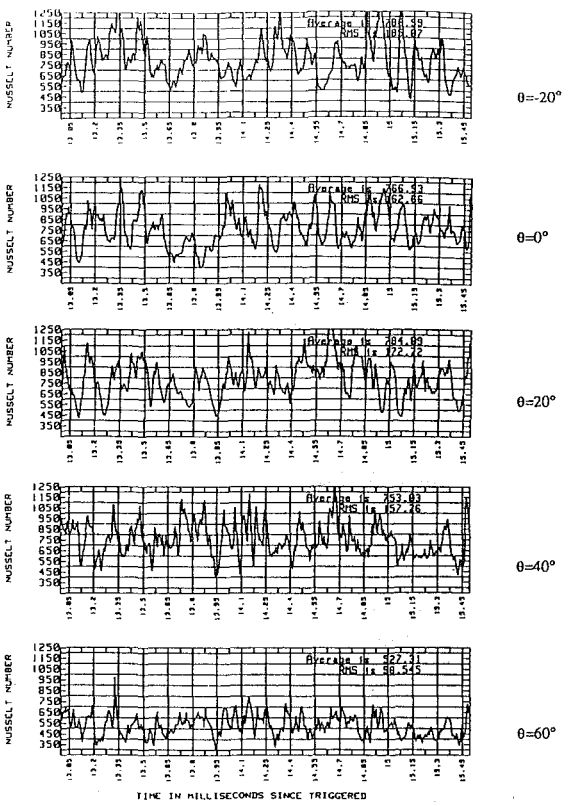

Fig. 10 Simultaneous heat transfer traces for M = 0.5, Re = 288,000, *Tu* = 0.4 percent, with *d/D* = 0.250 wake generator

bulence intensity free stream, possibly indicating that at these high wake turbulence intensities the stagnation-region boundary layer is turbulent or transitional at best.

Nondimensional power spectra of the heat transfer signals obtained from gages in the stagnation region are presented in Figs. 13 and 14 for the M_∞ = 0.08 and 0.5 cases. The only spectra that show a clear peak are those for the higher Mach number at locations off the stagnation line (e.g., 40 and 60 deg). The peak is relatively broad and has its center at a Strouhal number (based on the wake-generator diameter) of approximately 0.13, which is lower than that observed in the hot-wire spectra. The difference in Strouhal number is attributed to the upstream influence of the instrumented cylinder upon the wake-generator flow field. Figure 13 shows that at the lower Mach number a broadband peak seems to be appearing in the spectra at 60 deg with its center at a Strouhal number of approximately 0.2. This was more evident when the spectra were plotted on linear scales. Again, the Strouhal number is somewhat lower than that observed without the instrumented cylinder present in the wake. The spectra observed with the *d/D* = 0.125 wake generator are qualitatively similar at the higher Mach number. In this case the effect of vortex shedding was most evident at a circumferential location of 40 deg. The shedding frequency was not greatly affected by the instrumented cylinder for the small wake generator. No perceivable peaks in the spectra were noted at the lower Mach number with the small wake generator placed upstream.

There are several reasons that the power spectra may not clearly show the effect of the large-scale structures, the first reason being that spectral analysis is an inherent problem in short-duration testing because it requires relatively long records to obtain good resolution in the spectral domain. However, it was felt that the record length obtained by the ensembles of many ($\approx$15) runs at the same conditions provided enough

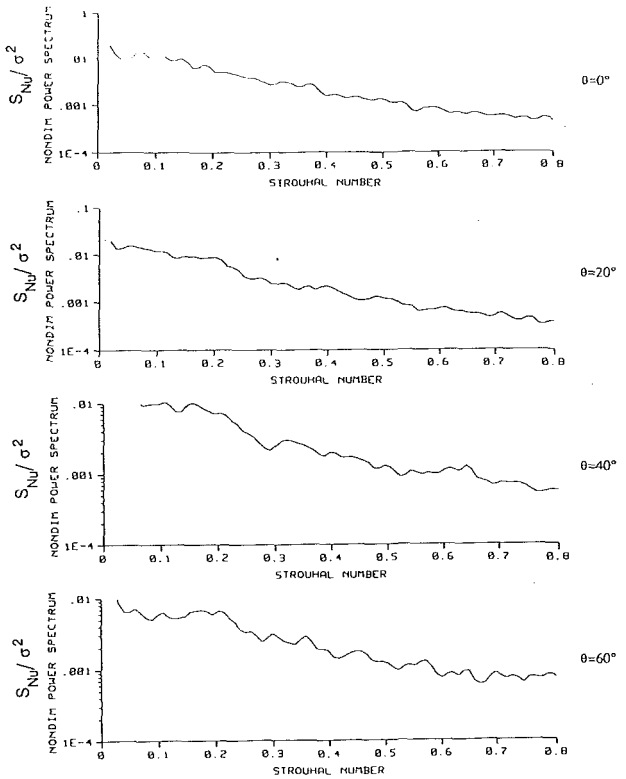

Fig. 13 Power spectrum at various locations for M = 0.08, Re = 112,000, *Tu* = 0.5 percent, with *d/D* = 0.250 wake generator

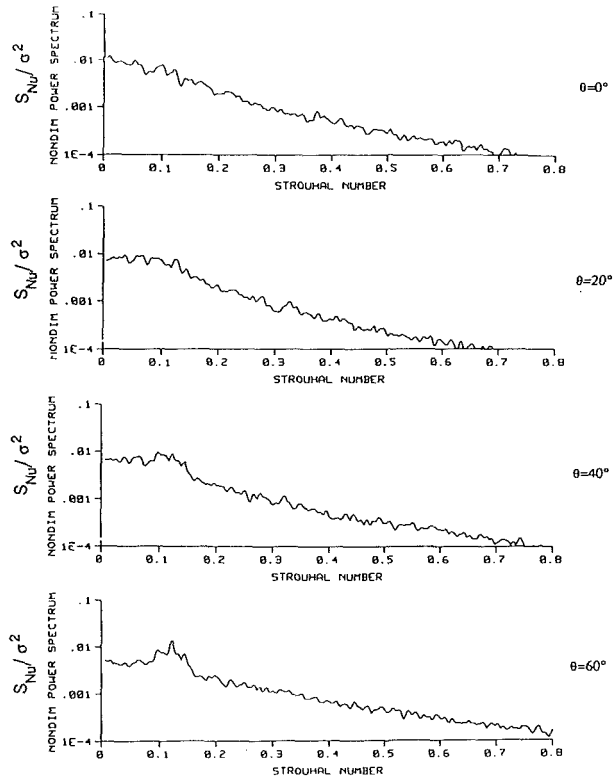

Fig. 14 Power spectrum at various locations for M = 0.5, Re = 288,000, *Tu* = 0.4 percent, with *d/D* = 0.25 wake generator

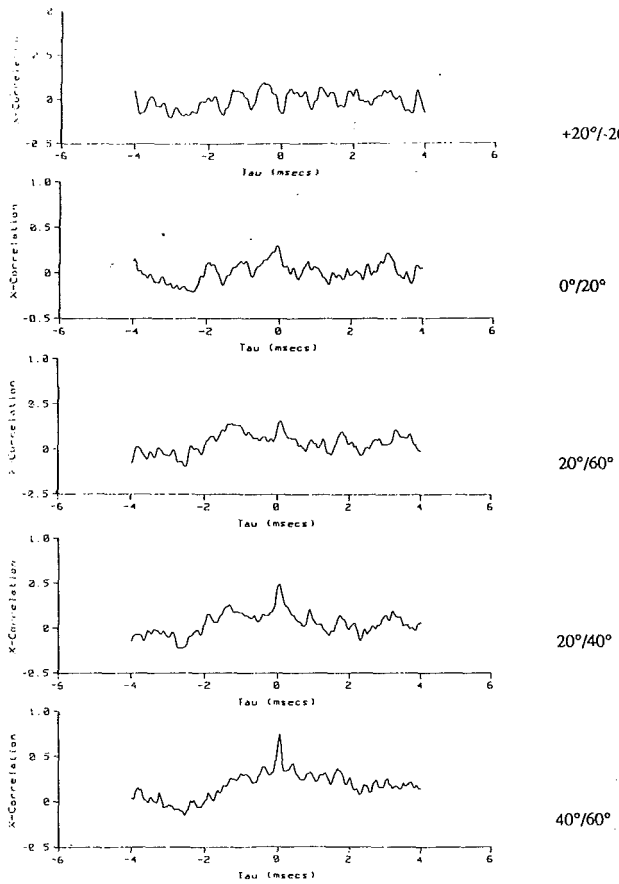

Fig. 15 Cross-correlation between various gages for M = 0.08, Re = 112,000, *Tu* = 0.5 percent, with *d/D* = 0.250 wake generator

ensembles so that adequate spectral resolution was achieved to make any dominant frequencies clear. Several more plausible reasons exist that may explain the apparent anomaly, however, one of these being that at a given location relative to the stagnation line, the large excursions in heat transfer rate tend to be intermittent: present for several milliseconds, disappearing, and then reappearing several milliseconds later. The reason for the intermittency is not clear, but is likely related to both the unsteady development of the boundary layer from the stagnation point and the unsteady nature of the wake itself. Because of this intermittency, standard spectral-analysis techniques can potentially average these events away if their relative duration is short and the nature of the background signal is broadband. Also, when the large excursions are present in the signal, there is an obvious phase shift between them that tends to "smear" the spectra even further. As a result of these findings it became clear that standard Fourier-series spectral-analysis techniques are not necessarily the best approach in this situation.

The cross-correlations corresponding to the instantaneous heat transfer signals of Figs. 9 and 10 are presented in Figs. 15 and 16. The correlations reflect the periodic behavior of the signals, particularly for the cases with the larger wake generator. The cross-correlations at the lower Mach number appear to sit on a pedestal because of a combination of the periodic nature of the signals and phase jitter. These two factors combined with the fact that the periodicity is intermittent and not apparent at all locations at all times could also diminish the magnitude of the correlations at $\tau = 0$. The correlation between the stagnation-point heat transfer and that at other circumferential locations is poor for all cases. As the boundary layer develops in the circumferential direction, the correlation between adjacent gages increases. The reason that the correlation between the stagnation point and other circumferential locations is so weak is likely related to the difference in re-

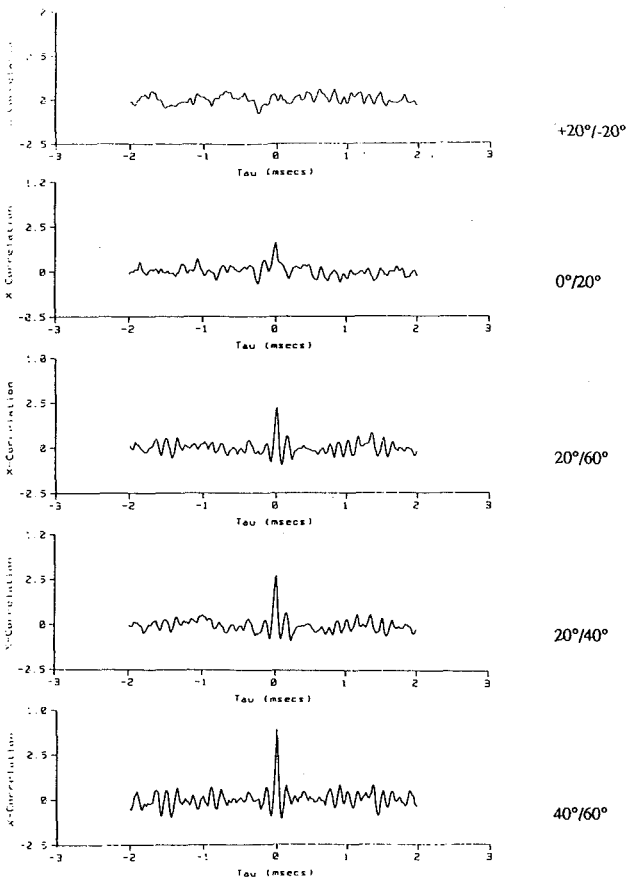

Fig. 16 Cross-correlation between various gages for M = 0.5, Re = 288,000, *Tu* = 0.4 percent, with *d/D* = 0.250 wake generator

ceptivity of the boundary layer as it develops away from the stagnation point. The stagnation-point boundary layer is very thin and as a result is very susceptible to free-stream disturbances. As the boundary layer develops away from the stagnation point, it thickens and becomes less susceptible to free-stream disturbances and more dependent upon its past history. The boundary layer at the stagnation point itself has no past history. The correlation between gages located on opposite sides of the stagnation point is relatively weak for all cases. However, for the larger wake generator at both Mach numbers, there is a weak negative correlation at $\tau = 0$ for the $+20$ and -20 deg locations. This indicates that at a particular measurement station there are a significant number of deviations from the mean with opposite sense at stations on the other side of the stagnation point. This fact is relatively apparent from the instantaneous signals directly. When the signals from two measurement stations from either side of the stagnation point are superimposed it is clear that many of the large positive excursions on one side of the stagnation point are associated with large negative excursions on the other side of the stagnation point.

Concluding Remarks

The experiments described in this paper detail the results obtained from a quasi-steady representation of the rotor/stator interaction in a gas turbine over a wide range of Mach number, Reynolds number, and free-stream turbulence intensity. The results support the following observations and conclusions:

1 The enhancement of the heat transfer in the stagnation region was documented by comparison with isolated cylinder tests under various conditions. Where previous data were available, the experimental results from these tests were found to compare well. No results have been presented in the literature concerning the heat transfer distribution on a cylinder at transonic Mach numbers. The results presented here show that the heat transfer data at supercritical Mach numbers are well collapsed by the $1/\sqrt{\text{Re}}$ scaling, and the heat transfer drops off much faster with θ for the compressible case.

2 The turbulence intensity behind the wake-generating cylinders was documented with hot-wire anemometry at the leading-edge location of the instrumented cylinder utilized. These tests documented the high level of turbulence intensity in the wake and the mass-flux defect. The wake-generator vortex-shedding frequency was found to be slightly greater than 0.2 for the $M_\infty = 0.08$ cases and slightly less than 0.2 for the $M_\infty = 0.5$ cases. The shedding frequency decreased when the instrumented cylinder was placed in the flow, and the effect was most pronounced for the larger wake generator at the higher Mach number.

3 Time-averaged heat transfer results from the instrumented cylinder with the wake generator in place indicate that the heat transfer rate, expressed in terms of the Frossling number, reached a maximum of approximately 1.6 independent of the Reynolds number. A comparison with the correlation of Lowery and Vachon (1975) for the stagnation-region Frossling in the presence of free-stream turbulence showed reasonable agreement if the Reynolds number used to calculate the Frossling number and $Tu\sqrt{\text{Re}}$ was adjusted for the mass-flux defect in the wake.

4 Time-resolved heat transfer measurements with the wake generator in place documented the high levels of unsteadiness in the stagnation-region heat transfer. The level of unsteadiness at the transonic Mach number was considerably higher than the incompressible case even though the turbulence intensity measured in the wake flow was lower at the higher Mach number. The high-frequency transients in instantaneous heat transfer reached levels of approximately 65 percent above the mean and 50 percent below the mean at the higher Mach number. The excursions were lower for the incompressible case, but still very significant. The periodicity of the heat transfer signals was most apparent at the higher Mach number, but the power spectra of the heat transfer signals at both Mach numbers indicated some peaking around the expected shedding frequency of the wake generator for locations away from the stagnation line. The effect of the periodic wake structures was not perceptible at the stagnation line itself through standard spectral-analysis techniques, but visual inspection of the raw data seemed to indicate that the effects of these vortices were present intermittently in the stagnation-point signals. Because of this intermittency and the broadband background signal, standard spectral techniques potentially average out the effects of these structures. Cross-correlations between various gages in the laminar boundary-layer region reflected the quasi-deterministic nature of the signals. The cross-correlation between the stagnation line and locations off the stagnation line was relatively weak, but the correlation between adjacent gages increased in the circumferential direction. This was attributed to the fact that as the boundary layer develops it becomes more dependent upon its past history and less susceptible to free-stream disturbances.

Acknowledgments

The work presented herein was supported by the National Aeronautics and Space Administration Lewis Research Center under grant number NAG 3-621. The grant technical officers were Drs. James O'Brien and Robert Simoneau, to whom the authors are indebted for their encouragement and assistance.

References

Ashworth, D. A., LaGraff, J. E., Schultz, D. L., and Grindrod, K. J., "Unsteady Aerodynamic and Heat-Transfer Processes in a Transonic Turbine

Stage," ASME *Journal of Engineering for Gas Turbines and Power*, Vol. 107, pp. 1022–1030.

Baines, W. D., and Peterson, E. G., 1950, "An Investigation of Flow Through Screens," ASME Paper No. 50-A-23.

Bayley, F. J., and Priddy, W. J., 1987, "Effects of Freestream Turbulence Intensity and Frequency on Heat Transfer to Turbine Blading," ASME JOURNAL OF ENGINEERING FOR POWER, Vol. 109, No. 2, pp. 60–64.

Doorly, D. J., and Oldfield, M. L. G., 1985, "Simulation of Wake-Passing in a Stationary Turbine-Rotor Cascade," *AIAA Journal of Propulsion and Power*, Vol. 1, No. 4, pp. 316–318.

Frossling, N., 1958, "Evaporation Heat Transfer and Velocity Distribution in Two-Dimensional and Rotationally-Symmetric Laminar Boundary Layer Flow," NACA TM-1432.

Gorla, R. S. R., 1984, "Effects of Unsteady Free Stream Velocity and Free Stream Turbulence on Stagnation-Point Heat Transfer and Skin Friction," NASA CR 3804.

Guenette, G. R., Epstein, A. H., Giles, M. B., Haimes, R., and Norton, R. J. G., 1989, "Fully-Scaled Transonic Turbine Rotor Heat Transfer Measurements," ASME JOURNAL OF TURBOMACHINERY, Vol. 111, No. 1, pp. 1–7.

Han, L. S., and Cox, W. R., 1983, "A Visual Study of Turbine Blade Pressure-Side Boundary Layers," ASME *Journal of Engineering for Power*, Vol. 105, pp. 42–52.

Kline, S. J., and McClintock, F. A., 1953, "Describing Uncertainties in Single-Sample Experiments," *Mechanical Engineering*, Vol. 75, No. 1, Jan.

LaGraff, J. E., Ashworth, D. A., and Schultz, D. L., 1989, "Measurement and Modeling of the Gas Turbine Blade Transition Process as Disturbed by Wakes," ASME JOURNAL OF TURBOMACHINERY, Vol. 111, pp. 315–322.

Lowery, G. W., and Vachon, R. I., 1975, "The Effect of Turbulence on Heat Transfer From Heated Cylinders," *International Journal of Heat and Mass Transfer*, Vol. 18, No. 11, pp. 1229–1242.

Magari, P. J., and LaGraff, J. E., 1991, "An Isentropic Compression-Heated Ludweig Tube Transient Wind Tunnel," *Experimental Thermal and Fluid Science*, Vol. 4, pp. 317–332.

Murthy, V. S., and Rose, W. C., 1978, "Detailed Measurements on a Circular Cylinder in Cross Flow," *AIAA Journal*, Vol. 16, No. 6, pp. 549–550.

Nagamatsu, H. J., and Duffy, R. E., 1984, "Investigation of the Effects of Pressure Gradient, Temperature and Wall Temperature Ratio on the Stagnation-Point Heat Transfer for Circular Cylinders and Gas Turbine Vanes," NASA CR 174667.

Naumman, A., Morsbach, M., and Kramer, C., 1966, "Separated Flow," AGARD CP4, pp. 539–574.

O'Brien, J. E., Simoneau, R. J., LaGraff, J. E., and Morehouse, K., 1986, "Unsteady Heat Transfer and a Direct Comparison to Steady-State Measurements in a Rotor-Wake Experiment," *8th International Heat Transfer Conference*, Hemisphere Publishing Co.

O'Brien, J. E., 1988, "Effects of Wake Passing on Stagnation-Region Heat Transfer," *Heat Transfer in Gas Turbine Engines and Three-Dimensional Flows*, E. Elovic, J. E. O'Brien, and D. W. Pepper, eds., ASME HTD-Vol. 103, pp. 17–28.

O'Brien, J. E., and Capp, S. P., 1988, "Two-Component Phase-Averaged Turbulence Statistics Downstream of a Rotating Spoked Wheel Wake Generator," ASME JOURNAL OF TURBOMACHINERY, Vol. 111, pp. 475–482.

Oldfield, M. L. G., Jones, T. V., and Schultz, D. L., 1973, "A Ludweig Tube With Light-Piston Isentropic Compression Heating," Aeronautical Research Council Paper No. 34255, HYP 935.

Oldfield, M. L. G., Burd, H. J., and Doe, M. G., 1984, "Design of Wide-Bandwidth Analog Circuits for Heat Transfer Instrumentation in Transient Tunnels," *Heat and Mass Transfer in Rotating Machinery*, papers from the 16th Symposium of the International Centre for Heat and Mass Transfer, D. E. Metzger and N. H. Agan, eds., pp. 233–258.

Pfeil, H., and Herbst, R., 1979, "Transition Procedure of Instationary Boundary Layers," ASME Paper No. 79-GT-128.

Rigby, D. L., and Rae, W. J., 1989, "Unsteady Stagnation-Point Heat Transfer During Passage of a Concentrated Vortex," NASA CR 18297.

Schultz, D. L., and Jones, T. V., 1973, "Heat Transfer Measurements in Short-Duration Hypersonic Facilities," AGARD Report No. AG-165.

Smith, M. C., and Kuethe, A. M., 1986, "Effects of Turbulence on Laminar Skin Friction and Heat Transfer," *Physics of Fluids*, Vol. 9, No. 12, pp. 2337–2344.

Sutera, S. P., Maeder, P. F., and Kestin, J., 1963, "On the Sensitivity of Heat Transfer in the Stagnation-Point Boundary Layer to Free-Stream Vorticity," *Journal of Fluid Mechanics*, Vol. 16, Part 4.

Van Dressar, N. T., and Mayle, R. E., 1989, "A Quasi-Steady Approach of Wake Effects on Leading Edge Transfer Rates," ASME JOURNAL OF TURBOMACHINERY, Vol. 111, pp. 483–490.

VanFossen, G. J., and Simoneau, R. J., 1985, "Preliminary Results of a Study of the Relationship Between Free-Stream Turbulence Intensity and Stagnation-Region Heat Transfer," ASME Paper No. 85-GT-84.

White, F. M., 1974, *Viscous Fluid Flow*, McGraw-Hill, NY.

Wittig, S., Schultz, A., Dullenkopf, K., and Fairbank, J., 1988, "Effects of Wake Characteristics on Heat Transfer Along a Cooled Turbine Blade," ASME Paper No. 88-GT-179.

Yardi, N. R., and Sukhatme, S. P., 1978, "Effects of Turbulence Intensity and Integral Length Scale of a Turbulent Free Stream on Forced Convection Heat Transfer From a Circular Cylinder in a Crossflow," ASME 6th International Heat Transfer Conference, Paper FC(6)-29.

Zukaskas, H. J., 1985, *Heat Transfer to a Cylinder in Crossflow*, Hemisphere Publishing.

M. Kumada

S. Iwata

Department of Mechanical Engineering,
Gifu University,
Yanagido, Gifu, Japan 501-11

M. Obata

Heat & Fluids Department,
Research Institute,
Ishikawajima-Harima
Heavy Industries Co., Ltd.,
Toyosu, Koto-ku, Tokyo, Japan 135

O. Watanabe

Toyo Denki Co., Ltd.,
2-156 Ajiyoshi-cho, Kasugai-city,
Aichi-pref, Japan 486

Tip Clearance Effect on Heat Transfer and Leakage Flows on the Shroud-Wall Surface in an Axial Flow Turbine

An axial flow turbine for a turbocharger is used as a test turbine, and the local heat transfer coefficient on the surface of the shroud is measured under uniform heat flux conditions. The nature of the tip clearance flow on the shroud surface and a flow pattern in the downstream region of the rotor blades are studied, and measurements are obtained by using a hot-wire anemometer in combination with a periodic multisampling and an ensemble-averaging technique. Data are obtained under on- and off-design conditions. The effects of inlet flow angle, rotational speed, and tip clearance on the local heat transfer coefficient are elucidated. The mean heat transfer coefficient is correlated with the tip clearance, and the mean velocity is calculated by the velocity triangle method for approximation. A leakage flow region exists in the downstream direction beyond the middle of the wall surface opposite the rotor blade, and a leakage vortex is recognized at the suction side near the trailing edge.

Introduction

Recently, in order to achieve high utilization efficiency in gas turbines, many efforts have been made to raise the turbine inlet temperature. It is necessary, for the development of these high-temperature gas turbines, to develop more effective cooling and thermal isolation techniques not only for rotor blades (Metzger et al., 1973; Kumada et al., 1981; Crawford et al., 1980) and stator vanes (Dunn and Hause, 1982), but also for flow path walls (Karimova et al., 1973; Guenette et al., 1985). In connection with the design of these components, further reliable data by which the heat transfer coefficient can be accurately predicted are still needed.

On the other hand, particularly the flow on the shroud surface opposite to the rotor blade tips is significantly affected by the turning and acceleration of the high-temperature and high-speed gas flowing through the blade row. This complex flow phenomenon on the shroud is attributed to a mutual interaction of the end-wall boundary layer, tip leakage flow, blade passage secondary flow, and the blade-surface boundary. Several efforts have been made to clarify this complex flow by means of a five-hole probe, a hot-wire anemometer, and an LDV anemometer, due to the need for higher efficiency or more reliable designs that minimize the loss in an axial flow compressor rotor (Hunter and Cumpsty, 1982; Lakshminarayana et al., 1982; Inoue and Kuroumaru, 1989). Furthermore, numerical studies have been performed for three-dimensional viscous flow inside a rotor, including tip clearance flow (Pouagare and Delaney, 1986; Dawes, 1987). These results are useful in understanding the basic phenomena that take place in the tip region, namely, the strong interaction of leakage flow with blade passage flow, vortex roll-up, and a separating zone between the leakage flow and the incoming main flow. However, as results were obtained only for model engines (Hunter and Cumpsty, 1982; Lakshminarayana et al., 1982; Inoue and Kuroumaru, 1989), it is uncertain whether the data are applicable to real gas turbines. Moreover, these studies (Dunn and Hause, 1982; Karimova et al., 1973; Guenette et al., 1985; Hunter and Cumpsty, 1982; Lakshminarayana et al., 1982; Inoue and Kuroumaru, 1989; Metzger et al., 1991) have not yet clarified how the structure varies with conditions of operation, that is, inlet flow angle.

Although many heat transfer studies have been devoted to measuring the heat transfer coefficient around a rotor blade for the axial flow turbine, there are few studies (Dunn and Hause, 1982; Karimova et al., 1973; Guenette et al., 1985; Metzger et al., 1991) that examine the coefficient on a shroud. Under the condition of uniform wall temperature, the empirical equation for the mean heat transfer coefficient was obtained by Karimova et al. (1973), who discussed the effect of tip clearance, but no measurements of the flow field were performed. It is not clear, in particular, to what degree their results are applicable to the general case. The flow field of the region near the shroud is unsteady, and it has an effect on the characteristics of the local heat transfer coefficient in connection with the shapes and sizes of the turbine stage.

In a previous report (Kumada et al., 1988), quantitative data were presented for the local heat transfer coefficient on the

Contributed by the International Gas Turbine Institute and presented at the 37th International Gas Turbine and Aeroengine Congress and Exposition, Cologne, Germany, June 1-4, 1992. Manuscript received by the International Gas Turbine Institute February 17, 1992. Paper 92-GT-200. Associate Technical Editor: L. S. Langston.

Table 1 Principal experimental conditions and rotor blade geometry

$Re = CmCr/\nu$	$1.39 \times 10^4 \sim 7.03 \times 10^4$
N [rpm]	2000 ~ 14,000
U [m/s]	17.7 ~ 123.9
Cr [mm]	13.14
C_3 [m/s]	30.8 ~ 112.2
C_4 [m/s]	7.4 ~ 80.1
ξ [deg]	36

shroud in the radial flow turbine for the turbocharger. In the present study, an axial flow turbine for the turbocharger was used for the test turbine. The local heat transfer coefficient on the shroud under the conditions of on- and off-design, which are equivalent to the conditions of zero, positive, and negative incidence, was measured, and an accurate measurement of tip clearance flow was made by inserting a hot-wire probe.

In this series of studies, the target is to establish a numerical prediction scheme for thermal stress in order to develop a ceramic abradable shroud.

Experimental Apparatus and Procedure

All measurements were performed for an axial flow turbine of the IHI VTR-161-type turbocharger, which has 53 rotor blades (169-mm-dia rotor, hub/tip ratio = 0.76). This turbocharger was chosen to facilitate handling and measurement. The principal experimental conditions and the rotor blade geometry are shown in Table 1. The basic velocity triangle for this machine is shown in Fig. 1. The blade profile corresponds to the tip section of the test turbine, and the blades have a three-dimensional, twisted shape similar to the actual case.

Driving air supplied by a blower through scroll and inlet guide vanes turned the rotor. The mass flow rate was linearly related to the rotational speed. The resultant uncertainty in the mass flow rate presently measured was ±5.5 percent at 20:1 odds, referring to Moffat (1982). In order to control the inlet flow angle of the rotor blades, the impellers of the compressor were partially cut off and/or the inlet of the compressor was partially sealed with thin aluminum tape. Although the discharge pressure of the blower used in the present study was low, the inlet flow condition under low revolution rate and change of flow incidence were produced in this way. The rotational speed, N, was measured by means of a pulse counter.

Measurement of the local heat transfer coefficient on the shroud surface was performed by using the well-established thin-film technique (stainless steel foil, 30 μm thick), which is equivalent to uniform heat flux conditions. As shown in Fig. 2, the stainless steel foil was glued onto the shroud (acrylic resin) and was directly energized by a stabilized DC source.

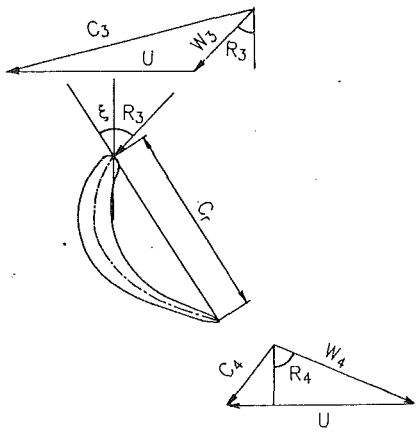

Fig. 1 Velocity triangle

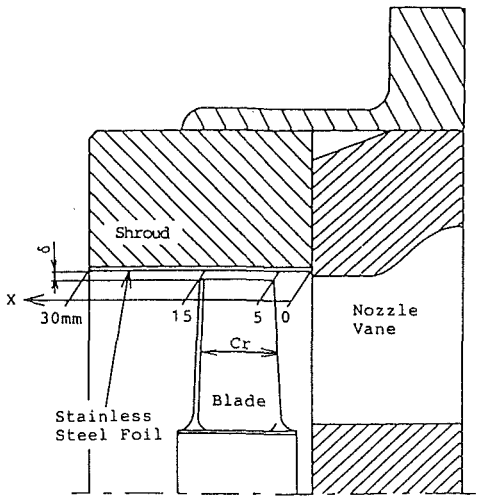

Fig. 2 Measuring section and coordinate system

The local wall temperature was measured with nine Cu–Co thermocouples (0.07 mm in diameter) soldered to the back of the foil. The temperature difference, ΔT, used in the definition of the heat transfer coefficient, h, was defined by the difference between the temperatures of the foil while being heated and not heated. This is because a heat drop caused by air passing through the rotor was taken into consideration. In order to avoid the effect of heat loss from the foil to the wall of acrylic resin on heating, a groove (5×4 mm^2 cross section) was cut into the contact-wall surface of thermocouples along the axial direction. A pile of glass wool was inserted carefully into the

Nomenclature

Bh = mean blade height, mm
C = absolute velocity at blade tip, m/s
Cm = mean absolute velocity $= (C_3 + C_4)/2$, m/s
Cr = chord length at blade tip, mm
h = local heat transfer coefficient, W/(m^{2}K)
N = rotor revolution, rpm
Nu = Nusselt number $= h\,Cr/\lambda$
R = inlet flow angle at blade tip against axial direction, deg
Re = Reynolds number $= Cm\,Cr/\nu$
ΔT = temperature difference between wall temperature while heated and not heated, K
U = blade tip speed, m/s
u = velocity component of X direction, m/s
v = velocity component of Y direction, m/s
W = relative velocity at blade tip, m/s
w = velocity component of Z direction, m/s
X = distance of axial direction, mm
Y = distance of tangential direction, mm
Z = distance of radius direction, mm
δ = blade tip clearance, mm
$\bar{\delta}$ = relative blade tip clearance $= \delta/Bh$
λ = thermal conductivity, W/(m K)
ν = kinematic viscosity, m^2/s
ξ = stagger angle, deg
τ = time, s

Subscripts

3 = rotor inlet
4 = rotor outlet

Superscripts

$(\bar{\ })$ = average

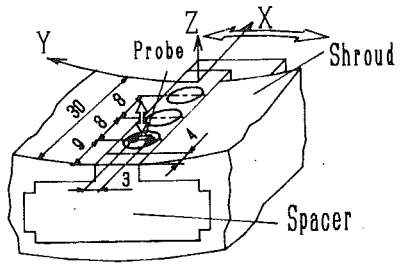

Fig. 3 Schematic view of a probe-setting device

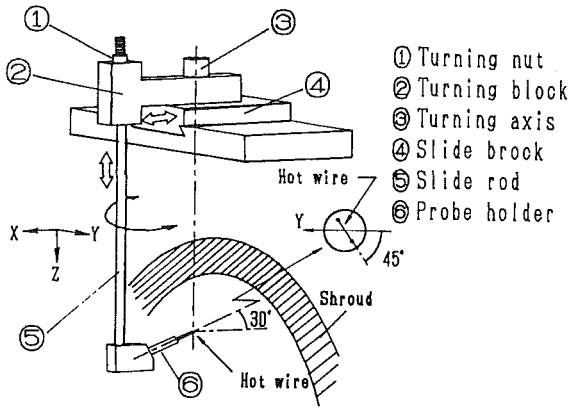

Fig. 4 Schematic view of a probe-turning device

groove and held there softly. Therefore, the fundamental heat loss in the heat transfer coefficient can be ignored. The resultant uncertainty in h was ± 6.5 percent at 20:1 odds. The coordinate system and principal symbols used are shown in Fig. 2. The local heat transfer coefficient was measured in two regions: the surface wall opposite to the rotor blade and that in the area downstream of the rotor. Six shrouds with different inner diameters were used primarily to investigate the effect of tip clearance. The tip clearance was measured at four positions along the circumference by a thickness gage. The tip clearance was distributed uniformly within ± 5 percent at each position. The tip clearance, δ, was varied from 0.3 mm to 1.2 mm.

Flow patterns on the shroud were obtained by a constant-temperature hot-wire anemometer using a periodic multi-sampling and averaging technique with a computerized data acquisition system. Velocity vectors were measured in three regions: the surface wall in the area upstream of the rotor, that opposite the rotor blade, and that in the area downstream of the rotor. The position of the blade was detected using a noninvasive, eddy-current-type displacement transducer (maximum frequency = 30,000 Hz). The hot-wire probe used was a single wire 5 μm in diameter with a 1 mm effective length.

In the Case of the Surface Wall Opposite to the Rotor Blade. In order to measure two-dimensional vectors, the hot-wire probe was inserted by a probe-setting device on the shroud, as shown in Fig. 3. The probe position could be moved at 8 mm intervals in the axial direction from $X = 9$ mm to 25 mm and, when taken out of the spacer, from $X = 5$ mm to 21 mm. The survey planes could be changed from $Z = 0.2$ mm to 1 mm continuously above the wall surface by using the slide bolt. At each measuring point on the survey plane, the hot-wire probe could be rotated from $+20$ to -20 deg against the axial direction. At each position, the hot-wire signals were acquired by a 10 μs sampling period summed up at each passage between blades during four revolutions of the rotor in order to avoid the effect of irregular revolution. In this measurement, the effects of the velocity component of the Z-direction and of reverse flow were involved in the obtained results. The

Table 2 Turning angle of the probe at each measuring point

X, mm	Angle of probe against the axial direction	
18	$-36 \sim 24$ deg,	6 deg intervals
21.5	$-45 \sim 35$ deg,	5 deg intervals
25	$-60 \sim 36$ deg,	6 deg intervals

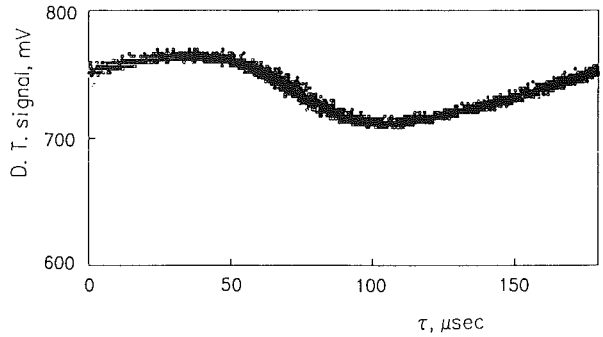

Fig. 5 Signals of the displacement transducer

obtained results, however, were useful in understanding the basic flow phenomena that would take place in the tip region of a real turbine.

Using the same device, the oncoming flow velocity on the surface near the leading edge of the rotor blade was measured.

In the Case of the Wall Surface in the Area Downstream of the Rotor. Three-dimensional vectors were obtained through use of the turning device, as shown in Fig. 4. This device can move a probe in the X and Z directions, and turn it on the Z axis. As shown in this figure, a hot-wire probe was attached inclined by 30 deg to the X axis, and the inclination of the sensor wire to the Y axis was adjusted to 45 deg by rotation of ⑥. The survey planes could be changed from $Z = 0.8$ mm to 8 mm using ①, and at each measuring point, the hot-wire probe was rotated, as shown in Table 2. At each sensor position, hot-wire signals were summed up during four revolutions of the rotor, that is, about 200 periods, and the sampling period was 10 μs. Hot-wire signals acquired were divided into 24 phases per period and were averaged for each phase. The three mean-velocity components can be obtained from a set of 12 or 17 ensemble averages of the hot-wire signal for each phase and the angles of the hot-wire probe, by solving the simultaneous quadratic equations by the least-squares method and the Newton–Raphson method (Hayashi and Nakaya, 1971). But, as shown in Fig. 5, a slight scatter of output signals of the displacement transducer, which was used to determine the blade position, can be seen. This was caused by the irregularity in the revolution, manufacture of blades, and their assembly. The resultant uncertainty in the position of the blade was ± 8.7 percent. Figure 6 shows a typical result of the hot-wire signals summed up during 200 periods. Data vary widely. The amount of this scatter, however, depends on the sensor position. Therefore, as the difference between the averaged values for 150 and 200 periods is very small, the velocity components are determined from (12 or 17) $\times$ 200 periods. They are accurate in the statistical sense.

Experimental Results and Discussion

Characteristics of Flow on the Shroud. Figure 7 shows the absolute velocity vector profile in the Z direction at $X = 3$ mm. The boundary layer thickness of the oncoming flow to rotor blades was about 0.8 mm regardless of the position in the Y direction, and the effects of incidence and revolution on it are very small in this experimental range. The inlet flow angle agrees well outside the boundary layer with the experimental condition; that is, the flow incidence is zero. However,

the incidence is about +5 deg in the boundary layer. It seems that the nature of the oncoming flow boundary layer is very important to heat transfer and tip leakage flow, although control of the boundary layer is not easy.

Figure 8 shows typical absolute velocity vector profiles in the Z direction. In this case, $\delta = 0.79$ mm and the hot-wire probe was moved from $Z = 0.2$ mm to 0.62 mm to avoid contact between the probe and blades. Although the flow passage between the blades is divided into twelve parts along the Y direction, the result of a six-way division is shown in this figure in order to avoid complication.

The change of velocity vectors in the Y and Z directions is very small in the front region of the blade ($X = 5$–9 mm). In the downstream direction past $X = 13$ mm, the velocity profiles show three-dimensional behavior. In particular, at $X = 13$ mm, the velocity vector becomes larger in the region directly under a blade, and this effect can be seen near the wall immediately after a blade is passed. This suggests the behavior of a tip leakage flow.

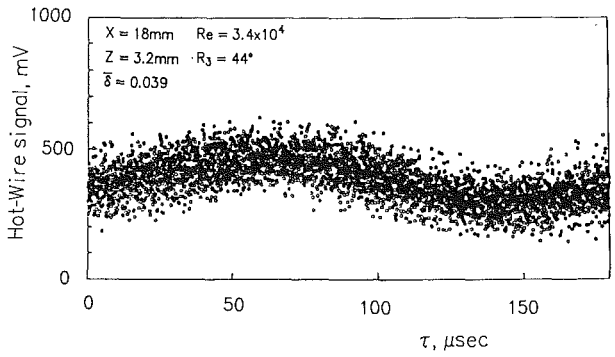

Fig. 6 Hot-wire signals

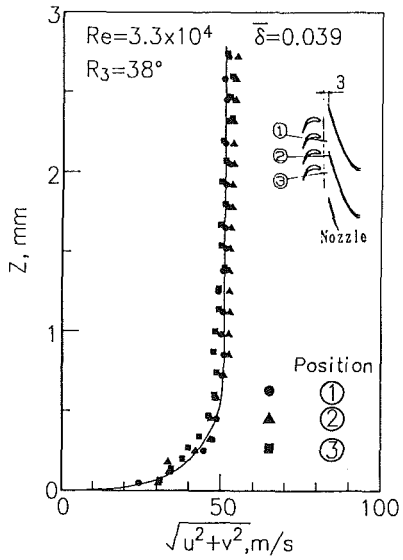

Fig. 7 Profile of absolute velocity vector in Z direction near the leading edge of rotor blade

Figures 9(*a*), 9(*b*), and 9(*c*) show typical relative velocity vectors on the survey plane near the surface of the shroud, at $Z = 0.2$ mm. These incidences are zero ($R_3 = 38$ deg), positive ($R_3 = 45$ deg), and negative ($R_3 = 23$ deg), respectively. What is obvious is that these figures are similar to each other, but the absolute values of the velocity vector all become larger in the order of positive, zero, and negative incidence. Tip leakage flow is the strongest, and the region is wide under the condition of $R_3 = 45$ deg. In contrast to this, in the case of negative incidence, leakage flow does not appear clearly. In this measurement, the flow is assumed to be two dimensional, and even if reverse flow appeared in some regions, it was impossible to determine the flow direction.

Figures 10(*a*), 10(*b*), and 10(*c*) show relative velocity vectors on the X-Y plane in the area downstream of the rotor, that is, at $X = 18$ mm, 21.5 mm, and 25 mm, respectively. Velocity vectors near the shroud surface, at $Z = 0.8$ mm, show tip leakage flow behind a rotor. Leakage flow and the incoming throughflow regions can be identified in this case, but the leakage flow becomes weak. The flow pattern at the suction side and in the region 2–3 mm away from the wall surface shows distortion due to the leakage vortex. This distortion becomes small in the flow direction.

To confirm the existence of the leakage vortex, Figs. 11(*a*), 11(*b*), and 11(*c*) show the secondary flow vector pattern under the same conditions as in Fig. 10. As expected, the vortex is shown at the same position as mentioned above. The shape of the vortex is slightly oblate due to the restriction of expression. From both Figs. 10 and 11, the leakage flow region can be distinguished from the throughflow region. The flow direction on the suction side is probably aligned nearly with the main flow at the radius slightly smaller than the blade tip radius. This means that a thin vortex sheet with high vorticity must exist between the leakage flow and the main flow, as indicated by Inoue et al. (1989), who measured the tip clearance flow in a low-speed rotating cascade facility. As a result, the vortex sheet may roll up due to the induced velocity. At the rotor end, this leakage vortex moves inward due to the presence of the adjacent blade surface and interacts with the blade wake.

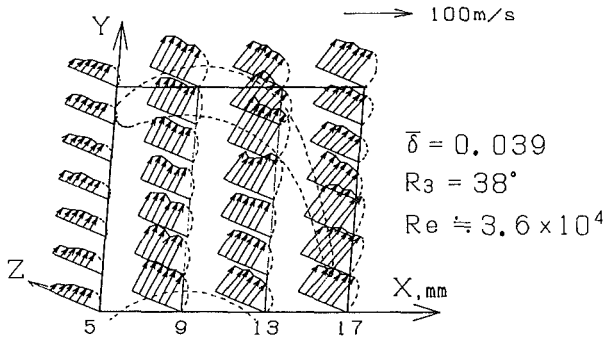

Fig. 8 Profile of absolute velocity vector in Z direction on the shroud opposite to the rotor blades

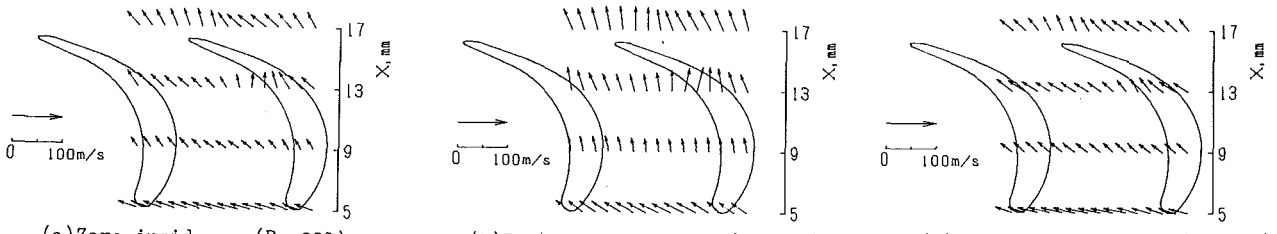

Fig. 9 Relative velocity vectors ($\bar{\delta} = 0.039$, $Re = 3.6 \times 10^4$, $Z = 0.20$ mm)

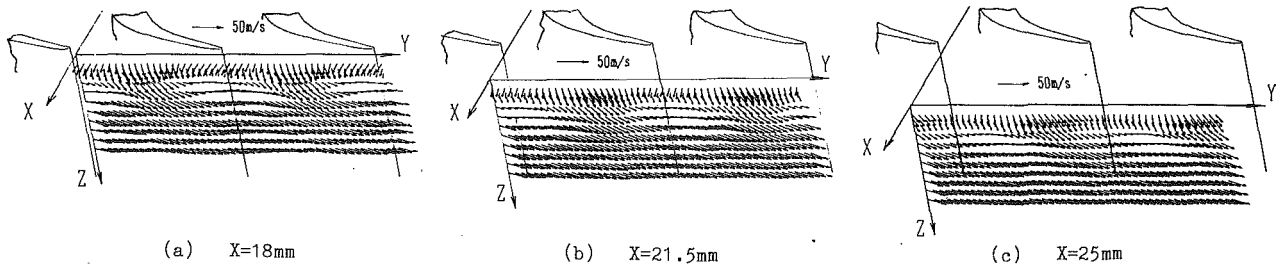

Fig. 10 Relative velocity behind the rotor

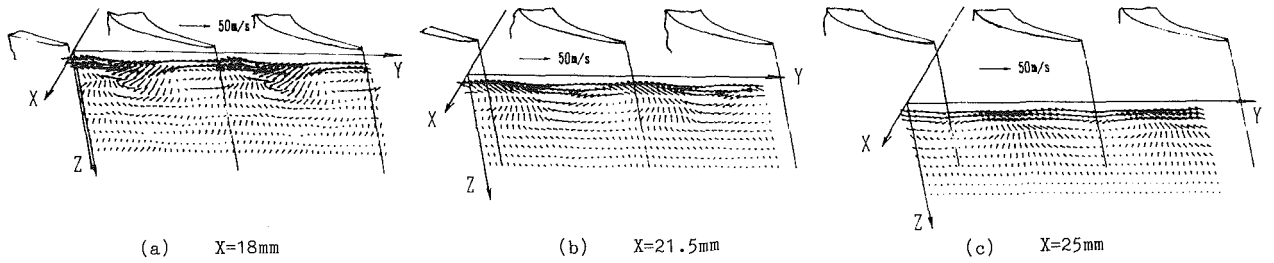

Fig. 11 Secondary flow velocity behind the rotor

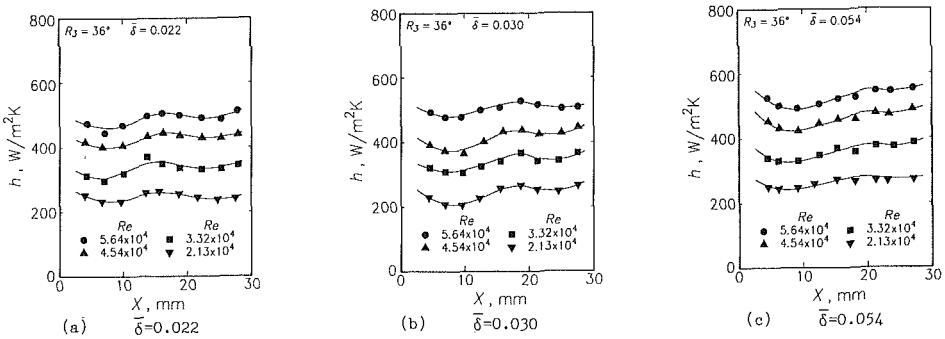

Fig. 12 Distribution of local heat transfer coefficient in the on-design condition

It seems to pass through the wake and is weakened by it as the flow proceeds downstream. In particular, it is worthy of note that the velocity component leaving the wall surface is large at the blade exit and becomes weaker along the flow direction, as shown in Figs. 11.

On the other hand, the phase-locked flow pattern is substantially similar to that of off-design conditions, though figures for this are not shown.

Local Heat Transfer Coefficient. Figures 12(*a*), 12(*b*), and 12(*c*) show typical distributions of the local heat transfer coefficient under the on-design point condition. R_3 is the relative angle included by the velocity at the blade tip against an axial direction, and is kept constant. Nondimensional tip clearances $\bar{\delta} = \delta/Bh$ are 0.022, 0.03, and 0.054, respectively. Although a slight scatter of data may be seen within experimental uncertainty, the value of h decreases monotonically in the direction of the outlet section and increases from near the middle of the wall surface opposite the rotor blades. The value of h reaches a maximum at the end of the rotor. Then h decreases again, and from nearly the length of one axial chord downstream to the end of the rotor blade, h increases again. These tendencies are generally evident regardless of rotational speed (change of Reynolds number, Re, is equivalent to one of revolution) and tip clearance.

The decrease and increase in these distributions of h in the region opposite to rotor blades seem to be due to the development of a boundary layer and the acceleration in velocity on the wall surface, as discussed above. The reason that h reaches the maximum value near the end of rotor blades has been considered to be a secondary flow, which is caused by leakage flow.

Furthermore, the value of h increases similarly with an increase in rotation speed, regardless of tip clearance. Although these tendencies of h were already observed in other experiments (Karimova et al., 1973; Guenette et al., 1985), the present result and their results are different in that the maximum value exists at a spot near the inlet of the rotor blade. The reason for this difference is the effect of the unheated region in the present experiment, as was discussed in the previous report (Kumada et al., 1988). The error due to this difference is very small, and these procedural results are within acceptable engineering accuracy.

Effect of Inlet Flow Angle on Local Heat Transfer Coefficient. Figures 13(*a*) and 13(*b*) show distributions of the local heat transfer coefficient under the off-design condition, that is, $R_3 = 59$ deg and $R_3 = 48$ deg, which correspond to the positive incidence condition and negative incidence condition, respectively. The nondimensional tip clearance is almost identical with the results shown in Fig. 12(*b*). These profiles are similar and there is a tendency for rotational speed to agree with the results of the on-design condition. The position of the maximum value near the end of the rotor blades moves slightly to the upstream direction in the case of the off-design condition. These characteristics in the distribution of h are similar, regardless of tip clearance.

Average Heat Transfer Coefficient. The average heat transfer coefficient was calculated by the numerical integration of the local heat transfer coefficient distribution over the range

from the leading edge, $X = 5$ mm, to the trailing edge, 15 mm. The characteristic length in the definition of the Nusselt number is the axial chord length of the blade.

In order to compare the sizes of $\overline{Nu}$ with respect to inlet flow angle, changes in the mean Nusselt number with respect to tip clearance are shown in Fig. 14. Each line indicated in this figure is the averaged line of several measurements. In general, $\overline{Nu}$ in the on-design condition is small, and $\overline{Nu}$ in positive incidence has the highest value regardless of δ. The $\overline{Nu}$ in negative incident changes with $\bar{\delta}$ substantially and is almost equal to the value of the on-design condition in the range of $\bar{\delta} = 0.04$. Although a slight scatter may be seen, $\overline{Nu}$ gradually becomes smaller with an increase in tip clearance regardless of rotational speed and inlet flow angle. This tendency agrees well with the results of Karimova et al. (1973). However, changes in $\overline{Nu}$ with respect to $\bar{\delta}$ become smaller in the order of negative, zero, and positive incidence. The change of $\overline{Nu}$ with respect to $\bar{\delta}$ can be neglected in the range of $\bar{\delta} > 0.04$ except under the condition of negative incidence.

Figures 15(*a*), 15(*b*), and 15(*c*) show a change in $\overline{Nu}$ with respect to the Reynolds number, in which the characteristic length is the same as that used in the definition of $\overline{Nu}$. The characteristic velocity, *Cm*, is the vector average of absolute velocity C_3 of the inlet and C_4 of the outlet at a tip of the rotor blade, where C_3 and C_4 were calculated by the velocity triangle method for approximation.

As shown in these figures, $\overline{Nu}$ is summarized by $Re^{0.8}$ regardless of inlet flow angle, and Karimova et al. (1973) reported that a similar expression can be obtained as

$$\overline{Nu} = 0.052\ Re^{0.8}(1 - 2\bar{\delta}^{0.8}). \quad (1)$$

Their result is plotted for reference in the same figures.

The above correlation, with $\overline{Nu}$ proportional to $Re^{0.8}$, is the same as the result obtained by Colburn (1933), which is the result of the heat transfer for a turbulent boundary layer on a flat plate. This similarity suggests that the flow behavior on the shroud segment is similar to the turbulent boundary layer flow. Recently, Metzger et al. (1991) reported that time-averaged shroud heat transfer levels are proportional to the 0.8 power of velocity. This was predicted with a turbulent correlation from the results of the simple one-dimensional model.

In comparison with the results of Karimova et al., the absolute value of $\overline{Nu}$ in the present experiment is almost the same as in the case of positive incidence, but under other conditions it is smaller. It is difficult at this stage to discuss the validity of Karimova et al.'s result because there is a great difference between the two experiments, including the range of Reynolds number, the velocity triangle, the type of turbine, and the blade profile.

Although local time-averaged heat transfer coefficients on the shroud are presented in this paper, it is necessary to measure the instantaneous heat transfer coefficient in order to clarify the relationship between the heat transport process and flow mechanism on the surface of a shroud wall. Further study is necessary and details will be reported at a later date.

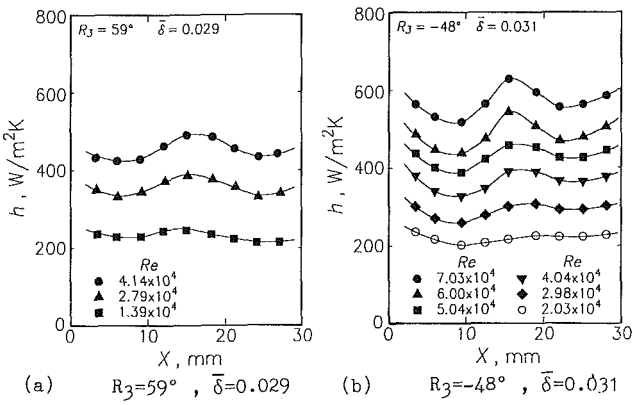

Fig. 13 Distribution of local heat transfer coefficient under off-design conditions

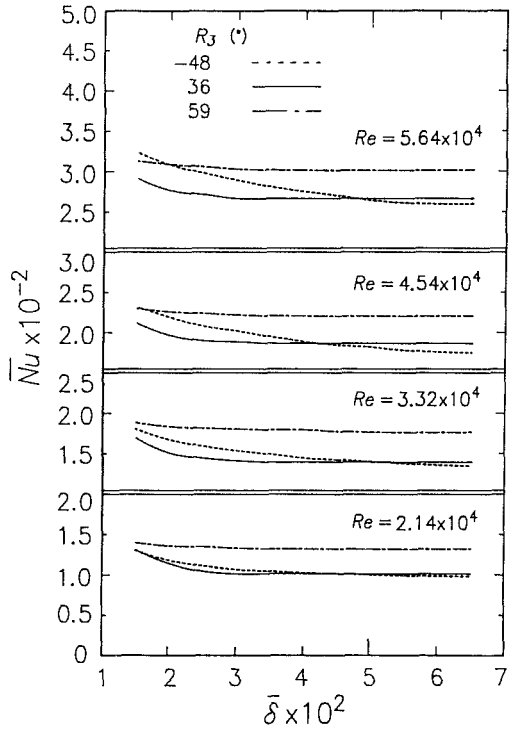

Fig. 14 Change of the distribution of mean Nusselt number with respect to $\bar{\delta}$ by condition of inlet flow angle

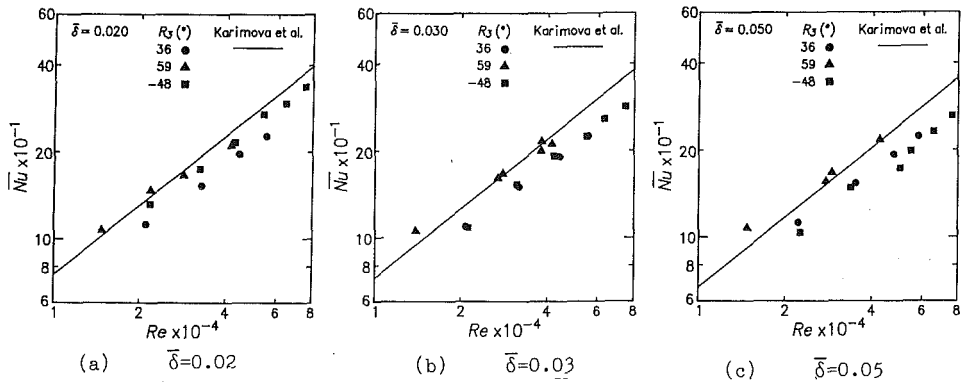

Fig. 15 Distribution of mean Nusselt number with respect to Reynolds number

Conclusions

Detailed measurements of the local heat transfer coefficient and tip clearance flow on the shroud opposite the turbine blade row have been made under the conditions of both on- and off-design, using the axial-flow type turbocharger. The results are summarized as follows:

1 In the downstream direction, beyond the middle of the wall surface opposite the rotor blade, the absolute velocity vector profiles exhibit three-dimensional behavior. In the middle region of the wall surface opposite the rotor blade, the velocity vector becomes larger in the region directly under a blade, and this effect can be seen near the wall surface in the region immediately after a blade passes through. This suggests the behavior of a tip leakage flow.

2 The velocity vector under the condition of positive incidence is always larger than that of the on-design condition.

3 A leakage flow region distinct from a throughflow region exists.

4 A leakage vortex is recognized at the suction side near the trailing edge of a blade, and a rolling-up leakage vortex decays downstream.

5 The local heat transfer coefficient decreases monotonically in the direction of the outlet section and increases from near the middle of the wall opposite the rotor blade row. Then h reaches a maximum value and decreases again, and from near one axial chord length downstream of the end of the rotor blade, h increases again. These tendencies are generally evident regardless of rotational speed, tip clearance, and the condition of the inlet flow angle.

6 The profile above, on the other hand, increases similarly with an increase in the rotational speed and a decrease in the tip clearance.

7 Mean Nusselt numbers in the region opposite the rotor blade are correlated with the tip clearance and Reynolds number. $\overline{Nu}$ is proportional to the 0.8 power of Re.

8 $\overline{Nu}$ gradually becomes smaller with an increase in tip clearance regardless of rotational speed and the condition of the inlet flow angle.

9 $\overline{Nu}$ in the condition of positive incidence is at its highest, and that in the on-design point is small.

10 The characteristics of the flow field on the shroud correspond to those of the local heat transfer.

Acknowledgments

The authors gratefully acknowledge the financial assistance provided through a Grant-in-Aid for Special Project Research (No. 01550171) by the Ministry of Education, Science, and Culture of Japan for fiscal 1989–1990.

References

Colburn, A. P., 1933, "A Method for Correlating Forced Convection Heat Transfer Data and a Comparison With Fluid Friction," *Trans. AIChE*, Vol. 29, pp. 174–181.

Crawford, M. E., Kays, W. M., and Moffat, R. J., 1980, "Full-Coverage Film Cooling. Part 1: Comparison of Heat Transfer Data for Three Injection Angles," ASME *Journal of Engineering for Power*, Vol. 102, pp. 1000–1007.

Dawes, W. N., 1987, "A Numerical Analysis of the Three-Dimensional Viscous Flow in a Transonic Compressor Rotor and Comparison With Experiments," ASME JOURNAL OF TURBOMACHINERY, Vol. 109, pp. 83–90.

Dunn, M. G., and Hause, A., 1982, "Measurement of Heat Flux and Pressure in a Turbine Stage," ASME *Journal of Engineering for Power*, Vol. 104, pp. 215–223.

Guenette, G. R., Epstein, A. H., Norton, R. J. G., and Yozhang, C., 1985, "Time Resolved Measurements of a Turbine Rotor Stationary Tip Casing Pressure and Heat Transfer Field," AIAA Paper No. 85-1220.

Hayashi, Y., and Nakaya, T., 1971, "Measurement of Three Dimensional Mean Velocity Vector and Reynolds Stress by a Single Rotatable Hot-Wire," Technical Report of National Aerospace Laboratory, Tr-242.

Hunter, I. H., and Cumpsty, N. A., 1982, "Casing Wall Boundary Layer Development Through an Isolated Compressor Rotor," ASME *Journal of Engineering for Power*, Vol. 104, pp. 805–818.

Inoue, M., and Kuroumaru, M., 1989, "Structure of Tip Clearance Flow in an Isolated Axial Compressor Rotor," ASME JOURNAL OF TURBOMACHINERY, Vol. 111, pp. 250–256.

Karimova, A. G., Lokai, V. I., and Tkachenko, N. S., 1973, "Investigation of Heat Release From a Gas to the Elements of a Turbine Body," *Izvestiya VUZ Aiatsinnaya Tekhnika*, Vol. 16, pp. 114–119.

Kumada, M., Hirata, M., and Kasagi, N., 1981, "Studies of Full-Coverage Film Cooling. Part 2: Measurement of Local Heat Transfer Coefficient," ASME Paper No. 81-GT-38.

Kumada, M., Asao, Y., Obata, M., and Funazaki, K., 1988, "Heat Transfer Measurement on the Casing Wall Surface Opposite to Turbine Blade Row," *Proc. of 1st World Conf. on Experimental Heat Transfer, Fluid Mechanics and Thermodynamics*, Dubrovnik, Yugoslavia, pp. 1027–1032.

Lakshminarayana, B., Pouagare, M., and Davino, R., 1982, "Three-Dimensional Flow Field in the Tip Region of a Compressor Rotor Passage—Part 1: Mean Velocity Profiles and Annulus Wall Boundary Layer," ASME *Journal of Engineering for Power*, Vol. 104, pp. 760–771.

Metzger, D. E., Takeuchi, D. I., and Kuenstler, P. A., 1973, "Effectiveness and Heat Transfer With Full-Coverage Film Cooling," ASME *Journal of Engineering for Power*, Vol. 95, pp. 180–186.

Metzger, D. E., Dunn, M. G., and Hah, C., 1991, "Turbine Tip and Shroud Heat Transfer," ASME JOURNAL OF TURBOMACHINERY, Vol. 113, pp. 502–507.

Moffat, R. J., 1982, "Contributions to the Theory of Single-Sample Uncertainty Analysis," ASME *Journal of Fluids Engineering*, Vol. 104, pp. 250–260.

Pouagare, M., and Delaney, R. A., 1986, "Study of Three-Dimensional Viscous Flows in an Axial Compressor Cascade Including Tip Leakage Effect Using a SIMPLE-Based Algorithm," ASME JOURNAL OF TURBOMACHINERY, Vol. 108, pp. 51–58.

The Effect of a Turbulent Wake on the Stagnation Point: Part II—Heat Transfer Results

A. J. Hanford

D. E. Wilson

Department of Mechanical Engineering,
The University of Texas,
Austin, TX 78712

A phenomenological model is proposed that relates the effect of free-stream turbulence to the increase in stagnation point heat transfer. The model requires both turbulence intensity and energy spectra as inputs to the unsteady velocity at the edge of the boundary layer. The form of the edge velocity contains both a pulsation of the incoming flow and an oscillation of the streamlines. The incompressible unsteady and time-averaged boundary layer response is determined by solving the momentum and energy equations. The model allows for arbitrary two-dimensional geometry; however, results are given only for a circular cylinder. The time-averaged Nusselt number is determined theoretically and compared to existing experimental data.

Introduction

Large increases in stagnation point heat transfer are often associated with a free stream, which contains unsteady spatial and temporal fluctuations. These fluctuations can be either vortical (turbulence) or irrotational. When the incoming flow is effectively incompressible, the increase can be a factor of two to three relative to the undisturbed value (Hoshizaki et al., 1975; Strahle, et al., 1987; Vanfossen and Simoneau, 1985). When the incoming flow is in the supersonic or even hypersonic range the increase can be much higher. For example, for Type III and Type IV shock/shock interactions the value can be 20–30 times the Fay-Riddell value (Edney, 1968; Keyes and Hains, 1973).

The actual location of the stagnation point will vary over a distance comparable to the undisturbed laminar stagnation point boundary layer thickness. The resulting boundary layer can be classified as pseudoturbulent (Taulbee and Tran, 1988) or disturbed laminar (Wilson and Hanford, 1990). A discussion of the basic physics and phenomenological model used in this analysis is given in an earlier paper by the authors (1990). However, the salient features will be outlined in the next section. The purpose of this paper is to report on recent results concerning the stagnation point heat transfer analysis when an incoming flow contains a quasi-coherent, large-scale turbulent structure that is characteristic of a turbulent wake impinging upon a body such as a turbine blade.

Turbulence modeling in the stagnation region has proceeded along several directions. One direction represents the effect of the free-stream turbulence using time-averaged boundary-layer equations and a standard turbulence model (Smith and Kuethe, 1966; Galloway, 1973; Traci and Wilcox, 1975; Wang, 1984). Reasonable agreement between experiment and theory can be obtained by adjusting the model parameters to fit a particular set of experimental data. Such models generally fail as predictive tools because they can produce unrealistic results when applied to flow fields with different turbulence intensities and spectra.

Vorticity stretching has been hypothesized as a significant mechanism for altering stagnation point properties (Sutera et al., 1963; Sutera, 1965; Sadeh et al., 1970a, 1970b). These mechanisms can account for three-dimensional effects and a significant percentage of the observed increase in heat transfer in the region of the stagnation point. However, the predicted flow field depends strongly upon arbitrary free-stream vorticity field parameters, specifically the wavelengths and orientation of the vortices.

A few researchers have attempted to solve the unsteady boundary-layer equations directly. However, most of the studies have been concerned with arbitrary small periodic fluctuations in the free stream. Recently, several papers have appeared that specifically address how a particular free-stream disturbance of engineering interest might alter the stagnation point flow field. For example, Cebeci et al. (1987) modeled a free-stream flow containing a wake passing perpendicular to the mean flow axis. Bogucz et al. (1988) considered an approaching flow, which included a pair of counterrotating vortices. Both of these studies reported significant unsteady components in the stagnation point velocity and temperature profiles. These investigations provide an understanding of how the spatial and temporal fluctuations of a free stream influence stagnation

Contributed by the International Gas Turbine Institute and presented at the 37th International Gas Turbine and Aeroengine Congress and Exposition, Cologne, Germany, June 1–4, 1992. Manuscript received by the International Gas Turbine Institute February 17, 1992. Paper No. 92-GT-197. Associate Technical Editor: L. S. Langston.

region skin friction and heat transfer. It is this basic methodology that is adopted in this investigation. Specifically, a model is proposed that simulates the effect of large-scale vortical structures in a turbulent free-stream flow upon the edge velocity in the unsteady boundary layer.

Phenomenological Model

Attempts at modeling the effect of free-stream turbulence in the stagnation region have been largely unsuccessful primarily because of a misunderstanding of the physical mechanisms. Many researchers have attempted to "force" turbulence into laminar stagnation point theories by simply adding a turbulence transport term into the time-averaged equations. However, most boundary layers are not fully turbulent at the stagnation region and, prior to transition, they are pseudolaminar and unsteady.

To be useful as an engineering analytical tool, the model must have two essential components. First, it must be relatively simple to use for a wide variety of flow field calculations. For example, the classical Fay and Riddell theory (1958) typifies this approach. Second, the model must include the essential physics to be truly predictive. That is, it must not contain arbitrary artificial parameters adjusted to reproduce experimental data accurately for some set of very specific flow conditions. For incompressible flows, the proposed model is simple to implement and contains the essential physics.

The phenomenological model requires a knowledge of both the turbulent intensity and energy spectra. Unfortunately, most experimental investigations of heat transfer augmentation due to free-stream turbulence report only the turbulent intensity. However, when the free-stream turbulence is generated by well-defined mechanisms such as bluff bodies, splitter plates, or turbulence grids, the spectra can generally be inferred from a knowledge of the flow physics. Therefore, this study focused upon wake-generated turbulence for which the intensity and spectra are reasonably well known.

The model isolates the important effects of the free-stream turbulence upon the stagnation point flow field. This is not the same as a model that accurately describes the complex time-dependent physical process occurring in the free stream, but rather *models its effect* in the near-wall stagnation point region.

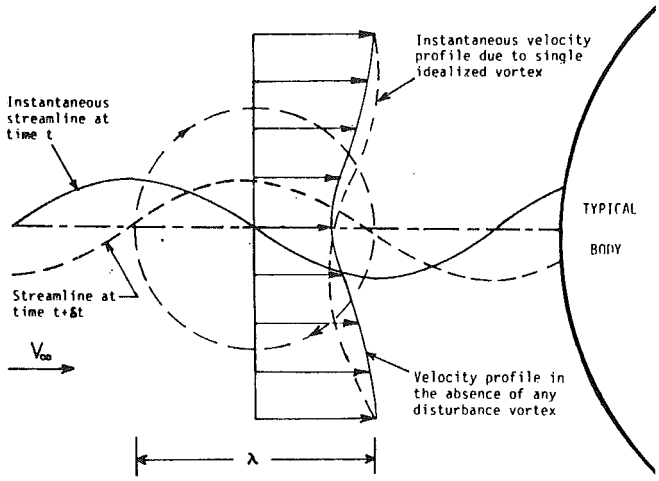

Fig. 1 Idealized model: stagnation point fluctuation due to a single wavelength vortical structure convected by the mean flow

With these caveats in mind, consider a fluctuation composed of a few dominant length (and frequency) scales in an otherwise uniform flow. This fluctuation would be produced, for example, by vortical structures of characteristic length, λ. As these structures are convected toward the stagnation point, the incoming flow pulsates and the instantaneous dividing streamline undergoes an oscillation in space and time. A picture of this process is shown in Fig. 1, where the oscillation is idealized as a traveling sinusoidal wave. The amplitude of this wave is proportional to the mean fluctuation velocity, $|v'|$. The frequency in the far field can be written as $\Omega \approx V_\infty/\lambda$. Near the body, but outside the boundary layer, the inviscid strain field alters both the length scale, λ, and the time scale, $1/\Omega$. As a

Nomenclature

A = geometric constant for inviscid stagnation point flow
a_n = pulsation parameter
$B_v(t)$ = an integration constant [see Eq. (3)]
b = characteristic nondimensional length scale
b_m = dimensional oscillation parameter
c = $d\bar{U}_e/dx$ at $x=0$
c_p = specific heat
D = characteristic length scale of the solid body
E = total nondimensional energy in all frequencies
Ec = Eckert number $=(cb)^2/c_p(T_w-T_\infty)$
e_n = nondimensional energy at a particular frequency
F = general function of η and τ associated with the ξ-dependent part of the stream function
f_n, g_n = η-dependent behavior of Fourier series expansion for F
H = general function of η and τ associated with the ξ-independent part of the stream function
h_n, k_n = η-dependent behavior of Fourier series expansion for H
k = thermal conductivity
M, N = finite series limits
Nu = Nusselt number [see Eq. (52)]
n = nondimensional frequency
Pr = Prandtl number
p = pressure
P_1, P_2 = apparent pressure gradient associated with the ξ-dependent and ξ-independent portion of the steady-stream function equation
Q_1, Q_2 = apparent volumetric heating associated with the ξ-dependent and ξ-independent portion of the steady thermal energy equation
q'' = heat flux
R = general function of η and τ associated with the ξ-dependent part of the temperature
r_n, q_n = η-dependent behavior of Fourier series expansion for R
Re = Reynolds number $=cb^2/\nu$
S = general function of η and τ associated with the ξ-independent part of the temperature
s_n, w_n = η-dependent behavior of Fourier series expansion for S
St = Strouhal number [see Eq. (46)]
T = dimensional temperature
Tu = turbulence intensity
t = dimensional time

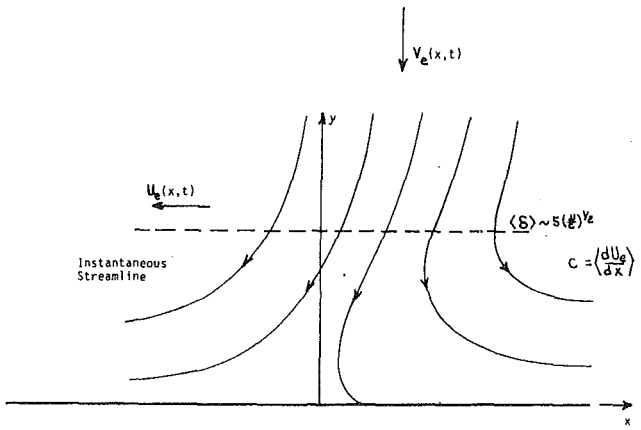

Fig. 2 Sketch of flow field and coordinate system in the stagnation point region

first approximation, however, the far-field scales will be used. Physically this is a valid approximation when the free-stream turbulence is frozen; that is, when the absolute dimensions of the vortical structures are not significantly altered compared with the change in the mean fluid velocities as the stagnation point is approached.

For this idealized model, we can now write the following expression for the unsteady edge velocity to which the laminar boundary layer must respond. Referring to Fig. 2, the result is given by

$$U_e(x, t) = c[1 - a_n \sin(\Omega_n t)][x - b_m \sin(\Omega_m t)] \quad (1)$$

where the repeated indices m and n indicate summation from one to some finite values, N and M. In this equation, the parameter, c, is the usual time-independent velocity gradient; that is, $c = dU_e/dx$ at $x = 0$. The nondimensional amplitude, a_n, is the ratio of the fluctuating velocity to the average velocity in the inviscid flow at the boundary layer edge. Thus, the first set of terms represents the pulsation of the incoming flow and a particular component, a_n, is proportional to $|v'|/U_c$, where U_c is a characteristic mean velocity outside the boundary layer. The dimensional parameter, b_m, represents the displacement amplitude of the incoming stagnation streamline. Consequently, this second set of terms represents the oscillation. The parameters appearing in Eq. (1) will be quantified below.

Mathematical Formulation

The simplified model of a free-stream turbulent fluctuation, shown in Fig. 1, is the basis for the unsteady stagnation point analysis. The stagnation streamline shown at the first instant is oscillating in a wavelike manner so that at the second instant it appears as shown by the broken line. It should be noted that the amplitude of this waviness in the stagnation streamline is highly exaggerated. Figure 2 shows the coordinate system and a schematic of the flow structure in the stagnation point region. The coordinate system is fixed on the body at the mean position of the stagnation streamline.

Based upon this model, the edge-velocity parallel to the wall can be written as

$$U_e(x, y, t) = c[1 - a_n \sin(\Omega_n t)][x - b_m \sin(\Omega_m t)] + \Gamma_{ob} y \quad (2)$$

where $N \geq M$, $\Omega = \Omega_n/n$, and Γ_{ob} accounts for shear in the incoming flow.

The relationship above assumes only N dominant frequencies are necessary to characterize the time dependence of the large-scale vortical structures. Values of N and M equal to one were used as an initial approximation; however, additional terms can easily be included.

It should be emphasized again that Eq. (2) does not represent the time-dependent vortical structures themselves, but is assumed to represent the essential effect of the unsteady structure of the shear layer, *insofar as the stagnation region is concerned.*

Using the incompressible continuity equation and assuming a constant free-stream vorticity, Ω_∞, the pulsating nature of the incoming flow can readily be seen from the expression for the edge velocity normal to the wall:

$$V_e(x, y, t) = (\Omega_\infty + \Gamma_{ob})x - c[1 - a_n \sin(\Omega_n t)]y + B_v(t) \quad (3)$$

Nomenclature (cont.)

γ_{ob} = nondimensional obliqueness parameter
γ_E = an unknown constant [see Eq. (42)]
U_e, V_e = boundary-layer edge velocity parallel and normal to the body surface, respectively
$|v'|$ = mean fluctuation velocity
u, v = boundary layer velocity parallel and normal to the body surface, respectively
V_∞ = far-field fluid velocity
x, y = dimensional boundary layer coordinates fixed on the body
α = nondimensional frequency $= (\Omega_1/c)^{1/2}$
β_m = nondimensional oscillation parameter $= b_n/b$
β_p = thermodynamic volume expansivity $= T^{-1}$ for an ideal gas
Γ_{ob} = dimensional obliqueness parameter
Δ = an appropriate inverse time scale
θ = nondimensional temperature difference
λ_n = characteristic length of vortical structures
ν = kinematic fluid viscosity
ξ, η = nondimensional boundary layer coordinates fixed on the body
ρ = fluid mass density
σ = $\sqrt{n/2}$
τ = nondimensional time
φ = dimensional two-dimensional stream function
ψ = nondimensional two-dimensional stream function
Ω = dimensional frequency of the periodic fluid motion
ω = a characteristic frequency of the periodic fluid motion
Ω_∞ = dimensional constant vorticity in the far field
ω_∞ = nondimensional constant vorticity in the far field

Subscripts

D = based on cylinder diameter, D
e = at the edge of the boundary layer
n = nth harmonic of time-dependent part of flow
o = time-independent part of flow
s = quantity evaluated at $\eta = 0$
w = quantity evaluated at $y = 0$
∞ = in the far field

Superscripts

$-$ = time-averaged quantity
$'$ = fluctuating quantity [when associated with a velocity; see Eq. (36)]
$'$ = ordinary derivative with respect to η
$*$ = nondimensional form of a quantity that is defined as dimensional

where $B_v(t)$ is a function of time. The pulsation parameters, a_n, specify the amplitude of the pulsation.

The system of differential equations that provides a description of the unsteady flow in the stagnation region for an incompressible, two-dimensional, laminar flow, in terms of primative variables is

$$\frac{\partial u}{\partial x}+\frac{\partial v}{\partial y}=0 \tag{4}$$

$$\frac{Du}{Dt}=-\frac{1}{\rho}\frac{dp}{dx}+\nu\left[\frac{\partial^2 u}{\partial x^2}+\frac{\partial^2 u}{\partial y^2}\right] \tag{5}$$

$$\frac{DT}{Dt}=\frac{k}{\rho c_p}\left[\frac{\partial^2 T}{\partial x^2}+\frac{\partial^2 T}{\partial y^2}\right]+\frac{\beta_p}{\rho c_p}T\frac{Dp}{Dt}+\frac{\mu}{\rho c_p}\left[2\left(\frac{\partial u}{\partial x}\right)^2+2\left(\frac{\partial v}{\partial y}\right)^2+\left(\frac{\partial u}{\partial y}+\frac{\partial v}{\partial x}\right)^2\right] \tag{6}$$

where D/Dt is the substantial time derivative operator in two dimensions.

The dimensional two-dimensional stream function, ϕ, is commonly defined as

$$u=\frac{\partial \phi}{\partial y} \qquad v=-\frac{\partial \phi}{\partial x} \tag{7}$$

The variables are nondimensionalized as follows:

$$\eta=\frac{y}{\sqrt{\nu/\Delta}} \qquad \psi=\frac{\phi}{cb}\left(\frac{\Delta}{\nu}\right)^{1/2}$$

$$\xi=x/b \qquad \tau=\Omega t$$

$$\omega_\infty=\Omega_\infty/\Omega \qquad \gamma_{ob}=\Gamma_{ob}/c$$

$$u^*=u/cb \qquad v^*=v\sqrt{\mathrm{Re}}/cb$$

$$p^*=\frac{p-p_o}{\rho(cb)^2} \qquad \theta=\frac{T-T_\infty}{T_w-T_\infty} \tag{8}$$

The dimensional parameters T_∞ and T_w are the mean free-steam and wall temperatures, respectively, and p_o is the mean stagnation pressure. The Reynolds number is defined as $\mathrm{Re}=cb^2/\nu$. The parameter c, which has units of inverse time, relates the two-dimensional body shape to the inviscid flow field. The parameter b is a length scale measured from the origin along the body surface. Furthermore, b is designated as one half the width of where the stream function varies approximately as x. In general, b is larger than the boundary layer thickness, δ, but the ratio of b to δ is of order unity. For a two-dimensional cylinder, $c=4V_\infty/D$ and b is equivalent to the surface length associated with a few degrees of circumference arc.

This particular nondimensionalization is selected so that the solution to the time-averaged part of the flow is independent of the particular body geometry. The parameter Δ^{-1} is a reminder that natural time scales for steady and unsteady flows differ. In a *steady* stagnation point flow Δ is c and $\sqrt{\nu/c}$ is the Hiemenz layer thickness. In an *unsteady* stagnation point flow the appropriate scale for the *time-dependent* equations is Ω and $\sqrt{\nu/\Omega}$ is the Stokes layer thickness. Because we eventually wish to divide the equations into steady and unsteady contributions and scale each by its natural time scale, both scales will be used to develop the simplified governing equations. However, because a consistent definition for η and ψ must eventually be adopted so that various solutions may be recombined, Δ will be equal to c, the steady flow scale, in all cases after the proper form of the unsteady equations are determined.

The resulting nondimensional x-momentum and energy equations, which have been further simplified by assuming that $\psi=\xi f(\eta, \tau)$, become

$$\alpha^2\frac{\partial^2\psi}{\partial\tau\partial\eta}+\frac{\partial\psi}{\partial\eta}\frac{\partial^2\psi}{\partial\xi\partial\eta}-\frac{\partial\psi}{\partial\xi}\frac{\partial^2\psi}{\partial\eta^2}=\alpha^2\frac{\partial U_e^*}{\partial\tau}+U_e^*\frac{\partial U_e^*}{\partial\xi}+\alpha^2\left(\frac{\Delta}{\Omega}\right)\frac{\partial^3\psi}{\partial\eta^3} \tag{9}$$

$$\alpha^2\frac{\partial\theta}{\partial\tau}+\frac{\partial\psi}{\partial\eta}\frac{\partial\theta}{\partial\xi}-\frac{\partial\psi}{\partial\xi}\frac{\partial\theta}{\partial\eta}=\alpha^2\left(\frac{\Delta}{\Omega}\right)\frac{1}{\mathrm{Pr}}\frac{\partial^2\theta}{\partial\eta^2}+\mathrm{Ec}\left[\alpha^2\frac{\partial p^*}{\partial\tau}+\frac{\partial\psi}{\partial\eta}\frac{\partial p^*}{\partial\xi}+\alpha^2\left(\frac{\Delta}{\Omega}\right)\left(\frac{\partial^2\psi}{\partial\eta^2}\right)^2\right] \tag{10}$$

where $\alpha^2=\Omega/c$ is the nondimensional frequency parameter, and $\mathrm{Ec}=(cb)^2/c_p(T_w-T_\infty)$ is the Eckert number. In a steady, low-speed stagnation point solution, the first term between the brackets in Eq. (10) is identically zero. The second term has quadratic variation in ξ and is negligible near $\xi=0$. Similarly, the last term is quadratic in ξ and is also negligible. However, in an unsteady flow, where the incoming stream undergoes large excursions, these terms make important contributions to the time-averaged solution.

The nondimensional edge velocity is

$$U_e^*(\xi, \eta, \tau)=[1-a_n\sin(n\tau)][\xi-\beta_m\sin(m\tau)]+O(\mathrm{Re}^{-1}) \tag{11}$$

with $\beta_m=b_m/b$.

The boundary conditions on ψ and θ are

$$\psi(\xi, 0, \tau)=0 \qquad \frac{\partial\psi}{\partial\eta}(\xi, 0, \tau)=0 \tag{12}$$

$$\frac{\partial\psi}{\partial\eta}(\xi, \eta\to\infty, \tau)=U_e^*(\xi, \eta, \tau)$$

$$\theta(\xi, \eta\to\infty, \tau)=0 \qquad \theta(\xi, 0, \tau)=\xi r_{os}+1 \tag{13}$$

where the constant r_{os} may be used to quantify a spatial variation at the wall in the energy equation boundary condition. For an isothermal body r_{os} would be zero.

Because this is a stagnation point flow, a solution will be sought in the form

$$\psi(\xi, \eta, \tau)=\xi F(\eta, \tau)+H(\eta, \tau) \tag{14}$$

$$\theta(\xi, \eta, \tau)=\xi R(\eta, \tau)+S(\eta, \tau) \tag{15}$$

Substitution of Eq. (14) for the stream function and Eq. (15) for the temperature into the partial differential Eqs. (9) and (10) and boundary conditions (12) and (13) allows the problem to be reformulated as four coupled partial differential equations with only two independent variables, η and τ.

Solution Methodology

The assumed solution given by Eqs. (14) and (15) allows the Navier–Stokes equations to be written in boundary layer form without approximation in the near-wall region. The equations may be solved using two independent approaches: The first is an unsteady, time-accurate integration of the resulting second-order and third-order, nonlinear partial differential equations; while the second is a high-frequency approximation. Wilson and Philips (1989) compared the time-accurate integration and high-frequency approximation using the momentum equation for a reattaching shear layer behind a backward facing step. They found that both techniques yielded almost identical results. However, the high-frequency approximation is far more revealing. It demonstrates how the unsteady nature of the flow produces an additional pressure gradient that induces over-

shoots in the velocity profiles near the wall, and also higher wall fluxes. Thus, only a solution using the high-frequency approximation is pursued here. Profiles of velocity, shear stress, and heat flux for the steady part of the flow appear to substantiate the basic postulate that large-scale unsteadiness, rather than small-scale turbulence, can induce the experimentally observed effects of relatively high wall flux quantities in the stagnation region.

High Frequency Approximation. Because the incoming flow is quasi-periodic (in fact we have represented it by only a few discrete frequencies) it is reasonable to seek a solution in which the functions $F(\eta, \tau)$, $H(\eta, \tau)$, $R(\eta, \tau)$, and $S(\eta, \tau)$ are expanded using a Fourier series in time. This in itself does not lead to any significant simplification. However, when the high-frequency approximation is exploited, the resulting unsteady components of the streamfunction have closed-form analytical solutions. As we will see, this produces a significant simplification and sheds considerable light upon the way in which the unsteadiness alters the time-averaged velocity profiles.

Using the forms of the streamfunction and temperature given by Eqs. (14) and (15) and representing the time-dependent behavior by finite Fourier series we have

$$\psi = \xi f_o(\eta) + h_o(\eta) + \sum_{n=1}^{N} \xi[f_n(\eta)\cos(n\tau) + g_n(\eta)\sin(n\tau)] + \sum_{n=1}^{N+M} [h_n(\eta)\cos(n\tau) + k_n(\eta)\sin(n\tau)] \quad (16)$$

$$\theta = \xi r_o(\eta) + s_o(\eta) + \sum_{n=1}^{N+M} \xi[r_n(\eta)\cos(n\tau) + q_n(\eta)\sin(n\tau)] + \sum_{n=1}^{N+M} [s_n(\eta)\cos(n\tau) + w_n(\eta)\sin(n\tau)] \quad (17)$$

where the series limits in Eqs. (16) and (17) are the largest values for which a set of nonzero functions might be obtained based on the input nonzero model parameters, a_n and β_m. Functions with a subscript (o) represent the time-independent component of the flow. They are, in effect, equivalent to the time-averaged solution.

Time-Independent Equations. The governing equations for the time-independent components of the solution (f_o, h_o, r_o, and s_o) are obtained by using the steady scaling with $\Delta = c$. Equations (16) and (17) are substituted into the x-momentum and energy equations, (9) and (10), and terms containing explicit functions of time are omitted. Setting the ξ-dependent and ξ-independent coefficients from these intermediate expressions independently to zero leads to four ordinary differential equations in η:

$$f_o''' + f_o f_o'' - f_o' f_o' + 1 + P_1 = 0 \quad (18)$$

where

$$P_1 = +\alpha^2\omega_\infty\gamma_{ob} + \gamma_{ob}^2 + \sum_{i=1}^{N}\frac{a_i a_i}{2} + \frac{1}{2}\sum_{i=1}^{N}(f_i f_i'' + g_i g_i'' - f_i' f_i' - g_i' g_i')$$

with $f_o = 0$ and $f_o' = 0$ at $\eta = 0$, and $f_o' \to 1$ as $\eta \to \infty$

$$h_o''' + f_o h_o'' - f_o' h_o' + \underbrace{\sum_{i=1}^{M} a_i\beta_i + \frac{1}{2}\sum_{i=1}^{N+M}(f_i h_i'' + g_i k_i'' - f_i' h_i' - g_i' k_i')}_{P_2} = 0 \quad (19)$$

with $h_o = 0$ and $h_o' = 0$ at $\eta = 0$, and $h_o' \to \sum_{i=1}^{M}\frac{a_i\beta_i}{2}$ as $\eta \to \infty$

$$\frac{r_o''}{\mathrm{Pr}} + f_o r_o' - f_o'' r_o + 2\,\mathrm{Ec} f_o'' h_o'' + Q_1 = 0 \quad (20)$$

where

$$Q_1 = -\mathrm{Ec}\left[\alpha^2\omega_\infty\gamma_{ob} + \gamma_{ob}^2 + \sum_{i=1}^{N\text{ or }M} a_i\beta_i\right] f_o' + \mathrm{Ec}\left[\frac{1}{2}\sum_{j=1}^{N\text{ or }M}\beta_j(j\alpha^2 f_j' + g_j')\right] - \mathrm{Ec}\left[\left(1 + \sum_{i=1}^{N}\frac{a_i a_i}{2}\right)h_o' + \sum_{j=1}^{N+M\text{ or }2N}\frac{E_j h_j'}{2}\right] + \frac{1}{2}\sum_{j=1}^{N}[f_j r_j' + g_j q_j' - f_j' r_j - g_j' q_j] + \frac{1}{2}\sum_{j=1}^{N}\left[\alpha^2\mathrm{Ec}\left(j a_j h_j' - \frac{B_j g_j'}{2}\right)\right] + \mathrm{Ec}\sum_{j=1}^{N}[f_j'' h_j'' + g_j'' k_j'' + a_j k_j'] + \mathrm{Ec}\sum_{j=1}^{N}\left[\frac{D_j g_j'}{2} - A_j f_j' + \frac{a_j g_j'}{2} - \sum_{i=1}^{N\text{ or }M}\frac{a_i\beta_i}{2}\right]$$

with $r_o = 0$ as $\eta \to \infty$, and $r_o = r_{os}$ at $\eta = 0$. The combined group Q_1 is defined as those terms that do not contain r_o or any of its derivative.

$$\frac{s_o''}{\mathrm{Pr}} + f_o s_o' - h_o' r_o + Q_2 = 0 \quad (21)$$

where

$$Q_2 = +\mathrm{Ec}\, h_o'' h_o'' - \mathrm{Ec}\left[\alpha^2\omega_\infty\gamma_{ob} + \gamma_{ob}^2 + \sum_{i=1}^{N\text{ or }M} a_i\beta_i\right] h_o' + \frac{\mathrm{Ec}}{2}\left[\sum_{j=1}^{M}\beta_j(j\alpha^2 h_j' + k_j') + \frac{1}{2}\sum_{j=1}^{N}(f_j s_j' + g_j w_j')\right] - \frac{\mathrm{Ec}}{2}\left[\sum_{j=1}^{N+M}(h_j' r_j + k_j' q_j) + \alpha^2\frac{B_j g_j'}{2}\right] + \frac{\mathrm{Ec}}{2}\sum_{j=1}^{N+M}[h_j'' h_j'' + k_j'' k_j'' - 2A_j h_j' + D_j k_j'] + \frac{\mathrm{Ec}}{2}\sum_{j=1}^{N}\left[a_j k_j' - \sum_{i=1}^{N\text{ or }M}\frac{a_i\beta_i}{2}\right]$$

with $s_o = 0$ as $\eta \to \infty$, and $s_o = 1$ at $\eta = 0$. The combined group Q_2 is defined as those terms that do not contain r_o or s_o or any derivatives of r_o or s_o. In Eqs. (18)–(21), $'$ denotes $d/d\eta$.

Note that the first line in Eq. (18) for f_o is exactly the equation for the Hiemenz stagnation point flow. The P_1 terms denoted by a brace are analogous to an additional pressure gradient plus Reynolds stresses due to the large-scale unsteadiness. The free-stream vorticity and the mean shear in the incoming flow also contribute to this term. Similarly, the P_2 terms in Eq. (19) for h_o are analogous to an additional pressure gradient and Reynolds stresses. The additional functions, Q_1 and Q_2, in the energy equations, (20) and (21), are comparable to induced volumetric heating terms from the unsteadiness, vorticity, and mean shear in the free-stream flow.

Time-Dependent Equations. Analytical expressions may be developed for the spatial variations in the induced unsteadiness that contribute to P_1 and P_2. However, the spatial variations in the induced unsteadiness from the expansion of the nondimensional temperature do not have closed-form analytical expressions. Instead, these functions may only be described without additional approximation by the numerical solution of ordinary differential equations.

As before, the x-momentum and energy equations, (9) and (10), are combined with the assumed solutions for ψ and θ given by Eqs. (16) and (17). The unsteady behavior is of interest here so the unsteady scaling with Δ equal to Ω is employed. The transient terms are retained and the steady equations are subtracted from the composite expressions for x-momentum and energy. After dividing each resulting expression by $\alpha^2 = \Omega/c$, the high-frequency approximation states that terms of order $1/\alpha^2$ and smaller are negligible. This approximation discards convection by mean fluid motion and simplifies the unsteady governing equations. In practice the high-frequency approximation requires only $\alpha^2 \geq 4$.

The limit of infinite frequency used in the high-frequency approximation removes convection due to steady fluid motion and retains diffusion and transient terms in the x-momentum and thermal energy balances. Physically, this process recognizes the greater importance of transient convection over mean flow convection when considering a rapidly oscillating flow. If the steady scaling had been used in place of the unsteady scaling, the diffusion terms would have been of order $1/\alpha^2$, requiring the remaining transient terms to balance with zero. Because the transient effects are observed experimentally to alter the surface fluxes, and therefore influence the x-momentum and thermal energy balances in the near wall region, such a formulation would contradict the known flow field physics. Thus, using purely physical arguments, the diffusion terms are important in the unsteady governing equations to balance the transient terms.

So that the unsteady and steady solutions are a function of the same nondimensional variable, η, the simplified unsteady x-momentum and thermal energy equations are transformed from the unsteady time scale to the steady time scale; that is, Δ is redefined as c. These reduced equations may be written entirely in terms of functions multiplying one of four trigonometric expressions: $\cos(n\tau)$, $\sin(n\tau)$, $\xi\cos(n\tau)$, and $\xi\sin(n\tau)$. Setting the coefficient functions of the trigonometric expressions separately to zero generates a closed system of linear, second-order and third-order, ordinary differential equations for f_n, g_n, h_n, k_n, r_n, q_n, s_n, and w_n.

The boundary conditions for the differential equations are determined in the same manner as the equations. The assumed solutions for ψ and θ, Eqs. (16) and (17), are substituted into the original boundary conditions, Eqs. (12) and (13). The steady portion of each composite boundary condition applies only to the steady equations, (18) to (21). After removing the steady contributions, the boundary conditions for the unsteady equations arise from what remains by setting the coefficients on $\xi\cos(n\tau)$, $\xi\sin(n\tau)$, $\cos(n\tau)$, and $\sin(n\tau)$ separately to zero.

The differential equations that describe the spatial functions associated with the time-dependent flow field are:

$$f_n''' - n\alpha^2 g_n' = n\alpha^2 a_n \tag{22}$$

where $a_n = 0$ when $n > N$. Also $f_n = 0$ and $f_n' = 0$ at $\eta = 0$, and $f_n' \to 0$ as $\eta \to \infty$.

$$g_n''' + n\alpha^2 f_n' = 0 \tag{23}$$

with $g_n = 0$ and $g_n' = 0$ at $\eta = 0$, and $g_n' \to -a_n$ as $\eta \to \infty$ for $n \leq N$.

$$h_n''' - n\alpha^2 k_n' = n\alpha^2 \beta_n \tag{24}$$

where $\beta_n = 0$ when $n > M$. Also $h_n = 0$ and $h_n' = 0$ at $\eta = 0$, and $h_n' \to A_n$ as $\eta \to \infty$ when $n \leq N+M$.

$$k_n''' + n\alpha^2 h_n' = -\frac{1}{2}\alpha^2 B_n \tag{25}$$

where $B_n = 0$ when $n > N+M$. Also $k_n = 0$ and $k_n' = 0$ at $\eta = 0$, and $k_n' \to -\beta_n$ (when $n \leq M$) or $k_n' \to 0$ (when $M < n \leq N+M$) as $\eta \to \infty$.

The differential equations that describe the time-dependent temperature field are:

$$\frac{r_n''}{\mathrm{Pr}} - n\alpha^2 q_n = \alpha^4 \frac{n}{2}\,\mathrm{Ec}\,B_n - 2\,\mathrm{Ec}\,(h_n'' f_o'' + f_n'' h_o'' + A_{6n}) - \alpha^2\,\mathrm{Ec}\,n\beta_n(1 + f_o') - \alpha^2\,\mathrm{Ec}\,[nD_n - \omega_\infty \gamma_{ob} f_n' + A_{F2n}] - \alpha^2\,\mathrm{Ec}\left[na_n\left(h_o' + \sum_{i=1}^{N \text{ or } M}\frac{a_i\beta_i}{2}\right) - A_{F3n} + A_{H1n}\right] \tag{26}$$

where $\beta_n = 0$ for $n > M$ and $f_n'' = 0$ for $n > N$. Also $r_n = 0$ at $\eta = 0$, and $r_n \to 0$ as $\eta \to \infty$ for $n \leq N+M$.

$$\frac{q_n''}{\mathrm{Pr}} + n\alpha^2 r_n = \alpha^4 n^2\,\mathrm{Ec}\,\beta_n - 2\,\mathrm{Ec}\,(k_n'' f_o'' + g_n'' h_o'' + B_{6n}) - \alpha^2\,\mathrm{Ec}\left[2nA_n - \frac{B_n}{2}f_o' - \omega_\infty \gamma_{ob} g_n' + B_{F2n} - B_{F3n} + B_{H1n}\right] \tag{27}$$

where $\beta_n = 0$ for $n > M$ and $g_n'' = 0$ for $n > N$. Also $q_n = 0$ at $\eta = 0$, and $q_n \to 0$ as $\eta \to \infty$ for $n \leq N+M$.

$$\frac{s_n''}{\mathrm{Pr}} - n\alpha^2 w_n = -\,\mathrm{Ec}\,(2h_n'' h_o'' + A_{7n}) - \alpha^2\,\mathrm{Ec}\,[n\beta_n h_o' - \omega_\infty \gamma_{ob} h_n' + A_{H2n} - A_{H3n}] \tag{28}$$

where $\beta_n = 0$ for $n > M$. Also $s_n = 0$ at $\eta = 0$, and $s_n \to 0$ as $\eta \to \infty$ for $n \leq N+M$.

$$\frac{w_n''}{\mathrm{Pr}} + n\alpha^2 s_n = -\,\mathrm{Ec}\,(2k_n'' h_o'' + B_{70n}) - \alpha^2\,\mathrm{Ec}\left[-\frac{B_n}{2}h_o' - \omega_\infty \gamma_{ob} k_n' + B_{H2n} - B_{H3n}\right] \tag{29}$$

with $w_n = 0$ at $\eta = 0$, and $w_n \to 0$ as $\eta \to \infty$ for $n \leq N+M$.

The terms A_n, B_n, D_n, E_n, A_{Fin}, A_{Hin}, B_{Fin}, and B_{Hin} are functions of η only and are presented in the appendix.

High-Frequency Solution of Time-Dependent Equations. The terms P_1, P_2, Q_1, and Q_2, in Eqs. (18) to (21) depend on the functions f_n, g_n, h_n, k_n, r_n, q_n, s_n, and w_n, which represent the effect of the free-stream vorticity on the stagnation point boundary layer. In general, the time-independent equations, (18) to (21), and the time-dependent equations, (22) to (29), must be solved simultaneously. However, because of the high-frequency approximation, the time-dependent equations decouple from the mean flow equations. The resulting linear boundary value problems can be solved analytically.

Solving Eqs. (22) to (25) for the spatial variation of the time-dependent stream function using the given boundary conditions leads to:

For $n \leq N$

$$f_n = \frac{a_n}{2\alpha\sigma}\{\exp(-\alpha\sigma\eta)[\cos(\alpha\sigma\eta) + \sin(\alpha\sigma\eta)]\} \tag{30}$$

$$g_n = \frac{a_n}{2\alpha\sigma}\{1 - \exp(-\alpha\sigma\eta)[\cos(\alpha\sigma\eta) - \sin(\alpha\sigma\eta)]\} - a_n\eta \tag{31}$$

For $n \leq M$

$$h_n = A_n\eta - \left(\frac{A_n+\beta_n}{2\alpha\sigma}\right) + \exp(-\alpha\sigma\eta)\left[\left(\frac{A_n+\beta_n}{2\alpha\sigma}\right)\cos(\alpha\sigma\eta) + \left(\frac{\beta_n - A_n}{2\alpha\sigma}\right)\sin(\alpha\sigma\eta)\right] \tag{32}$$

$$k_n = \left(\frac{\beta_n - A_n}{2\alpha\sigma}\right) - \beta_n\eta + \exp(-\alpha\sigma\eta)\left[\left(\frac{\beta_n - A_n}{2\alpha\sigma}\right)\cos(\alpha\sigma\eta) + \left(\frac{A_n+\beta_n}{2\alpha\sigma}\right)\sin(\alpha\sigma\eta)\right] \tag{33}$$

For $M < n \leq N+M$

$$h_n = \frac{A_n}{2\alpha\sigma}\{\exp(-\alpha\sigma\eta)[\cos(\alpha\sigma\eta) - \sin(\alpha\sigma\eta)] - 1\} + A_n\eta \quad (34)$$

$$k_n = \frac{A_n}{2\alpha\sigma}\{\exp(-\alpha\sigma\eta)[\cos(\alpha\sigma\eta) + \sin(\alpha\sigma\eta)] - 1\} \quad (35)$$

where $\sigma = \sqrt{n/2}$.

The above solutions for the unsteady spatial variations in the stream function are substituted back into the terms P_1, P_2, Q_1, and Q_2 in Eqs. (18) to (21) for the steady part of the flow and Eqs. (26) to (29) for the unsteady spatial variations in the temperature. These second-order and third-order, differential equations are solved numerically for the functions f_o, h_o, r_o, s_o, r_n, q_n, s_n, and w_n and their derivatives. A B-spline collocation code, COLSYS (Ascher et al., 1978), was used for the solution of these ordinary differential equations. This code automatically discretizes the domain of the independent variable η in a manner designed to capture large gradients and to satisfy prespecified tolerances on the solution. The applied tolerances restricted the relative error in the velocity and temperature components to less than 10^{-3}.

Quantifying the Edge Velocity Model

An important task associated with this numerical approach is to determine or assign values to the edge velocity constants, a_n, β_m, and c in Eq. (11). These constants depend on several physical flow parameters such as test article geometry, free-stream turbulence intensity, and Reynolds number.

General Characteristics of the Edge Velocity Parameters. The model parameters are functions of the free-stream vorticity and test article geometry. These parameters will be determined in a manner consistent with the following constraints:

- Physically, the constant c accounts for the alteration of the stagnation point flow field due to the test article geometry. The constant c may be determined from the mean flow field as dU_e/dx when x approaches zero.
- The constants a_n and β_m describe the spatial variations in the free-stream pulsation and stagnation point oscillation, respectively. Intuitively, these model constants should depend on the intensity and energy distribution of the turbulent structures that reach the edge of the boundary layer. Ideally, a_n and β_m would be determined from actual measurements of the instantaneous velocity parallel to the body at the edge of the boundary layer. Because such measurements are often not possible, a_n and β_m are inferred from free-stream values.
- Because the structure and energy distribution in the free-stream turbulence will vary depending on the mode of production, the constants a_n and β_m are expected to vary in functional form when the turbulence production mode changes.
- When the turbulence intensity in the upstream flow approaches zero, the governing equations, (18) to (21), should reduce to those for Hiemenz flow. This is equivalent to requiring that P_1, P_2, Q_1, and Q_2 approach zero when intensity approaches zero. Or, a_n must approach zero in the limit of zero turbulence.
- Because surface heat flux data correlate well as a function of $Tu\mathrm{Re}_D^{1/2}$ (Hoshizaki et al., 1975; Smith and Kuethe, 1966; Galloway, 1973; Traci and Wilcox, 1975; Wang, 1984), the model constants a_n and β_m may also be expected to vary with $Tu\mathrm{Re}_D^{1/2}$.
- The $a_i\beta_i$ product in P_2 of Eq. (19) accounts for alterations in the mean value of h_o due to the free-stream unsteadiness. The form of the governing equations suggests that this product strongly influences the surface flux quantities. Therefore, each a_n should have a corresponding β_n, and M should be equal to N.

As a specific example of a possible upstream flow with free-stream turbulence, we will consider the stagnation point region on a two-dimensional cylinder in a turbulent wake. Because the majority of the fluctuating energy in a turbulent wake is distributed among a few frequencies and length scales, this flow condition naturally provides a suitable initial test.

Characteristics of a Turbulent Wake. Turbulent wakes and free shear layers in general are characterized by large coherent vortical structures superimposed on fine-scale turbulence. The growth of the wake is controlled by these large organized structures, which are not greatly affected by the small-scale turbulence even at higher values of the Reynolds number. These vortical structures are convected along with the flow, maintaining their spacing and, at the same time, growing in size by diffusion. When vortices are close enough, they interact. This can be the pairing of two or more vortices into one larger vortex, or a stretching and elongation interaction, which decreases the cross-sectional diameter of the vortices. These vortical pairings continue to occur as the shear layer moves downstream. The vortical patterns appear to exist at all Reynolds numbers, and experiments verify their nearly two-dimensional character.

For a free-shear layer with no forcing applied, the vortices are usually formed periodically (Ho and Huang, 1982). The frequency spectrum of the vortical formations has a maximum that closely corresponds with the frequency of the most amplified disturbance predicted from linear stability analysis.

A summary of some of the important physical aspects established through experiments that are relevant to the mathematical model are summarized below:

- The large-scale vortical structures are the dominant feature of free shear layers over a wide range of Reynolds numbers and they persist far downstream (Browand and Ho, 1983).
- The large-scale vortical structures form a regular pattern at discrete frequencies that are decoupled from small-scale turbulence (Dimotakis and Brown, 1976).
- The large-scale vortical structures are quasi two-dimensional (Browand and Troutt, 1985).
- The large-scale structure contains over 50 percent of the fluctuating energy (Browand and Ho, 1983).

Based upon these observations, a simple model for these structures may be constructed.

Parameter Determination. Published experimental measurements are generally insufficient to allow all of the constants in the assumed edge velocity, Eq. (11), to be independently evaluated. As such, this study uses a number of unrelated data sets and approximations in order to fit the model constants and demonstrate the technique. Ideally, as was mentioned earlier, measurements of the boundary layer edge velocity specifically tailored for this model would provide a direct fit for the constants a_n, β_n, and c.

The specific example of a turbulent wake impinging normally upon a two-dimensional circular cylinder of diameter D will be considered. The fit for the constants will be at a Reynolds number, Re_D, of 24,650, and a Prandtl number, Pr, of 0.72, which are typical values for air flowing past a cylinder. An Eckert number, Ec, of -0.001 corresponding to a cold wall is assumed. The flow geometry dictates that both the free-steam vorticity, Ω_∞, and the imposed mean shear, Γ_{ob}, in the incoming flow are zero. One harmonic will be used ($N = 1$).

The edge velocities given by Eqs. (2) and (3) without the unknown function of integration, $B_v(t)$, may be decomposed into mean components and fluctuating components to give

$$U_e = cb\left[1 - \sum_{n=1}^{N} a_n \sin(nt)\right]\left[\xi - \sum_{m=1}^{M} \beta_m \sin(mt)\right]$$

$$V_e = -c\left(\frac{\nu}{\Delta}\right)^{1/2}\eta\left[1 - \sum_{n=1}^{N} a_n \sin(n\tau)\right]$$

$$U_e = \overline{U}_e + U_e' \qquad V_e = \overline{V}_e + V_e' \tag{36}$$

The mean velocities for an inviscid stagnation point may be expressed as

$$\overline{U}_e = cb\xi \qquad \overline{V}_e = -c\left(\frac{\nu}{\Delta}\right)^{1/2}\eta$$

Squaring Eqs. (36) and time-averaging the results then leads to expressions for Reynolds stresses at the edge of the boundary layer as

$$\overline{U_e' U_e'} = (cb)^2\left[\xi^2 \sum_{k=1}^{N} \frac{a_k a_k}{2} + 2\xi \sum_{k=1}^{N \text{ or } M} a_k \beta_k\right]$$
$$+ (cb)^2\left[\sum_{i=1}^{N \text{ or } M} \frac{a_i \beta_i}{2} \sum_{k=1}^{N \text{ or } M} \frac{a_k \beta_k}{2} + \sum_{k=1}^{M} \frac{\beta_k \beta_k}{2} + \sum_{k=1}^{N+M} \frac{A_k A_k}{2}\right]$$

$$\overline{V_e' V_e'} = (cb)^2 \frac{\eta^2}{\mathrm{Re}} \sum_{k=1}^{N} \frac{a_k a_k}{2}$$

At the boundary layer edge, the magnitude of the velocity vector, $|\mathbf{V}_e|$, and the turbulence intensity, Tu_e, may be defined as

$$|\mathbf{V}_e| = [\mathbf{V}_e \cdot \mathbf{V}_e]^{1/2} = cb\left[\xi^2 + \frac{\eta^2}{\mathrm{Re}}\right]^{1/2}$$

$$Tu_e = \frac{1}{|\mathbf{V}_e|}\left[\frac{\overline{U_e' U_e'} + \overline{V_e' V_e'}}{2}\right]^{1/2}$$

Therefore, the edge turbulence intensity may be expressed as

$$Tu_e = \left[\frac{\left(\xi^2 + \frac{\eta^2}{\mathrm{Re}}\right)\sum_{k=1}^{N} \frac{a_k a_k}{2} + 2\xi \sum_{k=1}^{N \text{ or } M} a_k \beta_k + \sum_{i=1}^{N \text{ or } M} \frac{a_i \beta_i}{2} \sum_{k=1}^{N \text{ or } M} \frac{a_k \beta_k}{2} + \sum_{k=1}^{M} \frac{\beta_k \beta_k}{2} + \sum_{k=1}^{N+M} \frac{A_k A_k}{2}}{2\left(\xi^2 + \frac{\eta^2}{\mathrm{Re}}\right)}\right]^{1/2} \tag{37}$$

Ideally, measurements for either the turbulence intensity or the velocities at the boundary layer edge could be used to obtain the pulsation and oscillation parameters, a_n and β_m. However, because variations in the edge velocities and in the edge turbulence intensity are generally unknown for available stagnation point data we will model the pulsation parameters, a_n, from knowledge of the turbulence intensity in a shear layer. The oscillation parameters, β_m, will be estimated using stagnation point heat transfer data. As an initial approximation we will consider only twice the leading term so that Eq. (37) reduces to

$$(Tu_e)^2 \cong \sum_{k=1}^{N} \frac{a_k a_k}{2} \tag{38}$$

To evaluate the pulsation parameters, a_n, we must first relate the turbulence intensity at the boundary layer edge, Tu_e, to that of the free stream, denoted here as Tu_∞ or simply as Tu.

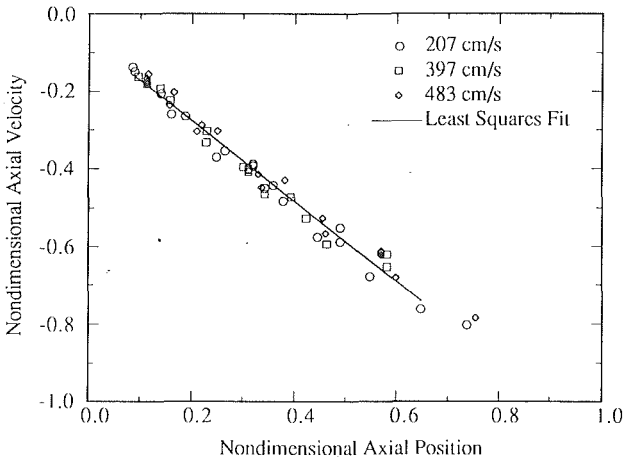

Fig. 3 Nondimensional axial velocity as a function of nondimensional axial distance from the stagnation plate from Johnson (1990). (The plate surface is at a nondimensional coordinate of zero, and the free stream is at one.)

The second hypothesis concerning the edge velocity parameters given above simplifies this exercise. Specifically, we assume that the absolute magnitudes of the large-scale fluctuations are unaltered by the inviscid strain field, provided we are at least eight viscous length scales from the wall. Thus, the physical coordinate becomes

$$y_e = 8\left(\frac{\nu}{c}\right)^{1/2}$$

It then follows that

$$|\overline{V}_e| = 8(c\nu)^{1/2}$$

or, for flow around a cylinder at high Reynolds numbers, we find

$$|\overline{V}_e| = 16\frac{V_\infty}{\mathrm{Re}_D^{1/2}} \tag{39}$$

To verify this hypothesis experimentally, data from Johnson (1990) for a turbulent air jet impinging upon a flat plate were used. In this study $Tu_\infty = 0.0511$ and $V_\infty = 4.83$ m/s. The parameter, c, determined from Fig. 3 had a value of 251 s^{-1}. At the boundary layer edge, $\eta_e = 8.0$, the turbulence intensity estimated by Eq. (38) is

$$Tu_e = Tu_\infty\left(\frac{V_\infty}{\overline{V}_e}\right) = 0.501 \tag{40}$$

Actual turbulence measurements at the boundary layer edge, shown in Fig. 4, confirm this to be an accurate value. For this example, the turbulence intensity at the boundary layer edge, Tu_e, is an *order of magnitude larger* than the free-stream value.

Because the pulsation parameters are a measure of the kinetic energy in the large-scale structures, each a_n is related to a corresponding frequency. Driver et al. (1987) present an energy spectrum for a reattaching shear layer as a function of nondimensional frequency. Theoretically, the nondimensional energy, E, frequency, n, and the fluctuating velocity component correlation are related by

$$(Tu_e)^2 = \int_{-\infty}^{+\infty} E(n)\,dn \tag{41}$$

By using these data, we assume turbulence within any shear flow has a similar energy distribution to that of a reattaching shear layer. Because the flow instabilities within shear-generated turbulence result from Kelvin–Helmholtz phenomena, this assumption is reasonable. More specifically, our assumption requires the *relative* energy distribution between different

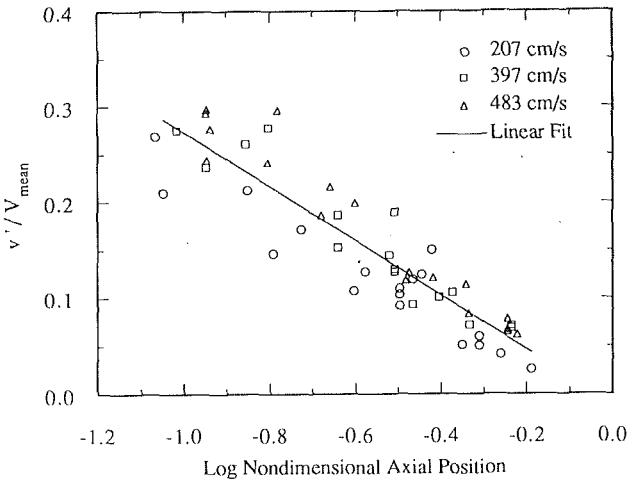

Fig. 4 The fluctuating velocity normalized by the local mean velocity versus the nondimensional axial position as the flow approaches a flat plate from Johnson (1990). (The plate surface is at a nondimensional coordinate of zero, and the free stream is at one.)

turbulence frequencies be similar to that in a reattaching shear layer; the absolute energy magnitude at a given frequency will be adjusted to agree with the overall energy condition dictated by Eq. (40). Thus, only the relative contributions at N frequencies, e_n, are determined using the data from Driver et al. Let a_n have the form

$$a_n = \gamma_E \sqrt{e_n}\ Tu\sqrt{\mathrm{Re}_D} \tag{42}$$

where γ_E is some unknown constant and e_n is the relative magnitude of the energy at frequency n from the energy spectrum of Driver et al. (1987). Employing Eq. (42) is equivalent to evaluating the energy integral in Eq. (41) numerically with a midpoint rule using N cells. Substituting Eqs. (40) and (42) into (38) yields an equation in γ_E. Thus, for $N=1$ we get

$$a_1 = 0.0883\ Tu\sqrt{\mathrm{Re}_D} \tag{43}$$

The numerical coefficient presented in Eq. (43) characterizes all turbulent free-stream flow fields in which the large-scale fluctuations are generated by a turbulent wake or more generally a turbulent shear layer, and therefore it is a fixed constant.

Currently, as discussed above, a rigorous method does not exist for evaluating β_n. Thus, instead of the more rigorous techniques employed to fit a_n, an empirical approach will prove useful. The simulation should reproduce well-documented engineering results, such as shear stress and heat flux at the surface. Therefore a reasonable approach is to choose values for β_n based on a trial-and-error algorithm using the known engineering results to provide an additional condition that any acceptable solution must satisfy. However, to minimize the number of empirical parameters in the current model, all β_n were set equal to each other. More than one independent value of β would not improve the current model's accuracy without additional information necessary to evaluate those constants.

Kestin and Wood (1970) developed a second-order correlation for stagnation point heat transfer on a body in a turbulent external flow as a function of turbulence intensity and Reynolds number:

$$\frac{\overline{\mathrm{Nu}_D}}{\sqrt{\mathrm{Re}_D}} = 0.945 + 3.48\left(\frac{Tu\sqrt{\mathrm{Re}_D}}{100}\right) - 3.99\left(\frac{Tu\sqrt{\mathrm{Re}_D}}{100}\right)^2 \tag{44}$$

This correlation is consistent with published experimental results, especially for high turbulence levels and Reynolds numbers. For a Reynolds number of 100,000, Traci and Wilcox (1975) give similar numerical results.

Matching the numerical simulation results with those of Kestin and Wood, Eq. (44), at $Tu\mathrm{Re}_D^{1/2}$ of 20 and 40, produces two values for β. Using a serpentine curve

$$\beta = \frac{243.7\ Tu\sqrt{\mathrm{Re}_D}}{108.6 + (Tu\sqrt{\mathrm{Re}_D})^2} \tag{45}$$

Equation (45) produces third-order surface heat flux variation with $Tu\mathrm{Re}_D^{1/2}$ similar to the second-order variation of Eq. (44). Numerical experiments with models employing constant, linear, quadratic, and sinusoidal variations in β with $Tu\mathrm{Re}_D^{1/2}$ all produced less satisfying results than the serpentine function. Thus, this current model contains the least amount of complexity necessary to satisfactorily model β.

The Strouhal number, St, expressed in terms of the frequency (in hertz), the vorticity thickness, λ_1, and the mean free-stream velocity is

$$\mathrm{St} \equiv \text{frequency}\ \frac{\lambda_1}{V_\infty} = \frac{\Omega_1 \lambda_1}{2\pi V_\infty} \tag{46}$$

From the definition of the nondimensional frequency

$$\alpha^2 \equiv \frac{\Omega_1}{c} = \frac{2\pi \mathrm{St} V_\infty / \lambda_1}{c}$$

which, for a turbulent wake impinging on a circular cylinder, reduces to

$$\alpha^2 = \frac{\pi}{2}\,\mathrm{St}\,\frac{D}{\lambda_1} \tag{47}$$

The length scale ratio , λ_1/D, represents the relative thickness of the wake to the characteristic body length, which is the diameter for a circular cylinder. From the experimental results discussed by Ho and Huang (1982) and Browand and Ho (1983), the Strouhal number is approximately 0.2 for a turbulent wake. The length scale ratio, according to Traci and Wilcox (1975), falls within the range $5 < (\lambda_1/D)\mathrm{Re}_D^{1/2} < 30$. We will adopt values of $\mathrm{St} = 0.2$ and $(\lambda_1/D)\mathrm{Re}_D^{1/2} = 10$, where the latter value duplicates that used by Traci and Wilcox. As such, the nondimensional frequency becomes

$$\alpha^2 = \frac{\pi}{100}\sqrt{\mathrm{Re}_D} \tag{48}$$

Thus, unlike other model parameters, α is a function only of the Reynolds number.

Wall Heat Flux Results

The ultimate test for any new theoretical model is: "How do the model predictions compare to experiment?" The key word here is predictions, because almost any model with phenomenologically developed parameters can produce results that compare favorably with experiments after proper adjustment of the model parameters.

Surface heat transfer and, to a lesser extent, skin friction measurements are the most readily available data for free-stream turbulence effects on stagnation point flows. Skin friction results, which here depend only upon the momentum solution, were given in a previous paper by the authors (1990). Thus, this paper concentrates on surface heat transfer results.

The local Nusselt number based on the cylinder diameter, D, the dimensional surface heat flux, q_w'', and the thermal conductivity of the fluid, k, is

$$\mathrm{Nu}_D \equiv \frac{q_w'' D}{k(T_w - T_\infty)} = -\frac{D}{(T_w - T_\infty)}\left(\frac{\partial T}{\partial y}\right)_{y=0}$$

or, in terms of nondimensional variables

$$\mathrm{Nu}_D = -2\sqrt{\mathrm{Re}_D}\left(\frac{\partial \theta}{\partial \eta}\right)_{\eta=0} \tag{49}$$

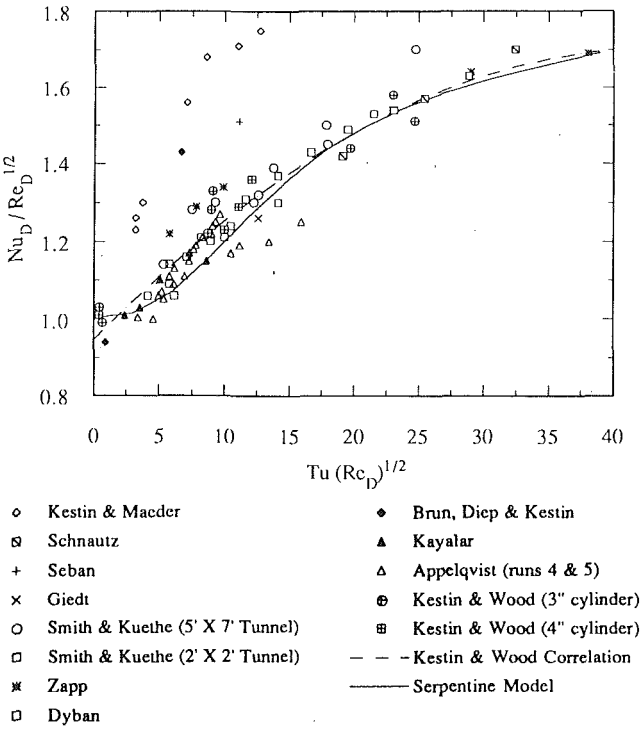

Fig. 5 Comparison of theoretical predictions, which are given here by the solid line, with wall heat transfer measurements. The experimental data, which are given here by the individual points, are summarized by Hoshizaki et al. (1975), and the correlation presented by Kestin and Wood (1970) is denoted by the dashed line.

The assumed form of the nondimensional temperature is given by Eq. (15) as

$$\theta(\xi, \eta, \tau) = \xi R(\eta, \tau) + S(\eta, \tau)$$

At the stagnation point, $\xi = 0$, the time-averaged temperature is given by

$$\bar{\theta}(\xi, \eta) = s_o(\eta) \tag{50}$$

or, Eq. (49) may be expressed as

$$\frac{\overline{Nu}_D}{\sqrt{Re_D}} = -2(s_o')_{\eta=0} \tag{51}$$

for an isothermal surface.

Goldstein (1938) gives the theoretical correlation for the Nusselt number at a two-dimensional stagnation point on a circular cylinder as

$$\frac{\overline{Nu}_D}{\sqrt{Re_D}} = 1.14\ Pr^{0.4} \tag{52}$$

assuming the fluid Prandtl number near unity and an undisturbed incoming flow. For a Prandtl number of 0.72, Eq. (52) gives $\overline{Nu}_D/Re_D^{1/2} = 1.00$.

Numerous experiments have examined stagnation point heat (or mass) transfer as a function of free-stream turbulence intensity, as summarized by Hoshizaki et al. (1975). These experimental results, the Kestin and Wood correlation given by Eq. (44), and the current model's predictions are displayed together on a traditional plot of $\overline{Nu}_D/Re_D^{1/2}$ versus $Tu(Re_D)^{1/2}$ in Fig. 5. The numerical model used parameter values of $Ec = -0.001$, $Pr = 0.72$, $Re_D = 100{,}000$, and $c = 251\ s^{-1}$. The model predictions do not exactly duplicate the Kestin and Wood correlation. However, considering that the experimental investigations did not report their turbulence frequency spectra, the model adequately represents the known data. Further, for an undisturbed free-stream flow ($Tu = 0$), the numerical model agrees with the theoretical value for surface heat transfer from Eq. (52).

Recalling that the turbulence energy spectra were represented by only one parameter, a_1, the present numerical results predict stagnation point heat transfer with an acceptable degree of accuracy over the entire range of turbulence intensity. While additional parameters should be included in the future to represent the turbulence spectra more accurately, the current model has sufficient terms to account for each of the significant physical mechanisms present in the actual flow. Thus, this numerical model is quasi-predictive and not just a phenomenological fit of observed results.

Summary

It should be noted that the analysis presented here is only a first approximation to the solution of a complex problem. It makes rather simplistic assumptions in order to describe a flow field that is vastly more complicated than is suggested by the mathematical model used to describe it. The following are the major assumptions made:

- The analysis totally ignores the existence of any isotropic small-scale unsteadiness that is convected into the stagnation point region.
- The large-scale unsteadiness is assumed to exist at only N, set here at one, dominant frequencies, which is a crude approximation to the continuous spectrum.
- As a result of the boundary conditions on the velocities, the vorticity in the prescribed incoming flow is time-independent, which is obviously at odds with the unsteady nature of the vortical structure in a turbulent wake.
- The analysis assumes that the unsteadiness in the stagnation point can be represented by a periodic, laminar model. In reality, the unsteadiness is a large-scale quasi-periodic motion with remnants of small-scale turbulence convected into the stagnation zone from the outer flow.

The proposed model does, however, have the essential parameters necessary for describing the effect of free-stream spatial and temporal nonuniformities on the stagnation point flow field.

Acknowledgments

This work has been supported by NASA Langley Research Center through research grant No. NAG 1-556.

References

Ascher, U., Christiansen, J., and Russell, R. D., 1978, "COLSYS—A Collocation Code for Boundary Value Problems," *Proceedings of Working Conference for Codes for Boundary Value Problems in ODE's*, Houston, TX.

Bogucz, E. A., Dirik, E. A., and Lyman, F. A., 1988, "Unsteady Stagnation-Point Heat Transfer Due to the Motion of Freestream Vortices," *AIAA/ASME/SIAM/APS 1st National Fluid Dynamics Congress*, Vol. 3, AIAA, Washington, DC, pp. 1893–1900.

Browand, F. K., and Ho, Chih-Ming, 1983, "The Mixing Layer: An Example of Quasi Two-Dimensional Turbulence," *Journal de Mecanique Theorique et Appliquee*, Numero Special, pp. 99–120.

Browand, F. K., and Troutt, T. R., 1985, "The Turbulent Mixing Layer: Geometry of Large Vortices," *Journal of Fluid Mechanics*, Vol. 158, pp. 489–509.

Cebeci, T., Krainer, A., Simoneau, R. J., and Platzer, M. F., 1987, "A General Method for Unsteady Stagnation Region Heat Transfer and Results for Model Turbine Flows," *Proceedings of the 1987 ASME-JSME Thermal Engineering Joint Conference*, Vol. 2, ASME, New York, pp. 541–646.

Dimotakis, P. E., and Brown, G. L., 1976, "The Mixing Layer at High Reynolds Number: Large-Structure Dynamics and Entrainment," *Journal of Fluid Mechanics*, Vol. 78, pp. 535–560.

Driver, D. M., Seegmiller, H. L., and Marvin, J. G., 1987, "Time-Dependent Behavior of a Reattaching Shear Layer," *AIAA Journal*, Vol. 25, pp. 914–919.

Edney, B., 1968, "Anomalous Heat Transfer and Pressure Distributions on Blunt Bodies at Hypersonic Speeds in the Presence of an Impinging Shock," FFA Report 115, The Aeronautical Research Institute of Sweden, Stockholm, Sweden.

Fay, J., and Riddell, R. F., 1958, "Theory of Stagnation Point Heat Transfer in Dissociated Air," *Journal of the Aeronautical Sciences*, Vol. 25.

Galloway, T. R., 1973, "Enhancement of Stagnation Flow Heat and Mass

Transfer Through Interactions of Free Stream Turbulence," *AIChE Journal*, Vol. 19, pp. 608–617.

Goldstein, S., 1938, *Modern Developments in Fluid Dynamics*, Vol. 2, Oxford University Press, London, United Kingdom.

Ho, Chih-Ming, and Huang, Lein-Saing, 1982, "Subharmonics and Vortex Marging in Mixing Layers," *Journal of Fluid Mechanics*, Vol. 119, pp. 443–473.

Hoshizaki, H., Chou, Y. S., Kulgein, N. G., and Meyer, J. W., 1975, "Critical Review of Stagnation Point Heat Transfer Theory," Technical Report AFFDL-TR-75-95, Wright Patterson Air Force Base, Dayton, OH.

Johnson, B. E., 1990, "Experimental and Numerical Studies of Solid Fuel Combustion in an Opposed Flow Configuration," Dissertation, The University of Texas, Austin, TX.

Kestin, J., and Wood, R. T., 1970, "The Influence of Turbulence on Mass Transfer From Cylinders," ASME *Journal of Heat Transfer*, Vol. 92, pp. 321–327.

Keyes, J. W., and Hains, F. D., 1973, "Analytical and Experimental Studies of Shock Interference and Heating in Hypersonic Flows," NASA Technical Note D-7139.

Sadeh, W. Z., Sutera, S. P., and Maeder, P. F., 1970a, "Analysis of Vorticity Amplification in the Flow Approaching a Two-Dimensional Stagnation Point," *Zeitschrift für Angewandte Mathematik und Physik*, Vol. 21, pp. 699–716.

Sadeh, W. Z., Sutera, S. P., and Maeder, P. F., 1970b, "An Investigation of Vorticity Amplification in Stagnation Flow," *Zeitschrift für Angewandte Mathematik und Physik*, Vol. 21, pp. 717–742.

Smith, M. C., and Kuethe, A. M., 1966, "Effects of Turbulence on Laminar Skin Friction and Heat Transfer," *The Physics of Fluids*, Vol. 9, pp. 2337–2344.

Strahle, W. C., Sigman, R. K., and Meyer, W. L., 1987, "Stagnating Turbulent Flows," *AIAA Journal*, Vol. 13, pp. 1071–1077.

Sutera, S. P., Maeder, P. F., and Kestin, J., 1963, "On the Sensitivity of Heat Transfer in the Stagnation-Point Boundary Layer to Free-Stream Vorticity," *Journal of Fluid Mechanics*, Vol. 16, pp. 497–520.

Sutera, S. P., 1965, "Vorticity Amplification in Stagnation-Point Flow and Its Effect on Heat Transfer," *Journal of Fluid Mechanics*, Vol. 21, pp. 513–534.

Taulbee, D. B., and Tran, L., 1988, "Stagnation Streamline Turbulence," *AIAA Journal*, Vol. 26, pp. 1011–1013.

Traci, R. M., and Wilcox, D. C., 1975, "Freestream Turbulence Effects on Stagnation Point Heat Transfer," *AIAA Journal*, Vol. 13, pp. 890–896.

Vanfossen, G. J., Jr., and Simoneau, R. J., 1985, "Preliminary Results of a Study of the Relationship Between Free Stream Turbulence and Stagnation Region Heat Transfer," ASME Paper 85-GT-84.

Wang, C. R., 1984, "Turbulence and Surface Heat Transfer Near the Stagnation Point of a Circular Cylinder in Turbulent Flow," ASME Paper No. 84-WA/HT-73.

Wilson, D. E., and Hanford, A. J., 1990, "The Effect of a Turbulent Wake on the Stagnation Point; Part I: Skin Friction Results," ASME Paper 90-GT-92.

Wilson, D. E., and Philips, P. K., 1989, "A Phenomenological Model for the Near Wall Structure due to a Turbulent Reattaching Flow behind a Backward Facing Step," *Computers and Experiments in Fluid Flow*; *Proceedings of the Fourth International Conference on Computational Methods and Experimental Measurements*, Computational Mechanics Publications, Southampton, United Kingdom, pp. 171–180.

APPENDIX

The coefficients A_n, B_n, D_n and E_n are defined as

$$A_n = \sum_{j=1}^{N} \frac{a_j}{2} [\beta_{j-n} + \beta_{j+n} - \beta_{n-j}] \tag{A1}$$

$$B_n = \sum_{i=1}^{M} \frac{\beta_i}{2} [(n-i)a_{n-i} + (n+i)a_{n+i} - (i-n)a_{i-n}] + \sum_{j=1}^{N} \frac{a_j}{2} [(n-j)\beta_{n-j} + (n+j)\beta_{n+j} - (j-n)\beta_{j-n}] \tag{A2}$$

$$D_n = \sum_{j=1}^{N} \frac{a_j}{2} [A_{n-j} + A_{n+j} - A_{j-n}] \tag{A3}$$

$$E_n = \sum_{j=1}^{N} \frac{a_j}{2} [a_{j-n} + a_{j+n} - a_{n-j}] \tag{A4}$$

The coefficients A_{in}, B_{in}, A_{Fin}, B_{Fin}, A_{Hin}, and B_{Hin} are defined as

$$A_{6n} = \sum_{j=1}^{N} \frac{f_j''}{2} (h_{j+n}'' + h_{j-n}'' + h_{n-j}'') + \sum_{j=1}^{N} \frac{g_j''}{2} (k_{j-n}'' + k_{j+n}'' - k_{n-j}'') \tag{A5}$$

$$B_{6n} = \sum_{j=1}^{N+M} \frac{k_j''}{2} (f_{n-j}'' + f_{n+j}'' - f_{j-n}'') + \sum_{j=1}^{N} \frac{g_j''}{2} (h_{n-j}'' + h_{n+j}'' - h_{j-n}'') \tag{A6}$$

$$A_{7n} = \sum_{j=1}^{N+M} \frac{h_j''}{2} (h_{j+n}'' + h_{j-n}'' + h_{n-j}'') + \sum_{j=1}^{N+M} \frac{k_j''}{2} (k_{j-n}'' + k_{j+n}'' - k_{n-j}'') \tag{A7}$$

$$B_{70n} = \sum_{j=1}^{N+M} \frac{k_j''}{2} (h_{n-j}'' + h_{n+j}'' - h_{j-n}'') \tag{A8}$$

$$A_{F2n} = \sum_{j=1}^{M} \frac{j\beta_j}{2} (f_{j+n}' + f_{j-n}' + f_{n-j}') \tag{A9}$$

$$B_{F2n} = \sum_{j=1}^{N} \frac{g_j'}{2} \begin{bmatrix} (n-j)\beta_{n-j} \\ +(n+j)\beta_{n+j} \\ -(j-n)\beta_{j-n} \end{bmatrix} \tag{A10}$$

$$A_{F3n} = \sum_{j=1}^{N} \frac{g_j'}{4} (B_{j-n} + B_{j+n} - B_{n-j}) \tag{A11}$$

$$B_{F3n} = \sum_{j=1}^{N+M} \frac{B_j}{4} (f_{n-j}' + f_{n+j}' - f_{j-n}') \tag{A12}$$

$$A_{H1n} = \sum_{j=1}^{N+M} \frac{h_j'}{2} \begin{bmatrix} (j+n)a_{j+n} \\ +(j-n)a_{j-n} \\ +(n-j)a_{n-j} \end{bmatrix} \tag{A13}$$

$$B_{H1n} = \sum_{j=1}^{N+M} \frac{k_j'}{2} \begin{bmatrix} (n-j)a_{n-j} \\ +(n+j)a_{n+j} \\ -(j-n)a_{j-n} \end{bmatrix} \tag{A14}$$

$$A_{H2n} = \sum_{j=1}^{N+M} \frac{h_j'}{2} \begin{bmatrix} (j+n)\beta_{j+n} \\ +(j-n)\beta_{j-n} \\ +(n-j)\beta_{n-j} \end{bmatrix} \tag{A15}$$

$$B_{H2n} = \sum_{j=1}^{N+M} \frac{k_j'}{2} \begin{bmatrix} (n-j)\beta_{n-j} \\ +(n+j)\beta_{n+j} \\ -(j-n)\beta_{j-n} \end{bmatrix} \tag{A16}$$

$$A_{H3n} = \sum_{j=1}^{N+M} \frac{B_j}{4} (k_{j-n}' + k_{j+n}' - k_{n-j}') \tag{A17}$$

$$B_{H3n} = \sum_{j=1}^{N+M} \frac{B_j}{4} (h_{n-j}' + h_{n+j}' - h_{j-n}') \tag{A18}$$

Heat Transfer on a Flat Surface Under a Region of Turbulent Separation

R. B. Rivir
Wright Laboratories,
Aero Propulsion and Power Directorate,
Wright-Patterson AFB, OH 45433

J. P. Johnston

J. K. Eaton

Mechanical Engineering Department,
Stanford University,
Stanford, CA 94305

Fluid dynamics and heat transfer measurements were performed for a separation bubble formed on a smooth, flat, constant-heat-flux plate. The separation was induced by an adverse pressure gradient created by deflection of the opposite wall of the wind tunnel. The heat transfer rate was found to decline monotonically approaching the separation point and reach a broad minimum approximately 60 percent below zero-pressure-gradient levels. The heat transfer rate increased rapidly approaching reattachment with a peak occurring slightly downstream of the mean reattachment point. The opposite wall shape was varied to reduce the applied adverse pressure gradient. The heat transfer results were similar as long as the pressure gradient was sufficient to cause full separation of the boundary layer.

Introduction

Separation of a turbulent boundary layer and subsequent reattachment of the shear layer to the solid surface occur in many different practical flow geometries. In some cases, the separation point is fixed by a sharp corner such as in the flow over a backward-facing step. In other cases such as the flow in a highly curved duct or over a bluff strut the boundary layer separates from a smoothly contoured surface due to the action of an adverse pressure gradient. Separated flow regions are characterized by high turbulence levels, large-scale unsteadiness, and rapid variations in the wall heat transfer coefficient. The heat transfer rate is often suppressed below attached boundary layer levels in the fully separated region, then strongly augmented near reattachment.

Separated flow heat transfer has been studied in detail for simple geometries where the separation point is fixed by a discontinuity in the wall contour (cf. reviews by Vogel and Eaton, 1984, and Sparrow, 1988). However, there has been little detailed study of heat transfer in flows where separation from a smooth wall occurs. Globally averaged heat transfer rates have been measured in flows containing smooth wall separations but there is no clear understanding of what happens to the heat transfer coefficient in the vicinity of separation. A boundary layer thickens rapidly as it approaches separation and the skin friction coefficient drops reaching zero at the time-mean separation point. This suggests that the heat transfer coefficient would fall rapidly. However, as the boundary layer thickens, both the turbulence intensity and the length scale of the eddies increase rapidly. These effects would be expected to increase the heat transfer rate. Which of these two effects dominates is unknown at this time. In the reattachment region where the skin friction also passes through zero the high turbulence levels dominate and the heat transfer coefficient is much larger than in attached boundary layers.

The objective of the present experiment was to find out what happens to the heat transfer coefficient in the neighborhood of a simple smooth-wall separation point. Separation of a two-dimensional boundary layer was forced on a flat wall by an imposed pressure gradient allowing detailed examination of the heat transfer behavior. In order to make the flow field well defined we chose to force the separated shear layer to reattach within the test section. It was then possible to study the heat transfer rate through a full separation bubble including a detachment region, a fully separated zone, and a reattachment zone.

Experimental Apparatus and Procedure

The experiments were performed in a closed-circuit wind tunnel with a test section as sketched in Fig. 1. The flat bottom wall of the test section acted as the test plate while the contoured opposite wall was adjusted to produce the appropriate pressure gradient. The flat wall had a leading edge in the contraction to avoid any nonuniformities in the wind tunnel wall boundary layer. Flow passing beneath the test plate was drawn out of the tunnel by a suction blower and returned to the tunnel downstream of the test section. With a test section geometry as shown, separation would occur on the contoured wall rather than on the flat wall. To prevent this, the upper wall boundary layer was removed through a suction slot just upstream of the region of strong adverse pressure gradient. The upper wall boundary layer was further energized by a row of longitudinal vortex generators placed near the point of strongest adverse

Contributed by the International Gas Turbine Institute and presented at the 37th International Gas Turbine and Aeroengine Congress and Exposition, Cologne, Germany, June 1–4, 1992. Manuscript received by the International Gas Turbine Institute February 17, 1992. Paper No. 92-GT-198. Associate Technical Editor: L. S. Langston.

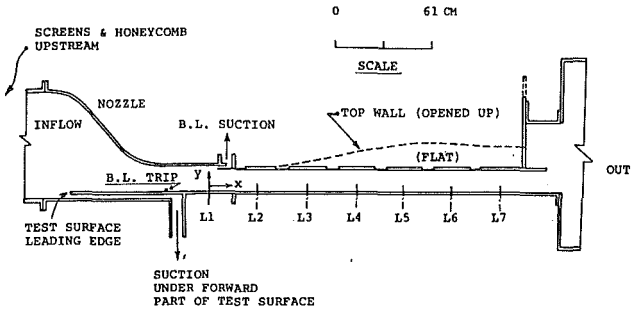

Fig. 1 Test section schematic

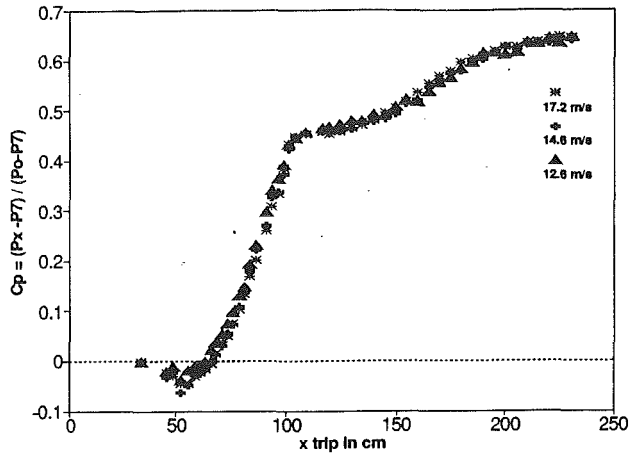

Fig. 2 Test section pressure coefficient base configuration

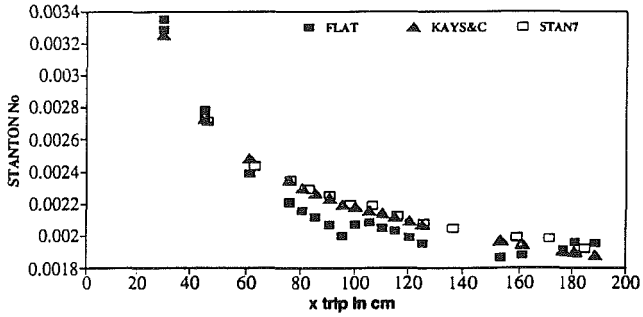

Fig. 3 Heat transfer for constant area channel 453 W/m²°C

pressure gradient. Vortex generators were also placed on the side walls to help prevent separation in the upper corners of the test section. With this treatment, the upper surface boundary layer remained attached and a reasonably two-dimensional separation bubble was formed on the flat surface.

The test plate boundary layer was tripped 53 cm downstream of the leading edge, near the contraction exit. Boundary layer profile measurements showed that the turbulent boundary layer had a virtual origin very near the trip so the trip location is taken as the origin of the streamwise (x) coordinate in the discussion that follows. The upper wall shape was adjusted to match the pressure distribution reported by Johnson and Nishi using the same tunnel. This shape will be referred to as the base case or standard geometry. The resulting pressure distribution has a strong adverse pressure gradient between $x = 80$ and 100 cm as shown in Fig. 2. Detachment of the boundary layer occurred at $x = 106$ cm and reattachment at $x = 176$ cm. It should be noted that separation and reattachment regions are generally quite unsteady with instantaneous flow reversals occurring over a wide region. The positions quoted here are just the time-mean detachment and reattachment locations as measured by Johnson and Nishi.

The flat test surface was made from two constant heat flux test plates used in previous studies: the large surface 61 cm × 119 cm with 180 thermocouples (Eibeck and Eaton, 1985) and the small surface 31 cm × 64 cm with 25 thermocouples (Abrahamson and Eaton, 1991). Each plate consisted of a 0.003-in. thick stainless steel foil glued to a 1.3-thickness balsa backing plate. The thermocouples were spot welded to the back of the larger plate and pressed firmly against the back of the smaller plate. The thermocouple locations in the two plates were not optimal for the present experiment requiring the use of three different test section configurations to get measurements over the entire surface. In Configuration 0, the larger plate was upstream and the positions were reversed in Configurations 1 and 2. The wall contour and fluid mechanics were identical for Configurations 0 and 1 but the heated surface began 24 cm downstream of the trip for Configuration 0 and 32 cm downstream of the trip for Configuration 1. Configuration 2 shifted the upper wall and the pressure distribution by 30 cm. The heat transfer surfaces were tested by setting the wind tunnel

Nomenclature

A = area of heat transfer surface, m²
c_p = specific heat at constant pressure, W-s/kg-°C
C_p = tunnel pressure coefficient = $(P_x - P_{\text{test section entrance}})/(P_o - P_{\text{test section entrance}})$
h = heat transfer coefficient = $q/[A(T_p - T_f)]$, W/(m² − °C)
P = pressure, Pa
$P_{\text{test section entrance}}$ = static pressure, 38 cm from boundary layer trip, Pa
q = heat flux per unit area, W/m²
Re_x = Reynolds number = $\rho U x_t/\mu$, $\rho U\theta/\mu$
St = Stanton number = $h/(\rho c_p U)$
U = mean velocity in the x direction, m/s
u' = rms component of velocity in the x direction, m/s
T_p = local constant heat flux wall surface temperature, K, °C
T_f = local free-stream fluid temperature K, °C
x_t = distance measured from boundary layer trip, cm
θ = momentum thickness, cm
μ = viscosity, Pa-s
ρ = density, kg/m³

Subscripts

0 = evaluated at stagnation conditions
∞ = evaluated at free-stream conditions

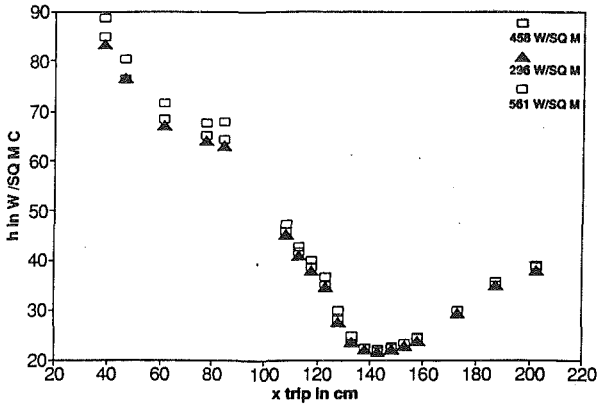

Fig. 4 Comparison of h for three heat fluxes—base configuration

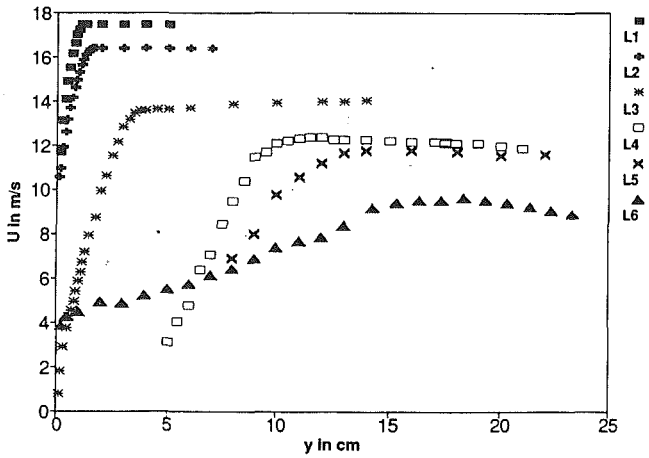

Fig. 5 Centerline velocity profiles at traverse stations

up to provide a constant area channel with a very small longitudinal pressure gradient. Normalized heat transfer coefficient data are shown in Fig. 3 for the constant area case. Also shown are a semi-analytical solution from Kays and Crawford (1980) and a solution from the STAN7 computer program. The agreement is within a few percent over the entire measurement region. Measurements were repeated at heat fluxes of 561, 458, and 295 W/m^2 for the base configuration. The collapse of the data was excellent, as shown in Fig. 4, indicating that conduction and radiation corrections applied to the data correctly accounted for the losses.

Mean velocity and turbulence intensity measurements were acquired using a single hot-wire boundary layer probe. The probe was operated with a 5-μm dia tungsten wire with the ends gold plated to give an active length of 1.25 mm. The probe was mounted on a gooseneck stem and traversed by a computer-controlled traverse mechanism. Data were acquired at the seven measurement stations labeled L1–L7 on Fig. 1. Measurement port L1 was located 38 cm downstream of the trip with subsequent measurement ports spaced 30.5 cm apart. The static pressure was measured using a set of 55 taps in the tunnel sidewall and a Validyne DP-45 pressure transducer connected through a scanivalve.

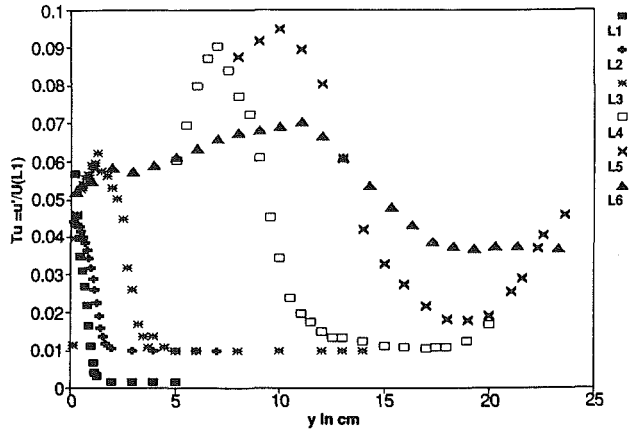

Fig. 6 Centerline turbulence profiles at traverse stations

Results

The majority of the experiments were performed in the base case geometry. The geometry was later changed to provide additional cases as discussed below. Three different wind tunnel flow velocities were used for the experiments reported here. The reference velocities measured at the test section entrance for the three tunnel settings were approximately 17.2, 14.6, and 12.6 m/s. At the highest wind tunnel speed, the momentum thickness Reynolds number of the boundary layer at port L1 was approximately 1500. Figures 5 and 6 document the mean centerline velocity and turbulence intensity profiles measured at each of the seven measurement stations. The boundary layer is very thin at stations L1 and L2 but grows very rapidly between L2 and L3. At L3 the boundary layer is very nearly separated and by position L4 there is a large region of reversed flow. The boundary layer reattaches somewhere between L5 and L6 and the profile at L6 is characteristic of reattached boundary layers. The turbulence profiles show the same trends. The profiles at L1 and L2 look like normal attached boundary layer profiles. By L3 the profile exhibits a peak away from the wall, the characteristic behavior of an adverse pressure gradient layer. Beyond separation, the profile develops a sharp peak characteristic of separated shear layers.

The heat transfer results are presented in Fig. 7. Here data have been taken from Configurations 0 and 1 to get complete coverage of the surface. Where thermocouple positions overlap, two symbols are plotted. The heat transfer coefficient decreases rapidly approaching separation to a minimum, which occurs very near the time-mean detachment point. The heat transfer rate rises slowly in the center of the separation bubble then rapidly in the reattachment region. The heat transfer rate apparently reaches a maximum around $x = 180$ cm, slightly downstream of the mean reattachment point. This contradicts previous findings in the backward-facing step flow where the peak heat transfer coefficient generally occurs a short distance upstream of the mean reattachment point (Vogel and Eaton, 1984). Perhaps the most significant finding here is that the heat transfer rate decreases monotonically approaching separation. Clearly the rapid reduction in the mean velocity near the wall causing a reduction in the heat transfer overwhelms any possible effect of increasing turbulent length scale.

The rapid divergence of the opposite wall in the base case experiments caused the separation streamline to lift well away from the wall. This was probably the cause of the rapid and monotonic decrease in the heat transfer rate. Different heat transfer behavior might be expected if the separation streamline lifted more slowly away from the surface. To investigate this the area expansion was reduced in steps and the heat transfer rate measured for each case. To accomplish this in a reasonable amount of time, the test section configuration was changed.

The two heat transfer surfaces were positioned the same as for Configuration 1 but with the upper wall deflection shifted downstream by 30 cm (Configuration 2). This moved the position of separation downstream by approximately 30 cm, allowing us to make heat transfer measurements in the separation zone without repeatedly changing the heat transfer surfaces. This new configuration did not allow for heat transfer measurements across the reattachment zone.

Six different cases were examined with proportionally reduced upper wall deflections. That is, the deflection of the upper wall from the flat state was reduced proportionally at every point along the wall. The reductions examined were 5, 10, 15, 20, 33, and 66 percent of the base case deflection. For example, in the 10 percent case, the wall deflection was reduced by 10 percent from the base case. The resulting pressure distributions are shown in Fig. 8. The pressure gradient reductions are approximately proportional to the area reductions. The heat transfer results are plotted in Figs. 9(*a–g*). Figure 9(*a*) shows the base case results. The position of the minimum is shifted downstream by 30 cm because of the shift in the wall deflection. Otherwise, the results appear the same as in Fig. 7. The results for 5, 10, 15, and 20 percent reductions shown in Figs. 9(*b–e*) all look similar to the base case. The position of the minimum shifts downstream with reduced deflection, indicating that the separation occurs later. The minimum becomes broader with decreased deflection and the actual minimum value increases slightly with decreasing deflection. The character of the results changes dramatically when the wall deflection is reduced by 33 percent. In this case, there is a broad shallow minimum with the results being quite sensitive to the wind tunnel speed. This suggests that the flow is only intermittently separating. It is interesting to note that even in this case, the strong adverse pressure gradient still causes a monotonic decrease in heat transfer through the separation zone. Finally, the case of 66 percent deflection reduction shows a much different behavior. Clearly the boundary layer never separates in this case. This then just shows the smooth variation of the heat transfer coefficient in a mild pressure gradient.

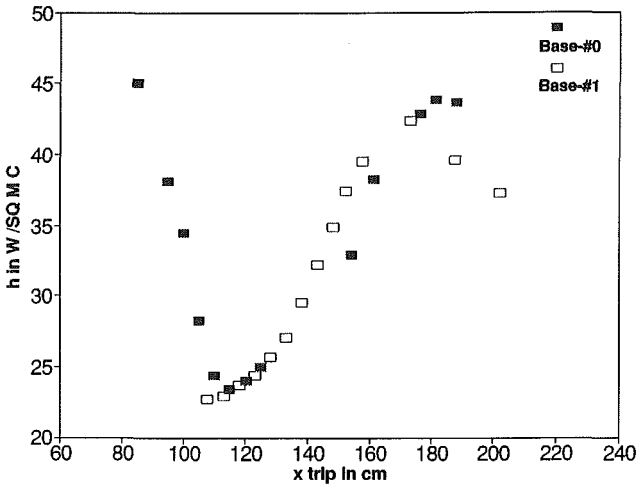

Fig. 7 Heat transfer coefficient through separation and reattachment

Conclusions

We have acquired fluid dynamics and heat transfer data for a nominally steady separation bubble on a smooth surface. The fluid dynamic measurements mimic the well-known behavior of a turbulent boundary layer in a strong adverse pressure gradient. The heat transfer coefficient drops monotonically approaching separation even though the peak turbulence intensity is increasing rapidly. The heat transfer coefficient rises rapidly in the reattachment region as expected from previous studies. However, unlike previous results, the peak in the heat transfer rate occurs downstream of the mean reattachment point. Additional experiments with reduced pressure gradient show that the minimum Stanton number achieved near separation is insensitive to the details of the flow.

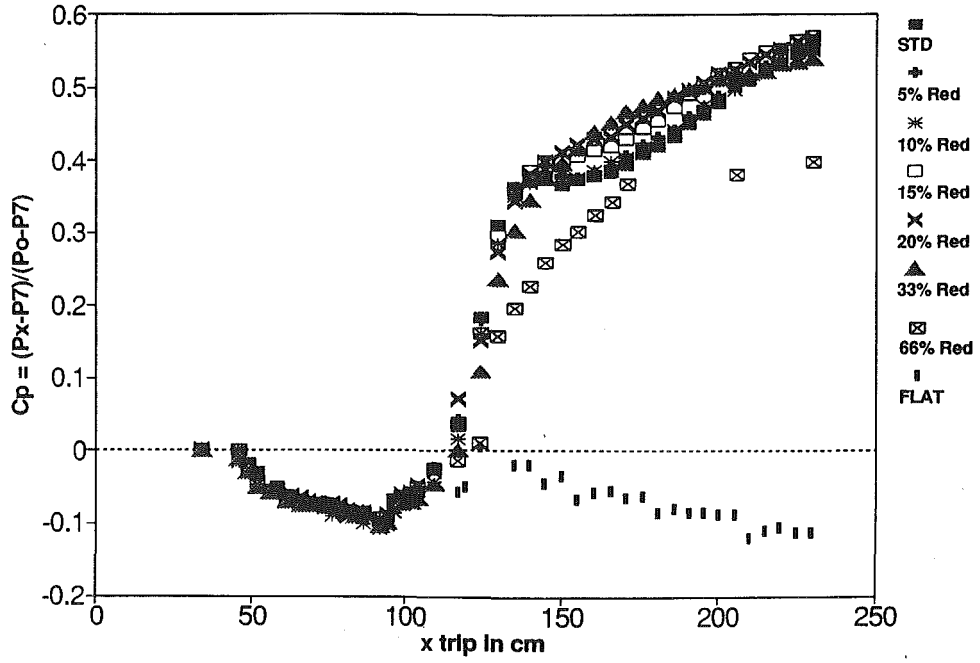

Fig. 8 Test section pressure coefficient for pressure gradient cases

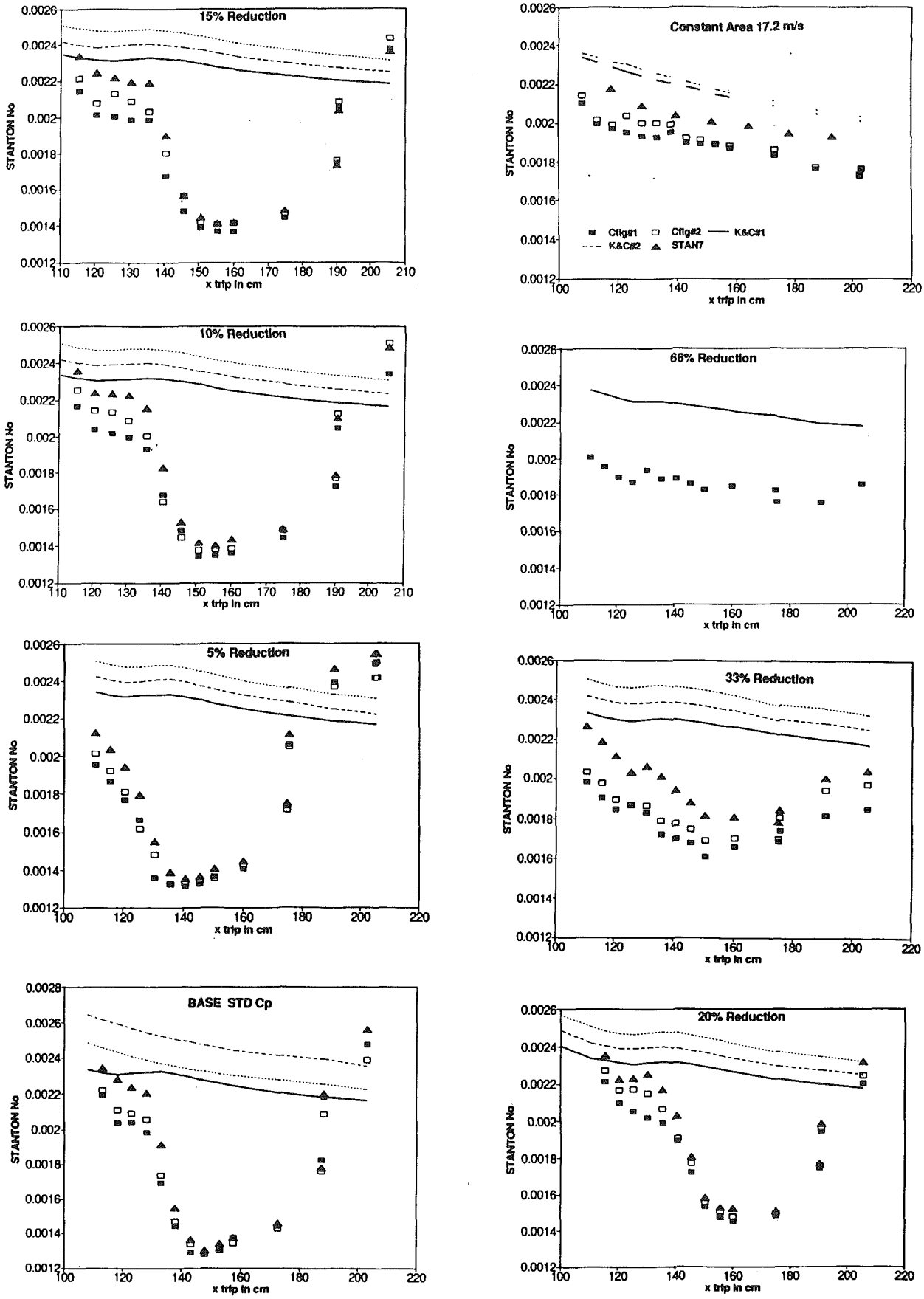

Fig. 9 Separation and reattachment heat transfer with pressure gradient—Configuration 2:

■ 17.2 m/s □ 14.6 m/s ▲ 12.6 m/s
— K&C 17.2 m/s - - - K&C 14.6 m/s · · · · K&C 12.6 m/s

References

Abrahamson, S. D., and Eaton, J. K., 1991, "Heat Transfer Through a Pressure-Driven Three-Dimensional Boundary Layer," ASME *Journal of Heat Transfer*, Vol. 113, pp. 355–362.

Eibeck, P. A., and Eaton, J. K., 1985, "An Experimental Investigation of the Heat-Transfer Effects of a Longitudinal Vortex Embedded in a Turbulent Boundary Layer," Thermosciences Division Department of Mechanical Engineering, Stanford University, Report MD-48.

Johnson, J. P., and Nishi, M., 1990, "Vortex Generator Jets—Means for Flow Separation Control," *AIAA Journal*, Vol. 28, pp. 989–994.

Kays, W. M., and Crawford, M. E., 1980, *Convective Heat and Mass Transfer*, 2nd ed., McGraw-Hill, New York, pp. 211–217.

Sparrow, E. M., 1988, "Heat Transfer in Fluid Flows Which Do Not Follow the Contour of Bounding Walls," ASME *Journal of Heat Transfer*, Vol. 110, pp. 1145–1153.

Vogel, J. C., and Eaton, J. K., 1984, "Heat Transfer and Fluid-Mechanics Measurements in the Turbulent Reattaching Flow Behind a Backward-Facing Step," Report MD-44, Thermo Sciences Division, Department of Mechanical Engineering, Stanford University, July.

An Experimental Study of Film Cooling in a Rotating Transonic Turbine

R. S. Abhari
Textron Lycoming,
Stratford, CT 06497

A. H. Epstein
Massachusetts Institute of Technology,
Cambridge, MA 02139

Time-resolved measurements of heat transfer on a fully cooled transonic turbine stage have been taken in a short duration turbine test facility, which simulates full engine nondimensional conditions. The time average of this data is compared to uncooled rotor data and cooled linear cascade measurements made on the same profile. The film cooling reduces the time-averaged heat transfer compared to the uncooled rotor on the blade suction surface by as much as 60 percent, but has relatively little effect on the pressure surface. The suction surface rotor heat transfer is lower than that measured in the cascade. The results are similar over the central 3/4 of the span, implying that the flow here is mainly two dimensional. The film cooling is shown to be much less effective at high blowing ratios than at low ones. Time-resolved measurements reveal that the cooling, when effective, both reduced the dc level of heat transfer and changed the shape of the unsteady waveform. Unsteady blowing is shown to be a principal driver of film cooling fluctuations, and a linear model is shown to do a good job in predicting the unsteady heat transfer. The unsteadiness results in a 12 percent decrease in heat transfer on the suction surface and a 5 percent increase on the pressure surface.

Introduction

The accurate prediction of film cooling on turbine profiles and the end-walls is a major factor in the continuing effort to increase turbine entry temperature. The designer's goal is to use the minimum amount of coolant necessary to insure adequate turbine life. To this end, there has been considerable research over the past 30 years to increase our understanding of coolant film behavior and its interaction with the free-stream flow. Film-cooled boundary layer behavior has been shown to be quite complex with wall curvature, three-dimensional external flow structure, free-stream turbulence, compressibility, and unsteadiness, all influencing cooling performance.

Many studies have focused on film cooling in simple geometries, on two-dimensional flat and curved plates in steady flow. For example, Ito et al. (1978) showed that the blade surface curvature influences the film cooling effectiveness particularly in the vicinity of the injection holes, with greater effectiveness on the convex surface and less on the concave surface, as compared to a flat plate case. On the concave surface, Schwarz and Goldstein (1989) suggested that the unstable flow along the concave surface promotes lateral mixing of the film cooling jets, which in turn results in a two-dimensional behavior of the film effectiveness.

More recently, studies of the steady flow in linear cascades have provided detailed measurements of film cooling performance on three-dimensional blade surfaces. Near the endwalls on the suction surface of the blade profile, Goldstein and Chen (1985) showed that the film cooling jets are swept away from the surface by the passage vortex, resulting in low levels of film effectiveness. On the concave surface, the film cooling was unaffected by endwall influences.

Relatively less work has been done in the unsteady rotating environment characteristic of a rotor blade. Dring et al. (1980) studied the performance of film cooling in a low-speed rotating facility. They observed a large radial displacement of the coolant jet on the pressure surface, which they concluded to be the main cause of the low level of effectiveness measured. Recently, Takeishi et al. (1992) reported measurements of film effectiveness on a rotating turbine stage. The overall conclusion of both studies was that on the rotor midspan, the suction surface film cooling effectiveness is similar to existing flat plate and cascade measurements, while on the pressure surface, a much higher decay rate of effectiveness was measured.

The influence of the NGV trailing edge slot coolant ejection on the downstream rotor time-averaged heat transfer was reported by Dunn (1986), who observed that NGV injection increased heat transfer on the downstream rotor by as much as 20 percent. Dunn's data also showed little effect on the heat transfer as the coolant to free-stream gas temperature was raised from 0.52 to 0.82.

The intent of the present study is to quantify experimentally the influence of three-dimensional and unsteady effects on the rotor film cooling process in a transonic rotating turbine stage. The approach is to measure the steady and time-resolved chord-

Contributed by the International Gas Turbine Institute and presented at the 37th International Gas Turbine and Aeroengine Congress and Exposition, Cologne, Germany, June 1–4, 1992. Manuscript received by the International Gas Turbine Institute February 17, 1992. Paper No. 92-GT-201. Associate Technical Editor: L. S. Langston.

Table 1 MIT blowdown turbine scaling

	Full Scale	MIT Blowdown
Fluid	Air	Ar-Fr 12
Ratio specific heats	1.28	1.28
Mean metal temperature	1118°K (1550°F)	295°K (72°F)
Metal/gas temp. ratio	0.63	0.63
Inlet total temperature	1780°K (2750°F)	478°K (400°F)
True NGV chord	8.0 cm	5.9 cm
Reynolds number*	2.7×10^6	2.7×10^6
Inlet pressure, atm	19.6	4.3
Outlet pressure, atm	4.5	1.0
Outlet total temperature	1280°K (1844°F)	343°K (160°F)
Prandtl number	0.752	0.755
Eckert number†	1.0	1.0
Rotor speed, rpm	12,734	6,190
Mass flow, kg/sec	49.0	16.6
Power, watts	24,880,000	1,078,000
Test time	Continuous	0.3 sec

* Based on NGV chord and isentropic exit conditions
† $(\gamma\text{-}1)M^2T/\Delta T$

wise heat flux distribution at three spanwise locations in a fully scaled short duration turbine rig. Here, we examine both the mean and time resolved heat transfer with film cooling and compare those results to measurements from an uncooled turbine with the same geometry and with cooled cascade data. An unsteady numerical calculation and analytical modeling is then used to elucidate the time-resolved fluid mechanics in the turbine rotor. Finally, the average heat transfer results are explained in terms of the time-resolved details.

Experimental Apparatus

These experiments were conducted in a short-duration (0.3 s) blowdown turbine test facility at MIT, which simulates full engine scale Reynolds number, Mach number, Prandtl number, gas to wall and coolant to mainstream temperature ratios, specific heat ratios, and flow geometry (Table 1) (Epstein et al., 1986). The corrected speed and weight flow where kept constant to better than 0.5 percent over the test time. The turbulent intensity at the nozzle guide vane inlet was less than 1 percent.

For the tests reported herein, a coolant injection system was added to the facility. The coolant system consisted of a refrigerated coolant supply tank (200 K minimum), metering orifice, and fast-acting (15 ms) shutoff valve. The flow path from the coolant tank to the NGV's and rotor spin-up nozzles was internally insulated with teflon and syntactic foam epoxy to reduced heat transfer. The coolant tank and metering orifice were sized such that the time rate of change of pressure in the coolant tank matched that the main flow supply tank. Thus, the coolant to main flow mass flux ratio (the blowing ratio) remains constant (±2 percent) over the test time. An argon/freon gas mixture was used for the coolant in order to match the ratio of specific heats of engine coolant (1.36). Freon-14 was selected (as opposed to freon-12 in the main flow) to prevent condensation at the low temperatures and high pressures of the coolant supply system.

High frequency response pressure transducers and thermocouples were installed in the NGV's and rotor blades to monitor the conditions in the coolant hole supply plenums. All worked well except for the rotor thermocouples, which were unreliable. Facility measurements for these tests included inlet total temperature and pressure, outlet total pressure, wall static pressures, and rotor speed.

Of interest here is the measurement of the time-resolved heat flux distribution about the rotor blade. The thermal inertia of the blades is such as to keep the blade wall temperature essentially constant during the test at the pretest initial temperature (room temperature). Thus, uncooled rotor blading behaves as though it were internally cooled, generating a heat flux from the free stream into the blade. This flux is measured with thin film heat flux gages distributed about the blade profile. These transducers are 25 μm thick with a rectangular sensing area (1.0×1.3 mm), oriented such that the longer dimension is in the chordwise direction. The frequency response of these instruments extends from dc to 100 kHz. The gages are individually calibrated and relative gage calibrations are accurate to better than 5 percent. Absolute calibration accuracy is about 10 percent. Uncertainty was evaluated for each transducer and is noted in the subsequent figures. Details of the gage theory, data reduction, and calibration may be found from Epstein et al. (1986). For the data presented herein, the signals from the heat flux gages were digitized at a 200 kHz sampling rate (33 times blade passing). Unless otherwise specified, the digital signal was then ensemble-averaged for 360 vane passed periods (Guenette et al., 1989). Nusselt numbers are defined in terms of rotor relative frame mass-averaged NGV exit temperature, the measured surface temperature, the gas thermal conductivity at that temperature, and the rotor axial chord.

The 0.5-m-dia turbine tested (Fig. 1) was a single-stage, 4:1 pressure ratio transonic machine whose design parameters are given in Table 2 (Rigby et al., 1990). This turbine geometry has been extensively studied in cooled and uncooled cascades

Nomenclature

$A(\omega)$ = Fourier coefficient at frequency ω
d = equivalent slot width
$f(x)$ = function of length
$G(\omega)$ = damping coefficient
h = heat transfer coefficient
L = length of coolant slot
M = Mach number
Nu = Nusselt number based on axial chord, inlet total temperature, wall temperature, and main gas conductivity at the wall
Pr = Prandtl number
Q = heat flux
Re_c = Reynolds number based on axial chord, isentropic exit Mach number, and properties at exit condition
S = surface length downstream of coolant holes
t = time
T = temperature
U = velocity
x = length scale
α = coolant injection angle relative to surface normal
η = effectiveness
θ = nondimensional coolant temperature
κ = modified reduced frequency
μ = viscosity
ξ, β = nondimensional blowing parameters
ρ = density
φ = perturbation potential
Ω = reduced frequency
ω = oscillation frequency

Subscripts

0 = uncooled
ad = adiabatic
aw = adiabatic wall
c = coolant
fc = film cooled
x, t = derivative with respect to x or t
∞ = free-stream conditions

Superscripts

$(\_)'$ = perturbation quantity
$\overline{(\ )}$ = time-averaged condition

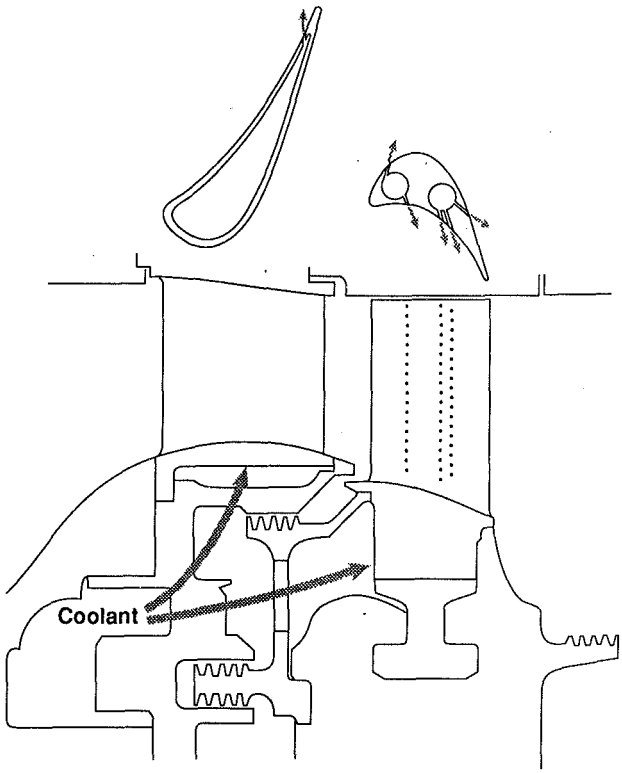

Fig. 1 Turbine geometry and cooling arrangement

Table 2 Turbine design parameters

Turbine loading, $\Delta H/U^2$	-2.3
Total pressure ratio	4.2
Velocity ratio, C_x/U	0.63
Rotor aspect ratio	1.5
NGV exit Mach No.	1.18
Rotor coolant/Main flow	6%
NGV Coolant/Main flow	3%

(Ashworth et al., 1987) and as an uncooled stage (Abhari et al., 1992). For these tests of cooled rotor heat transfer, thin walled nozzle guide vanes (NGV's) were used with slot injection near the pressure surface trailing edge sized to pass the flow of a fully cooled NGV. Solid rotor blading was used for the uncooled tests. For the cooled testing, the solid aluminum blades were drilled out for two coolant supply plenums. The film coolant hole configuration was chosen to provide the maximum information on coolant performance in rotating geometries rather than be representative of a production blade cooling configuration. The coolant hole internal diameters (0.5 mm) were 2 percent of axial chord. All rows had circular exit areas, except for the first row on the suction surface, which was D-shaped. The coolant hole and heat flux gage locations are shown in Fig. 2. The top chordwise row will be referred to as the tip location, the middle as midspan, and the bottom as the hub gages. These locations were chosen so as to elucidate the spanwise variation in the flow as far as possible without intruding into the endwall flow region (Norton, 1987). Unfortunately, several of the gages failed over the course of the testing (especially on the pressure surfaces), so not all measurement locations yielded data at all test conditions. All data taken during each test are reported.

Steady-State Measurements

As a prelude to measurements of the fully cooled stage, the uncooled rotor was tested behind cooled nozzle guide vanes.

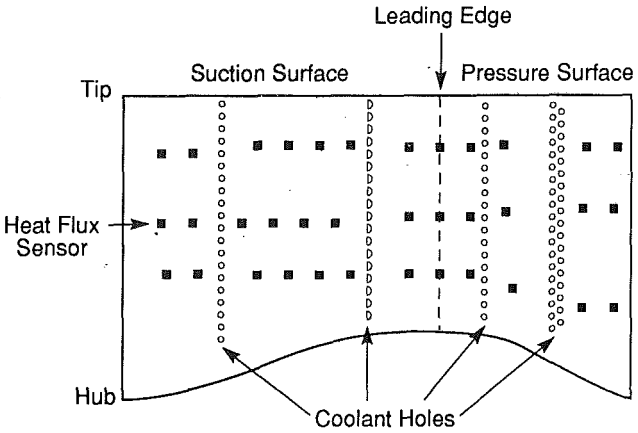

Fig. 2 Composite of the heat flux gauge and coolant hole positions on the projected blade surface. Note that each of the three chordwise rows of gages is on a separate blade.

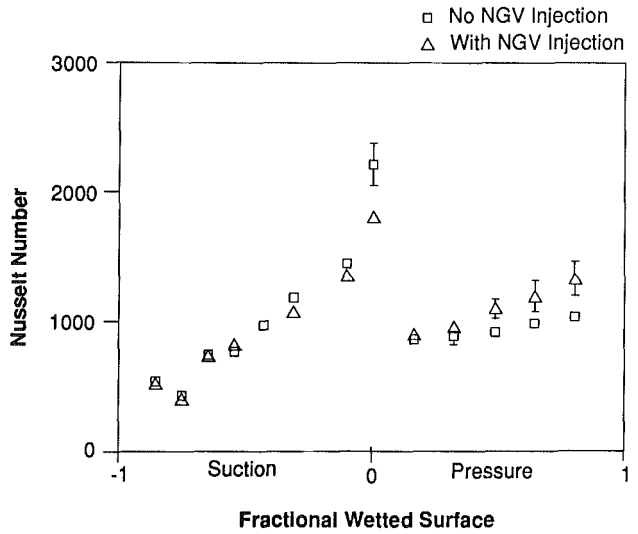

Fig. 3 Influence of nozzle guide vane trailing edge injection on uncooled rotor heat transfer

This was done to permit differentiation of the influence of the cold nozzle guide vane wakes (cold streaks to the rotor) from the effects of fully cooling the stage. (A cooled rotor behind uncooled NGV's may also be informative but was not done due to time constraints.) Figure 3 compares the steady-state heat transfer distribution about the uncooled rotor midspan behind both cooled and uncooled NGV's. (The chordwise sensor placement on the uncooled blade differs somewhat from the cooled blade placement illustrated in Fig. 2. The uncertainty in the measurements is indicated by a vertical bar unless it is less than the symbol size.) The coolant injection is 3.0 percent of the main mass flow rate and the coolant to free-stream temperature ratio is 0.63. The heat transfer at the leading edge drops by 18 percent with injection while the pressure surface heat transfer increases monotonically from the leading edge. Relatively little change is observed on the suction surface. Examination of the time-resolved data showed that the waveform shapes on the pressure surface were no different with and without injection, that only the dc levels changed. Tests run at different rotor speeds and blowing ratios showed similar results. At this time, we are uncertain as to the physical origin of these observed effects; changes in the NGV shock pattern due to the mass injection, increased NGV wake turbulence and velocity deflect, or changed wake temperature are all possible candidates. Work is currently under way to explain them in a quantitative fashion.

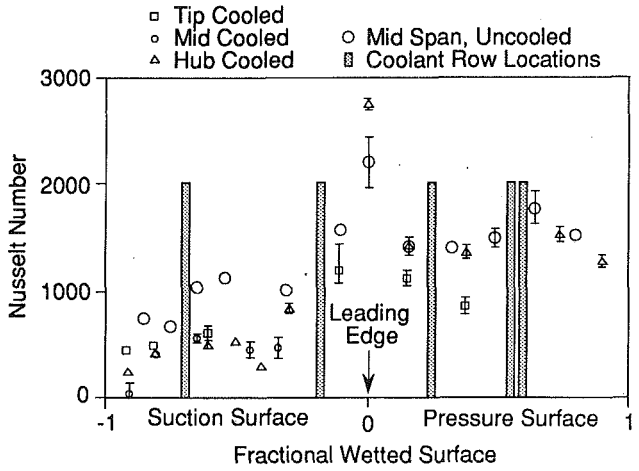

Fig. 4 Time-averaged heat transfer of fully cooled stage compared to that of the same profiles as an uncooled stage at – 10 deg rotor incidence and 120 percent of design Reynolds number

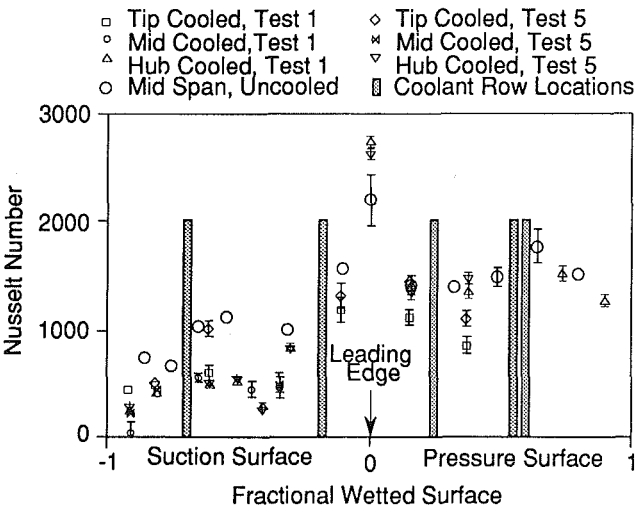

Fig. 5 Comparison of data from two tests illustrating level of measurement repeatability

Measurements made on the fully cooled stage are shown in Fig. 4, along with earlier uncooled stage results taken at the same operating condition (– 10 deg rotor incidence, 120 percent of the baseline Reynolds number). The shaded bars denote the location of the rows of coolant injection holes. Figure 5 presents the data of Fig. 4 along with that from a second test taken two months later to check repeatability. The results from the two tests are very similar with the exception of one tip section gage on the pressure and suction surfaces. It can be seen from the data in these plots that the suction and pressure surfaces behave quite differently. The film cooling is effective on the suction surface in reducing the blade heat transfer with similar results observed across the span, implying that the flow here is somewhat two dimensional. By comparison, little reduction in heat transfer is observed along the pressure surface except near the tip.

Rigby et al. (1990) performed measurements on the same cooled profile in a linear cascade. Figure 6 compares the cascade measurements with those from the rotating stage with both a cooled and uncooled rotor. The data show that heat transfer is reduced on the suction surface of the rotor compared to the cascade, by as much as 60 percent. On the pressure surface, the cooled cascade data show little influence of film cooling.

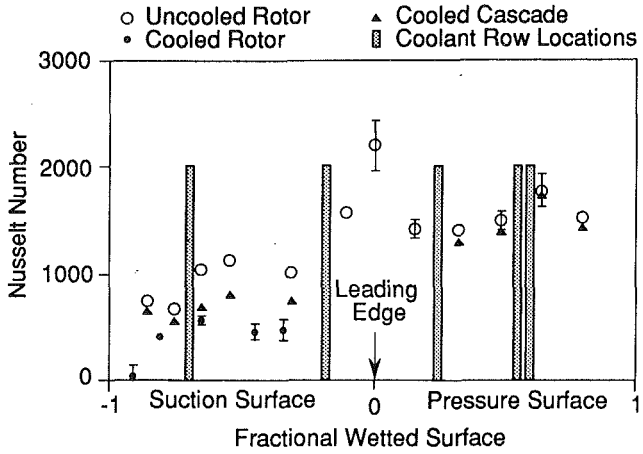

Fig. 6 Uncooled and film cooled rotating stage measurements compared with those from a cooled linear cascade

Table 3 Coolant test conditions

Temperature Ratios	
NGV Coolant/Freestream	0.54
Rotor Coolant/Freestream Relative	0.51
Rotor Coolant/Wall	0.74
Momentum Ratios, 1st Row of Holes	
Suction Surface	0.72
Pressure Surface	1.10
Blowing Ratios, 1st Row of Holes	
Suction Surface, High/Low	1.24/0.96
Pressure Surface, High/Low	1.52/1.1

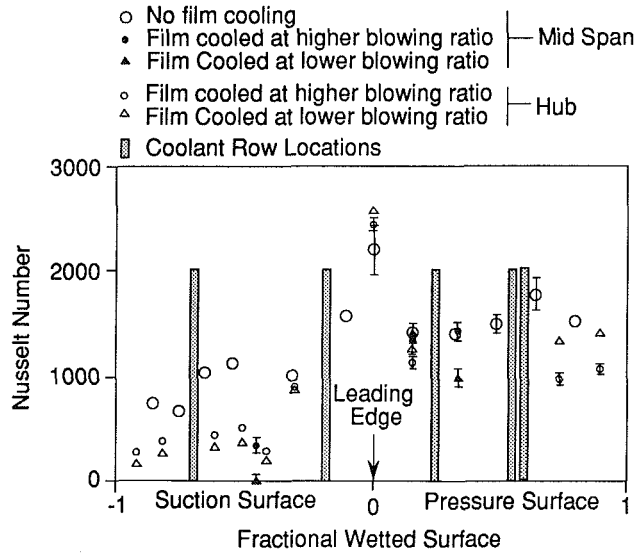

Fig. 7 The influence of blowing ratio on rotor heat transfer

The influence of blowing ratio (coolant mass flow/free-stream mass flow) on film cooling was examined by replacing the usual Argon-Freon 14 coolant with nitrogen, changing the coolant molecular weight and ratio of specific heats, thus reducing the blowing ratio without appreciably changing the momentum ratio (momentum of coolant flow/momentum of free-stream flow), Table 3. Although somewhat sparse, the data in Fig. 7 show that, on the suction surface, reducing the blowing ratio reduces the heat transfer. The data on the pressure surface are less uniform, with lowered blowing ratio reducing the heat transfer downstream of the first row of holes,

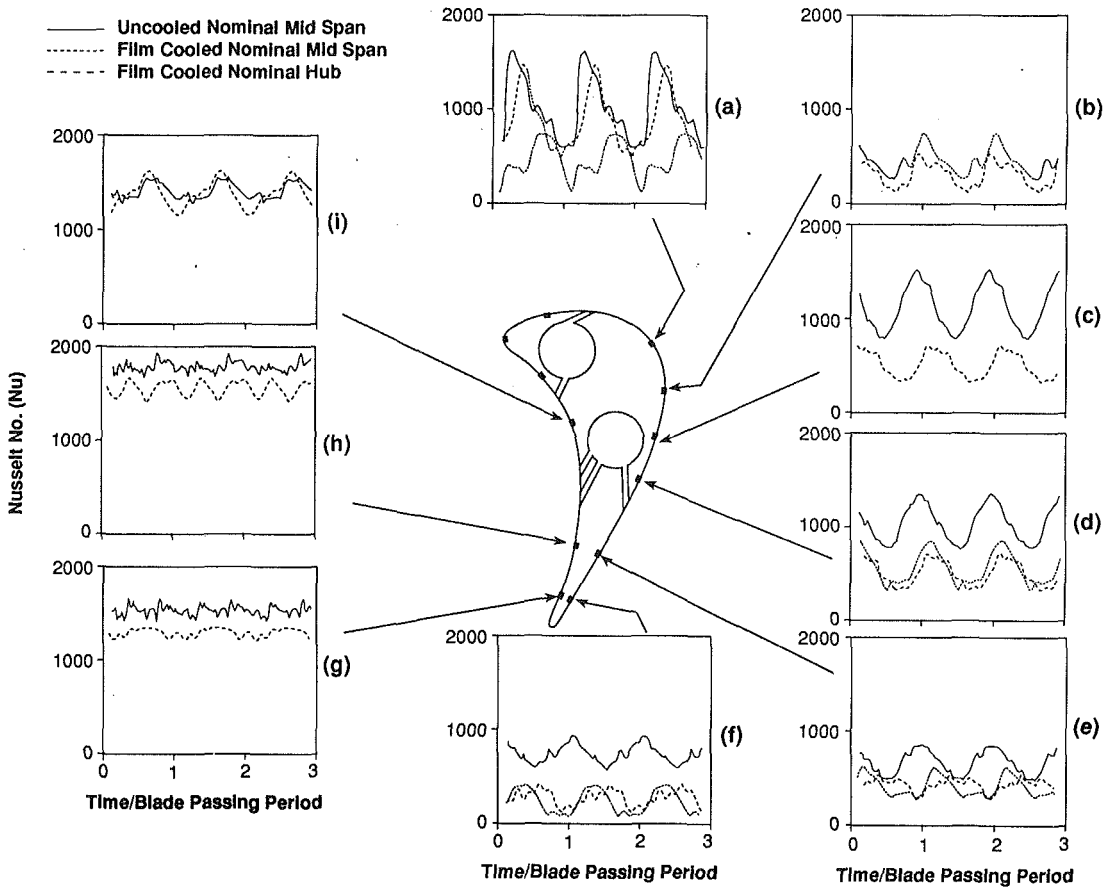

Fig. 8 Time-resolved rotor heat transfer measurements compared with those for an uncooled rotor

but downstream of the second row, the heat transfer is reduced at the higher blowing ratio. This behavior would be consistent with film lift-off at the higher blowing ratios.

Overall, we note that the film cooling appears effective on the rotor suction surface but much less so on the pressure surface. The lack of more detailed spatial coverage (due to instrumentation failures) inhibits more detailed conclusions from the steady state data. With the exception of Fig. 7, all the data in this paper were taken at the higher blowing ratio, corresponding to the design intent.

Time-Resolved Measurements

Time-resolved data are compared with uncooled rotor measurements in Fig. 8. Over the pressure surface, there is little or no reduction in heat transfer from the film cooling. On the suction surface, the influence of film cooling is more pronounced. At the crown of the suction surface (Fig. 8*a*), the cooling is pronounced at midspan but minimal at the hub. Elsewhere along the suction surface, the cooling is similar at hub and midspan. The influence of the film cooling is seen both to reduce the heat transfer and also to introduce a phase shift in the unsteady waveform.

The influence of blowing ratio on the pressure surface (position corresponding to Fig. 8*i*) is illustrated in Fig. 9. At the higher blowing ratio, the film provides no cooling at all while at the lower blowing ratio, the mean heat transfer is reduced by about 30 percent and the waveform is altered.

The fractional change in heat transfer (the isothermal film effectiveness) calculated from the midspan data on the crown of the suction surface (Fig. 8*a*) is shown in Fig. 10. Note that for about half of a vane passing period, the effectiveness is approximately constant at 0.7, but then drops rapidly to zero. In the following section, we examine the nature of this unsteadiness and present a simple time-resolved model of the process.

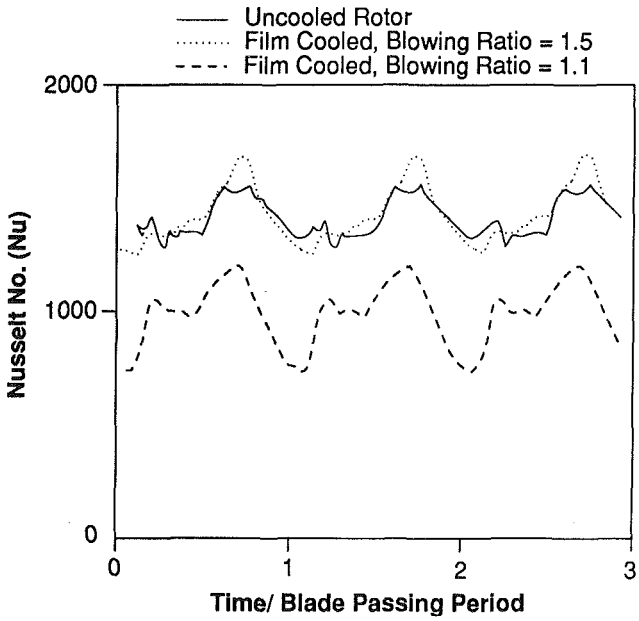

Fig. 9 The influence of blowing ratio of the upstream coolant hole on the pressure surface heat transfer corresponding to Fig. 8(*i*)

The Influence of Unsteadiness on Rotor Film Cooling

Turbine blade aerodynamic and cooling design is currently based on the assumption that the flow can be modeled as

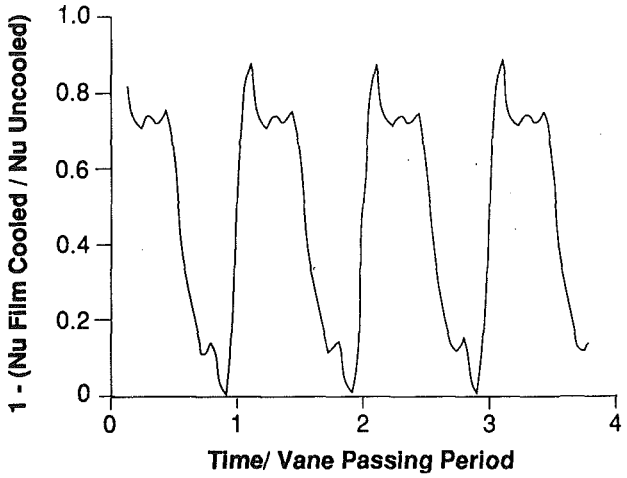

Fig. 10 Time-resolved isothermal effectiveness calculated from the midspan data on the crown of the rotor suction surface (Fig. 8*a*)

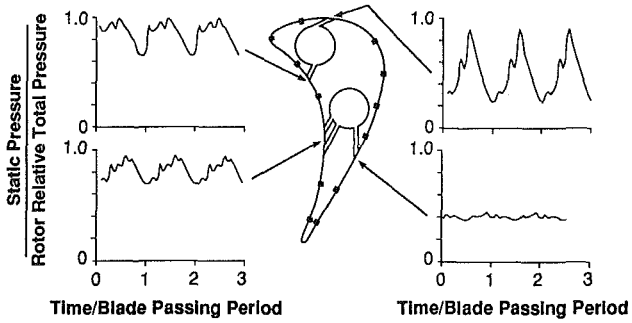

Fig. 11 Time-resolved wall static pressure at the coolant hole exit locations as predicted by an unsteady, multiblade row code

steady. The data presented here certainly show that blade heat transfer is unsteady over much of the airfoil surface. What are the sources of these fluctuations, which are dominant, how can they be modeled, and what are the turbine design implications of this unsteadiness?

There are many sources of unsteadiness in turbine rotors. Potential interactions between blade rows and impingement of NGV wakes and shock waves on the rotor are the predominant sources of free-stream unsteadiness. Abhari et al. (1992) showed that a two-dimensional, unsteady, multiblade row, viscous code (UNSFLO, Giles and Haimes, 1993) can quantitatively predict the time-resolved heat transfer in an uncooled configuration of this turbine stage.

The flow and heat transfer perturbations in a transonic turbine are large, of the order of the mean flow. Figure 11 presents the static pressure history calculated with the unsteady code for the uncooled turbine at the locations corresponding to the injection holes on the cooled rotor. This shows large fluctuations, especially near the front of the blade. The unsteady envelope of the rotor static pressure distribution is compared with the coolant supply plenum pressure in Fig. 12 and shows that the coolant driving pressure ratio can vary enormously, by more than 100 percent over some of the blade chord. Although in the time mean, the coolant minus wall static pressure difference is always positive, the instantaneous pressure difference is zero near the rotor leading edge over part of the vane passing period. On the suction surface, the variation in coolant driving pressure difference is sufficient to choke the coolant holes during part of the cycle and reverse the flow during another part! For this temporal pressure variation to influence the mass flow rate of coolant, the vane passing frequency must be low compared with the propagation time of

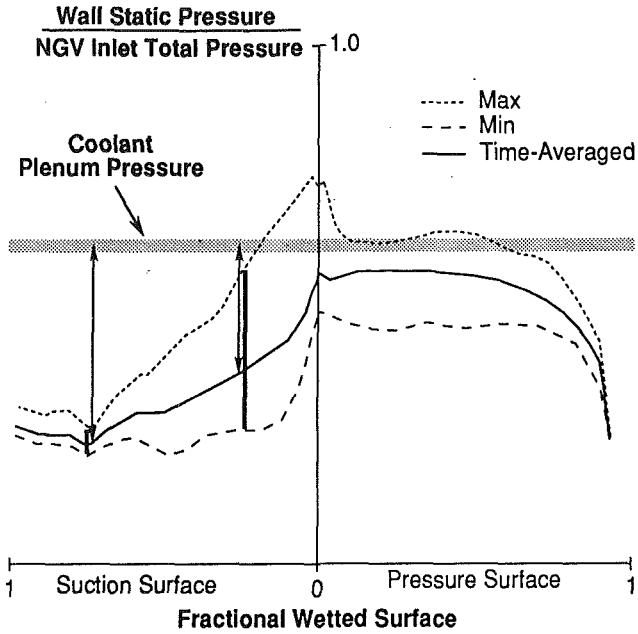

Fig. 12 Midspan rotor static pressure distribution as predicted by an unsteady, multiblade row, viscous code

disturbances through the coolant holes. For this turbine, the product of coolant mean flow Mach number and reduced frequency ($\Omega = \omega L/\overline{U}_c$) is 0.4, implying that pressure perturbations will indeed modify the coolant flow rate.

To model this process, we will formulate a simple unsteady, one-dimensional, subsonic compressible flow through a slot and drive it with the pressure perturbations calculated by the time-resolved multiblade row code. Linearized about the mean flow, the potential perturbation satisfies (Ashley and Landahl, 1965)

$$U = \overline{U} + U' = \overline{U}\left[1 + \frac{\partial \varphi(x, t)}{\partial x} + \ldots\right]. \tag{1}$$

and

$$(1 - \overline{M}^2)\varphi_{xx} - \frac{2\overline{M}^2}{\overline{U}}\varphi_{xt} - \frac{\overline{M}^2}{\overline{U}^2}\varphi_{tt} = 0 \tag{2}$$

Assuming a harmonic unsteady perturbation of the form $\varphi = f(x)e^{i\omega t}$, the above linear partial differential equation reduces to a linear ordinary differential equation, the solution of which provides the mean unsteady mass flux from the holes. Summing for all frequencies and ignoring the second-order terms (terms involving the square of the perturbation), the correction to the mean mass flow from the slot is given by

$$\overline{(\rho U)} = \overline{(\overline{\rho} + \rho')(\overline{U} + U')} = \overline{\rho}\,\overline{U} + \overline{(\rho' U')} \approx \overline{\rho}\,\overline{U}, \quad \text{when } \overline{(\rho' U')} \ll \overline{\rho}\,\overline{U} \tag{3}$$

where ρ is the coolant density, U is the velocity, the overbar corresponds to mean conditions, and the prime corresponds to the perturbation quantities. At the exit of the coolant holes, the unsteady mass flux from the coolant slot, including the first-order correction, is written as

$$\frac{\rho U}{\overline{\rho}\,\overline{U}} = \frac{\overline{\rho}\,\overline{U} + (\rho U)'}{\overline{\rho}\,\overline{U}} \approx \sum_{\omega = \omega_1}^{\infty} (1 - A(\omega)G(\omega)e^{i\omega t}) \tag{4}$$

where

$$G(\omega) = 1 - \overline{M}\,\frac{(1 - \overline{M})e^{-i\kappa} + (1 + \overline{M})e^{i\kappa}}{(1 - \overline{M})e^{-i\kappa} - (1 + \overline{M})e^{i\kappa}}, \text{ and } \kappa = \frac{\overline{M}\Omega}{1 - \overline{M}^2}$$

The term $A(\omega)$ is the Fourier coefficient of the periodic pressure at the exit of the coolant holes. Ω is the reduced frequency ($\omega L/\overline{U}_c$) based on the slot length (L), and the mean coolant

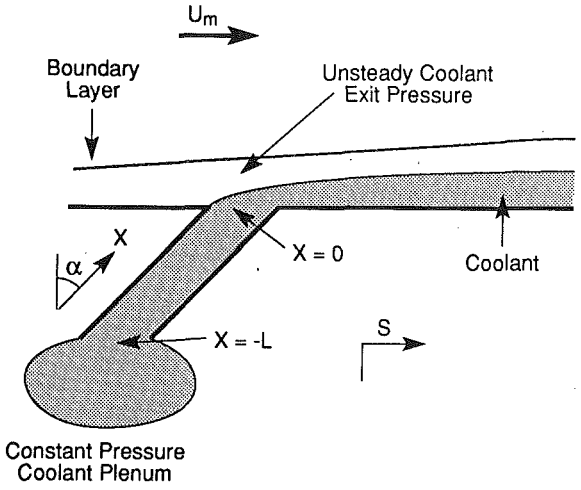

Fig. 13 Two-dimensional coolant slot model with unsteady external pressure field

velocity ($\overline{U}_c$). It is seen that as $\omega \to 0$, the term $G(\omega)$ also approaches zero and the quasi-steady conditions are recovered. For a Mach number of 0.8 and a reduced frequency of 0.4, Eq. (4) indicates that the fluctuation in the coolant mass flux through the slot is 30 percent.

Given that the mass flux from coolant holes is unsteady, the film cooling must be unsteady as well. Whitten et al. (1970) have shown that, in a turbulent boundary layer with nonuniform blowing, film cooling is influenced principally by the local boundary layer conditions and shows little effect of prior history. This suggests that, at distances relatively close to the cooling holes compared to the chord, film cooling with unsteady blowing may behave as if the local flow were quasi-steady. To test this assumption, we will use a steady-state film cooling correlation from the literature and drive it with the unsteady blowing as described in Eq. (4), using the unsteady, multiblade row calculation to supply the wall static pressure at coolant hole locations. The estimated cooling effectiveness will then be used to "correct" the heat flux measured about the uncooled rotor in order to predict the cooled blade heat transfer. For this purpose, we employ the film cooling correlation suggested by Goldstein and Haji-Sheik (1967) for the adiabatic cooling effectiveness:

$$\eta_{ad} \equiv (T_\infty - T_{ad})/(T_\infty - T_c) \tag{5}$$

$$\eta_{ad} = 5.75\ \mathrm{Pr}^{2/3}\xi^{-0.8}\left(\mathrm{Re}_c \frac{\mu_c}{\mu_\infty}\right)^{0.2}\beta^{-1} \tag{6}$$

where

$$\beta \equiv 1 + \left(1.5 \times 10^{-4} \cos \alpha \mathrm{Re}_c \frac{\mu_c}{\mu_\infty}\right)$$

$$\xi \equiv \left(\frac{S}{d}\right)\frac{(\rho U)_\infty}{(\rho U)_c}$$

α is the injection angle, Re_c is the Reynolds number based on the coolant fluid through the slot (Fig. 13). In this model, the coolant hole is a slot, so d represents an equivalent slot width defined as the hole area divided by the pitch between holes (Goldstein et al., 1974). It is assumed that the correction to the driving temperature due to the compressibility is negligible. The time lag required for the coolant fluid to reach any point S, is assumed to be 70 percent of the free-stream velocity, which corresponds to the mean propagation velocity of a turbulent patch within the boundary layer, as measured by Ashworth (1987).

Then, the ratio of heat transfer with film cooling ($\dot{Q}_{fc}$) to that without ($\dot{Q}_0$) is

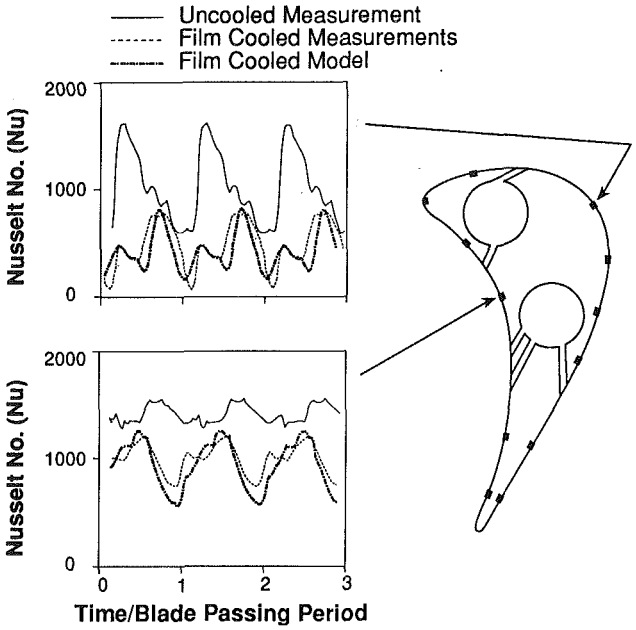

Fig. 14 A comparison of film-cooled measurements and predictions made with a simple, unsteady blowing model

$$\frac{\dot{Q}_{fc}}{\dot{Q}_0} = \frac{h_{fc}}{h_0}\left(\frac{T_{ad} - T_w}{T_\infty - T_w}\right) = \frac{h_{fc}}{h_0}(1 - \theta\eta_{ad})$$

$$\theta \equiv \left(\frac{T_\infty - T_c}{T_\infty - T_w}\right) \tag{7}$$

Assuming that the heat transfer coefficient is unchanged by the addition of the coolant, then Eq. (7) can be written in nondimensional form as

$$\mathrm{Nu}_{\text{film cooled}}(S, t) \approx \mathrm{Nu}_{\text{uncooled}}(S, t)(1 - \theta\eta_{ad}(S, t)) \tag{8}$$

We can now evaluate Eq. (8) using the uncooled rotor measurements to provide $\mathrm{Nu}_{\text{uncooled}}(S,t)$ and the unsteady, multiblade row calculation to provide the time history of the wall static pressure (i.e., the calculations in Fig. 11) needed to estimate the unsteady blowing rate.

Figure 14 compares the results of this calculation to the measured rotor film-cooled heat transfer and shows excellent agreement on both the pressure and suction surfaces. This agreement implies that film cooling at these locations is strongly influenced by unsteady blowing and that the above model captures the important physical features of the process. This result explains the apparent phase shift between the cooled and uncooled measurements as simply an artifact introduced by the unsteady blowing coupled to the propagation delay in the boundary layer. Additionally, the agreement between the model and data indicates that the boundary layer behavior is quasi-steady here and that film cooling performance can be successfully estimated in some cases without requiring film-cooled, unsteady, multiblade row codes (a great increase in complexity over the current state of the art).

The design of film-cooled turbines is presently done assuming steady flow. We can take the time-averaged static pressure distribution as presented in Fig. 12 and calculate the resulting blowing and heat transfer (which is the design intent). Compared to the results of the unsteady model and measurements (which agree), the steady-state predicted heat transfer is 12 percent too high on the suction surface and 5 percent too low on the pressure surface. Thus, the unsteady blowing can impact the mean blade heat transfer and may need to be accounted for in cooling design systems. The unsteadiness driving the process is larger for highly loaded transonic turbines than for

subsonic designs, so we would expect this effect to be somewhat exaggerated here compared to more lightly loaded designs.

Summary and Conclusions

The time-resolved heat transfer has been measured on the rotor of a fully cooled transonic turbine stage and compared with data from the same geometry operated in an uncooled configuration. The data show a considerable reduction in the average suction surface heat transfer with cooling but relatively little on the pressure surface. High blowing ratios were shown to provide much less effective cooling than lower ones. The results are similar over the center 3/4 of the span measured, implying that the flow in this region is mainly two dimensional.

Comparisons were also made with cooled cascade measurements of the same profile. The rotor heat transfer on the suction surface was considerably less than that in the cascade. The time-resolved data revealed that the cooling, when effective, both reduced the dc level of heat transfer and changed the shape of the unsteady wave form. The principal unsteady driver for the film cooling was shown to be the unsteady rotor blade surface pressure distribution caused by blade row interactions. These modulate the cooling flow over a wide range, which in turn generates fluctuations in cooling and heat transfer. A simple, linear model was shown to do a good job at predicting this effect. The unsteadiness resulted in a 12 percent heat transfer decrease at the suction surface location investigated, and a 5 percent increase on the pressure surface.

Acknowledgments

The authors would like to thank Dr. G. R. Guenette, Mr. C. W. Haldeman, and Dr. R. J. G. Norton for their generous assistance and stimulating comments, and Ms. D. Park for preparing the manuscript and figures. This work was supported by the Wright Laboratories, USAF, Dr. C. McArthur, program monitor, and Rolls-Royce Inc., Dr. R. J. G. Norton, technical monitor.

References

Abhari, R. S., 1991, "An Experimental Study of the Unsteady Heat Transfer Process in a Film Cooled Fully Scaled Transonic Turbine Stage," Ph.D. Dissertation, Massachusetts Institute of Technology, Cambridge, MA.

Abhari, R. S., Guenette, G. R., Epstein, A. H., and Giles, M. B., 1992, "Comparison of Time-Resolved Turbine Rotor Blade Heat Transfer Measurements and Numerical Calculations," ASME JOURNAL OF TURBOMACHINERY, Vol. 114, pp. 818–827.

Ashley, H., and Landahl, M., 1965, *Aerodynamics of Wings and Bodies*, Addison-Wesley, Boston, MA.

Ashworth, D. A., 1987, "Unsteady Aerodynamics and Heat Transfer Processes in a Transonic Turbine Stage," D. Phil. Thesis, Oxford University, United Kingdom.

Dring, R. P., Blair, M. F., and Joslyn, H. D., 1980, "An Experimental Investigation of Film Cooling on a Turbine Rotor Blade," ASME *Journal of Engineering for Power*, Vol. 102, pp. 81–87.

Dunn, M. G., 1986, "Heat-Flux Measurements for the Rotor of a Full-Stage Turbine: Part I—Time-Averaged Results," ASME JOURNAL OF TURBOMACHINERY, Vol. 108, pp. 90–97.

Epstein, A. H., Guenette, G. R., Norton, R. J. G., and Yuzhang, C., 1986, "High Frequency Response Heat Flux Gauge," *Review of Scientific Instruments*, Vol. 75, No. 4, pp. 639–649.

Giles, M. B., 1988, "UNSFLO: A Numerical Method for Unsteady Inviscid Flow in Turbomachinery," MIT Gas Turbine Laboratory Report No. 195.

Giles, M. B., and Haimes, R., 1993, "Validation of a Numerical Method for Unsteady Flow Calculations," ASME JOURNAL OF TURBOMACHINERY, Vol. 115, pp. 110–117.

Goldstein, R. J., and Haji-Sheik, A., 1967, *1967 Semi-International Symposium*, Japan Society of Mechanical Engineering, pp. 213–218, Tokyo.

Goldstein, R. J., Eckert, E. R. G., and Burggraf, F., 1974, "Effect of Hole Geometry and Density on Three-Dimensional Film Cooling," *International Journal of Heat and Mass Transfer*, Vol. 17, pp. 595–607.

Goldstein, R. J., and Chen, H. P., 1985, "Film Cooling on a Gas Turbine Blade Near the End Wall," ASME *Journal of Engineering for Gas Turbines and Power*, Vol. 107, pp. 117–122.

Guenette, G. R., Epstein, A. H., Giles, M. B., Haimes, R., and Norton, R. J. G., 1989, "Fully Scaled Transonic Turbine Rotor Heat Transfer Measurements," ASME JOURNAL OF TURBOMACHINERY, Vol. 111, pp. 1–7.

Ito, S., Goldstein, R. J., Eckert, E. R. G., 1978, "Film Cooling of a Gas Turbine," ASME *Journal of Engineering for Power*, Vol. 100, pp. 476–481.

Norton, R. J. G., 1987, Rolls Royce, Inc., Private Communications.

Rigby, M. J., Johnson, A. B., and Oldfield, M. L. G., 1990, "Gas Turbine Rotor Blade Film Cooling With and Without Simulated NGV Shock Waves and Wakes," ASME 90-GT-78.

Schwarz, S. G., and Goldstein, R. J., 1989, "The Two-Dimensional Behavior of Film Cooling Jets on Concave Surfaces," ASME JOURNAL OF TURBOMACHINERY, Vol. 111, pp. 124–130.

Takeishi, K., Aoki, S., Sato, T., and Tsukagoshi, K., 1992, "Film Cooling on a Gas Turbine Rotor Blade," ASME JOURNAL OF TURBOMACHINERY, Vol. 114, pp. 828–834.

Whitten, D. G., Moffat, R. J., and Kays, W. M., 1970, "Heat Transfer to a Turbulent Boundary Layer With Non-uniform Blowing and Surface Temperature," presented at the 4th International Heat Transfer Conference, Paris-Versailles.

An Experimental Study of Film Cooling Effectiveness Near the Leading Edge of a Turbine Blade

M. Salcudean
Professor and Head.

I. Gartshore
Professor.

K. Zhang
Research Engineer.

I. McLean
Postdoctoral Fellow.

Department of Mechanical Engineering,
University of British Columbia,
Vancouver, British Columbia, Canada

A flame ionization technique based on the heat/mass transfer analogy has been used in an experimental investigation of film cooling effectiveness. The measurements were made over the surface of a turbine blade model composed of a semi-cylindrical leading edge bonded to a flat after-body. The secondary flow was injected into the boundary layer through four rows of holes located at ±15 and ±44 deg about the stagnation line of the leading edge. These holes, of diameter d, had a 30 deg spanwise inclination and a 4d spanwise spacing. Adjacent rows of holes were staggered by 2d, and perfect geometry symmetry was maintained across the stagnation line. Discharge coefficients and flow division between the 15 and 44 deg rows of holes have also been measured. The strong pressure gradient near the leading edge produces a strongly nonuniform flow division between the first (±15 deg) and the second (±44 deg) row of holes at low overall mass flow ratios. This produced a total cutoff of the coolant from the first row of holes at mass flow ratios lower than approximately 0.4, leaving the leading edge unprotected near the stagnation line. Streamwise and spanwise plots of effectiveness show that the best effectiveness values are obtained in a very narrow range of mass flux ratios near 0.4 where there is also considerable sensitivity to changes in Reynolds number. The effectiveness values deteriorate abruptly with decreasing mass flow ratios, and substantially with increasing mass flow ratios. Therefore, it was concluded that the cooling arrangement investigated has poor characteristics, and some suggestions are made for alternate designs.

1 Introduction

Attempts to increase the efficiency of modern gas turbine engines lead to high gas temperatures at the inlet to the turbine. To improve the behavior of the turbine blades exposed to this hot gas, research can be aimed on one hand at the improvement of the materials used for the blades, and on the other hand, at improvements in the design of cooling schemes to protect the turbine blade. One of these cooling schemes is "film cooling" in which a cool gas is injected over the blade surface, protecting it from the action of hot gases. Film cooling has been extensively studied in the past. Most studies were concerned with obtaining high effectiveness for low-curvature surfaces that typify the blade downstream of the leading edge (see, for example, Hay et al., 1985). Far fewer studies have been directed at film cooling close to the leading edge, known as "shower head cooling."

The results of one study of shower head cooling have been published by Mick and Mayle (1988). They investigated the film cooling of the leading edge by using two rows of circular cooling holes located at 15 and 44 deg, respectively, from the stagnation line of semicircular nose coupled to a flat afterbody. They measured the film cooling effectiveness η (defined as $T_{aw}-T_\infty/T_c-T_\infty$, where the subscripts aw, ∞, and c refer to the adiabatic wall, free stream, and coolant, respectively) by injecting heated air through the "cooling" holes without heating the insulated surface of the body. The present study repeats some of their measurements, using a similar body, but using a different simulation method.

Karni and Goldstein (1990) studied the simulation of film cooling in the leading edge region through the mass transfer analogy using the naphthalene sublimation technique. The Sherwood numbers were investigated for different injection geometries. Nirmalan and Hylton (1990) studied the effect of blowing on Stanton number for a three-vane, linear, two-dimensional cascade. Mehendale and Han (1992) measured the heat transfer effectiveness near the leading edge and investigated the influence of high mainstream turbulence intensity.

Hay et al. measured the discharge coefficients using a flat plate with orifices. They reported that at low values of mass flow ratios M_∞ (expressed by them as pressure ratios) the discharge coefficient increased strongly with mass flow ratio. At high mass flow ratios the C_D reached a plateau with typical values around 0.7–0.8. Tillman and Jen (1984) have examined the effect of external flow on the coolant discharge coefficients for holes located in a circular cylinder. They have presented

Contributed by the International Gas Turbine Institute for publication in the JOURNAL OF TURBOMACHINERY. Manuscript received at ASME Headquarters October 16, 1992. Associate Technical Editor: H. Lukas.

the discharge coefficient variation as a function of the angular position of the hole for various mass flow rates. They did note the decrease of discharge coefficient with decreasing mass flow ratio. They also noted that the discharge coefficient decreased with decreasing Reynolds number of the flow through the coolant orifice. Values from their reports have been quoted later in this paper (Section 3.1).

The objectives of the present work are to analyze the flow division and to measure film cooling effectiveness. A new measurement technique and the heat mass transfer analogy are used.

The effectiveness measurements were carried out using a flame ionization detector technique, which, to the best knowledge of the authors, has been used here for the first time for film cooling effectiveness measurements. The present geometry differs from that of Mick and Mayle in that it uses four rows of holes at ± 15 and ± 44 deg placed symmetrically about the stagnation line (Mick and Mayle used three rows of holes at ± 15 and 44 deg in which those at ± 15 deg were staggered with respect to each other). Blockage ratios in the two experiments were also somewhat different. In all other aspects, the present model is like that of Mick and Mayle.

2 Experimental Arrangements

2.1 Model and Wind Tunnel Configuration. The present measurements were made in a large blower-type wind tunnel with a cross section 2.44 m wide by 1.6 m high. Turbulence intensities in the test section vary over the cross section but are never higher than 1/2 percent outside of the wall boundary layers. These intensities are much lower than those found in real engines, but they provide data that are a basis for comparison with higher intensity tests done elsewhere (Mehendale and Han, 1992). Mean velocities are uniform over the same central section to within ± 1 percent.

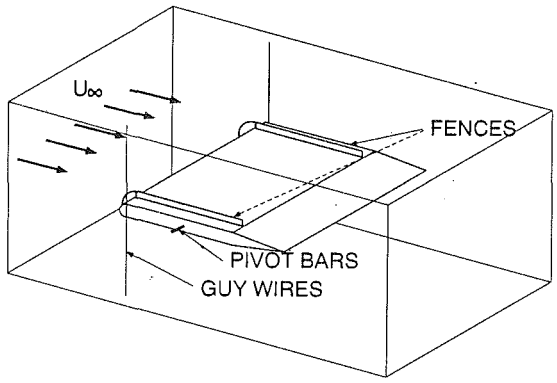

Fig. 1 Model turbine blade in test section

The model was mounted horizontally and spanned the test section as shown in Fig. 1. In common with the geometry of Mick and Mayle, the present model has a semicircular leading edge bonded smoothly to an afterbody, which consisted of parallel top and bottom surfaces and a tapered trailing edge. The model has a leading edge diameter (D) of 127 mm, parallel top and bottom lengths of 1.19 m, and an overall chordwise length of 2.28 m. Since the model spans the tunnel at zero

Nomenclature

A, B, C = empirical constants defined in concentration of contaminant

A_T = total cross-sectional area of all blowing holes

C_D = discharge coefficient for a blowing hole, equal to $\frac{(\rho_c U_c)_{\text{MEASURED}}}{(\rho_c U_c)_{\text{IDEAL}}}$. In these tests ρ is constant so that $C_D = \frac{U_{c\,\text{MEASURED}}}{U_{c\,\text{IDEAL}}}$

C_p = pressure coefficient, designating surface static pressure on the model and equal to $\frac{p_M - p_\infty}{\frac{1}{2}\rho U_\infty^2}$

C_{pp} = plenum pressure coefficient equal to $\frac{p_p - p_\infty}{\frac{1}{2}\rho U_\infty^2}$

d = coolant hole diameter (12.5 mm)

D = leading edge diameter (127 mm)

K = dimensionless constant defined in Eq. (A6)

M_1 = mass flow ratio for holes at 15 deg, equal to U_1/U_∞

M_2 = mass flow ratio for holes at 44 deg, equal to U_2/U_∞

M_∞ = overall mass flow ratio $\{\rho_c \overline{U}_c/\rho_\infty U_\infty\}$, which is equal to the velocity ratio $\overline{U}_c/U_\infty$ in these "incompressible" tests

p_M = static pressure at the surface of the model in the absence of blowing

p_∞ = static pressure upstream of the model

Q_{15} = volume flow rate for all holes at 15 deg

Q_{44} = volume flow rate for all holes at 44 deg

Q_T = total volume flow rate of discharge through all blowing holes

Re_c = coolant Reynolds number equal to $\overline{U}_c d/\nu$

T = temperature

U_1 = average discharge velocity through blowing holes located at $\theta = 15$ deg

U_2 = average discharge velocity through blowing holes located at $\theta = 44$ deg

$\overline{U}_c$ = average discharge velocity from all blowing holes; equal to $Q_T/A_T U_\infty$

U_∞ = free-stream velocity measured well in front of the model

x = streamwise distance along the curved surface of the model from the stagnation line

z = spanwise distance

η = film cooling effectiveness defined as $\frac{T_{aw} - T_\infty}{T_c - T_\infty}$ or $\frac{C_w - C_\infty}{C_c - C_\infty}$ or $\frac{C_w}{C_c}$

$\overline{\eta}$ = spanwise averaged values of η as described in text

θ = angle measured around the model leading edge from the leading edge stagnation line (line of symmetry)

ρ = density, assumed constant everywhere in these "incompressible" experiments

Subscripts

1, 2 = refer to holes located at 15 and 44 deg (respectively) from the stagnation line of the model

∞ = free stream, well ahead of the model

aw = adiabatic wall values

c = coolant hole values

M = at the surface of the model in the absence of blowing and (in the case of velocity), outside the model surface boundary layer

p = plenum values

w = wall values

incidence, the frontal blockage of the tunnel is 7.9 percent. This contrasts with the tests of Mick and Mayle for which the blockage ratio was 33 percent. The model was mounted at zero incidence in the wind tunnel by rotating it until the flat surfaces of the afterbody were parallel to the floor of the wind tunnel test section.

Tunnel or "free-stream" wind speeds can be calculated from given coolant hole Reynolds numbers Re_c (based on the average coolant velocity for all holes and the coolant hole diameter d), the mass flow ratio M_∞ (equal to the average coolant velocity divided by U_∞), and the given geometry of the model. In general, values of free-stream velocity between 2 and 20 m/s were used with many tests at 7 m/s. All these are in the low-speed incompressible range and were selected along with model size to maintain Reynolds numbers in the range found by real blades. Mach number effects are, of course, not modeled in these tests.

Because of the reports of flow separation on this geometry (see Bellows and Mayle, 1986), fences were placed on the model at spanwise positions ±0.95 m from the tunnel centerline, to reduce or eliminate spanwise flow in separation bubbles. Some indication of flow separation was found in the present tests, but because no particular studies were made to look for separation bubbles, no conclusions on this aspect of the work have been drawn.

The hollow semicylindrical forebody was bonded to a plenum, which slid inside the afterbody, as illustrated in Fig. 2(a). A flow baffle, two fine screens, and a perforated plate were installed in the plenum over its internal cross section to encourage uniform delivery of gas to the coolant holes at the leading edge. The plenum was fed with pure air (or air plus propane contaminant) through a 25 mm delivery hose near the trailing edge of the model. Plenum pressures were measured through appropriate internal pressure taps, while gas flow delivery rates were measured by suitable rotameters.

As already noted, coolant injection holes were located at ±15 and ±44 deg from the stagnation line as shown in Fig. 2(b). In this case, perfect symmetry of the holes about the stagnation line was maintained, four rows of holes being put in place.

All cooling holes were 12.7 mm in diameter (d) and were drilled with an inclination of 30 deg to a spanwise line on the cylindrical leading edge. Viewed from the direction of the cylinder axis, the hole centerlines are radial, forming angles of ±15 and ±44 deg with respect to the stagnation line. The injection hole geometry is illustrated in Fig. 2(c). The holes had a spanwise spacing of 4d in each row. The spacing and orientation of the holes as well as (d/D) are deliberately identical to those of Mick and Mayle. For the present studies, seven holes were drilled for each row. The center hole of each row was positioned close to the centerline of the model, effectively representing one of an infinite series of spanwise holes. The present model leading edge, through which the holes were drilled, had a thickness of 25.4 mm so that the hole length along its centerline is 4d.

2.2 Measurement of Discharge Coefficients and Flow Rate Division. A common definition of discharge coefficient is

$$C_D = \frac{(\rho_c U_c)_{\text{measured}}}{(\rho_c U_c)_{\text{ideal}}}$$

where $(\rho_c U_c)_{\text{ideal}}$ can be calculated using Bernoulli's equation for incompressible flow from the plenum pressure p_p to p_M, p_M being the static pressure at the exit location of the hole in the absence of blowing. The value of C_D may depend on hole length, Reynolds number, and entrance geometry as noted by Tillman and Jen (1984) but should not vary with location on the cylinder, except insofar as the velocities U_c and U_M vary. Here U_M is the fluid velocity approaching the hole from around the cylinder, excluding local boundary layers on the cylinder

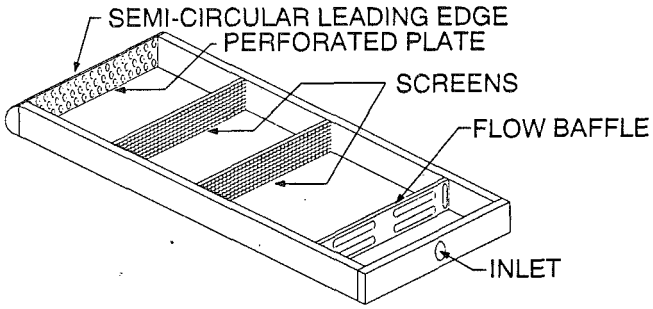

Fig. 2(a) Plenum interior

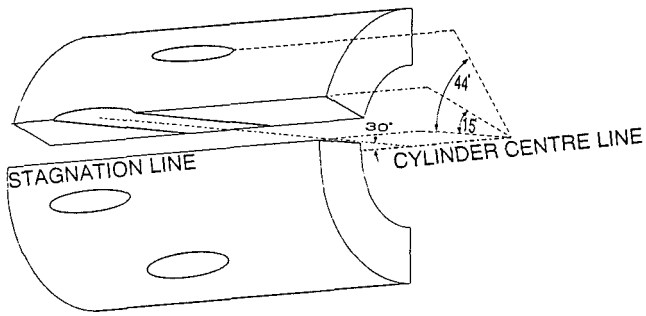

Fig. 2(b) Leading edge hole pattern

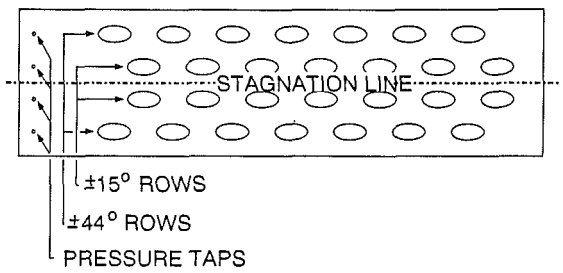

Fig. 2(c) Injection hole geometry

Fig. 2 Plenum and leading edge construction

surface. As shown by Gartshore et al. (1991) and indirectly by Tillman and Jen, C_D is strongly dependent on the ratio U_c/U_M, particularly for low values of this ratio.

Values of C_D were measured directly from the model during the present experiments. This was done by measuring the plenum pressure for various coolant flow rates and various free-stream velocities while having holes open at only one location (either ±15 or ±44 deg). Knowing the surface pressure coefficient C_p for the relevant hole location (15 or 44 deg), the value of discharge coefficient and the ratio of U_c/U_M could be found from the data, as described later in this paper, and in the Appendix.

The division of flow between the holes at ±15 deg and those at ±44 deg was also measured directly in the present case by the following procedure, adopted for any one tunnel velocity:

(a) With all the holes open, the volume flow rate through the plenum (Q_T) was measured using the rotameter. The plenum pressure at Q_T was also measured.

(b) With the holes at ±44 deg taped over (no flow out), the volume flow rate was adjusted until the plenum pressure obtained in (a) was found. The resulting flow rate, Q_{15}, was then measured.

(c) With holes at ±44 deg open and those at ±15 deg closed, the flow rate (Q_{44}), which occurred for the original plenum pressure, was measured.

The measured flow division Q_{15}/Q_{44} was then known and a

check was available from the fact that Q_T should equal the sum of Q_{15} and Q_{44}, within experimental accuracy. Values of average hole velocity U_1 or U_2 were found by dividing Q_{15} or Q_{44} by the total area of the holes in either of these rows (14 holes of 12.7 mm diameter in each row). The overall mass flow ratio M_∞ is found from $M_\infty = (Q_T/A_T U_\infty)$, where A_T is the summed cross-sectional area of all the coolant holes.

2.3 Measurement of Film Cooling Effectiveness. The film cooling effectiveness η as defined in Section 1 can be found by measuring temperature at an adiabatic wall, in the coolant and in the free stream (T_{aw}, T_c, and T_∞, respectively). Alternatively, greater simplicity can be obtained by using a mass transfer analogy, as discussed by Goldstein (1971). Using this technique, a foreign gas is used to mark or contaminate the coolant; the wall conditions are automatically and quite accurately "adiabatic" and the film cooling effectiveness may be defined in terms of the volume concentration of contaminant C as:

$$\eta = \frac{C_w - C_\infty}{C_c - C_\infty}$$

where the subscripts w, c, and ∞ indicate wall, coolant, and free-stream conditions, respectively. Injecting contaminant only from the coolant holes and not in the free stream forces C_∞ to zero, and η becomes simply C_w/C_c.

In the present case, propane was used as a contaminant gas and was injected in low (less than 3 percent) concentrations from the coolant holes. Measurements of C_w were made with a specially designed rake of very fine tubes (0.5 mm OD) designed to lie directly on the wall. Gas was sampled through these tubes and sent, through suitable fluid wafer switches, to a flame ionization detector, which accurately measured mean propane concentration (see Fackrell, 1980, for details of this instrument). Each tube was calibrated individually from a known concentration of propane before beginning the test. This calibration was then recorded in a microcomputer. By sampling alternately from the plenum to check C_c and then from a tube to find C_w, then switching to a new sampling tube, errors were minimized. The entire test was automated through the computer, which controlled the location of the rake (positioned by stepper motors driving a suitable traverse mechanism), the switching between tubes, and the processing of the results to produce values of η. The rake of fine sampling tubes contained 11 tubes, spaced $d/2$ apart, so that a spanwise length of $5d$ was covered by the rake. This test area is illustrated in Fig. 3, which shows typical measurement locations. In this and subsequent figures, x is the arc length of the curved surface measured from the stagnation line and z is the spanwise distance measured from the edge of one hole (as shown). Note that coolant fluid is discharged spanwise in the direction of increasing z.

The sampling tubes take fluid from about 0.25 mm above the wall, not *at* the wall as required. In general this error is difficult to quantify, but an explicit check on the accuracy of the method has been made in one case: For this test, propane-contaminated air was ejected from a two-dimensional *slot* in a flat plate into an uncontaminated stream. Measurements were then made of the velocity profile and the concentration profile at one position 5 slot widths downstream of the slot. Integration of the product of velocity and propane concentration over the entire profile height provided values of total propane flux (per unit length of slot) passing the measurement point. These values, found for several levels of propane concentration in the coolant, agreed within ±3 percent with the measured total propane flow into the plenum supplying the coolant mixture. We conclude that the flame ionization detector (FID) is able to measure local concentration with good accuracy. Other checks were made to ensure that the exact orientation of the FID sampling probe, with respect to the local velocity, did not affect the measured concentration significantly. We estimate that, within one hole diameter of ejection, the film cooling effectiveness is being measured correctly to within ±0.05, greater errors being possible very close to the coolant holes. Errors in tunnel velocity are less than 2 percent; errors in measuring coolant flow velocity are estimated as also less than 2 percent so that the overall uncertainty in the measurement of M_1 or M_∞ is less than 4 percent.

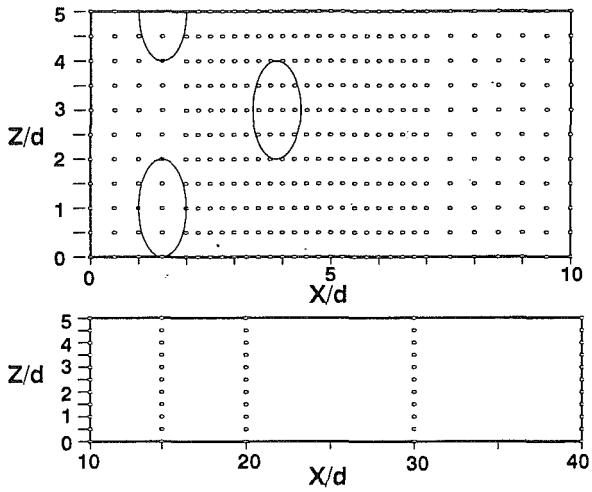

Fig. 3 Film cooling measurement stations

3 Results and Discussion

3.1 Flow Division Between Rows of Cooling Holes. An accurate description of the flow rate from individual holes is important for film cooling effectiveness. The flow division is complicated, however, by the strongly variable pressure and local velocity fields around the cylindrical leading edge of the present model, characterizing the "shower head" region of a turbine blade.

As has already been noted in Section 2.2 and by several earlier reports, discharge coefficients vary markedly with U_c/U_M where U_M is the local velocity approaching a coolant hole. The velocity U_M in this case varies from zero at the stagnation line to a maximum value near the junction between the cylindrical leading edge and the flat parallel sides of the model blade. The velocity U_M can be related to the local pressure on the cylinder through Bernoulli's equation. The appendix gives the equation relating the mass flow rate through holes at 15 and 44 deg to measured pressure distributions on the cylinder, measured discharge coefficients (varying with U_c/U_M) and measured overall mass flow ratios M_∞, defined in Section 2.2.

Discharge coefficients measured in the present tests are plotted in Fig. 4 together with values deduced from data reported by Gartshore et al. and by Tillman and Jen. The spanwise orientation of the coolant holes is 30 deg in each of the tests but coolant hole lengths and the exact geometry such as the curvature of the entrance to the holes from the plenum are probably slightly different in each case so that exact equality of C_D cannot be expected. The trends are clearly the same, however: low C_D at low U_c/U_M, rising to a constant C_D value for velocity ratios above about 2.

Gartshore et al. proposed a form for the C_D versus U_c/U_M curve (see appendix), which involves two empirical constants A and B. The constant A (in fact $A^{-1/2}$) describes the value of C_D reached at large U_c/U_M, while the constant B (in fact $B^{-1/2}$) describes the slope of the C_D versus U_c/U_M curve at the origin (zero U_c/U_M). Values of A and B found from the data from Gartshore et al., Tillman and Jen, and the present tests are given in Table 1 along with a composite constant K, which

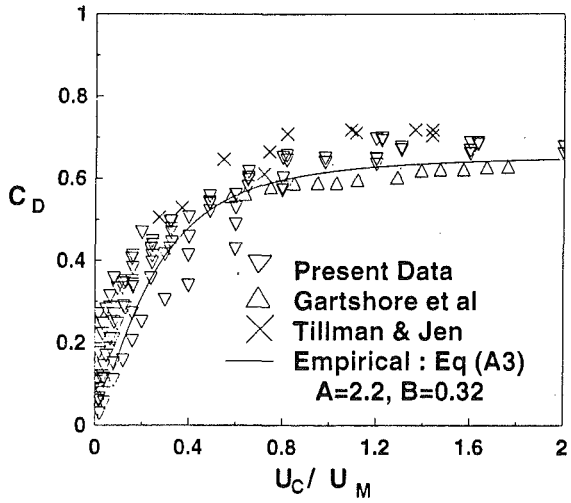

Fig. 4 Discharge coefficient variation with local velocity ratio

Table 1 Values of A, B, K describing measured discharge variations

Authors	A	B	Blockage Ratio	K
Tillman and Jen	2.0	0.20	33%	0.49
Gartshore et al.	2.5	0.23	5%	0.31
Present tests	2.2	0.32	7%	0.31

Notes: K is the value of M_∞ below which no flow would be expected from the holes at ± 15 deg, and is calculated from Eq. (A6). Appropriate values of C_{p_1} and C_{p_2} must be used in the calculation of K, and these vary significantly with position on the cylinder and with blockage ratio. Hole Reynolds numbers vary widely in tests for which U_c approaches zero and the average values of A and B in the table are necessarily somewhat approximate because they include such large Reynolds number changes.

describes the mass flow division between any two holes fed from a common plenum (see appendix).

The ratio of volume flow rates between the two rows of holes is shown in Fig. 5. Both the variation predicted by the analysis of the appendix and the measured ratios of Q_{15}/Q_{44} are shown, the predictions being based upon values of C_D measured from the present model. Good agreement can be seen between the measured and predicted values of flow rate division.

Figure 5 shows that, for an average mass flow ratio M_∞ between 0.3 and 0.4, the discharge from the holes at 15 deg drops to zero. This could be very dangerous as the critical region near the stagnation line is then completely unprotected.

The flow division reported by Mick and Mayle for their study is also shown on Fig. 5 and differs from the present measurements at low M_∞. In order to determine whether this difference could be due to the difference in geometry between the present model and that of Mick and Mayle, a new model was constructed for the present tests that more exactly duplicates Mick and Mayle's model: The new model has holes at ± 15 deg which are staggered with respect to each other, and holes at ± 44 deg which are also staggered with respect to adjacent rows. As shown in Fig. 5, measurements of the flow division between the two rows of holes in the new model gave values of flow rate Q_{15}/Q_{44}, which were essentially the same as those from the previous model despite the change in geometry. Therefore, the discrepancies in mass flow division between present and previous work cannot be attributed to the differences in hole location. A small difference in geometry or Reynolds number may promote or suppress transition in the holes, and may therefore give changes in C_D, as noted by Tillman and Jen. This may be responsible for the observed differences in flow rate between the two different studies, since

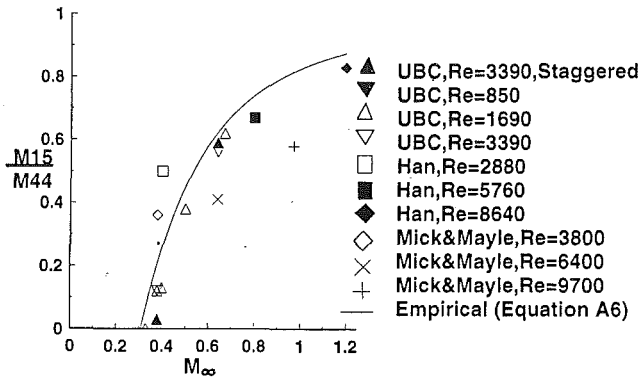

Fig. 5 Ratio of discharge flow rates from the two rows of coolant holes

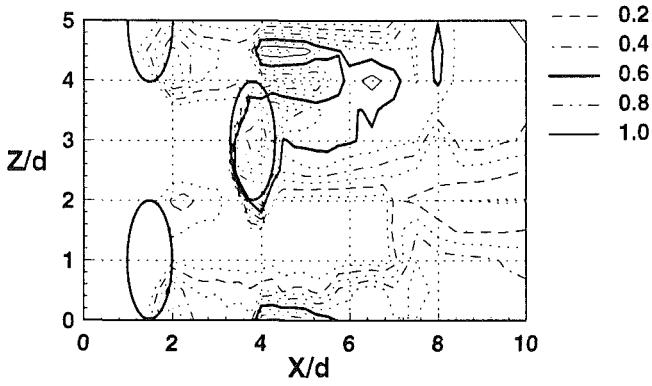

Fig. 6(*a*) $M_\infty = 0.40$

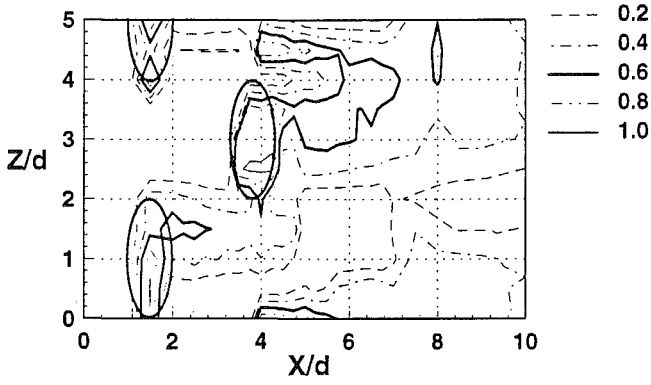

Fig. 6(*b*) $M_\infty = 0.64$

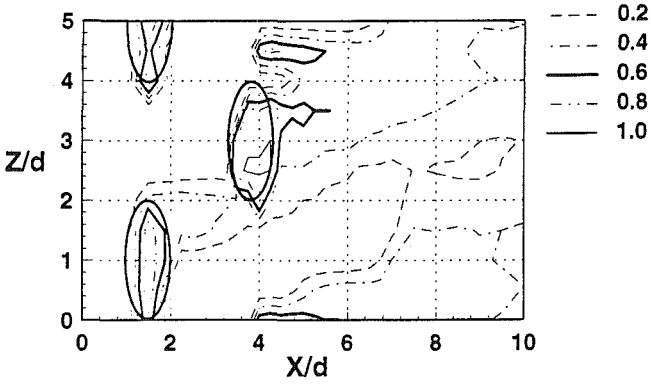

Fig. 6(*c*) $M_\infty = 0.97$

Fig. 6 Contours of iso-effectiveness for $Re_c = 3400$

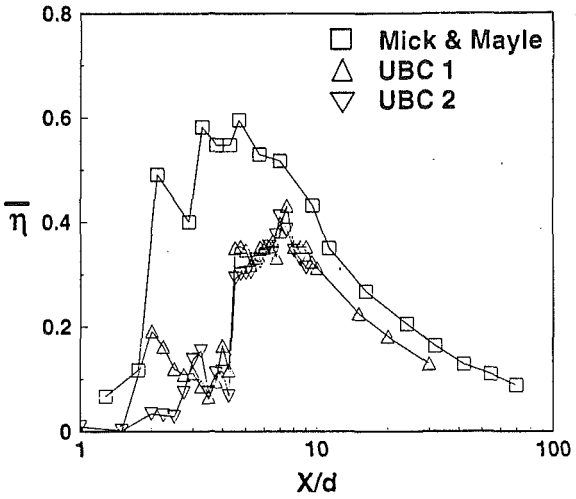

Fig. 7(*a*) $M_\infty = 0.40$

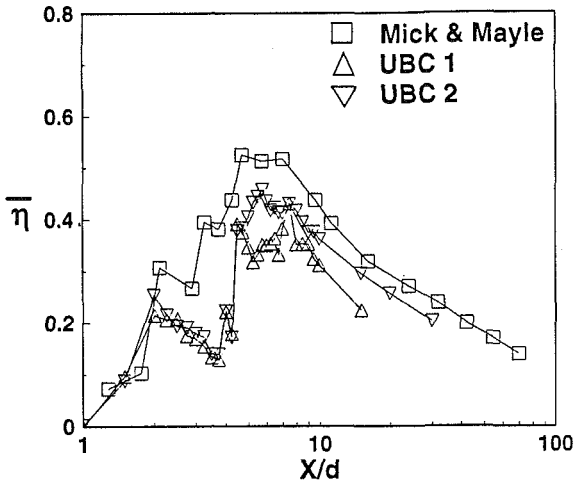

Fig. 7(*b*) $M_\infty = 0.64$

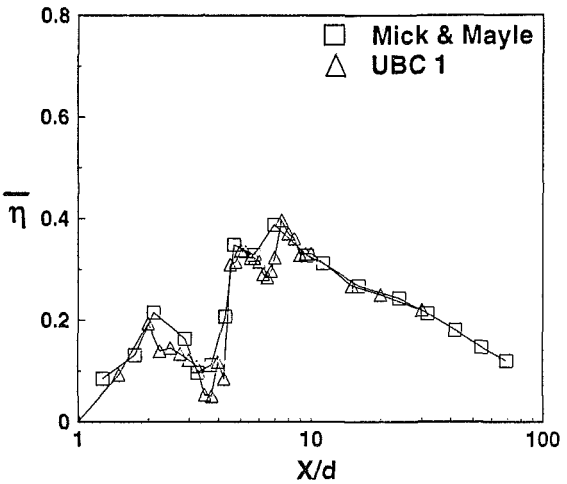

Fig. 7(*c*) $M_\infty = 0.97$

Fig. 7 Spanwise averaged effectiveness at $Re_c = 3400$

strong Reynolds number effects were noted in the present studies (see Section 3.3).

3.2 Film Cooling Effectiveness Variations With Mass Flux Ratio. From the measurements described in Section 2.3, at locations shown in Fig. 3, contours of equal effectiveness have been constructed for each M_∞. Typical results are shown in Fig. 6 for various values of M_∞ and for one coolant hole Reynolds number Re_c defined as $(\overline{U}_c d/\nu)$.

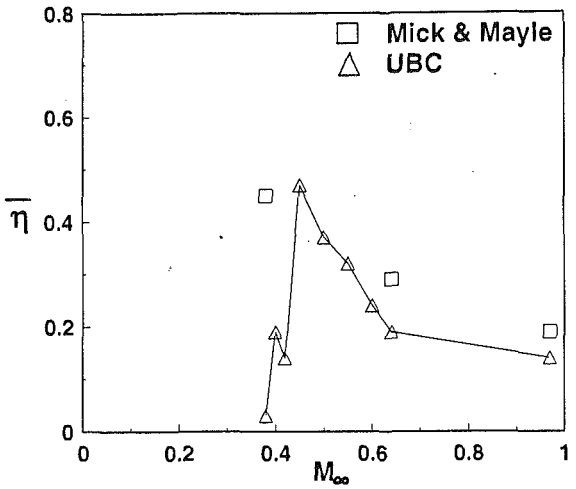

Fig. 8(*a*) $x = 2.5d$

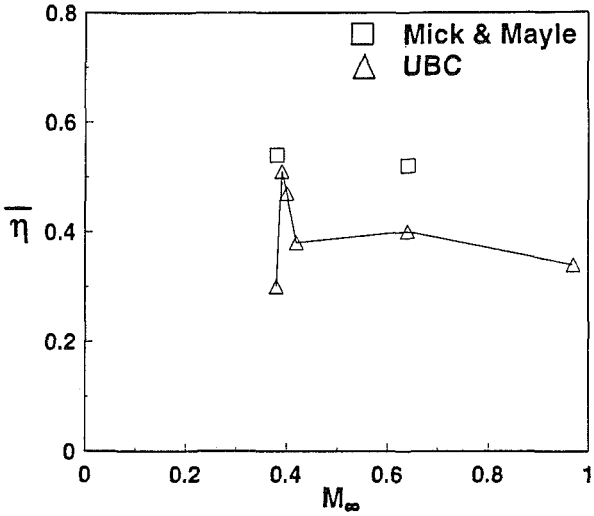

Fig. 8(*b*) $x = 5.0d$

Fig. 8 Spanwise-averaged effectiveness at one location versus M_∞

At $M_\infty = 0.4$, there is practically no coolant emerging from the 15 deg holes and therefore very little cooling effect between the two rows of holes. As M_∞ increases to 0.64, the cooling effect increases and the spanwise motion of the coolant from the first row of holes increases also. At $M_\infty = 0.97$, the coolant from the first row of holes blows directly over the holes of the second row, surely an undesirable pattern. The placement of the holes is worth reconsidering, based on this observation; a much better coverage could be obtained if the flow was directed from the first row to a place between the holes of the second row, and this could be done by moving the second row of holes to different spanwise positions. These observations confirm those made earlier by Mick and Mayle.

The spanwise-averaged film cooling effectiveness defined by $\overline{\eta} = 1/4d \int_0^{4d} \eta\, dZ$ is shown in Fig. 7 for the same mass flow ratios M_∞ as in Fig. 6. In every case, the region occupied by the hole exits has been omitted from the integral and the average since measured values of η in the hole are not thought to be particularly meaningful. This follows the procedure adopted by Mick and Mayle. Values of $\overline{\eta}$ measured by Mick and Mayle in their staggered geometry are also shown for comparison. Data designated UBC 1 and UBC 2 demonstrate repeatability over two different wind tunnel tests.

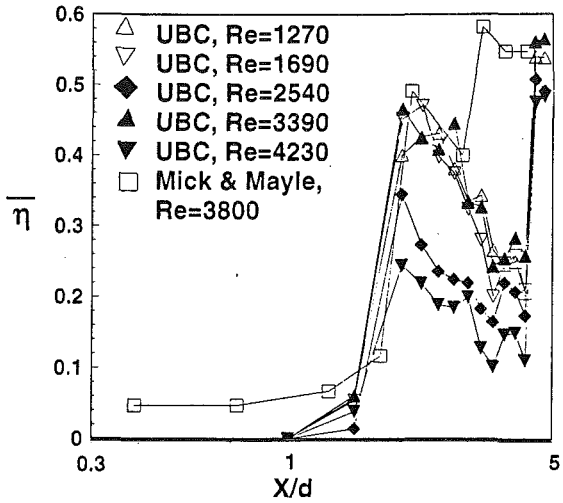

Fig. 9(a) $M_\infty = 0.40$

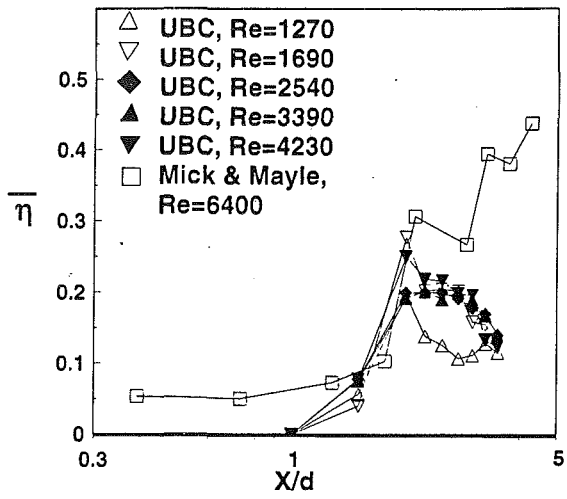

Fig. 9(c) $M_\infty = 0.64$

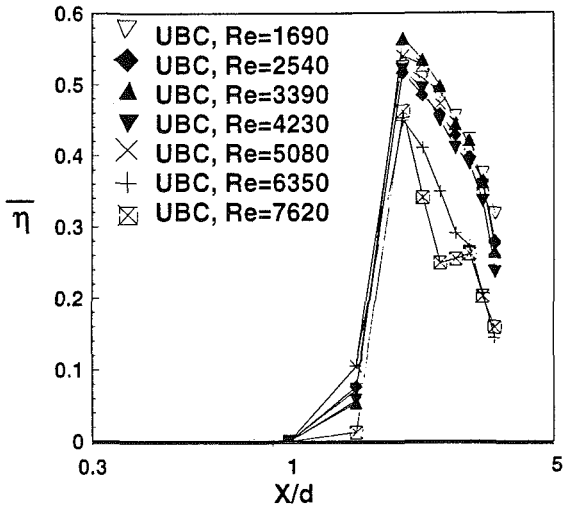

Fig. 9(b) $M_\infty = 0.45$

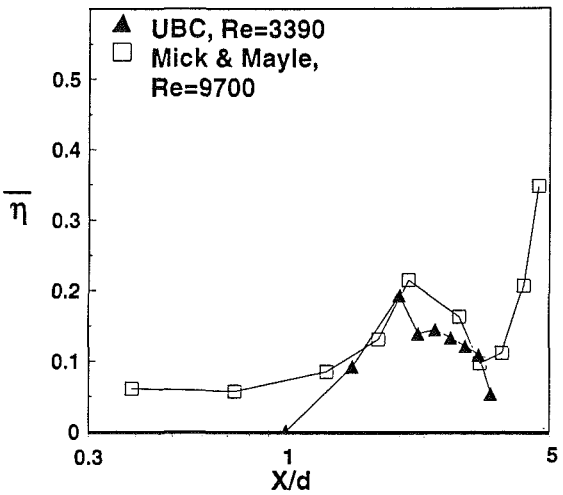

Fig. 9(d) $M_\infty = 0.97$

Fig. 9 Variations of spanwise-averaged effectiveness for various M_∞

Agreement between Mick and Mayle's results and the present measurements is poor at $M_\infty = 0.4$, somewhat improved at $M_\infty = 0.64$, and quite good at $M_\infty = 0.97$. Values of $\bar{\eta}$ are, however, quite low at the higher mass flow ratios, those typically used for film cooling of the leading edge. High M_∞ values are also well removed from the dangerous possibility of zero flow from the leading edge holes.

In Fig. 8, spanwise-averaged effectiveness is plotted at two locations ($x = 2.5d$ and $5.0d$) for various values of M_∞. Both graphs exhibit a very abrupt variation of $\bar{\eta}$ with M_∞, showing that the present cooling scheme is not robust around $M_\infty = 0.45$. Although high values of $\bar{\eta}$ occur near this mass flow ratio, the decrease in $\bar{\eta}$ is very dramatic for neighboring values of M_∞, suggesting impractically sensitive coolant requirements for high $\bar{\eta}$. It was thought that transition and/or separation and reattachment might be responsible for the abrupt variations of $\bar{\eta}$ seen in Fig. 8, and the effect of Reynolds number Re_c was therefore investigated.

3.3 Effects of Reynolds Number. To investigate the effect of Reynolds number on film cooling effectiveness, the mass flux ratio M_∞ was held constant while varying the value of Re_c. This necessitated a variation in both total mass flow rate and free-stream velocity such that the ratio M_∞ remained constant.

Typical results are shown in Fig. 9 where spanwise-averaged effectiveness $\bar{\eta}$ is plotted against x/d for various M_∞ and Re_c. At $M_\infty = 0.4$, the effect of Re_c is very dramatic. This may partially explain the differences observed between Mick and Mayle's results and the present measurements even though both were at essentially the same values of Re_c. Such strong Reynolds number effects would suggest great sensitivity of results to slight differences in experimental arrangements: different surface roughnesses, different turbulence levels in the coolant holes, etc. It is likely that laminar flow could be maintained at low Reynolds numbers, but the transition would occur at higher Re_c. The state of the flow was briefly investigated with a hot wire placed just downstream of the 15 deg coolant hole. Laminar flow with a clear dominant frequency was seen for $M_\infty = 0.45$ at low Re_c, suggesting either an acoustic or shear layer instability structure. The structure observed with the hot wire was not studied in detail, but the dominant frequency involved did not change with Re_c, which suggests an acoustic rather than velocity dependent origin. At higher Re_c or higher M_∞, turbulence was evident in the signal, supporting the transition ideas outlined above.

Weak Reynolds number dependence was observed at higher M_∞, with little effect being seen at $M_\infty = 0.97$. At this high value of M_∞, there is little sensitivity of results to the difference in apparatus between Mick and Mayle and the present exper-

iments, and therefore little difference in the variation of $\bar{\eta}$, as seen in Fig. 7(*c*).

4 Conclusions

Measurements of discharge coefficients, flow rates, and film cooling effectiveness for simulated showerhead cooling have shown the following:

1 Rapid changes in the flow rate from holes near the leading edge can occur at lower overall mass flux ratios. This can lead to a complete shutoff of flow from the first row of holes, which could seriously endanger the cooling of the leading edge of a blade. For this reason, low overall mass flux ratios should be avoided for all cooling systems in which several rows of holes are fed from a common plenum.

2 Measured effectiveness values are highest at low mass flux ratios (about $M_\infty = 0.45$) but decrease abruptly with both increasing or decreasing M_∞. This sensitivity to M_∞ is undesirable, since a slight variation in M_∞ could result in a large change in film cooling effectiveness. A more robust behavior is associated with higher M_∞, but here the values of $\bar{\eta}$ are much lower.

3 The coolant flow has a spanwise inclination at high M_∞, which directs the coolant ejected from the first row of holes toward the holes of the second row. This is therefore an inefficient arrangement and the relative positions of holes in the two rows need to be reconsidered. This confirms previous observations of Mick and Mayle.

4 One can conclude overall that the present arrangement of coolant holes has a poor performance: at low M_∞ the effectiveness is critically sensitive to Re_c and M_∞ and is not robust; at high M_∞ the effectiveness is low. Alternate designs should be investigated to obtain higher overall cooling at the high mass flux ratios, which are necessary to avoid cutoff of flow from the front holes, and to obtain more uniform cooling over a wide range of mass flux ratios.

Acknowledgments

The financial support of Pratt & Whitney Canada (PWC) and the Natural Sciences and Engineering Research Council are gratefully acknowledged. Very useful discussions were held with William Abdel-Messeh, Ardeshir Riahi, and Subhash Arora of PWC. The help of Michael Savage in model manufacturing and graphics preparation is also gratefully acknowledged.

References

Ainslie, B., 1991, "Measured and Calculated Flow Rates Through Inclined Two-Dimensional Slots," M.A.Sc. Thesis, Department of Mechanical Engineering, University of British Columbia.

Bellows, W. J., and Mayle, R. E., 1986, "Heat Transfer Downstream of a Leading Edge Separation Bubble," ASME JOURNAL OF TURBOMACHINERY, Vol. 108, pp. 131–136.

Fackrell, J. E., 1980, "A Flame Ionization Detector for Measuring Fluctuating Concentration," *J. of Phys. E: Sci. Inst.*, Vol. 13, pp. 888–893.

Gartshore, I., Salcudean, M., Riahi, A., and Djilali, N., 1991, "Measured and Calculated Values of Discharge Coefficients From Flush Inclined Holes: Application to the Film Cooling of Turbine Blades," *C.A.S.I. Journal*, Vol. 37, pp. 9–15.

Jubran, B., and Brown, A., 1985, "Film Cooling From Two Rows of Holes Inclined in the Streamwise and Spanwise Directions," ASME *Journal of Engineering for Gas Turbines and Power*, Vol. 107, pp. 84–91.

Hay, N., Lampard, D., and Saluja, C. L., 1985, "Effects of Cooling Films on the Heat Transfer Coefficient on a Flat Plate With Zero Mainstream Pressure Gradient," ASME *Journal of Engineering for Gas Turbines and Power*, Vol. 107, pp. 105–110.

Goldstein, R. J., 1971, "Film Cooling," *Advances in Heat Transfer*, Vol. 7, Academic Press, New York–London, pp. 321–379.

Karni, J., and Goldstein, R. J., 1990, "Surface Injection Effect on Mass Transfer From a Cylinder in Crossflow: A Simulation of Film Cooling in the Leading Edge Region of a Turbine Blade," ASME JOURNAL OF TURBOMACHINERY, Vol. 112, pp. 477–487.

Mehendale, A. B., and Han, J. C., 1992, "Influence of High Mainstream Turbulence on Leading Edge Film Cooling Heat Transfer," ASME JOURNAL OF TURBOMACHINERY, Vol. 114, pp. 707–715.

Mick, W. J., and Mayle, R. E., 1988, "Stagnation Film Cooling and Heat Transfer Including Its Effect Within the Hole Pattern," ASME JOURNAL OF TURBOMACHINERY, Vol. 110, pp. 66–72.

Nirmalan, V., and Hylton, L. D., 1990, "An Experimental Study of Turbine Vane Heat Transfer With Leading Edge and Downstream Film Cooling," ASME JOURNAL OF TURBOMACHINERY, Vol. 112, pp. 477–487.

Tillman, E. S., and Hen, H. F., 1984, "Cooling Airflow Studies at the Leading Edge of a Film-Cooled Airfoil," ASME *Journal of Engineering for Gas Turbines and Power*, Vol. 106, pp. 214–221.

APPENDIX

Mass Flow From Coolant Holes Located Near the Stagnation Line

Nomenclature

U_c = ejection velocity of coolant
P_∞, U_∞ = free-stream static pressure, and velocity
P_M = static pressure on the cylinder surface at an angle θ from stagnation in the absence of blowing
U_M = velocity (outside any boundary layer) at angle θ around the cylinder in the absence of blowing
P_p = total pressure in the plenum

Subscripts 1 or 2 refer to holes located at 15 deg (Hole 1) or 44 deg (Hole 2), where the angles are measured from the stagnation line at the leading edge of the cylindrical nose.

We define the "discharge coefficient" to be:

$$C_D = \frac{(\rho U_c)_{\text{MEASURED}}}{[(\rho U_c)]_{\text{IDEAL}}} = \frac{(U_c)_{\text{MEASURED}}}{(U_c)_{\text{IDEAL}}} \tag{A1}$$

where "ideal" discharge velocity would be found, for the present incompressible experiments, from Bernoulli's equation applied between the plenum (total pressure P_p) and the external pressure at the exit (in the absence of blowing) P_M.

Then:

$$P_p = P_M + \frac{1}{2}\rho (U_c^2)_{\text{IDEAL}}$$

so that:

$$C_D = \frac{U_c}{\left[\frac{2}{\rho}(P_p - P_M)\right]^{1/2}}$$

The discharge coefficient would be defined using an isentropic relationship for $(\rho U)_{\text{IDEAL}}$ if the flow were compressible. A different definition of terms was used by Gartshore et al. where values of blowing efficiency for a similar geometry are reported in terms of a different "discharge coefficient," which is defined as the inverse square of the present C_D.

It is worth noting that C_D is equal to 1 only if no losses are present *and* if there is no external flow at the exit ($U_M = 0$). Inviscid, ideal flow simulations confirm that C_D is less than 1 if $U_M > 0$ (Ainslie, 1991). In the limit, C_D approaches zero if U_M/U_c becomes very large.

The mass flow coefficient M in this incompressible flow is simply the velocity ratio:

$$M = \frac{U_c}{U_\infty}$$

and an overall mass flow coefficient M_∞ describing the average mass flow from Holes 1 and 2 is:

$$M_\infty = \frac{U_1 + U_2}{2U_\infty}$$

The usual definition of pressure coefficient C_p is:

$$C_p = \frac{P_M - P_\infty}{\frac{1}{2}\rho U_\infty^2}$$

A plenum pressure coefficient C_{pp} can be defined in a similar way as:

$$C_{pp}=\frac{P_p-P_\infty}{\frac{1}{2}\rho U_\infty^2}$$

From these definitions, C_D can be written in terms of mass flow and pressure coefficients as:

$$C_D=\frac{M}{\sqrt{C_{pp}-C_p}} \tag{A2}$$

Subscripts on C_D, M and C_p would identify Hole 1 or Hole 2. Gartshore et al. measured C_D values for a geometry similar to that used here and correlated their results using an expression of the form:

$$\frac{1}{C_D^2}=A+B\left(\frac{U_M}{U_c}\right)^2=A+\frac{B(1-C_p)}{M^2} \tag{A3}$$

From Eqs. (A2) and (A3):

$$\frac{C_{pp}-C_p}{M^2}=A+\frac{B(1-C_p)}{M^2}$$

or

$$C_{pp}=AM^2+B(1-C_p)+C_p$$

Since C_{pp} is the same for Holes 1 and 2, with the common plenum,

$$AM_1^2+B(1-C_{p_1})+C_{p_1}=AM_2^2+B(1-C_{p_2})+C_{p_2}$$

or

$$A(M_2^2-M_1^2)+(1-B)(C_{p_2}-C_{p_1})=0 \tag{A4}$$

M_1 and M_2 are related to M_∞ by the expression:

$$\frac{M_1+M_2}{2}=M_\infty.$$

Using this definition, Eq. (A4) can be written as:

$$M_1=M_\infty-\frac{(C_{p_1}-C_{p_2})(1-B)}{4AM_\infty} \tag{A5}$$

or as:

$$\frac{M_1}{M_2}=\frac{M_\infty^2-K^2}{M_\infty^2+K^2} \tag{A6}$$

where

$$K^2=\frac{(C_{p_1}-C_{p_2})(1-B)}{4A}.$$

The important limiting condition for which no flow would be expected through Hole 1 would be given by:

$$M_\infty=K \text{ for } M_1=0. \tag{A7}$$

For the present data, measurements show that:

C_{p_1} at $\theta_1=15$ deg is 0.75

C_{p_2} at $\theta_2=44$ deg is -0.5

For the Mick and Mayle data, which has about 30 percent blockage, the values of C_p can be found from Bellows and Mayle to be:

C_{p_1} at $\theta_1=15$ deg is 0.72

C_{p_2} at $\theta_2=44$ deg is -1.60

Values of A and B for Eqs. (A3) or (A6) can be found from the data reported by Gartshore et al. (denoted GSRD) or by Tillman and Jen (TJ), both of whom used geometries very similar to the present arrangement (see Fig. 5 of TJ's paper). Taking due account of the high blockage ratio in the TJ case, their data are well fitted by a curve of the form of Eq. (A3) with $A=2$ and $B=0.18$. GSRD suggest $A=2.5$ and $B=0.23$. Differences in these values are not surprising; hole length, hole entrance shape, internal crossflow, Reynolds number, and hole exit curvature would all affect A and B, as noted in the discussion of Tillman and Jen. Values of C_D measured in the present model are well described using $A=2.2$, $B=0.32$. These values are summarized in Table 1 and the data is shown in Fig. 4 of this paper.

A curve of the form of Eq. (A6) using $K=0.31$ describes the present data quite well as shown in Fig. 5 of this paper. We conclude that the present simple analysis, when used with appropriate discharge coefficient constants A and B, gives a good description of the division of flow between sets of holes fed from the same plenum but located in different pressure fields or in different crossflows.

Interactions Between Embedded Vortices and Injectant From Film Cooling Holes With Compound Angle Orientations in a Turbulent Boundary Layer

P. M. Ligrani
Associate Professor,
Department of Mechanical Engineering,
University of Utah,
Salt Lake City, UT 84112

S. W. Mitchell
Graduate Student,
Department of Mechanical Engineering,
Naval Postgraduate School,
Monterey, CA 93943-5000

Experimental results are presented that describe the effects of embedded, longitudinal vortices on heat transfer and film injectant downstream of two staggered rows of film cooling holes with compound angle orientations. Holes are oriented so that their angles with respect to the test surface are 30 deg in a spanwise/normal plane projection, and 35 deg in a streamwise/normal plane projection. A blowing ratio of 0.5, nondimensional injection temperature parameter θ of about 1.5, and free-stream velocity of 10 m/s are employed. Injection hole diameter is 0.945 cm to give a ratio of vortex core diameter to hole diameter of 1.6–1.67 just downstream of the injection holes ($x/d = 10.2$). At the same location, vortex circulation magnitudes range from 0.15 m^2/s to 0.18 m^2/s. By changing the sign of the angle of attack of the half-delta wings used to generate the vortices, vortices are produced that rotate either clockwise or counterclockwise when viewed looking downstream in spanwise/normal planes. The most important conclusion is that local heat transfer and injectant distributions are strongly affected by the longitudinal embedded vortices, including their directions of rotation and their spanwise positions with respect to film injection holes. Differences resulting from vortex rotation are due to secondary flow vectors, especially beneath vortex cores, which are in different directions with respect to the spanwise velocity components of injectant after it exits the holes. When secondary flow vectors near the wall are in the same direction as the spanwise components of the injectant velocity (clockwise rotating vortices R0–R4), the film injectant is more readily swept beneath vortex cores and into vortex upwash regions than for the opposite situation in which near-wall secondary flow vectors are opposite to the spanwise components of the injectant velocity (counter-clockwise rotating vortices L0–L4). Consequently, higher St/St_o are present over larger portions of the test surface with vortices R0–R4 than with vortices L0–L4. These disruptions to the injectant and heat transfer from the vortices are different from the disruptions that result when similar vortices interact with injectant from holes with simple angle orientations. Surveys of streamwise mean velocity, secondary flow vectors, total pressure, and streamwise mean vorticity are also presented that further substantiate these findings.

Introduction

Accounting for the presence of embedded longitudinal vortices is important for the design of cooling schemes for turbine blades and turbine endwalls. This is because embedded vortices are abundant in the passages between turbine blades. In addition, their presence results in significant perturbations to distributions of film coolant along with the accompanying thermal protection. Of importance are the magnitudes of perturbations to wall heat transfer and injectant distributions resulting from the interactions between the vortices and the film coolant, as illustrated by a number of recent studies. These include investigations of the interactions of embedded vortices with film injection from slots (Blair, 1974), with film injection from rows of holes (Goldstein and Chen, 1985, 1987; Ligrani

Contributed by the International Gas Turbine Institute and presented at the 37th International Gas Turbine and Aeroengine Congress and Exposition, Cologne, Germany, June 1–4, 1992. Manuscript received by the International Gas Turbine Institute February 17, 1992. Paper No. 92-GT-199. Associate Technical Editor: L. S. Langston.

et al., 1989a, 1991), as well as with film injectant from a single hole (Ligrani and Williams, 1990). According to Ligrani et al. (1991), the complicated nature of these physical situations results because of the dependence of local heat transfer and injection distributions on vortex strength, vortex size, and vortex location relative to a vast array of film cooling injection rates, hole sizes, geometries, and configurations.

Experimental studies of the interactions of embedded vortices and film cooling are scarce. Of earlier studies, Blair (1974) reports heat transfer distributions measured on an endwall film-cooled using a slot inclined at a 30 deg angle. The large vortex located in the corner between the endwall and the suction surface of their cascade was believed to cause significant variations of measured heat transfer and film cooling effectiveness. Nicolas and LeMeur (1974), Folayan and Whitelaw (1976), and Mayle et al. (1977) all focus on the effects of wall curvature, as well as the resulting arrays of vortex pairs, on the performance of film cooling over turbine blades. Goldstein and Chen (1985, 1987) describe results from a study on the influence of flows originating near the endwall on blade film cooling from one and two rows of holes. A triangular region is described that exists on the convex side of the blade where coolant was swept away from the surface by the passage vortex.

Ligrani et al. (1989a) describe the influences of embedded longitudinal vortices on film cooling from a single row of film cooling holes in a turbulent boundary layer. In that study, each hole is inclined at an angle of 30 deg with respect to the test surface, and spaced three hole diameters from neighboring holes. Surface heat transfer distributions, mean velocities, and mean temperatures show that film coolant is greatly disturbed and local Stanton numbers are altered significantly by the secondary flows within vortices. To clarify further the interactions between vortices and wall jets, Ligrani and Williams (1990) examined the effects of an embedded vortex on injectant from a single film-cooling hole in a turbulent boundary layer. Attention is focused on the effect of spanwise position of the vortices with respect to film injection holes. The main conclusion is that injection hole centerlines must be at least 2.9–3.4 vortex core diameters away from the vortex center in the lateral direction to avoid significant alterations to wall heat transfer and distributions of film coolant. Ligrani et al. (1991) then considered the influences of vortex strength on heat transfer and injectant distributions downstream of a single row of holes having the same geometry employed by Ligrani et al. (1989a). In Ligrani et al. (1991), a variety of vortex strengths are considered, with circulations as large as 0.150 m^2/s. One of the most important conclusions from this study is that magnitudes of perturbations to injectant distributions are dependent upon the ratio of vortex circulation to injection velocity times hole diameter ($S = \Gamma/U_c\, d$), and the ratio of vortex circulation to injection velocity times vortex core diameter ($S1 = \Gamma/U_c\, 2c$).

Of existing studies that focus on interactions between the vortices and injectant from one or more holes, hole geometries in all cases are oriented with simple angles. Simple angle injection refers to situations in which the film is injected from holes inclined to the test surface such that injectant is issued from the holes at an angle with respect to the test surface when viewed in the streamwise/normal plane, but approximately in the direction of the mainstream flow when viewed in the streamwise/spanwise plane.

More recently, gas turbine components include film holes with compound angle orientations, which are believed to produce injectant distributions over surfaces giving better protection and higher film effectivenesses than injectant from holes with simple angle orientations. Compound angle orientations are ones in which the film is injected with holes inclined to the test surface such that the injectant is issued with a spanwise velocity component relative to the mainstream flow (when viewed in the streamwise/spanwise plane). Consequently, interactions between vortices and film injection from holes with compound angle orientations are important because: (1) Compound angle holes are now quite common on gas turbine components, and (2) the interactions are different from ones existing when simple angle holes are employed. To the best of the authors' knowledge, no data are available in the archival literature on heat transfer and boundary layer behavior downstream of film cooling holes with compound angle orientations when the injectant interacts with embedded longitudinal vortices. Thus, the purpose of the present study is to provide new physical understanding of such interactions.

The present study is therefore different from Ligrani et al. (1989a, 1991) and Ligrani and Williams (1990) because interactions between the vortices and injectant from film holes with compound angle configurations, instead of simple angle configurations, are considered. Heat transfer, mean velocity components, and injection distributions are measured downstream of two staggered rows of injection holes with compound angle geometry with a blowing ratio of 0.5. Both clockwise rotating vortices and counterclockwise rotating vortices are employed, where vortex orientations are given as the vortices are viewed in spanwise/normal planes looking downstream. The direction of rotation of the vortices is important because rotation direction changes result in sign changes to the direction of secondary flow vectors near the wall beneath vortex cores. These are then opposed to or coincident with the spanwise velocity components of the injectant. Vortices are generated using half-delta wings placed on the wind tunnel test surface. The direction of vortex rotation is changed by altering the angle of delta wings with respect to the streamwise direction, and vortex spanwise positions with respect to the film injection holes are altered by changing the spanwise positions of the vortex generators.

Experimental Apparatus and Procedures

Wind Tunnel and Coordinate System. The wind tunnel is the same one used in the experiments of Ligrani et al. (1989a,

Nomenclature

A = vortex generator delta wing angle of attack
c = average vortex core radius
C_p = specific heat
d = injection hole diameter
m = blowing ratio = $\rho_c U_c/\rho_\infty U_\infty$
S = nondimensional circulation = $\Gamma/U_c\, d$
$S1$ = nondimensional circulation = $\Gamma/U_c\, 2\, c$
St = Stanton number with vortex and film injection
St_o = baseline Stanton number, no vortex, no film injection
St_f = Stanton number with film injection and no vortex
T = static temperature
U = mean velocity
X, x = streamwise distance
Y = distance normal to the surface
Z = spanwise distance from test surface centerline
Γ = circulation of streamwise vorticity
θ = nondimensional injection temperature = $(T_{r,c} - T_{r,\infty})/(T_W - T_{r,\infty})$
ξ = unheated starting length
ρ = density

Subscripts

c = injectant at exits of injection holes
r = recovery condition
w = wall
y = normal component
z = spanwise component
∞ = free-stream

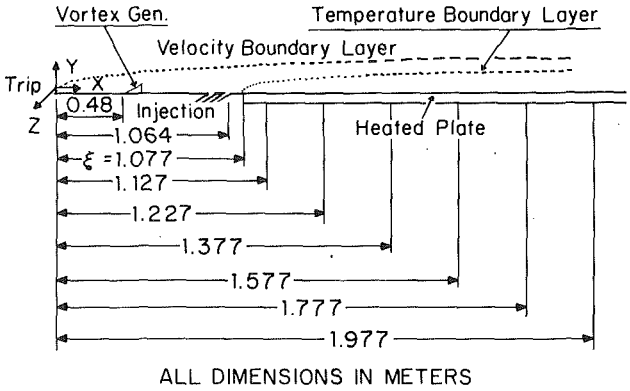

Fig. 1 Schematic of wind tunnel test section

1991). The facility is open-circuit and subsonic. A centrifugal blower is located at the upstream end, followed by a diffuser, a header containing a honeycomb and three screens, and then a 16-to-1 contraction ratio nozzle. The nozzle leads to the test section, which is a rectangular duct 3.05 m long and 0.61 m wide, with a topwall having adjustable height to permit changes in the streamwise pressure gradient.

A schematic showing the test section and coordinate system is presented in Fig. 1. The vortex generator base plate is shown to be located 0.48 m downstream of the boundary layer trip. The left edge of this base plate (looking downstream) is the base edge referred to in Table 1 as a location reference line. The downstream edge of the injection holes is then 0.584 m farther downstream from this base plate. The surface used for heat transfer measurements is then located a short distance farther downstream. With this surface at elevated temperature, an unheated starting length of 1.077 m exists, and the direction of heat transfer is then from the wall to the gas. Thermocouple row locations along the test surface are also labeled in Fig. 1. In regard to the coordinate system, Z is the spanwise coordinate measured from the test section centerline, X is measured from the upstream edge of the boundary layer trip, and Y is measured normal to the test surface. x is measured from the downstream edge of the injection holes and generally presented as x/d.

Injection System. The injection system is described by Ligrani et al. (1989a, 1991). Air for the injection system originates in a 1.5 hp DR513 Rotron Blower capable of producing 30 cfm at 2.5 psig. From the blower, air flows through a regulating valve, a Fisher and Porter rotometer, a diffuser, and finally into the injection heat exchanger and plenum chamber. The exchanger provides means to heat the injectant above ambient temperature. With this system and test plate heating, the nondimensional injection temperature parameter θ was maintained at about 1.5 for all tests to maintain conditions similar to ones existing in gas turbine components. The plenum connects to 13 plexiglass tubes, each 8 cm long with a length/diameter ratio of 8.4. With no vortex present, boundary layer displacement thickness at the injection location is $0.28d$.

Injection system performance was checked by measuring discharge coefficients which compared favorably with earlier measurements. Procedures to measure discharge coefficients and blowing ratios are described by Ligrani et al. (1989a).

Experimental Approach. In order to isolate the interactions between film injectant and the vortices embedded in turbulent boundary layers, measurements are made on a flat plate in a zero pressure gradient. Wind tunnel speed is 10 m/s, and temperature differences are maintained at levels less than 30°C so that viscous dissipation is negligible and fluid properties are maintained approximately constant. With this approach, many of the other effects present in high-temperature engines are not present (curvature, high free-stream turbulence, variable properties, stator/blade wake interactions, shock waves, compressibility, rotation, etc.) since these may obscure and complicate the interaction of interest.

Detailed measurements are made in spanwise planes at different streamwise locations in order to elucidate the development and evolution of flow behavior. In order to match the experimental conditions found in many practical applications, the boundary layer, embedded vortices, and wall injection are all turbulent.

Table 1 Spanwise positions of the vortices and vortex generators

Vortex Label	Spanwise location of the vortex generator baseplate reference line, a (cm)	a/2s	Centerline injection hole location with respect to the vortices	Vortex center z spanwise locations at x/d=10.2
R0	0.0	0.00	Beneath downwash	-3.05 (-3.05*)
R1	1.8	0.24	Beneath downwash & core	-1.25
R2	3.6	0.49	Beneath upwash & core	0.55
R3	5.4	0.73	Beneath upwash	2.35
R4	7.2	0.98	Beneath side of upwash	4.15(4.06*)
L0	0.0	0.00	Beneath downwash	2.54(2.54*)
L1	-1.8	-0.24	Beneath downwash & core	0.74
L2	-3.6	-0.49	Beneath upwash & core	-1.06
L3	-5.4	-0.73	Beneath upwash	-2.86
L4	-7.2	-0.98	Beneath side of upwash	-4.66(-5.08*)

* Determined from vorticity survey measurements.

Mean Velocity Components. Three mean velocity components were measured using a five-hole pressure probe with a conical tip manufactured by United Sensors Corporation. Celesco transducers and Carrier Demodulators are used to sense pressures when connected to probe output ports. Following Ligrani et al. (1989b), corrections were made to account for spatial resolution and downwash velocity effects. The same automated traverse used for injectant surveys was used to obtain surveys of secondary flow vectors, from which mean streamwise vorticity contours were calculated. These devices, the measurement procedures employed, as well as data acquisition equipment and procedures used are further detailed by Ligrani et al. (1989a, 1989c).

Stanton Number Measurements. Details on measurement of local Stanton numbers are given by Ortiz (1987), Bishop (1990), and Ligrani et al. (1989a, 1991). An overview of these procedures is repeated here for completeness.

The heat transfer surface is designed to provide a constant heat flux over its area. The surface next to the airstream is stainless steel foil painted flat black. Immediately beneath this is a liner containing 126 thermocouples, which is just above an Electrofilm Corp. etched foil heater rated at 120 volts and 1500 watts. Located below the heater are several layers of insulating materials including Lexan sheets, foam insulation, styrofoam, and balsa wood. Surface temperature levels and convective heat transfer rates are controlled by adjusting power into the heater using a Standard Electric Co. Variac, type 3000B. To determine the heat loss by conduction, an energy balance was performed. Radiation losses from the top of the test surface were analytically estimated. The thermal contact resistance between thermocouples and the foil top surface was estimated on the basis of outputs of the thermocouples and measurements from calibrated liquid crystals on the surface of the foil. This difference was then correlated as a function of heat flux through the foil. The convective heat flux q and surface temperature T_w are then used to determine Stanton numbers using $\mathrm{St} = q/((T_w - T_{r,\infty})\,\rho_\infty\,U_\infty\,Cp)$.

After the surface was completed, a variety of qualification tests were conducted to check its performance. These are described in detail by Ortiz (1987).

Mean Temperature Measurements. Copper-constantan thermocouples were used to measure temperatures along the surface of the test plate, the free-stream temperature, as well

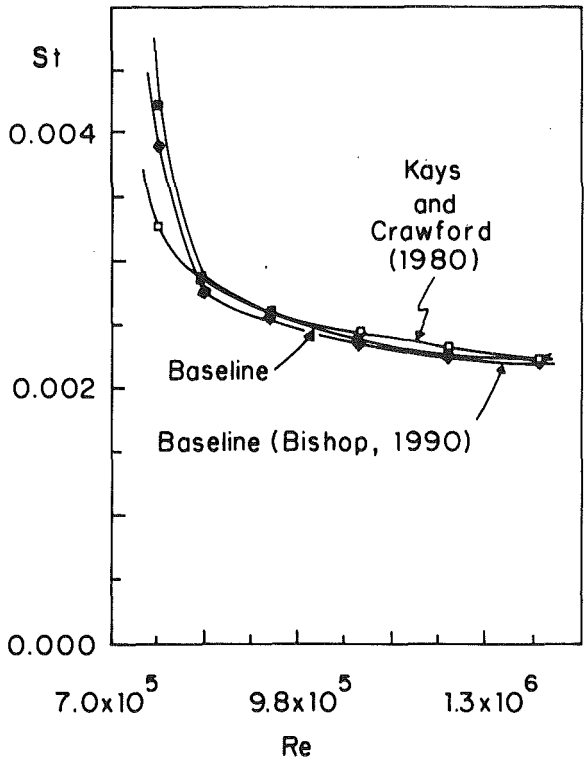

Fig. 2 Baseline heat transfer data with no vortices and no film cooling in the form of spanwise-averaged Stanton numbers as dependent upon Reynolds number

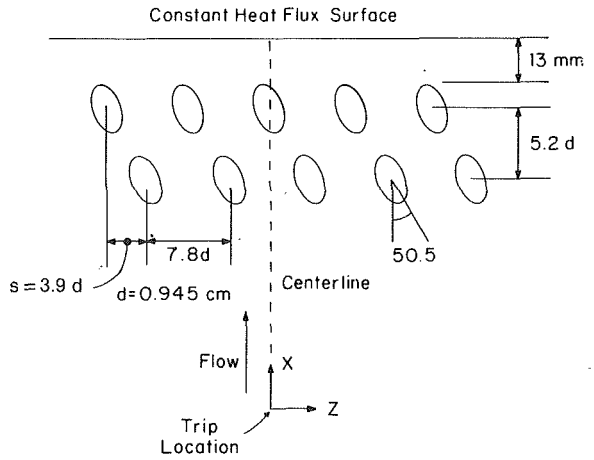

Fig. 3 Injection hole arrangement along the test surface to show compound angle film cooling hole geometry

as temperature distributions correlated to injection distributions. For the distributions, a thermocouple was traversed over spanwise/normal planes (800 probe locations) using an automated two-dimensional traversing system, which could be placed at different streamwise locations. Ligrani et al. (1989a, 1991) give additional details including procedures used for calibration.

Baseline Data Checks. Baseline data with no film injection already exist for similar test conditions (Ligrani et al., 1989a). Figure 2 shows that repeated measurements of spanwise-averaged Stanton numbers show good agreement (maximum deviation is 5 percent) with the correlation from Kays and Crawford (1980) for turbulent heat transfer to a flat plate with unheated starting length and constant heat flux boundary condition. Also included on this figure are results from Bishop (1990), which also show good agreement with the correlation of Kays and Crawford (1980). Local and spanwise-averaged Stanton numbers with injection at a blowing ratio of 0.5 (and no vortex) also show agreement with earlier results (Ligrani et al., 1989a). Further checks on measurement apparatus and procedures were made by measuring spatial variations of Stanton numbers along the test surface with different strength vortices (and no injection). These data are also consistent with other results in the literature (Ligrani et al., 1989a, 1991).

Experimental Uncertainties. Uncertainty analysis details are given by Ligrani et al. (1991). Uncertainty estimates are based upon 95 percent confidence levels, and determined following procedures described by Kline and McClintock (1953) and Moffat (1982). Typical nominal values of free-stream recovery temperature and wall temperature are 18.0 and 40.0°C, with respective uncertainties of 0.13 and 0.21°C. The free-stream density, free-stream velocity and specific heat uncertainties are 0.009 kg/m^3 (1.23 kg/m^3), 0.06 m/s (10.0 m/s) and 1 J/kgK (1006 J/kgK), where typical nominal values are given in parentheses. For convective heat transfer, heat transfer coefficient, and heat transfer area, 10.5 W (270 W), 1.03 W/m^2 K (24.2 W/m^{2}K), and 0.0065 m^2 (0.558 m^2) are typical uncertainties. The uncertainties of St, St/St$_o$, m, and x/d are 0.000086 (0.00196), 0.058 (1.05), 0.025 (0.50), and 0.36 (41.9).

In percentages, uncertainties of these quantities are as follows: free-stream recovery temperature: 0.7, wall temperature: 0.5, free-stream density: 0.7, free-stream velocity: 0.6, specific heat: 0.1, convective heat transfer: 3.9, heat transfer coefficient: 4.3, heat transfer area: 1.2, St: 4.4, St/St$_o$: 5.5, m: 5.0, and x/d: 0.9.

Injection Hole Arrangement

A schematic showing the compound angle film hole geometry along the test surface is shown in Fig. 3. Here, holes are arranged in two rows, which are staggered with respect to each other, with spanwise spacings between adjacent holes of $3.9d$. This spanwise spacing was chosen to allow sufficient space between adjacent injection holes as the spanwise locations of vortices are changed. The distance between two adjacent holes in the same row ($7.8d$) is equivalent to 4.7–4.9 vortex core diameters (as measured at $x/d = 10.2$). Determinations of vortex core sizes are discussed in the next section. Figure 3 also shows that centerlines of holes in separate rows are separated by $5.2d$ in the streamwise direction. Each row of holes contains five injection cooling holes with a nominal inside diameter of 0.945 cm. The centerline of the middle hole of the downstream row is located on the spanwise centerline ($Z = 0.0$ cm) of the test surface. The compound angle holes are employed with $\Omega = 35$ deg and $\beta = 30$ deg, where Ω is the angle of the injection holes with respect to the test surface as projected into the streamwise/normal plane, and β is the angle of the injection holes with respect to the test surface as projected into the spanwise/normal plane. The plane of each injection hole is angled at 50.5 deg from the streamwise/normal (X–Y) plane. Within the plane of each hole, hole centerlines are oriented at angles of 24 deg from the plane of the test surface (X–Z).

Generation and Control of Vortex Characteristics

The devices used to generate the vortices are shown in Fig. 4. In the present study, vortices are generated that rotate clockwise and counterclockwise when viewed in spanwise/normal planes. In each case, each vortex generator is a half-delta wing with 3.2 cm height and 7.6 cm base. Each wing is attached to a base plate, which is moved in the spanwise direction to produce vortices with different spanwise locations with respect to the film cooling holes. Delta wing arrangements used to

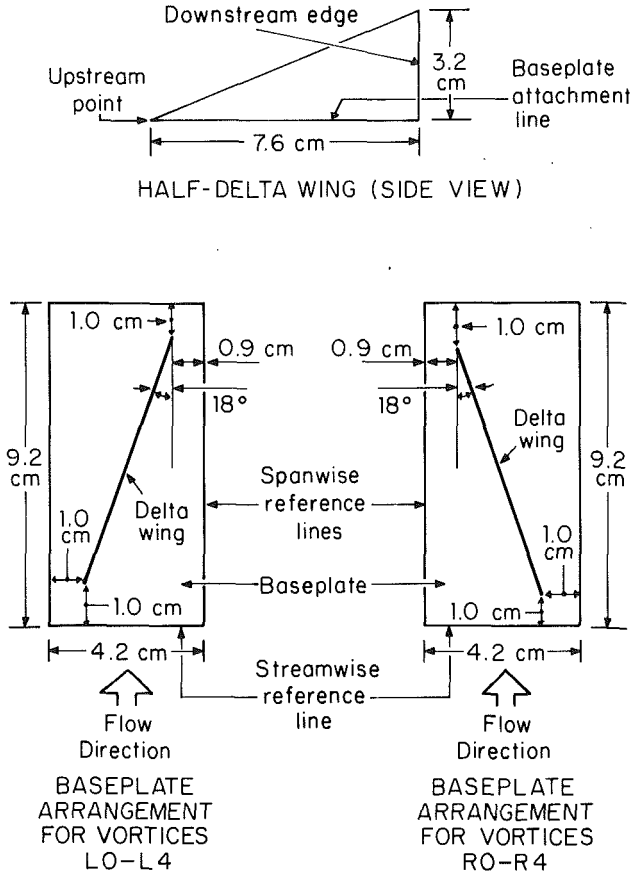

Fig. 4 Vortex generator geometries and orientations to produce clockwise and counterclockwise vortices (as viewed in spanwise/normal planes). Also shown are the dimensions of the vortex generator delta wing.

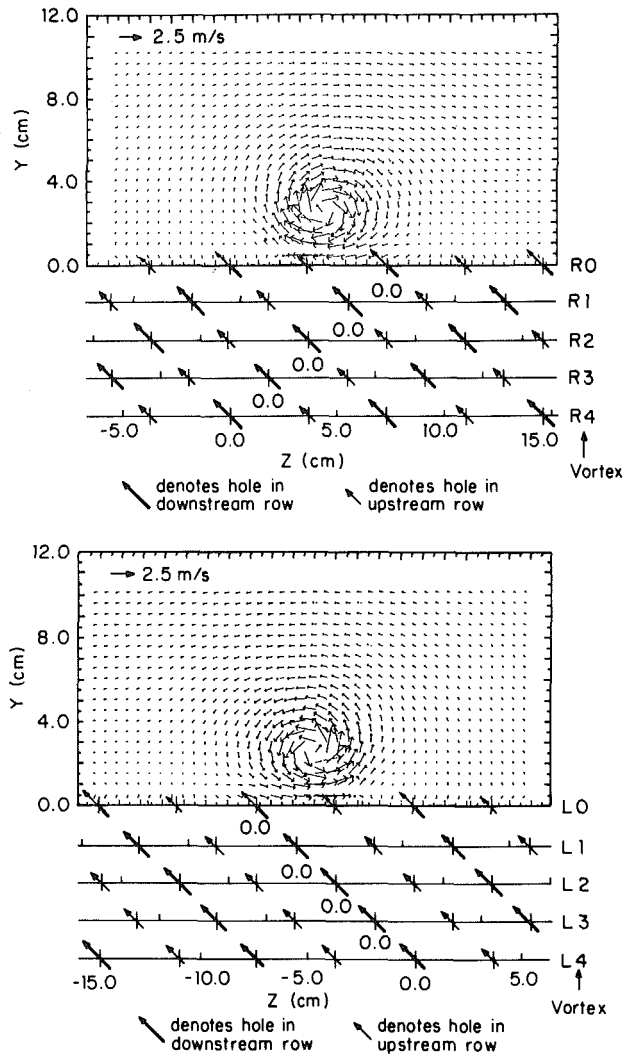

Fig. 5 Film cooling injection locations with respect to vortex center and secondary flow vectors (x/d = 10.2) (*a*) for vortices R0–R4, and (*b*) for vortices L0–L4. Each horizontal scale corresponds to a different vortex and different spanwise vortex position where Z = 0 corresponds to the centerline of the injection hole located on the wind tunnel centerline.

produce clockwise-rotating vortices R0–R4 and counterclockwise rotating vortices L0–L4 are shown in Fig. 4. The differences in the direction of vortex rotation result due to different delta wing placement on the baseplates relative to the mainstream flow direction.

With half-delta wing generators, vortices are produced with secondary flow vectors such as the ones shown in Figs. 5(*a*) and 5(*b*). In the first of these figures, the positions of the clockwise-rotating vortices R0–R4 are shown with respect to the film cooling hole locations. In the second figure, the positions of the counterclockwise rotating vortices L0–L4 are shown with respect to the film cooling hole locations. Large arrows denote the spanwise locations of holes in the downstream row and small arrows denote the spanwise locations of holes in the upstream row. The centerline of the central injection hole (hereafter referred to as the central hole) in the downstream row is located at Z = 0.0 cm. Secondary flow vectors in Figs. 5(*a*) and 5(*b*) were measured within vortices R0 and L0, respectively, just downstream of the injection holes at x/d = 10.2. The horizontal axis is then shifted in these figures so that the centerline of the central hole is appropriately oriented with respect to vortex centers for all vortices.

Table 1 provides a tabulation of the spanwise positions of vortices R0–R4 and vortices L0–L4, as well as the vortex generators used to produce them. This includes information on the spanwise locations of vortex generator baseplates, and the locations of the central hole with respect to the vortices. The spanwise spacing between vortices R0 and R1 (as well as between vortices R1 and R2, R2 and R3, L0 and L1, L1 and L2, etc.) is 1.8 cm or 24 percent of the spacing between two adjacent holes in the same row ($2s$ = 7.8d). This is 1.14–1.18 times $2c$, or just greater than the size of one vortex core diameter, where vortex core radius is denoted c. The spanwise spacing between vortices R0 and R4 and between vortices L0 and L4 are both 0.98 times $2s$, or just less than the spanwise spacing between two injection holes in the same row. Table 1 also includes estimated vortex center spanwise locations. These locations were also measured (at the locations of peak streamwise vorticity) for vortices R0, R4, L0, and L4. Good agreement between measured and estimated positions is evident for all four cases, with maximum deviation of 0.42 cm for vortex L4.

At x/d = 10.2, vortex core radii, c, of vortices R0–R4 and vortices L0–L4 are equal to 0.76–0.79 cm. c is determined as one half of the sum of average core radii in the Y and Z directions (as measured from vortex centers). These radii are determined for the area that encompasses all vorticity values greater than or equal to 40 percent of peak vorticity (at the center) for a particular vortex. The choice of 40 percent was made to give a good match to core radii determined at the locations of maximum secondary flow vectors. The area enclosed by secondary flow maxima is important, because for ideal Rankine vortices, it corresponds to the ideal core, which contains all vorticity. Secondary flow vector maxima are not used to determine core size as this gives results that are less

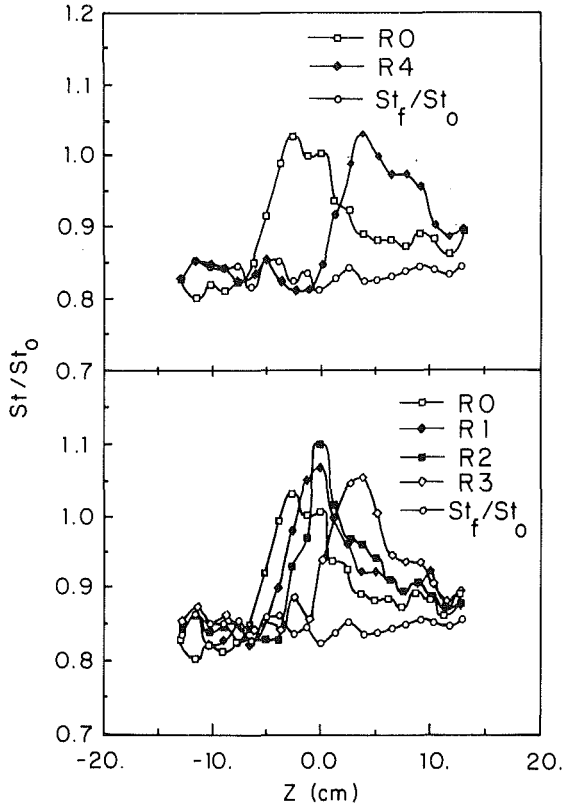

Fig. 6 Spanwise variations of local Stanton number ratios at x/d = 33.1 with m = 0.5 film cooling both with and without clockwise rotating vortices R0-R4. Free-stream velocity = 10 m/s. Vortex spanwise positions and locations with respect to film injection holes are given in Table 1.

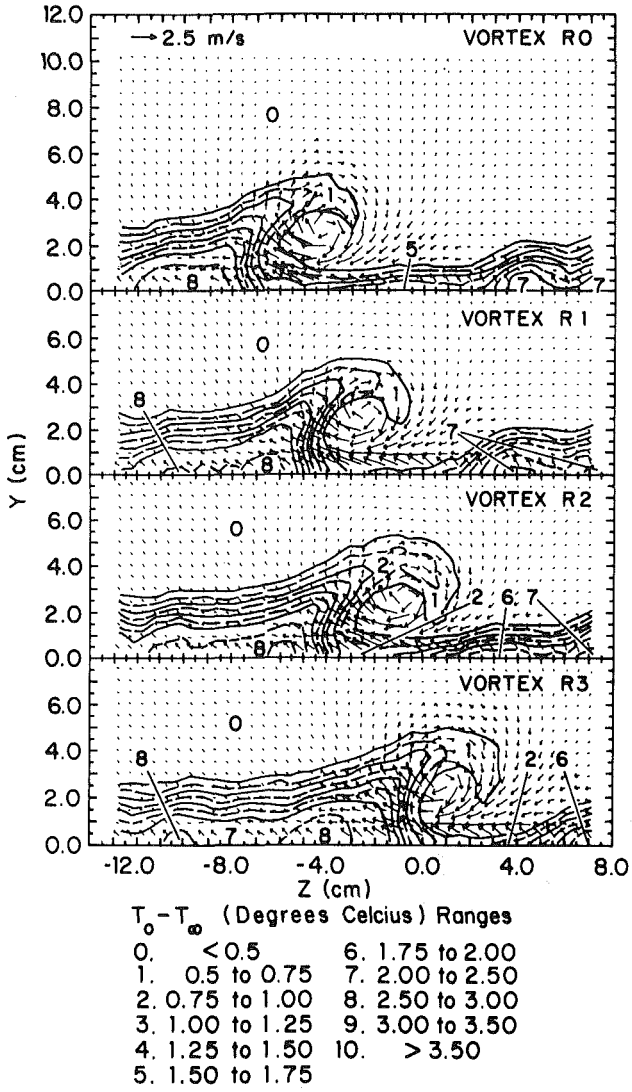

Fig. 7 Mean temperature field showing distributions of film injectant with secondary flow vectors at x/d = 45.8, with m = 0.5 film cooling and a free-stream velocity of 10 m/s. Data are given for clockwise rotating vortices R0-R4. Vortex spanwise positions and locations with respect to film injection holes are given in Table 1.

accurate than the 40 percent threshold approach. $2c/d$ then gives the ratio of vortex core diameter to injection hole diameter. At x/d = 10.2, this quantity is then about 1.6-1.67 for vortices R0-R4 as well as for vortices L0-L4.

Referring to Fig. 5(a) and Table 1, with vortex R0, the central hole is located beneath the vortex downwash. With vortex R1, the central hole is located beneath the vortex core near the downwash. Upwash regions of vortices R2 and R3 are located above the central hole, whereas vortex R4 passes injection locations such that the central hole lies to the side of the upwash. Vortices R0 and R4 are displaced a spanwise distance from each other, which about equals the spanwise spacing between two injection holes in the upstream row (7.8d). Thus, even though these two vortices are at different positions with respect to the central hole, they are at about the same positions relative to the hole placement pattern in upstream and downstream rows because of the spanwise periodicity of the injection hole locations. Consequently, spanwise variations of local heat transfer distributions are expected to be about the same for vortices R0 and R4 except for spanwise displacement of 7.8d or 7.37 cm.

In Fig. 5(b), it is evident that vortex L0 is located so that its downwash passes above the central hole as it passes x/d = 0.0. With vortex L1, the central hole is located beneath the vortex core near the downwash. Upwash regions of vortices L2 and L3 are located above the central hole, whereas vortex L4 passes injection locations such that the central hole lies to the side of the upwash. Compared to vortices R0-R4, vortices L0-L4 form a mirror image with respect to the Z axis. Just as for vortices R0 and R4, vortices L0 and L4 are displaced a spanwise distance from each other, which about equals the spanwise spacing between two injection holes in the upstream row (7.8d). Thus, even though vortices L0 and L4 are at different positions with respect to the central hole, they are at about the same positions relative to the hole placement pattern. Consequently, local heat transfer distributions are expected to be about the same for vortices L0 and L4 except for spanwise displacement of 7.8d or 7.37 cm.

Circulation magnitudes are calculated assuming that all vorticity values less than a threshold are equal to zero. The same numerical threshold of 100. (1/s) is used throughout this paper, chosen arbitrarily. It is about equal to 11 percent of the maximum vorticity of vortex R0 at x/d = 10.2 with no injection (909.8 1/s). At x/d = 10.2, circulation magnitudes (with no film cooling) range from 0.171 m^2/s to 0.177 m^2/s for vortices R0-R4, and from 0.149 m^2/s to 0.156 m^2/s for vortices L0-L4. Higher levels of vorticity evidence larger gradients of secondary flow vectors as one moves away from the vortex center. As vortex circulation becomes larger, secondary flow velocities between the main vortex center and wall increase, and amounts of spanwise vortex drift increase as the vortices are convected downstream.

With film injection at a blowing ratio of 0.5, parameter S ($= \Gamma/U_c\, d$) ranges from 3.62 to 3.75 for vortices R0-R4, and from 3.15 to 3.30 for vortices L0-L4. Parameter $S1$ ($= \Gamma/U_c\, 2c$) ranges from 2.19 to 2.24 for vortices R0-R4, and from

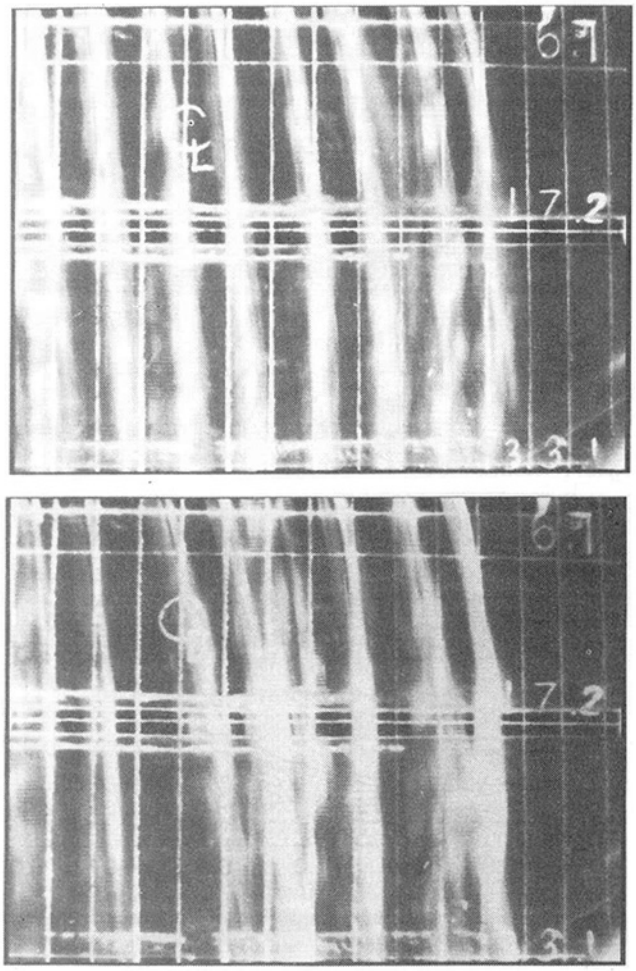

Fig. 8 Photographs of flow along the test surface showing distributions of injectant contaminated by fog fluid in streamwise/spanwise planes. The bulk flow (or streamwise direction) is down the page, and the spanwise direction is across the page. (*a*) No vortex and $m = 0.5$ film cooling. (*b*) Vortex R1 and $m = 0.5$ film cooling.

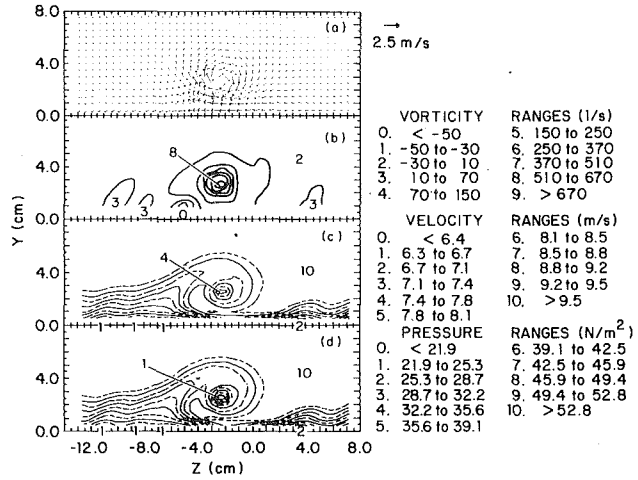

Fig. 9 Distributions of (*a*) secondary flow vectors, (*b*) streamwise vorticity, (*c*) streamwise mean velocity, and (*d*) total pressure with vortex *R*1 and film cooling at $m = 0.5$ as measured at $x/d = 45.8$ with a free-stream velocity of 10 m/s.

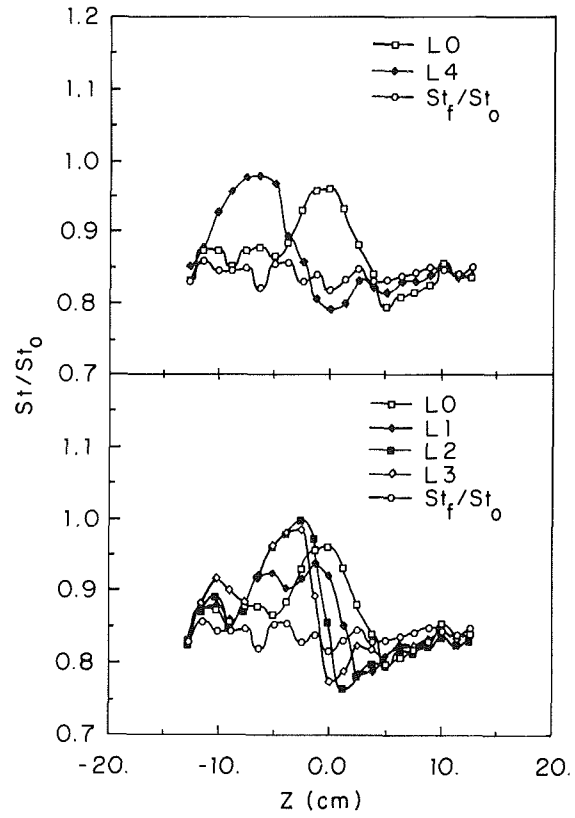

Fig. 10 Spanwise variations of local Stanton number ratios at $x/d = 33.1$ with $m = 0.5$ film cooling both with and without counterclockwise rotating vortices L0–L4. Free-stream velocity = 10 m/s. Vortex spanwise positions and locations with respect to film injection holes are given in Table 1.

1.96 to 1.99 for vortices L0–L4. These two parameters give measures of vortex strength relative to the injection velocity from measurements at $x/d = 10.2$ (Ligrani et al., 1991). According to Ligrani et al. (1991), S values higher than 1–1.5 and $S1$ values higher than 0.7–1.0 produce situations with simple angle film cooling in which injectant is swept into the vortex upwash and above the vortex core by secondary flows. In addition, local heat transfer measurements show evidence of injectant beneath vortex cores and downwash regions near the wall only for x/d up to 17.4.

Heat Transfer and Injectant Distributions

In the discussion that follows, results with vortices R0–R4 are presented in Figs. 6–9, and results with vortices L0–L4 are presented in Figs. 10 and 11. Information on the streamwise development of local Stanton numbers with $m = 0.5$ film cooling are presented in Fig. 12 for vortex R0 and in Fig. 13 for vortex L0.

Heat Transfer and Injectant Distributions With Vortices R0–R4. Distributions of St/St_o as dependent upon spanwise coordinate Z are presented in Fig. 6. These data were measured at $x/d = 33.1$ ($X = 1.377$ m) with film injection from both rows of holes at a blowing ratio m of 0.5 both with and without longitudinal vortices R0–R4 embedded in the turbulent boundary layer.

In the top portion of Fig. 6, St/St_o distributions are presented for vortices R0 and R4 along with St/St_o data obtained when no vortices are present in the flow. Of the features on this portion of Fig. 6, most apparent are the disturbances to local St/St_o distributions that result from the vortices. This is apparent where $St/St_o > St_f/St_o$, which occurs for $Z > -7$ cm for vortex R0 and for $Z > 0$ cm for vortex R4 as a consequence of the proximity of vortex downwash regions to these parts of the test surface. Here, St/St_o values are as high as 1.05 compared to St_f/St_o values from 0.80 to 0.85, where the latter are

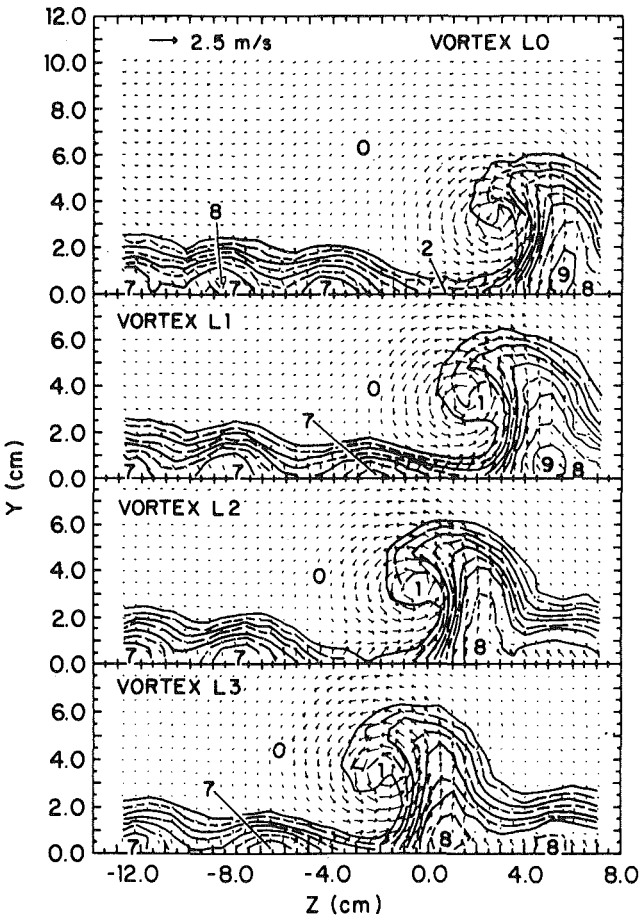

Fig. 11 Mean temperature field showing distributions of film injectant with secondary flow vectors at x/d = 45.8, with m = 0.5 film cooling and a free-stream velocity of 10 m/s. Data are given for counterclockwise rotating vortices L0–L4. Vortex spanwise positions and locations with respect to film injection holes are given in Table 1.

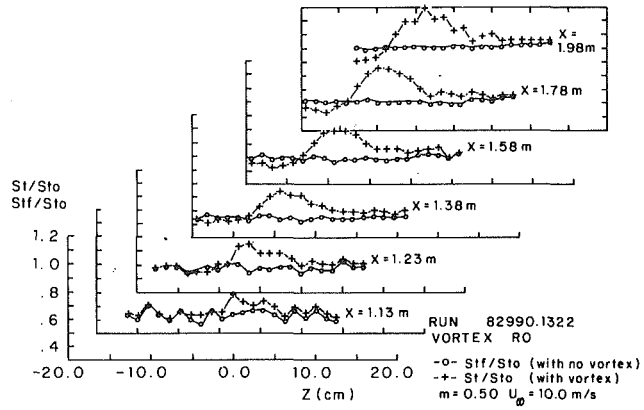

Fig. 12 Streamwise development of Stanton number ratios with m = 0.5 film cooling both with and without vortex R0. With this clockwise rotating vortex, the downwash passes over the central film cooling hole. Free-stream velocity = 10 m/s.

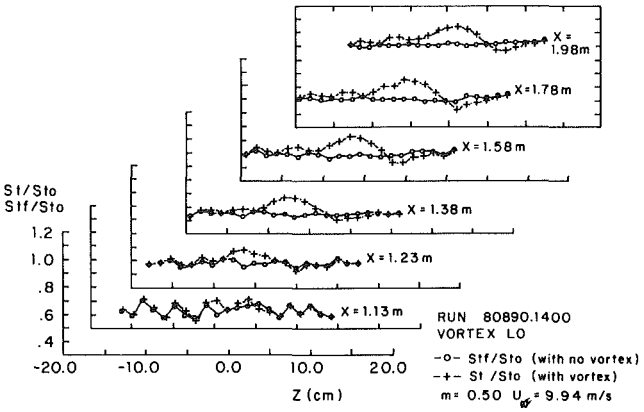

Fig. 13 Streamwise development of Stanton number ratios with m = 0.5 film cooling both with and without vortex L0. With this counterclockwise rotating vortex, the downwash passes over the central film cooling hole. Free-stream velocity = 10 m/s.

measured when no vortices are present. Test surface locations beneath vortex upwash regions correspond to $Z < -7$ cm for vortex R0 and to $Z < 0$ cm for vortex R4. Here, St/St_o values are generally lower than the St_f/St_o distribution.

The spanwise variations of local heat transfer are about the same for vortices R0 and R4 except for spanwise displacement with respect to each other a distance of about 7.2 cm. This validates the measurement apparatus and procedures employed to obtain local heat transfer distributions. The small quantitative differences between the two curves that occur locally result because of the strong dependence of local heat transfer distributions on the positions of the embedded longitudinal vortices as they pass the injection holes, and the fact that the spanwise displacement between the two vortices is slightly less than $2s$, the spanwise spacing between two adjacent holes in the downstream row. In this case the vortices are displaced from each other a distance of 7.2 cm or 98 percent of $2s$ (Table 1).

St/St_o distributions with vortices R0, R1, R2, and R3 are presented in the bottom portion of Fig. 6. Here, significant quantitative and qualitative variations are seen as the spanwise locations of the vortices are changed. When the St/St_o distributions are compared to each other, significant changes to the shapes of local maxima as well as to surrounding heat transfer distributions are apparent. Such variations evidence complicated interactions as the vortices interact simultaneously with injectant from several injection holes. One important similarity caused by all four vortices is the sharp spanwise gradient of St/St_o apparent at Z from -5 cm to 2 cm. As expected, this gradient moves in the $+Z$ direction as the spanwise locations of the vortices move in the $+Z$ direction. Away from this gradient, St/St_o values approach St_f/St_o both as large Z and at small Z at locations where the influences of the embedded vortices become less important. The highest local St/St_o value occurs with vortex R2, which convects downstream so that its core and upwash region pass over the central injection hole at Z = 0 cm. This situation is similar to one observed by Ligrani et al. (1989a) for injection from holes with simple angle orientations. In that study, the greatest disturbances to injectant occur when the vortex core passes over a film cooling hole, compared to situations in which the vortex core passes between two injection locations (i.e., vortices R1 and R3). According to Ligrani and Williams (1990), significant perturbations to injectant distributions (from simple angle holes) result when vortex cores pass with 1.67 core diameters on the downwash side, and 0.87 core diameters on the upwash side. The only vortices that meet this criterion with respect to the central hole are R1 and R2. However, the Ligrani and Williams (1990) criterion is expected to be somewhat different when compound angle injection is employed.

Figure 7 quantifies the distortion and rearrangement of injectant by vortices R0–R3. These data are given for a blowing ratio m of 0.5 at x/d = 45.8. As mentioned earlier, the spanwise locations of vortices R0–R3 with respect to the film cooling holes are given in Fig. 5(a) and Table 1. From these two sources,

it is evident that either downwash regions (vortices R0 and R1), core regions (vortices R1 and R2), or upwash regions (vortices R2 and R3) pass over the central injection hole as the vortices are convected downstream.

Measured secondary flow vectors are superimposed on each part of Fig. 7 to illustrate how their magnitudes and distributions relate to the reorganization of injectant by the different vortices. The same scaling for secondary flow vectors is used throughout all parts of Fig. 7. Procedures to determine injectant distributions were developed by Ligrani et al. (1989a) and later also used by Ligrani and Williams (1990). In these studies and the present one, injectant distributions are qualitatively correlated to mean temperature distributions. To do this, injectant is heated to 50°C without providing any heat to the test plate. Thus, because the injectant is the only source of thermal energy (relative to free-stream flow), higher temperatures (relative to free-stream temperature) generally indicate greater amounts of injectant. The temperature field is therefore given as $(T - T_\infty)$, and as such, shows how injectant accumulates and is rearranged mostly as a result of convective processes from the boundary layer and vortex secondary flows. Diffusion of injectant heat accounts for some of the temperature variations observed between injection hole exits and measuring stations, but compared to convection, this is of secondary importance.

If no vortex is present, concentrations of injectant are present in the boundary layer near the wall spaced about 3.7 cm apart in the spanwise direction at the same interval as the injection hole spacing. In Fig. 7, it is evident that all four vortices R0–R3 result in significant disturbances to the injectant because the distributions shown are different from the ones that would exist if no vortices are present. In each case, injectant is swept beneath the vortex centers in the negative Z direction, then into vortex upwash regions, and finally above the vortex centers. The spanwise locations of the centers of vortices R0, R1, R2, and R3 at $x/d = 45.8$ are at Z equal to -4.06 cm, -2.54 cm, -0.51 cm, and 1.52 cm, respectively. The Y coordinate of vortex centers is 2.5–2.6 cm. Centers are located at the point of maximum streamwise vorticity and are apparent in Fig. 7 at locations around which secondary flow vectors swirl.

Except for spanwise displacement, overall injectant distributions for vortices R0–R3 in Fig. 7 show some qualitative similarity. This is partially a result of the small spacing between holes in the spanwise direction, which results in abundant amounts of injectant at locations just downstream of $x/d = 0.0$. The small quantitative differences between the different injectant distributions result as different portions of different vortices interact with injectant from different film cooling holes as the vortices pass $x/d = 0$. Important injectant deficits are present in Fig. 7 beneath vortex cores, and near vortex cores beneath downwash regions because of the influences of vortex secondary flows. These deficits correspond to locally higher St/St_o values in Fig. 6 at the same Z locations. Injectant deficits are most severe for vortices R1 and R3 at respective Z locations of -4.0 cm to 0.0 cm, and 0.0 cm to 4.0 cm. The corresponding local maxima in Fig. 6 are large and broad and cover the same ranges of Z.

The redistribution of injectant by vortex R1 is further illustrated by the two photographs in Fig. 8. Each shows a streamwise/spanwise plane view of the test surface such that the streamwise direction is down the page, and the spanwise direction is across the page. Vertical white lines along the test surface in each photograph are spaced 2.54 cm apart in the spanwise direction, with the line along the spanwise centerline labeled accordingly. Horizontal lines are apparent at x/d of 6.7, 17.2, and 33.1. The injectant, which is contaminated with fog liquid, is clearly apparent in each photograph as it is convected downstream. For both cases, the injectant emerges from the two staggered rows of holes at a blowing ratio m of 0.5.

The top photograph of Fig. 8 shows flow along the test surface when no vortex is present, and the bottom one shows how the injectant is rearranged and distorted as vortex R1 is convected downstream. In the top photograph, injectant from each hole is immediately adjacent to injectant from neighboring holes across the span of the view shown. Slight spanwise components of injectant velocity are apparent near $x/d = 6.7$. As the smoke convects farther downstream, slight turning into the streamwise direction is apparent. However, the smoke continues to move at a slight angle with respect to the streamwise direction at x/d even as large as 33.1, as shown in the bottom portion of the photograph.

Similar behavior is evident in the bottom photograph of Fig. 8 except for significant disruptions of injectant by vortex R1. These are most apparent just to the left of the spanwise centerline for x/d from 6.7 to 17.2, and along the spanwise centerline for x/d from 17.2 to 33.1. At these locations, the scarcity of fog fluid evidences little injectant along the test surface. Such regions correspond to vortex downwash regions and regions beneath vortex cores, where St/St_o distributions like the ones in Fig. 6 show locally higher values compared to nearby magnitudes. Just to the right of the injectant deficits (i.e., at smaller Z), extra accumulations of injectant are apparent in Fig. 8 as a consequence of convection by secondary flows within upwash regions of vortex R1. In some cases, such extra accumulations of injectant result in local increases of film protection where values of St/St_o are locally lower than values of St_f/St_o that would exist if no vortex were present. At $x/d = 33.1$, the injectant in the bottom photograph of Fig. 8 is deficit at Z from -2.5 cm to 2.5 cm, with extra accumulations at Z from -7.6 cm to -2.5 cm. These values are consistent with injectant distributions in Fig. 7 for vortex R1 at $x/d = 45.8$ considering the negative spanwise convection of the vortex between the two streamwise locations. In the latter case, deficits of injectant are apparent along the wall at Z from -3.5 cm to 1.5 cm, and extra accumulations are apparent along the wall at Z from -8.5 cm to -3.5 cm.

Examples of flow properties measured in streamwise/normal planes at $x/d = 45.8$ with vortex R1 and $m = 0.5$ film cooling are presented in Fig. 9. These include secondary flow vectors, streamwise vorticity distributions, distributions of streamwise mean velocity, and distributions of mean total pressure. In Fig. 9(*a*), the rotation of the clockwise vortex is clearly apparent about the vortex center located at $Y = 2.48$ cm and $Z = -2.54$ cm. The center corresponds to the location of maximum streamwise vorticity which is clearly apparent in Fig. 9(*b*). The contours of streamwise vorticity that surround this center are approximately circular in shape with a region of negative vorticity located near the wall at Z from -4.0 cm to -6.0 cm (i.e., just to the left of the main vortex). Streamwise vorticity magnitudes are determined from secondary flow vector magnitudes using a finite difference form of the equation given by $\partial U_y/\partial Z - \partial U_z/\partial Y$. Distributions of streamwise mean velocity and total pressure in Figs. 9(*c, d*) are qualitatively similar. In both cases, a region where these quantities are locally higher is present near the wall within the vortex downwash. In addition, a region of low velocity and low pressure is present away from the wall within the vortex upwash, and deficits of velocity and pressure are present near the center of the vortex. Horizontal contour lines in Figs. 9(*c, d*) provide clear evidence of the turbulent boundary layer located on either side of the vortex. Within the boundary layer, additional deficits of pressure and velocity are present along the wall at locations of film injectant accumulation.

Heat Transfer and Injectant Distributions With Vortices L0–L4. In the discussion that follows, surface heat transfer results with vortices L0 and L4 are discussed first. This is followed by discussions of St/St_o results obtained with vortices L0–L4, and then by comparisons of these results with ones for

vortices R0–R4. Injectant distributions for vortices L0–L4 are then discussed last.

Spanwise distributions of St/St_o measured both with and without longitudinal vortices L0–L4 embedded in the turbulent boundary layer are shown in Fig. 10. As for the results shown in Fig. 6, the data in Fig. 10 were measured at $x/d = 33.1$ ($X = 1.377$ m) with film injection from both rows of holes at a blowing ratio m of 0.5. In the top portion of Fig. 10, St/St_o distributions are presented for vortices L0 and L4 along with St_f/St_o data obtained when no artificially induced vortices are present in the flow. As for the results in the top of Fig. 6, the ones in the top of Fig. 10 illustrate significant disturbances to local St/St_o distributions because of the vortices. This is particularly apparent in Fig. 10 for -5 cm $< Z < 4$ cm for vortex L0, and for $Z < -4$ cm for vortex L4 if the St/St_o distributions are compared to the St_f/St_o distribution obtained with no vortices in the flow. St/St_o are higher than St_f/St_o over these areas as a consequence of the proximity of vortex downwash regions to these portions of the test surface. Vortex secondary flows within downwash regions and beneath vortex cores first sweep injectant in the spanwise direction along the wall and then into upwash regions. Deficits of injectant then result beneath downwash regions, which give decreased protection, and increased St/St_o relative to St_f/St_o. The top portion of Fig. 10 also shows that St/St_o values for each vortex are generally lower than the St_f/St_o distribution for Z larger than 4 cm for vortex L0 and for Z larger than -4 cm for vortex L4. These locations correspond to regions beneath vortex upwash regions where extra injectant accumulates resulting in local increases of protection by the film.

The spanwise variations of local heat transfer are about the same for vortices L0 and L4 except for spanwise displacement with respect to each other a distance of about 7.2 cm, which is equivalent to 98 percent of $2s$ (Table 1). This provides validation of the measurement apparatus and procedures employed to obtain local heat transfer distributions in addition to that given by results in the top of Fig. 6. The small quantitative differences between the curves for vortices L0 and L4 in the top of Fig. 10 occur locally for the same reasons that data for vortices R0 and R4 in the top of Fig. 6 are locally different.

St/St_o distributions with vortices L0, L1, L2, and L3 are presented in the bottom portion of Fig. 10. Here, significant quantitative and qualitative variations are seen as the spanwise locations of the vortices are changed. When the St/St_o distributions are compared to each other, significant changes to the shapes of local maxima as well as to surrounding heat transfer distributions are apparent. Just like the results in Fig. 6, such variations evidence complicated interactions as the vortices interact simultaneously with injectant from several injection holes. In addition, vortices L0–L4 also result in sharp spanwise gradients of St/St_o. In Fig. 10, these gradients are apparent at Z from -2 cm to 4 cm, and move in the $-Z$ direction as the spanwise locations of the vortices move in the $-Z$ direction. The highest local St/St_o value just to the left of one such gradient (i.e., at smaller Z) occurs with vortex L2. This particular vortex convects downstream so that its core and upwash region pass over the central injection hole at $Z = 0$ cm (i.e., Fig. 5(b) and Table 1).

Vortices L0–L4 are different from vortices R0–R4 because of different directions of rotation (counterclockwise versus clockwise) when viewed looking downstream in spanwise/normal planes. This is important because secondary flow vectors, especially beneath vortex cores, are in different directions with respect to the spanwise coordinate Z as well as with respect to spanwise velocity components of injectant. Figure 3 shows the orientations of the film cooling holes with respect to streamwise and spanwise coordinate directions. Coolant is injected with a $-Z$ direction component. In Fig. 5(a), secondary flow vectors near the wall for vortices R0–R4 are then in the same direction as the spanwise components of the injectant velocity. The opposite is true in Fig. 5(b), where the near-wall secondary flow vectors for vortices L0–L4 have directions that are opposite to the direction of the spanwise components of the injectant velocity.

These differences between vortices R0–R4 and vortices L0–L4 are important because they result in significantly different local St/St_o distributions as the vortices interact with the film injectant. This is evident if St/St_o for vortices R0–R4 in Fig. 6 are compared to ones in Fig. 10 for vortices L0–L4. This comparison can be made for the same locations of vortex centers with respect to the central film injection hole with the only changes due to the direction of rotation of the vortices. It is evident from Figs. 5(a) and 5(b) and Table 1 that this is done by comparing results for vortices having the same numbers in their name labels (i.e., comparing results for vortex R0 with results for vortex L0, comparing results for vortex R1 with results for vortex L1, R2 with L2, etc.). Because they are the same in all parts of Figs. 6 and 10, St_f/St_o distributions (with film injection and no vortices) are appropriate to use in reference to distributions measured with vortices R0–R4 and L0–L4.

With each comparison, the same overall qualitative difference between the clockwise and counterclockwise vortices is evident. St/St_o distributions with the clockwise rotating vortices R0–R4 always show regions greater than St_f/St_o over larger portions of the test surface than the St/St_o distributions associated with counterclockwise rotating vortices L0–L4. In addition, St/St_o distributions with vortices R0–R4 show higher local maxima and maxima peaks, which are broader and spread over greater areas compared to St/St_o measured beneath vortices L0–L4. Such differences evidence different interactions between injectant and the two types of vortices. Higher St/St_o are present with vortices R0–R4 because the injectant is swept away from the wall (which results in decreased protection) more efficiently than with vortices L0–L4. The more efficient decimation of the injectant occurs since near-wall vortex secondary flows are in the same direction as the spanwise velocity components of the injectant. With vortices L0–L4, the opposite situation is present. Here, near-wall vortex secondary flows oppose the spanwise components of the film injectant resulting in greater resistance to injectant rearrangement by the vortices.

Figure 11 quantifies the distortion and rearrangement of injectant by vortices L0–L3. These data were obtained for a blowing ratio m of 0.5 at $x/d = 45.8$ using the same procedures employed to obtain the injectant distributions and secondary flow vectors given in Fig. 7. The spanwise locations of vortices L0–L3 with respect to the film cooling holes are given in Fig. 5(b) and Table 1. From these two sources, it is evident that either downwash regions (vortices L0 and L1), core regions (vortices L1 and L2), or upwash regions (vortices L2 and L3) pass over the central injection hole as the vortices are convected downstream.

Like the results presented in Fig. 7, the injectant distributions in Fig. 11 show that all four vortices L0–L3 produce significant disturbances to the injectant relative to distributions present if no vortices are present. Individual distributions in Fig. 11 are qualitatively similar to each other, except for variations due to spanwise displacement of the vortices with respect to the film injection holes. They also show some qualitative similarity to the ones in Fig. 7. The most important differences result because of different directions of vortex rotation. With vortices L0–L4, this causes much more injectant to be present next to the wall near the vortices, which is apparent if regions just to the right of vortex downwash regions in Fig. 7 are compared to regions just to the left of vortex downwash regions in Fig. 11. Such differences are particularly evident if the injection distribution for vortex L0 is compared to the one for vortex R0.

In Fig. 11, injectant is swept beneath the vortex centers in

the positive Z direction, then into vortex upwash regions, and finally above the vortex centers. The spanwise locations of the centers of vortices L0, L1, L2, and L3 are at Z equal to 3.05 cm, 1.52 cm, −0.51 cm, and −1.52 cm, respectively. The Y coordinates of vortex centers in Fig. 11 vary from 2.9 cm to 3.0 cm. In each case, injectant deficits are present near the wall in Fig. 11 located beneath vortex cores and near vortex cores beneath downwash regions. Of these, the most severe are located beneath vortices L0 and L2 at respective Z locations of 0.0 cm to 4.0 cm, and −4.0 cm to 0.0 cm. Corresponding St/St_o distributions in Fig. 10 show broad local maxima over nearly the same ranges of Z.

Streamwise Development of Heat Transfer Distributions With Film Cooling Both With and Without Vortices R0 and L0. Streamwise development of local St/St_o distributions with longitudinal vortices R0 and L0 are presented in Figs. 12 and 13, respectively. Also included on these figures are distributions of St_f/St_o obtained with film cooling only and no vortices embedded in the boundary layers. These two sets of results are presented together in each figure so that disturbances caused by the vortices to surface heat transfer in the film cooled boundary layers are apparent. In both figures, results are given for a blowing ratio m of 0.5 and a free-stream velocity of 10 m/s.

In examining results on Figs. 12 and 13, it is apparent that the disturbances caused by the vortices persist to the end of the test plate. This is evident since St/St_o values are higher than St_f/St_o at X = 1.98 m or x/d = 96.6. In fact, differences between St/St_o and St_f/St_o generally become greater with streamwise development, behavior that illustrates the coherence of the vortices as they are convected downstream. Differences are quite small just downstream of the injection holes at X = 1.13 m or x/d = 6.7, which indicates that the film, rather than the vortices, is most affecting local heat transfer behavior at this location. According to Ligrani et al. (1989a), such behavior probably results because the vortices are lifted off of the test surface by the film injectant. In addition, vortex secondary flows have not had enough time to rearrange the injectant at this streamwise station since it is just downstream of film hole exit locations, where the vortices initially interact with the injectant.

Comparing results in Fig. 12 to ones in Fig. 13 reveals important differences for vortices R0 and L0. In Fig. 12, regions where St/St_o are higher than St_f/St_o are at larger Z, and regions where St/St_o are lower than St_f/St_o are at smaller Z. The opposite trend is present in Fig. 13 because vortex L0 rotates in a direction opposite to vortex R0. However, in spite of these differences, both vortices R0 and L0 produce $St/St_o > St_f/St_o$ beneath downwash regions, and $St/St_o < St_f/St_o$ beneath upwash regions. Greater disturbances and higher St/St_o are present beneath the downwash regions of vortex R0 because injectant is swept away from the wall more efficiently than occurs with vortex L0. This is because near-wall secondary flows of vortex R0 are coincident with the spanwise velocity components of the film injectant. As mentioned earlier, this results in larger reductions in protection than if the secondary flows of a vortex are opposite to the spanwise component of injectant velocity, as with vortex L0. Regions where St/St_o are greater than St_f/St_o also cover larger spanwise portions of the test plate with vortex R0. This is consistent with the St/St_o results in Figs. 6 and 10. It is also consistent with the injectant distributions in Figs. 7 and 11, which show that injectant is present much closer to the downwash regions of vortices L0–L4 than to the downwash regions of vortices R0–R4.

Summary and Conclusions

Experimental results are presented that describe the effects of embedded, longitudinal vortices on heat transfer and film injectant downstream of two staggered rows of film cooling holes with compound angle orientations. Holes are oriented so that their angles with respect to the test surface are 30 deg in a spanwise/normal plane projection, and 35 deg in a streamwise/normal plane projection. A blowing ratio of 0.5, nondimensional injection temperature parameter θ of about 1.5, and free-stream velocity of 10 m/s are employed. Injection hole diameter is 0.945 cm to give a ratio of vortex core diameter to hole diameter of 1.6–1.67 just downstream of the injection holes (x/d = 10.2). At the same location, vortex circulation magnitudes range from 0.15 m^2/s to 0.18 m^2/s. With film injection at a blowing ratio of 0.5, the ratio of vortex circulation to injection velocity times hole diameter ($S = \Gamma/U_c\, d$) then ranges from 3.2 to 3.8, and the ratio of vortex circulation to injection velocity times vortex core diameter ($S1 = \Gamma/U_c\, 2c$) ranges from 2.0 to 2.2.

The most important major conclusion is that local heat transfer and injectant distributions are strongly affected by the longitudinal embedded vortices, including their directions of rotation and their spanwise positions with respect to film injection holes. Vortices are generated using half-delta wings attached to the test surface of the wind tunnel at 18 deg angles of attack with respect to the mainstream flow direction. By changing the sign of the angle of attack, vortices are produced that rotate either clockwise or counterclockwise when viewed looking downstream in spanwise/normal planes. By moving the delta wings in the spanwise direction, the spanwise locations of the vortices with respect to the film cooling holes are also changed.

Differences resulting from vortex rotation are due to secondary flow vectors, especially beneath vortex cores, which are in different directions with respect to the spanwise velocity components of injectant after it exits the holes. When secondary flow vectors near the wall are in the same direction as the spanwise components of the injectant velocity (clockwise-rotating vortices R0–R4), the film injectant is readily swept beneath vortex cores and into vortex upwash regions. Consequently, the protection provided by the injectant is reduced significantly and St/St_o may be as large as 1.05 compared to St_f/St_o values with no vortex from 0.80 to 0.85. With the opposite situation (counterclockwise rotating vortices L0–L4), the secondary flow vectors near the wall are directed opposite to the direction of the spanwise components of the injectant velocity, and the injectant is less likely to be rearranged by vortex secondary flows. As a result, higher St/St_o are present over larger portions of the test surface with vortices R0–R4 because the injectant is swept away from near wall regions (which results in decreased protection) more efficiently than with vortices L0–L4. Because of the design of the present experiment, these comparisons are made for the same locations of vortex centers with respect to the central film injection hole (located at Z/d = 0.0) such that the only changes are due to the direction of vortex rotation. With this type of comparison, St/St_o distributions with vortices R0–R4 show higher local maxima and maxima peaks that are broader and spread over greater areas compared to St/St_o measured beneath vortices L0–L4. Such behavior is consistent with injectant distribution surveys, which show larger quantities near the wall in proximity to vortices L0–L4, especially on the sides of vortex downwash regions away from the vortex centers.

A second major conclusion pertains to the compound angle orientations of the injection holes. Because of this, disruptions to the injectant and heat transfer caused by the vortices are different from the disruptions which result when similar vortices interact with injectant from holes with simple angle orientations. Ligrani et al. (1991) present results measured downstream of a single row of simple angle holes inclined at 30 deg with respect to the test surface and spaced 3.0 diameters apart in the spanwise direction. St/St_o results are given for a

blowing ratio of 0.5 with slightly weaker vortices than employed in the present study (vortex circulation magnitudes range from 0.13 m^2/s to 0.15 m^2/s, S = 1.58–1.61, $S1$ = 1.75–1.78). Relative to St_f/St_o distributions for x/d = 33.1, the Ligrani et al. (1991) St/St_o maxima are higher than the present results with counterclockwise rotating vortices (L0–L4), and lower than the present results with clockwise rotating vortices (R0–R4). Such behavior indicates that magnitudes of St/St_o maxima are qualitatively related to the angle between the injectant along the plane of the test surface and the direction of vortex secondary flow vectors near the wall (i.e., the spanwise or Z direction). With this dependence, smaller angles lead to greater disruptions to nominal injectant distributions and larger decreases in protection.

If one considers either the clockwise vortices or the counterclockwise vortices by themselves, significant St/St_o variations are seen as the spanwise positions of the vortices are changed. These result because different portions of different vortices interact with injectant from different film cooling holes as the vortices pass x/d = 0. Alterations resulting from different spanwise vortex positions include changes to local St/St_o maxima and to surrounding heat transfer distributions, as well as changes to injectant distributions measured in spanwise/normal planes. When near-wall vortex secondary flow vectors oppose the spanwise component of the injectant (vortices L0–L4), local St/St_o maxima are lowest when either the downwash or core pass over the central injection hole at Z = 0 cm (vortices L0 and L1). When near-wall vortex secondary flow vectors are coincident with the spanwise component of the injectant (vortices R0–R4), local St/St_o maxima are lowest when core regions of the vortices pass between injection holes in the downstream row of holes (vortices R0 and R3).

However, in spite of these quantitative variations, many overall qualitative features remain the same as the spanwise position of a vortex is changed. These include significant deficits of injectant beneath vortex cores, as well as near-vortex cores beneath downwash regions, which always correspond to St/St_o values, which are locally higher than St_f/St_o values at the same x/d and Z locations. Such variations persist as far as 97 hole diameters downstream of the injection holes (x/d = 96.6) as a consequence of vortex secondary flows, which first sweep injectant in the spanwise direction along the wall and then into upwash regions. St/St_o values are generally lower than St_f/St_o beneath vortex upwash regions since extra injectant accumulates resulting in local increases of protection by the film. In contrast, vortex disruptions are quite small just downstream of the injection holes at x/d = 6.7, which indicates that the film, rather than the vortices, is more affecting local heat transfer behavior at this streamwise location.

Acknowledgments

This study was supported, in part, by the Aero-Propulsion Laboratory of Wright Patterson Air Force Base, MIPR Number FY 1455-89-N0670. Dr. Bill Troha was program monitor. Some of the facilities used were purchased using funds from the Naval Postgraduate School Foundation Research Program.

References

Bishop, D. T., 1990, "Heat Transfer, Adiabatic Effectiveness and Injectant Distributions Downstream of Single and Double Rows of Film-Cooling Holes With Compound Angles," M. S. Thesis, Department of Mechanical Engineering, Naval Postgraduate School, Monterey, CA.

Blair, M. F., 1974, "An Experimental Study of Heat Transfer and Film Cooling on Large-Scale Turbine Endwalls," ASME *Journal of Heat Transfer*, Vol. 96, pp. 524–529.

Eibeck, P. A., and Eaton, J. K., 1987, "Heat Transfer Effects of a Longitudinal Vortex Embedded in a Turbulent Boundary Layer," ASME *Journal of Heat Transfer*, Vol. 109, pp. 16–24.

Folayan, C. O., and Whitelaw, J. H., 1976, "The Effectiveness of Two-Dimensional Film-Cooling Over Curved Surfaces," ASME Paper No. 76-HT-31.

Goldstein, R. J., and Chen, P. H., 1985, "Film Cooling on a Gas Turbine Blade Near the Endwall," ASME *Journal of Engineering for Gas Turbines and Power*, Vol. 107, pp. 117–122.

Goldstein, R. J., and Chen, P. H., 1987, "Film Cooling of a Turbine Blade With Injection Through Two Rows of Holes in the Near-Endwall Region," ASME JOURNAL OF TURBOMACHINERY, Vol. 109, pp. 588–593.

Kays, W. M., and Crawford, M. E., 1980, *Convective Heat and Mass Transfer*, 2nd ed., McGraw-Hill, New York.

Kline, S. J., and McClintock, F. A., 1953, "Describing Uncertainties in Single-Sample Experiments," *Mechanical Engineering*, Jan., pp. 3–8.

Ligrani, P. M., Oritz, A., Joseph, S. L., and Evans, D. L., 1989a, "Effects of Embedded Vortices on Film-Cooled Turbulent Boundary Layers," ASME JOURNAL OF TURBOMACHINERY, Vol. 111, pp. 71–77.

Ligrani, P. M., Singer, B. A., and Baun, L. R., 1989b, "Spatial Resolution and Downwash Velocity Corrections for Multiple-Hole Pressure Probes in Complex Flows," *Experiments in Fluids*, Vol. 7, No. 6, pp. 424–426.

Ligrani, P. M., Singer, B. A., and Baun, L. R., 1989c, "Miniature Five-Hole Pressure Probe for Measurement of Mean Velocity Components in Low Speed Flows," *Journal of Physics E—Scientific Instruments*, Vol. 22, No. 10, pp. 868–876.

Ligrani, P. M., and Williams, W. W., 1990, "Effects of an Embedded Vortex on Injectant From a Single Film-Cooling Hole in a Turbulent Boundary Layer," ASME JOURNAL OF TURBOMACHINERY, Vol. 112, pp. 428–436.

Ligrani, P. M., Subramanian, C. S., Craig, D. W., and Kaisuwan, P., 1991, "Effects of Vortices With Different Circulations on Heat Transfer and Injectant Downstream of a Row of Film-Cooling Holes in a Turbulent Boundary Layer," ASME *Journal of Heat Transfer*, Vol. 113, pp. 79–90.

Mayle, R. E., Kopper, F. C., Blair, M. F., and Bailey, D. A., 1977, "Effect of Streamline Curvature of Film Cooling," ASME *Journal of Engineering for Power*, Vol. 99, No. 1, pp. 77–82.

Moffat, R. J., 1982, "Contributions to the Theory of Single-Sample Uncertainty Analysis," ASME *Journal of Fluids Engineering*, Vol. 104, pp. 250–260.

Nicolas, J., and Le Meur, A., 1974, "Curvature Effects on a Turbine Blade Cooling Film," ASME Paper No. 74-GT-156.

Ortiz, A., 1987, "The Thermal Behavior of Film Cooled Turbulent Boundary Layers as Affected by Longitudinal Vortices," M. S. Thesis, Department of Mechanical Engineering, Naval Postgraduate School, Monterey, CA.

Discharge Coefficients of Holes Angled to the Flow Direction

N. Hay

S. E. Henshall

A. Manning

Department of Mechanical Engineering,
University of Nottingham,
Nottingham, United Kingdom

In the cooling passages of gas turbine blades, branches are often angled to the direction of the internal flow. This is particularly the case with film cooling holes. Accurate knowledge of the discharge coefficient of such holes at the design stage is vital so that the holes are correctly sized, thus avoiding wastage of coolant and the formation of hot spots on the blade. This paper describes an experimental investigation to determine the discharge coefficient of 30 deg inclined holes with various degrees of inlet radiusing and with the axis of the hole at various orientation angles to the direction of the flow. Results are given for nominal main flow Mach numbers of 0, 0.15, and 0.3. The effects of radiusing, orientation, and crossflow Mach number are quantified in the paper, the general trends are described, and the criteria for optimum performance are identified.

1 Introduction

A diverse range of geometries and flow conditions can arise in the cooling passages of gas turbines. The branches can be perpendicular or inclined to the main flow channel as indicated by the angle θ in Fig. 1, they can be sharp edged or radiused, r/d in Fig. 1, they can be angled to the direction of flow, as indicated by the angle α in Fig. 1. There could additionally be a crossflow present on either side of the hole and this crossflow could be flowing at various speeds or Mach number (M_c and M_∞ in Fig. 1). These parameters and the pressure ratio across the hole can occur in a variety of combinations. The designer is faced with the need to know the discharge coefficient, C_d, in these diverse situations in order to be able to size the holes and so control the flow through them in the desired way. This need is very critical for the film cooling holes where underfeed and overfeed of coolant through the hole can lead to the formation of hot spots on the blade surface and result in reduced blade life.

Prompted by this need a series of research projects have been undertaken at the University of Nottingham over a number of years, which aimed to quantify the discharge coefficient of cooling holes with emphasis on the blade film cooling situation.

Benmansour (1981) measured C_d for a range of angles of inclination ($\theta = 30$, 60, and 90 deg) and for a range of length to diameter ratios and crossflow. He found that for $l/d > 2$ the effect of l/d is very weak. Since film cooling holes usually have $l/d > 6$, all subsequent work was done at $l/d = 6$.

The effects of crossflow at inlet to the hole (coolant side) and exit from the hole (mainstream side) were described by Hay et al. (1983). At a low pressure ratio p_c^+/p_∞, the discharge coefficient is a strong function of pressure ratio, increasing with it. Beyond $p_c^+/p_\infty \simeq 1.4$, C_d reaches a plateau the level of which depends upon any crossflow present. Crossflow at inlet reduced C_d and the stronger the crossflow the larger this reduction. Crossflow at exit from the hole has a much weaker effect on C_d but also tends to reduce its value.

Khaldi (1987) looked at the effect of radiusing the holes and covered the same range of parameters as Benmansour. Radiusing was found to increase the discharge coefficient and also to make it less sensitive to crossflow. These results were published concisely by Hay et al. (1987).

Next, the nonalignment of the hole with the direction of the flow was investigated. This situation often occurs in film cool-

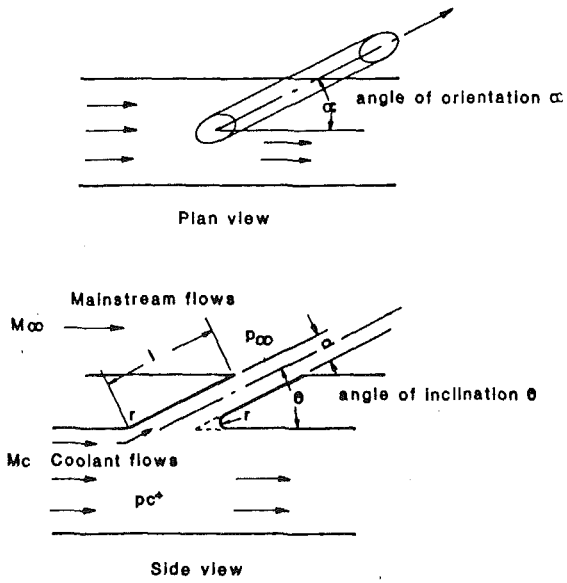

Fig. 1 Typical cooling hole geometric and flow parameters

Contributed by the International Gas Turbine Institute and presented at the 37th International Gas Turbine and Aeroengine Congress and Exposition, Cologne, Germany, June 1–4, 1992. Manuscript received by the International Gas Turbine Institute February 17, 1992. Paper No. 92-GT-192. Associate Technical Editor: L. S. Langston.

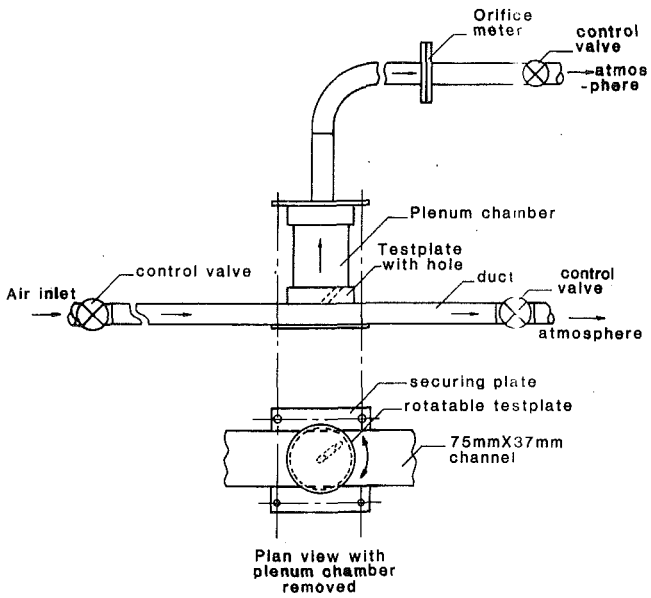

Fig. 2 General arrangement and details of the test rig

ing, particularly at the leading edge of rotor blades, and when the coolant is injected laterally. 30 deg inclined holes were used and tested at the full range of orientation angles α (i.e., 0–180 deg), and for a range of upstream cross flow Mach number. Evans (1985) looked at sharp-edged holes with and without crossflow; Henshall (1988) and Manning (1991) looked at the additional effect of radiusing the hole at inlet.

This paper reports these results. Values of C_d for 30 deg inclined holes oriented to the direction of the flow are presented together with the added effects of radiusing and crossflow at inlet for the full range of orientation angles.

Other authors have also published discharge coefficient data for various geometries, for example, Lichtarowicz et al. (1965), Dekker and Chang (1965), McGreehan and Schotsch (1987), and Briggs (1989). However, the effect of the orientation angle, α, has not been, as yet, addressed systematically.

2 Apparatus

The rig used is shown in Fig. 2. Basically it consists of a 2.5-m-long rectangular duct of 71 mm × 32 mm cross section. The duct has a circular hole cut into the top to accommodate the test plate in which the hole is formed. The angle of inclination of 30 deg was chosen as it is one often used for film cooling holes. The design of the rig allows the angle of orientation α to be varied over the full range of 0 to 180 deg simply by rotating the test plate and clamping it in position to give the desired angle of orientation. The test holes had to be inclined at 30 deg and also rounded to various extents. They had to be produced by an elaborate process consisting of casting in araldite over a core that was previously shaped to the desired r/d using a steel ball of the required radius and a soft filler.

Control valves are located at inlet and outlet of the channel. The flow through the test hole passes through a plenum chamber to an ISO orifice meter, and is then vented to the atmosphere through another control valve and a silencer.

The rig is fed from a screw compressor plant. The three control valves allow the pressure ratio across the test hole and the cross flow Mach number to be controlled independently.

All pressures were measured with water or mercury manometers. A thermocouple in the plenum chamber was used for temperature measurement. The test data were manually fed into a computer for processing.

The test holes had the following geometry:

r/d = 0, 0.25, 0.5, 0.75, 1.0
θ = 30 deg throughout
$1/d$ = 6 throughout
hole diameter = 7 mm for $r/d = 0$, and 6.35 mm (1/4 in.) for all other values of r/d.

3 Results

Measurements of C_d were made at various pressure ratios between 1.0 and 1.7 for the range of geometric parameters given in the previous section. Results were obtained for the three values of the crossflow Mach number M_c of 0, 0.15, and 0.3.

The calculation of the discharge coefficient was made using compressible flow relationships, i.e., the value of C_d is given by the ratio of the measured mass flow to the mass flow calculated for the same p_c^+/p_∞ using isentropic compressible flow relationships. The calculation procedure is detailed in Appendix 1.

The upstream pressure is taken as the stagnation pressure of the flow and is measured at a plane in the duct just upstream of the hole. The downstream pressure is taken as the static pressure downstream of the orifice and is measured in the plenum chamber.

The uncertainty in the measured values of C_d is estimated to be about ±3–4 percent.

A resumé of the results is given in Table 1 for just three values of pressure ratio, low, medium, and high. Reference to the table will be made later but at this stage it gives a good idea of the range of tests and of the parameters covered.

For $M_c = 0$ the orientation is not a variable and hence C_d, depends only on radiusing and on pressure ratio. Thus it is instructive to look at the effect of radiusing before that of orientation.

3.1 Effect of Radiusing. Figure 3 shows the variation of C_d with radiusing and with pressure ratio. The value of C_d increases with pressure ratio and reaches a plateau at $p_c^+/p_\infty \simeq 1.2$. This pattern of behavior has been noted before for 90 deg inclined holes (Hay and Spencer, 1992) and it is not surprising that it applies also to 30 deg inclined holes.

Figure 3 also shows that radiusing to an r/d of 0.25 produces a large increase in C_d and that further increase in r/d brings diminishing returns. Beyond $r/d = 0.75$ C_d values drop back slightly. This is also in line with previous results. Khaldi (1987) found that the major part of the gain in C_d with radiusing is obtained when r/d reaches 0.25, and he concludes that $r/d = 0.25$ is the optimum value for 90 deg inclined holes.

Nomenclature

a = velocity of sound
C_d = discharge coefficient
d = diameter of hole
l = length of hole
M = Mach number
p = static pressure
p^+ = stagnation pressure
r = radius of inlet to hole
α = orientation angle of the hole
θ = inclination angle of the hole

Subscripts

h = inside the test hole
c = upstream of test hole (coolant side)
p = plenum chamber
∞ = downstream of test hole (mainstream side)

Table 1 Representative selection of the C_d results

Pressure ratio p_c^+/p_∞		M_c = 0						M_c = 0.15					M_c = 0.3				
	α r/d	0	45	90	135	180	0	45	90	135	180	0	45	90	135	180
	1.1	0	0.69	0.68	0.68	-	-	0.75	0.7	0.58	0.5	0.48	0.71	0.59	0.42	0.45	0.29
		0.25	0.81	0.81	-	-	-	0.8	0.78	0.69	0.63	0.61	0.73	0.65	0.54	0.32	0.38
		0.5	0.82	0.83	0.83	-	-	0.83	0.8	0.77	-	-	0.67	0.65	0.5	0.4	0.49
		0.75	0.89	-	-	-	-	-	-	-	-	-	0.72	0.67	0.53	0.38	0.54
		1.0	0.86	-	-	-	-	-	-	-	-	-	0.71	0.7	0.51	0.45	0.54
	1.4	0	0.72	0.72	0.72	-	-	0.76	0.73	0.68	0.64	0.62	0.78	0.73	0.63	0.63	0.55
		0.25	0.86	0.81	0.82	-	-	0.84	0.83	0.8	0.78	0.77	0.82	0.8	0.74	0.68	0.68
		0.5	0.83	0.84	0.84	-	-	0.86	0.85	0.83	-	-	0.82	0.82	0.76	0.73	0.73
		0.75	0.89	-	-	-	-	0.88	-	0.87	-	-	0.86	0.85	0.8	0.79	0.8
		1.0	0.87	-	-	-	-	0.86	-	0.83	-	-	0.85	0.85	0.8	0.8	0.81
	1.6	0	-	-	-	-	-	0.76	-	0.7	0.67	0.65	0.79	0.75	0.66	0.65	0.59
		0.25	0.84	0.84	0.84	-	-	0.85	0.84	0.82	0.8	0.8	0.84	0.82	0.78	0.73	0.73
		0.5	0.85	0.85	0.85	-	-	0.87	0.86	0.84	-	-	0.85	0.84	0.79	0.77	0.78
		0.75	0.89	-	-	-	-	0.89	-	0.88	-	-	0.87	0.87	0.83	0.81	0.83
		1.0	0.87	-	-	-	-	0.87	-	0.85	-	-	0.88	0.88	0.83	0.82	0.84
Range of C_d for 1.1 < p_c^+/p_∞ < 1.6		0	0.03	0.04	0.04	-	-	0.01	0.03	0.12	0.17	0.17	0.08	0.16	0.24	0.2	0.3
		0.25	0.05	0.03	0.02	-	-	0.05	0.06	0.13	0.17	0.14	0.11	0.17	0.24	0.41	0.35
		0.5	0.03	0.02	0.02	-	-	0.04	0.06	0.07	-	-	0.18	0.19	0.29	0.37	0.29
		0.75	0.00	-	-	-	-	0.01	-	0.01	-	-	0.15	0.2	0.3	0.43	0.29
		1.0	0.01	-	-	-	-	0.01	-	0.02	-	-	0.17	0.18	0.32	0.37	0.3

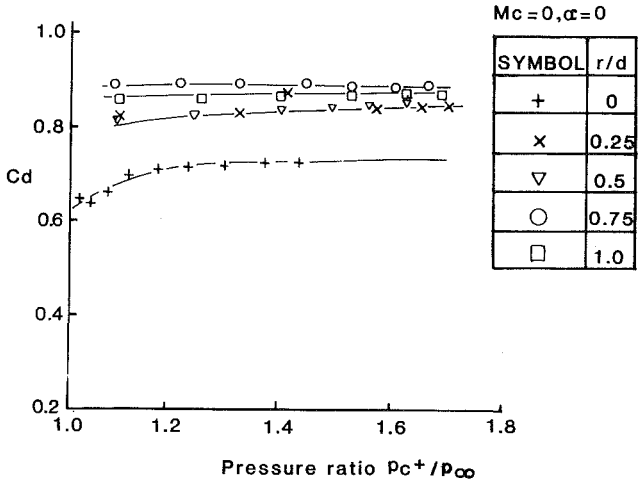

Fig. 3 Effect of radiusing on C_d in the absence of crossflow

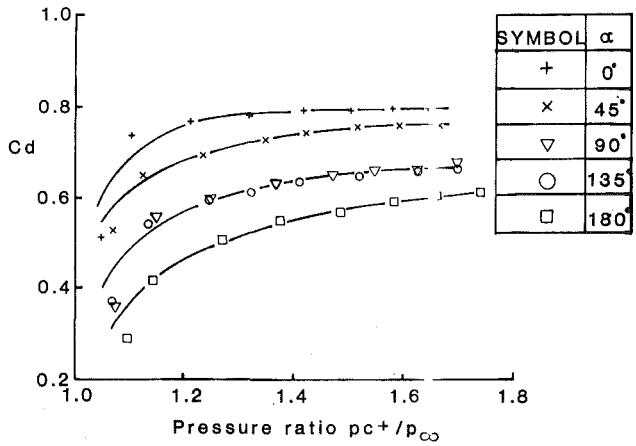

Fig. 4 Effect of angle of rotation on C_d at $M_c = 0.3$

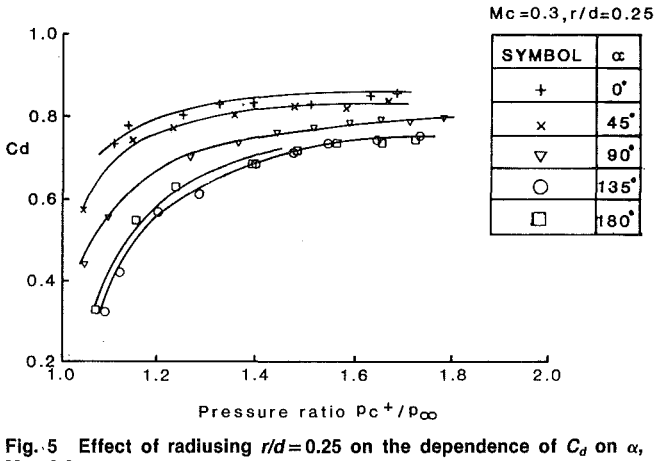

Fig. 5 Effect of radiusing $r/d = 0.25$ on the dependence of C_d on α, $M_c = 0.3$

3.2 Effect of Orientation. The effect of orientation is most pronounced for the sharp edged hole ($r/d = 0$) and the higher value of M_c. So we will take this case first. Figure 4 shows the effect of orientation at various pressure ratios. Increase in the angle of orientation leads to a decrease in C_d, a result to be expected as the flow has to turn more and more as the angle of orientation increases. Also a higher pressure ratio is needed before the variation in the value of C_d eases off into a plateau region.

The range in C_d (i.e., $C_{d\,\max} - C_{d\,\min}$) is quite large even at the higher values of pressure ratio. This is not a desirable behavior as it means that a given design will be sensitive to variations in the geometric and flow parameters.

This undesirable behavior is alleviated with rounding of the hole. Figure 5 shows the variation in C_d for $r/d = 0.25$. The absolute values of C_d are higher than for $r/d = 0$ and also the range in C_d has narrowed and the plateaux are reached at lower p_c^+/p_∞ values.

When the radiusing ratio is increased to 0.75, Fig. 6, C_d values are higher, the plateaux are reached earlier, and the range of C_d is narrower still. Thus not only does the flow need a smaller pressure drop to drive it through the hole, but it is also less sensitive to variations in the flow or the geometric parameters.

Radiusing seems to have the effect of making it easier for the flow to turn into the hole. In other words the loss coefficient due to turning is smaller when the hole is radiused.

3.3 Effect of the Crossflow. Constraints arising from requirements for accuracy in the measurement of C_d resulted in

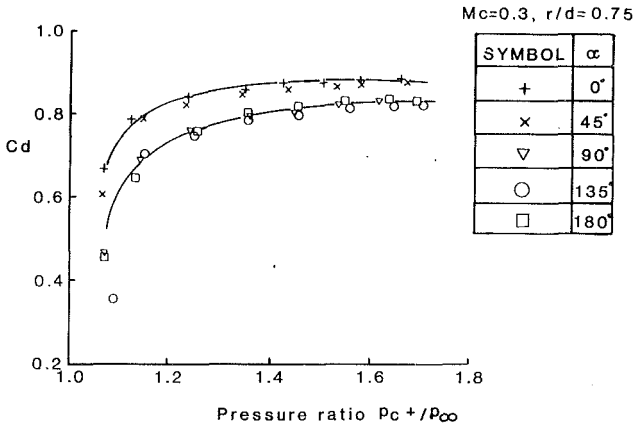

Fig. 6 Effect of further radiusing $r/d = 0.75$ on the dependence of C_d on α, $M_c = 0.3$

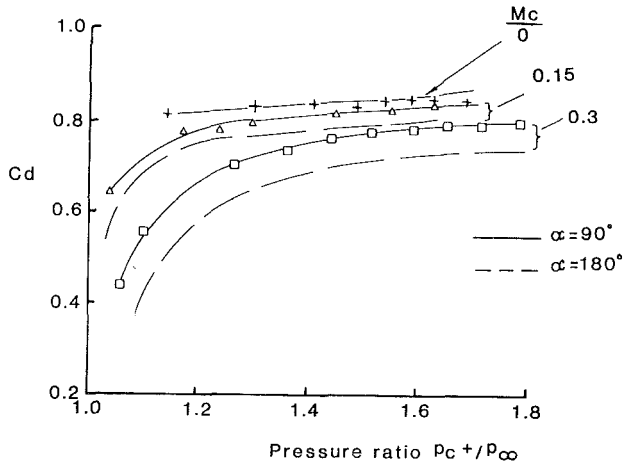

Fig. 7 Effect of crossflow on C_d at orientations of 90 and 180 deg

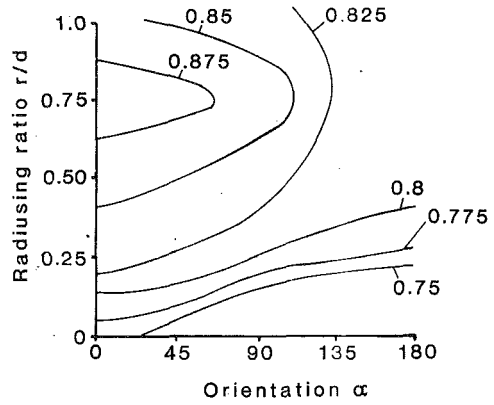

Fig. 8 Contour plot for C_d as a function of r/d and α at $M_c = 0.15$ and pressure ratio of 1.4

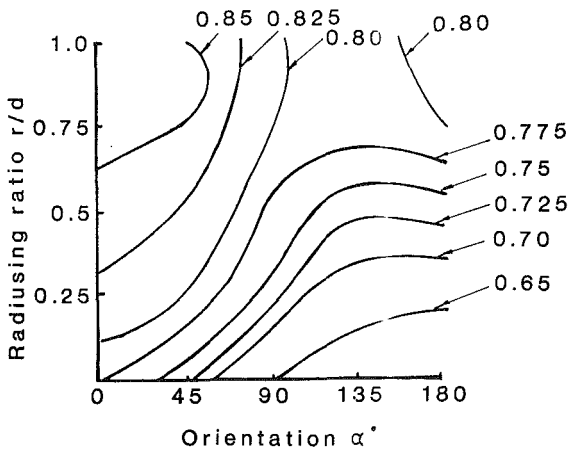

Fig. 9 Contour plot for C_d as a function of r/d and α at $M_c = 0.3$ and pressure ratio of 1.4

that the maximum value of the crossflow Mach number that could be achieved was 0.3. Thus results were obtained at $M_c = 0$, 0.15, and 0.3.

Figure 7 shows the effect of M_c at $r/d = 0.25$. For angles of inclination of 90 and 180 deg there is a drop in the value of C_d as M_c increases. Other results (omitted from Fig. 7 for clarity) show that for an orientation angle of 45 deg there is hardly any effect of M_c on C_d, while for $\alpha = 0$ there is a slight increase in C_d with M_c. This is consistent with the flow situation. For $\alpha = 0$ the momentum of the flow is in the direction of the hole and would be expected to help the flow into the hole. For $\alpha = 45$ deg the penalty of turning balances the help provided by the component of momentum in the direction of the hole. For $\alpha = 90$ deg and above there is a net loss reflected in the lower values of the discharge coefficient.

It is difficult to identify the physical flow phenomena that lead to the behavior described in the last three paragraphs. They obviously have to do with the way streamline curvature affects the position of the stagnation stream surface that separates the flow diverting into the hole from the continuing forward. Also the presence, position, and extent of the separation zones and their dependence on the local details of the flow will reflect in the discharge coefficient. Extensive flow visualization and numerical modeling would be needed in order to understand fully these complex flow phenomena.

3.4 Contour Plots. The amount of experimental data obtained in this work is fairly extensive and there does not seem to be an easy way of collapsing the data and expressing the variations in an all-embracing correlation. This being the case, a useful way of conveying the overall behavior is to condense the data in tabular form or present them in the form of contour plots.

Table 1, referred to earlier, shows the range of parameters covered and gives spot values of C_d at low, medium, and high values of pressure ratio. We have seen earlier that C_d values reach a plateau at around $p_c^+/p_\infty = 1.4$. This value was chosen as the "medium" pressure ratio for Table 1. The high pressure ratio was taken as the highest value of p_c^+/p_∞ set during the test program. The "low" value was an arbitrary choice as C_d varies strongly in this band of pressure ratio. The value of 1.1 was chosen as this exhibited the widest range in C_d.

At the bottom of Table 1 the range in C_d is given. This gives an indication of the sensitivity of C_d to pressure ratio. The sensitivity to r/d and α is not given explicitly but may be easily obtained from the tabulated values. For example, for a pressure ratio of 1.4 and $r/d = 0.75$ the range in C_d at $M_c = 0.3$ for variations in α is $C_{d\,\max} - C_{d\,\min} = 0.86 - 0.79 = 0.07$. ($C_{d\,\max}$ and $C_{d\,\min}$ above are shown underlined in Table 1.)

Contour plots of the results for $p_c^+/p_\infty = 1.4$ and $M_c = 0.15$ and 0.3 are shown in Figs. 8 and 9. The combined effects of radiusing and orientation may be seen easily: The area of highest C_d in both cases is that of zero orientation; the radius ratio of $r/d = 0.75$ gives the highest values for C_d and the least sensitivity of C_d to the orientation angle α. The absolute values of C_d are generally higher for $M_c = 0.15$. Also the range in C_d is narrower than for $M_c = 0.3$. Similar contour plots may be easily generated for other pressure ratios.

4 Conclusions

1 The effect of hole orientation on the coefficient of discharge of a 30 deg inclined hole has been quantified for two values of crossflow Mach number.

2 Increase in the angle of orientation leads to a decrease in the coefficient of discharge, which can be very substantial for sharp-edged holes.

3 Radiusing the hole entry produces an increase in the discharge coefficient and reduces its dependence on the angle of orientation.

4 A radiusing ratio of $r/d = 0.75$ gives the best results from the point of view of both increased C_d and reduced dependence on orientation.

5 The effect of crossflow Mach number is to increase C_d marginally for angles of orientation $\alpha < 45$ deg and decrease C_d for $\alpha > 45$ deg, the decrease being sizeable for $\alpha > 90$ deg.

6 A representative selection of the results has been presented in tabular and contour plot forms to convey the general trends.

References

Benmansour, S., 1981, "Discharge Coefficients of Film Cooling Holes," M. Phil Thesis, University of Nottingham, United Kingdom.

Briggs, P. A., 1989, "The Effects of Inlet Rounding on Orifice Discharge Coefficients," B. Eng. Third Year Project Report," University of Nottingham, United Kingdom.

Dekker, B. E. L., and Chang, U. F., 1965, 66, "An Investigation of Steady Compressible Flow Through Thick Orifices," *Proc. Inst. Mechanical Engineers*, Vol. 180, Part 3J.

Evans, R., 1985, "Discharge Coefficient of Inclined Long Orifices," B.Sc. Third Year Project Report, University of Nottingham, United Kingdom.

Hay, N., Lampard, D., and Benmansour, S., 1983, "Effects of Crossflows on the Discharge Coefficient of Film Cooling Holes," ASME *Journal of Engineering for Power*, Vol. 105, pp. 243-248.

Hay, N., Khaldi, A., and Lampard, D., 1987, "Effects of Crossflows on the Discharge Coefficient of Film Cooling Holes With Rounded Entries and Exits," *Proc. 2nd ASME-JSME Thermal Engineering Joint Conference* Honolulu, HI, Vol. 3, pp. 369-374.

Hay, N., and Spencer, A., 1992, "Discharge Coefficients of Cooling Holes With Radiused and Chamfered Inlets," ASME JOURNAL OF TURBOMACHINERY, Vol. 114, pp. 701-706.

Henshall, S. E., 1988, "Discharge Coefficient of Inclined Film Cooling Holes With Rounded Entry and Crossflow," B. Eng. Third Year Project Report, University of Nottingham, United Kingdom.

Khaldi, A., 1987, "Discharge Coefficient of Film Cooling Holes With Rounded Entries or Exits," Ph.D. Thesis, University of Nottingham, United Kingdom.

Lichtarowicz, A., Duggins, R. K., and Markland, E., 1965, "Discharge Coefficients for Incompressible, Noncavitating Flow Through Long Orifices," *Journal of Mechanical Engineering Science*, Vol. 7, No. 2, pp. 210-219.

Manning, A., 1991, "Discharge Coefficients of Holes Angled to the Flow Direction," B. Eng. Third Year Project Report, University of Nottingham, United Kingdom.

McGreehan, W. F., and Schotsch, M. J., 1988, "Flow Characteristics of Long Orifices With Rotation and Corner Radiusing," ASME JOURNAL OF TURBOMACHINERY, Vol. 110, pp. 213-217.

APPENDIX

Calculation of C_d

The discharge coefficient C_d is defined as:

$$C_d = \frac{\dot{m}}{\dot{m}_t}$$

where $\dot{m}$ is the measured mass flow (orifice meter) and $\dot{m}_t$ is the theoretical mass flow. The theoretical mass flow is calculated assuming isentropic compressible flow. The measured quantities needed for this calculation are p_c^+, p_∞, and T_p as detailed below.

Bearing in mind that $p_h = p_\infty$ and that $T_c^+ = T_h^+ = T_p$ (since the velocity in the plenum is very low) $\dot{m}_t$ is given by:

$$\dot{m}_t = \rho_h \, v_h \, A_h$$

A_h is the area of the hole $= \pi/4 \, d^2$. ρ_h is the density in the hole given by:

$$\rho_h = \frac{p_c^+}{RT_c^+} \cdot \frac{1}{(p_c^+/p_\infty)^{1/\gamma}}$$

and v_h, the velocity in the hole, is obtained from:

$$v_h = a_h \, \mathrm{M}_h$$

where

$$a_h = \{\gamma \, RT_h\}^{1/2} = \left\{ \frac{\gamma \, RT_p}{1 + \dfrac{\gamma - 1}{2} \mathrm{M}_h^2} \right\}^{1/2}$$

and M_h is given by:

$$\mathrm{M}_h = \left\{ \left[\left(\frac{p_c^+}{p_\infty} \right)^{\gamma - 1/\gamma} - 1 \right] \frac{2}{\gamma - 1} \right\}^{1/2}$$

Experimental Study on the Flow Characteristics of Streamwise Inclined Jets in Crossflow on Flat Plate

Sang Woo Lee[1]

Joon Sik Lee

Sung Tack Ro

Department of Mechanical Engineering,
Seoul National University,
Seoul 151-742, Korea

Experimental study has been conducted to investigate the flow characteristics of streamwise 35 deg inclined jets, injected into a turbulent crossflow boundary layer on a flat plate. Flow is visualized by schlieren photographs for both normal and inclined jets to determine the overall flow structure with the variation of the velocity ratio. A three-dimensional velocity field is measured for two velocity ratios of 1.0 and 2.0 by using a five-hole directional probe. The visualization study shows that the variation of the injection angle produces a significant change in the flow structure. It is recognized that the jet flow is mainly dominated by the turbulence for a small velocity ratio, but it is likely to be influenced by an inviscid vorticity dynamics for a large velocity ratio. Such a trend prevails in the streamwise inclined injection, compared with the normal injection. A pair of bound vortices accompanied with a complex three-dimensional flow is present in the downstream region of the jet exit as in the case of the normal injection, although its magnitude and range are different, and the strength of the bound vortex is strongly dependent on the velocity ratio. The interface between the jet and the crossflow is identified from the vorticity distribution.

Introduction

Many practical engineering applications involve jets in a crossflow. Depending on the flow configuration, two kinds of situations are encountered: internal and external flows. The internal flows include: jet injection to stabilize the flame or to dilute combustion products in a combustion chamber; jet impingement cooling of a gas turbine blade leading edge; and the jet flow during the take off or landing of a V/STOL. The external flows include: flow from a cooling tower or chimney; flow associated with waste water or cooling water discharged into a river or sea; and film cooling to protect a gas turbine blade surface from hot gas flow.

The injection of a jet into the crossflow can alter the flow field substantially and result in a very complex three-dimensional flow structure. Many works on normally injected jets in the crossflow have been performed since Morton (1961), and Keffer and Bains (1963). Kamotani and Greber (1972) measured the average velocity, turbulent components and temperature distributions for the normally injected round jet in a crossflow. They found that the measured quantities were mainly dependent on the momentum flux ratio of the jet to the crossflow, and that a pair of counterrotating vortices existed. Chassaing et al. (1974) defined a universal axial velocity profile from velocity measurements in the symmetry plane of cylindrical and coaxial jets. Bergeles et al. (1976) studied the flow characteristics with the variation of velocity ratio through the flow visualization and static pressure measurement at the wall in the neighborhood of the jet exit. Moussa et al. (1977) found from three-dimensional velocity measurements in the near field of the jet exit that a pair of bound vortices are formed in the downstream region due to the reorientation of ring vortices emerging from the jet exit. They also suggested a method to identify the jet and crossflow interface based on mean vorticity distribution. Crabb et al. (1981) confirmed double vortex characteristics from turbulent component data and showed that this is associated with the fluid that escaped from the jet exit. Andreopoulos and Rodi (1984) experimentally studied the normally injected round jet in the presence of boundary layer flow on a flat wall, and showed that the jet structure is strongly dependent on the velocity ratio. They also suggested two kinds of flow pattern with respect to the velocity ratio. Using a conditional sampling technique, Andreopoulos (1985) clarified that the jet from the injection hole affects the mean turbulent velocity components more than the crossflow, and suggested a new vorticity pattern and flow structure of normal injection jets in the crossflow. Studies on jets in the crossflow were reviewed by Rajaratnam (1976) and Demuren (1986).

In the film cooling application, the jet is usually injected making an acute angle with the crossflow, rather than the

[1]Present address: Department of Mechanical Engineering, Kum-Oh National University of Technology, Kumi, Kyungbook 730-701 Korea.

Contributed by the International Gas Turbine Institute and presented at the 37th International Gas Turbine and Aeroengine Congress and Exposition, Cologne, Germany, June 1-4, 1992. Manuscript received by the International Gas Turbine Institute February 17, 1992. Paper No. 92-GT-181. Associate Technical Editor: L. S. Langston.

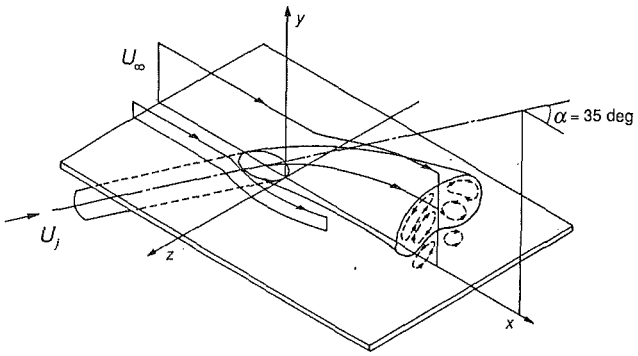

Fig. 1 Early flow description of a streamwise inclined jet in a crossflow and coordinates of present study

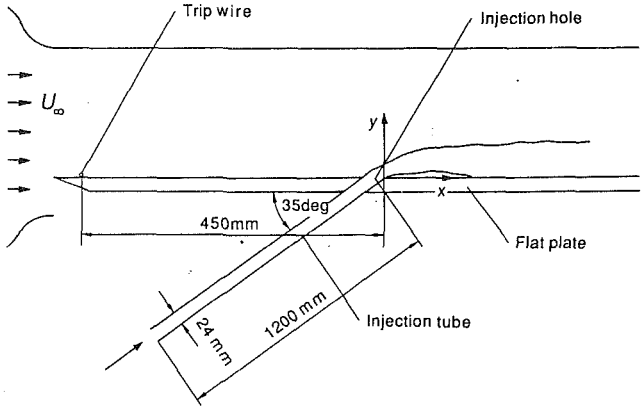

Fig. 2 Schematic diagram of experimental arrangement

normal injection. Figure 1 shows the early flow model of a streamwise inclined jet in a crossflow suggested by Goldstein et al. (1968). This qualitative description was drawn mainly based on studies such as Abramovich (1963) and Keffer and Baines (1963), not on three-dimensional flow measurements. As for the inclined jet, most of the studies were concerned with the measurement of the film cooling effectiveness and the heat transfer coefficient, although limited studies were conducted for the flow fields. There are some investigations (Yoshida and Goldstein, 1984; Jubran and Brown, 1985; Pietrzyk et al., 1989) that contain only two-dimensional velocity measurements in the jet symmetry plane, but no detailed three-dimensional measurements have been performed on the streamwise inclined jet in the crossflow.

In the process of examining the previous researches on inclined jets in the crossflow, some difficulties were encountered in figuring out the overall flow structure because of the lack of three-dimensional velocity data. In this study, experiments have been conducted to investigate the flow characteristics of the streamwise 35 deg inclined jets into a turbulent boundary layer on a flat plate. Flow is visualized by schlieren photographs for both normal and inclined jets of different velocity ratios or momentum flux ratios. Three-dimensional velocity components are measured with a five-hole directional probe, and streamwise vorticities are evaluated to define the jet and crossflow interface.

Experimental Apparatus and Procedure

The wind tunnel used in this experiment is an open-circuit type with a cross section of 0.4 m × 0.28 m. At a mean velocity of 10 m/s, uniformity and turbulent level are about 0.5 percent and 0.2 percent, respectively. As shown in Fig. 2, the flow coming out from the wind tunnel is developing to the turbulent boundary layer flow right after the trip wire of the radius 0.5 mm. The channel is made of a rectangular duct of 0.4 m × 0.2 m. The jet exit is located at 0.45 m downstream from the trip wire. The injection pipe is 24 mm in inner diameter and 1.2 m in length in order to make the pipe flow fully turbulent. Before entering the injection pipe, the injected air from the blower passes through a heat exchanger and a plenum chamber. The temperature difference between the crossflow and jet is maintained within 0.5°C.

A five-hole three-dimensional directional probe (United Sensor & Control model DC125) 3.2 mm in diameter is used to measure three-dimensional velocity components in the neighborhood of the jet exit, and is positioned by a two-dimensional drive mechanism with stepping motors (Oriental Motors, PH266-03GK) and linear heads (Oriental Motors, 2LB10-3). Three-dimensional velocity components are determined by calibration curves obtained from the relations among the pressures, flow angles, and velocity magnitude. Figure 3 is the schematic of a data acquisition system for the velocity and pressure. Probe traversing and velocity measurement are controlled by a personal computer (IBM XT) in an on-line system using a pulse-generating adaptor and GPIB. Scanivalve (Scanivalve Corp.), which is also controlled by the computer, is used to measure the pressures from the five-hole probe in a proper sequence. Pressure signals are transformed to electric ones by a calibrated digital manometer (YEW 2573) and from these signals, 1024 data are sampled and averaged in a signal analyzer (IWATSU SM-2100) in which a 12-bit A-D converter is in-

Nomenclature

D = inner diameter of injection pipe
J = momentum flux ratio = $\rho_j U_j^2/\rho_\infty U_\infty^2$
R = velocity ratio = U_j/U_∞
r = radial distance from the center of the injection pipe
Re_D = Reynolds number = $U_\infty D/\nu_\infty$
U = x velocity component
U_e = injection velocity at jet exit in the case of no crossflow
U_j = spatially averaged mean velocity at jet exit = $\frac{4}{\pi D^2} \cdot \int_0^{D/2} U_e 2\pi r dr$
U_∞ = free-stream velocity
V = y velocity component
W = z velocity component
x = coordinate in streamwise direction, Fig. 1
y = coordinate in upward direction, Fig. 1
z = coordinate in spanwise direction, Fig. 1
α = angle of inclination of injection pipe, Fig. 1
δ^* = displacement thickness at origin of coordinates
θ = momentum thickness at origin of coordinates
ν_∞ = kinematic viscosity of crossflow fluid
ρ_j = density of injection fluid
ρ_∞ = density of crossflow fluid
Φ_j = mean vorticity flux at jet exit = $\int_0^{D/2} |\Omega| \cdot U_e \cdot 2\pi r dr$
Ω = vorticity vector
Ω_j = spatially averaged mean vorticity at jet exit = $\Phi_j/U_j A$
Ω_x = streamwise vorticity
Ω_z = spanwise vorticity

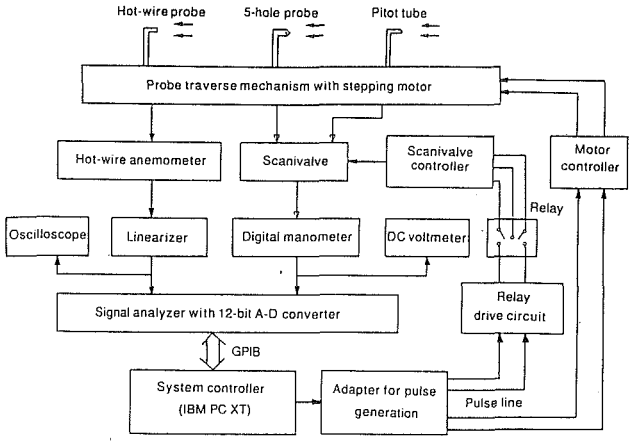

Fig. 3 Schematic diagram of data acquisition system

stalled. The average values are transferred to the computer through the GPIB.

Free-stream velocity, U_∞, is maintained at 9.65 m/s and at the origin of the coordinates, the displacement and momentum thicknesses are 2.10 mm and 1.62 mm, respectively. Two dimensionality of the crossflow boundary layer near the jet exit in the spanwise direction is confirmed by measuring velocity profiles at two spanwise positions where $z/D = 4$ and -4. The Reynolds number based on the diameter of the injection pipe and free-stream velocity, $\mathrm{Re}_D = U_\infty D/\nu_\infty$, is 1.47×10^4. For flow visualization, schlieren photographs are taken by introducing CO_2 gas of mass concentration 0.99 into the injection pipe instead of air, and four different velocity ratios are considered to be $R = 0.5$, 1.0, 1.5, and 2.0, all with $\rho_j/\rho_\infty = 1.53$. The three-dimensional velocity measurements are conducted for $R = 1.0$ and 2.0 on the six y–z planes, the locations of which are $x/D = -1$, 0, 1, 2, 4, and 6. In each y–z plane, the measuring points are: y/D from 0 to 2.0 with an interval of $D/12$ in upward direction; and z/D from 0 to 1.5 with an interval of $D/6$ in the spanwise direction. The experimental conditions are summarized in Table 1.

The measurement error in the flow angle is estimated within about 1 deg. The accuracy of the measured pressures is roughly within 1 percent of dynamic pressure outside of the boundary layer. In order to have a precise global estimate on the accuracy of the measurements, the mass flux was calculated at each boundary surface of the velocity measurement arrays. As a result, the net mass flux across all the surfaces of the measurement control volume is balanced to within 0.5 percent of the total inlet mass flux, in spite of a high turbulence level in the near field of the jet exit. The results are compared with those of Yoshida and Goldstein (1984), which shows a good agreement (Lee, 1990).

General Flow Structure of Normally Injected Jet in Crossflow

The most important feature of the jet in a crossflow may be mutual deformation by the interaction between each other. The trajectory of the jet is deflected into the crossflow direction, while the crossflow is altered as if it is blocked by a rigid obstacle. Moreover, the jet entrains the fluid from the crossflow during the interaction. This results in a different flow pattern from the one with a rigid obstacle. In addition, regardless of the velocity ratios, a very complex three-dimensional wake flow occurs in the downstream of the jet exit. In this region, the streamwise velocity is relatively small and the wake region grows proportional to the velocity ratio. Pressure drop in this region induces an inward motion transporting the fluid from the crossflow toward the jet symmetry plane with

Table 1 Experimental conditions

	U_∞(m/s)	D(mm)	α(deg)	δ^*(mm)	θ(mm)	Re_D	ρ_j/ρ_∞	R, J
Flow visualization	9.65	10	35, 90	2.10	1.62	0.59×10^4	1.53	R = 0.5, 1.0, 2.0 J = 0.38, 1.53, 6.12
Velocity measurement	9.65	24	35	2.10	1.62	1.47×10^4	1.00	R = 1.0, 2.0 J = 1.0, 4.0

downwash of the jet. As the velocity ratio increases, this effect becomes more and more significant and the inward motion shows a behavior like a wall jet. Due to this effect, the wake is separated from the wall. For all the velocity ratios, a shear layer exists above the wake region, in which the streamwise velocity changes greatly.

While moving downstream, both the shear layer and the wall jet region are reduced and the flow returns to the boundary layer type with a decrease in the jet effect. In the downstream region of the jet exit, there are two vortices rotating in opposite directions with respect to each other. It is known that these vortices originate from the vortex rings emanating from the jet exit and make the jet cross section the form of a kidney. As the jet flow is approaching its exit with a large velocity ratio, vortex lines build up concentric rings and the ring in the vicinity of the pipe wall has the maximum strength, while in the crossflow boundary layer, there exists a spanwise vorticity, $-\Omega_z$. As these vortex rings are escaping from the exit, a pair of bound vortices are formed as a consequence of reorientation and stretching (Moussa et al., 1977). Though this secondary flow of bound vortex type is originally generated from the pipe flow, this may also be produced by shearing between the jet and the crossflow. In particular, when the velocity ratio is large, the shear at the boundary surface plays an important role in the formation of vorticity (Andreopoulos and Rodi, 1984). On the other hand, the spanwise vorticity in the crossflow boundary is stretched and converted into streamwise vorticity due to the turning of the crossflow around the jet near the wall right before the jet exit. This converted streamwise vorticity forms a horseshoe vortex similar to that encountered in the boundary layer flow with a rigid obstacle. This horseshoe vortex always rotates in the opposite direction with respect to the bound vortex. However, since its strength is much weaker compared with the bound vortex, this seems to be suppressed by the bound vortex except in the case of a large velocity ratio. There is some evidence given by Andreopoulos and Rodi (1984) that the horseshoe vortex is swept into the hollow of the kidney-shaped jet field underneath the bound vortex.

Results and Discussion

Flow Visualization. The previous visualization studies on jets in a crossflow by using a fog of paraffin oil droplets (Andreopoulos, 1985) or dry ice vapor (Ramsey and Goldstein, 1971; Goldstein et al., 1974) could not clearly explain the flow field near the jet exit, especially in the case of a relatively large injection velocity. In this study, the above-mentioned difficulties were avoided by using a schlieren optical system and spark light source, with which we were able to visualize the instantaneous flow structures clearly.

Figure 4 shows the instantaneous pictures of normal injection jets in the crossflow with the variation of velocity ratio, $R = U_j/U_\infty$, or momentum flux ratio, $J = \rho_j U_j^2/\rho_\infty U_\infty^2$. The results are presented for $R = 0.5$, 1.0, and 2.0, which are equivalent to $J = 0.38$, 1.53, and 6.12, respectively. As the velocity ratio increases, the injected jet penetrates the crossflow more deeply. When R is 0.5, the fluid from the jet exit is significantly bent toward the wall near the jet exit, and the flow is converted into a very complex turbulent motion with large-scale eddies. The interface between the injected jet and crossflow exhibits a highly intermittent behavior and a large-eddy structure. Also, the irregular CO_2 mass concentration near the jet exit shows

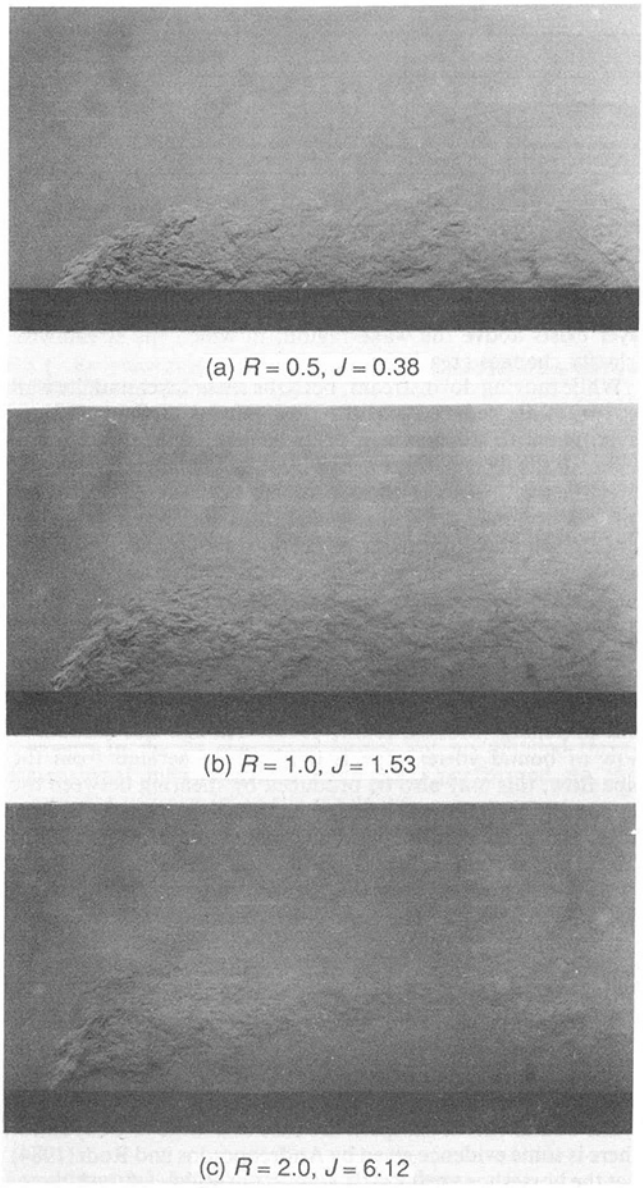

Fig. 4 Short-exposure schlieren photographs for normal injection

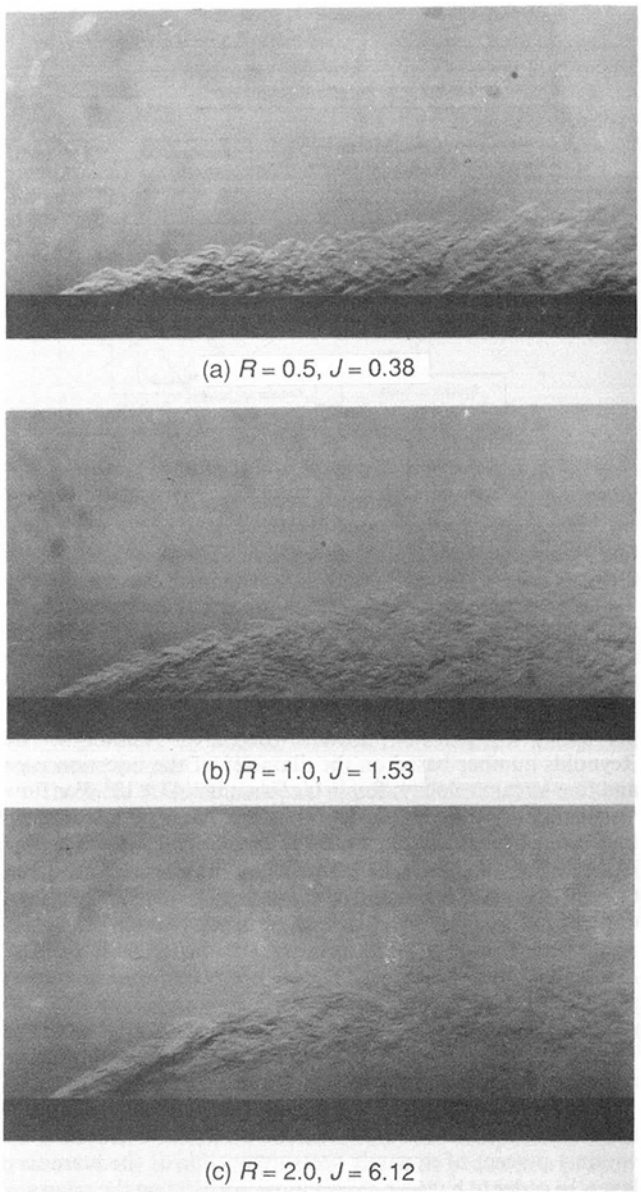

Fig. 5 Short-exposure schlieren photographs for streamwise inclined injection

a strong interaction of the jet with the crossflow. On escaping from the jet exit, the injected jet is bent toward the wall and fills up the near-wall region in the downstream. This means that there is little inward motion induced by the pressure drop caused by the presence of the jet. Therefore, in a small velocity ratio, the flow in the downstream region of the jet exit is mainly occupied by the injected fluid. When the velocity ratio becomes 1.0, the scale of the turbulence is smaller than that of $R = 0.5$, but the jet region is more widely extended. In the upstream edge of the jet exit, the injected fluid tends to decelerate with the crossflow and a rolling-up of the shear layer is observed just as in a turbulent free jet from a circular pipe injected into stationary surroundings. On the other hand, in the downstream edge of the jet exit, the ring vortices emanating from the injection pipe are considerably deformed due to the acceleration with the crossflow. These vortices are stretched in the z direction near the downstream edge of the jet exit and are bundled up to form bound vortices as proposed by Andreopoulos (1985). When the velocity ratio reaches 2.0, the jet is clearly separated from the wall, and no injection fluid can be seen near the wall. In the normal injection case, a rolling-up of the shear layer and tilting process of ring vortices always exists regardless of the velocity ratios. Accordingly, the reorientation of ring vortices dominates the downstream flow of the jets in the crossflow and results in a very complex three-dimensional turbulent flow.

Short-exposure schlieren photographs of streamwise 35 deg inclined jets are shown in Fig. 5. Flow conditions of these photographs are the same as those of normal injection except for the injection angle. For a small velocity ratio, $R = 0.5$, the injected fluid is confined to the restricted region near the wall and the downstream flow is affected by the crossflow significantly. In the case of the inclined injection, the jet trajectory approaches the wall and the flow scale is smaller, compared to that of the normal injection. When the velocity ratio becomes 1.0, the injected jet influences the flow fields more widely and near the wall, there is a region where CO_2 concentration is nearly zero. But the rolling-up of the shear layer, observed in the upstream edge of the jet exit in the normal injection case, does not exist in the inclined injection case. As the velocity ratio reaches 2.0, the injected jet is separated from the wall abruptly, and it seems that the jet is not affected by the crossflow. Moreover, the injected jet maintains its structure far downstream with a relatively small interaction with the crossflow, and the potential core region is extended to the down-

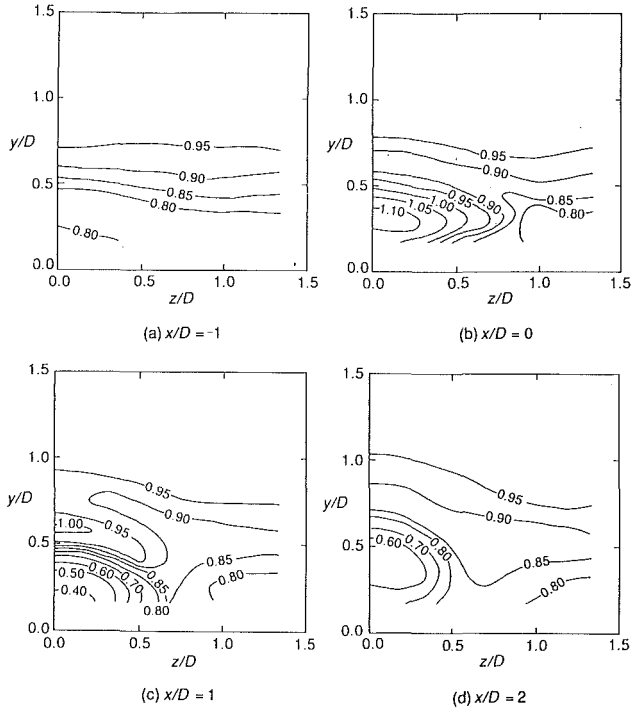

Fig. 6 Contours of x-directional velocity, U/U_∞, for $R = 1.0$

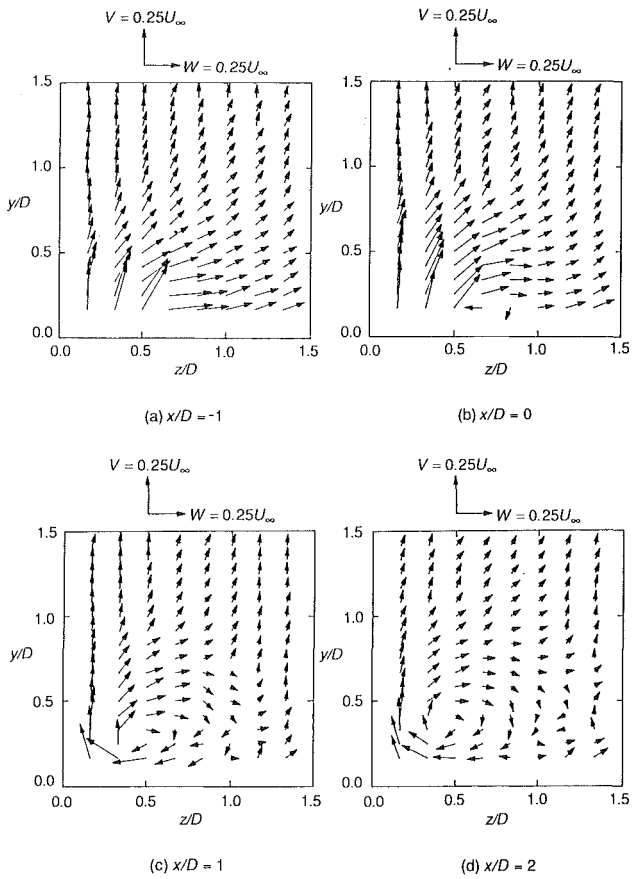

Fig. 7 Projection of velocity vectors on y-z plane for $R = 1.0$

stream region of the jet exit by about three times of the pipe diameter. In the downstream region, the flow field can be divided into three regions: wake region, jet region, and free-stream region. At some distance downstream, a region with no injected fluid can be observed between the wall and the jet. The presence of this region with nearly zero CO_2 concentration implies that a strong inward motion toward the jet symmetry plane due to the pressure drop in the wake region is produced underneath the jet trajectory. In addition, by studying the schlieren photograph for $R = 2.0$, we found that the jet region was also divided into two parts by a dark strip starting from the downstream edge of the jet exit, which diminishes while moving downstream. This strip is attributed to the changes in the optical path in the y direction, resulting from the kidney-shaped jet cross section. The two sections of fluid moving toward the jet symmetry plane in each side of the jet near the wall inevitably collide with each other, and then the collision forces the crossflow fluid near the symmetry plane to move in the upward direction. Accordingly, the jet cross section is deformed into a kidney shape as a result of the upward motion. On moving downstream, the CO_2 concentration is lowered and is uniformly distributed by the three-dimensional mixing of the injected fluid with the crossflow fluid.

In the streamwise inclined injection, the entrainment of crossflow fluid near the jet boundary is much less compared to that of normal injection, and the jet boundary is well defined. Regardless of the injection angle, the jet flow is mainly dominated by the turbulent transport for the small velocity ratios. On the other hand, it is influenced by the inviscid vorticity dynamics for the large velocity ratios. Such a trend prevails in the inclined jet.

Mean Velocity. Distributions of streamwise velocity, U/U_∞, for $R = 1.0$ at each measurement plane in the case of the inclined injection are presented in Fig. 6. From the overview, while moving downstream, the jet boundary is growing and after the jet escapes from the exit completely, it is significantly bent by the crossflow. Figure 6(a) shows the velocity contours in the y-z plane at $x/D = -1$. In this plane, the velocity distribution is similar to that of the boundary layer except for the near-field of the jet exit. At $x/D = 0$, the velocity distribution changes remarkably. The result shows that the injected jet is accelerated in the streamwise direction and is forced to move toward the wall by the crossflow, which pushes the boundary layer fluid out in the z direction. The jet effect is extended up to where z/D is about 1.0. When x/D reaches unity, a wake region exists where U/U_∞ is very small just below the jet, which is located at about $y/D = 0.5$. Between the jet and the wake region, there exists a shear layer with a large velocity gradient. In the y-z plane where x/D is 2, the jet region is extended to the outer side of the boundary layer, but the velocity gradient is reduced by the momentum diffusion and shearing between the jet and the crossflow.

Figure 7 shows the secondary flow pattern in the y-z planes for $R = 1.0$. At $x/D = -1$, it can be seen that over the jet exit, the y-directional velocity component has a relatively large value. But in the region where z/D is larger than 0.5, only the spanwise velocity exists near the wall. The flow parallel to the wall is due to the injection of the jet, which results in pushing the boundary layer fluid out in the spanwise direction. At $x/D = 0$, the overall trend of the secondary flow is similar to that at $x/D = -1$, but near the wall, the flow in the $-z$ direction is observed in a very narrow region at about $z/D = 0.75$. In spite of the presence of the inward motion, there is still an outward flow in the region where z/D is larger than 1.0. At $x/D = 1$, the secondary flow forms a complete streamwise vortex, the so-called bound vortex. The somewhat irregular motion at about $z/D = 1.0$ near the wall is due to the inward motion induced by the bound vortex, which is balanced to the outward flow generated by the jet on either side of the jet exit. When x/D reaches 2, the center of the bound vortex moves upward, and the bound vortex seems to be fully established. In particular, a separation of the secondary flow near $z/D = 1.0$ occurs, which is due to the momentum balance between the inward and outward flows.

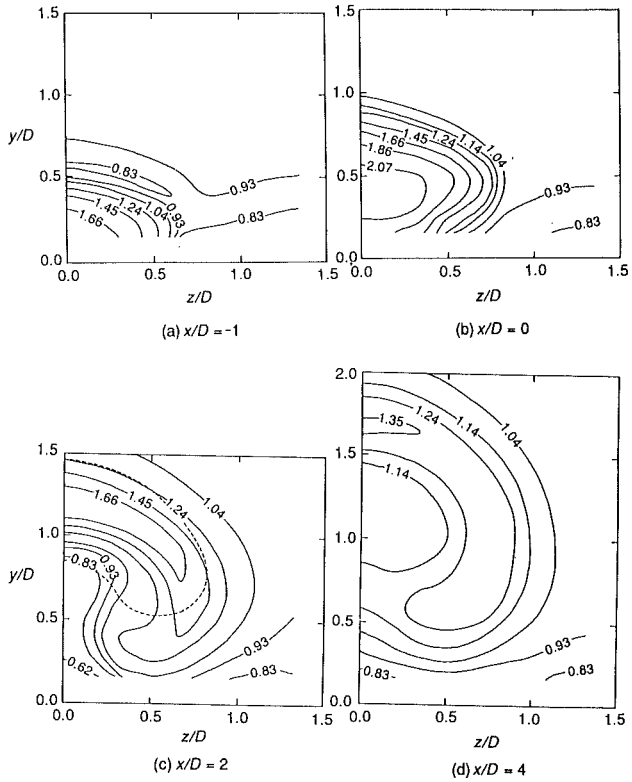

Fig. 8 Contours of x-directional velocity, U/U_∞, for $R = 2.0$

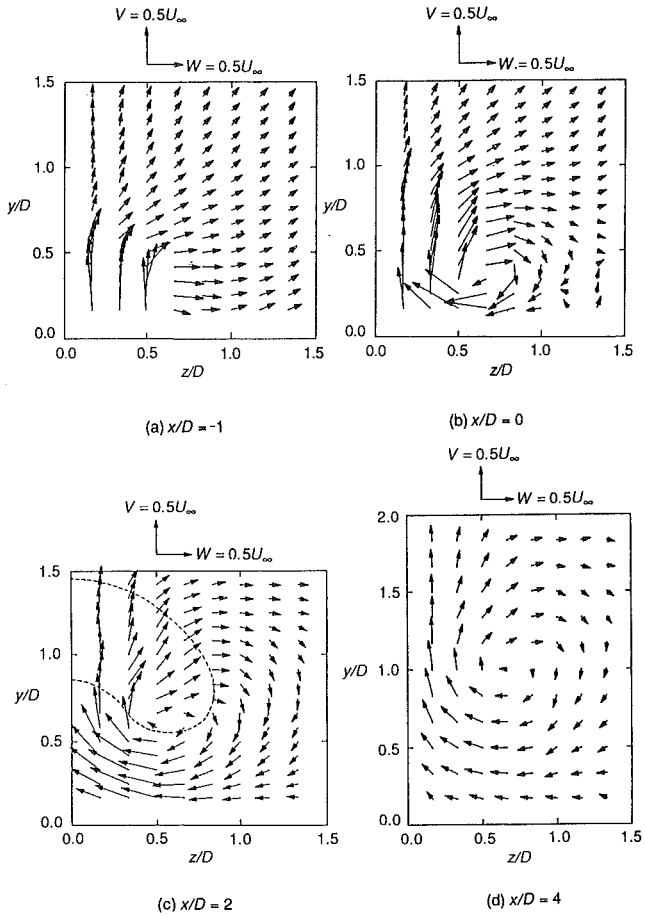

Fig. 9 Projection of velocity vectors on y-z plane for $R = 2.0$

Figure 8 represents the velocity contours of U/U_∞ for $R = 2.0$. While moving downstream, the jet region where U/U_∞ is larger than the free-stream velocity is extended, and after escaping from the jet exit, the jet cross section is converted into the kidney shape. Just above the exit, the velocity contours are concentrated near the jet exit with a large velocity gradient. When x/D reaches 2, the jet effect spreads out to the whole measuring region and the maximum velocity location moves up to about $y/D = 1.2$. In Fig. 8(c), the dotted line indicates the jet and the crossflow interface defined by the method proposed by Moussa et al. (1977). The procedure to determine the interface will be discussed later. In the jet symmetry plane, where $z/D = 0$, it can be seen that the flow may be divided into three regions: wake region, jet region, and free-stream region along the y direction. Between each region, two shear layers exist where the velocity gradient is large. The velocity gradient in the shear layer between the wake and jet is much larger. Such a flow structure is sustained by the crossflow fluid entering the wake where a large pressure drop has taken place under the jet region. The inward motion makes the velocity contours bend toward the jet symmetry plane near $z/D = 0.5$. In the y-z plane where $x/D = 4$ (Fig. 8(d)), the shear layers at $x/D = 2$ become extinct due to the shearing between the jet and the crossflow, and the flow returns to the boundary-layer type.

Figure 9 shows the secondary flow pattern in the y-z plane for $R = 2.0$. At $x/D = -1$, we observed that the injected jet forced the fluid in the boundary layer to move in both upward and spanwise directions. In particular, when z/D is more than 0.5, the outward motion parallel to the wall is much stronger. In contrast to the result of $R = 1.0$, there is little spanwise velocity component right above the jet exit, which indicates that for $R = 2.0$, the injected jet is less influenced by the crossflow than for $R = 1.0$. When x/D reaches 0, the streamwise vortex develops as in the case of $R = 1.0$, although the strength and range of the vortex are quite different from each other. The inward flow of the crossflow fluid toward the jet symmetry plane produces a pair of vortices. It is noted that on the right side of the bound vortex near the wall, an irregular secondary motion is produced due to the interaction between the outward flow shown in Fig. 9(a) and the inward motion caused by the bound vortex. When x/D reaches 2, the center of the bound vortex moves upward, and a strong inward flow under the center of the bound vortex is present. In addition, a pair of well-organized vortices in the streamwise direction is developed. However, the irregular motion generated at $x/D = 0$ is swept away by the strong inward flow here. This inward motion toward the jet symmetry plane colliding with one from the other side of the symmetry plane results in an upward flow near the symmetry plane. Such a flow structure forms the jet and crossflow interface into a kidney shape denoted by a dotted line in Fig. 9(c), and this movement of the crossflow fluid plays an important role in maintaining the jet structure far downstream. At $x/D = 4.0$, the bound vortex still keeps its structure, but loses its strength significantly.

Figure 10 shows contours of V/U_∞ at $x/D = 2$ for $R = 2.0$. When x/D reaches 2, the position of the maximum of V/U_∞ lies just below the jet trajectory, which indicates that in the region where x/D is larger than 2, the crossflow fluid in the wake region has a larger y-directional momentum than the injected fluid. Therefore, the indirect contribution of the pressure drop induced by the presence of the jet is more important than the direct contribution of the y-directional momentum out of the jet exit, to preserve the V/U_∞ at some downstream positions.

Contours of W/U_∞ is shown in Fig. 11. At $x/D = 2$, the inward flow toward the jet symmetry plane is developed well below the jet and the maximum value of W/U_∞ reaches about half the free-stream velocity and decreases while moving downstream.

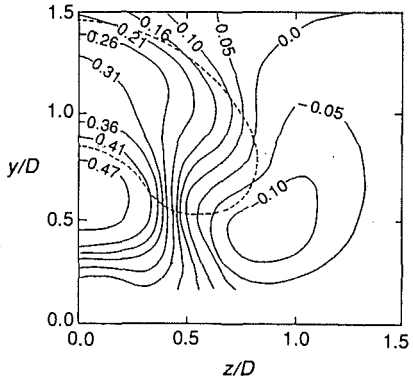

Fig. 10 Contours of y-direction velocity, V/U_∞, at $x/D=2$ for $R=2.0$

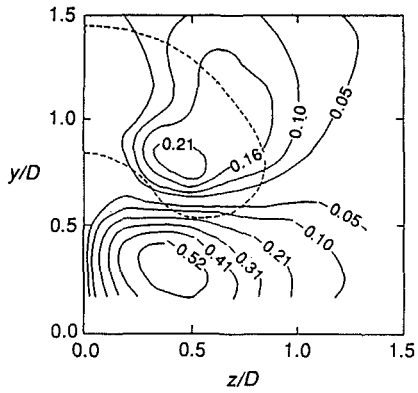

Fig. 11 Contours of z-direction velocity, W/U_∞, at $x/D=2$ for $R=2.0$

Comparison of the velocity profiles of the present 35 deg inclined jet with those of the normal jet obtained by Andreopoulos and Rodi (1984) is shown in Fig. 12. In their study, the origin of coordinates is positioned at the center of the jet exit, not on the downstream edge of jet exit. In addition, free-stream velocity was maintained at 13.9 m/s and the Reynolds number based on the free-stream velocity and injection-hole diameter was 4.1×10^4. The dotted lines stand for the results of the normal injection and the symbols represents the present results. Figure 12(a) shows that in the case of the normal injection, the velocity deficit in the wake region is much larger than that of the 35 deg inclined injection. Generally, in the case of a normal jet, a reverse-flow region is always found in the wake region, especially for a large velocity ratio such as $R=2.0$. However, in the present inclined injection, no reverse flow zone has been observed even for $R=2.0$. Figure 12(b) shows the y-directional velocity component variation along the y direction. In the normal injection case, we can see two downward flow regions near the wall and $y/D=2$, but no such flow exists in the present inclined injection case. Moreover, the magnitude of the y-directional velocity component is much larger in the inclined injection case than in the normal injection case, even though the y component of normal jet velocity is larger than that of inclined jet velocity for the same velocity ratio. This implies that the induced flow into the wake is much stronger in the inclined injection case than in the normal injection case. z-directional velocity profiles at $z/D=0.5$ (Fig. 12(c)) also show that the bound vortex region in the 35 deg injection case is much closer to the wall compared to the normal injection case. From the above comparisons, it is noted that the secondary motion in the inclined injection is much stronger and the gradient of pressure drop in the wake of the inclined jet may be much larger than that of the normally injected jet.

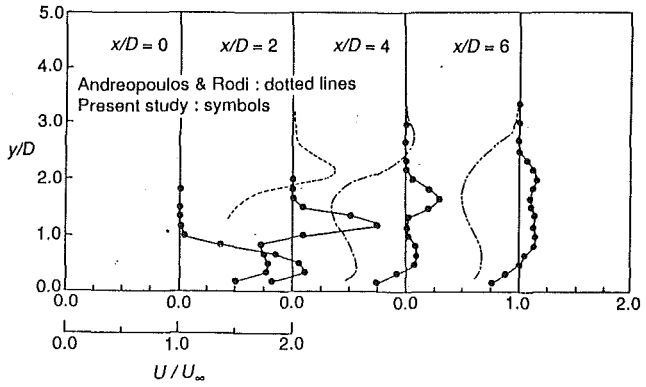

(a) x-directional velocity in jet symmetry plane(z/D = 0)

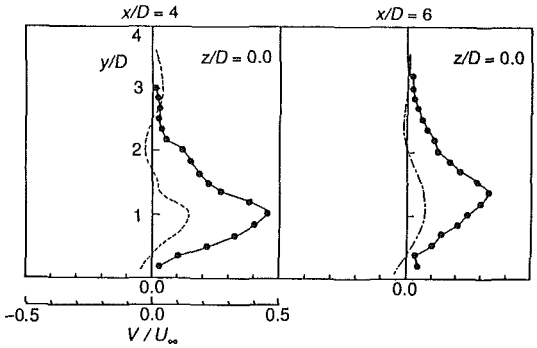

(b) y-directional velocity in jet symmetry plane(z/D = 0)

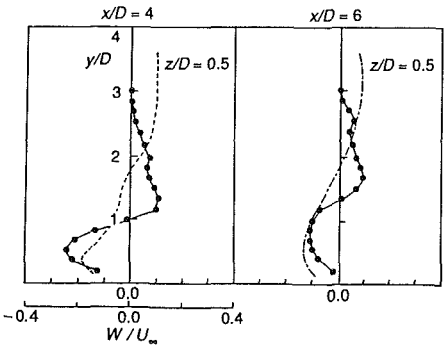

(c) z-directional velocity at z/D = 0.5

Fig. 12 Comparison of velocities of present study (35 deg injection) with those of Andreopoulos and Rodi (90 deg injection) for $R=2.0$

In the near field and some downstream region of the jet, the result of the velocity measurement is compared with that of the flow visualization, even though the flow conditions are somewhat different. Figure 13 shows the superposition of the velocity vectors in the jet symmetry plane for $J=4.0$ ($R=2.0$) upon the schlieren photograph for $J=3.45$ ($R=1.5$). When $x/D=0$, the jet boundary in the photograph coincides with the position where the velocity magnitude is significantly decreasing. As discussed in the previous flow visualization, the jet trajectory is divided into two parts by a dark strip. This strip is attributed to the change in optical disturbance resulting from the kidney-shaped cross section. Between the strip and wall is the wake region. At $x/D=2$, velocity vectors show that in wake region, the x-directional velocity component is very small compared with the free-stream velocity, but the y-directional velocity component has a relatively large value. While moving downstream, the velocity profile is flattened and finally becomes the boundary-layer type. It is also noted that at $x/D=2$,

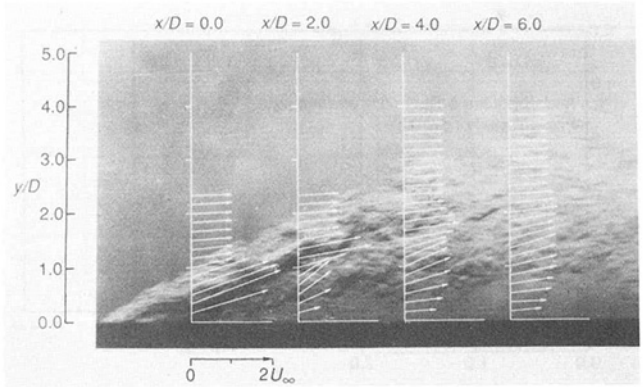

Fig. 13 Comparison of the result of velocity measurement in jet symmetry plane ($J = 4.0$) with that of flow visualization ($J = 3.45$)

the boundary of the jet trajectory near the wall coincides approximately with the center of the bound vortex, which is located at $y/D = 0.5$ in Fig. 9(*c*).

The early flow description shown in Fig. 1 seems to be quite misleading in comparison with the present results. Contrary to Fig. 1, only one pair of streamwise vortices exist in the jet cross section as can be seen in Fig. 9(*c*). From the present three-dimensional measurements, we confirmed that the secondary motion in the jet cross section is strong enough to alter the whole flow structure, especially for a large velocity ratio. Accordingly, the pre-existing investigations based on two-dimensional velocity measurements of the inclined jet in the crossflow are not sufficient to account for the actual flow phenomenon.

Mean Vorticity Distribution. We observed from the flow visualization that the flow characteristics of the jet in a crossflow are dominated by an inviscid vorticity dynamics for a large velocity ratio, especially in the case of a streamwise inclined jet. Accordingly, for a clear understanding of a vorticity structure and identification of the jet and crossflow interface, the vorticity in the flow direction, Ω_x, is evaluated from the cross-sectional velocities, V and W. Ω_x may be determined from the circulation in the y–z plane. In the following figure, Ω_x is nondimensionalized by the spatial mean vorticity at pipe, Ω_j.

Since the direction of the vorticity coming from the jet pipe is always parallel to the pipe wall, the mean vorticity flux may be defined as

$$\Phi_j = \int_0^{D/2} |\Omega| \cdot U_e \cdot 2\pi r dr = \pi \int_0^{D/2} r \cdot dU_e^2 \qquad (1)$$

From this equation, the spatial mean vorticity averaged over the jet exit is evaluated as

$$\Omega_j = \frac{\Phi_j}{U_j A} = \frac{\pi}{U_j A} \int_0^{D/2} r \cdot dU_e^2 \qquad (2)$$

where A is the cross-sectional area of the pipe and U_e is the velocity measured at the jet exit when there is no crossflow. The values of the mean vorticity flux, Φ_j, and the mean vorticity, Ω_j, calculated from the above equations, are 15.9 m^2/s^2 and 1832/s, respectively.

Figure 14 shows the dimensionless vorticity, Ω_x/Ω_j at each cross section. In the present coordinate system, vorticity due to the bound vortex always has a positive value. In Fig. 14(*a*), Ω_x/Ω_j has its maximum value at $z/D = 0.5$. This coincides well with the jet and crossflow interface. Along the downstream, the bounds containing positive vorticity, the bound vortex region, is enlarged and the maximum location of the positive vorticity corresponds approximately to the bound vortex center. The vorticity in the streamwise direction has its maximum in the plane of $x/D = 0$, and a gradual decrease in the magnitude in the downstream region brings about weakening of the bound

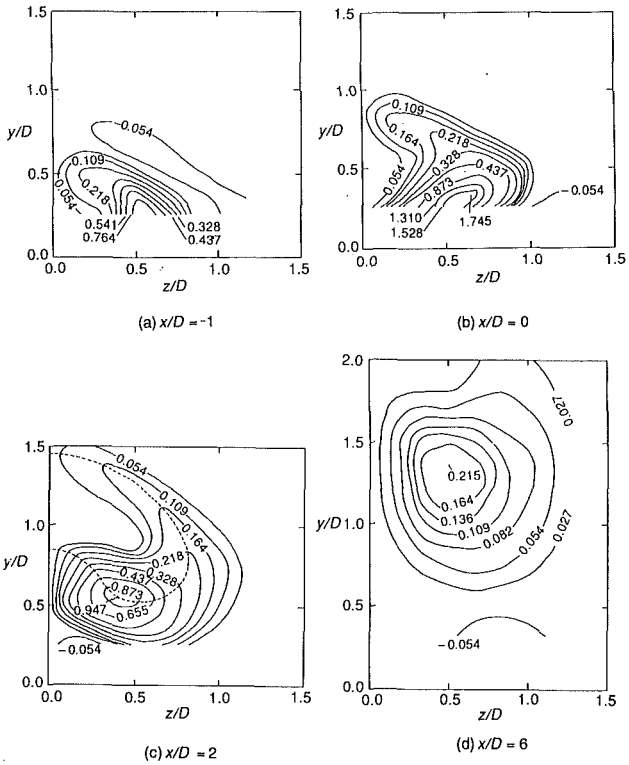

Fig. 14 Contours of streamwise vorticity, Ω_x/Ω_j, for $R = 2.0$

vortex. At $x/D = 2$, near jet symmetry plane where y/D is roughly 1.0, there exists a region where Ω_x/Ω_j is relatively small, which is surrounded by the region with positive vorticity. This region is considered as the potential core observed in the present flow visualization, and coincides with the inside of the jet and crossflow interface.

Jet and Crossflow Interface. As for the turbulent mixing flow, it is very difficult to define the interface clearly. In general, since flow variables and its derivatives vary continuously, many problems are concerned with determining the interface between the jet and the crossflow. Despite the difficulties, there are several yardsticks to measure the interface. These include turbulent intensity, velocity profile, turbulent microscale, and mean vorticity.

Generally speaking, the locations where turbulent intensity, shear force associated with mean velocity gradient, and mean vorticity have their maxima, do not usually coincide with each other. However, from the results of Moussa et al. (1977), it has been found that the ridges of the maximum values in turbulent intensity and mean vorticity are sufficiently close to each other. Therefore, in this study, the interface is determined using the mean vorticity. Since the jet is injected with an acute angle to the crossflow, it is reasonable to define the interface using the vorticity in the flow direction, Ω_x. Figure 14(*c*) shows how the interface is determined from the vorticity distribution. When moving from the crossflow region to the jet region, a point with a maximum of Ω_x/Ω_j has to be encountered. The trajectory connecting the points is defined as the jet and crossflow interface. In Fig. 15, the development of the jet and crossflow interface in the streamwise direction is illustrated. While moving downstream, the interface is extended in both y and z directions. When x/D reaches unity, the lower part of the interface is separated from the wall, and the jet cross section is finally deformed into kidney shape at $x/D = 2$.

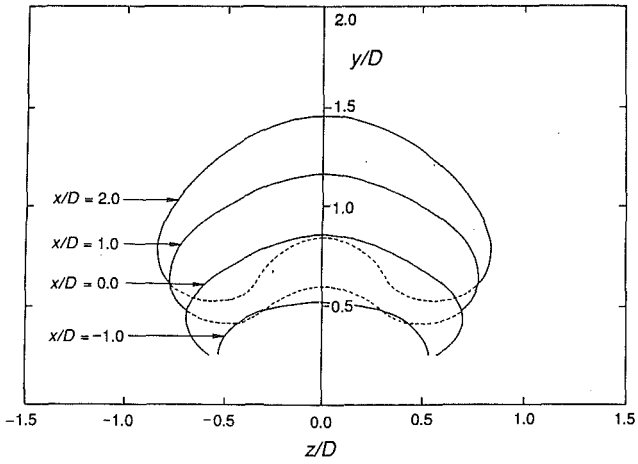

Fig. 15 Streamwise development of jet boundaries for $R = 2.0$

Conclusion

In the present study, experiment on the streamwise 35 deg inclined jets injected into the crossflow boundary layer on a flat plate has been conducted by flow visualizations and three-dimensional velocity measurements. Several observations are noted and summarized below.

From the flow visualization study, we found that the jet flow was mainly dominated by the turbulence for a small velocity ratio, but it is likely to be influenced by an inviscid vorticity dynamics for a large velocity ratio. Such a trend prevails in the streamwise inclined injection, in comparison with the normal injection. When the velocity ratio is small, the fluid from the jet exit is bent toward the wall. Therefore, it seems that only injected fluid in some downstream region of the jet exit exists. But for a large velocity ratio, the injected jet is separated from the wall abruptly, so only the crossflow fluid is filled in the region between the wall and the jet trajectory. In the inclined injection, the jet maintains its structure far downstream with a relatively small interaction with the crossflow and the potential core region is extended to a certain downstream position. In addition, the entrainment of the crossflow fluid near the jet and crossflow interface is much less in comparison with the normal injection.

Three-dimensional velocity measurements show that a pair of bound vortices accompanied with a complex three-dimensional flow exist in the downstream region of the jet exit as in the case of the normal injection, and the range and strength of the bound vortices are strongly dependent on the velocity ratio. However, in the present inclined injection, no reverse flow zone can be observed even for $R = 2.0$ and the secondary motion is much stronger. The occasion of the secondary flow in the y direction is mainly due to the pressure drop in the wake region, whereas the y directional momentum of the jet makes a minor contribution.

From the present results, it can be confirmed that the secondary flow pattern in the early flow model is not realistic and moreover, the three-dimensional flow characteristics are so dominant that the previous two-dimensional measurements in the jet symmetry plane are not sufficient to account for the flow structure of the jets in the crossflow, especially for a large velocity ratio.

Acknowledgments

The authors are grateful for the support provided by a grant from The Korea Science & Engineering Foundation and Turbo and Power Machinery Research Center.

References

Abramovich, G. N., 1963, *The Theory of Turbulent Jets*, MIT Press, Cambridge, MA, pp. 3–25, 195–201, 541–556.

Andreopoulos, J., 1985, "On the Structure of Jets in a Crossflow," *Journal of Fluid Mechanics*, Vol. 157, pp. 163–197.

Andreopoulos, J., and Rodi, W., 1984, "Experimental Investigation of Jets in a Crossflow," *Journal of Fluid Mechanics*, Vol. 138, pp. 93–127.

Bergles, G., Gosman, A. D., and Launder, B. E., 1976, "The Near-Field Character of a Jet Discharged Normal to a Main Stream," ASME *Journal of Heat Transfer*, Vol. 98, pp. 373–378.

Chassaing, P., George, J., Claria, A., and Sananes, F., 1974, "Physical Characteristics of Subsonic Jets in a Cross-Stream," *Journal of Fluid Mechanics*, Vol. 62, pp. 41–64.

Crabb, D., Durão, D. F. G., and Whitelaw, J. H., 1981, "A Round Jet Normal to a Crossflow," ASME *Journal of Fluids Engineering*, Vol. 103, pp. 142–153.

Demuren, A. O., 1986, "Modeling Turbulent Jets in Crossflow," *Encyclopedia of Fluid Mechanics*, N. P. Cheremisinoff, ed., Vol. 2–1, Gulf Publishing Company, pp. 431–465.

Goldstein, R. J., Eckert, E. G. R., and Ramsey, J. W., 1968, "Film Cooling With Injection Through Holes: Adiabatic Wall Temperatures Downstream of a Circular Hole," ASME *Journal of Engineering for Power*, Vol. 90, pp. 384–395.

Goldstein, R. J., Eckert, E. R. G., and Burggraf, F., 1974, "Effect of Hole Geometry and Density on Three-Dimensional Film Cooling," *Int. J. Heat Mass Transfer*, Vol. 17, pp. 595–607.

Jubran, B., and Brown, A., 1985, "Film Cooling From Two Rows of Holes Inclined in the Streamwise and Spanwise Directions," ASME *Journal of Engineering for Gas Turbines and Power*, Vol. 107, pp. 84–91.

Kamotani, Y, and Greber, I., 1972, "Experiments on a Turbulent Jet in a Cross Flow," *AIAA J.*, Vol. 10, pp. 1425–1429.

Keffer, J. F., and Baines, W. D., 1963, "The Round Turbulent Jet in a Cross-wind," *Journal of Fluid Mechanics*, Vol. 15, pp. 481–496.

Lee, S. W., 1990, "Experimental Studies on the Flow and Heat Transfer Characteristics on Film-Cooled Surfaces," Ph.D. Thesis, Seoul National University, Korea.

Morton, B. R., 1961, "On a Momentum-Mass Flux Diagram for Turbulent Jets, Plumes and Wakes," *Journal of Fluid Mechanics*, Vol. 10, pp. 101–108.

Moussa, Z. M., Trischka, J. W., and Eskinazi, S., 1977, "The Near Field in the Mixing of a Round Jet With a Cross-Stream," *Journal of Fluid Mechanics*, Vol. 80, pp. 49–80.

Pietrzyk, J. R., Bogard, D. G., and Crawford, M. E., 1989, "Hydrodynamic Measurements of Jets in Crossflow for Gas Turbine Film Cooling Application," ASME JOURNAL OF TURBOMACHINERY, Vol 111, pp. 139–145.

Rajaratnam, N., 1976, "Jets in Crossflow," *Turbulent Jets*, Elsevier Publishing Company Inc., New York, pp. 184–208.

Ramsey, J. W., and Goldstein, R. J., 1971, "Interaction of a Heated Jet With a Deflecting Stream," ASME *Journal of Heat Transfer*, Vol. 93, pp. 365–372.

Yoshida, T., and Goldstein, R. J., 1984, "On the Nature of Jets Issuing From a Row of Holes Into a Low Reynolds Number Mainstream Flow," ASME *Journal of Engineering for Gas Turbines and Power*, Vol. 106, pp. 612–618.

Behavior of the Laterally Injected Jet in Film Cooling: Measurements of Surface Temperature and Velocity/Temperature Field Within the Jet

S. Honami

T. Shizawa

Mechanical Engineering Department,
Science University of Tokyo,
Kagurazaka, Shinjuku, Tokyo 162, Japan

A. Uchiyama

Takasago Machinery Works,
Mitsubishi Heavy Industries Ltd.,
Takasago, Hyogo 676, Japan

This paper describes the behavior of the injected jet on the flat surface in lateral injection of the film cooling. Simultaneous velocity and temperature measurements were made by the double-wire probe. The test surface was also covered with an encapsulated temperature-sensitive liquid crystal. The image processing system based on the temperature and hue of the liquid crystal calibration provides the surface temperature distributions. The tests were conducted at three mass flux ratios, 0.5, 0.85, and 1.2. The laterally injected jet has an asymmetric structure with a large scale of vortex motion on one side caused by the interaction with the primary stream. Asymmetry is promoted with mass flux ratio increased, resulting in low film-cooling effectiveness.

Introduction

A continued effort to increase the turbine inlet temperature has been made over the last decades. Film cooling is one of techniques that may satisfy the requirements for thermal protection of the exposed turbine blade from hot combustion gases. Although many experimental works on film cooling have been undertaken to provide design data, recent emphasis is placed on more detailed work on the jet behavior or a combined effect of the individual parameters by Sinha et al. (1991) and Honami and Fukagawa (1987). The interaction of the vortex generator and the injected jet through a single hole was investigated in the application of the film cooling by Ligrani et al. (1991). Even though there has been a lack of understanding of the behavior of the laterally injected jet, Compton and Johnston (1992) studied the fluid dynamics behaviors of the jet from a single hole from the viewpoint of the control or suppression of turbulent boundary layer separation by a vortex generator jet. Discrete-hole injection offers some complexity such as the three-dimensional nature on the fluid dynamics and heat transfer behaviors. As most of the studies have been made individually on the surface heat transfer or the fluid dynamics behaviors of the injected fluid in lateral injection, there has been no detailed study dealing with the integrated results of the individual aspects.

The objective of the present research is to obtain under-

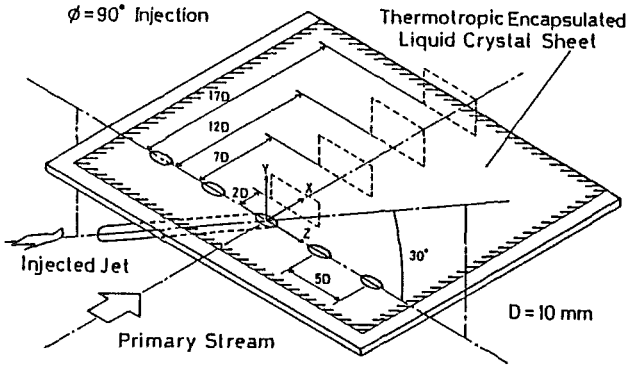

Fig. 1(*a*) Experimental apparatus (dimensions in mm)

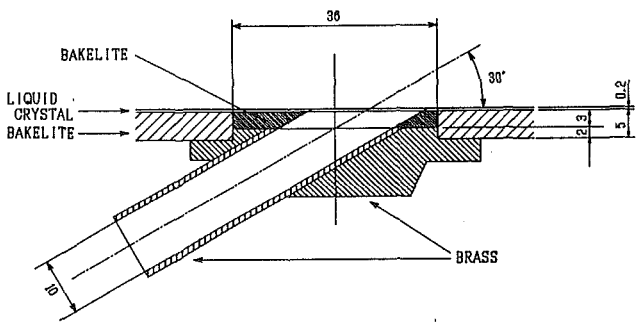

Fig. 1(*b*) Cross section of injection hole

Contributed by the International Gas Turbine Institute and presented at the 37th International Gas Turbine and Aeroengine Congress and Exposition, Cologne, Germany, June 1-4, 1992. Manuscript received by the International Gas Turbine Institute February 17, 1992. Paper No. 92-GT-180. Associate Technical Editor: L. S. Langston.

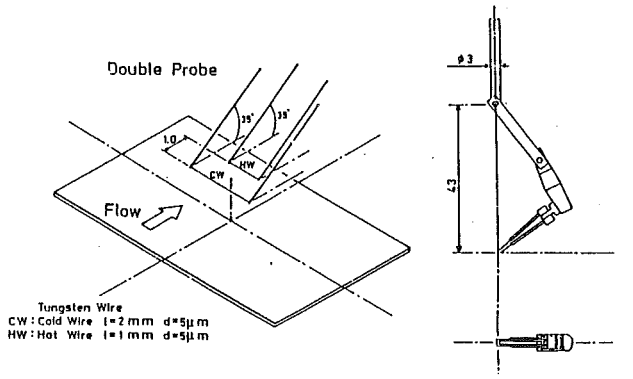

Fig. 2 Double-wire probe

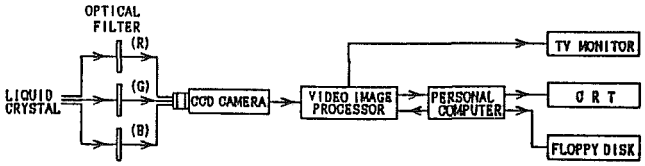

Fig. 3 Image processing system

standing of the injected jet behavior and its film-cooling effectiveness in lateral injection with mass flux ratio varied. The present paper provides detailed data of both velocity/temperature fields within the injected jet and temperature field on the surface in lateral (spanwise) injection from a row of the holes. Emphasis is placed on the measurement of the velocity/temperature fields in the jet by using a double-wire probe, i.e., a constant-temperature type of hot-wire anemometer and a constant current type of thermo-resistance meter. Another measurement also focuses on the temperature fields on the surface, i.e., film-cooling effectiveness from the image processing of temperature sensitive liquid crystal. The results obtained for the three mass flux ratios of 0.5, 0.85, and 1.2 will be discussed.

Experimental Apparatus and Techniques

Figure 1(*a*) shows a schematic of the experimental test rig. A two-dimensional 10:1 contraction nozzle is followed by a flat surface test section of 900 mm in length, 600 mm in width, and 100 mm in height. The tripping wire was installed at the inlet of the flat surface to provide a turbulent boundary layer over the test region.

Figure 1(*b*) shows a cross section of an injection hole looking downstream. Five holes in a row spaced five hole diameters apart are located 430 mm downstream of the trip. The hole pitch of five was selected, since a wide spread of the injectant is expected in lateral injection. A row of injection holes having a diameter of 10 mm is arranged at a pitching angle of 30 deg to the surface and an injection angle of 90 deg to the streamwise direction. The secondary air is injected at a higher temperature than the primary stream as in many studies of film cooling. The injected air is heated through the brass tube wrapped with a ribbon type of nickel-chrome heater and insulator.

Figure 2 shows a double-wire probe. It provides simultaneous velocity and temperature measurements by a constant-temperature hot-wire anemometer with a tungsten wire 5 μm in diameter and 1 mm in length and a constant current thermo-resistance meter with a tungsten wire 5μm in diameter and 2 mm in length. Temperature compensation of the hot wire was made by an output voltage of the thermo-resistance meter. The injected air temperature was maintained 55 K above that of the primary stream.

Figure 3 shows an image processing system by taking the image of the thermotropic liquid crystal by a black and white CCD camera. The test surface was covered with a thin sheet of encapsulated temperature-sensitive liquid crystal to visualize

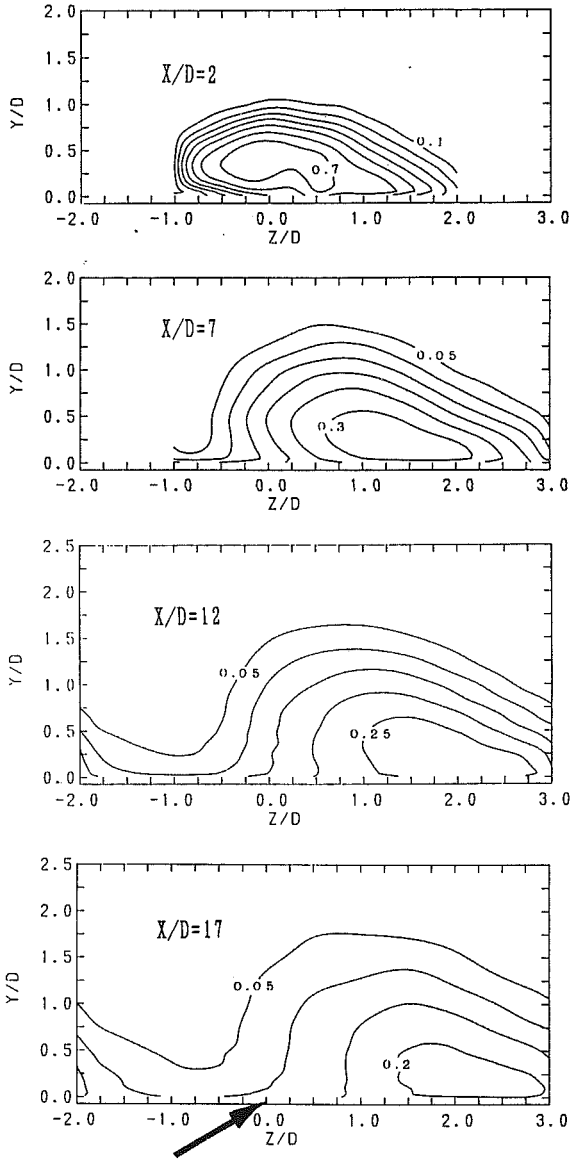

Fig. 4(*a*) $M = 0.50$

Nomenclature

D = injection hole diameter
I = momentum flux ratio = $\rho_2 U_2^2/\rho_\infty U_\infty^2$
M = mass flux ratio = $\rho_2 U_2/\rho_\infty U_\infty$
T = time-averaged temperature
U = time averaged velocity
X, Y, Z = coordinate, see Fig. 1(*a*)
θ = nondimensional temperature = $(T-T_\infty)/(T_2-T_\infty)$
ϕ = injection angle to streamwise direction

Subscripts

∞ = primary stream
2 = secondary injected jet
w = surface

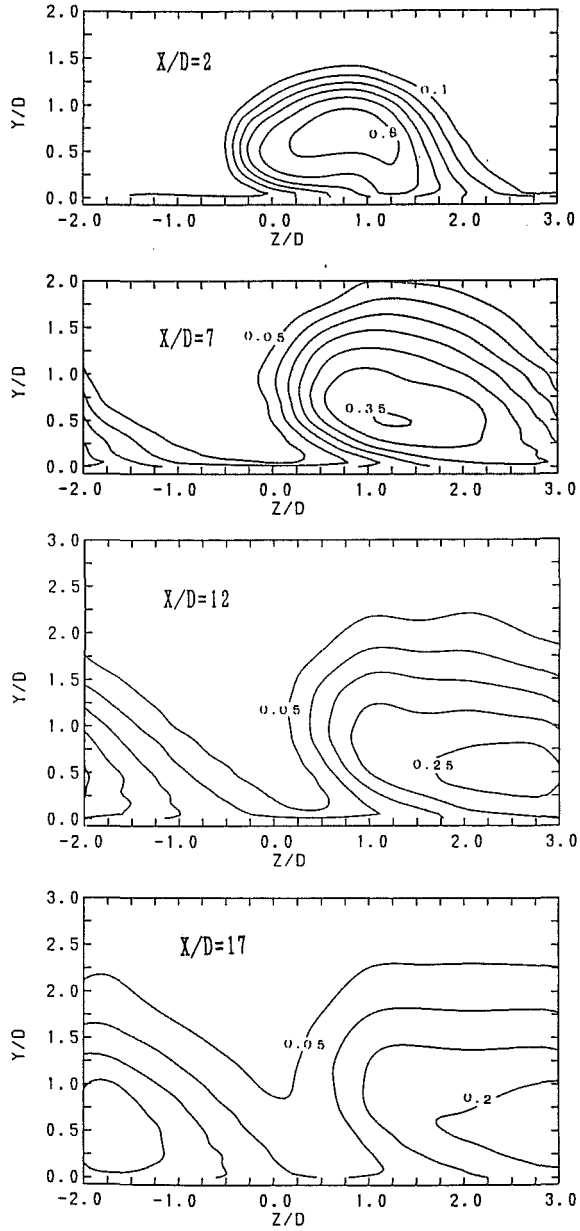

Fig. 4(*b*) $M = 0.85$

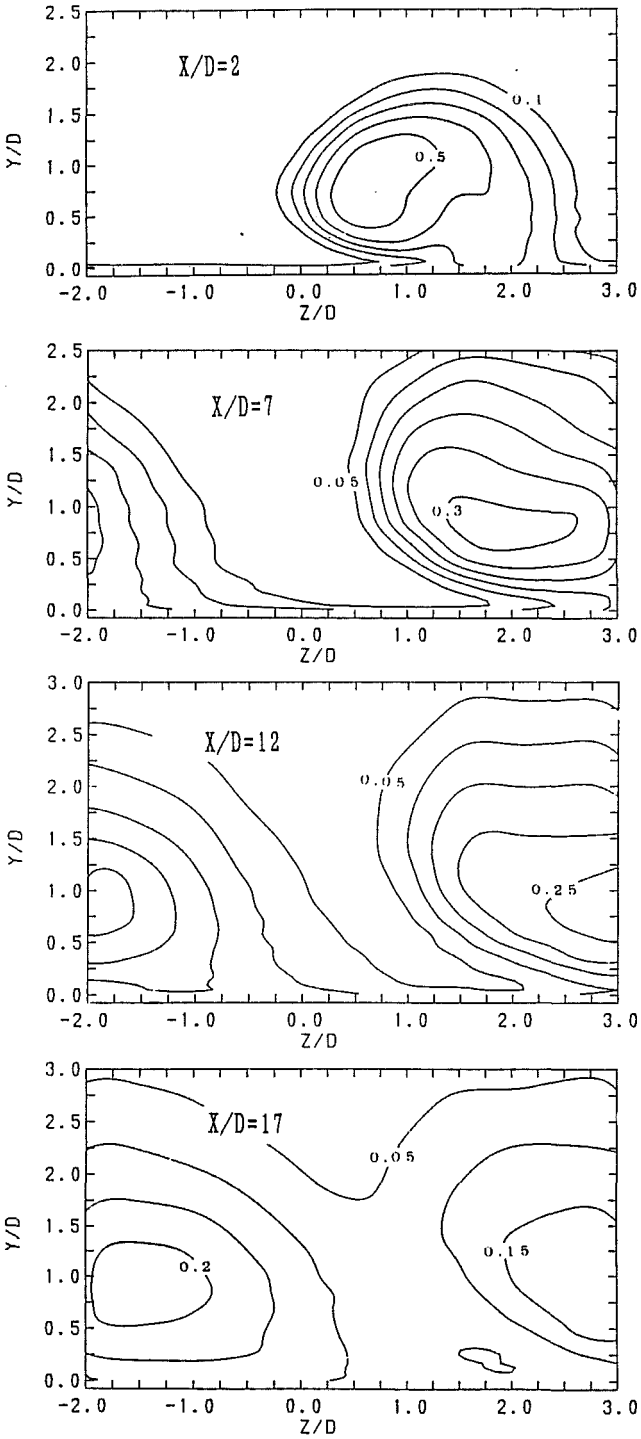

Fig. 4(*c*) $M = 1.2$

Fig. 4 Time-averaged temperature contours, θ

Table 1 Experimental conditions

Mass flux ratio	Density ratio	Momentum flux ratio
0.50	0.85	0.294
	0.95	0.263
0.85	0.85	0.850
	0.95	0.761
1.20	0.85	1.694
	0.95	1.516

the surface temperature fields. The individual image data of three principal colors were taken through the camera with three kinds of optical filter resolved into red, green, and blue. The hue is obtained through the reduction process of the data above; noise is eliminated by a spatial filter by using an image processor and a personal computer. The image processor with high resolution of 512 by 512 pixels and intensity resolution of 8 bits was employed. The hue and temperature calibration for the liquid crystal was conducted at the outlet of the calibration wind tunnel in which the air temperature can be controlled by a heater. The temperature of the injected air is 18 K above the fluid temperature of the primary stream because of the limitation of measurable range of the liquid crystal.

All the tests were conducted in the primary air with the free-stream velocity of 13.5 m/s. The momentum thickness Reynolds number at the test section is 1100. The ratio of displacement thickness to the injection hole diameter is 0.18–0.20 at the test section. Table 1 shows the test condition of the secondary injected air and the primary stream. The density ratio is kept constant at 0.85 for the double-wire measurement and at 0.95 for the liquid crystal one.

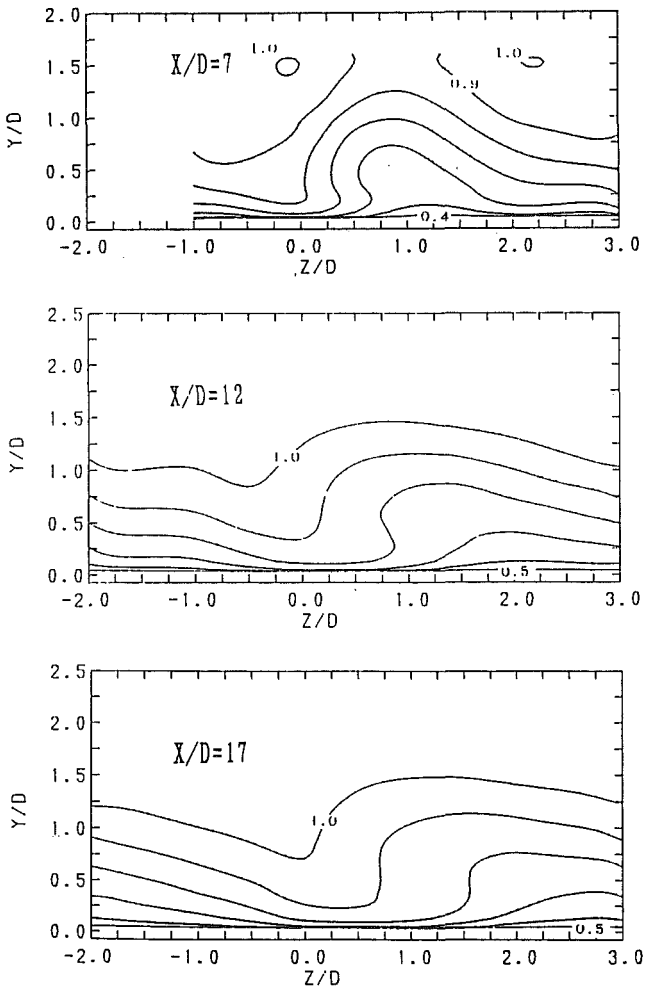

Fig. 5(*a*) M = 0.50

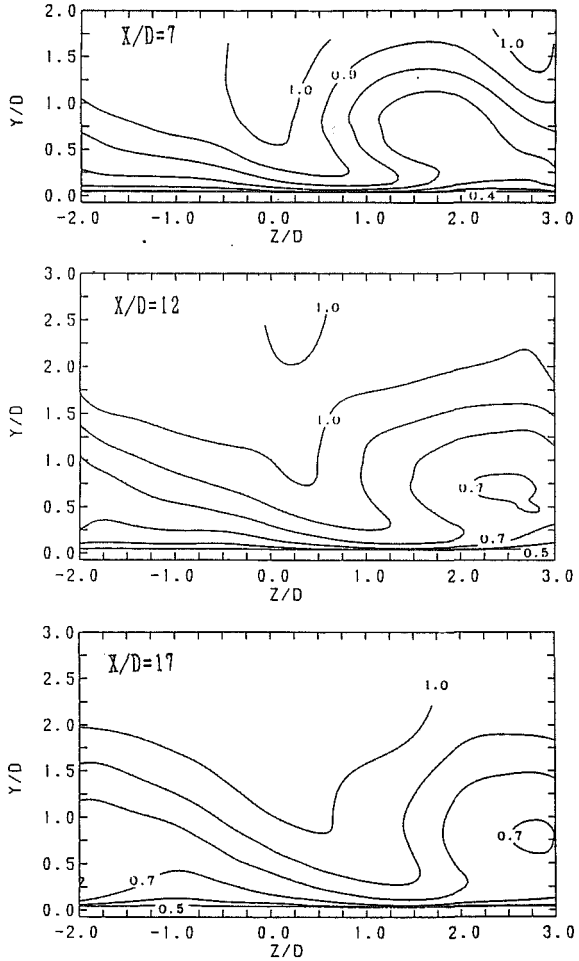

Fig. 5(*b*) M = 0.85

Results and Discussion

Temperature Profiles in the Jet. Figure 4 shows contours of the nondimensional time-averaged temperature measured by the double-wire probe for different mass flux ratios. The injection hole center is located at $Z = 0$ in the figure. An arrow indicates the injected jet orientation at the hole. The pattern of isotherms shows asymmetry with respect to the jet center in lateral injection. The primary stream with low temperature penetrates into the bottom of the jet in the left side of the injected jet looking downstream, whereas no penetration of the low-temperature fluid occurs in the right side.

Such asymmetry is maintained in the downstream direction. The peak temperature in the jet center decreases rapidly near the injection hole and more slowly in the farther downstream region. For higher mass flux ratio, the injected jet lifts up into the primary stream. The primary stream penetrates deeply into the left side of the jet and the jet bottom in the right side still remains near the surface. The high-temperature region in the jet center among the different mass flux ratios near the injection hole is located near the surface for low mass flux ratio, but far from the surface for higher mass flux ratio. In particular, it is observed in the upper left side at mass flux ratio of 1.2.

Velocity Profiles in the Jet. Figure 5 shows the time-averaged velocity contours, U/U_∞. The data at $X/D = 2$ were discarded, since the injected jet was forced to change from lateral to streamwise direction of the flow by the primary stream near the hole, and then the single hot wire was not suitable for the measurement in the highly three-dimensional flow field with high turbulence intensity. The profiles show asymmetry with respect to the jet center as in the temperature profiles, although asymmetry was not so clear as the temperature ones for low mass flux ratio. The local, high-velocity region is observed around the jet, because the primary stream is accelerated by getting over the injected jet. At the farther downstream station, boundary layer becomes thin in the left side of the jet. As the mass flux ratio is increased, the local acceleration of the primary stream and the thinning of the boundary layer are promoted. The injected jet shows the isolated contours that correspond to the jet center, since the location of the locally low velocity region coincides with that of the locally high temperature region, i.e., the jet center.

Compton and Johnston (1992) obtained velocity vector and velocity contours in the experiments of the vortex generator jet, as shown in Fig. 6. Their experiment is almost the same as the present one, except for the pitching angle of 45 deg and the hole diameter of 6.35 mm. They observed a clear vortex motion in the laterally injected jet at the velocity ratio of 1.0, which corresponds to a mass flux ratio of 0.85 in the present experimental condition, the density ratio being 0.85. They also found that the maximum vorticity became large with increasing velocity ratio, VR, from 0.7 to 1.3. The jet boundary indicated asymmetry like the present injected jet. The maximum vorticity levels were strongly dependent on the velocity ratio, VR, and

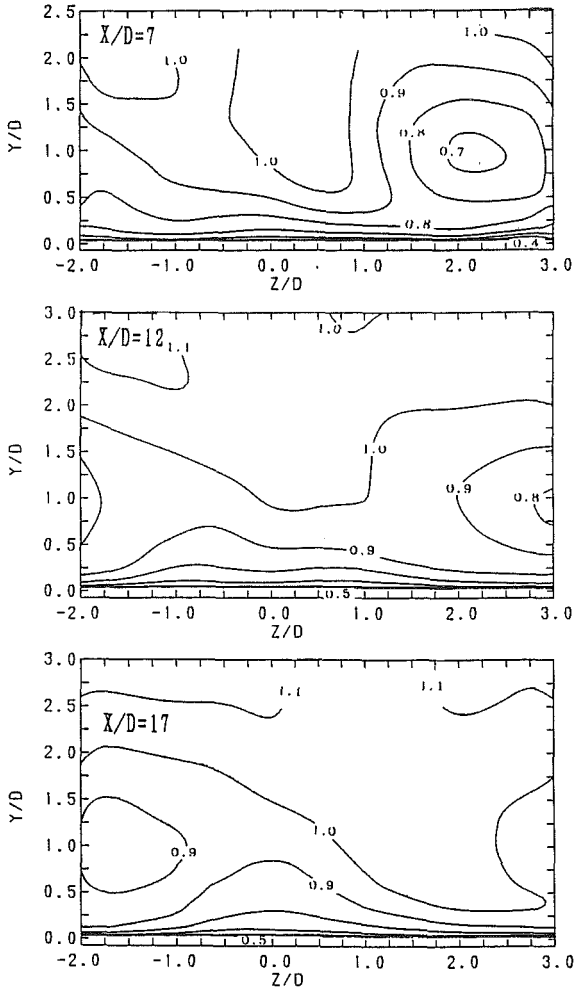

Fig. 5(c) $M = 1.2$

Fig. 5 Time-averaged velocity contours, U/U_∞

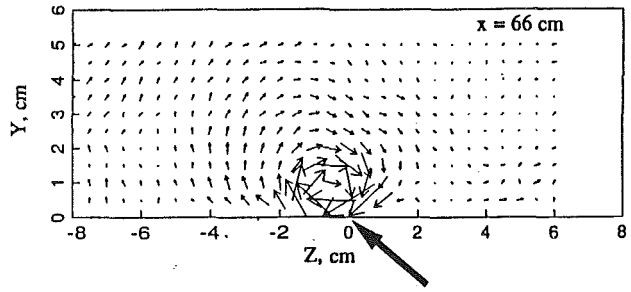

(a) Secondary velocity vectors for VR=1.0. Large arrow indicates jet orientation.

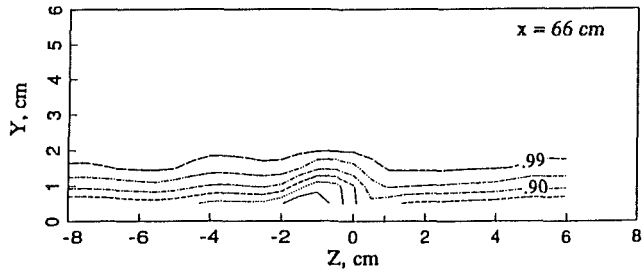

(b) U/U_∞ contours. Intervals are by 0.05, except the final contour, which is located at boundary layer edge.

Fig. 6 Experiment of vortex generator jet from Fig. 2 by Compton and Johnston (1991)

a skew angle, which was the injection angle in the present paper. An optimal skew angle that might offer the best performance in suppression of separation, in other words, strong vortex motion, might be between 45 and 90 deg.

As a result, a large scale of one vortex motion was confirmed in the laterally injected jet by Compton's experiment. It is shown through comparison with their result that the jet behavior is dependent on the vortex intensity induced by the primary stream, i.e., the vorticity in the jet. Hence, the primary stream promotes the vortex motion in the left side of the jet and suppresses it in the right side. This vortex motion causes the injected jet to detach from the surface with increased mass flux ratio.

Surface Temperature Profiles. Figure 7 shows the temperature contours on the surface of the test section in lateral injection. The nondimensional surface temperature corresponds to film cooling effectiveness, since the definition is the same as each other. The direction of the injection is in the positive spanwise z-direction. The broad band of the temperature contours of 0.2 is observed due to the calibration of the liquid crystal in which the curve has a weak sensitivity to temperature in this temperature range. The high-temperature region is located in the positive spanwise direction as the mass flux ratio becomes large. The injected jet for mass flux ratio of 0.5 covers the wide region of higher temperature, while the low temperature region is obtained for the high mass flux ratio of 1.2.

The locally low temperature region is observed near the injection hole, i.e., $X/D = 1$ and $Z/D = -1$, even though the effect of the thermal conductivity near the injection hole is considered because of the thinner insulator than that of the test surface, as shown in Fig. 1(*b*). This feature becomes more marked with increasing the mass flux ratio. The sharp kink of isotherms of $\theta = 0.35$ for mass flux ratio of 0.5, and $\theta = 0.30$ for mass flux ratio of 0.85 and 1.2, are shown in the figures.

Injected Jet Behavior. Figure 8 shows the combined temperature fields obtained from the measurements by the double-wire probe and the liquid crystal. The near-surface temperature in the injected jet measured by the probe corresponds to the surface temperature distribution by the liquid crystal. Maximum surface temperature shifts in the spanwise direction as the jet proceeds in the downstream direction. The spanwise location of the maximum temperature in the jet deviates from the geometric center of the jet with increasing mass flux ratio, because the rolling down of the primary stream results in the low surface temperature in the downwash region of the left side of the jet. But the high surface temperature is obtained in the right side due to the attached jet without the vortex motion. The exact behavior of the injected jet could not be expected from only the measurement of the surface temperature field in lateral injection. Furthermore, the isothermal line downstream of the hole shows a large kink, as mentioned before. This is more evidence that the rolling down of the mainstream beyond the injected jet occurs close to the injection hole. Such behavior of the jet produces a local change in film-cooling effectiveness, and causes damage of the blade material near the hole because of unexpected thermal stress. It is worth noting that the asymmetric feature of the laterally injected jet is easily understood by the combined results on the temperature measurements on the surface and within the injected jet.

Figure 9 shows a sketch of the jet behavior and the interaction of the jet and the primary stream based on the results

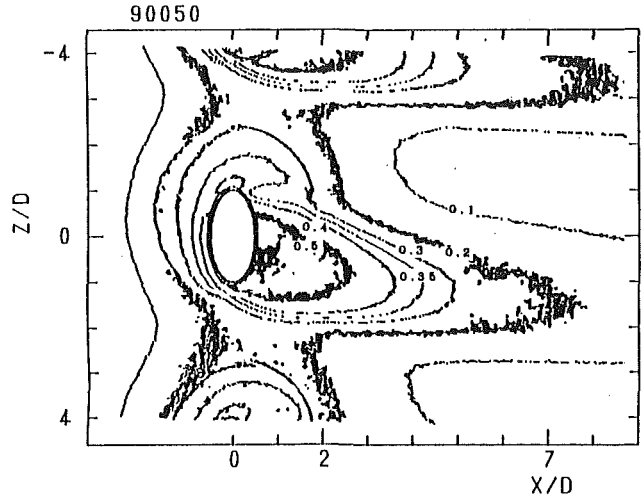

(a) M = 0.50

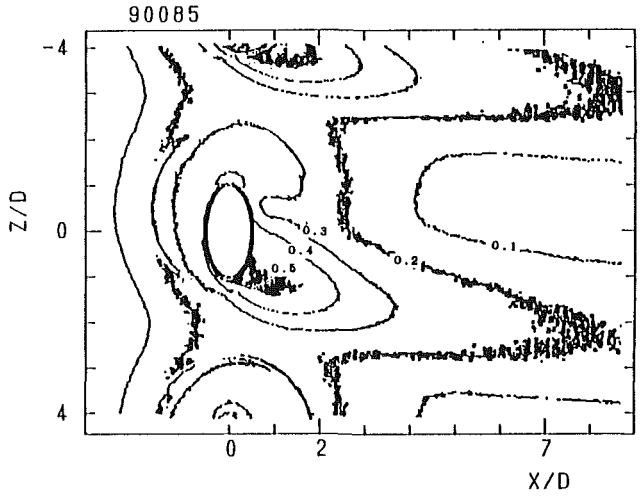

(b) M = 0.85

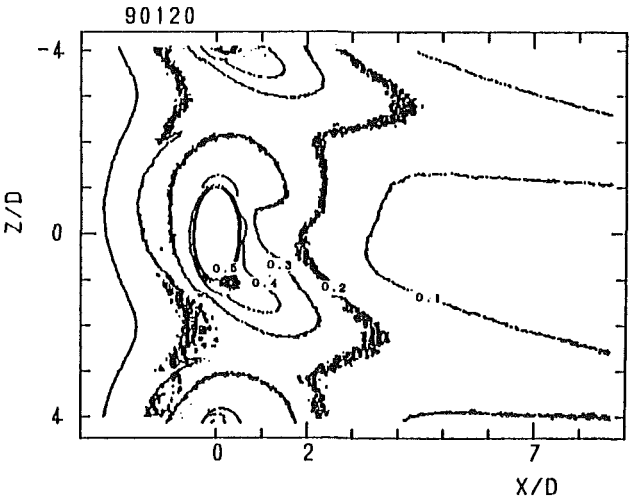

(c) M = 1.2

Fig. 7 Temperature contours on the surface

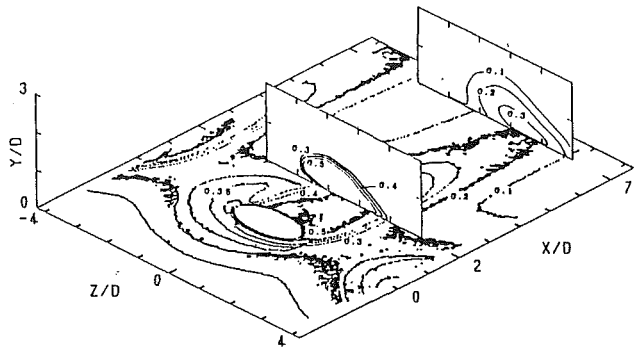

(a) M = 0.50

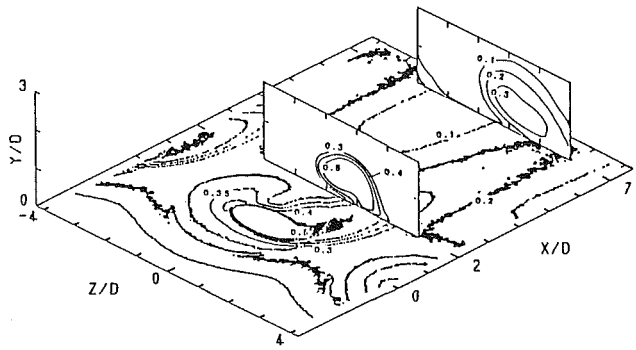

(b) M = 0.85

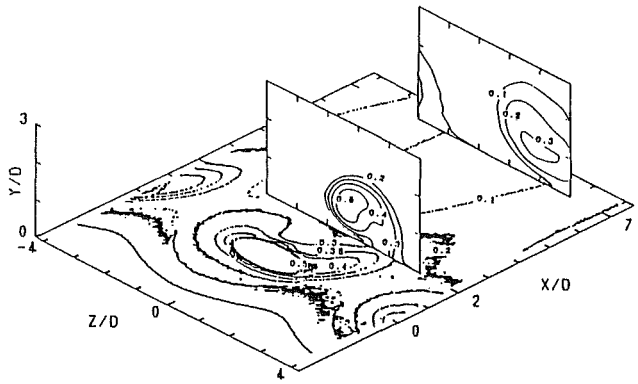

(c) M = 1.2

Fig. 8 Time-averaged temperature field

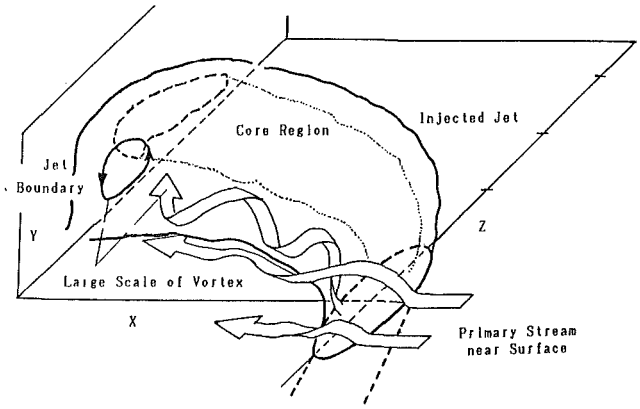

Fig. 9 Jet behavior in lateral injection for low mass flux ratio

obtained from the above-mentioned measurements for low mass flux ratio. Goldstein et al. (1970) showed the flow field associated with a laterally inclined jet with a large-scale, two-vortex structure. The laterally injected jet observed by the present experiment has the asymmetric structure with a large-scale, one-vortex motion promoted by the primary stream in the left side of the jet. The question is why the vortex motion cannot be observed in the right side as in streamwise injection. It may be considered that a skewed boundary layer develops on the surface close to the hole because of strong streamline curvature of the jet, and then the vorticity in the skewed boundary layer is canceled by the rolling up of the primary stream in the right side because of the opposite sign of the vorticity. Therefore, understanding of such features results in improvements in film-cooling performance. The suppression of the vortex motion in the left side is a key technology to obtain a higher film-cooling effectiveness, besides the wide spread of the jet in the spanwise direction with the mass flux ratio increased.

Conclusions

Detailed measurements of the laterally injected jet on the velocity/temperature field by a hot-wire anemometer and a thermo-resistance meter and the surface temperature field by the temperature-sensitive liquid crystal were conducted. The following conclusions were obtained:

1 The laterally injected jet has an asymmetric structure with a large-scale vortex motion promoted by the primary stream on one side of the jet, but suppressed on the other side.

2 There is a little contribution to the film-cooling on one side with the vortex motion, whereas high film-cooling effectiveness is obtained on the other side.

3 The asymmetric structure in lateral injection is promoted with mass flux ratio increased, resulting in low film-cooling effectiveness.

Acknowledgements

We wish to thank Messrs. M. Kayama, H. Maseda, A. Namie, and M. Yamamoto who assisted in the data acquisition. We also acknowledge the help of Mr. Y. Tanaka, who constructed the data reduction system of the image processing.

References

Compton, D. A., and Johnston, J. P., 1992, "Streamwise Vortex Production by Pitched and Skewed Jets in a Turbulent Boundary Layer," AIAA *Journal*, Vol. 30, pp. 640–647.

Goldstein, R. J., Eckert, E. R. G., Eriksen, V. L., and Ramsey, J. W., 1970, "Film Cooling Following Injection Through Inclined Circular Tubes," *Israel Journal of Technology*, Vol. 8, pp. 145–154.

Honami, S., and Fukagawa, M., 1987, "A Study on Film Cooling Behavior of a Cooling Jet Over a Concave Surface," *Proceedings of 1987 Tokyo International Gas Turbine Congress*, Vol. 3, pp. 209–216.

Ligrani, P. M., Subramanian, C. S., Craig, D. W., and Kaisuwan, P., 1991, "Effects of Vortices With Different Circulations on Heat Transfer and Injectant Downstream of a Single Film-Cooling Hole in a Turbulent Boundary Layer," ASME JOURNAL OF TURBOMACHINERY, Vol. 113, pp. 433–441.

Sinha, A. K., Bogard, D. G., and Crawford, M. E., 1991, "Film-Cooling Effectiveness Downstream of a Single Row of Holes With Variable Density Ratio," ASME JOUNRAL OF TURBOMACHINERY, Vol. 113, pp. 441–449.

Heat Transfer in Rotating Serpentine Passages With Trips Skewed to the Flow

B. V. Johnson

J. H. Wagner

United Technologies Research Center,
East Hartford, CT 06108

G. D. Steuber
Pratt & Whitney,
East Hartford, CT 06108

F. C. Yeh
NASA Lewis Research Center,
Cleveland, OH 44135

Experiments were conducted to determine the effects of buoyancy and Coriolis forces on heat transfer in turbine blade internal coolant passages. The experiments were conducted with a large-scale, multipass, heat transfer model with both radially inward and outward flow. Trip strips, skewed at 45 deg to the flow direction, were machined on the leading and trailing surfaces of the radial coolant passages. An analysis of the governing flow equations showed that four parameters influence the heat transfer in rotating passages: coolant-to-wall temperature ratio, rotation number, Reynolds number, and radius-to-passage hydraulic diameter ratio. The first three of these four parameters were varied over ranges that are typical of advanced gas turbine engine operating conditions. Results were correlated and compared to previous results from similar stationary and rotating models with smooth walls and with trip strips normal to the flow direction. The heat transfer coefficients on surfaces, where the heat transfer decreased with rotation and buoyancy, decreased to as low as 40 percent of the value without rotation. However, the maximum values of the heat transfer coefficients with high rotation were only slightly above the highest levels previously obtained with the smooth wall model. It was concluded that (1) both Coriolis and buoyancy effects must be considered in turbine blade cooling designs with trip strips, (2) the effects of rotation are markedly different depending upon the flow direction, and (3) the heat transfer with skewed trip strips is less sensitive to buoyancy than the heat transfer in models with either smooth walls or normal trips. Therefore, skewed trip strips rather than normal trip strips are recommended and geometry-specific tests will be required for accurate design information.

Introduction

Advanced gas turbine airfoils are subjected to high heat loads that require escalating cooling requirements to satisfy airfoil life goals. The efficient management of cooling air dictates detailed knowledge of local heat load and cooling air flow distribution for temperature and life predictions. However, predictions of heat transfer and pressure loss in airfoil coolant passages currently rely primarily on correlations derived from the results of stationary experiments. Adjustment factors are usually applied to these correlations to bring them into nominal correspondence with engine experience. This is unsatisfactory when blade cooling conditions for new designs lie outside the range of previous experience.

Rotation of turbine blade cooling passages gives rise to Coriolis and buoyancy forces, which can significantly alter the local heat transfer in the internal coolant passages due to the development of cross-stream (Coriolis) as well as radial (buoyant) secondary flows. Buoyancy forces in gas turbine blades are substantial because of high rotational speeds and coolant temperature gradients. Earlier investigations (Eckert et al., 1953) with stationary, single pass, co- and counterflowing coolant passages indicated that there can also be substantial differences in the heat transfer when the buoyancy forces are aligned with or counter to the forced convection direction. A better understanding of Coriolis and buoyancy effects and the capability to predict the heat transfer response to these effects will allow the turbine blade designer to achieve cooling configurations that utilize less flow and reduce thermal stresses in the airfoil.

An extensive analytical and experimental program was originated and sponsored by NASA at the Lewis Research Center as part of the Hot Section Technology (HOST) program. The objectives of this program were (1) to gain insight regarding the effect of rotation on heat transfer in turbine blade passages, (2) to develop a broad data base for heat transfer and pressure drop in rotating coolant passages, and (3) to improve computational techniques and develop correlations that can be useful to the gas turbine industry for turbine blade design. The attainment of these objectives became even more critical with

Contributed by the International Gas Turbine Institute and presented at the 37th International Gas Turbine and Aeroengine Congress and Exposition, Cologne, Germany, June 1-4, 1992. Manuscript received by the International Gas Turbine Institute February 17, 1992. Paper No. 92-GT-191. Associate Technical Editor: L. S. Langston.

the advent of the Integrated High Performance Turbine Engine Technology (IHPTET) initiative. As part of the IHPTET goal, the turbine would operate at near stoichiometric, i.e., 2200–2500 K (3500–4000°F) inlet temperatures, maintain efficiencies in the 88–94 percent range, and require total coolant flows of only 5 percent of the engine air flow rate (Ref. IHPTET Brochure, circa 1984). To attain these ambitious goals, a thorough understanding of the rotational effects of heat transfer and flow in turbine blade coolant passages is mandatory.

Previous Studies. Heat transfer experiments in multiple-pass coolant passages with skewed trips have been conducted in stationary models by several investigators to obtain a data base for the thermal design of gas turbine airfoils, e.g., Boyle (1984), Han et al. (1986), Metzger et al. (1988). These data bases are directly applicable to the cooling designs of stationary vanes. However, the effects of Coriolis forces and buoyancy, due to the large rotational gravity forces (up to 50,000 g), are not accounted for.

The complex coupling of the Coriolis and buoyancy forces has prompted many investigators to study the flow field generated in unheated, rotating circular and rectangular smooth wall passages without the added complexity of buoyancy, i.e., Moore (1967), Hart (1971), Wagner and Velkoff (1972), and Johnston et al. (1972). These investigators have documented strong secondary flows and have identified aspects of flow stability that produce streamwise oriented, vortex-like structures in the flow of rotating radial passages. The effect of rotation on the location of flow reattachment after a backward facing step was presented by Rothe and Johnston (1979). This work was especially helpful in understanding the effects of rotation on heat transfer in passages with normal trips. However, the secondary flow patterns associated with skewed trips and Coriolis forces can produce additional complex interactions.

The combined effects of Coriolis and buoyancy forces on heat transfer have been studied by a number of investigators during the past twenty years. Heat transfer experiments in rotating models with smooth walls has been reported by Wagner et al. (1991a, 1991b), Guidez (1989), Iskakov and Trushin (1983), Morris (1981), Morris and Ayhan (1979), Lokai and Gunchenko (1979), Johnson (1978), and Mori et al. (1971). Heat transfer experiments in rotating models with normal trips have been reported by Wagner et al. (1992) and Taslim et al. (1991a). Heat transfer in a rotating model with criss-cross skewed trips was recently reported by Taslim et al. (1991b). Large increases and decreases in local heat transfer from smooth walls or walls with trips were found by some investigators under certain conditions of rotation while other investigators showed lesser effects. Analysis of these results does not show consistent trends. The inconsistency of the previous results is attributed to differences in the measurement techniques, models, and test conditions.

Objectives. Under the NASA HOST program, a comprehensive experimental project was formulated to identify and separate effects of Coriolis and buoyancy forces for the range of dimensionless flow parameters encountered in axial flow, aircraft gas turbines. The specific objective of this experimental project was to acquire and correlate benchmark-quality heat transfer data for a multipass, coolant passage under conditions similar to those experienced in the blades of advanced aircraft gas turbines. A comprehensive test matrix was formulated, encompassing the range of Reynolds numbers, rotation numbers, and density ratios expected in modern gas turbine engines.

The results presented in this paper are from the third phase of a three-phase program, directed at studying the effects of rotation on a multipass model with smooth and rough wall configurations. The first phase utilized the smooth wall configuration. Initial results for outward flow in the first passage were previously presented by Wagner et al. (1991a). The effects of flow direction and buoyancy with smooth walls were presented by Wagner et al. (1991b). The second phase utilized a configuration with normal trips on the leading and trailing surfaces of the straight passages and were presented by Wagner et al. (1992). The heat transfer results with normal trips showed that large decreases in heat transfer could occur on certain surfaces due to rotation and that the heat transfer coefficients could also have a large sensitivity to buoyancy. The present paper covers the phase with surface roughness elements oriented at 45 deg to the flow direction. Comparisons will be made with the results for smooth walls and the walls with normal trips in the same model and with concurrent rotating and stationary experiments employing trips skewed to the flow direction.

The results from the present work will show that large decreases in heat transfer coefficients can occur due to rotation. However, the heat transfer coefficients for the model with skewed trips show much less sensitivity to buoyancy than the results from the models with either smooth walls or normal trips. Physical models to account for these heat transfer characteristics will be proposed in the discussion herein.

The facility, data acquisition, and data reduction techniques employed in this experiment were discussed in the Wagner et al. (1991a) paper and will not be repeated. However, the description of the model will be repeated for the convenience of the reader.

Description of Experimental Equipment

Heat Transfer Model. The heat transfer model was designed to simulate the internal multipassage geometry of a cooled turbine blade (Fig. 1). The model consists of three straight sections and three turn sections, which were instrumented, followed by one uninstrumented straight section, as shown in Fig. 2. The model orientations with respect to the

Nomenclature

A = area of passage cross section
d = hydraulic diameter
e = trip height
Gr = rotational Grashof number
h = heat transfer coefficient
J = rotational Reynolds number
k = thermal conductivity
m = mass flow rate
Nu = Nusselt number = hd/k
P = trip spacing, i.e., pitch
R = local radius
Re = Reynolds number = $(md/(\mu A)$
Ro = Rotation number = $\Omega d/V$
T = temperature
V = mean coolant velocity
X = streamwise distance from inlet
μ = absolute viscosity
ν = kinematic viscosity
ρ = coolant density
$\Delta\rho/\rho$ = density ratio = $(\rho_b - \rho_w)/\rho_b$
Ω = rotational speed

Subscripts

b = bulk property
f = film property
i = inlet to model
w = heated surface location
∞ = fully developed, smooth tube

Superscripts

$-$ = average
$'$ = distance from beginning of second passage
$''$ = distance from beginning of third passage

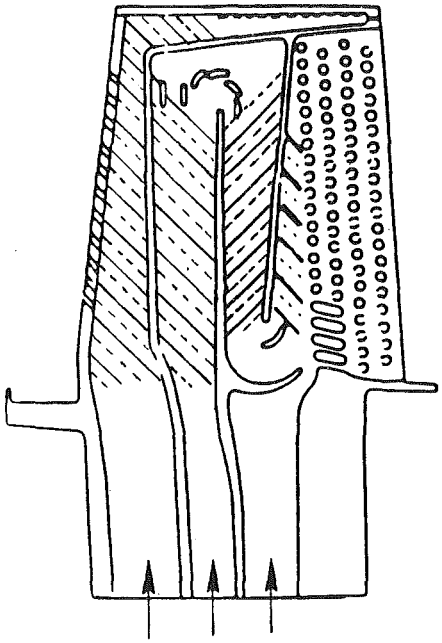

Fig. 1 Typical coolant passage configuration for aircraft gas turbine rotating airfoils

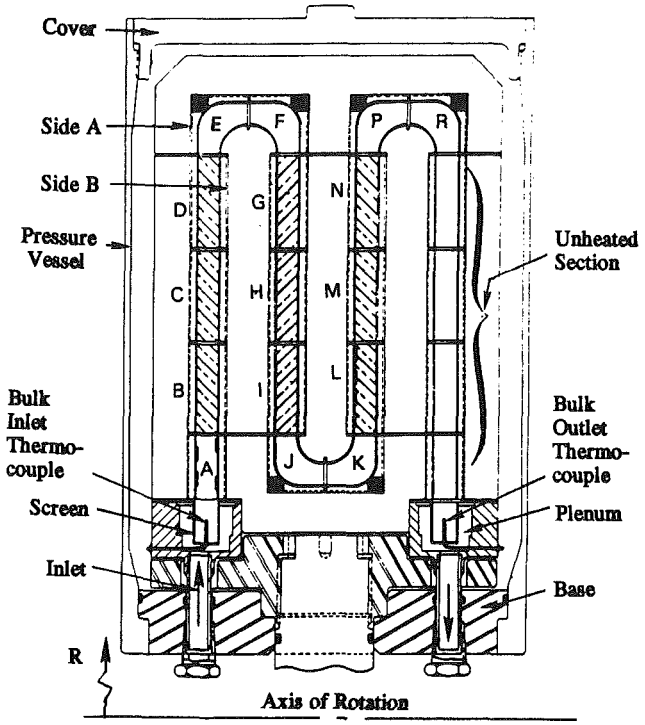

Fig. 2 Cross-sectional view of coolant passage heat transfer model assembly with skewed trip rough walls; view through center of model toward leading surfaces with $\Omega > 0$, dotted ribs show locations on the trailing surfaces

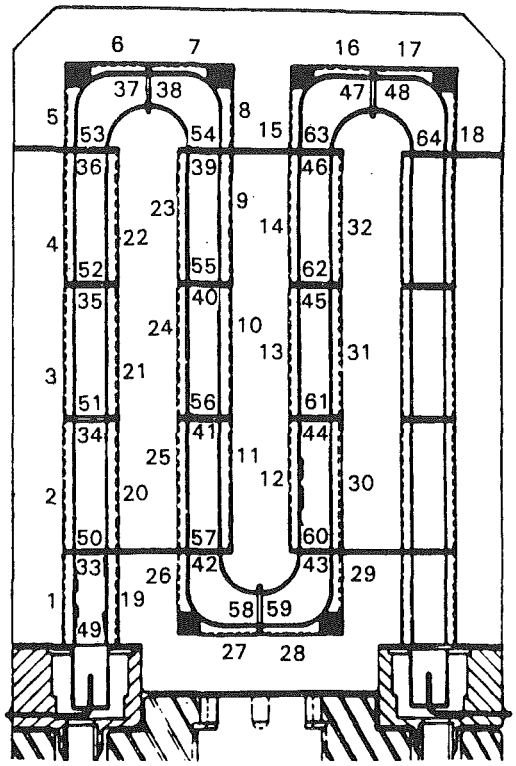

Fig. 3(*a*) Cross-sectional view of test surface identification plan for coolant passage heat transfer; side wall test section surfaces 1-32 are in plane perpendicular to view shown, test section surfaces 33-48 are on "$+\Omega$" leading plane, test section surfaces 49-64 are on "$+\Omega$" trailing plane

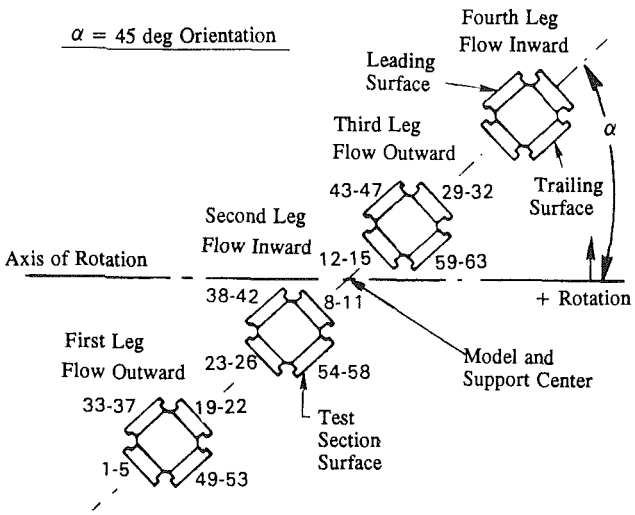

Fig. 3(*b*) Test surface identification plan for coolant passage heat transfer; view from outer turn sections

rotational centerline for $\alpha = 45$ deg are shown in Fig. 3(*b*). Data presented herein were obtained in the first, second, and third passages with radially outward, inward, and outward flows, respectively. The model passages are approximately square with a characteristic dimension of 12.7 mm (0.5 in.). Four elements form the walls of the square coolant passage at each streamwise location. The heated length of the first passage is 14 hydraulic diameters and is comprised of sixteen heated copper elements at four streamwise locations. The heated copper elements at the first streamwise location were all smooth walls and were used as guard heaters.

The cross-sectional views of Figs. 2 and 3 show the orientation of the leading, trailing, and sidewall surfaces. The streamwise locations, *A* through *R*, are shown in Fig. 2. The test surface identification plan for each heated surface is shown in Figs. 3(*a*) and 3(*b*). Each copper element is heated on the side opposite the test surface with a thin film, 0.1 mm (0.003 in.), resistance heater. Each element is 3.8 mm (0.150 in.) thick and is thermally isolated from surrounding elements by 1.5 mm (0.060 in.) thick fiberglass insulators. The insulating material separating the copper elements at each streamwise lo-

cation resulted in a 1.0 mm (0.04 in.) chamfer in the corners, which yielded a hydraulic diameter, d, in the straight sections of 13.2 mm (0.518 in.). The radius at the center of the heat transfer test sections with trips, i.e., average model radius, was 663 mm (26.1 in.). The power to each element was adjusted to obtain an isothermal wall boundary condition. In practice, temperature differences less than 1°C (2°F) were achieved. The heat flux between the elements with a 1°C (2°F) temperature difference was estimated to be less than 2 percent of a typical stationary surface-to-coolant heat flux.

Trips strips were machined in a staggered pattern on the leading and trailing surfaces of the 152.4 mm (6 in). straight length of each passage as shown in Fig. 2. No trips were on the Side A or Side B walls or on the guard elements ($X/d<3$) in the first passage. The height ($e/d=0.1$), shape (circular), and streamwise spacing or pitch ($P/e=10$) of the trips are typical of the trips cast on the coolant passage walls of turbine blades.

Testing was conducted with air at dimensionless flow conditions typical of advanced gas turbine designs in the Rotating Heat Transfer Laboratory at United Technologies Research Center. The required dimensionless rotation numbers were obtained with rotation rates of 875 rpm or less by operating the model at a pressure of approximately 10 atm. The model inlet air temperature was typically 27°C (80°F) and the copper elements were held at 49°C, 71°C, 93°C, 116°C (120°F, 160°F, 200°F, and 240°F) for coolant-to-wall temperature differences of 22°C, 44°C, 67°C and 89°C (40°F, 80°F, 120°F, and 160°F), respectively. Temperatures of the copper elements were measured with two chromel alumel thermocouples inserted in drilled holes in each element. Heat transfer coefficients were determined by performing an energy balance on each copper element to obtain the convective heat flux and the local coolant bulk temperature. The heat transfer coefficients were based on the projected are rather than the total heat transfer surface area due to trip geometry. The total heat transfer surface area for the test surfaces with trip strips was 1.15 times the projected area. See Wagner et al. (1991a) for additional information about the data reduction procedure.

Nusselt numbers and Reynolds numbers were calculated for each element. The fluid properties in the Nusselt and Reynolds numbers were evaluated at the film temperature, i.e., $T_f=(T_w+T_b)/2$. All of the heat transfer results presented herein have been normalized with a correlation for fully developed, turbulent flow in a smooth tube. The constant heat flux Colburn equation, adjusted for constant wall temperature, was used to obtain the Nusselt number for fully developed, turbulent flow in a smooth tube (Kays and Perkins, 1973). The resulting equation for the constant wall temperature condition with a Prandtl number equal to 0.72 is as follows:

$$\mathrm{Nu}_\infty = 0.0176\ \mathrm{Re}^{0.8}$$

An uncertainty analysis of the data reduction equations using the methods of Kline and McClintock (1953) showed that approximately 3/4 of the uncertainty in calculating the heat transfer coefficient was due to the measurement of temperatures in the model. The uncertainty of the heat transfer coefficient is influenced mainly by the wall-to-coolant temperature difference and the net heat flux from each element. Uncertainty in the heat transfer coefficient increases when either the temperature difference or the net heat flux decreases. For increasing X/d, the uncertainty increases because the wall-to-coolant temperature difference decreases. For low heat fluxes (i.e., low Reynolds numbers and on leading surfaces with rotation), the uncertainty in the heat transfer also increased. Estimates of the error in calculating heat transfer coefficient typically varied from approximately ±6 percent at the inlet to ±30 percent at the exit of the heat transfer model for the baseline stationary test conditions. The uncertainty in the lowest heat transfer coefficient on the leading side of the third passage with rotation is estimated to be 40 percent, primarily due to the uncertainty in the calculated bulk temperature. Although the uncertainty analysis was useful in quantifying the maximum possible uncertainty in calculating the heat transfer coefficient, multiple experiments at the same test condition were repeatable to within ranges smaller than those suggested by the analysis.

Results

Foreword. Heat transfer in stationary experiments with augmentation devices on the passage walls is primarily a function of the Reynolds number (a flow parameter), the streamwise distance from the inlet, X/d (a geometric parameter), and the geometry of the augmentation device. However, when rotation is applied, the heat transfer is also strongly influenced by the coupled effects of Coriolis and buoyancy and becomes asymmetric around the passage. An analysis of the equations of motion by Suo (1980, i.e., Appendix 10.1 of Hajek et al., 1991), similar to that of Guidez (1989), showed that the basic dimensionless fluid dynamic parameters governing the flow in a radial coolant passage were the Reynolds number, the rotation number, Ro, the fluid density ratio, $\Delta\rho/\rho$, and the geometric parameter, R/d. An alternate analysis of the equations of motion produces the rotational Reynolds number, $J=d\Omega^2/\nu$ as one of the governing parameters. Note also that Ro equals J/Re. Note that the rotation number, Ro is the reciprocal of the Rossby number, $V/\Omega d$, and governs the formation of cross-stream secondary flow due to Coriolis forces. The rotation number, Ro, the fluids density ratio, $\Delta\rho/\rho$, and the geometric parameter, R/d, appear in the governing equation as a buoyancy parameter. This buoyancy parameter, $(\Delta\rho/\rho)\ (R/d)(\Omega d/V)^2$, is similar to $\mathrm{Gr}/\mathrm{Re}^2$ for stationary heat transfer. The difference between our rotational buoyancy parameter and the stationary $\mathrm{Gr}/\mathrm{Re}^2$ is that $\Delta\rho/\rho=(T_w-T_b)/T_w$ rather than $\beta\Delta T=(T_w-T_b)/T_b$. The difference between the parameters decreases as T_w approaches T_b. Thus, with rotation, the heat transfer in the first passage is a function of three geometric parameters (surface roughness geometry, X/d, and surface orientation relative to the direction of rotation) and three flow parameters (Reynolds number, rotation number, and the buoyancy parameter). The heat transfer in the turns and other passages are functions of the aforementioned parameters and the serpentine geometry.

Due to the vector nature of the equations of motion, the combinations of buoyancy forces and the flow direction are expected to have a significant effect on the coolant flow and heat transfer (e.g., Eckert et al., 1953). In the parallel flow case, the flow is radially inward, coincident with buoyancy-driven flow for heated walls. For the counterflow case where the flow is radially outward, the flow direction is opposite to the direction of the buoyancy-driven flow. Flow direction (i.e., radially inward or outward) and a fixed radially outward directed force field, created by the rotating reference frame, establish the potential for parallel and counterflow situations.

The nomenclature used in the text for low and high-pressure surfaces is consistent with the leading to trailing side, Coriolis-generated, pressure gradients due to the secondary flows. In general, high-pressure surfaces have normal components of flow toward the surface while low-pressure surfaces have normal components of flow away from the surface. Therefore, trailing surfaces in the first passage with outward flow are on the high-pressure side of the passage. Similarly, leading surfaces in the second passage with inward flow are on the high-pressure side. For turbine airfoils, the leading surfaces of the coolant passage are adjacent to the suction side of the airfoil and the trailing surfaces of the coolant passage are adjacent to the pressure side of the airfoil.

The format of this paper is to show the effects of each of the primary variables (X/d, rotation number, density ratio) on the heat transfer about a baseline flow condition to develop

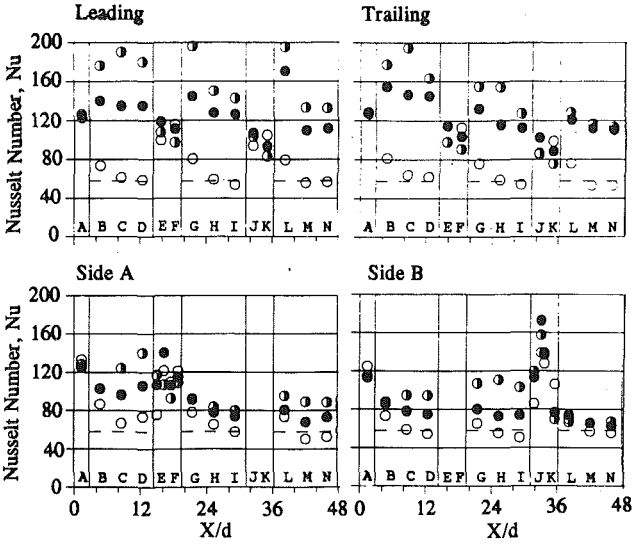

Fig. 4 Effect of trip configuration of heat transfer for stationary baseline flow conditions; $\Omega = 0$ rpm, Re = 25000, $R/d = 49$, $\alpha = 0$, $(\Delta\rho/\rho)_{in} = 0.13$, ○ —smooth wall, ● —normal trips, ◑ —skewed trips; - - - smooth wall correlation for Nu_∞, leading and trailing notation for $\Omega > 0$

an understanding of the cause/effect relationships. At the same time, the results for the skewed trips will be compared with results from smooth walls and walls with normal trips in the same test section. The entire body experimental results are then examined to determine the effects of the buoyancy parameter on the heat transfer in selected locations of the coolant passage. A complete set of results for the walls with trips is also available in a NASA contractor's report by Johnson et al. (1993).

Heat Transfer Results for Baseline Flow Conditions

The baseline experiments in the three instrumented passages had dimensionless flow conditions, which consisted of a Reynolds number of 25,000 and an inlet density ratio, $(\rho_b - \rho_w)/\rho_b = (T_w - T_b)/T_w$, of 0.13. The rotating baseline experiments had a rotation number, $\Omega d/V$, of 0.24 and a radius ratio at the average model radius, R/d, equal to 49. These values were selected because they are in the central region of the operating range of current large aircraft gas turbine engines.

Stationary Baseline Flow Conditions. Streamwise variations of Nusselt number for the stationary baseline test with skewed trips are shown in Fig. 4. The Nusselt numbers, (*a*) for fully developed, turbulent flow in a smooth tube with constant wall temperature (Kays and Perkins, 1973), (*b*) for the model with smooth walls (Wagner et al., 1991b) and (*c*) for the model with normal trips (Wagner et al., 1992), are shown for comparison. The heat transfer from the walls with skewed trips (denoted leading and trailing surface) in the first outward straight ($3 < X/d < 14$) passage have heat transfer coefficients more than three times the fully developed, smooth-wall correlation and more than 50 percent greater than that with normal trips. Note that the heat transfer coefficients on the leading and trailing surfaces with the skewed trips do not decrease significantly with X/d in the first passage as they did for the model with smooth walls. Some differences in heat transfer are observed between the leading and trailing surfaces for this stationary baseline condition. The exact cause of the difference is not known but may be due to the staggering of the trips on the two surfaces (Fig. 2).

The heat transfer coefficients on the side walls with smooth surfaces were less than those on the leading and trailing surfaces with trips. However, the heat transfer with either set of trips was 20 to 100 percent greater than with the smooth walls. This increase in heat transfer on the side walls was attributed to increased velocity due to blockage of the trips for $X/d = 4$ and to the increased turbulence level in the coolant passage for $X/d = 8$ and 12. Note also that the heat transfer from the test surfaces of Side A (Fig. 2) of the skewed trip model increases markedly at $X/d = 8$ and 12. This increase was attributed to the secondary flow, from the center of the coolant passage, with a colder temperature toward the sidewall with element numbers 1 through 4. The secondary flow was caused by the trips skewed at 45 deg to the flow direction. The heat transfer coefficients on the trip model with skewed trips are 10 to 30 percent greater than those on the model with normal trips. The model with skewed trips has approximately five percent greater surface area on the leading surface than the model with normal trips. Therefore most of the increase in heat transfer with skewed trips compared to that with normal trips is attributed to the changes in the flow characteristics.

The heat transfer coefficients measured in the remaining two passages (i.e., $20 < X/d < 31$) show similar characteristics. The heat transfer characteristics in the second passage are generally similar to those in the first passage with heat transfer on all walls for the model. The large increase in heat transfer on the leading side of the model at $X/d = 21$ (streamwise location *G*) and at $X/d = 38$ (streamwise location *L*) was attributed to the convection interaction of the secondary flow patterns in the first channel through the first 180 deg turn and the concentration of streamwise vorticity adjacent to the leading surface.

The heat transfer in the turn regions was generally the same for the present experiment with skewed trips, compared to the previous smooth wall and normal trip experiments. The modest changes on the leading and trailing surfaces of the turn sections are attributed in part to the differences in the velocity profiles expected at the entrance to the turn regions. For the smooth wall flow condition, the velocities are expected to be high in the corners of the duct (e.g., Schlichting, 1968). For flow over normal trips, the velocity can be expected to peak in the center of the channel due to the large momentum losses at each trip. The changes in heat transfer on the sides (outside walls of turn sections) attest to the complexity of the flow structure in the turns and are not yet explained.

Rotating Baseline Flow Condition. The streamwise distributions of the Nusselt number for the Rotating Baseline Flow Condition are presented in Fig. 5. Also shown are the results for the heat transfer model with smooth walls and with normal trips and the smooth wall correlation for Nu_∞. The heat transfer characteristics for the models with trips and rotation are similar to those for the model with smoother walls. That is, in the first passage with flow outward, the heat transfer increases on the trailing side and decreases on the leading side. In addition, in the straight passages, the relative position of the heat transfer coefficients remain the same as for the Stationary Baseline Flow Condition. (The model with the skewed trips has the highest heat transfer coefficients and the model with the smooth walls has the lowest heat transfer coefficients on the leading and trailing sides and on most of the side wall heat transfer surfaces.) However, the ratio of the heat transfer coefficients at each streamwise location varies. At some locations, the heat transfer with the skewed trips is only 5 percent greater than those with normal trips; increases are commensurate with the increases in the surface area. (Recall that the heat transfer coefficients are based on projected surface area.)

The largest difference between the heat transfer from the models with skewed and normal trips occurs on the trailing surfaces in the second passage streamwise locations, *G*, *H*, and *I* or $19 < X/d < 31$. In this region, the heat transfer with the normal trips is closer to the smooth wall value than that with the skewed trips. This behavior was previously (Wagner et al., 1992) attributed to the formation of buoyancy-driven cells between the normal trips on this trailing surface with flow

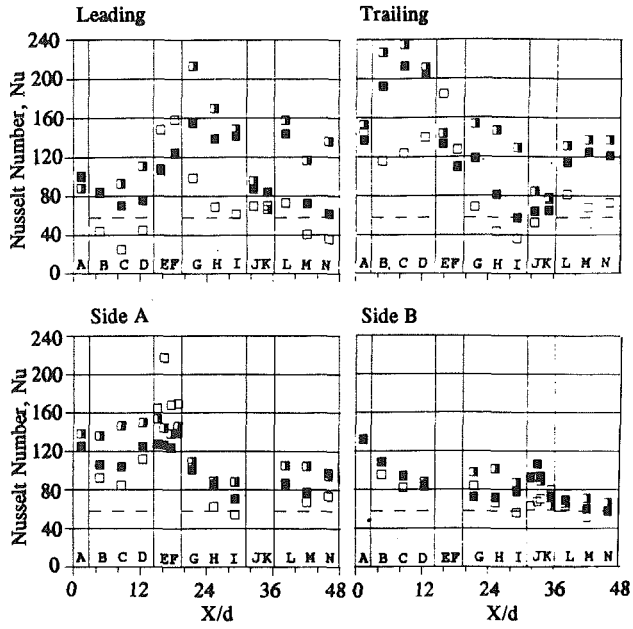

Fig. 5 Effect of trip configuration on heat transfer for rotating baseline flow conditions; $\Omega = 550$ rpm, Re = 25,000, $R/d = 49$, $\alpha = 0$, $(\Delta\rho/\rho)_{in} = 0.13$, □ —smooth wall, ■ —normal trips, ◨ —skewed trips, - - - smooth wall correlation for Nu_∞

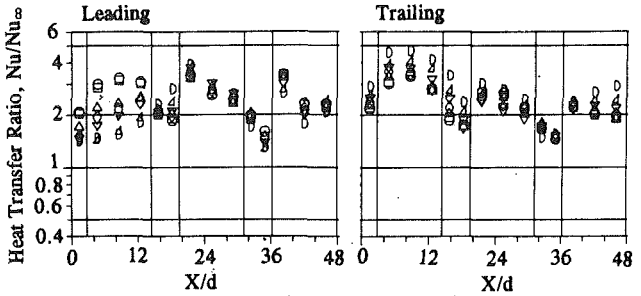

Fig. 6 Effect of rotation number on heat transfer ratio; Re = 25,000, R/d = 49, $\alpha = 0$, $(\Delta\rho/\rho)_{in} = 0.13$, rotation Nos. ○ —0.00, □ —0.006, △ —0.06, ◇ —0.12, ▽ —0.18, ◿ —0.23, ▷ —0.34.

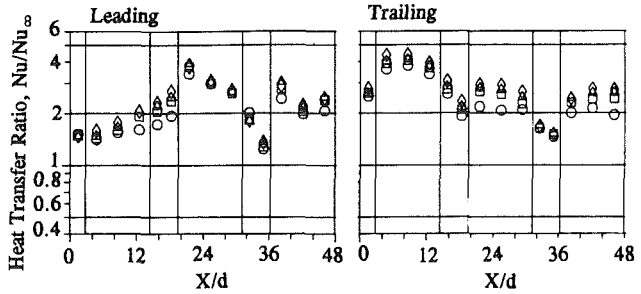

Fig. 7 Effect of density ratio on heat transfer ratio; Re = 25,000, $R/d = 49$, $\alpha = 0$, $Ro = 0.24$, $(\Delta\rho/\rho)_{in}$ values; ○ —0.07, □ —0.12, △ —0.18, ◇ —0.23

radially inward. The authors' hypothesis is that the secondary flow produced by the skewed trips precludes such a radially recirculating flow and the accompanying lower heat transfer coefficients. This model is compatible with the results for calculated flows in circular ducts with square trips (Taylor et al., 1991).

The increase in heat transfer from the models with the trips in the second and third passages was generally less than that obtained in the first outward straight section. This general reduction in heat transfer was attributed primarily to the development of well-mixed flow in the coolant passages downstream of the turns and, possibly, the increased uncertainty in the bulk temperature at these downstream locations. (The increased heat transfer compared to the smooth wall model causes the difference between bulk temperature and the wall temperature to decrease and hence the uncertainty of the heat transfer coefficient determined to increase.)

The heat transfer in the turn regions with rotation is also complex. For the first turn at the model tip (outside radius, *E* and *F*), the heat transfer coefficients with the smooth wall model are the highest on all three surfaces. For the second turn at the model root (inside radius; *J* and *K*), the heat transfer with the smooth model is the lowest. These effects are attributed to the complex flows produced during the convection of secondary flow patterns produced in the straight passage sections upstream of each turn by each of the three types of wall surfaces (smooth, normal trips, skewed trips). Additional analytical effort will be required to delineate the causes for these effects.

Heat Transfer Results for Variation of Parameters About Baseline Flow Conditions

Effect of Rotation. The rotation number, $\Omega d/V$, was varied from 0 to 0.35 for this series of flow conditions. The Reynolds number, inlet density ratio, and radius ratio were held constant at the nominal values of 25,000, 0.13, and 49, respectively. The streamwise distribution of the heat transfer ratios are presented in Fig. 6.

The heat transfer ratios vary significantly, i.e., by a factor of 2, on the leading surface. The decrease in heat transfer coefficient due to rotation on the leading surface of the first passage is approximately the same as previously shown for the models with smooth walls or with normal trips. That is, the heat transfer decreases to approximately one-half the stationary value for $Ro = 0.24$. The heat transfer in the trailing segments of the first passage increased 30 to 40 percent when the rotation number was increased from 0 to 0.34.

The effects of rotation are markedly less in the second and third passages. This lack of large variation is attributed to (1) the secondary flow patterns induced by the skewed trip configurations and (2) the effects of the conservation of vorticity through turn regions on the heat transfer in the second and third passage. The heat transfer from each of the leading and trailing segments in the second passage, $19 < X/d < 31$, with flow radially inward is generally within 20 percent of the respective values for $\Omega = 0$. The heat transfer from the trailing segments in the third passage with flow radially outward, $36 < X/d < 48$, does increase as much as 50 percent of their respective values for $\Omega = 0$. Although these effects were previously recognized, their relative importance regarding the heat transfer was difficult to estimate. The current (e.g., Prakash and Zerkle, 1991) analyses of flows in complex rotating coolant passages are providing insight into the flow and heat transfer characteristics of turbine blade internal cooling.

Effect of Density Ratio. The inlet density ratio, $(\Delta\rho/\rho)_i$, was varied from 0.07 to 0.22 for this series of flow conditions. The Reynolds number, rotation number, and radius ratio were held constant at the baseline values of 25,000, 0.24, and 49, respectively. Heat transfer was obtained at a fixed rotation number and, therefore, conclusions can be obtained regarding the effects of buoyancy for flow conditions near the rotating baseline flow conditions.

Increasing the inlet density ratio (i.e., the wall-to-coolant temperature difference) from 0.07 to 0.22 causes the heat transfer ratio in the first passage of the model with skewed trips to increase on the trailing surfaces by as much as 25 percent and on the leading surfaces by as much as 20 percent (Fig. 7). The

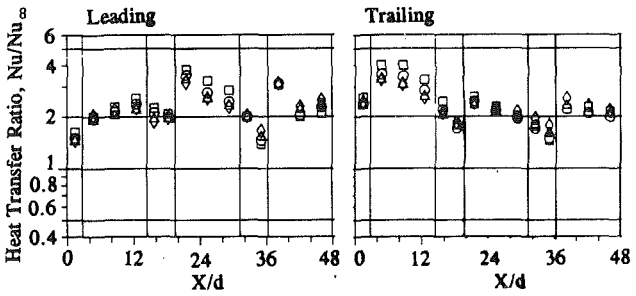

Fig. 8 Effect of Reynolds number on heat transfer ratio for a rotation number of 0.12; $R/d = 49$, $\alpha = 0$, $(\Delta\rho/\rho)_{in} = 0.13$, $Ro = 0.12$, Reynolds Nos.: □ —12,500, ○ —25,000, Δ—50,000, ◇ —75,000

exception to the general increase in heat transfer with increasing density ratio occurred near the inlet of the first passage on the leading side, where the heat transfer ratio is relatively unaffected by varying density ratio. In the second passage, with flow radially inward on the low-pressure (trailing edge) side, heat transfer increased as much as 60 percent with increases in the temperature difference. (Larger effects of density ratio were obtained for a rotation number of 0.35).

The increase in the heat transfer ratio in the third passage with flow radially outward was also as much as 60 percent as the inlet density was increased. In the third passage, the effects of density ratio on the heat transfer from the leading and trailing surfaces are larger for the model with skewed trips than were measured for the model with normal trips for $Ro = 0.24$.

Effects of Reynolds Number. The streamwise variation of heat transfer ratio, Nu/Nu_∞, is presented in Fig. 8 for Reynolds numbers from 12,500 to 75,000, a fixed rotation number, $Ro = 0.12$, and a fixed inlet density ratio, $\Delta\rho/\rho_{inlet} = 0.13$. The heat transfer ratios for $Re = 50{,}000$ and 75,000 at all locations are well correlated by use of the Kays and Perkins correlation, i.e., with the Nusselt number proportional to Reynolds number to the 0.8 power. The variations between the heat transfer ratios for Reynolds number equal 25,000 and those for 50,000 and 75,000 are generally less than 10 percent. The variation for Reynolds numbers of 12,500 is greater, especially in regions with the highest heat transfer coefficients.

The conclusion from these rotating and stationary experiments was that the relationship for fully developed flow in a square duct with smooth walls, $Nu_\infty = 0.0176\ Re^{0.8}$, would be adequate for scaling the effects of Reynolds number on the heat transfer ratio.

Effects of Passage Orientation. Heat transfer experiments were conducted with the plane of the coolant passages rotated 45 deg to the axis of rotation ($\alpha = 45$ deg) for the model with skewed trips. See Fig. 3(*b*) for the model orientation. The effect of model orientation on the streamwise distribution of the heat transfer ratio for the four surfaces is presented in Fig. 9. The heat transfer ratios for the Rotating Baseline Flow Conditions are presented for $\alpha = 0$ and 45 deg. In the first coolant passage, rotation of the model from $\alpha = 0$ to $\alpha = 45$ deg caused the heat transfer ratio to decrease on both side walls and the trailing side and to increase or remain the same on the leading side. In the second passage small decreases in the heat transfer ratio occurred on all four sides of the coolant passage. The conclusion from this comparison is that the heat transfer ratios can increase or decrease 20 to 30 percent with the coolant passage orientation up to 45 deg from the $\alpha = 0$ orientation for this trip strip geometry and coolant passage aspect ratio.

Correlating Parameters

In this section, the heat transfer ratios will be presented for

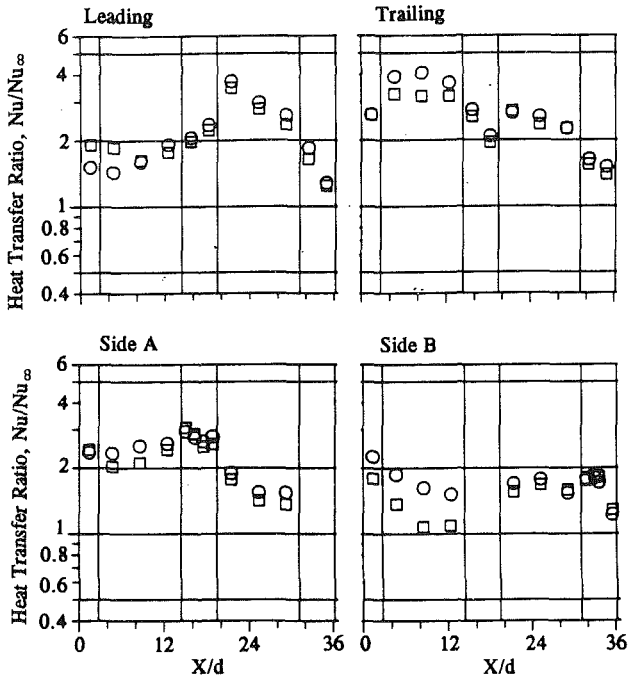

Fig. 9 Effect of model orientation (alpha) on heat transfer ratio of skewed trips; $Re = 25{,}000$ $R/d = 49$, $(\Delta\rho/\rho)_{in} = 0.13$, $Ro = 0.23$, alpha values: ○ —0 deg, □ —45 deg

specific locations on the leading and trailing surfaces in the three passages. The heat transfer ratios will be presented as

1 the variation of local rotation number with each inlet density ratio noted, and
2 the variation of the local buoyancy parameter with each rotation rate and inlet density ratio noted.

The results from the models with smooth walls and with normal trips are also presented for comparison. With these two presentations, the similarities and differences of the heat transfer characteristics from the three models with normal and skewed trips and with smooth walls can be identified and discussed.

Variation With Rotation Number. The heat transfer ratios for the downstream leading and trailing surfaces in the three straight passages are presented in Fig. 10. The test surface identification number (Figs. 2 and 3), the streamwise location and the X/d, X'/d, or X''/d ratio from the start of each straight section are also shown on each panel of the figure.

High-Pressure Surfaces. The trailing surfaces of the first and third passages and the leading surface of the second passage are denoted as the high-pressure surfaces. In the first and third passages of both models with trips, the heat transfer coefficients increase with increasing rotation number at approximately half the slope as these for the model with smooth walls. The increases in heat transfer ratios, due to rotation, are as much as 75 percent compared to the heat transfer ratios for the same models with trips and no rotation. Also, the heat transfer ratios in the second passage with flow radially inward are essentially independent of rotation. Note that the heat transfer from the models with trips is essentially independent of inlet density for $Ro \leq 0.24$ in the first two passages. The uncertainty in the heat transfer measurements in the third channel increases due to small bulk to wall temperature differences for the low inlet density ratios. However, the results for the third passages with trips show characteristics similar to those for the third passage with smooth walls.

Low-Pressure Surfaces. The heat transfer from the low-pressure surfaces is more complex than that from the high-

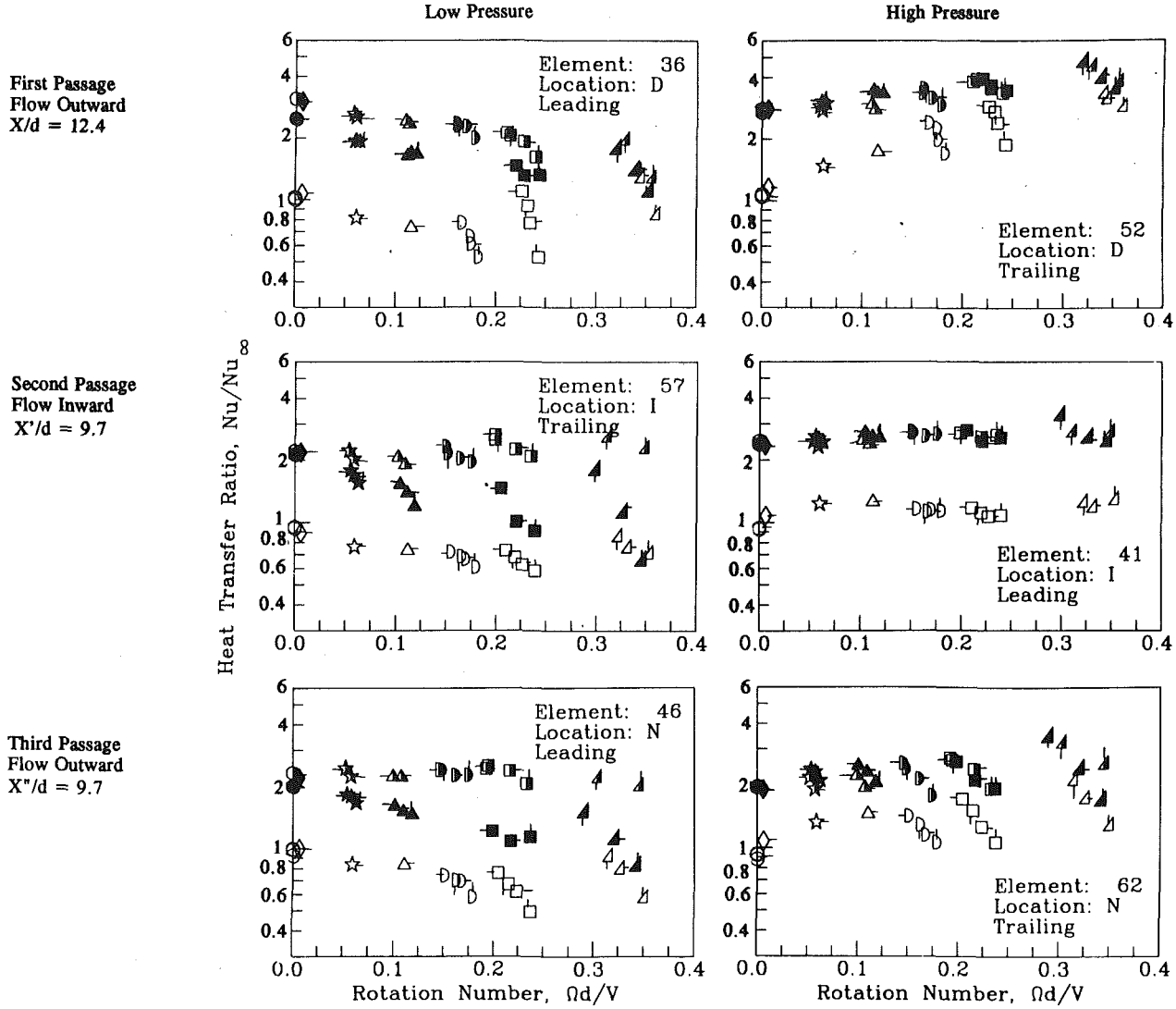

Fig. 10 Effect of rotation number on heat transfer ratios in the first, second and third passages; Re = 25,000 R/d = 49, open symbols—smooth wall data, solid symbols—normal trip data half solid symbols—skewed trip data

pressure surfaces. The heat transfer ratio in the first passage with both the normal and skewed trips decreases with increasing rotation number at the downstream location for the range of values tested, i.e., $\Omega d/V < 0.36$. At the larger values of $\Omega d/V$, 0.24–0.36, the heat transfer ratio increases with increases in the density ratio, similar to the results obtained for the trailing surface of the first passage.

The effects of inlet density ratio on the heat transfer ratio in the second passage are of order 10 percent for the model with skewed trips and with flow radially inward. Note that large variations of order 300 percent were obtained for the model with normal trips in this passage for $\Omega d/V = 0.34$. Note also that the local density ratios in the second passage are about half of the inlet values.

The heat transfer characteristics of the third passage are more similar to those of the second passage than those of the first passage for each model. The model with skewed trips showed less decrease in heat transfer with increasing rotation than the models with the normal trips or the smooth walls.

The more complicated heat transfer distributions on the low-pressure surfaces of the coolant passages are attributed to (1) the combination of buoyancy forces and the stabilization of the near-wall flow for low values of the rotation number, (2) the developing, Coriolis-driven secondary flows cells, and (3) the increases in flow reattachment lengths after trips for the larger values of the rotation number. It is postulated that the relatively small effects from variations in density ratio near the inlet of the second passage and the large effects near the end of the second passage are due to the development of the near-wall thermal layers (i.e., thickening for the normal trip model compared to thinning for the smooth wall model). Near the inlet of the second passage, the thermal layers are postulated to be thin because of the strong secondary flows in the first turn region. With increasing X/d, the turn-dominated secondary flows diminish and the counteracting effects of buoyancy and the Coriolis-generated secondary flow increase.

Variations With Buoyancy Parameter. The buoyancy parameter, $(\Delta\rho/\rho)(\Omega R/V)$ $(\Omega d/V)$, has been effective for the correlation of heat transfer results from the model with smooth walls (Wagner et al., 1991a, 1991b). The best correlation was made for streamwise locations of X/d = 12 and for values of the buoyancy parameter greater than 0.20. In this section, the heat transfer ratios from the leading and trailing surfaces in the three passages are presented and compared with results from the models with smooth walls and with normal trips.

The variations of the local heat transfer ratio with the buoyancy parameter in the first passage with flow outward are shown in Fig. 11. The heat transfer from the trailing surfaces is correlated better with the buoyancy parameter than with the

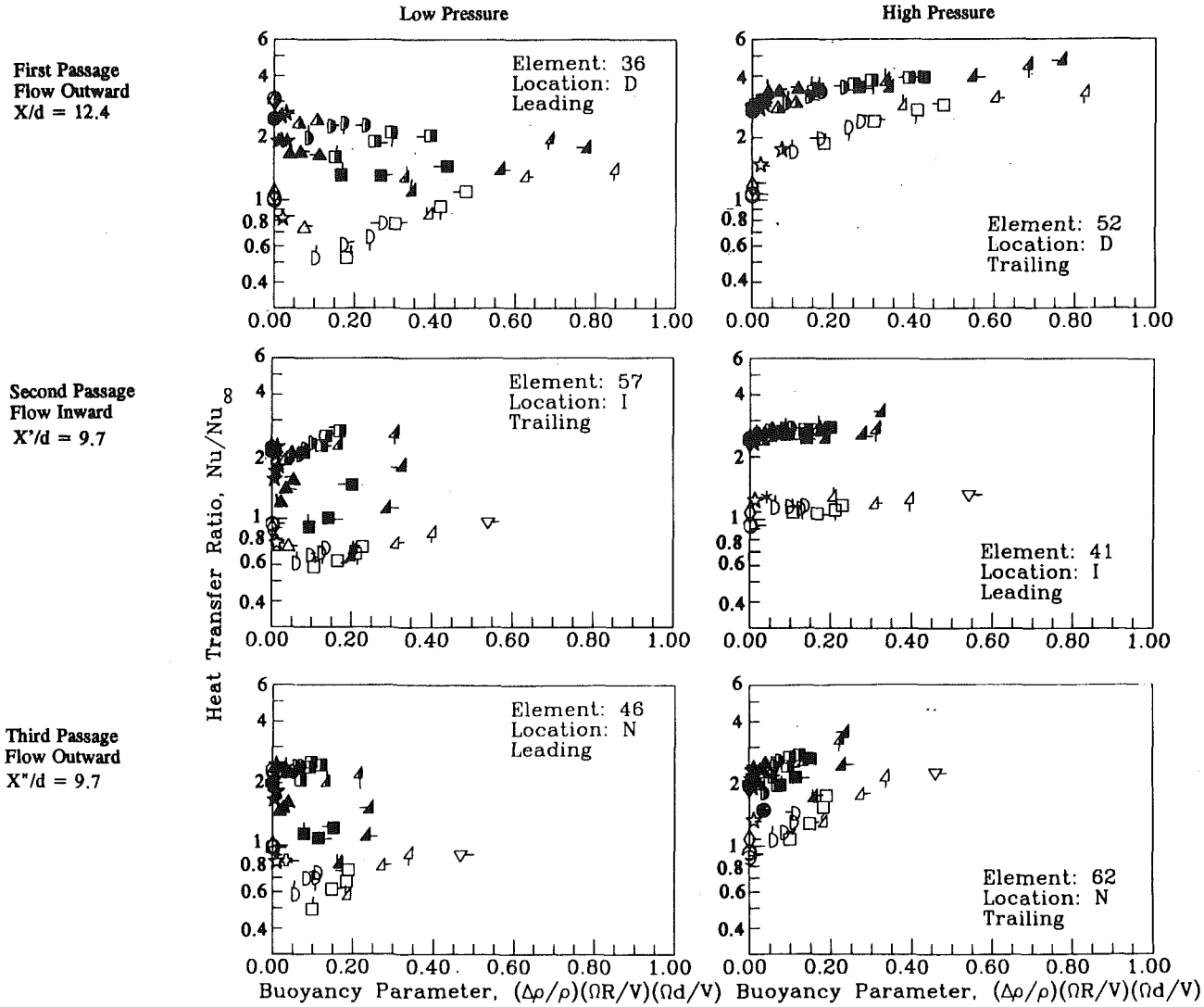

Fig. 11 Effect of buoyancy parameter on heat transfer ratios in the first, second, and third passages; Re = 25,000, *R/d* = 49, open symbols—smooth wall data, solid symbols—normal trip data, half solid symbols—skewed trip data

Table 1 Symbol flags for Figs. 10 and 11

Symbol	ΔT_{in}(°C)	ΔT_{in}(°F)	$(\Delta\rho/\rho)_{in}$
○	22.4	40	0.07
○–	44.7	80	0.13
◐	67.1	120	0.18
–○	89.1	160	0.22

rotation number (Fig. 10) or the inlet density ratio (not shown). Note that the heat transfer ratios of test surface 52 for both the skewed and normal trips are 25 and 20 percent greater than the heat transfer ratios for the smooth walls and for buoyancy parameters > 0.6. Recall that the total surface areas for the skewed and normal trips are 15 and 10 percent greater than for the smooth walls, respectively, and that the heat transfer coefficients and hence heat transfer ratios are based on the projected area. The conclusion is that half or more of the increase in heat transfer occurs due to the increased surface area. The increase in local heat transfer coefficient due to trips (10 percent) for high rotation numbers and high values of the buoyancy parameter is a small fraction of the 150 and 200 percent increase due to the trips at zero rotation.

The variations of heat transfer ratio with the buoyancy parameter for the leading (low pressure) surfaces in the first passage show several of the same characteristics previously shown for the results from the smooth model. However, for $Ro < 0.25$, the heat transfer ratios are correlated better by the rotation number (Fig. 10) than by the buoyancy parameter. For test surface 36 and at values of the buoyancy parameters greater than 0.6, the increase in the heat transfer ratio with skewed trips is as much as 35 percent greater than with the smooth walls. For the same condition with normal trips, the heat transfer coefficients were only 20 percent greater than with the smooth wall. However, the heat transfer on both surfaces with trips is as much as 50 percent less than the values obtained without rotation!

The variation of the heat transfer ratio with the buoyancy parameter in the second passage with flow radially inward shows markedly different results between the current model and previous model with normal trips. For the current model with skewed trips, the leading surfaces, e.g., element 41, are well correlated by the buoyancy parameter but have values of the heat transfer ratio that are not more than 10 to 20 percent greater than the value for the stationary model. The trailing surfaces, e.g., element 57, are reasonably well correlated by the buoyancy parameter. However, the maximum decrease in heat transfer ratio from the stationary ratio is less than 30 percent, whereas the smooth wall model had decreases of approximately 40 percent. It should be noted that the decrease

in absolute values are greater for the model with skewed trips (0.75 Nu_∞) than for the model with smooth walls (0.45 Nu_∞).

Summary of Results and Conclusions

Results from the present experiments with skewed trips in rotating, radial square coolant passages show that Coriolis forces and buoyancy effects can strongly influence heat transfer. However, the heat transfer coefficients were much less sensitive to buoyancy effects than were those previously measured with normal trips. The maximum effects of buoyancy on surfaces with skewed trips were also less than occurred on smooth surfaces. The authors's conclusions from these observations are that skewed trips provided higher heat transfer coefficients and less sensitivity to buoyancy effects and that skewed trips, rather than normal trips, should be employed for rotating coolant passages.

The comparison of results from the present experiments with previous results for models with smooth wall and with normal trips shows that flow and heat transfer in rotating coolant passages can be complex, especially when no single flow mechanism dominates the heat transfer process. The present results were obtained for skewed trips with values of trip streamwise pitch to trip height $(P/e) = 10$ and trip height to coolant passage width $(e/D) = 0.1$, typical of those used in coolant passages. For stationary coolant passage, these trip geometries generally produce heat transfer coefficients that are three times those obtained with smooth wall passages with fully developed flow. The wide range of heat transfer coefficients obtained with rotation (1.2 to 5.0 times the values for fully developed flow in smooth passages) indicates that it is prudent to have a data base available for the design of specific coolant passages used in rotating turbine blades.

Following is a summary of comments regarding the importance of each of the parameters previously identified.

- Reynolds Number. The heat transfer ratios for stationary and rotating conditions are reasonably well correlated by a $Nu \sim Re^{0.8}$ relationship. For low Reynolds numbers, i.e., $Re \sim 12{,}500$, the exponent may be less.
- Rotation Number. The rotation number correlates the heat transfer ratios better for more surface locations and flow conditions when the heat transfer surfaces have skewed ribs than it did for the model with smooth walls. The decrease in heat transfer ratio from the stationary value on the low-pressure side of the first coolant passage is well correlated by the rotation number for $Ro \leq 0.24$. The percentage decrease on the low-pressure side of the first coolant passage was essentially independent of the three wall surface geometries.
- Density Ratio and Buoyancy Parameter. For these tests with a constant value of R/d, the density ratio, the rotation number, and the Reynolds numbers are independent flow parameters and the buoyancy is determined by the variations of the density ratio and the rotation number, i.e., $(\Delta\rho/\rho)(\Omega d/V)^2(R/d)$. The density ratio is a lesser factor in heat transfer when the flow in the coolant passage is well mixed. For most flow situations with the skewed trips, the flow is apparently well mixed and the effects of density ratio are minimal for $Ro < 0.25$.
- Streamwise Location. The heat transfer with skewed trips does not vary as much with streamwise location compared to the smooth wall model. The large decrease in heat transfer with increasing distance from the inlet measured in the model with smooth walls does not occur with the trips. The exception occurs for flow downstream of turns with the skewed trips where the upstream vorticity has been convected to one side of the model and the flow readjusts in the new passage.
- Trip Orientation. The secondary flows produced by the trips can have a large effect on heat transfer. The skewed trips apparently caused secondary flow patterns that did not produce strong effects of density ratio. The normal trips apparently caused flow patterns that produced strong effects of density ratio (Wagner et al., 1992).
- Flow Direction. The effects of flow direction were generally less for the models with trips compared to the model with smooth walls.

Acknowledgments

The work published in this paper was supported by the NASA/Lewis Research Center under the HOST Program, Contract No. NAS3-23691 to the Pratt and Whitney Commercial Engine Business/Engineering Division and by the United Technology Corporation's independent research program. The authors gratefully acknowledge the assistance of Ms. S. Orr (UTRC) and Mr. J. Minguy (UTRC) in the performance of this program. The authors are appreciative of the support and guidance by the HOST management team at NASA/Lewis Research Center and by their colleagues at P&W and UTRC.

References

Boyle, R. J., 1984, "Heat Transfer in Serpentine Passages With Turbulence Promoters," ASME Paper No. 84-HT-24; NASA Technical Memorandum 83614.

Eckert, E. R. G., Diaguila, A. J., and Curren, A. N., 1953, "Experiments on Mixed-, Free- and Forced-Convective Heat Transfer Connected With Turbulent Flow Through a Short Tube," NACA Technical Note 2974.

Guidez, J., 1989, "Study of the Convective Heat Transfer in Rotating Coolant Channel," ASME JOURNAL OF TURBOMACHINERY, Vol. 111, pp. 43–50.

Hajek, T. J., Wagner, J. H., Johnson, B. V., Higgens, A. W., and Steuber, G. D., 1991, "Effects of Rotation on Coolant Passage Heat Transfer: Volume I—Coolant Passages With Smooth Walls," NASA Contractor's Report 4396, Vol. I.

Han, J. C., Park, J. S., and Ibrahim, M. Y., 1986, "Measurement of Heat Transfer and Pressure Drop in Rectangular Channels With Turbulence Promoters," NASA Contractor Report 4015.

Hart, J. E., 1971, "Instability and Secondary Motion in a Rotating Channel Flow," *J. Fluid Mech.*, Vol. 45, Part 2, pp. 341–351.

Iskakov, K. M., and Trushin, V. A., 1983, "Influence of Rotation on Heat Transfer in a Turbine-Blade Radial Slot Channel," *Izvestiya VUZ. Aviatsionnaya Tekhnika*, Vol. 26, No. 1, pp. 97–99.

Johnson, B. V., 1978, "Heat Transfer Experiments in Rotating Radial Passages With Supercritical Water," *Gas Turbine Heat Transfer*, ASME HTD-Vol. 125.

Johnson, B. V., Wagner, J. H., and Steuber, G. D., 1993, "Effect of Rotation on Coolant Passage Heat Transfer: Volume II—Coolant Passages With Trips Normal and Skew to the Flow," NASA Contractors Report 4396, Vol. II.

Johnston, J. P., Halleen, R. M., and Lezius, D. K., 1972, "Effects of Spanwise Rotation on the Structure of Two-Dimensional Fully Developed Turbulent Channel Flow," *J. Fluid Mech.*, Vol. 56, Part 3, pp. 533–557.

Kays, W. M., and Perkins, H. C., 1973, "Forced Convection, Internal Flow in Ducts," in: *Handbook of Heat Transfer*, W. M. Rohsenow and J. P. Hartnett, eds., McGraw-Hill, pp. 7-28 and 7-33.

Kline, S. J., and McClintock, F. A., 1953, "Describing Uncertainties in Single Sample Experiments," *Mechanical Engineering*, Vol. 75, Jan., pp. 3–8.

Lokai, V. I., and Gunchenko, E. I., 1979, "Heat Transfer Over the Initial Section of Turbine Blade Cooling Channels Under Conditions of Rotation," *Therm. Enging.*, Vol. 26, pp. 93–95.

Metzger, D. E., Fan, C. S., and Plevich, C. W., 1988, "Effects of Transverse Rib Roughness on Heat Transfer and Pressure Losses in Rectangular Ducts With Sharp 180 Degree Turns," AIAA Paper No. 88-0166.

Moore, J., 1967, "Effects of Coriolis on Turbulent Flow in Rotating Rectangular Channels," M.I.T. Gas Turbine Laboratory Report No. 89.

Mori, Y., Fukada, T., and Nakayama, W., 1971, "Convective Heat Transfer in a Rotating Radial Circular Pipe (2nd Report)," *Int. J. Heat Mass Transfer*, Vol. 14, pp. 1807–1824.

Morris, W. D., and Ayhan, T. 1979, "Observations on the Influence of Rotation on Heat Transfer in the Coolant Channels of Gas Turbine Rotor Blades," *Proc. IMechE*, Vol. 193, pp. 303—311.

Morris, W., 1981, *Heat Transfer and Fluid Flow in Rotating Coolant Channels*, Research Studies Press.

Prakash, C., and Zerkle, R., 1991, "Prediction of Turbulent Flow and Heat Transfer in a Radially Rotating Square Duct," *Heat Transfer in Gas Turbine Engines*, E. Elovic and H. Martin, eds., ASME HTD-Vol. 188.

Rothe, P. H., and Johnston, J. P., 1979, "Free Shear Layer Behavior in Rotating Systems," ASME *Journal of Fluids Engineering*, Vol. 101, pp. 117–120.

Schlichting, H., 1968, *Boundary-Layer Theory*, 6th ed., McGraw-Hill, New York, p. 575.

Suo, M., 1980, "Dimensionless Analysis Notes," United Technologies Research Center; included as "Analysis of Equations of Motion" (Section 10.1), *Effects of Rotation on Coolant Passages Heat Transfer: Vol. I—Coolant Passages With Smooth Walls*, NASA Contractor Report 4396, Vol. I, Sept. 1991.

Taslim, M. E., Rahman, A., and Spring, S. D., 1991a, "An Experimental Investigation of Heat Transfer Coefficients in a Spanwise Rotating Channel With Two Opposite Rib-Roughened Walls," ASME JOURNAL OF TURBOMACHINERY, Vol. 113, pp. 75–82.

Taslim, M. E., Bondi, L. A., and Kercher, D. M., 1991b, "An Experimental Investigation of Heat Transfer in an Orthogonally Rotating Channel Roughened With 45 deg Criss-Cross Ribs on Two Opposite Walls," ASME JOURNAL OF TURBOMACHINERY, Vol. 113, pp. 346–353.

Taylor, C., Xia, J. Y., Medwell, J. O., and Morris, W. D., 1991, "Numerical Simulation of Three Dimensional Turbulent Flow and Heat Transfer Within a Multi-ribbed Cylindrical Duct," ASME Paper No. 91-GT-8.

Wagner, J. H., Johnson, B.V., and Hajek, T. J., 1991a, "Heat Transfer in Rotating Passages With Smooth Walls and Radial Outward Flow," ASME JOURNAL OF TURBOMACHINERY, Vol. 113, pp. 42–51.

Wagner, J. H., Johnson, B. V., and Kopper, F. C., 1991b, "Heat Transfer in Rotating Serpentine Passages With Smooth Walls," ASME JOURNAL OF TURBOMACHINERY, Vol. 113, pp. 321–330.

Wagner, J. H., Johnson, B. V., Graziani, R. A., and Yeh, F. C., 1992, "Heat Transfer in Rotating Serpentine Passages With Trips Normal to the Flow," ASME JOURNAL OF TURBOMACHINERY, Vol. 114, pp. 847–857; NASA TM 103758.

Wagner, R. E., and Velkoff, H. R. 1972, "Measurements of Secondary Flows in a Rotating Duct," ASME *Journal of Engineering for Power*, Vol. 94, pp. 261–270.

Experimental Heat Transfer Investigation of Stationary and Orthogonally Rotating Asymmetric and Symmetric Heated Smooth and Turbulated Channels

H. A. El-Husayni
Graduate Student.

M. E. Taslim
Professor.

Mechanical Engineering Department,
Northeastern University,
Boston, MA 02115

D. M. Kercher
Principal Engineer,
GE Aircraft Engines,
Lynn, MA 01910

An experimental investigation was conducted to determine the effects of variations in wall thermal boundary conditions on local heat transfer coefficients in stationary and orthogonally rotating smooth wall and two opposite-wall turbulated square channels. Results were obtained for three distributions of uniform wall heat flux: asymmetric, applied to the primary wall only; symmetric, applied to two opposite walls only; and fully symmetric, applied to all four channel walls. Measured stationary and rotating smooth channel average heat transfer coefficients at channel location $L/D_h = 9.53$ were not significantly sensitive to wall heat flux distributions. Trailing side heat transfer generally increased with Rotation number, whereas the leading wall results showed a decreasing trend at low Rotation numbers to a minimum and then an increasing trend with further increase in Rotation number. The stationary turbulated wall heat transfer coefficients did not vary markedly with the varaitions in wall heat flux distributions. Rotating leading wall heat transfer decreased with Rotation number and showed little sensitivity to heat flux distributions except for the fully symmetric heated wall case at the highest Reynolds number tested. Trailing wall heat transfer coefficients were sensitive to the thermal wall distributions generally at all Reynolds numbers tested and particularly with increasing Rotation number. While the asymmetric case showed a slight deficit in trailing wall heat transfer coefficients due to rotation, the symmetric case indicated little change, whereas the fully symmetric case exhibited an enhancement.

Introduction

Fluid traveling in the axial direction inside an orthogonally rotating channel experiences the effect of the Coriolis acceleration created by the rotation of the channel. This force has a significant effect on the flow field and can create secondary flows on planes perpendicular to the main flow direction. When heat transfer occurs between the fluid and the channel walls, density variations due to temperature gradients can create buoyancy forces that directly affect the heat transfer characteristics of the flow.

Heat transfer in pipe flow with a circumferentially uniform (fully symmetric) heat flux boundary condition with and without rotation has been the focus of a number of theoretical and experimental studies. An extensive body of theoretical work has been developed to support experimental results. Heat transfer characteristics for noncircular duct geometries with nonsymmetric thermal boundary conditions, however, have been studied to a lesser extent, especially in the rotating mode. Correlations developed for a circular duct geometry in the turbulent regime can be adapted to flows in noncircular ducts when the hydraulic diameter is substituted for the diameter of the circular cross section. Dimensional analysis and experimental studies have demonstrated that forced convection heat transfer in ducts can be correlated with parameters such as fluid velocity, fluid properties, channel geometry, and the thermal boundary conditions applied to the channel walls. Dittus and Boelter's (1930) classic correlation for stationary, fully symmetric wall heat flux at fully developed turbulent flow in smooth tubes with heat transfer to the fluid is an example of such experimental correlations. More recent duct heat transfer investigations have focused on turbulated noncircular channels with and without rotation and symmetric and asymmetric thermal wall conditions.

The application of the aforementioned studies to the analysis

Contributed by the International Gas Turbine Institute and presented at the 37th International Gas Turbine and Aeroengine Congress and Exposition, Cologne, Germany, June 1-4, 1992. Manuscript received by the International Gas Turbine Institute February 17, 1992. Paper No. 92-GT-189. Associate Technical Editor: L. S. Langston.

of heat transfer in the serpentine turbulated cooling passages of turbine blades requires consideration of measured heat transfer effects of Coriolis and centripetal acceleration buoyancy fields and perhaps to a lesser extent the impact of various wall thermal conditions associated with the rotation of the cooling passage. In the past it has been a practice to use classic duct heat transfer correlations developed from flow in stationary channels to predict the heat transfer characteristics in rotating cooling passages. Failure to consider these rotationally induced effects particularly on the heat transfer in rib-roughened channels, such as in the design and analysis of blade cooling passages, could result in unreliable and erroneous channel heat transfer coefficients, metal temperatures, and engine blade operating life predictions.

Over the last several years stationary and rotating turbulated channel experimental investigations were either asymmetric, symmetric, or fully symmetric wall thermal boundary conditions effects on heat transfer coefficient distributions. However, no known systematic test comparisons have been investigated among these three types of wall thermal boundary conditions for the same geometry and environmental conditions.

In the present measurements local and integrated-average heat transfer coefficient distribution comparisons are made for stationary and orthogonally rotating smooth and opposite-wall turbulated square outflow channels. Smooth and rib-roughened channel wall thermal conditions were comprised of imposed uniform asymmetric, symmetric, and fully symmetric heat flux distributions on one wall, two opposite walls, and all four walls, respectively.

Liquid crystal thermography measured the detailed surface temperature distributions for the orthogonal surface between two adjacent ribs in the turbulated channel and similarly for the smooth channel walls. From these measurements local and average heat transfer coefficients (Nusselt numbers) were determined over a wide range of air flow (Reynolds number) and rotational speeds (Rotation number). Liquid crystals laid over constant heat flux wall heaters resulted in detailed photographs of surface isotherms at discrete test conditions. This technique appears to be an effective and accurate measurement device for heat transfer investigations, especially in the rotating frame and thermal wall boundary conditions studied.

Literature Review

Effects of Stationary Wall Thermal Boundary Conditions. Barrow (1962) reported the results of a theoretical and experimental study of asymmetric heat transfer in fully developed turbulent air flow between two smooth parallel plates. Flow between two parallel plates in the second and third parts of the study was simulated by a long duct of low aspect ratio ($AR = 0.034$). The asymmetric heating results showed that the heat transfer coefficient was lower than accepted values for the symmetric heating. The decrease in heat transfer coefficient was observed to intensity as the degree of asymmetry increased. A decrease of the order of 40 percent was measured. It was concluded that the heat transfer coefficient is dependent on the circumferential heat flux distribution perpendicular to the flow direction.

Hatton and Quarmby (1963) presented the results of a comprehensive study of the turbulent heat transfer situation between parallel plates with heating on one side. Using the two basic solutions of uniform tempertaure and uniform heat flux in conjunction with the superposition technique, a solution for unequal but uniform heat fluxes was obtained. The effect of heat fluxes on the heat transfer coefficient showed, under identical conditions, that Nusselt numbers for the asymmetric heating analysis were lower than those for the symmetric.

Novotny et al. (1964) investigated the heat transfer characteristics of three rectangular ducts with different aspects ratios to determine whether heat transfer characteristics were greatly affected by the choice of thermal boundary conditions. They reported experimental heat transfer results for fully developed turbulent flow in rectangular smooth ducts with aspect ratios of 1, 0.2, and 0.1. The top and bottom walls were uniformly heated while the side walls were unheated. The experimental results for this symmetric thermal boundary condition were found to be lower than those obtained by the fully symmetric circular tube empirical correlation of Colburn et al. (1945), especially at higher Reynolds numbers.

Sparrow et al. (1966) conducted an experimental investigation to determine the effect of asymmetric heating on the fully developed turbulent heat transfer. The rectangular duct, with a low aspect ratio of 0.2, was similar in construction to Novotny's as well as the testing procedure and experimental

Nomenclature

a = height of the channel (Fig. 2)
b = width of the channel (Fig.2)
AR = aspect ratio of the channel $= a/b$
D_h = hydraulic diameter of the channel $= 2ab/(a + b)$
e = turbulator (rib) height
Gr = Grashof number $= (r/D_h) \cdot Ro^2 \mathrm{Re}^2 (T_s - T_i)/T_s$
h = heat transfer coefficient
$\bar{h}_t$ = area-weighted average heat transfer coefficient on the surface between a pair of turbulators
J = rotational Reynolds number based on hydraulic diameter $= \Omega D_h^2/\nu = \mathrm{Re}Ro$; (+) for trailing surface, (−) for leading surface
k = thermal conductivity of air
L = channel entrance-to-camera distance (Fig. 2)
Nu = Nusselt number $= hD_h/k$
$\overline{\mathrm{Nu}}$ = area-weighted average Nusselt number $= \bar{h}_t D_h/k$
Nu_{st} = Nusselt number for stationary case
$\mathrm{Nu}_{\mathrm{rot}}$ = Nusselt number for rotating case
Nu_∞ = fully developed smooth wall channel Nusselt number (Wagner et al., 1991, 1992; $\mathrm{Nu}_\infty = 0.0176\ \mathrm{Re}^{0.8}$)
Nu_o = Dittus–Boelter fully developed smooth channel flow Nusselt number $= 0.023 \cdot \mathrm{Re}^{0.8}\ \mathrm{Pr}^{0.4}$
$\dot{q}''$ = heat flux generated by electric heater
$\dot{q}_b''$ = heat flux lost through back of test section
$\dot{q}_T''$ = heat flux lost by radiation
r = radial distance from the camera centerline to the axis of rotation
Re = Reynolds number based on hydraulic diameter
Ro = Rotation number $= \Omega D_h/U_m$; (+) for trailing surface, (−) for leading surface
S = turbulator (rib) pitch
T_i = air temperature at the channel inlet
T_m = air mixed mean temperature
T_s = surface temperature
T_f = film temperature $= (T_m + T_s)/2$
$\Delta T/T$ = temperature-induced density ratio $= (T_s - T_i)/T_s$
U_m = mean velocity of air
ν = kinematic viscosity of air
Ω = angular velocity

setup. In comparing the findings with those of Novotny et al. (1964), the effect of symmetric heating was shown to increase the value of Nusselt number by 10 to 15 percent. Moreover, the results showed for unequally heated walls, the wall with higher heat flux exhibited lower heat transfer coefficients than those of the symmetric wall and higher than those of asymmetric walls. However, heat transfer coefficients for the less heated wall were higher than those of the symmetric heating case by 15 percent. The results were found to compare favorably with a number of analytical studies of the limiting case of asymmetrically heated parallel-plate channels.

Tan and Charters (1970) undertook an experimental investigation to determine heat transfer coefficients in a rectangular duct with asymmetric heating. The duct had an aspect ratio of 0.33 and was constructed to simulate a flat-plate solar-air heater with rectangular flow passage. Results reaffirmed the findings of previous authors that asymmetric heating produced lower heat transfer coefficients than those obtained under symmetric heating.

Mass transfer experiments were conducted by Sparrow and Cur (1982), for asymmetrically heated flat (low aspect ratio $\sim$ 0.055) rectangular duct with flow separation at the inlet. The naphthalene sublimation technique in conjunction with the analogy between heat and mass transfer was used to obtain heat transfer results. In these experiments, the investigators studied the influence of the sharp-edged inlet on the flow development in the entrance region and the fully developed heat transfer coefficient. Mass transfer differences between asymmetric and symmetric heating were not observed in the thermally developing region; however, the effect of symmetric heating was to reduce the thermal entrance length to 5–7 D_h compared with 10–13 D_h for the asymmetric heating. It was further noted that the asymmetric heat transfer results fell below the symmetric heating results farther downstream by a maximum of 7.5 percent.

Sparrow et al. (1986), in an experimental and a complementary numerical work, studied the heat transfer characteristics of hydrodynamically developed turbulent flow in a rectangular duct (AR = 0.18), in which one wall was maintained at a constant temperature while the other walls were adiabatic. The naphthalene sublimation technique and the analogy between mass and heat transfer was used in the experimental part of the study. These results reaffirmed the previous finding that one-sided heating produced relatively longer thermal entrance lengths. The fully developed heat transfer results also compared favorably with those reported by other investigators noted above.

Kostic and Hartnett (1986) summarized the heat transfer in rectangular ducts of various thermal boundary conditions. On the bases of experimental and analytical studies in an asymmetrically heated duct, the lower heat flux wall produced higher heat transfer coefficients than those in a symmetrically heated duct. However, the higher heat flux wall in an asymmetrically heated duct gave lower Nusselt numbers than those of the symmetrically heated duct. The effect of asymmetric heating was found to decrease with the increase in Prandtl number.

The investigative conclusion from the heat transfer studies summarized is that the consistent overall effect of asymmetric heating condition in rectangular ducts is to produce lower heat transfer coefficients than those obtained by a symmetric or fully symmetric heating. The heat transfer trends of this paper for both smooth and turbulated square asymmetric and symmetric heated channels are in general agreement with the previous investigations sighted.

Effects of Rotation. Morris and Harasgama (1985) presented experimental results of local and mean heat transfer coefficients on the leading and trailing walls of a square-sectioned smooth duct rotated in an orthogonal mode with both radially outward and inward flow. Results indicated that for radially outward flow, the overall effect of rotation was to produce regions of reduced heat transfer coefficient on the leading wall relative to the stationary case. This rotating phenomenon was attributed to the hypothesis that the wall temperature was higher on the leading side hence creating a higher rotational buoyancy effect which would degrade the near-wall radial velocity and thus lower heat transfer coefficients.

Harasgama and Morris (1988) performed a study to examine the influence of the secondary flows induced by the rotation of smooth circular, square, and triangular ducts on the heat transfer characteristics of the walls. Local heat transfer coefficients on the trailing wall of a square duct were found to be consistently higher than those on the leading wall. They also detected a possible increase in heat transfer coefficients on the leading wall with the increase in rotational Rayleigh number. This observation created uncertainty about the overall influence of rotational buoyancy on the heat transfer process.

Experiments conducted by Wagner et al. (1991) examined heat transfer characteristics of a turbulent flow in a rotating, square, smooth, serpentine passage. While the coolant heat transfer model was constructed to simulate a typical multipass turbine blade coolant passage, only results for the first outward flow passage were reported. Coolant flow Reynolds number was maintained at 25,000, while four sets of wall-to-coolant temperature differences were examined. Results showed that, for all values of fluid density ratios examined, locally averaged heat transfer ratios (Nu/Nu_∞) on the leading wall exhibited a consistent trend of decreasing with Ro to a minimum and then increasing with further increase in Ro while the trailing wall continued increasing.

Morris and Salemi (1992) presented results of an experimental study on the combined effects of Coriolis and buoyancy forces on the heat transfer process in rotating smooth circular tubes. Tests were performed for four Reynolds numbers (15,000 to 30,000) and at four rotational speeds (0 to 2700 rpm). Five heat flux settings were used for each Reynolds number–speed combination to study the influence of surface-to-coolant temperature differences on the heat transfer process. Results indicated circumferential variation in the heat transfer coefficient with an enhancement on the trailing side relative to the leading side.

Effects of Turbulence Promoting Ribs. Turbulated wall heat transfer enhancement relative to smooth walls in stationary and orthogonally rotating ducts has been the focus of a number of investigators. The reader is referred to the work of, for example, Han et al. (1978, 1984, 1985, 1992), Lau et al. (1991), Metzger et al. (1983, 1988, 1990), Taslim et al. (1988, 1989a, 1989b, 1991), and Wagner et al. (1986, 1992).

Experimental Apparatus

A schematic of the rotating test facility, test sections, and relevant dimensions are shown in Figs. 1 and 2. The top, bottom, and front walls were made of 1.27-cm-thick plexiglass sheets that formed the three walls of a 1.17-m-long channel. The fourth wall (the back wall), on which all measurements were taken, was made of a 4.13-cm-thick polyurethane board. The smooth and turbulated test section channels in their final assembly had a width of 7.62 cm and height of 8.13 cm corresponding to an aspect ratio of 1.067. A total of 15 custom-made etched foil heaters were laid on all four walls of the test sections. These heaters, with a width equal to the spanwise dimension of the surface on which they were affixed, were 31.75 cm long on the front wall and 27.94 cm long on the other three walls. The heating element was made of a 0.00127 cm inconel sheet sandwiched between two 0.00254-cm Kapton layers. To display isotherm contours, a liquid crystal sheet with a total thickness of 0.0254 cm was laid on top of the heaters

affixed to the polyurethane wall. A small window on the plexiglass wall opposite the polyurethane wall was left uncovered for a camera to record the isochrome areas formed on the liquid crystal sheet as illustrated in Fig. 2. Power was supplied to the heaters by a 20-channel silver–silver contact slip ring assembly. The ohmic power supplied to each heater was individually controlled by a transformer to assure uniform heat flux on each wall.

The turbulated channel was identical to the all-smooth-wall test section in all aspects except that opposite walls were roughened with plexiglass turbulators of square cross-sectional area (1.91 × 1.91 cm with sharp edges). The turbulators were arranged in a staggered configuration at a 60 deg angle of attack with the flow direction and had a pitch-to-height ratio (S/e) of 10 as shown in Fig. 2. The blockage ratio of the turbulator height-to-channel hydraulic diameter (e/D_h) was 0.24, which is a typical value for the cooling channels in a small turbine blade. It should be noted that although the turbulator ribs lay on the heater–liquid crystal assembly and were not covered by heaters themselves, the measured results are for heat transfer coefficients on the surface area between two adjacent turbulators.

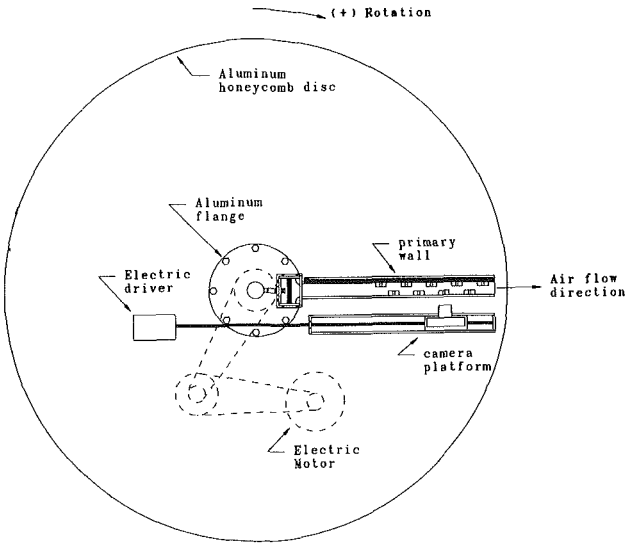

Fig. 1 Rotating test facility (top view)

Each test section was placed radially on the test facility's light-weight aluminum honeycomb rotating disk. Air was the working fluid and the flow direction for the rotating tests were radially outward. Air mass-flow rate was measured using a custom-made critical venturi. After passing through a single-pass baffled counterflow shell-and-tube water cooler and two stages of filtration, air was delivered to the plenum section by means of a rotating air seal. The air was then directed through a honeycomb flow straightener and a bellmouth opening into the test section. The air cooler condensed any residual moisture in the air before entering the second filtering stage. Cooling the air to approximately 20°C (68°F) also resulted in higher surface-to-air bulk temperature differences, thereby reducing the uncertainty in heat transfer coefficient measurements.

Test Procedure

Prior to testing, the liquid crystal sheet was calibrated with procedures explained in detail by El-Husayni (1991). The shade of green corresponding to a temperature of 37°C (98.6°F), more distinct than other colors, was chosen as the reference color.

East test section was rotated at nominal speeds of 50, 100, and 200 rpm, in both clockwise (+) and counterclockwise (−) directions. Reversal of the direction of rotation permitted measurements on both the trailing and leading surfaces of the channel at the same camera location. For each rotational speed, Reynolds number was varied between 5000 and 23,000 in five steps for the turbulated test section. The smooth test section, however, was tested for only two Reynolds numbers (9600 and 20,600) for each rotational speed. Stationary tests were also performed for the specified range of Reynolds numbers.

The testing procedure followed in the present investigation can be summarized as follows. For a given air mass flow rate and rotational speed, enough power was supplied to the heaters

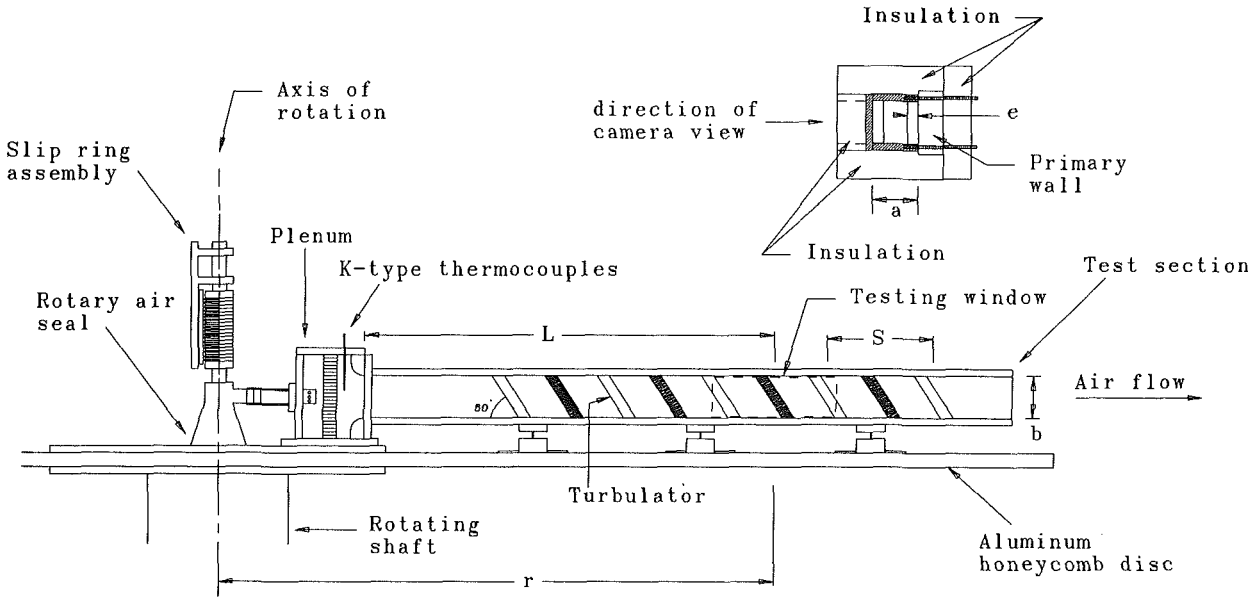

▨ denotes front wall turbulators (otherwise, on back wall)
L - distance from entrance to camera center line
Heaters and insulation are not shown for clarity

Fig. 2 Rotating test facility (side view)

to produce the first isochrome on the liquid crystal sheet in the measurement area. This area corresponded to a location at an L/D_h of 9.53 (r/D_h = 12.92) for the smooth case or an area between a pair of ribs centered also at the L/D_h of 9.53 for the turbulated test section. This L/D_h is typical of a small turbine blade airfoil cooling passage pitch-line location. After the system reached thermal equilibrium, i.e., the isochromes on the liquid crystal sheet remained stagnant, a photograph was taken of the entire measurement area. For the turbulated channel, the power level was then increased, forcing isochromes to move so that another segment of the region of interest could be recorded on film. This procedure was repeated until the reference isochrome covered the entire area between two turbulators. An average of 15 photographs was required to cover that area of interest with the reference temperature. This concluded a set of data for a single combination of Reynolds number and rotational speed. Then the flow rate was increased and the above process was repeated for all the remaining Reynolds numbers and rotational speeds. Data were archived and organized using an interactive computer program on a VAX 8650 main frame. The heat transfer coefficient corresponding to each picture was then calculated from:

$$h = \frac{\dot{q}'' - \dot{q}_b'' - \dot{q}_T''}{T_s - T_m}$$

where T_s is the surface temperature and T_m is the air mixed mean temperature calculated from an energy balance between the test section entrance and the camera location. It should be noted that the small temperature drop across the liquid crystal sheet (a fraction of a degree) was taken into consideration when surface temperature was measured. $\dot{q}_b''$ is the heat loss through the back of the primary wall and $\dot{q}_T''$ is the radiational loss from the primary wall to the other three walls of the test duct. Air properties were evaluated at the local film temperature, T_f.

The final process in data reduction was to digitize the reference color on the printed photographs for the calculation of the area-weighted average heat transfer coefficient. A dedicated software package with an active tablet and a magnetic-field mouse was utilized to evaluate the area covered by the reference isochrome. Area values associated with each photograph were stored in a data file for use in conjunction with the raw data to obtain heat transfer coefficients. The area-weighted average heat transfer coefficient was then calculated from:

$$\bar{h}_t = \sum_{1}^{np} \left(\frac{h_1 a_1 + h_2 a_2 + \cdots + h_{np} a_{np}}{a_1 + a_2 \cdots + a_{np}} \right)$$

where np is the total number of photographs taken for a given Reynolds number-rotational speed combination, a_1 through a_{np} are the areas covered with the reference color, and h_1 through h_{np} are the measured heat transfer coefficients corresponding to those areas. Maximum experimental uncertainty for the heat transfer coefficients, following the method of Kline and McClintock (1953), was calculated to be about ±8 percent for the case of asymmetric heating at the highest rotation number.

Results and Discussion

Smooth Test Section. Variations of the local Nusselt number with Reynolds number for all thermal boundary conditions are shown in Fig. 3. Heat transfer coefficients corresponding to the stationary case (Ro = 0) show little sensitivity to the choice of thermal boundary conditions but do show the classic abrupt entrance enhancement effects associated with developing boundary layers at the measurement location of L/D_h = 9.53. On both leading and trailing sides, especially for the lower range of the Rotation number, the rotating flow results

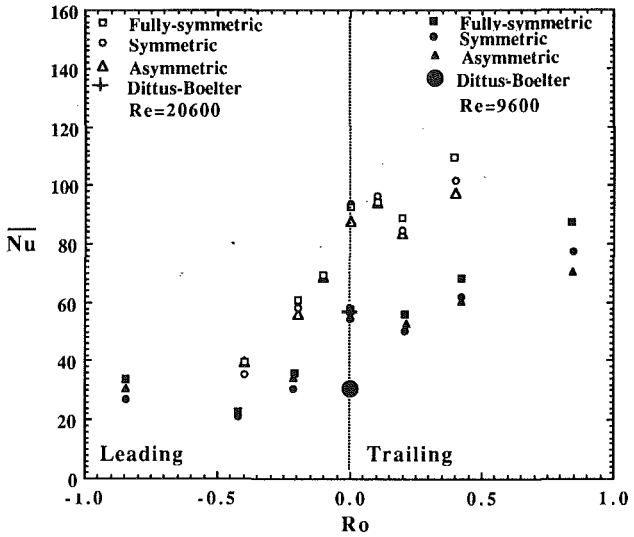

Fig. 3 Thermal boundary conditions and rotational effects on smooth channel heat transfer

show only a slight sensitivity to the choice of thermal boundary conditions. the fully symmetric heating shows a higher heat transfer coefficient than that in the asymmetric heating case.

The maximum difference in heat transfer coefficient between the fully symmetric and asymmetric heating cases occurred at the higher end of the Rotation number and the lower value of the Reynolds number. These conditions correspond to the highest Coriolis acceleration and the lowest fluid inertia. The results also show a local minimum in trailing heat transfer coefficient at low Rotation numbers and an apparent minimum on the leading walls at higher rotation. Those tests corresponding to the minimum points were repeated and the results, each time, showed a persistent minimum. Since it is generally concluded that centripetal buoyancy has a degrading effect on the heat transfer coefficient in a radially outward flow, a physical explanation for such behavior must be attributed to: (*a*) an initial domination of centripetal buoyancy over the Coriolis accelerations at low Rotation numbers on the trailing side and (*b*) the apparent upturn in the heat transfer, also noted by Wagner et al. (1991), on the leading side may be attributed to higher levels of turbulence intensity at high Rotation numbers (Mityakov et al., 1984) caused here primarily by higher buoyancy forces, which increase near-wall velocity gradients and thus generate higher turbulent kinetic energy near the wall.

It is noted that for the asymmetric heating case, the radiative heat flux from the heated walls to the three unheated walls was substantial. Depending on the heat flux generated on the test section wall, the amount of radiative heat flux reached as high as 30 percent of the total heat flux generated on that surface. As expected, the amount of radiative heat flux for the symmetric case was less than that of asymmetric case and in the fully symmetric case it was almost negligible.

Results of the present work are compared with those obtained by Wagner et al. (1991) in Fig. 4 in terms of the buoyancy number Gr/Re^2. Reasonable agreement, considering the fact that variation of the buoyancy number in the present work was accomplished through the change of the Rotation number and not $\Delta T/T$, is apparent. The higher levels of heat transfer in the present work may be attributed mainly to these data being taken earlier in both the hydrodynamically and thermally developing regions of the channel when compared to the data of Wagner et al. The present limited smooth channel data, however, suggest future investigations to expand the range of test parameters and geometry to verify levels and trends of wall heat transfer over the full range of buoyancy number simulation for blade cooling design application.

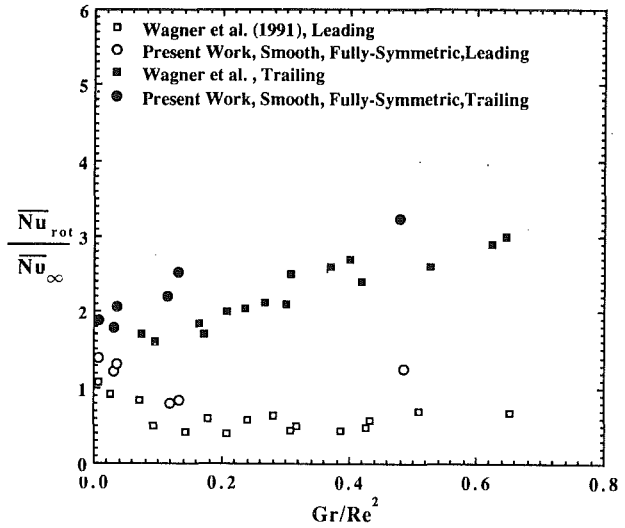

Fig. 4 Fully symmetric heated smooth channel rotational heat transfer enhancement comparison for variations in buoyancy parameter

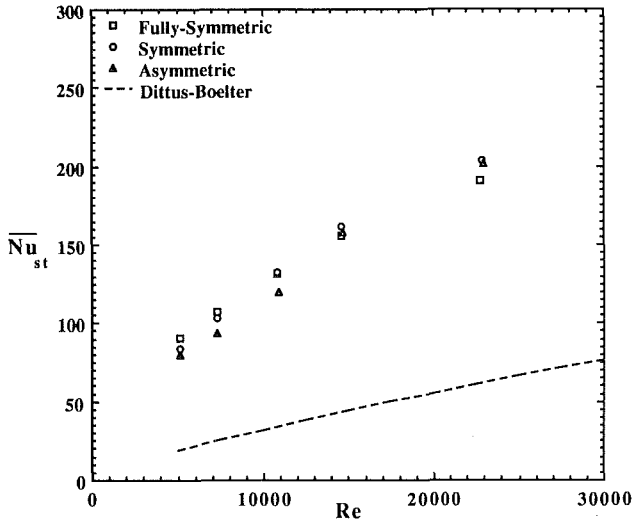

Fig. 5 Stationary turbulated channel wall heat transfer for variations in uniform heat flux distributions

Turbulated Test Section. The smooth test section was roughened with a total of nine staggered turbulators as shown in Fig. 2. Results are presented for the area between the third and fourth turbulators on the primary (liquid crystal) wall. The effects that various thermal boundary conditions have on the heat transfer coefficient in the turbulated test section in a stationary mode are shown in Fig. 5. The asymmetric heated case generally produced the lowest Nusselt number values for the range of Reynolds number investigated. While the heat transfer coefficients for the symmetric case were higher than those for the asymmetric case, the fully symmetric case produced the highest heat transfer coefficients in the low range of Reynolds numbers and the lowest heat transfer coefficients in the higher range of Reynolds numbers. To the authors' knowledge no data for a blockage ratio as high as e/D_h = 0.24, tested in this investigation, are available in the open literature for comparison. Reported 60 deg staggered data were for blockage ratios in the order of 4–6 percent (Metzger et al., 1990; Lau et al., 1991). Furthermore, highly conductive turbulators were utilized in the latter study with the turbulators fin effects included in the reported results. These factors made the comparisons inappropriate.

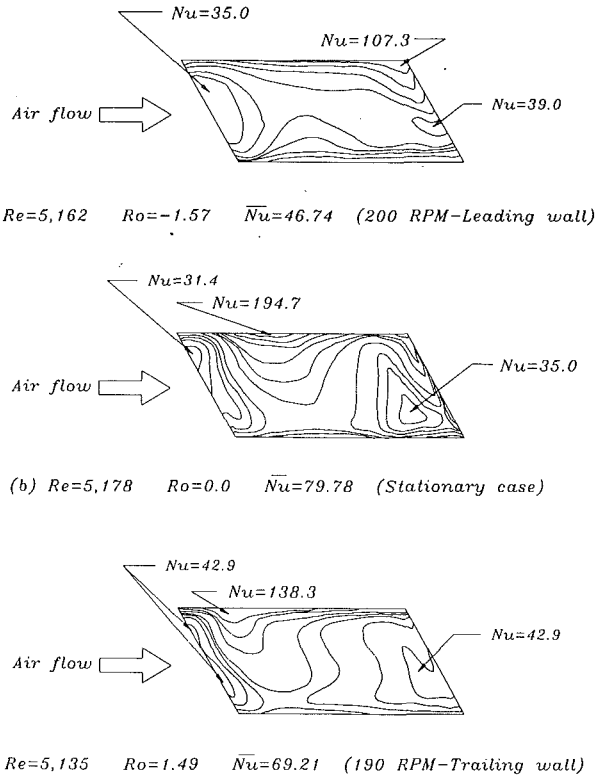

Fig. 6 Variations in iso-Nu contours between two consecutive turbulators for asymmetrically heated stationary and rotating channels

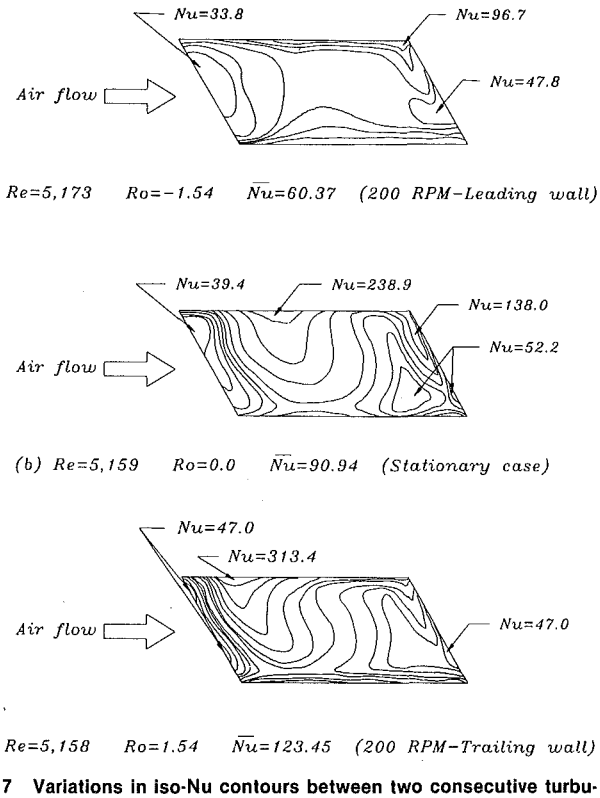

Fig. 7 Variations in iso-Nu contours between two consecutive turbulators for fully symmetric heated stationary and rotating channels

Figures 6 and 7 show typical displays of isochromes corresponding to iso-h areas in a region between a pair of turbulators on the leading and trailing walls and for the stationary,

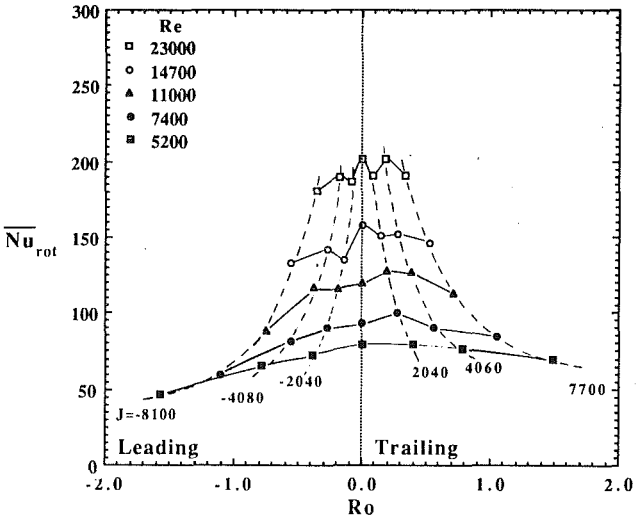

Fig. 8 Asymmetrically heated turbulated wall heat transfer at various Reynolds numbers

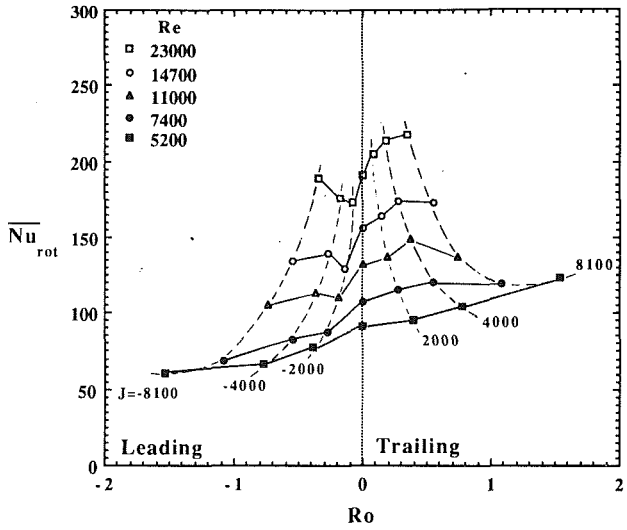

Fig. 10 Fully symmetric heated turbulated wall heat transfer at various Reynolds numbers

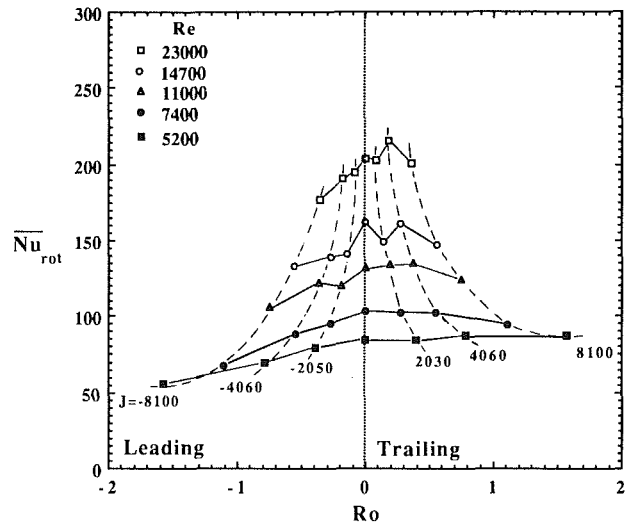

Fig. 9 Symmetrically heated turbulated wall heat transfer at various Reynolds numbers

asymmetrically, and fully symmetrically heated cases. These figures, which represent the flow "footprints" on the turbulated surface, are very helpful in interpreting the heat transfer behavior of each surface and perhaps is the major benefit of liquid crystal thermography. It is observed that there are significant differences between the iso-h patterns on the stationary wall and those on the rotating leading wall, but relatively minor differences between the iso-h patterns on the rotating trailing and stationary walls. Although minimal differences are noticed in the iso-h patterns on the trailing wall between the asymmetric and fully symmetric heated cases, a significant difference in the average heat transfer coefficient was measured. These data correspond to the highest Rotation number with the lowest Reynolds number. Hence it can be conjectured that the centripetal buoyancy effects would be most pronounced under such operating parameters and therefore suppress any possible enhancement in the asymmetric heating case.

Figures 8–10 show the thermal wall variation of average turbulated wall heat transfer coefficient with Rotation number at different Reynolds numbers for both the leading and trailing walls. The solid lines between data points are constant Reynolds number whereas the broken lines are constant rotational Reynolds number. This data representation illustrates the trend of heat transfer coefficient behavior as Reynolds number, Rotation number, and wall thermal boundary conditions vary. Several observations are noted. First, effects of the thermal boundary conditions on the leading wall heat transfer coefficients and trends are more significant as Reynolds number increases, whereas the trailing wall heat transfer coefficients and trends are generally sensitive to the choice of thermal boundary conditions at all Reynolds numbers. The maximum differences appear to occur at the highest end of the Rotation number and lowest Reynolds number. Second, while the heat transfer coefficient shows a definite rotational deficit on the leading wall for all thermal boundary conditions, only the fully symmetric thermal boundary condition shows an appreciable trailing wall enhancement at all rotational speeds. Third, a comparison between the fully symmetric case in Figs. 3 and 10 shows that the rotational heat transfer minimum, discussed previously for the smooth channel, occurs on the leading side of the turbulated channel with an increasing strength as the Reynolds number increases and rotational speed decreases. However, on the trailing side, the local minima are apparent only for the asymmetric and symmetric cases. For the fully symmetric case with the apparent downturn trend at higher Reynolds numbers, it can be speculated that those minimums will occur at higher Rotation numbers.

To show the effects of rotation on the heat transfer coefficient for all Reynolds numbers, the measured rotating heat transfer coefficients were normalized with those measured in the stationary mode at the same Reynolds number. The three thermal boundary condition results are shown in Figs. 11–13. All thermal boundary conditions show a deficit in heat transfer coefficient on the leading surface. This deficit increases with the Rotation number. At low Rotation numbers, corresponding to either high flow velocity or low angular velocity, fluid inertia overcomes forces caused by Coriolis accelerations. Therefore, the effects of rotation on heat transfer coefficient at low rotation numbers are minimal. At the highest end of the Rotation number on the leading side, however, the situation is reversed. The Coriolis accelerations are strong enough to force the flow away from the leading wall. As discussed before, the display of the iso-h lines on the leading wall at high Rotation number (Figs. 6 and 7) show a significant change in the flow "footprint" and corresponding lower heat transfer levels compared to that of stationary case.

Finally, whereas the change in deficit heat transfer due to rotation on the leading surface appears to be almost insignif-

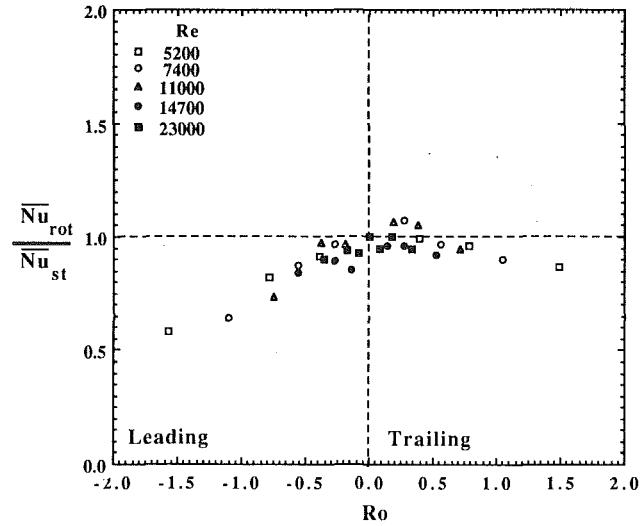

Fig. 11 Asymmetrically heated rotating turbulated channel effects on wall heat transfer

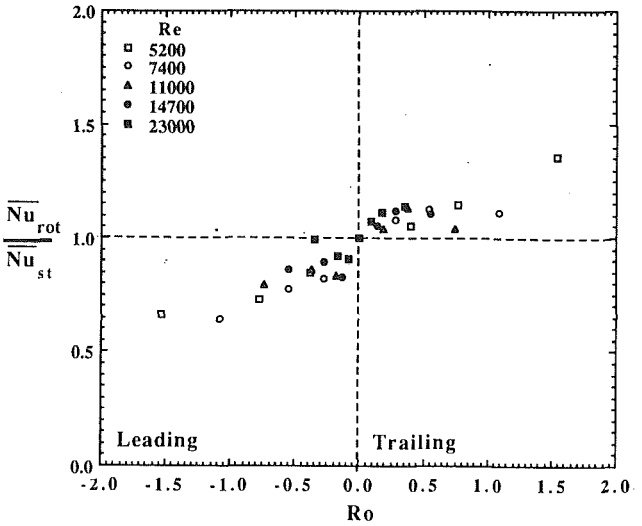

Fig. 13 Fully symmetric heated rotating turbulated channel effects on wall heat transfer

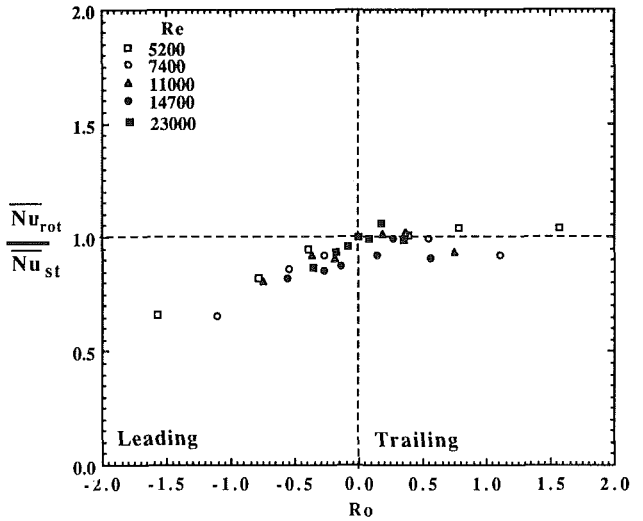

Fig. 12 Symmetrically heated rotating turbulated channel effects on wall heat transfer

icant as the number of heated walls increases, the enhancement in heat transfer coefficients on the trailing wall increases as the number of heated walls increases. It is speculated that a higher near-wall temperature gradient caused by the secondary flows in the asymmetric case produces higher centripetal buoyancy forces, which are known to have degrading effects on the heat transfer coefficients for the radially outward rotating flows. Furthermore, this behavior is consistent with the previous conclusion for rotating smooth and roughened test sections in stationary mode where, for most cases, the heat transfer coefficients increased as the number of heated walls increased.

Conclusions

Smooth Test Section

(*a*) Heat transfer coefficients for the smooth passage in stationary mode did not exhibit any appreciable sensitivity to the choice of thermal boundary condition. The same conclusion was made for the rotating mode with the exception of the results obtained at the highest Rotation number tested. Nevertheless, the fully symmetric case exhibited the highest heat transfer coefficients.

(*b*) The heat transfer coefficients on the leading side of the smooth passage showed a decreasing trend at low Rotation numbers to a minimum at about $Ro = -0.4$ and then increased with further increase of the Rotation number.

Turbulated Test Section

(*a*) In the stationary mode, the heat transfer coefficients did not vary markedly with the change of the thermal boundary conditions except that the heat transfer increased slightly with increased number of heated walls at low Reynolds numbers but decreased at higher Reynolds numbers.

(*b*) Heat transfer coefficients on the leading side of the turbulated passage in rotating mode decreased with Rotation number for all thermal boundary conditions, but appeared almost insignificantly affected by the thermal wall conditions imposed.

(*c*) Heat transfer coefficients on the trailing side were more sensitive to the choice of thermal boundary conditions. While the asymmetric case showed a slight increasing deficit in heat transfer with increased rotation, the symmetric wall indicated little change, whereas the fully symmetric case exhibited an enhancement.

Acknowledgments

Support of General Electric Aircraft Engines, Lynn, Massachusetts, is gratefully acknowledged. The authors would also like to thank Professor Tiegang Li for his valuable contribution in the data gathering process.

References

Barrow, H., 1962, "An Analytical and Experimental Study of Turbulent Gas Flow Between Two Smooth Parallel Walls With Unequal Heat Fluxes," *Int. J. Heat Mass Transfer*, Vol. 5, pp. 469–487.

Colburn, A. P., Schoenborn, E. M., and Sietton, C. S., 1945, Natl. Advisory Comm. Aeronaut. Rept. No. UD-NI.

Dittus, F. W., and Boelter, L. M. K., 1930, "Heat Transfer in Automobile Radiators of the Tubular Type," *Univ. of Cal. Publ. in Engineering*, Vol. 2, No. 13, pp. 443–461.

El-Husayni, H., 1991, "An Experimental Investigation of Heat Transfer Coefficients in Stationary and Orthogonally Rotating Smooth and Rib-Roughened Test Sections Heated on One, Two and Four Walls," M.S. Thesis, Mechanical Engineering Department, Northeastern University, Boston, MA.

Han, J. C., Glicksman, L. R., and Rohsenow, W. M., 1978, "An Investigation of Heat Transfer and Friction for Rib-Roughened Surfaces," *Int. J. Heat Mass Transfer*, Vol. 21, pp. 1143–1156.

Han, J. C., 1984, "Heat Transfer and Friction in Channels With Two Opposite Rib-Roughened Walls," ASME *Journal of Heat Transfer*, Vol. 106, pp. 774–781.

Han, J. C., Park, J. S., and Lei, C. K., 1985, "Heat Transfer Enhancement in Channels With Turbulence Promoters," ASME *Journal of Engineering for Gas Turbines and Power*, Vol. 107, pp. 628–635.

Han, J. C., Zhang, Y. M., and Lee, C. P., 1992, "Influence of Surface Heat Flux Ratio on Heat Transfer Augmentation in Square Channels With Parallel, Crossed, and V-Shaped Angled Ribs," ASME JOURNAL OF TURBOMACHINERY, Vol. 114, pp. 872–880.

Harasgama, S. P., and Morris, W. D., 1988, "The Influence of Rotation on the Heat Transfer Characteristics of Circular, Triangular and Square-Sectioned Coolant Passages of Gas Turbine Rotor Blades," ASME JOURNAL OF TURBOMACHINERY, Vol. 110, pp. 44–50.

Hatton, A. P., and Quarmby, A., 1963, "The Effect of Axially Varying and Unsymmetrical Boundary Conditions on Heat Transfer With Turbulent Flow Between Parallel Plates," *Int. J. Heat Mass Transfer*, Vol. 6, pp. 903–914.

Kline, S. J., and McClintock, F. A., 1953, "Describing Uncertainties in Single-Sample Experiments," *Mechanical Engineering*, Vol. 75, Jan., pp. 3–8.

Kostic, M., and Hartnett, J. P., 1986, "Heat Transfer to Water Flowing Turbulently Through a Rectangular Duct With Asymmetric Heating," *Int. J. Heat Mass Transfer*, Vol. 29, No. 8, pp. 1283–1291.

Lau, S. C., McMillin, R. D., and Han, J. C., 1991, "Heat Transfer Characteristics of Turbulent Flow in a Square Channel With Angled Discrete Ribs," ASME JOURNAL OF TURBOMACHINERY, Vol. 113, pp. 367–374.

Metzger, D. E., Fan, C. S., and Pennington, J. W., 1983, "Heat Transfer and Flow Friction Characteristics of Very Rough Transverse Ribbed Surfaces With and Without Pin Fins," *Proc. ASME-JSME Thermal Engineering Joint Conference*, Vol. 1, pp. 429–436.

Metzger, D. E., Fan, C. S., and Plevich, C. W., 1988, "Effects of Transverse Rib Roughness on Heat Transfer and Pressure Losses in Rectangular Ducts With Sharp 180° Turns," AIAA Paper No. 88-0166.

Metzger, D. E., Fan, C. S., and Yu, Y., 1990, "Effects of Rib Angle and Orientation on Local Heat Transfer in Square Channels With Angled Roughness Ribs," *Compact Heat Exchangers: A Festschrift for A. L. London*, Hemisphere Publishing Corp., pp. 151–167.

Morris, W. D., and Harasgama, S. P., 1985, "Local and Mean Heat Transfer on the Leading and Trailing Surfaces of a Square Sectioned Duct Rotating in the Orthogonal Mode," *Heat Transfer and Cooling in Gas Turbines*, AGARD-CP-390.

Morris, W. D., and Salemi, R., 1992, "An Attempt to Uncouple the Effect of Coriolis and Buoyancy Forces Experimentally on Heat Transfer in Smooth Circular Tubes That Rotate in the Orthongonal Mode," ASME JOURNAL OF TURBOMACHINERY, Vol. 114, pp. 858–864.

Mityakov, V. Y., Petropavlovsky, R. R., Ris, V. V., Smirnov, E. M., and Smirnov, S. A., 1984, "Turbulent Flow and Heat Transfer in Rotating Channels and Tubes," *Heat and Mass Transfer in Rotating Machinery*, D. M. Metzger and N. H. Afgan, eds., Hemisphere Publishing Corp.

Novotny, J. L., McComas, S. T., Sparrow, E. M., and Eckert, E. R. G., 1964, "Heat Transfer for Turbulent Flow in Rectangular Ducts With Two Heated and Two Unheated Walls," *AIChE J.*, Vol. 10, No. 4, pp. 466–470.

Sparrow, E. M., Lloyd, J. R.., and Hixon, C. W., 1966, "Experiments on Turbulent Heat Transfer in an Asymmetrically Heated Rectangular Duct," ASME *Journal of Heat Transfer*, Vol. 88, pp. 170–174.

Sparrow, E. M., and Cur, N., 1982, "Turbulent Heat Transfer in a Symmetrically or Asymmetrically Heated Flat Rectangular Duct With Flow Separation at the Inlet," ASME *Journal of Heat Transfer*, Vol. 104, pp. 82–89.

Sparrow, E. M., Garcia, A., and Chuck, W., 1986, "Numerical and Experimental Turbulent Heat Transfer Results for a One Sided Heated Rectangular Duct," *Num. Heat Transfer;* Vol. 9, pp. 301–322.

Tan, H. M., and Charters, W. W. S., 1969, "Effect of Thermal Entrance Region on Turbulent Forced-Convective Heat Transfer for an Asymmetrically Heated Rectangular Duct," *Solar Energy*, Vol. 12, pp. 513–516.

Tan, H. M., and Charters, W. W. S., 1970, "An Experimental Investigation of Forced-Convective Heat Transfer for Fully-Developed Turbulent Flow in a Rectangular Duct With Asymmetric Heating," *Solar Energy*, Vol. 13, pp. 121–125.

Taslim, M. E., and Spring, S. D., 1988, "Experimental Heat Transfer and Friction Factors in Turbulated Cooling Passages of Different Aspect Ratios, Where Turbulators are Staggered," Paper No. AIAA-88-3014.

Taslim, M. E., Rahman, A., and Spring, S. D., 1989a, "An Experimental Investigation of Heat Transfer Coefficients in a Spanwise Rotating Channel With Two Opposite Rib-Roughened Walls," ASME JOURNAL OF TURBOMACHINERY, Vol. 113, pp. 75–82.

Taslim, M. E., Chrysafis, C., and Kercher, D. M., 1989b, "An Experimental Study of Heat Transfer in a Spanwise Rotating Channel Turbulated With 45 Degree Criss-Cross Ribs," ASHE HTD-Vol. 120, pp. 11–23.

Taslim, M. E., Bondi, L. A., and Kercher, D. M., 1991, "An Experimental Investigation of Heat Transfer in an Orthogonally Rotating Channel Roughened With 45 deg Criss-Cross Ribs on Two Opposite Walls," ASME JOURNAL OF TURBOMACHINERY, Vol. 113, pp. 346–353.

Wagner, J. H., Kim, J. C., and Johnson, B. V., 1986, "Rotating Heat Transfer Experiments With Turbine Airfoil Internal Flow Passages," ASME Paper No. 86-GT-133.

Wagner, J. H., Johnson, B. V., and Hajek, T. J., 1991, "Heat Transfer in Rotating Passage With Smooth Walls and Radial Outward Flow," ASME JOURNAL OF TURBOMACHINERY, Vol. 113, p. 42–51.

Wagner, J. H., Johnson, B. V., Graziani, R. A., and Yeh, F. C., 1992, "Heat Transfer in Rotating Serpentine Passages With Trips Normal to the Flow," ASME JOURNAL OF TURBOMACHINERY, Vol. 114, pp. 847–857.

S. Mochizuki

J. Takamura

Department of Mechanical Engineering,
Tokyo University of Agriculture and Technology,
Koganei, Tokyo, Japan

S. Yamawaki

R&D Department,
Aeroengine and Space Operations,
Ishikawajima-Harima Heavy Industries,
Mizuho, Tokyo, Japan

Wen-Jei Yang

Department of Mechanical Engineering and Applied Mechanics,
The University of Michigan,
Ann Arbor, MI 48109-2125

Heat Transfer in Serpentine Flow Passages With Rotation

Heat transfer characteristics of a three-pass serpentine flow passage with rotation are experimentally studied. The walls of the square flow passage are plated with thin stainless-steel foils through which electrical current is applied to generate heat. The local heat transfer performance on the four side walls of the three straight flow passages and two turning elbows are determined for both stationary and rotating cases. The throughflow Reynolds, Rayleigh (centrifugal type), and rotation numbers are varied. It is revealed that three-dimensional flow structures cause the heat transfer rate at the bends to be substantially higher than at the straight flow passages. This mechanism is revealed by means of a flow visualization experiment for a nonrotating case. Along the first straight flow passage, the heat transfer rate is increased on the trailing surface but is reduced on the leading surface, due to the action of secondary streams induced by the Coriolis force. At low Reynolds numbers, the local heat transfer performance is primarily a function of buoyancy force. In the higher Reynolds number range, however, the circumferentially averaged Nusselt number is only a weak function of the Rayleigh and rotation numbers.

Introduction

In modern high-performance gas turbines, the effective cooling of gas turbine blades (especially nozzle blades, and first-stage moving blades, which are under severe thermal conditions) is essential to the enhancement of their performance. In general, film cooling is imposed on external surface of turbine blades, while forced-convection cooling is often performed inside the blades, by means of a winding cooling passage, as depicted in Fig. 1. In the case of moving blades, the flow and heat transfer mechanisms are extremely complex, since both the Coriolis force and the buoyancy force in the centrifugal acceleration field exert the same order of effects on flows in the passage. Morris and Ayhan (1979) investigated the influence of rotation on heat transfer in the coolant channel of gas turbine rotor blades. Wagner et al. (1991a) treated the buoyancy-force-controlled heat transfer phenomena in rotating passages with radial outward flow. Wagner et al. (1991b) conducted experimental studies on heat transfer performance in rotating serpentine passages of square cross section. It was revealed that significant changes occurred in the heat transfer performance at the turning sections, and there were considerable differences between the inward and outward flows in the straight sections of the flow passage. The Rayleigh number was higher than the Reynolds number, implying that the heat transfer performance was buoyancy controlled. Wagner et al. (1991a) and Taslim et al. (1991) reviewed the existing literature on rotating passages with smooth walls, and experimentally studied the effects of rotation on heat transfer performance in rotating, square passages with smooth walls and with opposite rib-roughened walls, respectively. Iacovides and Launder (1991) studied fully developed flow in rotating rectangular ducts under constant wall heat flux conditions. Other studies on heat transfer performance inside rotating channels and tubes include those of Siegel (1985), Guidez (1989), and Medwell et al. (1991). However, the flow and heat transfer characteristics in serpentine flow passages are not yet sufficiently clear.

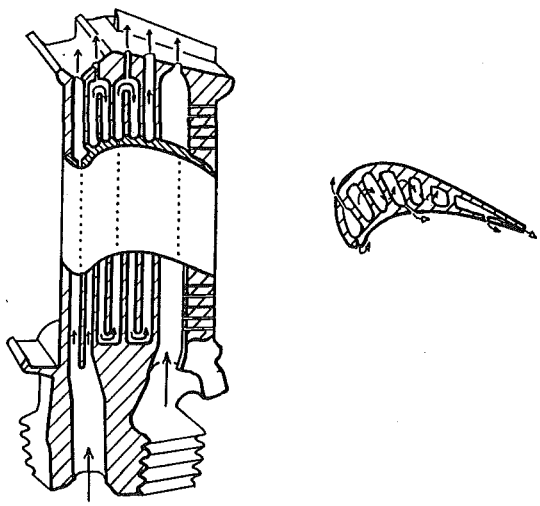

Fig. 1 A schematic of a winding flow passage inside a moving turbine blade

Contributed by the International Gas Turbine Institute and presented at the 37th International Gas Turbine and Aeroengine Congress and Exposition, Cologne, Germany, June 1-4, 1992. Manuscript received by the International Gas Turbine Institute February 17, 1992. Paper No. 92-GT-190. Associate Technical Editor: L. S. Langston.

In the present paper, an experimental study is performed to determine convective heat transfer inside a serpentine flow passage of square cross section, rotating about an axis that is perpendicular to the straight flow passage. The purpose of the study is to disclose the general, fundamental characteristics of basic elements (outward and inward straight flow passages and bends) in an internal convective cooling passage of axial-flow-type gas turbine blades. The four walls of the square flow passage are maintained at constant heat flux condition, which is different from the constant wall temperature case used in the previous study by Wagner et al. (1991a, b). The thermal boundary condition on the walls of cooling passages in actual turbine blades is under neither constant temperature nor constant heat flux but is in between the two. The difference in the heat transfer coefficients, resulting from the two thermal boundary conditions, is insignificant. The effects of both the secondary stream (induced by the Coriolis force) and the buoyancy force (caused by the centrifugal force) on heat transfer characteristics are investigated.

Experimental Apparatus and Procedure

A variety of geometries and dimensions are used for the winding flow passages within actual turbine blades. The average equivalent (or hydraulic) diameter d_e is about 3 mm; the length of a straight flow portion L is 6 to 15 times d_e; and the average rotating arm length of blades R is 30 to 70 times d_e. In this study, an enlarged model about 7 times the actual size of a turbine blade is employed. For the model, d_e = 20 mm (square flow cross section with 20 mm sides), L = 210 mm, and R = 880 mm. The inlet air temperature was 18 to 25°C (i.e., room temperature under one atmosphere).

The test section is illustrated schematically in Fig. 2. It consists of two radially outward, straight flow sections, one radially inward straight flow section, and two 180-deg flow bends. These flow sections rotate about the axis, which is perpendicular to the straight flow passages, as shown. In order to distinguish the four side walls of the square flow passage, the front and rear walls, relative to the rotating direction, are called the leading and trailing surfaces, respectively. The other two side walls are named the right and left surfaces, in reference to an observer facing the flow direction.

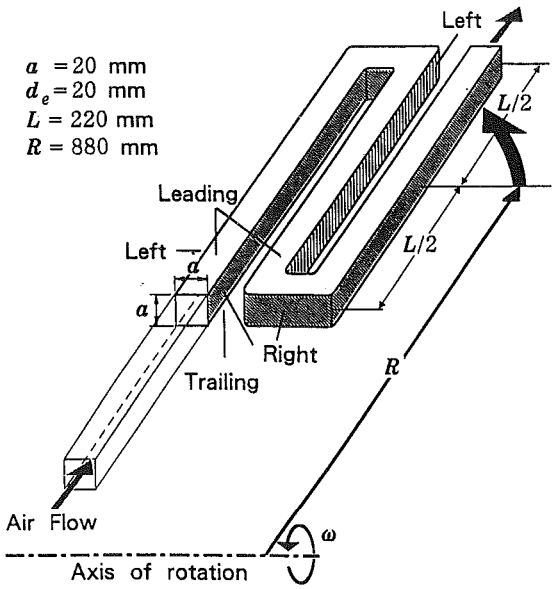

Fig. 2 Geometry and dimensions of a serpentine flow passage and its axis of rotation

Figure 3 depicts the details of the test section and the position of thermocouples for measuring the heat transfer surface temperature. The flow passages are made of a Bakelite plate, which is fabricated by means of precision machine cutting. The values of the curvature r at the inner and outer corners of the bends are 4 mm and 10 mm, respectively. One 50-μm-thick piece of stainless steel foil covers each of the four side walls. By passing electric current through the steel, the foils become heating surfaces of uniform heat flux. The entire test section is covered with insulating material. As shown in Fig. 3, the K type (alumel-chromel) thermocouples are positioned on each of the four side walls at 17 different locations along the flow direction,

Nomenclature

a = side length of passage cross section, m
C_p = specific heat, kJ/kg-°C
d_e = mean equivalent (i.e., hydraulic) diameter, m
f = force, N; f_{CE}, centrifugal, f_{CO}, Coriolis
Gr = Grashof number = $R\omega^2\beta d_e\Delta T_m/\nu^2$
k = thermal conductivity of air, W/m-°C
L = length of straight flow passage, m
l_s = length of entrance region, m
$\dot{m}$ = mass flow rate, kg/s
Nu = Nusselt number as defined by Eq. (2); Nu_∞, stationary and fully developed both hydrodynamically and thermally
Nu_m = average Nusselt number over the entire first straight flow passage = $\alpha_m d_e/k$
Nu′ = circumferential average Nusselt number as defined by Eq. (3)
n = number of revolutions per minute
Pr = Prandtl number
$\dot{q}_w$ = heat flux of passage walls, W/m^2
R = mean radius of rotating blade, m
Ra = Rayleigh number, as defined by Eq. (2)
Re = Reynolds number, as defined by Eq. (2)
Ro = rotation number, as defined by Eq. (2)
T = temperature, °C; T_b, of bulk fluid, T_w, of passage wall
T_o = inlet fluid temperature
T_w' = circumferential average wall temperature as defined by Eq. (4), °C
ΔT_m = mean temperature difference = $(z_1, z_2, [T_w'(z) - T_b(z)]dz/(z_2 - z_1))$
u = fluid velocity in flow passage, m/s
u_m = mean fluid velocity in flow passage
z = flow distance from the place where wall heating begins, m
α = convective heat transfer coefficient as defined by Eq. (1) W/m^2-°C; α_∞, stationary and fully developed both hydrodynamically and thermally
α_m = average heat transfer coefficient = $\dot{q}_w/\Delta T_m$
α' = circumferential average heat transfer coefficient as defined by Eq. (4), W/m^2-°C
β = coefficient of thermal expansion, 1/K
ν = kinematic viscosity, m^2/s
ω = angular velocity of rotation, rad/s

Subscripts

b = bulk fluid
e = equivalent
m = average over entire first straight flow passage
w = passage wall
∞ = stationary case, fully developed

Superscript

′ = circumferential average

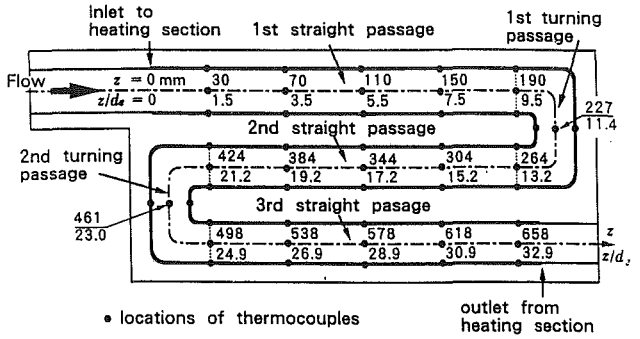

Fig. 3 Location of thermocouples in serpentine flow passage

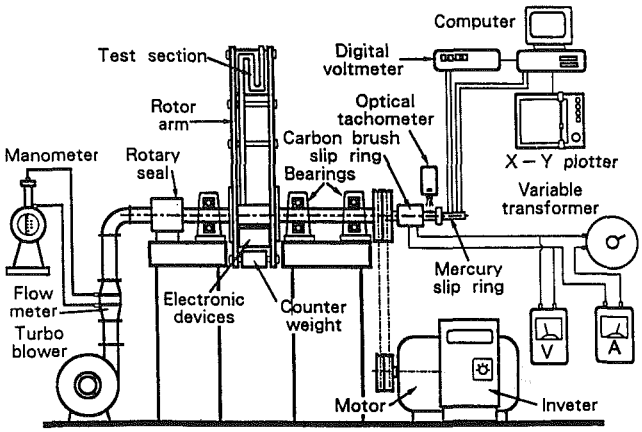

Fig. 4 A schematic of the experimental apparatus

to monitor the heating surface temperature T_w. The distance z is measured along the centerline of the flow passage, from the point at which heating begins. The portions of flow passage beginning at z/d_e = 0, 9.5, 13.2, 21.2, 24.9, . . . are called the first straight passage, first turning passage, second straight passage, and second turning passage, . . ., respectively.

A schematic of the experimental apparatus is shown in Fig. 4. The test section is joined to the tip of a rotor arm, which is attached to the rotating shaft. An induction motor drives the shaft via a V belt. The rotating speed of the motor is controlled by an inverter, while the rotor speed is monitored by means of an optical-type digital tachometer. The air from a turbo fan flows through a laminar flow meter and a rotary seal into the hollow rotating shaft. It then changes flow direction by 90 deg and flows into the test section after traveling through a straight entrance region (length l_s = 660 mm, l_s/d_e = 30), which has a square flow cross section identical to the flow passage inside the test section. The air that exits the test section releases into the atmosphere. The voltage of the electric power used for heating the heat transfer surface is regulated by a variable transformer. The power is supplied to the test section via a carbon brush slip ring. The air temperature at the inlet of the test section is measured by means of the K-type thermocouples 300 μm in diameter.

It is not an easy task to transfer many signals from a rotating body to a stationary system. In the present experimental apparatus, an electronic device is incorporated into the rotating system in order to extract 70 thermocouple outputs. Figure 5 illustrates the diagram of the circuit used for these temperature measurements. The outputs from all thermocouples are led first to cold junctions, installed inside the rotating body, and then to microrelay switches. A signal from the computer activates a digital circuit inside the rotating body, which turns microrelay switches to select the desired thermocouple. The signal from the selected thermocouple is amplified by means

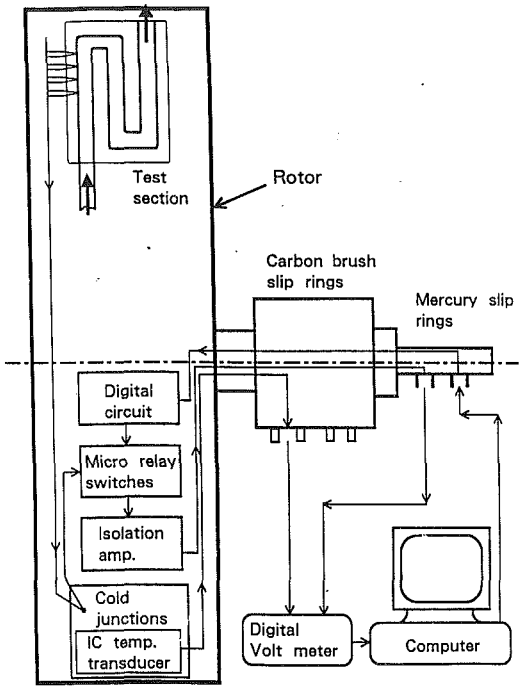

Fig. 5 A circuit for temperature measurements

of an isolation amplifier in order to raise the S/N ratio. It is then transmitted out of the rotating body via a mercury slip ring. All thermocouple outputs are thus transmitted from the rotating body to the stationary space, and automatically recorded. The mercury slip ring employed in the present study has two channels: one for transmitting the input signal from the computer, the other for extracting the output signals of the thermocouples.

Experimental Results and Discussion

The local heat transfer coefficient α is defined as

$$\alpha = \dot{q}_w/(T_w - T_b) \tag{1}$$

The Nusselt, Reynolds, rotation, and Rayleigh numbers are defined respectively as

$$\left.\begin{aligned} &\mathrm{Nu} = \alpha d_e/k,\ \mathrm{Re} = u_m d_e/\nu, \\ &Ro = \omega d_e/u_m,\ \mathrm{Ra} = (\beta \dot{q}_w R/k)(\mathrm{Re}Ro)^2\mathrm{Pr} \end{aligned}\right\} \tag{2}$$

Here, Ra denotes the modified Rayleigh number commonly employed in natural convective heat transfer, under the uniform wall heat flux condition. The use of this Rayleigh number is convenient for the constant wall heat flux case, since it is relatively simple to impose a desired value of the heat flux q_w, while to produce a desired value of the wall temperature (equivalently the wall-fluid temperature difference) is rather difficult. One can rewrite Ra as

$$\mathrm{Ra} = \mathrm{Nu}_m \mathrm{GrPr}$$

where

$$\mathrm{Gr} = R\omega^2 \beta d_e^3 \Delta T_m/\nu^2$$

The air flow rate, rotational speed of the rotor, and heating rate are varied to change the values of Re, Ro, and Ra. The heat transfer performance, in the form of the dimensionless parameter Nu, is measured. An uncertainty analysis was conducted following the principles described by Kline and McClintock (1953). The uncertainty in heat transfer measurements (i.e., heat transfer coefficients) was estimated to be within ±15 percent.

One of the most important features of heat transfer in wind-

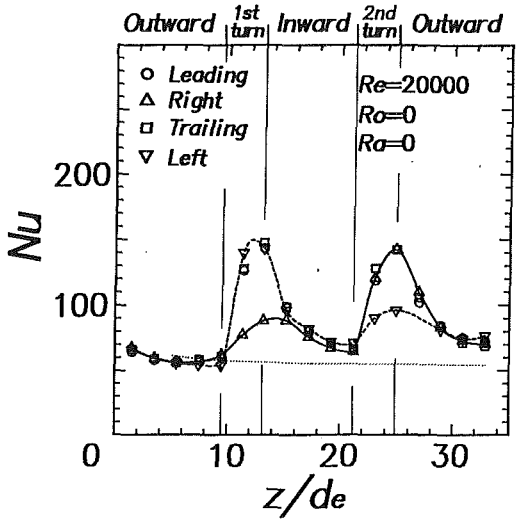

Fig. 6 Distribution of Nusselt numbers in the serpentine flow passage at Re = 20,000 and Ra = *Ro* = 0

ing flow passages may be found at the 180-deg bends, where complex flow phenomena exert strong effects on heat transfer characteristics.

1 Stationary Case. An example is shown in Fig. 6 for the distribution of local Nusselt numbers in the flow direction at Re = 20,000 for the stationary case (corresponding to Ra = *Ro* = 0). It is disclosed that:

(*i*) In the first outward straight flow passage, the values of Nu at the four side walls coincide and agree well with those in the thermal entrance region of turbulent flow inside a long, straight tube (Kays and Crawford, 1980), as shown by the dotted line. It should be noted that, in the present test setup, a fully developed turbulent flow enters the thermal entrance region, due to the hydrodynamic region prior to the test section.

(*ii*) In both the first and second bends, the values of Nu at all four side walls increase. The increase in Nu at the curved outer wall is especially notable. The values of Nu at the leading and trailing surfaces are identical and as high as those at the curved outer wall. The Nu at the curved inner wall is the lowest of the four side walls.

(*iii*) The second (inward) and third (outward) straight flow passages are subject to the influence of the circulating flow in their upstream bends, resulting in higher values of Nu at the left wall surface (∇) at the entrance of the second straight flow passage and the right wall surface (Δ) at the entrance of the third straight flow passage. Further downstream, however, the values of Nu for the four side walls coincide again.

(*iv*) All local Nu values downstream of the first straight flow passage are higher than that of a long straight tube, as represented by the dotted line in Fig. 6.

From the above observations, one concludes that in the stationary case, heat transfer downstream of the first bend is strongly influenced by the flow characteristics in the bend. That is, the left and right surfaces have markedly distinct heat transfer characteristics, while the leading and trailing surfaces exhibit the same thermal behavior.

To aid in understanding heat transfer mechanisms at the first bend, a flow visualization study is performed on a physical model, which is identical to the test section, except that the Bakelite cover plate of the leading surface is replaced by transparent plexiglass. Paraffin mist is used as the tracer to observe the flow patterns in and around the first bend, as depicted in Fig. 7. Figures 7(*a*), (*b*), and 7(*c*) correspond to the cases where the mist is injected (*a*) near the left wall, (*b*) at the midway between (*a*) and (*c*), and (*c*) along the passage axis. The air

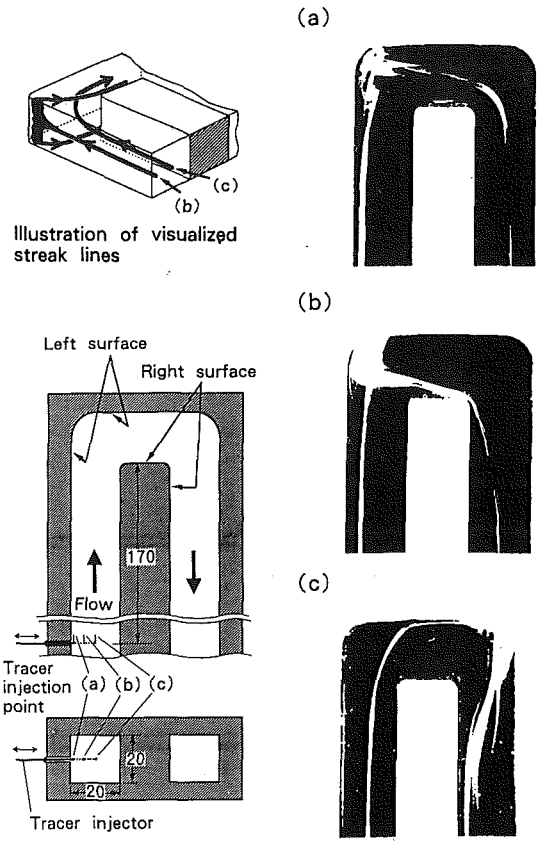

Fig. 7 Flow visualization in first bend of stationary passage with mist injected in the first straight section, (*a*) near left surface, (*c*) along passage axis, and (*b*) midway between (*a*) and (*c*), Re = 300

flow is set at Re = 300, for reference purposes. In case (*c*), the mist traveling along the passage axis collides with the left wall of the bend. It then switches to follow the right wall in the second straight flow passage. Both cases (*a*) and (*b*) are characterized by a large inverse flow region at the left corner of the bend. A visual, observation reveals that the mist follows the left wall into the bend, where it takes a head-on collision and splits into two streams, one upward and one downward, to wash the left corner, then separately follow the main flow. In short, the flow in the bend is three dimensional and extremely complex as shown in the illustration of visualized streak lines. The aforementioned phenomena in items (*ii*) and (*iv*) result from three-dimensional flow structures.

2 Rotating Case. Examples of the local T_w and Nu distributions along the flow passage are illustrated in Figs. 8(*a*) and 8(*b*), respectively, for the flow passage in rotation, with Re = 20,000, *Ro* = 0.046, and Ra = 1.25×10^8. It is disclosed from Fig. 8(*a*) that, as a general trend, the wall temperatures are higher at the straight channel sections and lower in the bend regions. Since the wall heat flux is constant in the present study, the bulk mean air temperature increases with the flow distance z/d_e as shown. Figure 8 illustrates that, in spite of an increase in the cooling air temperature along the flow passage, the maximum wall temperature is achieved not at the downstream region, but at the leading surface, in the first straight flow passage. This is one of the special phenomena observed when the flow passage is in rotation. Figure 8(*b*) shows that:

(*i*) In the first straight flow passage, Nu increases along the trailing surface, decreases along the leading surface, and increases slightly along the right and left surfaces.

(*ii*) In contrast to the first straight flow passage, in the second passage the local Nu increases along the leading surface and decreases along the trailing surface. This reversal of Nu

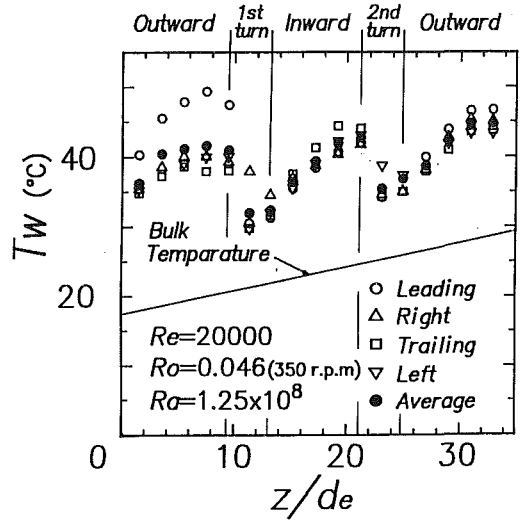

Fig. 8(*a*) Variation of local wall temperature along rotating flow passage at Re = 20,000, *Ro* = 0.046 (i.e., 350 rpm), and Ra = 1.25 × 10^8

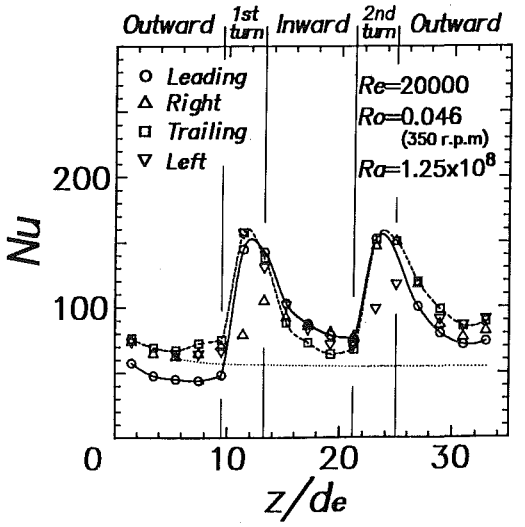

Fig. 8(*b*) Variation of local Nu's along rotating flow passage at Re = 20,000 *Ro* = 0.046 (i.e., 350 rpm), and Ra = 12.5 × 10^8

between the two surfaces is repeated again in the third straight flow passage.

(*iii*) As in the stationary case, the values of Nu on the four side walls of the bends are all significantly higher than that of a straight tube (shown by the dotted lines). The Nu of the curved inner side wall is lower than the Nu values of the other three side walls, but is higher than the stationary case. In short, the basic trend of heat transfer characteristics at the bends is not much different from that of the stationary case.

3 First Straight Flow Passage in Rotation. As shown above, the heat transfer characteristics in the rotating serpentine flow passage are extremely complex. Each flow passage has a distinct heat transfer mechanism that requires detailed investigation. The present study focuses on heat transfer in the first straight flow passage: Figs. 9 and 10 depict the variations of heat transfer coefficient ratios, Nu/Nu_∞, in the first straight flow passage, for Re = 4,000, $\dot{q}_w$ = 315 W/m^2, and Re = 20,000, $\dot{q}_w$ = 1650 W/m^2, respectively. The rotating speed ranges from 0 to 500 rpm. Only results for the leading and trailing surfaces are included because only they are significantly influenced by rotation. Nu_∞ is the Nusselt number in a stationary straight tube with fully developed hydrodynamic

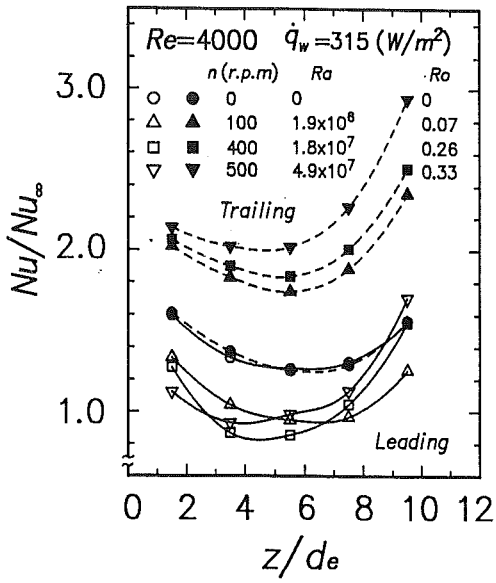

Fig. 9 Variation of heat Nusselt number in the first straight flow passage at Re = 4000 and $\dot{q}_w$ = 315 W/m^2 with $\beta\Delta T$ = 0.037 to 0.11

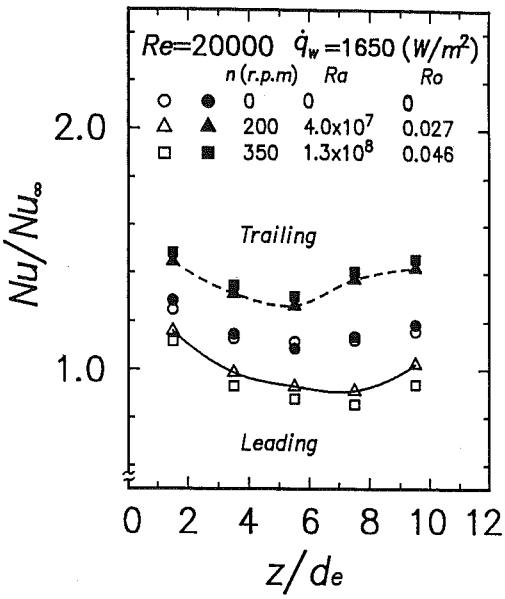

Fig. 10 Variation of heat Nusselt number in the first straight flow passage at Re = 20,000 and $\dot{q}_w$ = 1650 W/m^2 with $\beta\Delta T$ = 0.037 to 0.11

and thermal fields (Kays and Crawford, 1980). The Kays–Crawford formula reads

$$\mathrm{Nu}(z) = \mathrm{Nu}_\infty[1.0 + C/(z/d_e)]$$

where

$$\mathrm{Nu}_\infty = 0.022\ \mathrm{Re}^{0.8}\mathrm{Pr}^{0.5}$$

$$C = 0.8[1.0 + (\mathrm{Re}/1700)^{-1.5}],\ 3000 < \mathrm{Re} < 5 \times 10^5$$

$$z/d_e > 5,\ \mathrm{Pr} = 0.717$$

Figures 9 (Re = 4000) and 10 (Re = 20,000) represent the lower and higher flow rate cases, respectively.

The following is deduced from these figures:

(*i*) In the stationary case (n = 0), the distributions of heat transfer coefficients on the leading (open circle) and trailing (solid circle) surfaces coincide. They first decrease along the flow, but then rebound near the end of the straight passage.

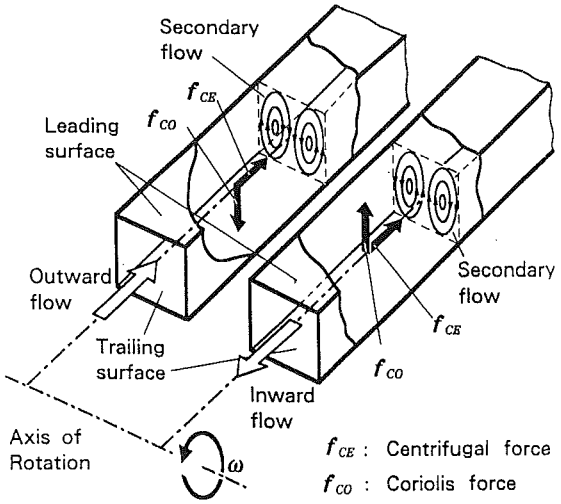

Fig. 11 Generation of secondary flows in the first and second straight flow passages due to rotation

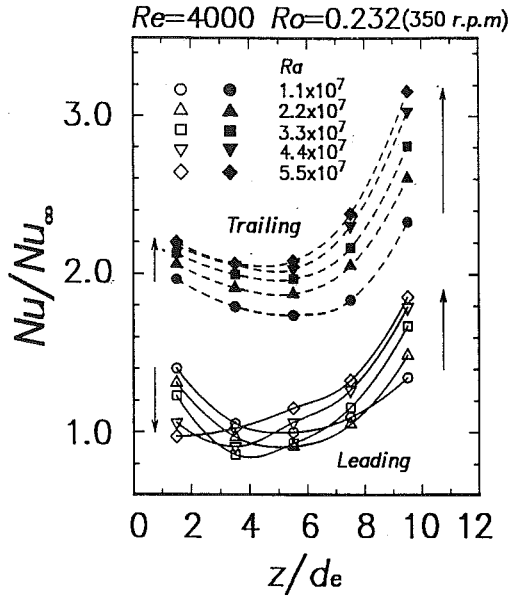

Fig. 12 Variation of Nusselt numbers along first straight flow passage in rotation at Re = 4000 and Ro = 0.232 (i.e., 350 rpm) with $\beta\Delta T$ = 0.037 to 0.11

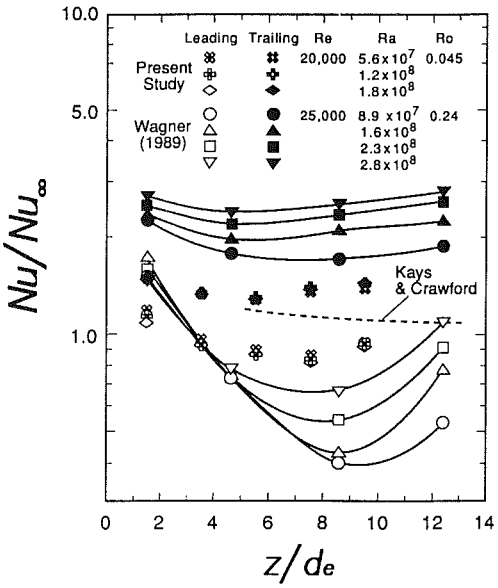

Fig. 13 Variation of Nusselt numbers along first straight flow passage in rotation with $\beta\Delta T$ = 0.037 to 0.11

The rebound is due to the effects of the bend propagating upstream into the straight passage. (z/d_e = 9.5 corresponds to the exit of the straight passage, i.e., the inlet of the bend).

(*ii*) When the flow passage is in rotation, Nu of the trailing surface increases over the entire passage, while Nu of the leading surface declines, even to a value below Nu_∞. As a result, Nu of the trailing surface is higher than Nu of the leading surface over the whole flow passage. For example, at Re = 4,000 in Fig. 9, Nu of the trailing surface is roughly twice that of the leading surface.

(*iii*) In the rotating cases, the distribution of Nu on the trailing surface first diminishes along the flow passage, and then rebounds. The location of this "rebound" migrates upstream with increasing rotation number R_o.

The aforementioned phenomena observed in the rotating flow passage result from a combination of both the Coriolis and centrifugal forces, in addition to a contribution of forced convection by the mainstream. Figure 11 illustrates a schematic diagram of secondary flow patterns that are induced in the rotating flow passages, both when the fluid is flowing outward from, and inward toward, the axis of rotation. The figure is used to explain the mechanisms that induce the previously mentioned phenomena: When a fluid flows in a tube rotating about an axis that is perpendicular to the tube axis, a centrifugal force f_{CE} acts on every part of the fluid. In addition, a Coriolis force f_{CO}, whose magnitude is proportional to the flow velocity u (radial component), acts in the direction perpendicular to u. The direction of f_{CO} varies with the direction of u (outward or inward flow), as depicted in the figure. Due to the action of viscosity, u is small near the tube walls and large near the tube axis. As a result, a relatively large Coriolis force appears in the central portion of the flow cross section, and consequently a secondary flow is produced, as shown schematically in the figure. The rotational directions of this secondary flow are completely opposite that of the outward and inward flows. In the presence of such a secondary flow, the heat transfer performance of the side wall (i.e., the trailing surface for outward flow, or the leading surface for inward flow), which receives relatively cold fluid from the tube center will be enhanced. This trend becomes more pronounced with an increase in the rotational speed. This explains item (*ii*) concerning the trailing surface having a higher heat transfer rate than the leading surface.

The heat transfer performance in a rotating flow passage is subject to forced convection due to the main stream flow (flow in the tube-axis direction), the secondary flow induced by the Coriolis force, and the buoyancy effect caused by the centrifugal force. The magnitudes of their effects are represented by the Reynolds, rotation, and Rayleigh numbers, respectively.

Re (i.e., throughflow rate) and Ro (number of revolutions per minute) are held constant while Ra (heat flux $\dot{q}_w$) is varied to investigate the effects of the buoyancy force. Representative results are shown in Figs. 12 and 13 for Re = 4000, Ro = 0.232, and Re = 20,000, Ro = 0.045, respectively. These figures reveal that:

(*i*) When Ro is relatively high (Fig. 12), the heat transfer characteristics of both the leading and trailing surfaces are significantly affected by Ra. The heat transfer performance is controlled by Ra.

(*ii*) Ra has little influence on Nu when Ro is relatively low (Fig. 13). This is the case of heat transfer controlled by Re.

(*iii*) When the effect of Ra is significant (Fig. 12), an

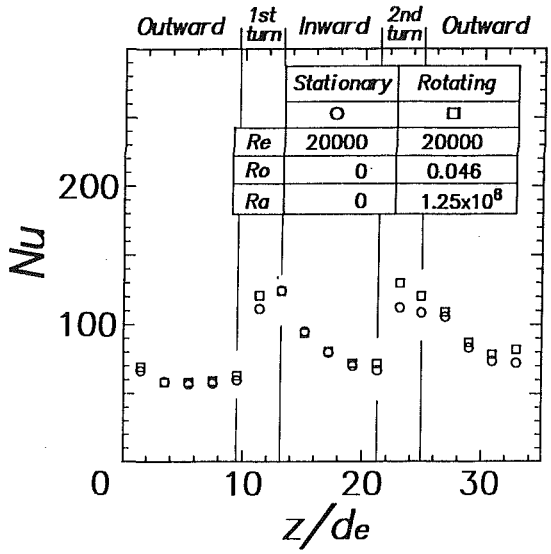

Fig. 14 Variations of circumferential average Nusselt numbers in the three-pass serpentine flow passage in stationary and rotating cases

increase in Ra is accompanied by increased Nu at the trailing surface throughout the entire flow passage, while Nu at the leading surface diminishes at the passage inlet and increases at the exit. (This appears to happen at both leading and trailing surfaces.)

Some test data of Wagner et al. (1991a) are superimposed in Fig. 13 for comparison. It is seen that these results support the observations described in items (*i*) and (*iii*).

Since the leading and trailing surfaces have markedly different heat transfer characteristics, the designers of cooling flow passages in rotor blades must take this finding into consideration.

Because Nu increases on the trailing surface but decreases on the leading surface, the circumferential average Nusselt number Nu′ would not change much in rotating flow passages. Nu′ is defined as

$$\mathrm{Nu}'(z) = \alpha'(z) d_e / k \tag{3}$$

where

$$\left.\begin{aligned} \alpha'(z) &= \dot{q}_w / (T_w'(z) - T_b(z)) \\ T_w'(z) &= (T_{w_{\text{leading}}} + T_{w_{\text{trailing}}} + T_{w_{\text{right}}} + T_{w_{\text{left}}})/4 \\ T_b(z) &= T_o + 4az\dot{q}_w/(\dot{m}C_p) \end{aligned}\right\} \tag{4}$$

Figure 14 is an example showing the variations of Nu′ along the entire flow passage for both the stationary (shown by circles) and rotating (shown by squares) cases. It is seen that rotation augments Nu′ in the bends as well as the third straight flow passage, but only slightly in the first and second straight flow passages.

Since the flow velocity diminishes in both the main flow and circumferential direction at all four corners of a square flow cross section, it is easy to expect a retardation in the local heat transfer coefficients there. In other words, one realizes that the local heat transfer coefficients are not uniform in the circumferential direction. In the present study, thermocouples are installed at the center of each of the four walls at several locations along the flow passage to measure the representative temperatures of each surface. The readings from these thermocouples are substituted into Eq. (4), which yields the average heat transfer coefficient based on the center temperatures of the four walls. It is anticipated that the present results are somewhat higher than the circumferentially averaged heat transfer coefficient including the four corners and their vicinity.

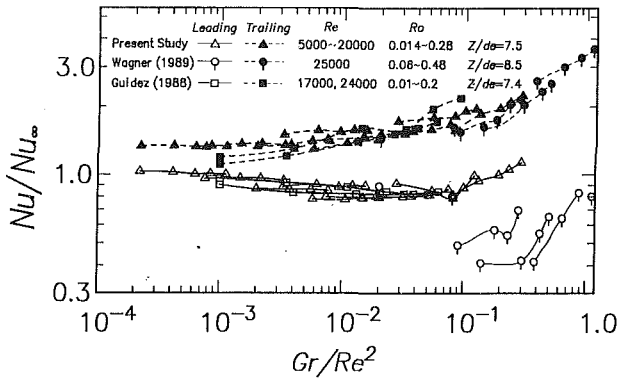

Fig. 15 Comparison with previous experimental results

4 Comparison With Previous Experimental Results. Figure 15 depicts the effects of Gr/Re^2 on Nu/Nu_∞ for the leading and trailing surfaces, at $z/d_e = 7.5$ in the radially outward flow passage (indicated by open and solid triangles). The existing data of Wagner et al. at $z/d_e = 8.5$ (open and solid circles) and Guidez at $z/d_e = 7.4$ (open and solid squares) are superimposed on Guidez at $z/d_e = 7.4$ (open and solid squares) are superimposed on the figure for comparison. Note that Gr is defined as $R\omega^2\beta\, d_e{}^3\Delta T/\nu^2$. Both the present and Guidez's (1989) studies were under uniform wall heat flux, while the study of Wagner et al. (1991a) utilized uniform wall temperature and all used a square flow passage.

It is seen in the figure that the three studies agree fairly well in the Nusselt numbers on the trailing surface over the entire range of Gr/Re^2 and also in those on the leading surface up to Gr/Re^2 of 0.1. The agreement in the Nusselt numbers on the leading surface breaks down when Gr/Re^2 exceeds 0.1. The data of Wagner et al. fall drastically below those of the present study beginning at Gr/Re^2 of approximately 0.1. The reason is uncertain. Nevertheless, it is important to point out that the Nu curves for both the trailing and leading surfaces deflect at $Gr/Re^2 \approx 0.1$. It is conjectured that the buoyancy effects begin to change at $Gr/Re^2 \approx 0.1$. A further study is needed to explore its mechanism.

Conclusions

Heat transfer performance in a rotating serpentine flow passage of square cross section is experimentally investigated. The test section is preceded by a hydrodynamic calming region. The test model is a blow-up (by seven times) model of actual winding flow passages in rotor blades. It is concluded from the study that:

(*i*) The flow in the 180-deg bends exhibits strong three-dimensional structure.

(*ii*) The heat transfer coefficient in the bend is substantially higher than in the straight flow passages. Hence, the average heat transfer characteristics over the entire flow passage is greatly affected by flow at the 180-deg bends.

(*iii*) Due to secondary flow induced by the Coriolis force, the heat transfer coefficient in the radially outward flow passages diminishes on the leading surface, but increases on the trailing surface, with an increase in rotational speed. The trend is reversed in the radially inward flow passages.

(*iv*) In the radially outward flow passages:

(*a*) For relatively high rotation numbers, the Nusselt numbers on the leading and trailing surfaces are governed by buoyancy effects, namely the Raleigh number.

(*b*) Since changes of the Nusselt numbers on the leading and trailing surfaces are in opposite directions, the average heat transfer coefficient of the entire flow passage is a weak function of the Rayleigh and Rossby numbers.

Acknowledgments

The authors wish to thank Messrs. Y. Yamanaka and S. Higuchi for their efforts in fabricating the experimental apparatus and conducting the tests.

References

Guidez, J., 1989, "Study of the Convective Heat Transfer in a Rotating Coolant Channel," ASME JOURNAL OF TURBOMACHINERY, Vol. 111, pp. 43–50.

Iacovides, H., and Launder, B. E., 1991, "Parametric and Numerical Study of Fully Developed Flow and Heat Transfer in Rotating Rectangular Ducts," ASME JOURNAL OF TURBOMACHINERY, Vol. 113, pp. 331–338.

Kays, W. M., and Crawford, M. E., 1980, *Convective Heat and Mass Transfer*, 2nd ed., McGraw-Hill, New York, p. 243.

Kline, S. J., and McClintock, F. A., 1953, "Describing Uncertainties in Single Sample Experiments," *Mechanical Engineering*, Vol. 75, Jan., pp. 3–8.

Medwell, J. O., Morris, W. O., Xia, J. Y., and Taylor, C., 1991, "An Investigation of Convective Heat Transfer in a Rotating Coolant Channel," ASME JOURNAL OF TURBOMACHINERY, Vol. 113, pp. 354–359.

Morris, W. D., and Ayhan, T., 1979, "Observations on the Influence of Rotation on Heat Transfer in the Coolant Channels of Gas Turbine Rotor Blades," *Proc. Instn. Mech. Engrs.*, Vol. 193, pp. 303–311.

Siegel, R., 1985, "Analysis of Buoyancy Effect on Fully Developed Laminar Heat Transfer in a Rotating Tube," ASME *Journal of Heat Transfer*, Vol. 107, pp. 338–344.

Taslim, M. E., Rahman, A., and Spring, S. D., 1991, "An Experimental Investigation of Heat Transfer Coefficients in a Spanwise Rotating Channel With Two Opposite Rib-Roughened Walls," ASME JOURNAL OF TURBOMACHINERY, Vol. 113, pp. 75–82.

Wagner, J. H., Johnson, B. V., and Hajek, T. J., 1991a, "Heat Transfer in Rotating Passages With Smooth Walls and Radial Outward Flow," ASME JOURNAL OF TURBOMACHINERY, Vol. 113, pp. 42–51.

Wagner, J. H., Johnson, B. V., and Kopper, F. C., 1991b, "Heat Transfer in Rotating Serpentine Passages With Smooth Walls," ASME JOURNAL OF TURBOMACHINERY, Vol. 113, pp. 321–330.

The Solution-Adaptive Numerical Simulation of the Three-Dimensional Viscous Flow in the Serpentine Coolant Passage of a Radial Inflow Turbine Blade

W. N. Dawes
Whittle Laboratory,
University Engineering Department,
Cambridge, United Kingdom

This paper describes the application of a solution-adaptive, three-dimensional Navier–Stokes solver to the problem of the flow in turbine internal coolant passages. First, the variation of Nusselt number in a cylindrical, multiribbed duct is predicted and found to be in acceptable agreement with experimental data. Then the flow is computed in the serpentine coolant passage of a radial inflow turbine including modeling the internal baffles and pin fins. The aerodynamics of the passage, particularly that associated with the pin fins, is found to be complex. The predicted heat transfer coefficients allow zones of poor coolant penetration and potential hot spots to be identified.

Introduction

The continual trend to increase turbine inlet temperatures, to improve thermal efficiency, places ever-increasing demands on our ability to cool the turbine blades. It is common practice to use cooler air from upstream in the engine and to make this pass through a passage internal to the blade, exiting through the trailing edges. This passage is usually "serpentine" in its overall form and may contain several baffles and pin fins. From the point of view of design, it would be very useful to be able to simulate this flow numerically. However, both the geometry and the flow field are extremely complex, far more so than on the primary gas side.

The design problem is essentially to use the minimum mass flow rate of coolant and pump it with minimum head loss. To achieve this requires an understanding of the aerodynamics of the coolant passage itself. The distribution of the coolant within the passage is complicated by strong, three-dimensional secondary motions. These are driven by Coriolis and centrifugal pressure gradients and by the strong cross-stream pressure gradients generated by 180 deg bends. Baffles and distributions of pin fins are used to try and control the tendency of the fluid to migrate radially outboard. These add complications to the passage aerodynamics and in turn impact on the head losses associated with the passage. Typical design trade-offs are illustrated in Fig. 1 (taken from Snyder and Roelke, 1988).

Current design methods (see Kumar and Roelke, 1989, and Kumar and Deanna, 1988, for examples) are empirical and are based on combinations of one-dimensional lumped parameter models for passage friction loss, bend losses, branching losses, pumping effects, and temperature changes due to both heat transfer and rotational effects. Only just recently have attempts been started (Steinthorsson et al., 1991a, b) to apply to three-dimensional Navier–Stokes solvers to the problem. Here the key difficulty in the analysis is the ability to represent the complex geometry by a suitable mesh system.

The purpose of this paper is to show how a recently developed, unstructured mesh, solution adaptive, three-dimensional Navier–Stokes solver can readily be applied to the complex geometry of a serpentine passage in a cooled radial inflow turbine rotor blade. The work has two objectives: first to predict the complex aerodynamics of the coolant passage; and second to attempt to predict the variation of heat transfer coefficient within the coolant passage.

Mesh Generation and Adaptive Refinement

The geometry chosen for the present study is that developed jointly between Allison Gas Turbines and NASA under the HOST program (Snyder and Roelke, 1988). The actual geometry is not yet in the public domain but enough data are given in their paper to construct a very similar looking configuration; this is shown in Fig. 2. The coolant passage consists of an initial serpentine bend followed by three exit branches separated by baffles. Twelve pin fins are located to control the flow split. The channel cross section is not well defined in the publications listed above and was therefore assumed to be rectangular.

Contributed by the International Gas Turbine Institute and presented at the 37th International Gas Turbine and Aeroengine Congress and Exposition, Cologne, Germany, June 1–4, 1992. Manuscript received by the International Gas Turbine Institute February 17, 1992. Paper No. 92-GT-193. Associate Technical Editor: L. S. Langston.

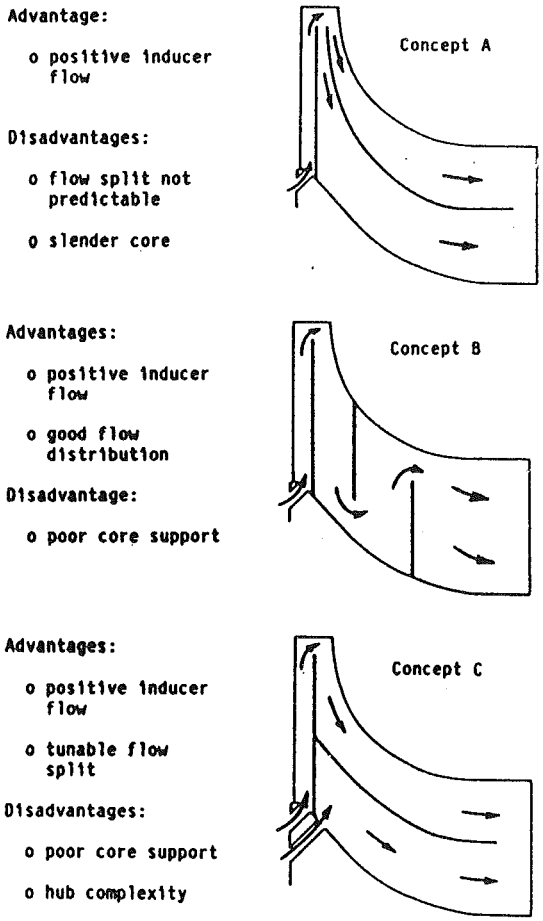

Fig. 1 Typical design trade-offs for a radial inflow turbine internal coolant passage (taken from Snyder and Roelke, 1988)

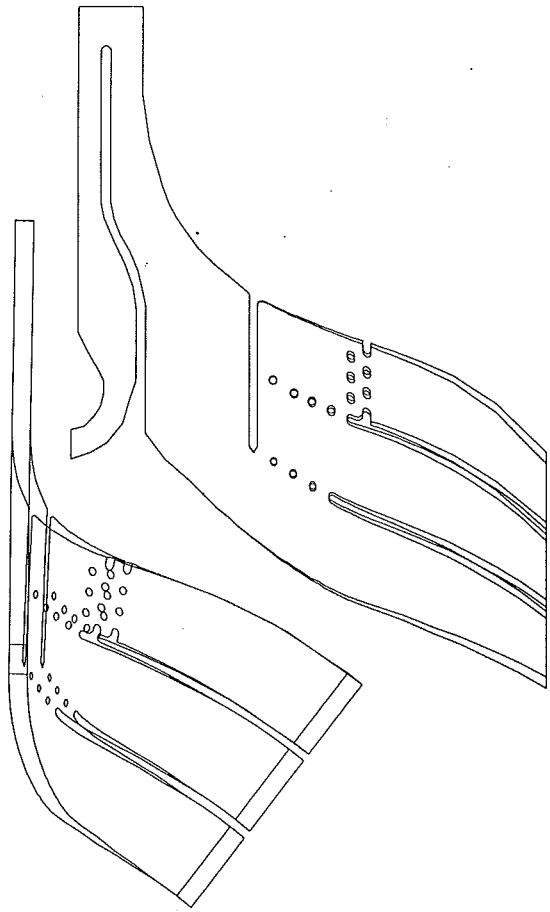

Fig. 2 The basic geometry of the coolant passage

The basic unstructured mesh generation procedure consists of a multiblock approach described in much more detail in Dawes (1992b); Fig. 3 shows the five blocks forming the data input. Within each block, a topologically cuboidal mesh is generated and this in turn is converted to an unstructured list of tetrahedral control volumes. The lists for each block are then added together and boundary face data, edge data, etc., extracted. The baffles and pin fins are introduced interactively during the mesh generation session by deletion of sets of cells and thus represent no particular burden on data preparation. The pin fins have a circular cross section and when they are introduced the mesh is distorted locally automatically to accommodate this.

Once an unstructured mesh has been produced it can be refined with great freedom based both on geometric parameters (proximity to wetted surfaces, etc.) and on features of the flow field (like gradients of a chosen variable). The refinement process permits tetrahedra to divide into 2, 4, or 8, as illustrated in Fig. 4, and takes place interactively by accepting a particular refinement criterion from the user and then automatically processing all cells that meet that criterion. In the case of the present study the *final* mesh is shown in Fig. 5 and contains 75,626 nodes. The refinement has in part been triggered by geometric parameters (the pin fins have a particularly fine mesh near them) and partly by the evolving solution itself. Figure 5 also shows the mesh structure in the crossflow plane at the flow exit.

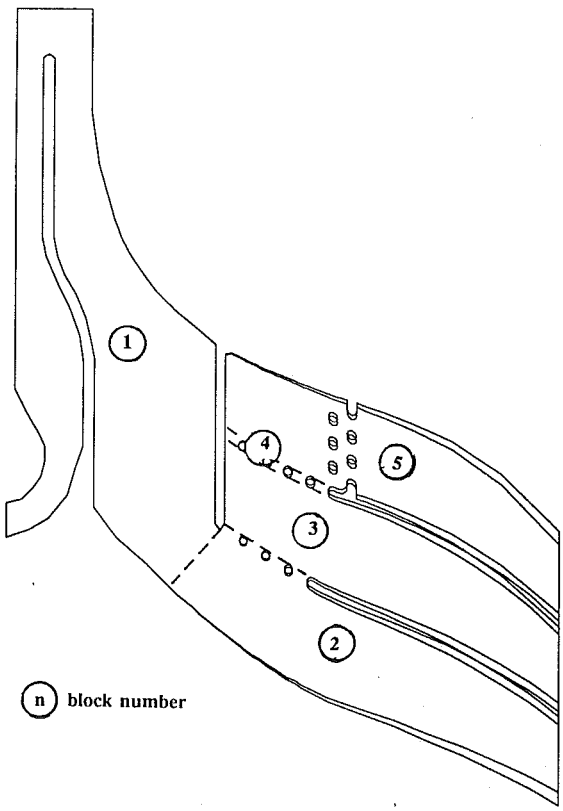

Fig. 3 Division of the passage into five blocks for the mesh generator

Equations of Motion and Solution Algorithm

The equations solved are the fully three-dimensional Reynolds-averaged Navier–Stokes equations expressed in strong

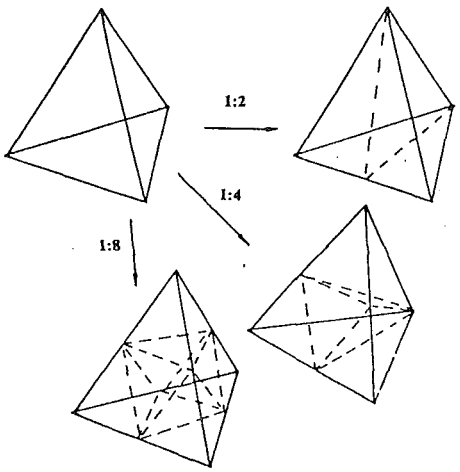

Fig. 4 The three possible cell refinements

conservation form and retaining the full stress tensor (including the full energy equation). Turbulence is modeled via k–ϵ transport equations (Patel et al., 1985) together with appropriate low Reynolds number terms (Lam and Bremhorst, 1981) to handle smoothly the approach to the blade surfaces. In an (x, t, r) Cartesian coordinate system rotating about the x axis:

$$\frac{\partial}{\partial t}\oint_{\mathrm{VOL}} \overline{U}\, d\,\mathrm{VOL} = \oint \overline{H}\cdot d\overline{\mathrm{AREA}} + \oint_{\mathrm{VOL}} \rho\overline{S}\, d\mathrm{VOL} \quad (1)$$

where

$$\overline{U} = \begin{bmatrix} \rho \\ \rho V_x \\ \rho V_t \\ \rho V_r \\ \rho E \\ \rho k \\ \rho \epsilon \end{bmatrix}$$

$$\overline{H} = \begin{bmatrix} \rho\overline{q} \\ \rho V_x\,\overline{q} + \overline{\overline{\sigma}}\hat{i}_x \\ \rho V_t\,\overline{q} + \overline{\overline{\sigma}}\hat{i}_t \\ \rho V_r\,\overline{q} + \overline{\overline{\sigma}}\hat{i}_r \\ \rho I\overline{q} + \overline{q}\cdot\overline{\overline{\sigma}} + \lambda\nabla T \\ \rho k\overline{q} + (c_2\mu/\rho)\nabla k \\ \rho\epsilon\overline{q} + (c_3\mu/\rho)\nabla\epsilon \end{bmatrix} \quad \overline{S} = \begin{bmatrix} 0 \\ 0 \\ t\,\Omega^2 - 2\Omega V_r \\ r\,\Omega^2 + 2\Omega V_t \\ 0 \\ G - \rho\epsilon \\ f_1\dfrac{c_4\epsilon G}{k} - f_2\dfrac{c_5\rho\epsilon^2}{k} \end{bmatrix}$$

with

$\overline{q}$ = $V_x\hat{i}_x + V_t\hat{i}_t + V_f\hat{i}_r$, the relative velocity
Ω = rotation speed
I = $c_pT_{o_{\mathrm{rel}}} - 1/2(\Omega r)^2$, the rothalpy
$\overline{\overline{\sigma}}$ = the stress tensor, $-p\overline{\overline{I}} + \overline{\tau}$, $\overline{\tau} = 2\mu\ \mathrm{def}(\overline{q}) - 2/3\mu(\nabla\overline{q})\overline{\overline{I}}$
$\mathrm{def}(\overline{q})$ = $1/2(\nabla\overline{q} + (\nabla\overline{q})^T)$
μ = $\mu_{\mathrm{lam}} + \mu_T$
μ_T = $\rho f_\mu c_1 k^2/\epsilon$
G = $2\mu(\mathrm{def}(\overline{q}))^2 - 2/3\mu(\nabla\overline{q})^2$
λ = $c_p\,(\mu_{\mathrm{lam}}/\mathrm{Pr} + \mu_T/\mathrm{Pr}_T)$

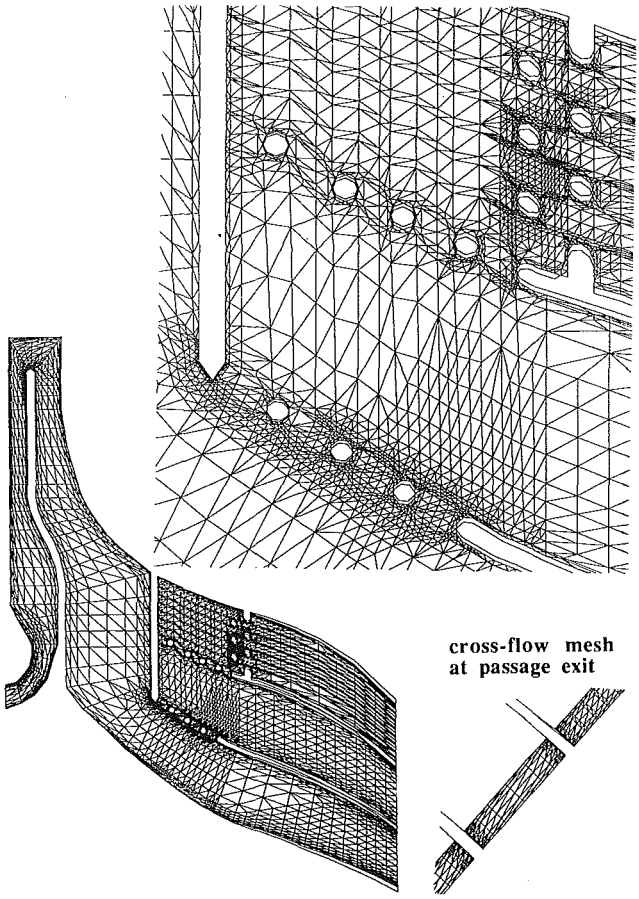

Fig. 5 The final mesh in the center plane of the coolant passage after adaptive refinement and containing a total of 75,626 nodes

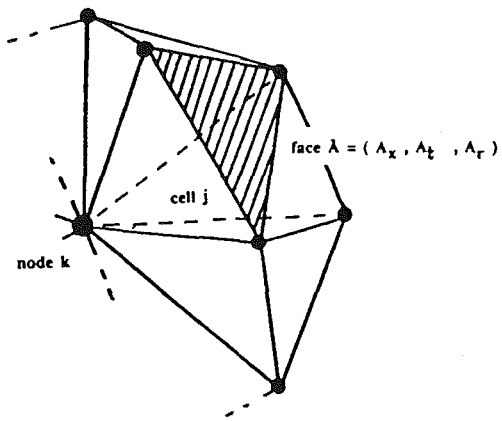

Fig. 6 A typical control volume (j) contributing to node k

and f_μ, f_1, and f_2 are the low Reynolds number damping terms. The various constants in the k–ϵ model take their standard values and the turbulent Prandtl number, Pr_T, is taken as 0.9.

Full details of the numerical solution procedure are given by Dawes (1991, 1992a); here only an outline will be given. The seven equations of motion are discretized in finite volume form on each of the tetrahedral control volumes with vertex variable storage. Figure 6 illustrates a typical set of tetrahedal cells, j, surrounding and influencing a node, k. The seven primary variables (density, three momentum, energy and turbulent kinetic energy, and dissipation rate) are assumed to have a piecewise linear variation over cell faces between the vertices so that the flux sum for a given cell is evaluated to

second-order accuracy in space. The derivative terms in the viscous stresses are piecewise constant over the cell (since the primary variables are piecewise linear) and are computed by simple application of the Gauss divergence theorem. Using all the cells surrounding the node, k, as a control volume then allows the evaluation of the viscous stress terms at k. Assembling for convenience all the viscous terms into a vector D_k allows the definition of a residue, R_k, at each node as:

$$R_k = \frac{1}{\text{VOL}_k} \sum_{\text{cell } j} \text{fluxes}_j + D_k \tag{2}$$

Artificial diffusion is added to control shock capture and solution decoupling and is controlled in magnitude by the local strength of the pressure gradient. It is particularly important to construct the artificial smoothing carefully in the unstructured environment to guarantee that the smoothing involves no derivatives of flow variables normal to viscous surfaces and to scale the smoothing in accordance with the highly nonuniform mesh. The formulation adopted guarantees that functions with trilinear variation return a zero smoothing term even on highly nonuniform meshes. In practice this very simple and economical smoother performs perfectly satisfactorily and is capable of crisp shock capture (over 2–3 cells).

The net flux imbalance into each cell is used to update the flow variables themselves via a two-step Runge–Kutta time-marching algorithm with residual smoothing.

Various boundary conditions must be imposed. At inflow the total pressure, total temperature, turbulent kinetic energy and dissipation rate, and two flow angles are fixed and the derivative of static pressure in the streamwise direction set to zero. At the outflow boundaries the static pressure is held constant and the other variables extrapolated from the interior.

On solid surfaces zero normal fluxes of mass, momentum, and energy are imposed. The wall shear stress is computed either from the laminar sublayer or log law equations depending on whether the local value of the wall coordinate Y^+ is less than or greater than 10, respectively. The log law is applied in the form:

$$U/u_\tau = (1/\kappa)\log\,(E\,y^+) \tag{3}$$

where U is the local fluid velocity, κ is the von Karman constant, 0.41, and E is set to force $U/u_\tau = 10$ at $y^+ = 10$. Similarly the wall heat flux is computed either from the wall normal temperature derivative if Y^+ is less than 10 or from a wall function based on Reynolds analogy:

$$q_w = \rho u_\tau c_p (T - T_w) \tag{4}$$

where q_w is the wall heat flux, T is the local fluid temperature, and T_w the specified wall temperature.

In a similar spirit if Y^+ is less than 10 the turbulent kinetic energy and the normal gradient of dissipation rate are set to zero on the surface; otherwise k and ϵ are set to be consistent with the assumed log law at values of $u_\tau^2/\sqrt{c_1}$ and $u_\tau^3/\kappa Y_w$, respectively, with Y_w the normal distance to the wall.

Results

Calibration: Multiribbed Duct. As experimental results are not yet available for the radial inflow turbine, a preliminary calibration exercise was performed. The flow and heat transfer were predicted in a multiribbed cylindrical duct (Taylor et al., 1991) typical of internal coolant passages and for which other comparative data are available. The geometry and mesh are shown in Fig. 7. The duct is cylindrical with an internal diameter of 0.010 m and overall length of 0.125 m. Five ribs are located within the duct, each rib having a square cross section of 0.002 m. The flow in the test was essentially incompressible but the present computations were run at a Mach number level of around 0.3. The Reynolds number based on duct diameter

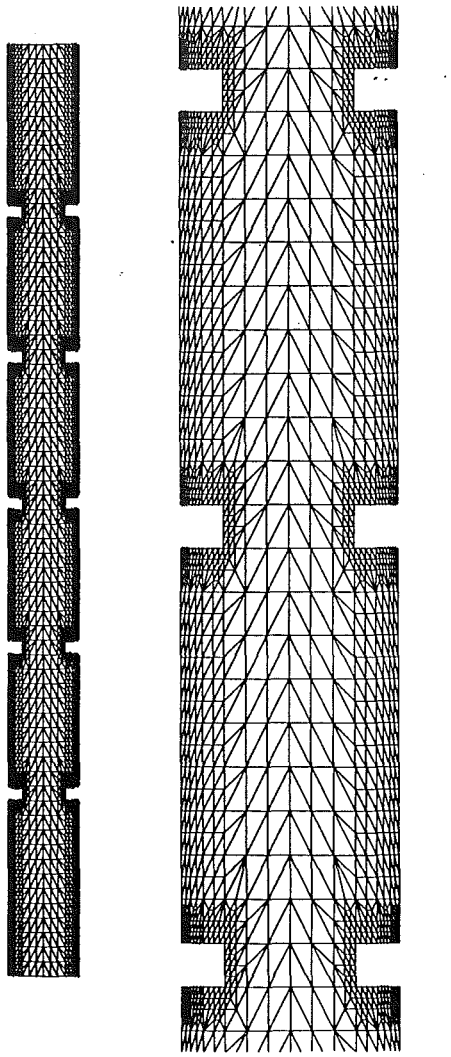

Fig. 7 Cross section through the mesh generated for the multiribbed duct

was 15,000. An unstructured mesh containing 49,085 nodes was generated semi-automatically from a cylinder (which is one of the building blocks available in the mesh generator) with the ribs formed by deleting circumferential sets of cells and then by prerefining near the ribs for improved resolution; this is an example of geometric-adaptive refinement and is a powerful advantage of the present approach.

Predicted Mach number contours and velocity vectors are shown in Fig. 8. From the second rib onward the flow is essentially repeatable and characterized by strong recirculations downstream of each rib with the bulk flow forming a jetlike structure along the centerline. The re-attachment location of the flow separation from each rib is around 9 rib heights downstream. The zoomed velocity vectors display some wiggles and this is because the artificial dissipation in the solver is deliberately set just low enough that wiggles just appear; this is a sign that the absolute minimum smoothing is being used and causing the minimum possible contamination of the solution. The impermeable surface boundary conditions are set in a "weak" manner by overwriting computed fluxes of mass, momentum, and energy with zero; this guarantees that there is no flow through the boundary even though in the zoomed vector view the very high velocities just near the rib corners appear to have a wall-normal component.

The predicted Nusselt numbers are compared with meas-

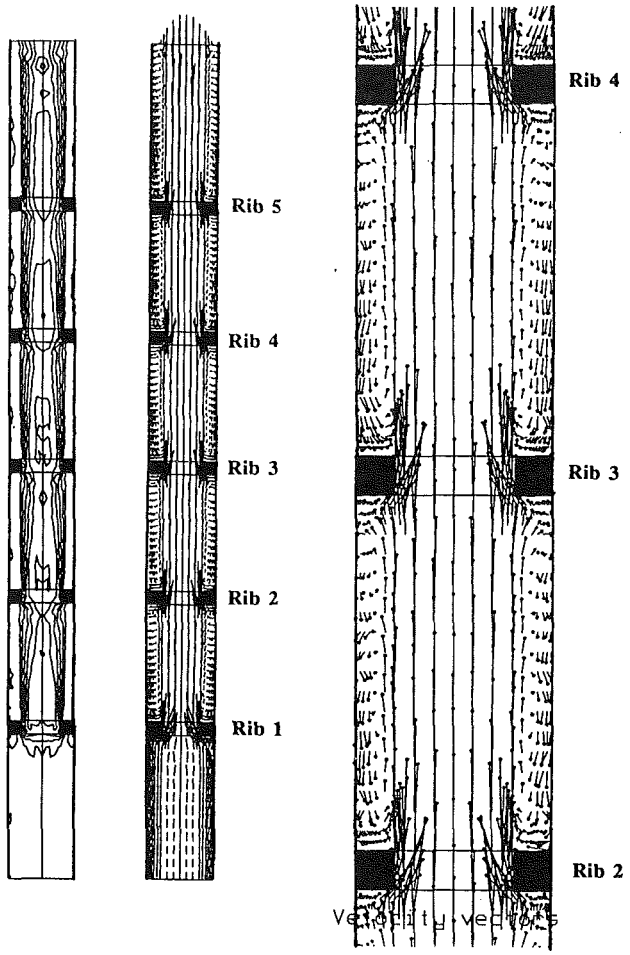

Fig. 8 Predicted Mach number contours and velocity vectors for the multiribbed duct

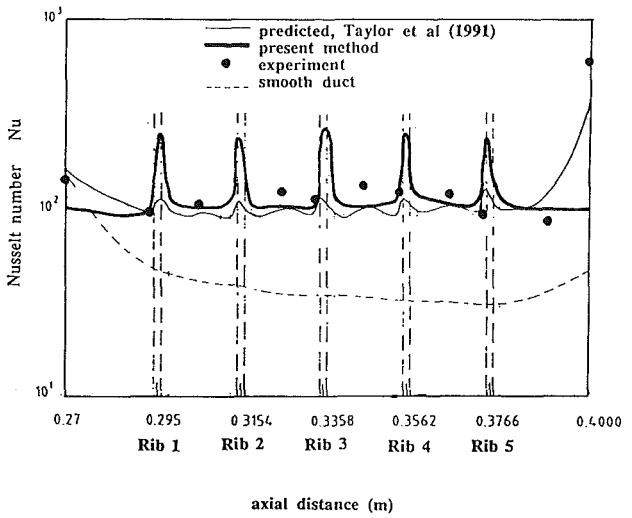

Fig. 9 Comparison of predicted and measured Nusselt numbers for the multiribbed duct

urement and another prediction (Taylor et al., 1991) in Fig. 9. The presence of the ribs greatly enhances the level of heat transfer (up to 50 percent more than for the smooth duct). The higher velocity levels over the ribs themselves produce local peaks of heat transfer and this tendency is more visible in the present predictions than those of Taylor et al. (1991) (the measurements have insufficient resolution to confirm this).

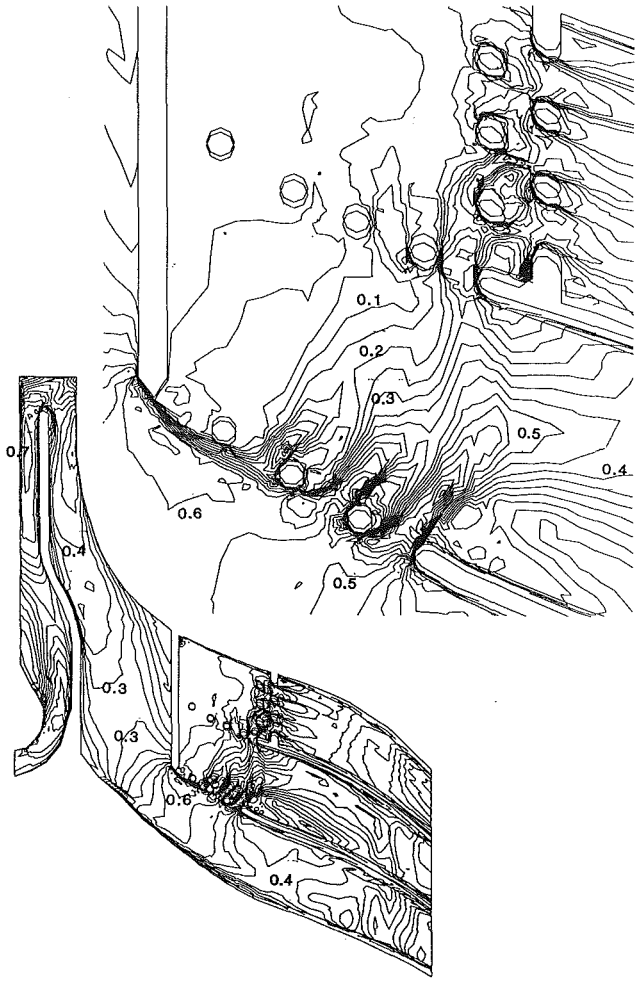

Fig. 10 Predicted midpassage Mach number contours

Such short wavelength peaks are very sensitive to levels of artificial smoothing; Taylor et al. (1991) make no mention of what levels they used. Nevertheless, overall the level of agreement is very satisfactory.

The Radial Inflow Turbine Internal Coolant Passage

As described in an earlier section, a mesh was developed for the internal coolant passage of the NASA radial inflow turbine. The geometry used represents in fact the 1.8 scale cold test model and the simulation used the following basic parameters (taken from Steinthorsson et al., 1991a):

Rotational speed	21,596	rpm
Inlet absolute P_o	267366	Pa
Inlet absolute T_o	276.	K
Exit hub static p	64262	Pa
Exit tip static p	61366	Pa

The Reynolds number based on inlet to exit path length is of order one million. The wall temperature was for simplicity everywhere specified as 500 K; a more general variation could have been used but nevertheless the heat transfer rate to the fluid can still be computed in dimensionless form. No experimental measurements are available at the time of writing and the sole three-dimensional simulation attempted previously for this geometry (Steinthorsson et al., 1991b) is incomplete and only encompasses aerodynamic data for the first serpentine bend.

The objectives of the present simulation are first to gain some insight into a complex flow and second to attempt to predict the heat transfer to the coolant gas.

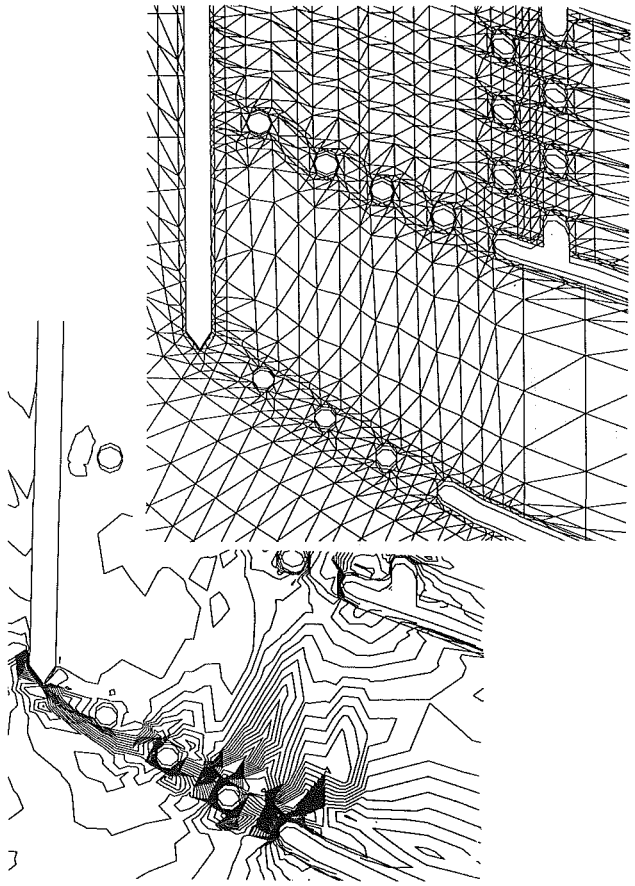

Fig. 11 Zoom view near the first set of pin fins of Mach numbers in midpassage predicted on the *initial* mesh *before* solution-adaptive refinement

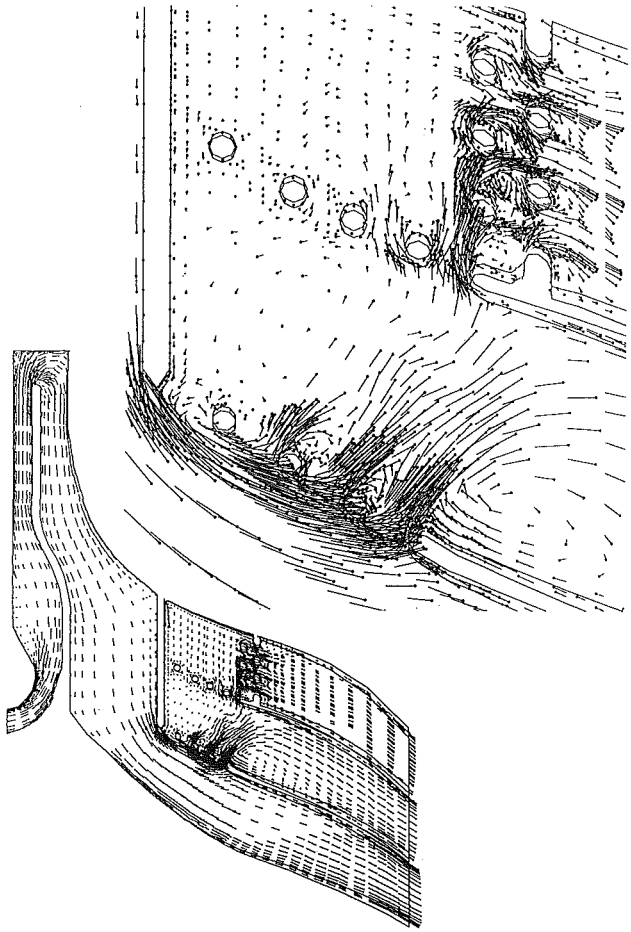

Fig. 12 Predicted midpassage velocity vectors

The predicted midpassage Mach number field is shown in Fig. 10. At this pressure ratio the flow is highly compressible with peak Mach numbers of order 0.8. The extent of the detail contained in the present predictions is illustrated by the clearly visible wake structures associated with the pin fins; this impacts, as will be described later, on the local heat transfer quite considerably. To illustrate the benefit of the present solution-adaptive refinement capability, Fig. 11 shows a zoom view near the first set of pin fins of the Mach numbers predicted in midpassage on the *initial* mesh *before* the solution-adaptive refinement, which led to the "final" mesh shown in Fig. 5. The contrast in the resolution of the wake structures between the "initial" and the "final," shown in Fig. 10, is striking. The adaptation was carried out by refining every cell with greater than a 10 percent variation of entropy across it. It would be much less convenient and much more costly to achieve a similar level of refinement in a conventional structured solver.

The predicted midpassage velocity vectors in Fig. 12 add considerably to our understanding of the flow field. The serpentine bend contains three separated zones: one associated with the diffusing section just after the inlet; one small one just after the tight bend in the farthest outboard portion of the bend; and one in the corner between the bend and the radial baffle. Downstream of the radial baffle, as the flow turns toward the axial direction, the flow starts to attempt to centrifuge outward through the gaps between the pin fins. As the detail shows the bulk of the flow is through the second, third, and fourth gaps (especially the latter two, which are in fact predicted to be nearly choked) into the middle exit passage. From there some flow is centrifuged to the upper exit passage, the majority of this passing through the gap between the last pin fin and the leading edge of the upper baffle, while the remainder passes over a large recirculating zone and thence to the middle exit. The coolant is predicted to penetrate very poorly into the zone between the radial baffle and toward the casing with obvious implications for heat transfer. The wake/vortex structure of each pin fin is strikingly predicted; the ability to predict this sort of local detail by local mesh refinement is one of the strong advantages of the present solution-adaptive approach.

The distributions of predicted heat transfer coefficient (W/m^2 K) on the suction and pressure sides of the coolant passage are shown in Figs. 13 and 14. In general the heat transfer coefficient correlates to the local velocity level: higher velocity levels permit greater removal of heat from the sidewall and vice versa. The general background level of heat transfer coefficient is predicted to be between 200 and 400 W/m^2 K. In the serpentine bend the coefficient increases to a peak of around 1000 near the 180 deg bend itself although the actual volume of heat that can be extracted from the external primary flow will be restricted somewhat as the coolant temperature of course rises naturally as it moves radially outward (rothalpy is conserved in the absence of any heat transfer). Within the bend, reduced coefficients are observed associated with the three separated zones. Any reduction in heat transfer on the secondary gas side implies the possibility of a hot spot on the primary gas side.

As mentioned earlier, there is very poor coolant penetration into the zone downstream of the radial baffle and toward the casing. Correspondingly this zone is predicted to have the lowest levels of heat transfer coefficient in the whole passage (below 200 W/m^2K).

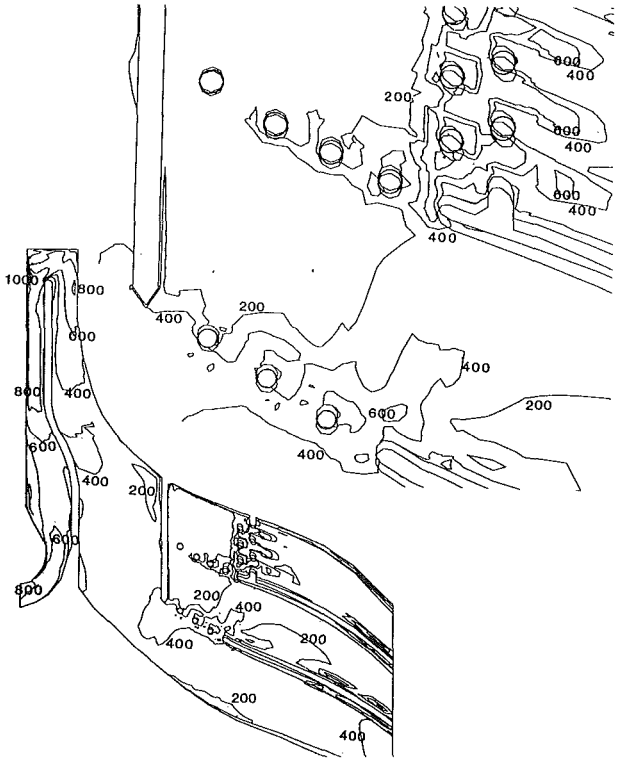

Fig. 13 Predicted heat transfer coefficient (W/m^{2}K) on the suction side of the coolant passage

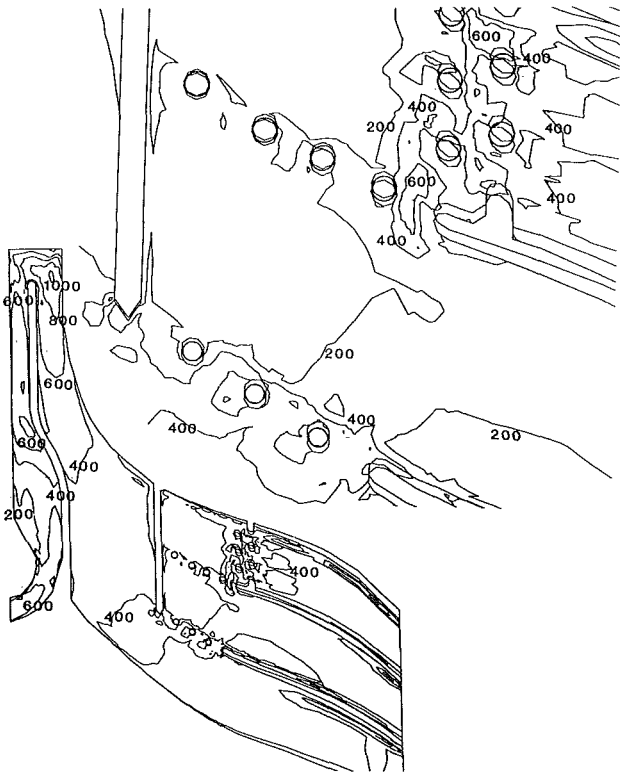

Fig. 14 Predicted heat transfer coefficient (W/m^{2}K) on the pressure side of the coolant passage

There is a highly nonuniform distribution of heat transfer coefficient associated with the pin fins with values of over 600 W/m^2 K in zones influenced by the strong jets through the gaps between the pins and values as low as 200 W/m^2 K in the immediate wake region of each pin. Clearly the metal sidewalls may attenuate somewhat the dramatic spatial variations of the coefficient as seen by the primary gas side, but nevertheless the detail achieved in these predictions might lead to crucial information regarding potential primary side hot spots.

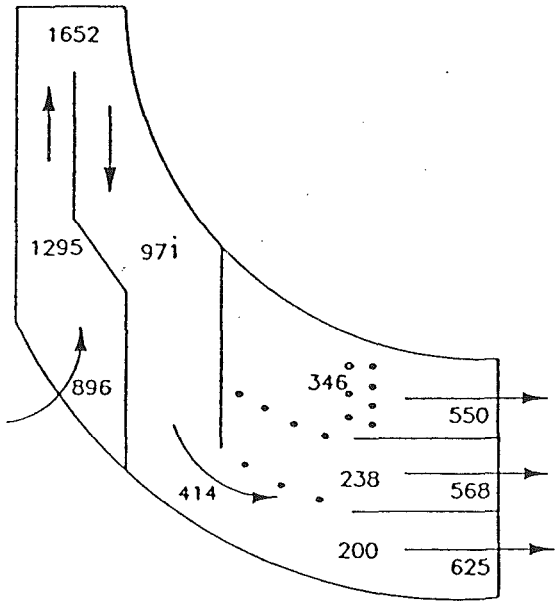

Fig. 15 Passage-mean heat transfer coefficient (W/m^{2}K) predicted by a simple one-dimensional model (Kumar et al., 1988)

The three dimensionality of the predictions is evidenced by the quite large differences in predicted heat transfer coefficient between the suction and pressure sides of the passage, particularly near the serpentine bend and the first row of pin fins.

Although no experiments have yet been made on the NASA turbine, Kumar et al. (1988) have predicted heat transfer coefficients by a simple one-dimensional model of the passage; their result is shown in Fig. 15. Their general level of predicted heat transfer is about 25 percent higher than in the present calculations. Currently the reason for the differences is not known.

Concluding Remarks

The Nusselt number variation in a multiribbed duct has been predicted with an acceptable level of agreement with the experimental data.

The very complex flow inside a radial inflow turbine coolant passage has been predicted and, as a first effort, the results are very encouraging. The level of aerodynamic detail predicted, particularly of the flow associated with the pin fins, is striking. In terms of the design of the coolant passage, the predictions suggest that the principal weakness in the concept is poor coolant penetration into a zone downstream of the radial baffle and toward the casing.

The solution could be improved still further: physically by improved turbulence and transition modeling; numerically by improving the implementation of the wall boundary conditions in the corner between the two exit baffles and the suction and pressure sides and by smoothing the mesh somewhat. These are being pursued actively at the moment.

References

Dawes, W. N., 1991, "The Development of a Solution-Adaptive 3D Navier-Stokes Solver for Turbomachinery," Paper No. AIAA-91-2469.

Dawes, W. N., 1992a, "The Simulation of Three-Dimensional Viscous Flow in Turbomachinery Geometries Using a Solution-Adaptive Unstructured Mesh Methodology," ASME JOURNAL OF TURBOMACHINERY, Vol. 114, pp. 528–537.

Dawes, W. N., 1992b, "The Extension of a 3D Navier–Stokes Solver Towards Geometries of Arbitrary Complexity," ASME Paper No. 92-GT-???

Kumar, G. N., and Deanna, R. G., 1988, "Development of a Thermal and Structural Analysis Procedure for Cooled Radial Turbines," ASME Paper No. 88-GT-18.

Kumar, G. N., and Roelke, R. G., 1989, "A Generalised One Dimensional Computer Code for Turbomachinery Cooling Passage Flow Calculations," NASA Technical Memorandum 102079.

Lam, C. K. G., and Bremhorst, K. A., 1981, "Modified Form of the k–ϵ Model for Predicting Wall Turbulence," ASME *Journal of Fluids Engineering*, Vol. 103, pp. xx-00.

Patel, V. C., Rodi, W. S., and Scheuerer, G., 1985, "Turbulence Models for Near-Wall Flows and Low Reynolds Numbers: A Review," *AIAA Journal*, Vol. 23, No. 9.

Snyder, P. H., and Roelke, R. J., 1988, "The Design of an Air-Cooled Metallic High Temperature Radial Turbine," Paper No. AIAA-88-2872.

Steinthorsson, E., Shih, T.I.-P., and Roelke, R. J., 1991a, "Computation of the Three-Dimensional Flow and Heat Transfer Within a Coolant Passage of a Radial Flow Turbine," Paper No. AIAA-91-2238.

Steinthorsson, E., Shih, T.I.-P., and Roelke, R. J., 1991b, "Algebraic Grid Generation for Coolant Passages of Turbine Blades With Serpentine Channels and Pin Fins," Paper No. AIAA-91-2366..

Taylor, C., Xia, J. Y., Medwell, J. O., and Morris, W. D., 1991, "Numerical Simulation of Three Dimensional Turbulent Flow and Heat Transfer Within a Multi-ribbed Cylindrical Duct," ASME Paper No. 91-GT-8.

Influence of Surface Heating Condition on Local Heat Transfer in a Rotating Square Channel With Smooth Walls and Radial Outward Flow

J. C. Han
HTRI Professor.
Fellow ASME

Y. M. Zhang
Research Associate.
Mem. ASME

Turbine Heat Transfer Laboratory,
Department of Mechanical Engineering,
Texas A&M University,
College Station, TX 77843-3123

C. P. Lee
Manager,
Turbine Aero & Cooling Design,
General Electric Company,
Cincinnati, OH 45215
Mem. ASME

The effect of a surface heating condition on the local heat transfer coefficient in a rotating square channel with smooth walls and radial outward flow was investigated for Reynolds numbers from 2500 to 25,000 and rotation numbers from 0 to 0.352. The square channel, composed of six isolated copper sections, has a length-to-hydraulic diameter ratio of 12. The mean rotating radius to the channel hydraulic diameter ratio is kept at a constant value of 30. Four surface heating conditions were tested: (1) four walls at uniform temperature, (2) temperature ratio of leading surface to side wall and trailing surface to side wall is 1.05 and 1.10, respectively, (3) trailing surface hot and remaining three walls cold, and (4) leading surface hot and remaining three walls cold. The results show that the heat transfer coefficients on the leading surface are much lower than that of the trailing surface due to rotation. For case (1) of four walls at uniform temperature, the leading surface heat transfer coefficient decreases and then increases with increasing rotation numbers, and the trailing surface heat transfer coefficient increases monotonically with rotation numbers. However, the trailing surface heat transfer coefficients for cases (2) and (3) are slightly lower than case (1), and the leading surface heat transfer coefficients for cases (2) and (4) are significantly higher than for case (1). The results suggest that the local wall heating condition creates the local buoyancy forces, which reduce the effects of the bulk buoyancy and Coriolis forces. Therefore, the local heat transfer coefficients on the leading and trailing surfaces are altered by the surface local heating condition.

Introduction

The trend in advanced aeroengine design for high thermal efficiency and high power density is toward high entry gas temperature (1400°–1500°C), which is far above the allowable metal temperature. Therefore, highly sophisticated cooling technologies such as film cooling, impingement cooling, and augmented convection cooling must be employed to maintain the structural integrity of blades and vanes used in advanced gas turbine engines. This investigation considers the local heat transfer characteristics in turbine coolant passages with rotation. Since heat is transferred from both the pressure and suction surfaces, rib turbulators (turbulence promoters) are often cast on two opposite walls of the cooling passages (i.e., inner walls of the pressure-trailing and suction-leading surface) to enhance heat transfer to the cooling air. A typical coolant passage can be modeled as a single pass or multipass rectangular channel with four smooth walls or with two opposite rib-roughened walls. This paper focuses on the effect of surface heating condition on the local heat transfer coefficient in a rotating, square channel with four smooth walls and radial outward flow.

Most of the available data/correlations in the literature on internal turbine blade cooling are from tests performed with nonrotating flow condition (Han, 1984, 1988; Han and Zhang, 1991; Han et al., 1992). Adjustment factors are applied to these correlations to bring them into nominal correspondence with engine experience. These design methods become unacceptable when turbine blade cooling conditions for advanced engines are outside the range of previous experience. Rotation of turbine blade cooling passages gives rise to Coriolis and buoyancy forces. These forces can substantially affect coolant flow patterns and influence the local heat transfer distributions inside the turbine blade cooling passages. Heat transfer data are difficult and expensive to obtain under rotation; therefore, only limited amounts of data are available in the open literature. Mori et al. (1971) studied the mean convective heat

Contributed by the International Gas Turbine Institute and presented at the 37th International Gas Turbine and Aeroengine Congress and Exposition, Cologne, Germany, June 1–4, 1992. Manuscript received by the International Gas Turbine Institute February 17, 1992. Paper No. 92-GT-188. Associate Technical Editor: L. S. Langston.

transfer in a rotating radial circular pipe. Clifford et al. (1984) reported the local and mean transfer in a triangular-sectioned duct rotating in the orthogonal mode. Morris et al. (1988), Morris and Ghavami-Nasr (1991), and Morris and Salemi (1992) studied the effect of rotation on the heat transfer characteristics of circular, triangular, rectangular and square-sectioned coolant passages of gas turbine rotor blades. Guïdez (1989) presented the study of convective heat transfer in a rotating coolant channel. Taslim et al. (1991) studied heat transfer coefficients in a rotating channel with ribbed walls. Wagner et al. (1986, 1991a, b, 1992) investigated the local heat transfer in rotating serpentine passages with smooth walls and two opposite ribbed walls. With the exception of Taslim et al. (1991), Wagner (1986, 1992), and Clifford et al. (1984), all of the above-mentioned work was conducted with smooth wall models, and with the exception of Wagner (1991b, 1992), the aforementioned studies were tested for straight channels. Some investigators found that large increases and decreases in trailing and leading surface heat transfer were found to occur under certain conditions of rotation, while other investigators found lesser effects. Some inconsistencies exist between investigators due to differences in measurement techniques, models and test conditions.

Wagner et al. (1991a, b) made the most systematic investigation of the effects of Coriolis and buoyancy forces on local heat transfer coefficient distributions of a two-pass square channel with smooth walls. In summary, the difference in heat transfer between rotating and nonrotating flow conditions is primarily due to secondary flows associated with Coriolis acceleration (due to rotation) and the centripetal buoyancy (due to large wall-to-coolant temperature differences). The rotating trailing surface heat transfer coefficient can be increased up to 3.5 times the nonrotating fully developed smooth tube values, but the leading surface heat transfer coefficient can be decreased to 40 percent of the fully developed circular tube values. The local heat transfer coefficient on the trailing (pressure) surface of the first coolant passage (radial outward flow) increases with increasing rotational speed and wall-to-coolant temperature difference. This is because the rotation induces the thinner destabilization boundary layer on the trailing surface (see Fig. 1) and the buoyancy causes the near-wall counterflow interaction with the mainstream on the trailing surface of the first coolant passage. However, the local heat transfer coefficient on the leading surface of the first coolant passage decreases with increasing rotational speed but increases with wall-to-coolant temperature differences. This is because the rotation causes a thicker stabilization boundary layer (see Fig. 1) as well as the cross-stream flow patterns that induce heated,

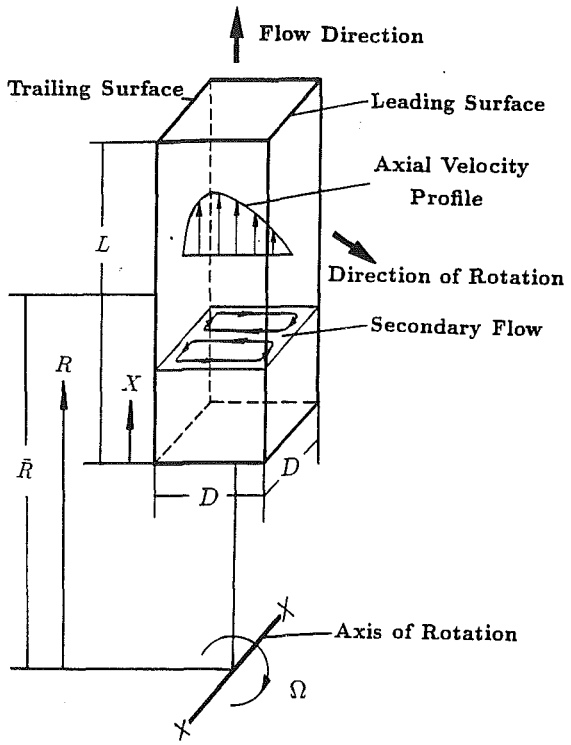

Fig. 1 Conceptual view of rotating coolant flow distribution

near-wall fluid from the trailing and sidewall surfaces to accumulate near the leading side of the coolant passage. This results in reduced heat transfer on the leading surface. Meanwhile, the buoyancy causes the near-wall counterflow interaction with the mainstream on the leading surface of the first coolant passage and tends to enhance heat transfer. Since the Coriolis effect is greater than the buoyancy effect, the local heat transfer coefficient on the leading surface is lower than the fully developed circular tube values.

The studies mentioned above were limited to uniform wall temperatures (Wagner et al., 1991a) or uniform wall heat flux (Morris et al., 1988) of the square channel. However, the heat flux from the leading surface is quite different from that of the trailing surface and sidewall in advanced gas turbine blades (Han et al., 1992). Since the cross-stream secondary flow and buoyancy-induced near-wall turbulence are very sensitive to

Nomenclature

A = heat transfer surface area
D = hydraulic diameter; square channel width or height
h = heat transfer coefficient
K = thermal conductivity of coolant
L = heated channel length
Nu = Nusselt number = hD/K
Nu_o = Nusselt number in fully developed tube flow
Pr = Prandtl number
q = heat generation rate from heaters, W
q_{loss} = heat loss rate through test model insulation, W
q_{net} = net heat transfer rate, W
R = rotating radius
$\bar{R}$ = mean rotating radius
Re = Reynolds number = $\rho DV/\mu$
Ro = rotation number = $\Omega D/V$
T_b = local bulk mean coolant temperature, °C or K
T_{bi} = inlet bulk mean coolant temperature, °C or K
T_w = local wall temperature, °C or K
T_{wA} = local wall temperature of side A surface, °C or K
T_{wB} = local wall temperature of side B surface, °C or K
T_{wL} = local wall temperature of leading surface, °C or K
T_{wT} = local wall temperature of trailing surface, °C or K
V = mean coolant velocity
X = axial distance from heated channel inlet
$\Delta\rho/\rho$ = coolant-to-wall density ratio based on local bulk mean coolant temperature = $(\rho_b - \rho_w)/\rho_b = (T_w - T_b)/T_w$
$(\Delta\rho/\rho)_i$ = coolant-to-wall density ratio based on inlet bulk mean coolant temperature = $(\rho_{bi} - \rho_w)/\rho_{bi} = (T_w - T_{bi})/T_w$
μ = coolant dynamic viscosity
ρ = coolant density
ρ_b = coolant density based on local bulk mean coolant temperature
ρ_{bi} = coolant density based on inlet bulk mean coolant temperature
ρ_w = coolant density based on local wall temperature
Ω = rotational speed, rpm

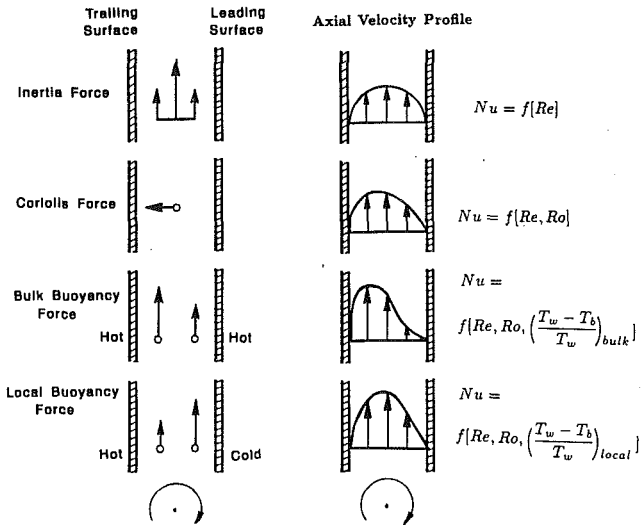

Fig. 2 Conceptual view of effect of inertia, Coriolis, and buoyancy forces on axial velocity profile

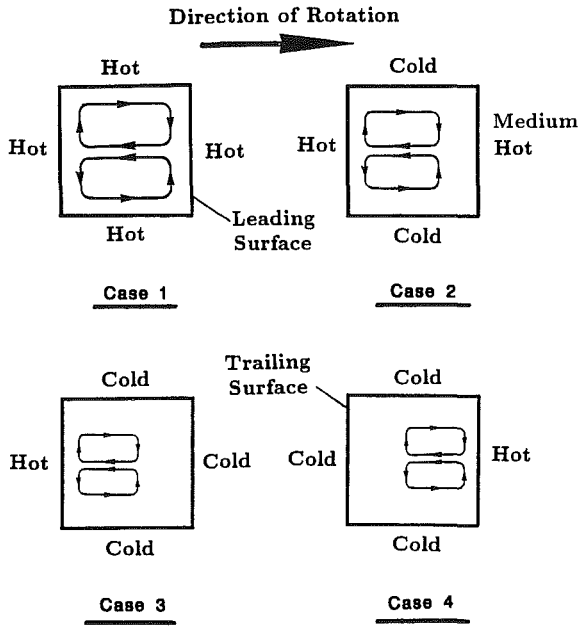

Fig. 3 Conceptual view of effect of different surface heating conditions on secondary cross-stream flow

Table 1 Four surface heating conditions studied

Case No.	Surface Heating Conditions	T_{wT}/T_{wA}	T_{wL}/T_{wA}
1	Uniform surface temperature - trailing, leading, and sidewalls hot	1.0	1.0
2	Uneven surface temperature - trailing hot, leading medium hot, and sidewalls cold	1.10	1.05
3	Uneven surface temperature - trailing hot, leading and sidewalls cold	1.10	1.0
4	Uneven surface temperature - leading hot, trailing and sidewalls cold	1.0	1.10

Note: Surface temperatures were evaluated at °K
Sidewall A temperature = Sidewall B temperature, i.e., $T_{wA} = T_{wB}$

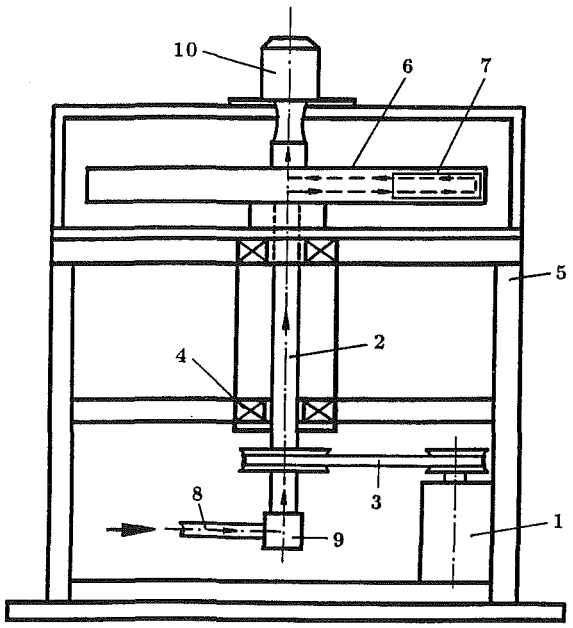

1. Electric Motor with Controller
2. Rotating Shaft
3. Belt Drive Pulley System
4. Bearing Support System
5. Steel Table
6. Rotating Arm
7. Test Section
8. Compressor Air
9. Rotary Seal
10. Slip Ring

Fig. 4 Schematic of the rotating rig

wall thermal boundary conditions, it is of interest to study the effects of different wall heating conditions on the leading and trailing surface of the first coolant passage under rotation conditions. Figure 2 depicts the effect of local buoyancy force on the coolant flow profile when the pressure side (trailing) is hot but the suction side (leading) is cold. This local buoyancy force, due to uneven wall temperature, is an additional parameter that can alter the coolant flow profile and change the heat transfer coefficients on the leading and trailing surfaces of the square channel with rotation.

The objective of this study is to investigate the effect of wall heating condition on the local heat transfer coefficient in a rotating square channel with smooth walls and radial outward flow. Four surface heating conditions were tested (see Fig. 3 and Table 1): (1) four walls at uniform temperature (a baseline test to compare the data of Wagner et al., 1991a), (2) the absolute temperature ratio of leading surface to side wall and trailing surface to side wall is 1.05 and 1.10, respectively (a surface heating condition to simulate turbine engine operating conditions), (3) trailing surface hot and remaining three walls cold (a special case to check the local buoyancy effect), and (4) leading surface hot and remaining three walls cold (a special case that is the opposite of case 3). Three rotational speeds (Ω = 0, 400, and 800 rpm) and four Reynolds numbers (Re = 2500, 5000, 10,000, and 25,000) were tested. Seven corresponding rotation numbers (Ro = 0.0, 0.0176, 0.0352, 0.044, 0.088, 0.176, and 0.352) were obtained. The experiment was performed by varying each parameter while holding the remaining parameters constant.

The square channel, composed of six isolated copper sections, has a length-to-hydraulic diameter ratio (L/D) of 12. The mean rotating radius to the channel hydraulic diameter ratio ($\bar{R}/D$) is kept at a constant value of 30. The local heat transfer coefficients on the leading and trailing surfaces of the square duct are determined from the channel entrance to the downstream region. The experimental results of uniform wall temperature (case 1) are used to demonstrate the effect of rotation number (Coriolis forces) on the local heat transfer

coefficients (leading and trailing surfaces) and compared to the previous data (Wagner et al., 1991a), at similar rotation number and density ratio (buoyancy forces). The effects of nonuniform wall heating conditions (cases 2, 3, and 4) on the local heat transfer coefficients (leading and trailing surfaces) are then identified by similar rotational speed and Reynolds number.

Experimental Facility

Figure 4 shows a schematic of the rotating rig. The hollow rotating shaft (2) is driven by a 25-hp AC motor (1) with a toothed belt drive pulley system (3) through a frequency-controlled motor controller with a maximum rotating speed of 3400 rpm. The rotating shaft and supporting bearing system (4) are vertically mounted on a rigid table (5) made of heavy steel structure. The rotating arm (6) is perpendicularly connected to the rotating shaft. The test model (7), a two-pass square channel with a sharp 180 deg turn (see Fig. 5 for details), is inserted to the end portion of one side of the rotating arm. One side of the rotating arm has the same two-pass square channel in order to duct the coolant flow through the test model. The other side of the arm serves as a balance during rotation. To simulate engine configuration, the ratio of the mean rotating arm radius to the channel hydraulic diameter ($\bar{R}/D$) is 30. The regulated compressor air (8) is routed through an orifice meter to the entrance (bottom) of the rotating shaft through a rotary seal (9). The coolant flows through the hollow rotating arm and the test model (two-pass channel) and is exhausted into the atmosphere at the exit (top) of the rotating shaft. The slip ring systems (10) are attached to the exit portion of the rotating shaft. A 100 contact slip ring is used to transfer outputs from thermocouples attached to the rotating channel to a 100 point data logger interfaced to an IBM computer. A second 32 contact slip ring is used to transfer outputs from heaters attached to the rotating channels to a 32 point variac connected with digital multimeters. The local surface temperature and heat flux can be measured through these slip ring systems. The rotating speed is measured by a digital photo-tachometer.

To obtain the true regionally averaged heat transfer coefficients for turbine cooling design, it is better to have a test section that can determine the regionally averaged heat transfer coefficients in the duct streamwise flow direction. The two-pass square duct is divided into twelve short copper sections as shown in Fig. 5. Each copper section is composed of four copper plates and has an inner cross section of 1.27 cm by 1.27 cm (1/2 in. by 1/2 in.). Thin Teflon strips are machined along the periphery contact surface between copper sections as insulation to prevent possible heat conduction. The square test duct length-to-hydraulic diameter ratio (L/D) is 12. The local wall temperature of the test duct is measured by 48 copper-constantan thermocouples distributed along the length and across the circumference of the copper duct. The inlet air temperature was measured by a thermocouple at the inlet central plane of the heated duct. There is an unheated Teflon entrance duct (not shown in Fig. 5) that has the same cross section and length as that of the test duct. This entrance duct serves to establish hydrodynamically fully developed flow at the entrance to the test duct. The inlet velocity profiles were not measured.

Figure 5 also shows the cross section of the test duct. The test duct orientation is such that the leading and trailing walls of the square cross sections are vertical and the two opposite side walls horizontal. The resistance heaters are uniformly cemented between the copper plate backface grooves and the Teflon wall to insure good contact. Each of the four duct walls has its own heater with each heater independently controlled by a variac transformer. Each heater provides a controllable heat flux for each duct wall. The smooth side walls are isolated

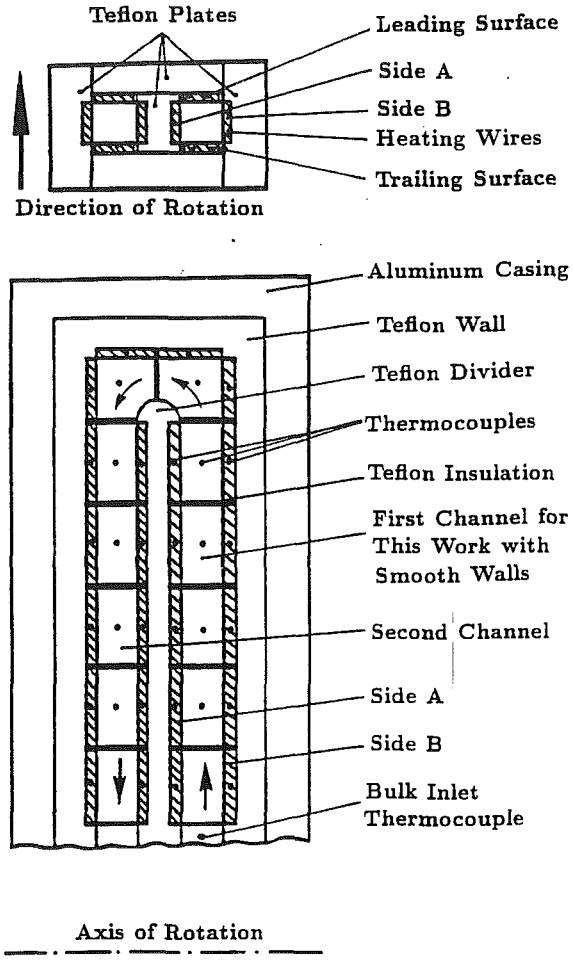

Fig. 5 Schematic of the heat transfer test model

from the leading and trailing walls to eliminate heat conduction. The entire heated test duct is insulated by Teflon material. Note that the test model was originally designed for a two-pass square channel with smooth or ribbed walls. However, only the first pass smooth wall results are presented in this paper. The objective is to investigate systematically the effect of varying wall heating condition on the leading and trailing surface heat transfer coefficients in a rotating square duct with smooth walls and radial outward flow.

Data Reduction

The local heat transfer coefficient was calculated from the local net heat transfer rate per unit surface area to the cooling air, the local wall temperature on each copper plate, and the local bulk mean air temperature as:

$$h = (q_{net})/[A(T_w - T_b)] \quad (1)$$

Equation (1) was used for the local leading, trailing, and side surface heat transfer coefficient calculations. The local net heat transfer rate (q_{net}) was the electrical power generated from the heaters (q) minus the heat loss outside the test duct (q_{loss}). The electrical power generated from the heater was determined from the measured heater resistance and voltage on each wall of the test duct. The effect of the local wall temperature variation on the local heater resistance was estimated to be less than 2 percent but was included in the data reduction. The effect of axial wall conduction between copper sections on the local net heat transfer rate was less than 2 percent but was also included in the data analysis. Loss tests were performed to determine the total heat loss from each of the test model walls for a no-flow condition (with rotation but without coolant

flow). The loss calibration was performed by supplying power to the test model for steady state. This was done for several different power inputs to obtain the relation between the total heat loss from each surface and the corresponding surface temperature. The heat loss calibration was performed for four different surface heating conditions (cases 1, 2, 3, and 4) and for three rotation speeds (0, 400, and 800 rpm), respectively. The amount of heat loss from the test model varied from 1000 W/m^2 to 2500 W/m^2 depending on the rotating speed and surface heating condition.

The local wall temperatures used in Eq. (1) were read from the thermocouple output of each copper plate. The local bulk mean air temperature used in Eq. (1) was calculated from the local net heat input to the coolant flow through each set of heated surfaces. The local bulk mean temperature was determined by marching along the test duct and calculating the temperature rise due to the local net heat input to the coolant. The calculation was started at the inlet of the heated test duct where the coolant temperature was measured by a single thermocouple (about 30°C). The local bulk mean air temperature for each heated surface was determined by averaging the inlet and exit calculated bulk mean air temperatures for each set of four heated walls. Figure 6 shows the typical variations of local wall to bulk mean air temperature along the test duct for four different surface heating conditions at rotation numbers of 0.0 and 0.08 (0.0 and 800 rpm at Re ≈ 10,000).

The local heat transfer coefficient calculated from Eq. (1) was converted to the dimensionless Nusselt number for a given flow Reynolds number. The properties in the Nusselt and Reynolds number were evaluated at the average of the inlet and outlet bulk mean coolant temperatures. To reduce the influence of flow Reynolds number on the heat transfer coefficient with rotation, the local Nusselt number of the present study was normalized by the Nusselt number for fully developed turbulent flow in smooth circular tubes with no rotation correlated by Dittus-Boelter/McAdams (Rohsenow and Choi, 1961) as:

$$\mathrm{Nu}/\mathrm{Nu}_0 = (hD/K)/[0.023\ \mathrm{Re}^{0.8}\mathrm{Pr}^{0.4}] \qquad (2)$$

with Pr = 0.72. The uncertainty of the local heat transfer coefficient is affected by the local wall-to-coolant temperature difference and the net heat input to the coolant flow from each heated copper plate. The uncertainty of the local heat transfer coefficient increases when decreasing $(T_w - T_b)$ and the net heat input. The uncertainty also increases for low heat inputs such as low Reynolds numbers and on the leading surfaces. Based on the method described by Kline and McClintock (1953), the typical uncertainty in the Nusselt number was estimated to be less than 8 percent for Reynolds numbers larger than 10,000. The maximum certainty, however, could be up to 20–25 percent for the lowest heat transfer coefficient on the leading surface of the test duct at the lowest Reynolds number tested.

Experimental Results and Discussion

The Nusselt number is a function of Reynolds and Prandtl numbers for fully developed turbulent forced convection in nonrotating channels. As previously discussed (Wagner et al., 1991a), the classical forced convection mechanism present in the channel is influenced by the presence of Coriolis forces (rotation number) and centripetal buoyancy (wall-to-coolant temperature difference, $\Delta\rho/\rho$). The net results of these parameters due to rotation in the known forced convection heat transfer correlation may be written as:

$$\mathrm{Nu} = f(\overline{R}/D,\ X/D,\ \mathrm{Re},\ \mathrm{Pr},\ Ro,\ \Delta\rho/\rho) \qquad (3)$$

where Pr = 0.72 and $\overline{R}/D$ = 30. The tests were performed for four Reynolds numbers (Re = 2500, 5000, 10,000, and 25,000) and three rotational speeds (Ω = 0, 400, and 800 rpm). Seven rotation numbers (Ro = 0.0, 0.0176, 0.0352, 0.044, 0.088, 0.176, and 0.352) were obtained. This study considers

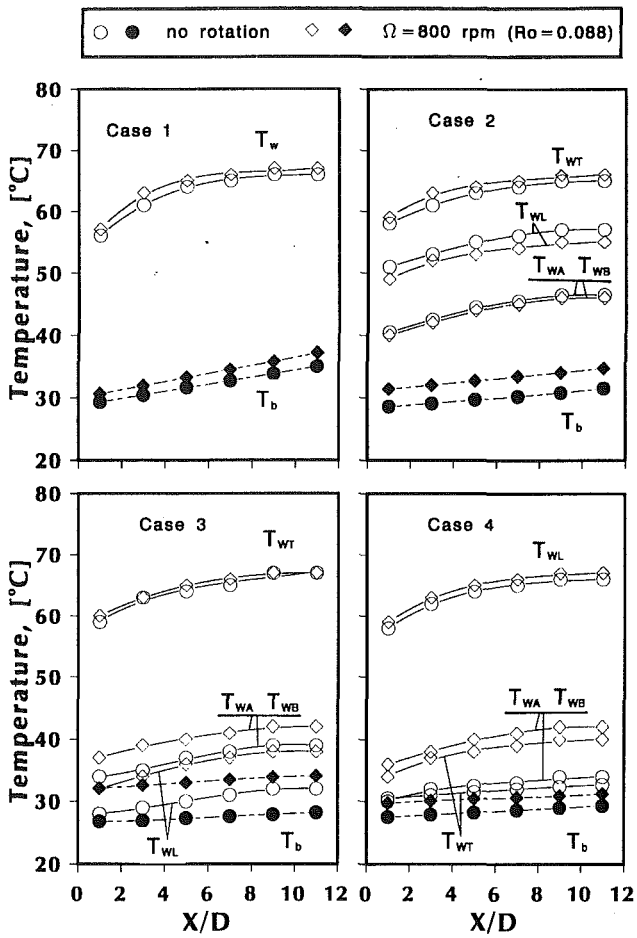

Fig. 6 Variation of surface and coolant temperature with axial location for studied four cases at Re = 10,000

the effect of local surface heating condition on the local heat transfer coefficients. This was done for one uniform wall temperature condition (case 1, $(\Delta\rho/\rho)_i$ = 0.11) and three uneven wall temperature conditions (Cases 2, 3, and 4). The results of all tests were evaluated on a local basis (i.e., on the leading and trailing surfaces along the X/D streamwise direction) by varying each parameter while holding the remaining parameters constant.

The effect of each parameter on the local heat transfer coefficients is presented in the following order: effect of rotation relative to nonrotation, effect of rotation number, effect of surface heating condition, correlating data and comparison with the previous investigators results and effect of Reynolds number.

Effect of Rotation Relative to Nonrotation. The regionally averaged heat transfer results are presented as the axial distributions of a normalized Nusselt number ratio ($\mathrm{Nu}/\mathrm{Nu}_0$ versus X/D). Figure 7 shows the effect of rotation on the leading, trailing, and side wall Nusselt number ratio distributions with Ro = 0.352, 0.176, 0.088, and 0.0352 (based on Ω = 800 rpm and Re = 2500, 5000, 10,000, and 25,000, respectively) for the case of uniform wall temperature (case 1, $(\Delta\rho/\rho)_i$ = 0.11). The results for these corresponding nonrotation tests (Re = 2500, 5000, 10,000, and 25,000) are also shown for comparison. Note that the nonrotating heat transfer ratios on the leading, trailing, side A and side B surfaces are close to each other, within 5 percent for the four Reynolds numbers studied. Therefore, a single curve along the axial location is presented (see Fig. 7, legend +). The nonrotating heat transfer ratio decreases monotonically from 1.5 near the thermal entrance of the first passage to about 1.0 near the downstream (X/D = 9) and then

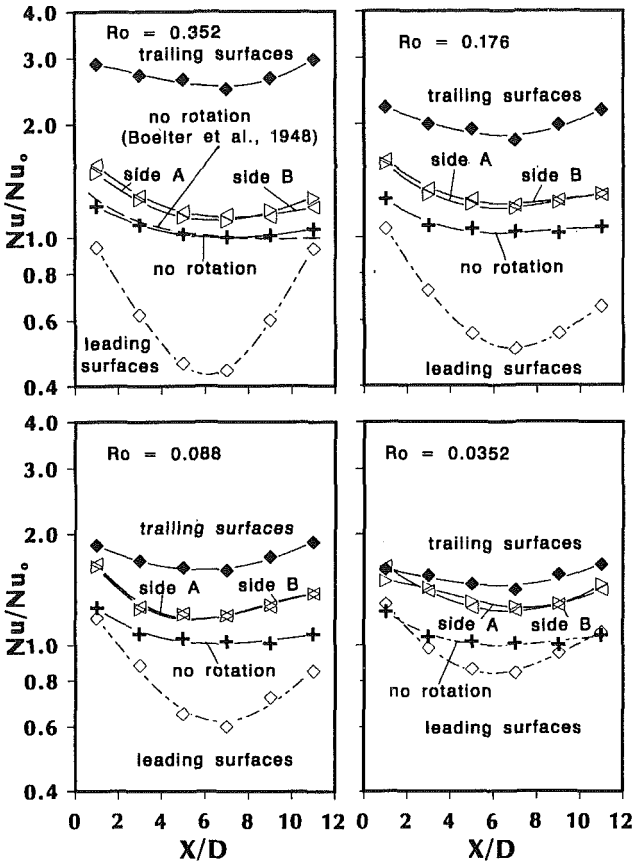

Fig. 7 Comparison of Nusselt number ratio variation between no rotation and rotation for Case 1

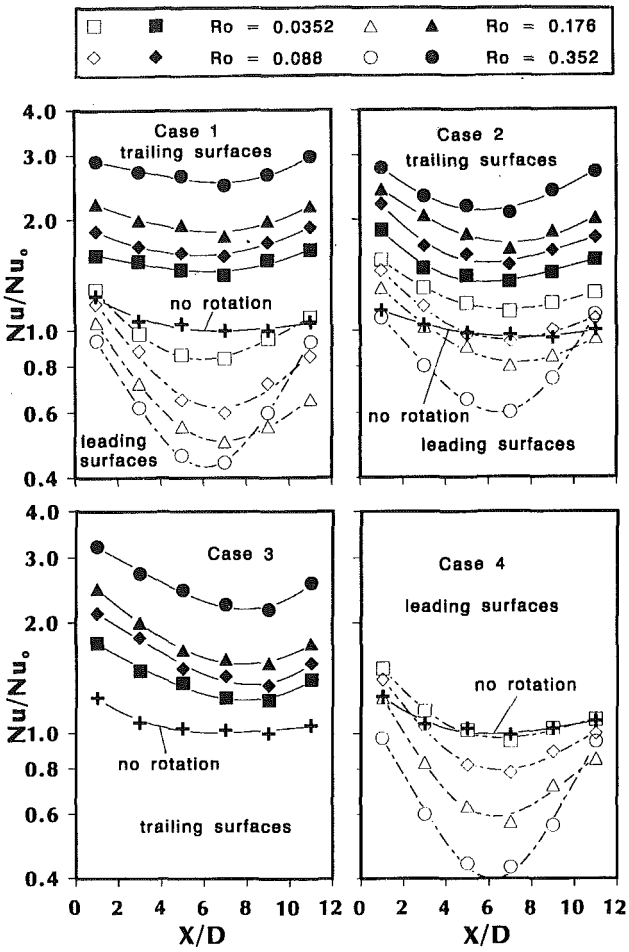

Fig. 8 Effect of rotation number on Nusselt number ratio variation for four cases studied

increases slightly near $X/D = 11$ because of flow entering the sharp 180 deg turn. The nonrotating results agree with the previous study of local heat transfer ratios in the entry region of a circular tube with fully developed flow condition (Boelter et al., 1948).

With a rotation number of 0.352 (based on Ω = 800 rpm and Re = 2500) heat transfer ratio decreases and increases by factors of more than two from the leading and trailing surfaces, respectively, compared to the heat transfer ratio from the nonrotating condition. The heat transfer ratios from the side A and side B surfaces are about the same and about 20–30 percent higher than the nonrotating results. The heat transfer ratio on the leading surface decreases sharply from the entrance to about 40 percent of the nonrotating value at $X/D = 6$ and then increases rapidly at the larger X/D location. The heat transfer ratio on the trailing surface is fairly uniform in the axial location and about 2.5 times that of the nonrotating results. This means that the trailing surface heat transfer coefficients can be 6 times higher than that of the leading surface due to a rotation number of 0.352. However, as seen from Fig. 7, the difference of the heat transfer coefficients between the trailing and leading surfaces reduces with decreasing rotation number from 0.352 to 0.0352 (based on Ω = 800 rpm and Re = 25,000). However, the heat transfer coefficients on the surfaces of sides A and B are fairly insensitive to the rotation number from 0.352 to 0.0352.

As previously discussed by Wagner et al. (1991a), the difference of the heat transfer coefficients between the rotating and nonrotating conditions on the leading, trailing, and sidewall surfaces is attributed to both the increasing strength of the secondary cross-stream flow vortices due to the Coriolis force and the centripetal buoyancy. The higher trailing surface heat transfer coefficients are because (1) the coolant impingement (due to rotation) on the trailing surface creates a thinner boundary layer and (2) the coolant profile distortion (due to rotation) produces a stronger centripetal buoyancy-induced wall turbulence near the destabilized trailing surface thin boundary layer. The decreases in heat transfer coefficients near the inlet of the channel on the leading surfaces are due to a thicker stabilized boundary layer, and the subsequent increase in heat transfer coefficients near the end of the channel is attributed to the stronger centripetal buoyancy-induced, destabilized wall turbulence boundary layer. These are the typical combined effects of Coriolis and buoyancy forces due to rotation on the leading, trailing, and sidewall surfaces of a square channel with radially outward flow.

Effect of Rotation Number. Figure 8 shows the effect of rotation number on the leading and trailing surface Nusselt number ratio for different surface heating conditions (cases 1, 2, 3, and 4, respectively). As discussed above, the trailing surface heat transfer ratio increases up to 2.5 times with increasing rotation number from 0.0 to 0.352 for the uniform wall temperature condition (case 1, $(\Delta\rho/\rho)_i = 0.11$). Similar trends are observed for the cases of uneven wall temperature conditions (cases 2 and 3). Note that the Nusselt number ratios on the trailing surface were not measured for case 4. Unlike the trailing surface, the leading surface Nusselt number ratio decreases to 0.4 with increasing rotation number from 0.0 to 0.352 for case 1, except that the Nusselt number ratio decreases and then increases again near the end region of the channel for the larger rotation number. In contrast to the uniform wall temperature condition (case 1), the leading surface Nusselt number ratio for the uneven wall temperature (case 2) increases (Ro = 0.0 to 0.0352) and then decreases again with increasing rotation number (Ro = 0.0352 to 0.352). Note that the heat transfer coefficients on the leading surface for case 2 are much

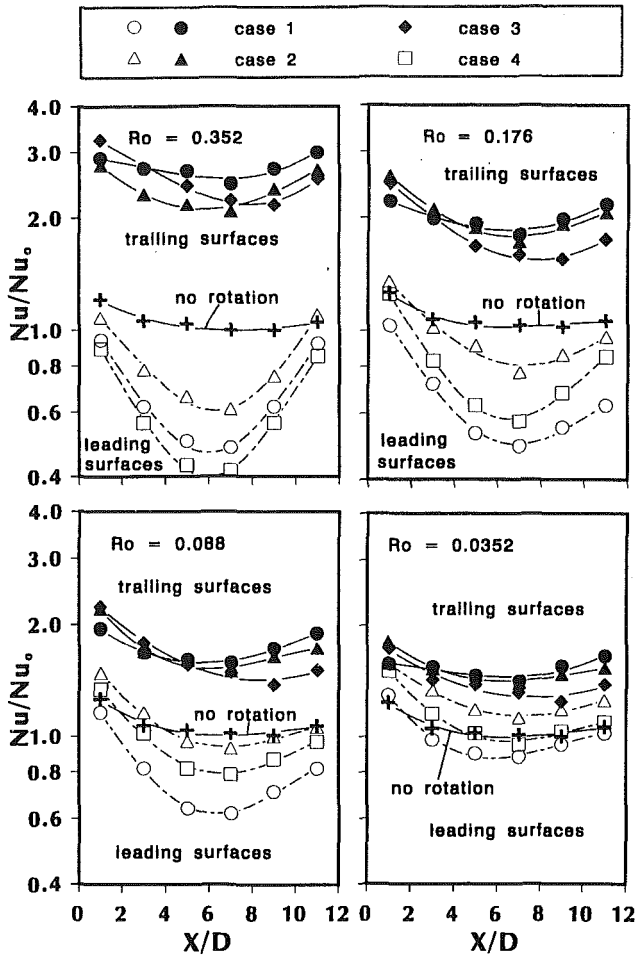

Fig. 9 Effect of surface heating condition on Nusselt number ratio variation at selected rotation numbers

higher than the corresponding values for case 1. The leading surface heat transfer coefficients for case 3 were not measured. The leading surface heat transfer coefficients for case 4 are almost unchanging for a rotation number between 0.0 and 0.0352 and then decrease steadily while increasing the rotation number to 0.352.

This suggests that the leading surface heat transfer coefficients are strongly altered by the uneven wall temperature condition. A more detailed discussion on the cause and effect relationships is presented in the following section.

Effect of Surface Heating Condition. Figure 9 shows the effect of surface heating condition on the leading and trailing surface Nusselt number ratio for the rotation numbers studied between 0.0352 and 0.352. Four surface heating conditions are studied (see Fig. 3 and Table 1): (1) four walls at uniform temperature, (2) trailing surface temperature higher than the leading and sidewall surface temperature, (3) trailing surface hot and remaining surfaces cold, and (4) leading surface hot and remaining surfaces cold. Note that the test results for the nonrotating Nusselt number ratios on the leading and trailing surface for the four surface heating conditions are about the same within 5 percent. Therefore, the nonrotating Nusselt number ratios are presented as a single curve and included in Fig. 9 for comparison (read legend +).

The results show that the trailing surface Nusselt number ratio for case 2 is 5–15 percent lower than that of case 1, and the trailing surface Nusselt number ratio for case 3 is 5–25 percent lower than that of case 1. However, the results show that the leading surface Nusselt number ratio for case 2 is 20–80 percent higher than that of case 1, and the leading surface Nusselt number ratio for case 4 is 10–40 percent higher than case 1 for all studied rotation numbers except for the one with the larger rotation number (R_o = 0.352).

The trailing surface temperature being higher than the leading and sidewall surface can result in more cooler fluid near the sidewall and leading surfaces. These cooler fluids are accelerated and a thinner boundary layer is created near the leading surface. Additionally, these cooler fluids tend to stay with the leading surface and reduce the amount of secondary cross-stream flow between the leading and trailing surface due to rotation (see Fig. 3). The reduced secondary cross-stream flow cuts down the effect of Coriolis force and centripetal buoyancy-induced force on the leading and trailing surface (see Fig. 2). Figure 9 shows that the trailing surface heat transfer coefficients for case 2 are not as high as case 1 and the leading surface heat transfer coefficients for case 2 are not as low as case 1. The difference in the heat transfer coefficients between the trailing and leading surface becomes smaller for case 2.

The cooler fluid stays with the leading surface for the case of hot trailing surface, which further reduces the amount of secondary cross-stream flow between the leading and trailing surface due to rotation (see Fig. 3). Figure 9 shows that the trailing surface heat transfer coefficients for case 3 are lower than case 1. For the case of hot leading surface, the cooler fluid stays with the trailing surface and cuts down the activity of cross-stream flow due to rotation (see Fig. 3). Figure 9 also shows that the leading surface heat transfer coefficients for case 4 are higher than case 1. Although the cross-stream flow effect is important for the case of higher rotation number (Ro = 0.352), the cooler fluids are staying with the leading surface for case 4 than for case 1.

Figure 2 summarizes the effects of inertia force (Reynolds number), Coriolis force (rotation number), bulk buoyancy force (for the case of uniform wall temperature), and local buoyancy force (for the case of uneven wall temperature) on the coolant flow profile and the associated heat transfer coefficient. For the case of uniform wall temperature, the Coriolis force turns the coolant flow to the trailing surface and the bulk buoyancy force further keeps the coolant flow closer to the trailing surface. Therefore, the trailing surface heat transfer coefficient is much higher than the leading surface due to rotation. For the case of trailing hotter than leading, however, the uneven wall temperature superimposed on the coolant flow profile creates cooler fluid near the leading surface and produces more buoyancy force near the leading surface than the trailing surface. This unequal local buoyancy force shifts the coolant flow back a little to the leading surface and suppresses the amount of secondary cross-stream flow induced by the Coriolis force. Therefore, the uneven wall temperature between the leading and trailing surface eventually degrades the effect of rotation on the trailing and leading heat transfer coefficients.

Comparison With Previous Results. As discussed above, the convective heat transfer coefficients on the leading and trailing surface of a rotating channel with radial outward flow can be affected by the Coriolis force (rotation number) and the surface heating condition (bulk or local buoyancy force). Figure 10 shows the variation of Nusselt number ratio with rotation number at selected axial locations for the four surface heating conditions studied. The experimental results from Wagner et al. (1991a) for the case of uniform wall temperature are also included for comparison. Note that Wagner et al. results are based on the following conditions and axial locations: Ro calculated from Re = 25,000 by varying rotational speed, $(\Delta\rho/\rho)_i$ = 0.13, $\overline{R}/D$ = 49, and X/D = 4.7, 8.5, and 12.4, respectively. The present data for the case of uniform wall temperature (case 1) are based on: Ro calculated from Ω = 800 rpm by varying Re between 2500 and 25,000, $(\Delta\rho/\rho)_i$ = 0.11, $\overline{R}/D$ = 30, and X/D = 5, 9, and 11, respectively. The results show that the present Nusselt number ratio on the trailing and leading surface for the case of uniform wall tem-

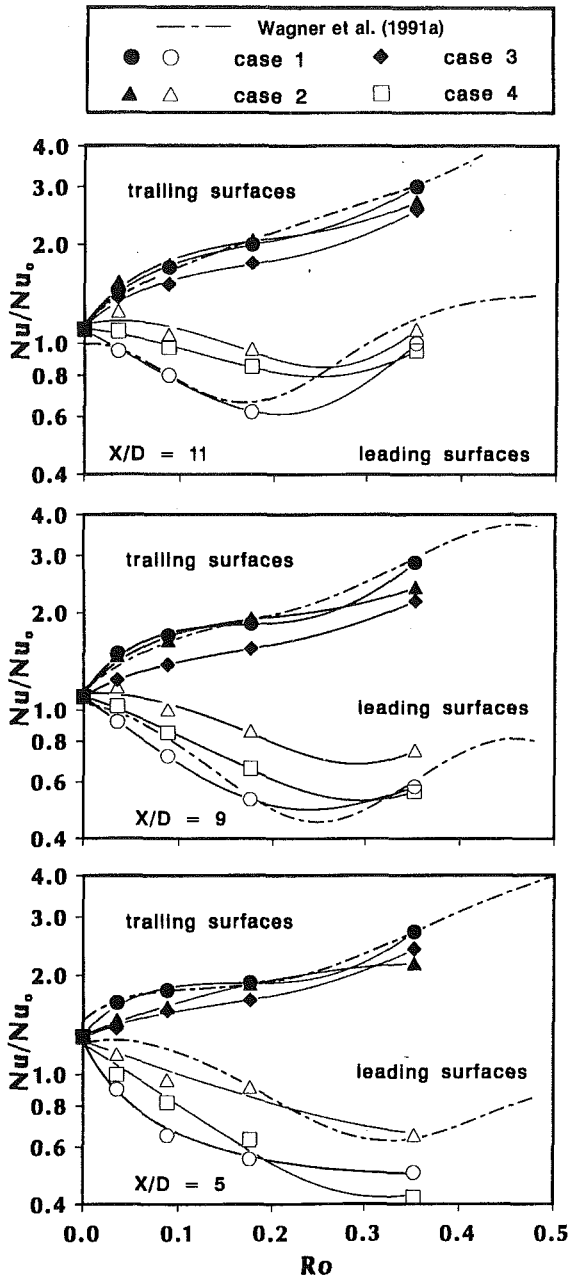

Fig. 10 Effect of rotation number on Nusselt number ratio variation for studied four cases at selected axial locations and comparison with the previous results (Wagner et al., 1991a)

perature condition agrees with those of Wagner et al. except that $X/D = 5$. This confirms that the trailing surface Nusselt number ratio increases with an increasing rotation number, whereas the leading surface Nusselt number ratio decreases and then increases with an increasing rotation number for the case of uniform wall temperature condition. At $X/D = 5$, the leading surface Nusselt number ratios of this study are much lower than those of Wagner et al. The difference may be caused by the flow inlet condition used in each study: a fully developed flow entrance for this study versus a sharp developing flow entrance for Wagner et al. The fully developed flow profile with a thicker boundary layer can be more easily effected by the Coriolis force than the developing accelerating flow with a thinner boundary layer. Therefore, the leading surface Nusselt number ratios of this study are much lower.

As previously discussed, the uneven surface temperature on both the leading and trailing surface creates unequal local buoyancy forces that alter the heat transfer coefficients. Figure 10 shows that, as a result, the trailing surface Nusselt number ratios for cases 2 and 3 are 15–25 percent lower than that for case 1, whereas the leading surface Nusselt number ratios for cases 2 and 4 are 40–80 percent higher than that for case 1. It is clear that the local buoyancy force interacts with the Coriolis force and reduces the effect of the rotation number on the trailing and leading surface heat transfer coefficients (see Fig. 2).

A buoyancy parameter $(\Delta\rho/\rho)(R/D)\,(Ro)^2$ was used by Wagner et al. (1991a) to consider the combined effects of Coriolis and buoyancy forces on heat transfer. The buoyancy parameter includes the effects of axial coolant-to-wall density ratio $(\Delta\rho/\rho = (T_w - T_b)/T_w$, buoyancy force), secondary cross-stream flow (Coriolis force, R_o), and rotating radius to hydraulic diameter ratio (R/D). Figure 11 shows the variation of the Nusselt number ratio with the buoyancy parameter at selected axial locations for the four surface heating conditions. The experimental results from Wagner et al. (1991a) for the case of uniform wall temperature are also included for comparison. The shaded area shown in Fig. 11 represents the data from Wagner from two sets of mean rotating radius ($\overline{R}/D = 49$ and 33) and Ro between 0.0 and 0.48. Note that the R/D ratio of the present study is 30 and R_o between 0.0 and 0.352. They indicated that the Nusselt number ratio is insensitive to the mean rotating radius for $\overline{R}/D$ between 33 and 49. They also indicated that the Nusselt number variation for a given buoyancy parameter is primarily due to the range of rotation numbers studied. The results show that the present Nusselt number ratios on the trailing and leading surface for the case of uniform wall temperature (case 1) are in the range of their data variation (except that the leading surface Nusselt number ratios are much lower at $X/D = 5$ as discussed above). Again, the results show that the effect of uneven surface temperature is to increase the leading surface heat transfer coefficients for cases 2 and 4 and to decrease the trailing surface heat transfer coefficients for cases 2 and 3, respectively, at a given buoyancy parameter condition.

Effect of Reynolds Number. Since the rotation number is defined as $Ro = \Omega D/V$, the same Ro can be obtained by using larger or smaller values of Ω and V. Figure 12 shows the effect of the Reynolds number on the leading and trailing surface Nusselt number ratio for the studied four surface heating conditions. The comparisons are based on: (1) $Ro = 0.088$ for Re = 5000 and 10,000, (2) $Ro = 0.176$ for Re = 2500 and 5000. The results show that Nusselt number ratio for both the leading and trailing surface decreases slightly with an increasing Reynolds number for the given rotation number. The effect of a Reynolds number is found to be more severe for case 2 than cases 1, 3, and 4.

Concluding Remarks

The influence of surface heating condition on the local heat transfer coefficients in a rotating square channel with smooth walls and radial outward flow has been studied for rotating numbers from 0.0 to 0.352 and Reynolds numbers from 2500 to 25,000. The main findings are:

1 The local trailing surface Nusselt number ratio can be as high as 2.5–3.0, whereas the local leading surface Nusselt number ratio can be as low as 0.4 for the case of uniform wall temperature condition $[(\Delta\rho/\rho)_i = 0.11]$ due to the effect of rotation ($Ro = 0.352$).

2 The general trend of the effect of rotation on heat transfer is that the trailing surface Nusselt number ratio increases but the leading surface Nusselt number ratio decreases with an increasing rotation for the four surface heating conditions studied. The increased (or decreased) heat transfer coefficients on the trailing or leading surface are due to the cross-stream and centripetal buoyancy-induced flows from rotation.

3 The uneven wall temperature creates unequal buoyancy

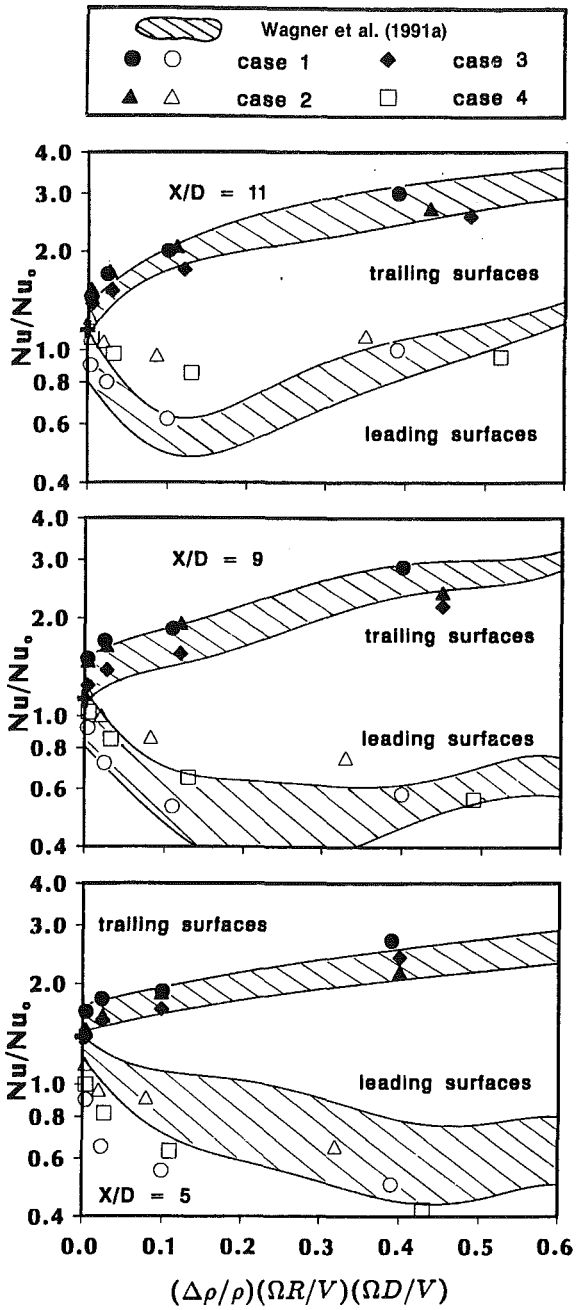

Fig. 11 Effect of buoyancy parameter on Nusselt number ratio variation for studied four cases at selected axial locations and comparison with the previous results (Wagner et al., 1991a)

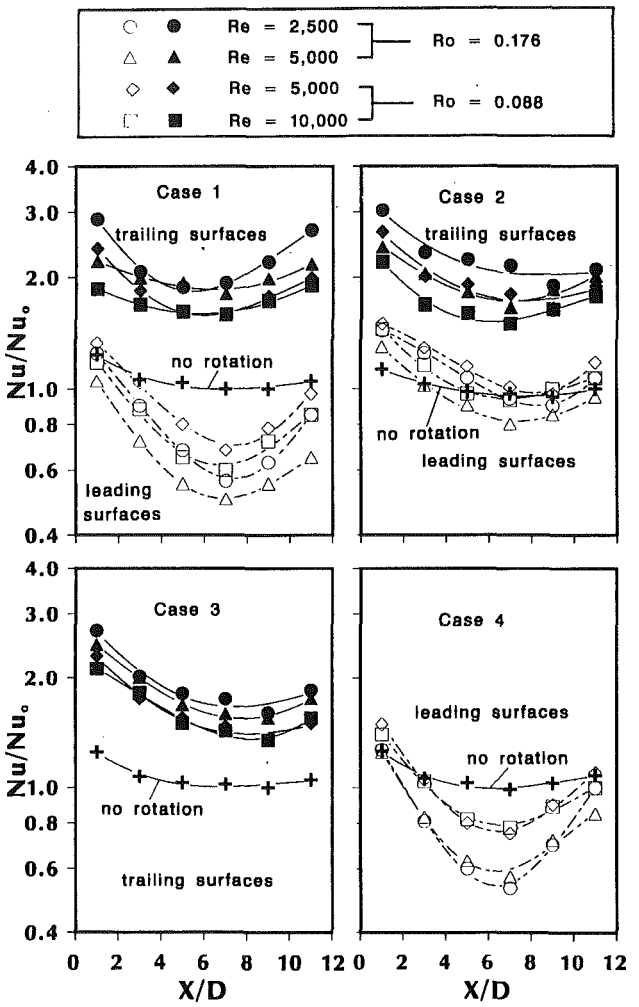

Fig. 12 Effect of Reynolds number on Nusselt number ratio variation for studied four cases

forces between the leading and trailing surface. The unequal local buoyancy forces reduce the amounts of cross-stream flow between the leading and trailing surfaces and degrades the effect of rotation on the local leading and trailing heat transfer coefficients.

4 The trailing surface heat transfer coefficients for uneven surface temperature conditions (cases 2 and 3) are lower than that for uniform surface temperature (case 1). The leading surface heat transfer coefficients for uneven surface temperature conditions (cases 2 and 4) are much higher than that for uniform surface temperature (case 1). This implies that the difference between the leading and trailing heat transfer coefficient with uneven wall temperature becomes smaller compared to the uniform wall temperature case.

5 The Nusselt number ratio for both the trailing and leading surface decreases slightly with an increasing Reynolds number for a given rotation number for the four cases of surface heating conditions studied.

6 The Nusselt number ratios on the trailing and leading surface agree with the previous experimental results for similar ranges of rotation numbers and for the buoyancy parameter for the case of uniform wall temperature condition (case 1) except the leading surface entrance region. This confirms that the trailing surface heat transfer coefficients increase with increasing rotation numbers (or buoyancy parameters), whereas the leading surface heat transfer coefficients decrease and then increase with increasing rotation number (or buoyancy parameters).

7 The trailing surface Nusselt number ratios for uneven surface temperature conditions (cases 2 and 3) are 15–25 percent lower than that for uniform surface temperature (case 1) at a given buoyancy parameter (or rotation number), whereas the leading surface Nusselt number ratios for uneven surface temperature conditions (cases 2 and 4) are 40–80 percent higher than that for uniform surface temperatures (case 1) at a given buoyancy parameter (or rotation number).

Acknowledgments

The investigation was supported by the General Electric Company.

References

Boelter, L. M. K., Young, G., and Iverson, H. W., 1948, "An Investigation of Aircraft Heaters—Distribution of Heat Transfer Rate in the Entrance Section of a Circular Tube," NACA TN 1451, Washington, DC.

Clifford, R. J., Morris, W. D., and Harasgama, S. P., 1984, "An Experi-

mental Study of Local and Mean Heat Transfer in a Triangular-Sectioned Duct Rotating in the Orthogonal Mode," ASME *Journal of Engineering for Gas Turbines and Power*, Vol. 106, pp. 661–667.

Guidez, J., 1989, "Study of the Convective Heat Transfer in a Rotating Coolant Channel," ASME JOURNAL OF TURBOMACHINERY, Vol. 111, pp. 43–50.

Han, J. C., 1984, "Heat Transfer and Friction in Channels With Two Opposite Rib-Roughened Walls," ASME *Journal of Heat Transfer*, Vol. 106, pp. 774–781.

Han, J. C., 1988, "Heat Transfer and Friction Characteristics in Rectangular Channels With Rib Turbulators," ASME *Journal of Heat Transfer*, Vol. 110, pp. 321–328.

Han, J. C., and Zhang, P., 1991, "Effect of Rib-Angle Orientation on Local Mass Transfer Distribution in a Three-Pass Rib-Roughened Channel," ASME JOURNAL OF TURBOMACHINERY, Vol. 113, pp. 123–130.

Han, J. C., Zhang, Y. M., and Lee, C. P., 1992, "Influence of Surface Heat Flux Ratio on Heat Transfer Augmentation in Square Channels With Parallel, Crossed, and V-Shaped Angled Ribs," ASME JOURNAL OF TURBOMACHINERY, Vol. 114, pp. 872–880.

Harasgama, S. P., and Morris, W. D., 1988, "The Influence of Rotation on the Heat Transfer Characteristics of Circular, Triangular, and Square-Sectioned Coolant Passages of Gas Turbine Rotor Blades," ASME JOURNAL OF TURBOMACHINERY, Vol. 110, pp. 44–50.

Kline, S. J., and McClintock, F. A., 1953, "Describing Uncertainties in Single-Sample Experiments," *Mechanical Engineering*, Jan., pp. 3–8.

Mori, Y., Fukada, T., and Nakayama, W., 1971, "Convective Heat Transfer in a Rotating Radial Circular Pipe (2nd Report)," *International Journal of Heat and Mass Transfer*, Vol. 14, pp. 1807–1824.

Morris, W. D., Harasgama, S. P., and Salemi, R., 1988, "Measurements of Turbulent Heat Transfer on the Leading and Trailing Surfaces of a Square Duct Rotating About an Orthogonal Axis," ASME Paper No. 88-GT-114.

Morris, W. D., and Ghavami-Nasr, G., 1991, "Heat Transfer Measurements in Rectangular Channels With Orthogonal Mode Rotation," ASME JOURNAL OF TURBOMACHINERY, Vol. 113, pp. 339–345.

Morris, W. D., and Salemi, R., 1992, "An Attempt to Uncouple the Effect of Coriolis and Buoyancy Forces Experimentally on Heat Transfer in Smooth Circular Tubes That Rotate in the Orthogonal Mode," ASME JOURNAL OF TURBOMACHINERY, Vol. 114, pp. 858–864.

Rohsenow, W. M., and Choi, H., 1961, *Heat, Mass and Momentum Transfer*, Prentice-Hall, Inc., New Jersey, pp. 192–193.

Taslim, M. E., Rahman, A., and Spring, S. D., 1991, "An Experimental Investigation of Heat Transfer Coefficients in a Spanwise Rotating Channel With Two Opposite Rib-Roughened Walls," ASME JOURNAL OF TURBOMACHINERY, Vol. 113, pp. 75–82.

Wagner, J. H., Kim, J. C., and Johnson, B. V., 1986, "Rotating Heat Transfer Experiments With Turbine Airfoil Internal Passages," ASME Paper No. 86-GT-133.

Wagner, J. H., Johnson, B. V., and Hajek, T. J., 1991a, "Heat Transfer in Rotating Passages With Smooth Walls and Radial Outward Flow," ASME JOURNAL OF TURBOMACHINERY, Vol. 113, pp. 42–51.

Wagner, J. H., Johnson, B. V., and Kopper, F. C., 1991b, "Heat Transfer in Rotating Serpentine Passages With Smooth Walls," ASME JOURNAL OF TURBOMACHINERY, Vol. 113, pp. 321–330.

Wagner, J. H., Johnson, B. V., Graziani, R. A., and Yeh, F. C., 1992, "Heat Transfer in Rotating Serpentine Passages With Trips Normal to the Flow," ASME JOURNAL OF TURBOMACHINERY, Vol. 114, pp. 847–857.

Effect of Trailing-Edge Ejection on Local Heat (Mass) Transfer in Pin Fin Cooling Channels in Turbine Blades

R. D. McMillin

S. C. Lau

Department of Mechanical Engineering,
Texas A&M University,
College Station, TX 77843-3123

Experiments are conducted to study the local heat transfer distribution and pressure drop in a pin fin channel that models the cooling passages in modern gas turbine blades. The detailed heat/mass transfer distribution is determined via the naphthalene sublimation technique for flow through a channel with a 16-row, staggered 3 × 2 array of short pin fins (with a height-to-diameter ratio of 1.0, and streamwise and spanwise spacing-to-diameter ratios of 2.5) and with flow ejection through holes in one of the side walls and at the straight flow exit (to simulate ejection through holes along the trailing edges and through tip bleed holes of turbine blades). The pin fin heat/mass transfer and the channel wall heat/mass transfer are obtained for the straight-flow-only and the ejection-flow cases. The results show that the regional pin heat/mass transfer coefficients are generally higher than the corresponding regional wall heat/mass transfer coefficients in both cases. When there is side wall flow ejection, a portion of the flow turns to exit through the ejection holes and the rate of heat/mass transfer decreases in the straight flow direction as a result of the reducing mass flow rate along the channel. The rate of cooling air flow through a pin fin channel in a gas turbine blade must be increased to compensate for the "loss" of the cooling air through trailing edge ejection holes, so that the blade tip is cooled sufficiently.

Introduction

Cooling of the tail regions of the blades in modern high-performance gas turbine engines is enhanced by forcing air through internal pin fin channels. Due to the small spacing between the pressure wall and the suction wall near the trailing edge of a blade, the pin fins in the cooling channel typically have a height-to-diameter ratio of about one. The short pin fins enhance the removal of heat from the walls of the blades by periodically interrupting the flow of the cooling air, promoting turbulence, and increasing the heat transfer area. The increase of the heat transfer from the walls to the cooling air, however, is generally accompanied by a significant increase of the pressure drop in the pin fin channel, and, therefore, an increase of the required pumping power.

Compressed air enters the pin fin channel in a gas turbine blade at the base of the blade and exits either through ejection holes along the trailing edge of the blade or through bleed holes at the tip of the blade. The rate of mass flow of air decreases along the channel as air exits through the trailing edge ejection holes. Thus, the rate of cooling air flow must be increased to compensate for the ejection flow through the trailing edge holes, so that the tip of the blade is cooled sufficiently.

Heat transfer and friction characteristics of the flow of air in straight channels with short pin fins have been studied by a number of researchers, such as Brown et al. (1980), VanFossen (1982), Brigham and VanFossen (1984), Simoneau and VanFossen (1984), Metzger and Haley (1982), Metzger et al. (1982, 1984, 1986), Lau et al. (1987), and Chyu (1990). Metzger et al. (1982) conducted experiments to study the heat transfer characteristics of turbulent air flow in a wide channel with ten rows of pin fins. They presented results that showed the row-average heat transfer coefficient along the pin fin channel increased, reached a maximum in the third (or fourth) pin row, then decreased gradually.

Lau et al. (1989a, 1989b) demonstrated that, when air was allowed to eject through an array of small holes in one side wall of a pin fin channel, the decreasing rate of mass flow in the channel significantly affected the overall heat transfer from the channel and the overall pressure drop across the channel.

Lau et al. (1991) conducted heat transfer and pressure drop experiments to study the effect of varying the ejection hole configuration on the regional heat transfer for turbulent air flow in a pin fin channel. With a rectangular test channel that had 8 identical aluminum segments and 32 staggered rows of pins, they obtained regional heat transfer results for various ejection hole geometries and a wide range of flow rate. The

Contributed by the International Gas Turbine Institute and presented at the 37th International Gas Turbine and Aeroengine Congress and Exposition, Cologne, Germany, June 1–4, 1992. Manuscript received by the International Gas Turbine Institute February 17, 1992. Paper No. 92-GT-178. Associate Technical Editor: L. S. Langston.

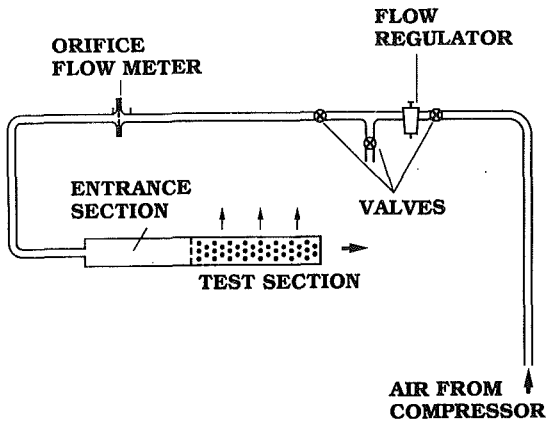

Fig. 1 Schematic of test apparatus

results showed that the segmental heat transfer coefficients in the ejection-flow cases decrease along the pin fin channel much faster than that in the straight-flow-only case.

The objective of the present investigation is to study the detailed distribution of the local heat transfer coefficient in the internal cooling channel near the trailing edge of a gas turbine blade. Mass transfer experiments are conducted with a pin fin test channel whose interior surfaces exposed to the flow of air are all coated with naphthalene. A naphthalene-coated surface in a mass transfer experiment is analogous to a surface maintained at a uniform temperature in a corresponding heat transfer experiment. By measuring the rates of sublimation on the naphthalene-coated surfaces, the detailed distribution of the local heat transfer coefficient is determined. By applying the analogy between heat transfer and mass transfer, the distribution of the local heat transfer coefficient on the surfaces in a geometrically similar pin fin channel may be evaluated (Eckert and Goldstein, 1976).

The test section is a wide rectangular channel with a staggered array of short pin fins that models the pin fin cooling passage in a gas turbine blade. In one set of experiments, air is forced to flow straight through the channel. In another set of experiments, air is forced to exit the channel through small holes in one side wall and in the straight flow exit. The holes model the ejection holes along the trailing edge of a gas turbine blade and the bleed holes at the tip of the blade. Results are obtained for a wide range of flow rate corresponding to that typical for cooling of gas turbine blades. By comparing the results from the two sets of experiments, the effect of trailing edge flow ejection on the local heat transfer distribution in a pin fin channel in a gas turbine blade is examined.

Experimental Apparatus

The naphthalene sublimation experiments are conducted with an open flow loop. The flow loop and all instrumentations for the experiments are located in an air-conditioned laboratory that is maintained at 22°C. Air from a building compressor flows through a dryer, a filter, a regulator, two control valves, a calibrated orifice flow meter, and an entrance section, before entering the test section (Fig. 1). From the test section exit, the mixture of air and naphthalene vapor is ducted with a large flexible vinyl tube to the outside of the laboratory (through a fume hood with an exhaust fan).

For a set of calibration experiments, the test section is a 7.5:1 rectangular channel with smooth walls. The flow cross section of the channel is 47.6 mm wide and 6.35 mm high. The four walls of the channel are made of aluminum. By removing a 3.18-mm-thick layer of the aluminum with a milling machine from the inside surface of each of the top and bottom walls, each wall has a shallow cavity with a 3.18-mm-thick rim (Fig. 2*a*). In a casting process, the cavity is filled with naphthalene. The naphthalene surface is smooth and flat, and is flush with the rim of the cavity.

Each of the two vertical side walls also has a naphthalene-filled cavity. The naphthalene, however, does not have a rim on all sides. During the casting of a side wall, two long, straight, 3.18-mm-thick, rectangular aluminum bars serve as part of the rim. Upon removal of the bars at the end of the casting process, a long rectangular block of naphthalene is raised above the interior surface of the side wall and is bound at its two ends only.

Nomenclature

A_{min} = minimum flow area across span of pin fin channel, m^2
D = diameter of pins, m
D_h = hydraulic diameter, m
H = height of pins, m
h_m = mass transfer coefficient, Eq. (1), m/s
$\bar{h}_m$ = regionally averaged mass transfer coefficient, Eq. (3), m/s
$\dot{m}$ = total mass flow rate of air, kg/s
$\dot{m}''$ = mass diffusion flux of naphthalene, Eq. (2), kg/(m^2•s)
N = number of pin rows in channel
p_{exit} = exit pressure, N/m^2
p_{inlet} = inlet pressure, N/m^2
p_{local} = local pressure in pin fin channel, N/m^2
Re_D = Reynolds number based on pin diameter, Eq. (5)
Re_{Dh} = Reynolds number based on hydraulic diameter and average velocity
S = spanwise pin spacing, m
Sc = Schmidt number
Sh_D = local Sherwood number, Eq. (4)
$\overline{Sh}_D$ = regional Sherwood number over segment of pin fin channel with two rows of pins
Sh_{Dh} = local Sherwood number for flow through smooth rectangular channel
$Sh_{0,Dh}$ = Sherwood number for fully developed flow through a smooth rectangular channel, Eq. (6)
Sh_r = relative Sherwood number, Eq. (9)
u_{max} = average velocity of flow at minimum flow cross section in pin fin channel, m/s
x = distance from channel entrance, m
X = pin spacing in straight flow direction, m
y = distance from left side wall, Figs. 9 and 11, m
ΔP_{total} = dimensionless total pressure drop across pin fin channel, Eq. (7)
ΔP_{local} = dimensionless local pressure in pin fin channel, Eq. (8)
Δt = duration of test run, s
Δz = change of elevation of naphthalene surface at measurement point, m
μ = dynamic viscosity of air, N•s/m^2
ν = kinematic viscosity of air, m^2/s
ρ = density of air, kg/m^3
ρ_b = bulk vapor density of naphthalene, kg/m^3
ρ_w = local vapor density of naphthalene at surface, kg/m^3
ρ_s = density of solid naphthalene, kg/m^3
σ = diffusion coefficient, m^2/s

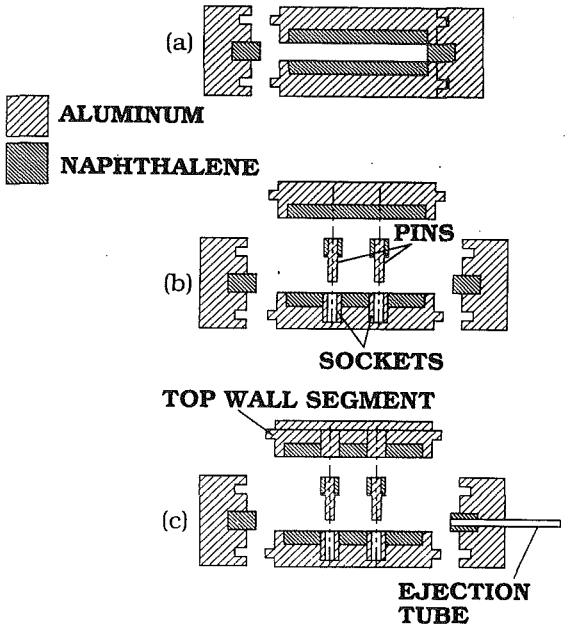

Fig. 2 Cross section of test channel: (*a*) with smooth walls, (*b*) with pin fins, (*c*) with ejection holes in one side wall

During the process of assembling the test section, rectangular ribs on the long sides of the top and bottom walls are matched against grooves on the sides of the two side walls. The naphthalene blocks on the two side walls cover the aluminum rims of the naphthalene cavity of the top and bottom walls (Fig. 2*a*). Thus, all interior surfaces of the smooth channel are active surfaces.

Teflon tape in the grooves on the two side walls and adhesive tape over the interfaces between the adjacent walls are used to prevent air leakage during an experiment. Quick release clamps hold the four walls of the test section in place.

To study the heat/mass transfer characteristics of flow in a pin fin channel, the bottom wall of the rectangular channel is replaced with one that has a staggered array of 40 aluminum sockets in the cavity (Fig. 2*b*). Each socket is a short aluminum rod with a concentric hole for the insertion of a pin fin and with a top surface that is flush with the top of the rim of the cavity. The array has alternating rows of three and two sockets, and the streamwise and spanwise center-to-center spacings between adjacent sockets are both 15.9 mm.

The pin fins are machined from aluminum rods 6.35 mm in diameter (Fig. 2*b*). The narrower lower half of each pin fin is for insertion into a socket. The upper half of each pin is covered with a cylindrical layer of naphthalene, which has an outside diameter of 6.35 mm, in a casting process using a matching female mold. The female mold is a small aluminum rectangular plate that has 20 countersunk holes such that 20 pins may be prepared at one time. The countersunk holes have the same dimensions as those of the naphthalene-coated pins. The casting process involves placing the aluminum frames of the pins to be cast in the countersunk holes, filling the holes with molten naphthalene, allowing the naphthalene to solidify, shaving off excess naphthalene from the top of the pins with a sharp razor blade, and removing the pins from the mold.

After the pins are inserted into the sockets in the bottom wall and the four walls of the test section are assembled, all interior surfaces of the test section (actually about 98.8 percent, a 0.41-mm-wide ring at the base of each pin is not covered with naphthalene) are active mass transfer surfaces. The pin fins have a height-to-diameter ratio of 1.0 and the pin fin array has streamwise and spanwise center-to-center spacings of 15.9 mm (that is, $H/D = 1.0$, $X/D = S/D = 2.5$).

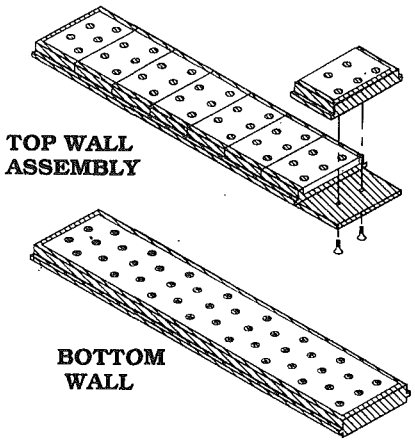

Fig. 3 Schematic of top and bottom walls of pin fin channel

For experiments with ejection, one of the side walls of the test section is replaced with one that has 64 equally spaced holes (Fig. 2*c*). Thin wall aluminum tubes with a length of 31.8 mm and an inside diameter of 1.59 mm are inserted into the 64 holes and are affixed with epoxy. The upstream ends of the tubes are flush with the naphthalene surface (after the cavity in the side wall is filled with naphthalene). The straight flow exit of the test section is blocked with a 6.35-mm-thick aluminum end plate that has five equally spaced holes of diameter 1.59 mm. The end plate is affixed to the four test channel walls with small machine screws. A rubber gasket prevents air leakage between the end plate and the channel walls. During an experiment with ejection, air exits the test section laterally through the 64 ejection holes on one of the side walls and in the straight flow direction through the five ejection holes in the end plate (to model cooling air through trailing edge ejection holes and tip bleed holes in a gas turbine blade).

In a separate set of experiments, the top wall of the test section is replaced with one that has eight identical segments (Fig. 2*c*). The segments are joined end to end and are attached to a 3.18-mm-thick aluminum support plate with small flat head machine screws (Fig. 3). Each segment is 31.8 mm long and has a 3.18-mm-deep cavity filled with naphthalene. In the cavity, there is a staggered array of five short aluminum rods 6.35 mm in diameter affixed to the bottom of the cavity. The top surfaces of the rods are flush with the top surface of the rim of the cavity. When the test section is assembled, the five rods are aligned with two rows of pin fins. This set of experiments using a segmental top wall determines the regionally averaged mass transfer from the channel walls over two rows of pin fins. The regional mass transfer results also validate the local results.

The entrance section is made entirely of aluminum. It has the same cross section as the test section and is 0.203 m long. The test section is mated to the entrance section with two flanges and cap screws. The two flanges are designed to ensure good alignment of the interior surfaces. Rubber gaskets prevent air leakage at the interfaces during an experiment.

The flow loop for the pressure measurement experiments is that for the mass transfer experiments. The test section and the entrance section are made entirely of aluminum and are geometrically similar to those for the mass transfer experiments. Their interior dimensions, however, are twice the corresponding dimensions of the test section and the entrance section for the mass transfer experiments. That is, the channel cross section is 95.3 mm wide and 12.7 mm high, and the pin fins are 12.7 mm in diameter. The pin fins are affixed to both the top and bottom walls with silicone adhesive. One of the side walls is 63.5 mm thick and has 64 lateral ejection holes

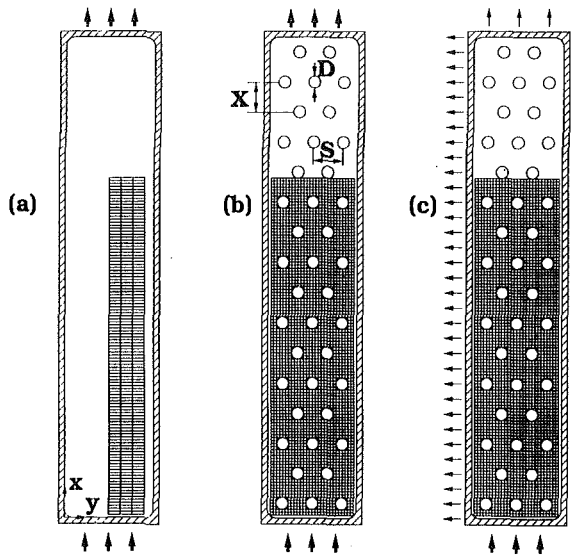

Fig. 4 Measurement grid on bottom channel wall: (*a*) channel with smooth walls, (*b*) pin fin channel with no side wall ejection holes, (*c*) pin fin channel with side wall ejection holes

3.18 mm in diameter. An end plate with five ejection holes blocks the straight flow exit. To study the pressure drop for straight flow through the pin fin channel, the lateral ejection holes are blocked with adhesive tape and the end plate is removed.

All dimensions of the various test sections have a tolerance of ±0.05 mm.

Instrumentations

Three small-gage thermocouples are used to measure the temperature of the naphthalene in the bottom wall of the test section during a mass transfer experiment. The junctions of these thermocouples are placed at strategic locations just beneath the exposed naphthalene surface. The average surface temperature is needed to calculate the vapor density of naphthalene at the measurement points. Another thermocouple at the entrance section measures the air temperature. A digital multichannel temperature indicator with a resolution of 0.1°C reads the thermocouple outputs.

The distribution of the local mass transfer on the bottom wall of the test section is determined by measuring the elevations at a grid of up to 3,277 points (see Fig. 4) with a Starret electronic depth gage before and after air is allowed to flow through the test section, at the beginning and at the end of a test run, respectively. The electronic gage has a range of ±0.2 mm and a resolution of 0.0001 mm. A coordinate table enables the traversing of the naphthalene-coated bottom wall in two perpendicular directions in a horizontal plane relative to the sensor of the electronic gage, which is mounted rigidly on a platform. The platform is affixed to the stationary base of the coordinate table and can be raised or lowered slightly. The coordinate table is equipped with two step motors that are controlled with a programmable indexer. In the electronic gage, the deflection of the tip of the sensor is converted to a voltage output that is proportional to the deflection. A microcomputer is programmed to read the voltage output from the electronic depth gage 40 times over a period of less than 1 second, take the arithmetic average, and record the average.

To determine the rates of mass transfer from the 40 pin fins, the pin fins are weighed one at a time with a Sartorius electronic balance before and after air is allowed to flow through the test section, at the beginning and at the end of a test run, respectively. The balance has a range of 0–32 g and a resolution of 0.01 mg (or a range of 0–160 g and a resolution of 0.1 mg). Similarly, to determine the regionally averaged mass transfer from the channel walls, the eight top wall segments are weighed one at a time at the beginning and at the end of a test run.

Fifteen and eight pressure taps are installed along two straight lines parallel to the two side walls on the top wall of the pressure measurement test section. The taps along the two lines are located at x/X = 1.0, 2.0, 3.0, . . . , and at x/X = 2.0, 4.0, 6.0, . . . , respectively. Two additional pressure taps are located on the top wall at the test section entrance. The local pressures at these taps are measured with respect to the atmospheric pressure with a U-tube manometer.

The pressure drop across the orifice and the gage pressure at the tap upstream of the orifice in the flow meter are measured with a water or mercury U-tube manometer, or an oil inclined manometer, depending on the measurement range. Atmospheric pressure is measured with a mercury barometer.

Experimental Procedure

After casting the various components of the mass transfer test section walls, the components are sealed in plastic storage bags and allowed to reach equilibrium with the laboratory overnight. After casting the 40 pin fins, they are placed in a plastic container with 40 separate compartments. On each compartment of the container is marked the position of each pin fin when it is installed in the test section. The casting phase of a mass transfer experiment usually lasts 4 to 5 hours.

At the beginning of the experiment, the local elevations at a grid of points on the naphthalene surface of the bottom wall of the test section are measured. Since the local elevation measurements are automated, the weights of the 40 pin fins (and those of the eight top wall segments in some experiments) are measured one at a time with the electronic balance during this time. The weights of up to five additional pins are measured for the estimation of the mass losses due to natural convection during the measurement period.

The test section is designed such that the walls can be assembled and disassembled quickly, and that the test section can be attached to and detached from the entrance section by simply tightening a few small cap screws. Once the test section is affixed to the entrance section, adhesive tape is used on the outside surfaces of the test section at the interfaces between adjacent walls to ensure that there is no air leakage during an experiment.

By opening a control valve, air is allowed to flow through the test flow loop at a predetermined rate for a period of between 30 minutes and 1.5 hours, depending on the overall air mass flow rate. The duration of an experiment is determined for a given air flow rate in a series of preliminary experiments to ensure that the mass transfer from the naphthalene surfaces changes the surface elevations enough to minimize the uncertainty of the local measurements but not excessively to change the flatness of the naphthalene surfaces and the roundness of the pin surfaces (and thus, the flow cross section) significantly.

The pressure drop across the orifice flow meter is monitored and recorded periodically. The naphthalene surface temperature and the air temperature are also recorded several times during the experiment. The gage pressure upstream of the orifice and the atmospheric pressure are read at the beginning and at the end of the experiment.

At the conclusion of the mass transfer experiment, the control valve is closed and the duration of the experiment is recorded. The test section is detached from the flow loop and disassembled. The local measurements are repeated, and the pin fins (and the top wall segments) are weighed again.

Auxiliary experiments are conducted to determine the mass losses from the channel walls and the top wall segments due to natural convection during the time required to assemble and

disassemble the test section and to measure the local and regional mass transfer.

Data Reduction

The local mass transfer coefficient, h_m, is defined as

$$h_m = \frac{\dot{m}''}{(\rho_w - \rho_b)} \tag{1}$$

where $\dot{m}''$ is the rate of mass transfer per unit area, ρ_w is the local vapor density at the naphthalene surface, and ρ_b is the local bulk density in the flow. The mass flux at any measurement point is calculated from

$$\dot{m}'' = \rho_s \left(\frac{\Delta z}{\Delta t}\right) \tag{2}$$

where ρ_s is the density of solid naphthalene, Δz is the measured elevation change at the measurement point, and Δt is the elapsed time of the test run.

The regional mass transfer coefficient for a wall segment or a pin is defined as

$$\bar{h}_m = \frac{\overline{\dot{m}''}}{(\rho_w - \rho_b)} \tag{3}$$

where the average mass flux is evaluated from the measured change of the mass of the segment or the pin, the area of the exposed naphthalene surface on the wall segment or the pin, and the elapsed time of the test run.

The vapor density at the naphthalene surface is determined from the vapor pressure-temperature relationship for naphthalene (Ambrose et al., 1975) and the ideal gas law, based on the measured naphthalene temperature. In the straight-flow-only case, the bulk density in the flow is evaluated by dividing the cumulative mass of naphthalene that is transferred to the airstream per unit time from the wall and pin surfaces up to the measurement point, the segment, or the pin of interest, by the volumetric rate of air flow. Since the mass transfer from the two naphthalene-coated side walls is not measured, in the calculation of the cumulative mass of naphthalene in the airstream, the spanwise-averaged side wall mass flux is approximated as the spanwise-averaged top and bottom wall mass flux at a given location. The cumulative mass of naphthalene in the airstream is generally very small; therefore, ρ_b is much smaller than ρ_w (the maximum value of ρ_b occurs at the channel exit; its value never exceeds 4.8 percent of that of ρ_w), and the approximation for the side wall mass transfer does not cause significant errors in the evaluation of the mass transfer coefficients (even a 20 percent error in the estimated value of ρ_b will cause only up to 1 percent error in h_m or $\bar{h}_m$).

In the ejection-flow case, the volumetric flow rate decreases in the straight flow direction. The volumetric flow rate at any cross section in the straight flow direction in the channel is not known. To obtain the distribution of the average volumetric flow rate at a channel cross section, the rate of flow through each ejection hole must be determined. By measuring the pressure drop across each ejection hole and assuming isentropic flow (the friction coefficient for each hole is dependent on the flow rate and is not known), the rate of air flow through each hole may be calculated. Such an estimation of the rates of air flow through the ejection holes and the distribution of the air flow rate in the channel, however, may be subjected to substantial errors. Since ρ_b is not small compared with ρ_w near the straight flow exit, where the volumetric flow rate of air may be very small, the rough estimation of the volumetric flow rate will result in a high degree of uncertainty in the distributions of the local and regional mass transfer coefficients.

To evaluate the local and regional mass transfer coefficients for the ejection-flow case, the local bulk density is replaced with a pseudo-local bulk density calculated by assuming a constant mass flow rate in the channel (that is, no flow ejection). With this assumption of constant mass flow rate in the channel, ρ_b is again very small compared with ρ_w (up to 4.8 percent of ρ_w near the channel straight flow exit) and the distributions of the local and regional mass transfer coefficients are lower than corresponding distributions based on the actual local bulk density.

Should h_m or $\bar{h}_m$ be calculated with the bulk density at the channel entrance, which is equal to zero, the values of h_m or $\bar{h}_m$ would have been lower only slightly (no more than 3.6 percent near the channel straight flow exit). If the distributions of the local and regional mass transfer coefficients for the ejection-flow case were obtained by estimating the local bulk density and volumetric flow rate with a rough model described above (by estimating the rates of mass flow through the holes, assuming a constant friction coefficient for all holes), the distributions would be up to 12 percent higher near the straight flow exit.

The local Sherwood number is a dimensionless mass transfer coefficient defined as

$$\mathrm{Sh}_D = \frac{h_m D}{\sigma} = h_m D \left(\frac{\mathrm{Sc}}{\nu}\right) \tag{4}$$

where D is the pin diameter, σ is the diffusion coefficient, Sc is the Schmidt number (Sc = 2.5 for naphthalene in air), and ν is the kinematic viscosity of air. Similarly, the regional Sherwood number is defined in terms of the regional mass transfer coefficient.

The Reynolds number is defined as

$$\mathrm{Re}_D = \frac{\rho u_{\max} D}{\mu} = \frac{\dot{m} D}{A_{\min} \mu} \tag{5}$$

where $\dot{m}$ is the mass flow rate of air at the pin fin channel entrance, $A_{\min}$ is the minimum flow cross-sectional area in the pin fin channel, and μ is the dynamic viscosity of air.

The local and regional Sherwood number results are compared with the Sherwood number for fully developed flow in a smooth channel, given by the Dittus–Boelter equation:

$$\mathrm{Sh}_{0,Dh} = 0.023 \mathrm{Re}_{Dh}^{0.8} \mathrm{Sc}^{0.33} \tag{6}$$

The overall pressure drop across the pin fin channel and the local pressure relative to the exit pressure are normalized with the dynamic pressure and are, respectively, defined as

$$\Delta P_{\text{total}} = \frac{p_{\text{inlet}} - p_{\text{exit}}}{\frac{1}{2} \rho u_{\max}^2 N} \tag{7}$$

$$\Delta P_{\text{local}} = \frac{p_{\text{local}} - p_{\text{exit}}}{\frac{1}{2} \rho u_{\max}^2 N} \tag{8}$$

where N is the number of pin rows in the test section and is equal to 16.

The pressure drop across the orifice does not fluctuate more than ±2.0 percent during any of the test runs. The orifice is rated at ±1.0 percent accuracy. The uncertainty of the total mass flow rate through the test section is estimated to be ±1.7 percent (Kline and McClintock, 1953). Using Eq. (5), the estimated uncertainties of ±1.0, ±3.5, and ±2.2 percent for the properties of air, the minimum area, and the pin diameter, respectively, the maximum uncertainty of the calculated Reynolds number is ±4.6 percent.

For a 0.56°C variation of the naphthalene surface temperature, there is approximately a 6.0 percent change in the local naphthalene vapor density, using the vapor pressure-temperature relationship of Ambrose et al. (1975). Each of the measured naphthalene surface temperatures varies by less than this amount for any test run. The bulk vapor density is generally small compared with the wall vapor density. Although the value of the bulk vapor density depends on the approximation of

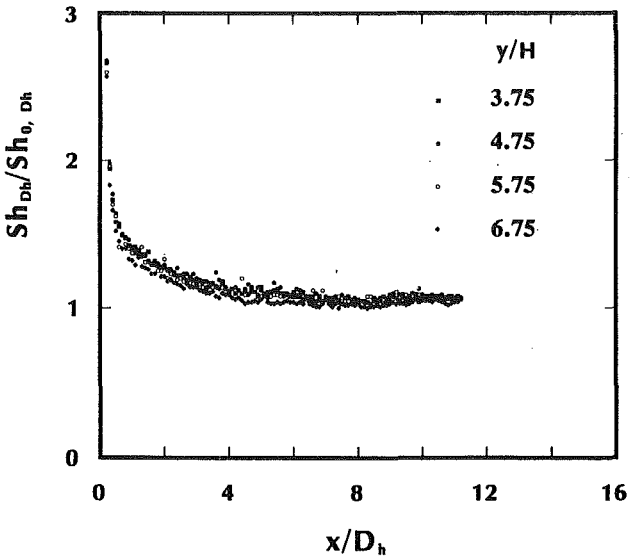

Fig. 5 Sh_{Dh} distributions, channel with smooth walls

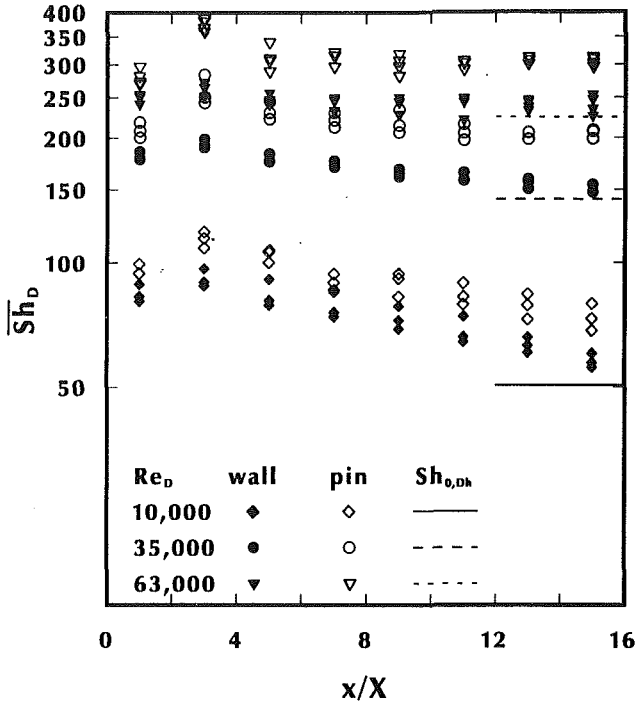

Fig. 6 $\overline{Sh}_D$ distributions, straight-flow-only case

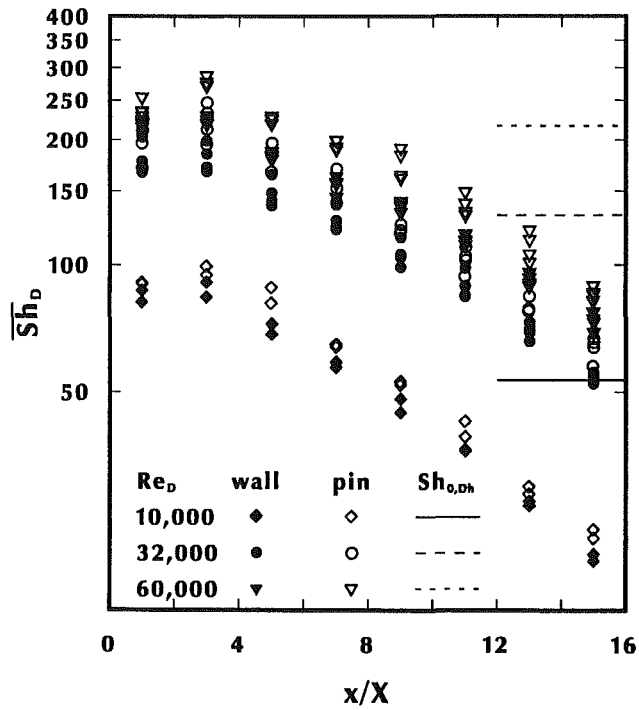

Fig. 7 $\overline{Sh}_D$ distributions, ejection-flow case

the average mass flux on the side walls as that on the top and bottom walls, the wall/bulk density difference has an estimated maximum uncertainty of ±6.3 percent. Using Eqs. (1) and (3) and an uncertainty of ±5.0 percent for the mass fluxes, the uncertainties of the local and average mass transfer coefficients are conservatively estimated to be ±8.0 percent. As a result, the local and averaged Sherwood numbers are accurate to about ±8.4 percent.

Similarly, the overall and local pressure drops are estimated to be accurate to ±4.5 percent.

Presentation of Results

The local Sherwood number, Sh_{Dh}, for flow in a 7.5:1 straight rectangular channel with smooth walls, normalized with the corresponding value of $Sh_{0,Dh}$ from Eq. (5), is plotted as a function of x/D_h in Fig. 5. The calibration data are for $Re_{Dh} \approx 30{,}000$ and are obtained along four axial lines along $y/H = 3.75$, 4.75, 5.75, and 6.75. The expected asymptotic drop of $Sh_{Dh}/Sh_{0,Dh}$ toward a value of 1.0 with increasing distance from the channel entrance is the result of the development of the concentration boundary layer. No significant spanwise variation of the local Sherwood number is evident. The $Sh_{Dh}/Sh_{0,Dh}$ distributions for test runs with two other values of Re_{Dh} are similar to those of $Re_{Dh} \approx 30{,}000$ and are not shown. The calibration data, along with all regional and local results to be presented here, are available in a dissertation by McMillin (1992).

The regional mass transfer results for turbulent flow in a pin fin channel are given in Figs. 6 and 7 for $Re_D \approx 10{,}000$, 30,000, and 60,000. Two regional Sherwood numbers are determined, respectively, from the average mass transfer from the exposed surfaces of (*a*) the top and bottom walls and (*b*) the five pins, separately, over a two-row segment of the pin fin channel. The two regional Sherwood numbers are plotted as functions of the distance from the channel entrance that is normalized with the pin spacing in the straight flow direction, x/X.

Figure 6 displays the regional results for the straight-flow-only case (with no side wall ejection). For all three Reynolds numbers, an initial increase of $\overline{Sh}_D$ from the entrance to the third and fourth pin rows in the second segment is followed by a gradual decrease from the third segment toward the channel exit. This trend is consistent with previously reported data, for example, Metzger et al. (1982). The distributions of the row-averaged heat/mass transfer coefficient are believed to be caused by the increasing-then-decreasing turbulence intensity along the pin fin channels. Metzger and Haley (1982) and Simoneau and VanFossen (1984) measured the turbulence intensities in rectangular channels with short pin fins and presented results that showed a peak in the turbulence level at the third pin row to the fourth pin row. It is observed that the relatively low mass transfer from the walls in the "unobstructed" regions between the pins in the first row as the concentration boundary layer develops also contributes to the relatively low values of $\overline{Sh}_D$ on the channel walls in the first segment.

In the case of a smaller value of Re_D, the $\overline{Sh}_D$ distribution is lower and has a steeper slope beyond the third segment. The larger drop of the $\overline{Sh}_D$ distribution beyond the second segement in the case of a smaller value of Re_D was also observed by Lau et al. (1991). The present regional results also compare reasonably well with the heat transfer results of Metzger et al. (1982) and Lau et al. (1991), and the mass transfer results of Chyu (1990), although the test sections for the studies are all different.

For the range of Re_D studied, the pin mass transfer coefficient is 15 to 30 percent higher than the corresponding wall mass transfer coefficient. Higher heat/mass flux from the pins than that from the walls has also been reported in the literature. VanFossen (1982) estimated that the pin heat transfer coefficient was about 35 percent higher than the wall heat transfer coefficient; Metzger et al. (1982) and Chyu (1990) showed that the pin heat/mass transfer coefficient is about 10 percent higher than the wall heat/mass transfer coefficient. Thus, all studies have shown that the regional pin heat/mass transfer coefficient is higher than the corresponding regional wall heat/mass transfer coefficient. The discrepancies among the results in these studies are due to the differences in the test section configurations and boundary conditions, and the accuracies of the various experimental methods.

The regional results for the ejection-flow case are presented in Fig. 7. Comparing corresponding Sherwood numbers in the ejection-flow case and in the straight-flow-only case shows that the values of $\overline{Sh}_D$ in the ejection-flow case are consistently lower. The difference between corresponding values of $\overline{Sh}_D$ in the two cases increases steadily with increasing x/X. The lower $\overline{Sh}_D$ values in the ejection case are due to the decreasing rate of mass flow of air in the channel as x/X increases. As in the straight-flow-only case, the values of the pin Sherwood number are consistently higher than those of the wall Sherwood number. The ratio of the pin Sherwood number to the wall Sherwood number is generally in the range of 1.07 to 1.20. Thus, it appears that the turning of the flow toward the ejection holes on one side wall also reduces the difference between the mass fluxes on the pins and on the walls.

Although it is interesting to see that the ratio of the pin Sherwood number to the wall Sherwood number is reduced when there is side wall flow ejection, the $\overline{Sh}_D$ results are averaged over a segment with two rows of pins and do not tell how the mass transfer coefficient varies on the exposed surfaces of the pins and the walls. Results show that the average mass flux on the pin nearest the side wall with the ejection holes in an odd-numbered row (with three pins) is always higher than those on the other two pins in the same row, while the average mass fluxes on the other two pins are about the same. The differences among the mass fluxes on the three pins in an odd-numbered row decrease with increasing distance from the entrance. Near the straight flow exit, the mass fluxes on the three pins in an odd-numbered row are about the same.

The average mass fluxes on the pins in any even-numbered row (with two pins) are lower than those on the three pins in the odd-numbered row immediately upstream, as a result of the lower average flow velocity past the two pins. With flow ejection, the average mass flux on the pin closer to the ejection holes is slightly higher than that on the other pin in the same row near the channel entrance. Farther downstream, no difference between the mass fluxes on the two pins in an even-numbered row is observed. The local results to be presented next show that the turning of some of the flow toward the ejection holes also causes the mass flux on the exposed surfaces of the walls to be higher near the ejection holes.

The rate of mass transfer from the exposed surface of the bottom wall is determined at a uniform grid of 3277 points, along 29 lines with 113 measurement points on each line. The distance between adjacent points is 1.59 mm. At the base of a pin, four measurement points are located right at the interface between the naphthalene and the socket for the insertion of the pin; the mass transfer coefficients at the points are not determined. The mass transfer data at eight other points nearest the base of a pin may be subjected to a relatively higher degree of uncertainty, since these points are only 0.37 mm from the outer edge of the aluminum socket while the depth gage probe has a spherical tip with a diameter of 1.59 mm.

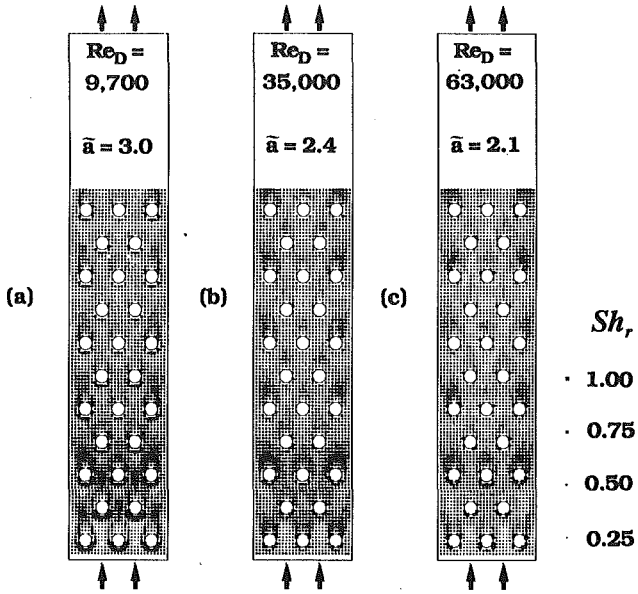

Fig. 8 Sh_r distributions, straight-flow-only case

The distributions of the local mass transfer coefficient in the straight-flow-only case and in the ejection-flow case are obtained for $Re_D \approx 10{,}000$, 30,000, and 60,000. The local results are presented as two-dimensional distributions of a relative Sherwood number, defined as

$$Sh_r = \frac{Sh_D - 0.25Sh_{0,Dh}}{\tilde{a}Sh_{0,Dh} - 0.25Sh_{0,Dh}} \tag{9}$$

where $\tilde{a}$ = 3.0, 2.4, and 2.1 for $Re_D \approx 10{,}000$, 30,000, and 60,000, respectively. The constants $\tilde{a}$ and 0.25 in the definition of Sh_r are chosen such that $Sh_r = 1.0$ when $Sh_D \geq \tilde{a}Sh_{0,Dh}$, and $Sh_r = 0.0$ when $Sh_D \leq 0.25\ Sh_{0,Dh}$. Between the upper and lower limits, Sh_r varies linearly with Sh_D. For a given Re_D, the majority of the Sh_D data falls between 0.25 and $\tilde{a}$ times the corresponding $Sh_{0,Dh}$.

To facilitate the graphic presentation of the two-dimensional local mass transfer distribution, the value of Sh_r at a measurement point is given in terms of the size of a square whose center is located at the measurement point. In the measurement region over 11 rows of pins on the surface of the bottom channel wall, a grid of 29 × 113 squares is plotted, with the largest possible size of a square indicating that $Sh_r = 1.0$ and a very small square $Sh_r \approx 0.0$. By defining Sh_r as in Eq. (9) and by presenting the local results in terms of a grid of squares whose sizes are proportional to the values of Sh_r at the measurement points, it is possible to compare the local mass transfer distributions on the channel walls in the straight-flow-only case with those in the ejection-flow case.

In Figs. 8(*a*), 8(*b*), and 8(*c*), the Sh_r distributions are given for straight flow through the pin fin channel with $Re_D \approx$ 10,000, 30,000, and 60,000, respectively. In all three cases, the Sh_r distributions are symmetric with respect to the midplane of the channel. The local mass transfer near the pins in the first several rows is generally higher than that near the pins in the rows further downstream. In the first row, however, the local mass transfer between two pins is very low. The local mass transfer decreases with increasing x/X as the mass con-

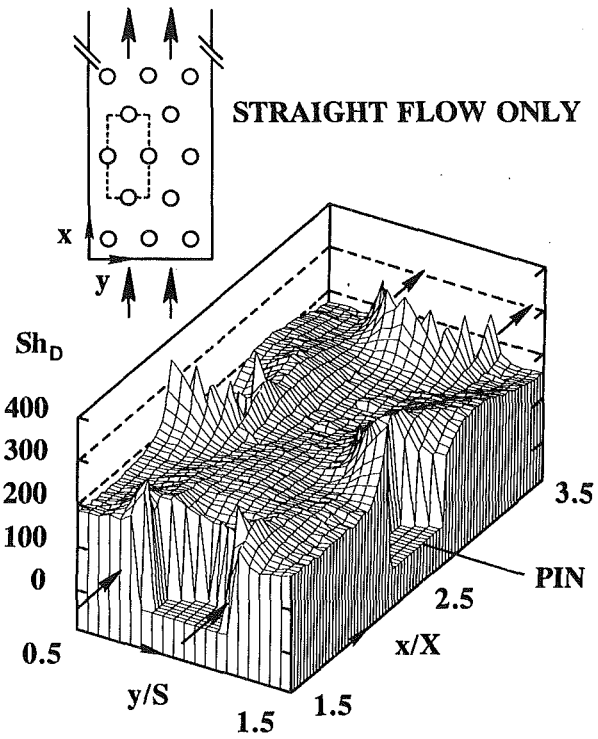

Fig. 9 Detailed Sh_D distribution in a focused region, straight-flow-only case

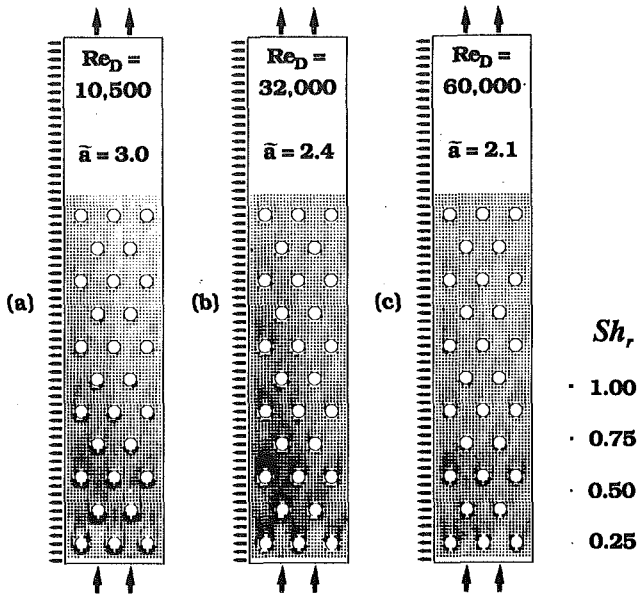

Fig. 10 Sh_r distributions, ejection-flow case

centration boundary layer grows and then increases rapidly as the two pins in the second row are encountered. The low mass transfer between two pins in the first row lowers the average wall mass transfer in the first and second rows.

Comparing Figs. 8(*a*) and 8(*c*), the local mass transfer between the pins in the first row increases more abruptly immediately upstream of the pins in the second row in the lower Re_D case. The values of Sh_r in the lower Re_D case are generally higher in the next several rows and lower in the rows farther downstream than those in the higher Re_D case. The generally more gradual drop of the local mass transfer with increasing x/X when Re_D is larger than when Re_D is small is consistent with the regional results.

In the first several rows, the mass transfer is very high immediately upstream of a pin and decreases gradually along the base of the pin as the flow negotiates around the base of the pin. Along any line through the centers of two pins in two consecutive odd-numbered or even-numbered rows, the local mass transfer increases in the main flow direction, reaches a maximum, drops to a minimum gradually, and then increases to a large value immediately upstream of the downstream pin. The approximate locations of the local maximum and minimum coincide with the regions of high and low turbulence intensities downstream of a pin in a staggered array observed by Simoneau and VanFossen (1984).

The local mass transfer in the region between two pins in a row is generally low. The local mass transfer in the wake regions downstream of the two pins near the side walls in an odd-numbered row (with three pins) is higher than that in the wake region downstream of the pin in the middle of the row. The flows around the two outer pins also appear to turn toward the side walls, as shown by the asymmetry of the wake regions downstream of the two pins. The resistance for air to flow through the narrower spaces between the outer pins and the side walls is larger than that for air to flow through the wider spaces (with twice the minimum cross-sectional area) between the pins. The larger flow resistance between the two pins in the next row (resulting from the 25 percent smaller minimum cross-sectional area) compared with that between the pins and the side walls also contributes to forcing the flow to turn toward the side walls and away from the pin in the middle of the odd-numbered row, reducing the mass transfer on the channel wall around the middle pin.

Figure 9 gives a close-up look of the detailed distribution of the local mass transfer around the bases of four pins between the second and the fourth rows ($1.5 \le x/X \le 3.5$ and $0.5 \le y/S \le 1.5$) in the $Re_D \approx 30{,}000$ case. The local mass transfer in the focused region is obtained at 1701 points (a grid of 21 $\times$ 81 points with spacings between points of 0.79 mm and 0.40 mm, in the spanwise and straight flow directions, respectively). The very large values of Sh_D immediately upstream of a pin and the slightly lower values around the upstream half of the base of a pin give the locations of high mass transfer on the wall near the pin. Figure 9 clearly shows that, along $y/S = 0.5$ and 1.5, the local mass transfer downstream of the two points at $x/X = 2.5$ increases, reaches a maximum, and drops to a relatively flat minimum gradually. Although not shown in the figure, the local mass transfer then increases to a large value immediately upstream of the two downstream pins at $x/X = 4.5$, similar to the abrupt increase of Sh_D immediately upstream of the two pins at $x/X = 2.5$. The slightly higher mass transfer downstream of the pin at $x/X = 2.5$ and $y/S = 0.5$ than that downstream of the other pin in the same row appears to be caused by the aforementioned turning of the flow toward the side wall.

The Sh_r distributions in the ejection-flow case are presented in Fig. 10. The distributions are significantly different from those in the straight-flow-only case, although they also retain some of the features of the straight flow distributions. The turning of some of the flow toward the ejection holes and the decrease of the rate of mass flow with increasing distance from the channel entrance are evident. The mass transfer in the half of the channel closer to the side wall with the ejection holes is generally higher than that in the opposite half of the channel. The regional mass transfer drops with increasing distance from the channel entrance much faster than that in the straight-flow-only case. In the several rows near the channel entrance, the mass transfer is always higher near the base of a pin closer to the side wall with the ejection holes. The trend continues in the rows farther downstream, although the degree of asymmetry appears to decrease with increasing distance from the channel entrance.

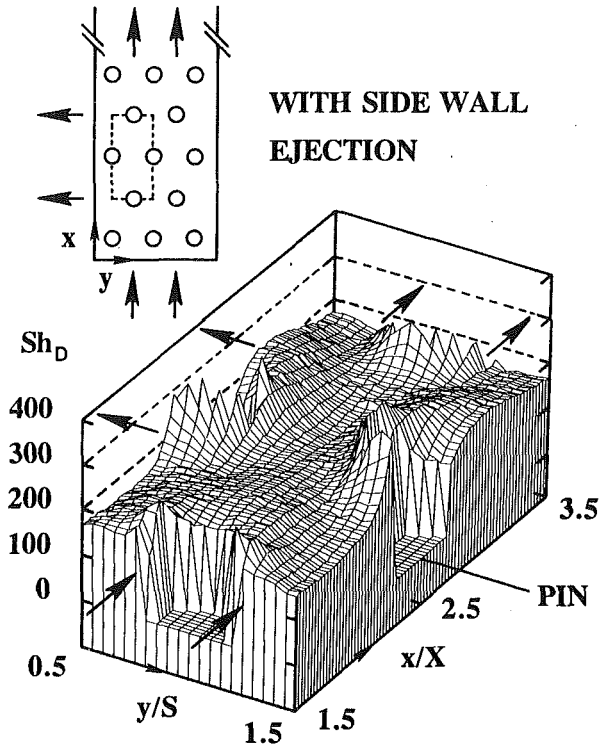

Fig. 11 Detailed Sh_D distribution in a focused region, ejection-flow case

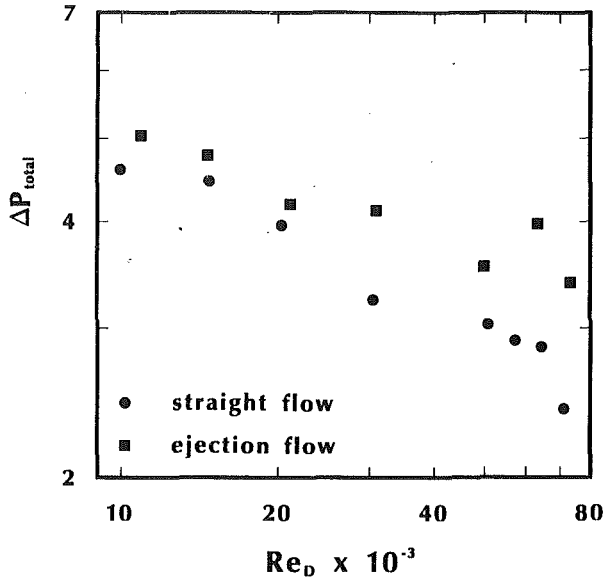

Fig. 12 Overall pressure across test channel

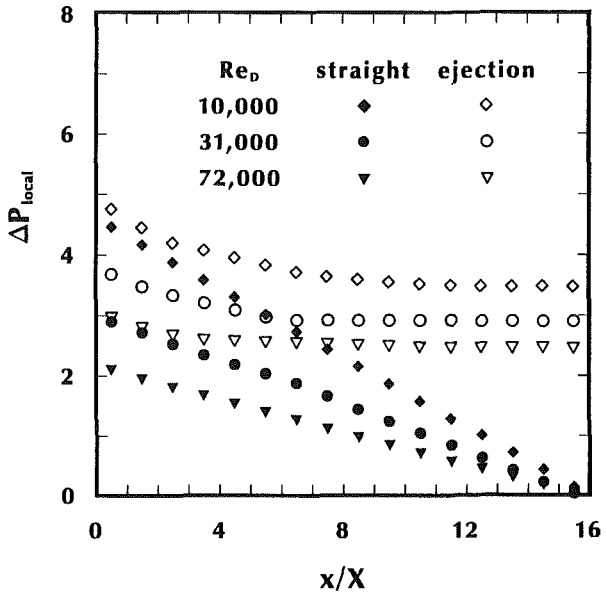

Fig. 13 Local pressure distribution in test channel

Despite the turning of a portion of the main flow (toward the side wall with the ejection holes) to exit through the ejection holes, the flow around the pin in an odd-numbered row nearest the solid side wall (the side wall with no ejection holes) turns toward the solid side wall. As in the straight-flow-only case, this is due to the large flow resistance between the solid side wall and the closest pin in an odd-numbered row and the slightly larger flow resistance between the two pins in the next even-numbered row (caused by the 25 percent smaller minimum cross-sectional area).

As in the straight-flow-only case, the local mass transfer is determined at a grid of 21 × 81 points in a rectangular region between the pins in the second row and the pins in the fourth row in the ejection-flow case with $Re_D \approx 30{,}000$. The detailed Sh_D distribution is given in Fig. 11. The distribution clearly shows that the loss of cooling air through the ejection holes lowers the mass transfer coefficient around the bases of the four pins. Comparing the Sh_D distributions in Figs. 9 and 11, the values of Sh_D around the front half of each pin are lower in the ejection-flow case than in the straight-flow-only case. Downstream of the outer pin in the third row (the pin at $x/X = 2.5$ and $y/S = 0.5$), there is a region of high mass transfer, indicating the turning of the cooling air toward the ejection holes. Otherwise, the Sh_D distribution in Fig. 11 has many of the features of that in Fig. 9: a relatively low mass transfer region between two pins in a row; a local peak at a distance of about one pin diameter downstream of a pin in the odd-numbered row with three pins (at $x/X = 2.5$) but a relatively flat region downstream of a pin in the even-numbered row (at $x/X = 1.5$).

The overall and local pressure drop results are presented in Figs. 12 and 13, respectively. The normalized overall pressure drop across the channel decreases with increasing Reynolds number in both the straight-flow-only case and the ejection-flow case. At any Reynolds number, the value of ΔP_{total} in the ejection-flow case is 10 to 30 percent higher than that in the straight-flow-only case. Thus, it requires more pumping power to supply a given mass flow rate of cooling air through a pin fin channel with ejection holes than through the same channel without ejection holes (with a wide open straight flow exit only).

The local pressure in the straight-flow-only case decreases linearly with increasing distance from the channel entrance. The local pressure in the ejection-flow case decreases with increasing x/X near the channel entrance and levels off to almost a constant value when $x/X \geq 8.0$ and $x/X \geq 4.0$ for $Re_D \approx 10{,}000$ and 70,000, respectively. The leveling off of the local pressure distributions (that is, the decrease of the absolute value of the pressure gradient along x/X) is the result of the decrease of the mass flow in the channel. Since the rate of mass flow through an ejection hole is driven by the local pressure drop across the hole, the rate of ejection mass flow is expected to be high near the channel entrance, and low and relatively constant near the straight flow exit. In both the straight-flow-only case and the ejection-flow case, the ΔP_{local} distribution is higher when Re_D is small than when Re_D is large.

Conclusions

Mass transfer experiments are conducted for turbulent air flow through a rectangular pin fin channel whose interior surfaces are mass transfer active. The staggered 3 × 2 pin fin array in the channel has $H/D = 1.0$, $X/D = S/D = 2.5$ and the Reynolds number ranges from 10,000 to 60,000. The distributions of the mass transfer coefficient are obtained are obtained for straight flow through the pin fin channel and for flow through the pin fin channel with small ejection holes in one side wall and at the straight flow exit of the channel. The following conclusions are drawn:

1 In the straight-flow-only case, the average pin mass transfer coefficient over a segment of the channel with two pin rows is 15 to 30 percent higher than the corresponding average wall mass transfer coefficient. When there is side wall flow ejection, the regionally averaged pin mass transfer coefficient is only 7 to 20 percent higher than the corresponding average wall mass transfer coefficient.

2 The turning of the flow toward the ejection holes causes generally higher wall mass transfer near the side wall with the ejection holes and lower wall mass transfer near the opposite solid side wall.

3 Flow ejection through holes in one side wall lowers the mass flow rate of air in the channel. The continually decreasing mass flow rate along the channel causes the mass transfer coefficient to drop significantly toward the straight flow exit of the channel.

4 In both the straight-flow-only case and the ejection-flow case, the wall mass transfer is generally high around the base of a pin. In the ejection-flow case, the turning of the flow toward the ejection holes causes the wake regions behind the pins near the side wall with the ejection holes to be asymmetric.

5 For straight flow through the 3 × 2 pin fin array, the wall mass transfer around the bases of the two off-centered pins in a row of three pins is generally higher than that around the base of the pin in the middle as the flow seeks paths with the least resistance. Along the centerline through corresponding pins in consecutive odd-numbered or even-numbered rows, the wall mass transfer increases with increasing distance from the upstream pin, reaches a maximum, decreases to a minimum, and then increases abruptly immediately upstream of the downstream pin.

6 In the straight-flow-only case, the local pressure decreases linearly along the pin fin channel. In the ejection-flow case, the local pressure decreases initially along the pin fin channel but levels off to almost a constant value downstream of the eighth pin row.

Since the test section and the conditions of the present investigation are chosen to model the cooling of the tail region of a gas turbine blade and the distribution of the mass transfer coefficient is analogous to that of the heat transfer coefficient, the results and conclusions given here are applicable to the design of pin fin cooling passages in gas turbine blades.

Acknowledgments

The authors appreciate the support of this research by the National Science Foundation (Grant No. CBT8713833).

References

Ambrose, D., Lawenson, I. J., and Sprake, C. H. S., 1975, "The Vapor Pressure of Naphthalene," *J. Chem. Thermo.*, Vol. 7, pp. 1172–1176.

Brigham, B. A., and VanFossen, G. J., 1984, "Length-to-Diameter Ratio and Row Number Effects in Short Pin Fin Heat Transfer," ASME *Journal of Engineering for Gas Turbines and Power*, Vol. 106, pp. 241–246.

Brown, A., Mandjikas, B., and Mudyiwa, J. M., 1980, "Blade Trailing Edge Heat Transfer," ASME Paper No. 80-GT-45.

Chyu, M. K., 1990, "Heat Transfer and Pressure Drop for Short Pin Fin Arrays With Fin-Endwall Fillet," ASME *Journal of Heat Transfer*, Vol. 112, pp. 926–932.

Eckert, E. R. G., and Goldstein, R., 1976, *Measurements in Heat Transfer*, 2nd ed., McGraw-Hill, New York, pp. 399–412.

Kline, S. J., and McClintock, F. A., 1953, "Describing Uncertainties in Single-Sample Experiments," *Mechanical Engineering*, Vol. 75, Jan., pp. 3–8.

Lau, S. C., Han, J. C., and Kim, Y. S., 1989a, "Turbulent Heat Transfer and Friction in Pin Fin Channels With Lateral Flow Ejection," ASME *Journal of Heat Transfer*, Vol. 111, pp. 51–58.

Lau, S. C., Han, J. C., and Batten, T., 1989b, "Heat Transfer, Pressure Drop, and Mass Flow Rate in Pin Fin Channels With Long and Short Trailing Edge Ejection Holes," ASME JOURNAL OF TURBOMACHINERY, Vol. 111, pp. 116–123.

Lau, S. C., Kim, Y. S., and Han J. C., 1987, "Local Endwall Heat/Mass Transfer Distributions in Pin Fin Channels," *AIAA J. of Thermophysics and Heat Transfer*, Vol. 1, pp. 365–372.

Lau, S. C., McMillin, R. D., and Kukreja, R. T., 1991, "Segmental Heat Transfer in a Pin Fin Channel With Ejection Holes," *Int. J. Heat Mass Transfer*, in press.

McMillin, R. D., 1992, "Heat (Mass) Transfer Characteristics of Turbulent Flow in Cooling Channels in Turbine Airfoils," Ph.D. Dissertation, Texas A&M University, College Station, TX.

Metzger, D. E., Berry, R. A., and Bronson, J. P., 1982, "Developing Heat Transfer in Rectangular Ducts With Staggered Arrays of Short Pin Fins," ASME *Journal of Heat Transfer*, Vol. 104, pp. 700–706.

Metzger, D. E., Fan, C. S., and Haley, S. W., 1984, "Effects of Pin Shape and Array Orientation on Heat Transfer and Pressure Loss in Pin Fin Arrays," ASME *Journal of Engineering for Gas Turbines and Power*, Vol. 106, pp. 252–257.

Metzger, D. E., and Haley, S. W., 1982, "Heat Transfer Experiments and Flow Visualization for Arrays of Short Pin Fins," ASME Paper No. 82-GT-138.

Metzger, D. E., Shepard, W. B., and Haley, S. W., 1986, "Row Resolved Heat Transfer Variations in Pin Fin Arrays Including Effects of Non-uniform Arrays and Flow Convergence," ASME Paper No. 86-GT-132.

Simoneau, R. J., and VanFossen, G. J., 1984, "Effect of Location in an Array on Heat Transfer to a Short Cylinder in Crossflow," ASME *Journal of Heat Transfer*, Vol. 106, pp. 42–48.

VanFossen, G. J., 1982, "Heat Transfer Coefficients for Staggered Arrays of Short Pin Fins," ASME *Journal of Engineering for Power*, Vol. 104, pp. 268–274.

Heat Transfer and Turbulence in a Turbulated Blade Cooling Circuit

N. Abuaf
Corporate Research & Development,
General Electric Company,
Schenectady, NY 12301

D. M. Kercher
GE Aircraft Engines,
Lynn, MA 01910

The aerothermal performance of a typical turbine blade three-pass turbulated cooling circuit geometry was investigated in a 10X plexiglass test model. The model closely duplicated the blade's leading edge, midchord, and trailing edge cooling passage geometries. Steady-state heat transfer coefficient distributions along the blade pressure side wall (convex surface) of the cooling circuit passages were measured with a thin-foil heater and a liquid crystal temperature sensor assembly. The heat transfer experiments were conducted on rib-roughened channels with staggered turbulators along the convex and concave surfaces of the cooling passages. Midchannel axial velocity and turbulence intensity measurements were taken by hot-wire anemometry at each passage end of the three-pass cooling circuit to characterize and relate the local thermal performance to the turbulence intensity levels. The near-atmospheric experimental data are compared with results of a Computational Fluid Dynamics (CFD) analysis at the operating internal environment for a 1X rotating model of the blade cooling circuit and other turbulator channel geometry heat transfer data investigations. The comparison between the measurements and analysis is encouraging. Differences with other heat transfer data appear reasonably understood and explainable.

1 Introduction

To design and maintain high-pressure turbine blade airfoil acceptable metal temperatures and material life, many modern gas turbine blades are internally cooled by circulating compressor air through multipass rib-roughened passages. The serpentine passages are connected by 180-deg turns, which may or may not be equipped with ribbed turbulence promoters. The trailing edge passage has trailing edge holes, which discharge air to cool the blade trailing edge and thus deplete the cooling air flow rate as it proceeds from the passage base toward the tip of the airfoil. Knowledge of the local enhancements of the heat transfer coefficient distributions and the associated frictional pressure losses as a function of the flow parameters, the passage geometries, and turbulence promoter geometries is essential for gas turbine designers to produce efficiently cooled airfoils.

In the stationary investigations reported in the literature, the internal cooling passages have been approximately modeled by either square or rectangular channels having two opposite walls equipped with turbulence promoters. Han et al. (1978) undertook a systematic investigation of the heat transfer and friction losses in ribbed rectangular channels with two parallel plates. Metzger et al. (1983) investigated the effect of various rib configurations in a rectangular duct. Han and Lei (1983), Han et al. (1985), and Han (1984) conducted tests in a square duct and developed correlations to predict the average friction factor and the local and average Stanton number as a function of the flow characteristics and the passage and turbulence promoter geometries as well as the angle of attack between the flow direction and the turbulence promoter ribs. Han and Park (1986) measured the local heat transfer coefficients on the ribbed and smooth side walls of a square channel, thus providing information on the local heat transfer coefficient distributions. Taslim and Spring (1987, 1988, 1991) used stationary rectangular turbulated passage geometries and studied the effect of passage aspect ratio and various rib geometries. Their turbulator height-to-passage hydraulic diameter ratios were larger than the previous investigations. Taslim et al. (1991) extended the stationary work on high blockage turbulators ribs to an investigation of rotating Coriolis heat transfer effects. Han and Park (1988) and Han (1988) extended their work to rectangular channels with turbulence promoters and presented correlations for the frictional pressure losses and heat transfer data. Although developing flow and heat transfer data have been obtained (Han and Park, 1986, 1988), there is no quantitative correlation that characterizes the straight duct entrance effects for turbulated walls.

In typical airfoils with multipass cooling circuits, the radial passages have curved turbulated side walls and cross-sectional aspect ratios, which vary considerably along the passage from root to tip. The passage cross sections also change in shape from the leading edge to the midchord. The blade trailing edge passage becomes nearly triangular in shape and generally has a very low aspect ratio cross section. Multipass cooling circuits have 180-deg turns, which connect the consecutive passages. The local variations in the heat transfer coefficients upstream and downstream of the turns, their range of influence, and the pressure head losses associated with the turns are also important factors to be investigated. Boyle (1984) studied the

Contributed by the International Gas Turbine Institute and presented at the 37th International Gas Turbine and Aeroengine Congress and Exposition, Cologne, Germany, June 1-4, 1992. Manuscript received by the International Gas Turbine Institute February 17, 1992. Paper No. 92-GT-187. Associate Technical Editor: L. S. Langston.

local heat transfer coefficients and the pressure losses associated with smooth and turbulated square passages with sharp 180-deg turns. The first passage of the two-pass serpentine cooling circuit, fed through a 90-deg turn at the entrance, resulted in strong entrance effects. The local heat transfer coefficient enhancements obtained were high and similar for the turbulated and smooth duct configurations. Metzger et al. (1984) and Metzger and Sahm (1986) studied the pressure losses and local heat transfer coefficients as a function of the channel geometries, the aspect ratios of the passages before and after the turn, and the flow Reynolds numbers in smooth rectangular channels with a sharp 180-deg turn. Metzger et al. (1988) extended their investigations to rib-roughened channels with rectangular cross sections. In addition to the turbulated ducts they also studied the effect of radially oriented turbulence promoters on the top and bottom walls of the 180-deg turns. Han et al. (1988) measured detailed mass transfer distributions around sharp 180-deg turns in a two-pass cooling circuit with smooth and turbulated square channels using the naphthalene sublimation technique. This provided detailed data between two consecutive turbulators and in the different regions of the 180-deg turn. Chyu (1991), using the same sublimation technique, measured heat transfer in two- and three-pass circuits with sharp 180-deg turns.

The trailing edge channels of typical serpentine blade airfoil designs have the cooling air entering the channel at the base and discharging through the tip and a multitude of trailing edge holes distributed along the channel. The cooling air is thus depleted along the channel with the complex flow distribution and varying passage geometry affecting the local heat transfer coefficients. Lau et al. (1989) investigated such a flow configuration in a pin-fin channel with several ejection holes.

The effects of free-stream turbulence on the local heat transfer coefficient distributions for the gas side surfaces of the turbine blades have been well recognized and several systematic investigations have been and are being carried out to evaluate its relative importance (Moffat and Maciejewski, 1985; Zerkle and Lounsbury, 1989; Krishnamoorthy and Sukhatme, 1989). As noted detailed heat transfer studies have been conducted to characterize the effect of geometric parameters and flow variables on the performance of channels with rib roughnesses. However, there are no known measurements, but some CFD information (Fodemski, 1988) relating the turbulence intensity levels generated by these surface roughnesses in the cooling passages.

In the present investigation detailed distributions of the local steady-state heat transfer coefficients were measured along the convex turbulated wall (blade pressure side) of a 10X scaled

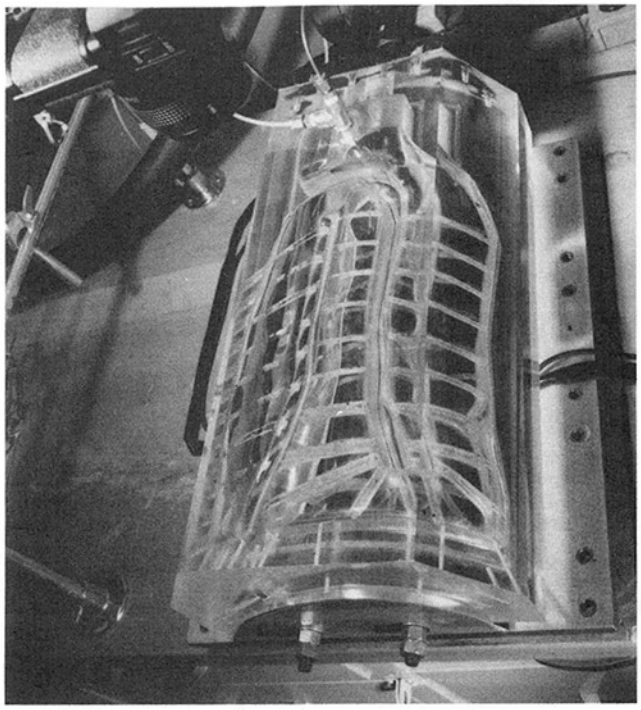

Fig. 1 Turbulated serpentine blade 10X test model

three-pass cooling circuit model with curved walls and actual design features of a typical serpentine blade. Axial midchannel velocities and turbulence intensity measurements were also performed in the same model at six discrete locations, i.e., each channel end to relate with the local heat transfer observations. Comparisons of the measured midchannel turbulence measurements and surface heat transfer coefficients were made with an adiabatic CFD analysis of the actual blade three-pass serpentine at engine operating conditions and a correlation with other turbulator geometry heat transfer data investigations.

2 Experimental Setup

The test rig consists of a high-pressure air supply, a flow control valve, a calibrated venturi meter, and the three-pass serpentine passage test section.

The test section shown in Fig. 1 consists of a three-pass serpentine passage including a 90-deg bent inlet between the supply chamber and the leading edge passage, a turbulated

Nomenclature

A_h = heater total area
A_{hp} = portion of heater area in contact with air
$A_{\min}$ = minimum flow area or open area
$A_{\max}$ = maximum full flow area
AR = aspect ratio = b/a
a = passage width (turbulated)
b = passage height (smooth)
c_p = specific heat
D = local hydraulic diameter without ribs
e = turbulator rib height
h = heat transfer coefficient
h_t = turbulated wall heat transfer coefficient
k = turbulent kinetic energy
k_{Air} = air thermal conductivity
k_{Mylar} = thermal conductivity of Mylar
$\dot{m}$ = air mass flow rate
m^* = $A_{\min}/A_{\max}$
Nu_{SD} = smooth duct Nusselt number
Nu_t = turbulated wall Nusselt number
n = Reynolds number exponent
P = channel cross-sectional perimeter
Pr = Prandtl number
Q = total power dissipated by heater
$\dot{q}$ = net uniform heat flux
Re = flow Reynolds number based on hydraulic diameter
s = turbulator pitch
T_f = air bulk temperature
T_{LC} = liquid crystal temperature
T_o = supply chamber air temperature
T_w = wall temperature
Tu = percentage of midchannel turbulence intensity
$\overline{U}_{\text{Local}}$ = midchannel time-averaged local axial flow velocity
u' = fluctuating velocity
V_{DC} = hot-wire DC volts
V_{rms} = hot wire rms volts
v = velocity
x = distance
α = rib-to-flow angle
μ = viscosity
ρ = density
Δx_{Mylar} = thickness of Mylar layer

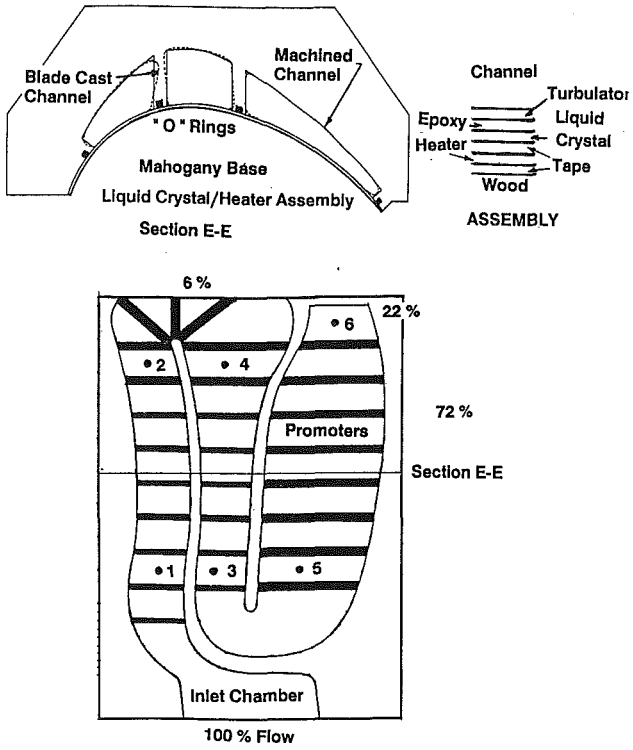

Fig. 2 Typical cross section, comparing the 10X model with the blade geometries, and model core projection onto the concave surface with test flow distribution

180-deg sharp turn between the leading edge and the midchord, another 180-deg (smooth) turn between the midchord and the trailing edge. The trailing edge passage has twelve trailing edge holes. Small bleed holes were drilled at the tip wall of the three passages. Varying height staggered turbulence promoters were placed on the two opposite chordwise walls of the passages and fan-mounted radial rib roughnesses exist at the first 180-deg turn as indicated in Fig. 2.

The test section model is a 10X scale of a typical serpentine cooling circuit. The camber or twist of a typical airfoil design was eliminated and the pressure side curved wall of the airfoil was approximated with two arcs of circles. The wall curvatures, the passage cross section shape, and aspect ratios are typical for small turbine blades. Figure 2 shows the core projection of the model base outline of the entrance region, the leading edge, midchord, and trailing edge channels and the two 180-deg turns with the specific turbulence promoter locations. The plexiglass test sections with the machined channels were positioned on a hardwood (mahogany) base as illustrated by the pitch-section EE. The broken lines represent the blade cast channel shapes while the solid lines represent the machined shapes of the test model.

The heat transfer coefficient distributions on the convex wall of the turbulence promoted serpentine passage were determined using a liquid crystal element over a thin-foil heater (Simonich and Moffat, 1982) as illustrated in Fig. 2. The one-wall heating was selected in order to accommodate easy photographic recordings of the heated surface. Tests performed with air by Sparrow et al. (1966) and with water by Kostic and Hartnett (1986) have shown that for smooth ducts with non-symmetric heating, the heat transfer coefficients measured for the heated wall were respectively 15 to 8 percent lower than the uniformly heated case. The 25.4 cm wide 30.2 cm long thin-foil heater consisted of a 0.0013 cm Inconel layer deposited on a 0.005 cm Kapton back. Two copper electrodes were deposited along the length of the heater element parallel to the channel axial direction. The thin-foil heater was calibrated by applying a voltage across the electrodes and measuring the voltage distribution to assure uniformity of constant heat flux. The liquid crystal element had an active range from 35 to 40°C and was calibrated in a well-mixed uniform temperature water bath. The yellow color of the liquid crystal spectra occurred at 36.4°C within an accuracy of 0.1°C. The thin-foil heater was held against the wood base by a double-sticking tape with the liquid crystal-covered Mylar sheet taped onto the heater surface. Leakage between the neighboring channels and the external channel walls and ambient was prevented by "o" ring seals placed in grooves under the separating walls shown in Fig. 2. The plexiglass test section was clamped onto the wood base by means of a metallic assembly shown in Fig. 1.

The top surfaces of the plexiglass block were cut at the appropriate angles and polished in order to permit normal observation of the passage bottom areas for photographic recordings. Turbulence promoters consisting of plexiglass square ribs were glued on the convex and concave surfaces of the channels at the design positions in a staggered configuration. The leading edge channel had seven turbulence ribs placed at a pitch of ten turbulence promoter heights and two double-the-size at a pitch of five. The last promoter before the first 180-deg turn was tapered. Three radial ribs at 40, 90, and 140 deg with respect to the inlet flow direction were glued on the convex bottom liquid crystal-heater assembly-wood wall while radial ribs at 15, 65, 115, and 165 deg were glued on the concave top wall (plexiglass surface). The midchord passage had two larger turbulence ribs at the tip, followed by six smaller ribs to accommodate the cross-sectional area changes along the midchord passage. The trailing edge channel had the larger chordwise tapered ribs extending along the low-aspect-ratio rectangular cross section. All the promoter ribs along the passage were square (except the trailing edge), sharp-cornered, and normal to the flow direction.

The thin-foil heater DC power supply was measured by means of a voltmeter connected across the two copper electrodes and a shunt measuring the current. To determine the local heat transfer coefficient distributions for the given flow Reynolds number, the dissipated heat flux was increased in specified steps. When steady state was reached, the color field of the liquid crystal surface was recorded photographically. Iso-h contours for a multitude of heat fluxes were obtained by sweeping through a given heat flux range covering the first appearance and disappearance of the yellow color. The iso-h contours were then superimposed onto a composite sketch shown in Fig. 3.

The near-ambient heat transfer tests were conducted at the blade design Reynolds number, which scales to an air mass flow rate of 0.016 kg/s, resulting in a mean Reynolds number of 23400 at the leading edge and midchord passages. At this flow rate the Reynolds numbers in the trailing edge passage varied between 16,000 at the root to 4400 near the tip discharge area.

Turbulence intensity measurements were performed at six strategic midchannel locations: one in each end of each passage shown in Fig. 2. Location 1 is at the inlet of the leading edge passage between the second and third ribs while location 2 is at the end of the same passage between the two last ribs before the first 180-deg turn. Location 4 is at the inlet of the midchord passage downstream of the 180-deg turn, while location 3 is at the exit of this passage before the second 180-deg turn. Locations 5 and 6 are at the inlet and exit of the trailing edge passage.

3 Data Reduction

3.1 Turbulence Intensity. Adiabatic time-averaged axial velocity and turbulence intensity measurements were per-

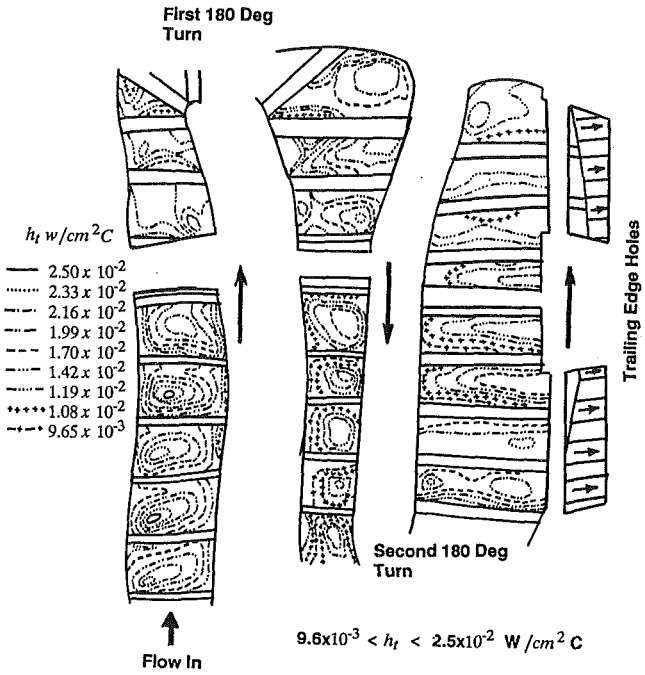

Fig. 3 Model test three-pass serpentine passage convex surface iso-heat transfer coefficient distributions at design Reynolds number

formed with a DISA Type 55DO5 portable battery-operated constant-temperature anemometer, using a hot wire as a transducer. The DC output of a DISA Type 55D Linearizer, corresponding to the time-averaged axial velocity, was measured with a FLUKE 8050A Digital Multimeter. The rms values of the output corresponding to the velocity turbulence in the axial direction were measured with a Hewlett-Packard 3456A Digital Voltmeter. The percentage of turbulence intensity was calculated from

$$Tu = 100\,\frac{V_{\text{rms}}}{V_{DC}} = 100\,\frac{u'}{U_{\text{local}}} \tag{1}$$

where V_{rms} or u' represent the local midchannel velocity fluctuations and V_{DC} and U_{Local} are representative of the midchannel local mean flow velocities. The voltage integration time was set to 1.667 s/sample. Ten samples were recorded and averaged for the rms value of the voltage. The hot-wire anemometer measures the quantity (ρv), or mass velocity where ρ is the local density. To evaluate the local velocities from the hot-wire calibration curves, it was necessary to establish the density (temperature and pressure) at the points of measurement, to perform the necessary density corrections.

A series of adiabatic tests was performed where the pressure drops across the various measurement locations were recorded as a function of air flow rate. These tests provided the necessary information to find the local pressure for each air flow rate at the specific location. With the knowledge of the inlet air temperature, the density correction was applied to each velocity measurement.

3.2 Heat Transfer. The heat transfer data consisted of a series of photographs showing the yellow color iso-h lines obtained at an ascending heat flux while all the other flow parameters remained constant. The local turbulated heat transfer coefficients were evaluated from

$$h_t = \frac{\dot{q}}{T_w - T_f} \tag{2}$$

where $\dot{q}$ is the net uniform heat flux dissipated by the foil heater, T_w is the wall temperature, and T_f is the local air bulk temperature. The net heat flux $(\dot{q})$ was determined from the measured DC voltage across the foil heater, the DC current passing through it, and the total foil heater area, A_h. The radiation losses from the heated wall were neglected in Eq. (2) and in the following calculations, since it was estimated to be less than a few percent of the measured average convective heat transfer coefficients.

The local air bulk temperature was evaluated from the energy balance,

$$T_f = T_o + \frac{Q}{A_h}\,\frac{A_{hp}}{\dot{m}c_p} \tag{3}$$

where T_o is the supply chamber air temperature, T_f is the local air bulk temperature, Q is the total power dissipated by the foil heater, A_{hp} is the inlet-to-local heater area in contact with the flowing air, $\dot{m}$ is the air mass flow rate, c_p is the specific heat of air, and A_h is the total foil heater area. To evaluate the local bulk temperature, further assessment was required of the air mass flow distribution through each passage with the air flow discharged through the eight holes at the tip region and the twelve trailing edge slots. A flow network of the serpentine circuit was analyzed by using a one-dimensional flow circuit analysis program. Results of the percent inlet flow distribution are shown in Fig. 2.

The local heat transfer coefficients are based on the local surface wall temperatures (T_w), while the temperatures indicated by the yellow color of the liquid crystal exist at a point underneath the Mylar sheet. The liquid crystal 36.4°C temperature is extrapolated to the Mylar surface temperature from the relationship

$$\frac{T_{LC} - T_w}{T_{LC} - T_f} = \frac{\dfrac{\Delta x_{\text{Mylar}}}{k_{\text{Mylar}}}}{\dfrac{1}{h} + \dfrac{\Delta x_{\text{Mylar}}}{k_{\text{Mylar}}}} \tag{4}$$

In Eq. (4) T_{LC} is the liquid crystal yellow color temperature, T_w, is the wall temperature in Eq. (2), T_f is the local air bulk temperature calculated from the energy balance Eq. (3), h is the local heat transfer coefficient, and the Mylar conductance $k_{\text{Mylar}}/\Delta x_{\text{Mylar}}$ was evaluated to be 1447.9 W/m^2°C for Mylar sheet thickness of 0.013 cm.

The nondimensional turbulated heat transfer results $(h_t D/k_{\text{Air}})$ were compared with the fully developed smooth duct turbulent pipe flow heat transfer,

$$\text{Nu}_{SD} = 0.023\text{Re}^{0.8}\text{Pr}^{0.4} \tag{5}$$

in terms of an enhancement factor, $\text{Nu}_t/\text{Nu}_{SD}$, where Pr is the local bulk Prandtl number for air, and Re is the flow channel hydraulic diameter Reynolds number without ribs.

To estimate the errors expected in the heat transfer coefficients calculated from Eq. (2) an uncertainty analysis was performed following the methodology suggested by Kline and McClintock (1953). The typical percent error in the heat transfer coefficients was found to be less than 2 percent.

4 Results

4.1 Heat Transfer Coefficients. Nine iso-h lines were photographically recorded for each passage as illustrated in Fig. 3. They were obtained at a flow rate of 0.016 kg/s at nine ascending heat fluxes. The recorded maximum and minimum and area-averaged Nusselt numbers for the leading edge, midchord, and trailing edge passages are shown in Figs. 4(*a*), 4(*b*), and 4(*c*), as a function of the dimensionless distance x/D, where x is the axial distance measured from the channel inlet and D is the local hydraulic diameter. The local ranges of Nusselt numbers between two consecutive turbulence promoters are presented as bars with the minimum recorded value corresponding to the first appearance of the yellow color and the maximum recorded value to the last appearance of the same

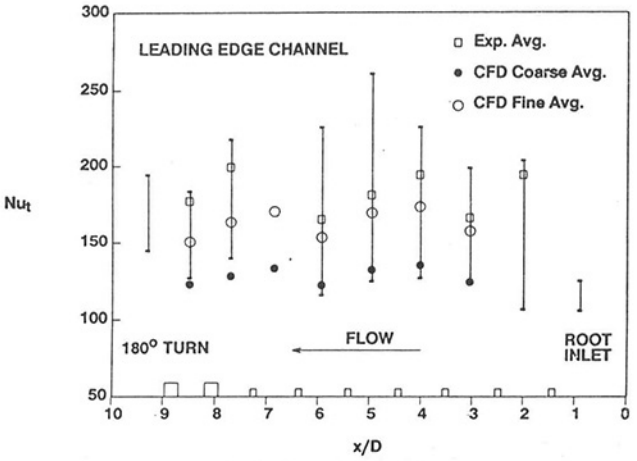

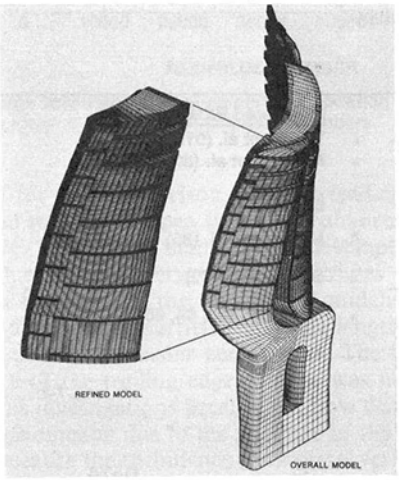

CFD BLADE AND LEADING EDGE MODELS
Marinaccio (1989, 1990, 1991)

Fig. 4(*a*) Leading edge channel heat transfer distribution with distance from the inlet. Comparison of model turbulated convex surface maximum, minimum, and average measurements with blade CFD average predictions.

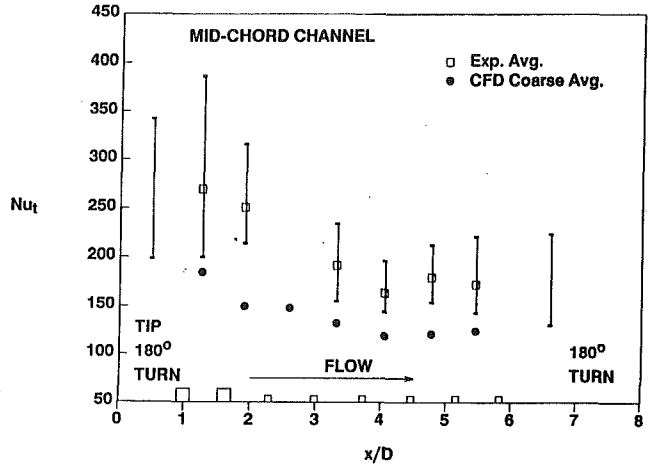

Fig. 4(*b*) Midchord channel heat transfer distribution with distance from the tip. Comparison of model turbulated convex surface maximum, minimum, and average measurements with blade CFD average predictions.

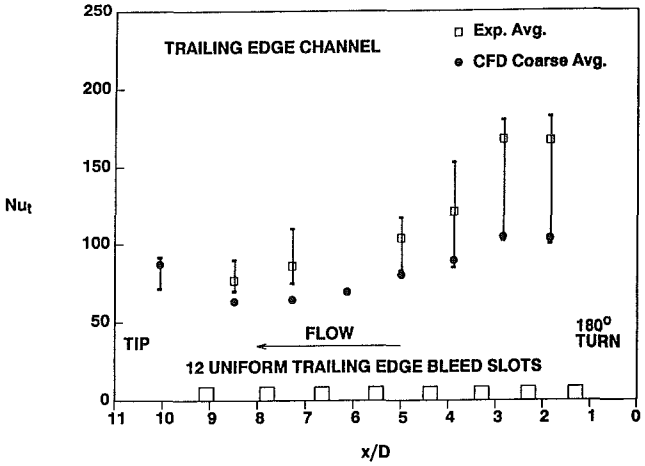

Fig. 4(*c*) Trailing edge channel heat transfer distribution with distance from the root turn. Comparison of model turbulated convex surface maximum, minimum, and average measurements with blade CFD average predictions.

color along each channel and turn. The area-averaged heat transfer coefficients presented as open squares were calculated from the detailed iso-h lines in Fig. 3. Figures 5(*a*), 5(*b*), and 5(*c*) show the local turbulated coefficient enhancement factors relative to the fully developed turbulent coefficients in smooth pipes (Eq. (5)). The missing values at some specific locations in Figs. 4 and 5 are due to the metallic structure blocking the direct view of the area. The highest enhancement factors evaluated are due to turn-entrance effects and turbulated flow conditions existing after each run. The maximum length-to-diameter ratios for the three channels vary between seven and ten. Therefore it is expected that the flows in the leading edge and midchord passages probably do not have sufficient length to become fully developed and to recuperate from the three-dimensional effects introduced by the sharp turns. This is substantiated in Fig. 7 discussed below along with a separate remark about the trailing edge passage flow.

A CFD analysis of the cooling circuit passages was performed with the STAR-CD code (Marinaccio, 1989, 1990, 1991), by modeling the actual full-size blade cooling circuit operating under operational engine pressure, temperature, and rotational conditions (nonbuoyancy). The tip holes present in the existing blade were not modeled in this analysis. Since the CFD calculations and the present experiments were not conducted for similar conditions, the CFD Nusselt and the approximately 2:1 off-design Reynolds numbers were adjusted to account for the geometric scaling, the air flow rates, and the air thermal conductivity and viscosity. The turbulated wall Nusselt numbers were assumed to be proportional to the Reynolds number to the power n ($\mathrm{Nu} \propto \mathrm{Re}^n$). The Reynolds number exponents for the leading edge, midchord, and trailing edge passages were taken from Fig. 6, which is a plot of the exponent n as a function of a dimensionless geometric parameter ($2e/(b - 2e)$), where e is the turbulator rib height and b is the passage height. The results of Fig. 6 (squares) were obtained from a compilation of data presented by Taslim et al. (1991) for high and low blockage rib-roughened passages. The respective exponents for the leading edge, midchord, and trailing edge passages ranged from 0.52 to 0.59, which are lower than the classical value of 0.8.

The CFD average results (Marinaccio, 1990, 1991), of the coarse (dark bullets) and fine (open circles) mesh density are compared with the 10X measurements in Figs. 4 and 5 at several locations along the three passages. The 8X fine-mesh leading edge average results agree quite reasonably with the average data at the leading edge passage (Figs. 4*a* and 5*a*). The coarse-mesh results are generally lower than the data. The comparison of fine-mesh and coarse-mesh CFD results with measurements illustrates the importance of proper mesh density for complex separating flows where increased density improves the wall velocity gradient definition and near-wall turbulent kinetic energy generation and thus heat transfer coefficient prediction.

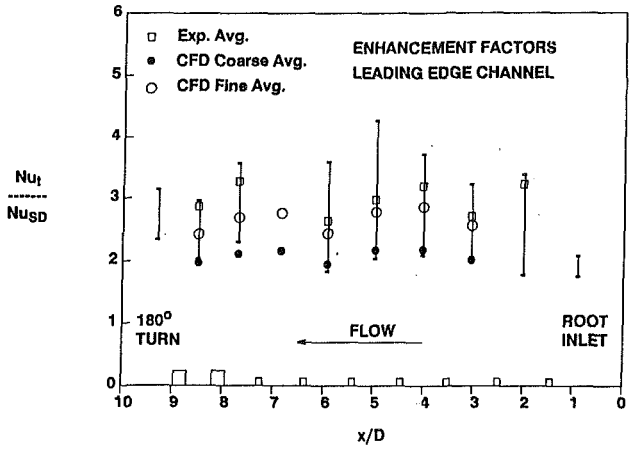

Fig. 5(*a*) Leading edge channel heat transfer enhancement factor distribution with distance from the inlet. Comparison of model turbulated convex surface maximum, minimum, and average measurements with blade CFD average predictions.

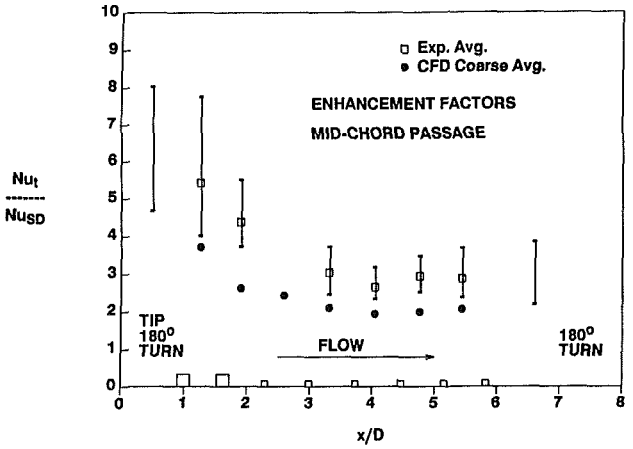

Fig. 5(*b*) Midchord channel heat transfer enhancement factor distribution with distance from the tip. Comparison of model turbulated convex surface maximum, minimum, and average measurements with blade CFD average predictions.

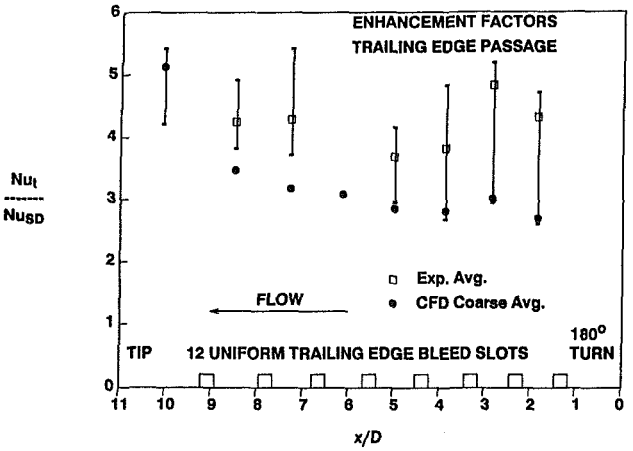

Fig. 5(*c*) Trailing edge channel heat transfer enhancement factor distribution with distance from the root turn. Comparison with model turbulated convex surface maximum, minimum, and average measurements with blade CFD average predictions.

An approximate evaluation of the rotational effects for the CFD case, based on data existing in the literature (Wagner et al., 1991; Host, 1987), shows that the effect of rotation on the average Nusselt numbers on the leading and trailing channel

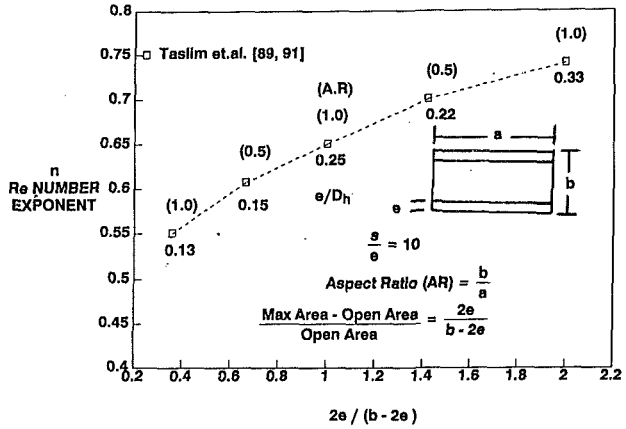

Fig. 6 Variation of Reynolds number exponent for staggered square rib turbulated rectangular stationary channel Nusselt number-Reynolds number correlation

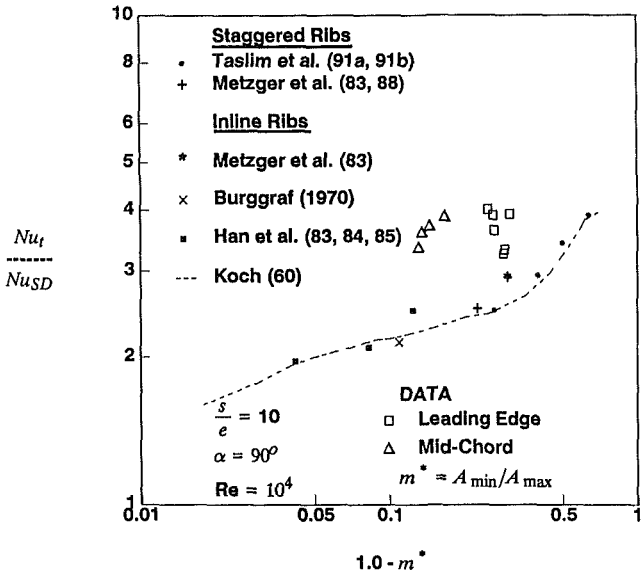

Fig. 7 Rectangular stationary channel staggered turbulated heat transfer enhancement factors compared to in-line turbulator data and circular tube data. Comparison of leading edge and midchord test enhancement factors with fully developed flow data.

outflow angled pressure side surfaces of the passages should be expected to be less than 10 percent of the stationary case, considering the leading and trailing channel cross-section shallow angles relative to the direction of rotation, and on the insignificant difference on the midchord in-flow channel after the 180-deg turn.

Figure 7 is a compilation of data for fully developed turbulated channel enhancement factors (Nu_t/Nu_{SD}) measured with rectangular staggered (Taslim et al., 1991; Taslim and Spring, 1991; Metzger et al., 1983, 1988), rectangular in-line (Metzger et al., 1983; Burggraf, 1970; Han and Lei, 1983; Han, 1984; Han and Park, 1985) and circular tubes (Koch, 1960) plotted versus the passage geometric parameter of $(1.0 - A_{min}/A_{max})$. A_{min} and A_{max} are the minimum and maximum flow cross-sectional areas. The ratio (A_{min}/A_{max}) equals $(1 - 2e/b)$ for a rectangular channel and $(1 - 2e/D)^2$ for a circular channel. e is the turbulator height; b is the rectangular passage height, and D is the circular tube diameter. For the present comparison the data considered were for a rib pitch-to-rib height ratio of ten ($s/e = 10$), for a flow-to-rib angle of ninety degrees ($\alpha = 90$ deg) and for a flow Reynolds number of 10^4. Since the present heat transfer data were taken at Reynolds numbers different from 10^4, the measured enhancement factors

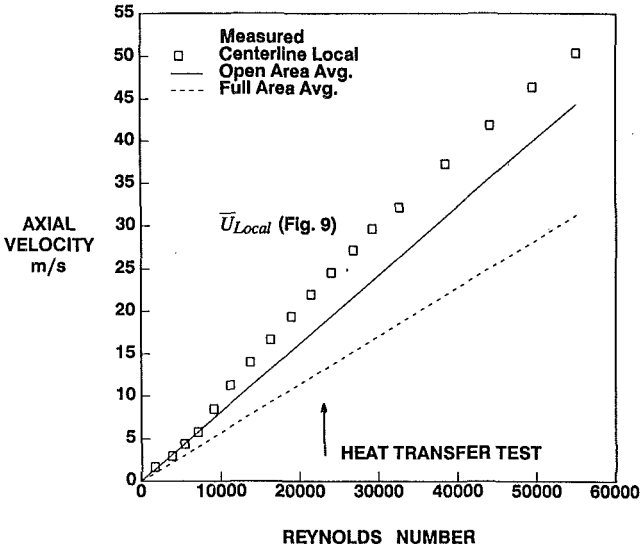

Fig. 8 Average midchannel axial velocity at Location 1 (inlet of the leading edge channel) versus flow Reynolds numbers

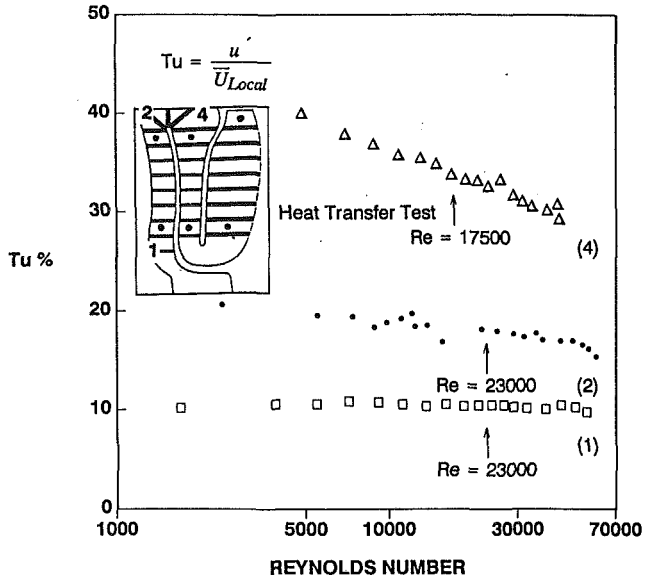

Fig. 9 Midchannel axial turbulence intensity at locations 1, 2, and 4 versus Reynolds numbers

were scaled for this comparison. The test leading edge (open squares) and midchord (open triangles) enhancement factors shown in Fig. 7 are higher than the fully developed turbulated channel values. This observation substantiates the previous remark that the flows in the leading and midchord channels apparently do not have sufficient passage length to generate fully developed heat transfer coefficients. The heat transfer performance of the trailing edge passage was not compared with previous investigations because the flow distribution is a complex phenomenon due to the presence of the trailing edge holes and because the turbulence promoters were rectangular and tapered in shape and had a pitch-to-average rib height ratio of 6.6 instead of 10 (as specified in Fig. 7).

4.2 Axial Velocities and Turbulence Intensities. Figure 8 shows the measured passage centerline axial velocities at Location 1 (Fig. 2) as a function of the local flow Reynolds numbers. The flow Reynolds numbers varied between 2000 and 55,000 and were calculated from:

$$\mathrm{Re} = \frac{4\dot{m}}{P\mu} \tag{6}$$

where P is the cross sectional perimeter of the channel location. Figure 8 also shows the local average axial velocities calculated from the measured air mass flow rate, local pressure and local flow area. The lower velocities were calculated with the passage full flow area without accounting for the presence of the turbulence promoters. Higher velocities were evaluated by subtracting the rib areas from the total passage flow area. The measured axial velocities are approximately 15–20 percent higher than the average velocities with the open area between the ribs. Local velocity measurements for the other measurement locations, 2 to 5, are very similar in nature and thus will not be presented. The axial midchannel turbulence intensities measured (based on the local axial velocity) at locations 1, 2, and 4 are presented in Fig. 9 as a function of the local flow Reynolds numbers. The turbulence intensities at Location 1 have an average value of 0.1 (10 percent) and do not show a strong variation with the Reynolds number. The increasing turbulence intensities generated by the staggered ribs up to location 2 decreased about 25 percent from about 0.2 to 0.15 with increasing Reynolds numbers. The turbulence intensities at Location 4 decreases also about 25 percent from 0.4 to 0.3 as the Reynolds numbers increase an order of magnitude from 4900 to 46,400. Location 4, located downstream of the first

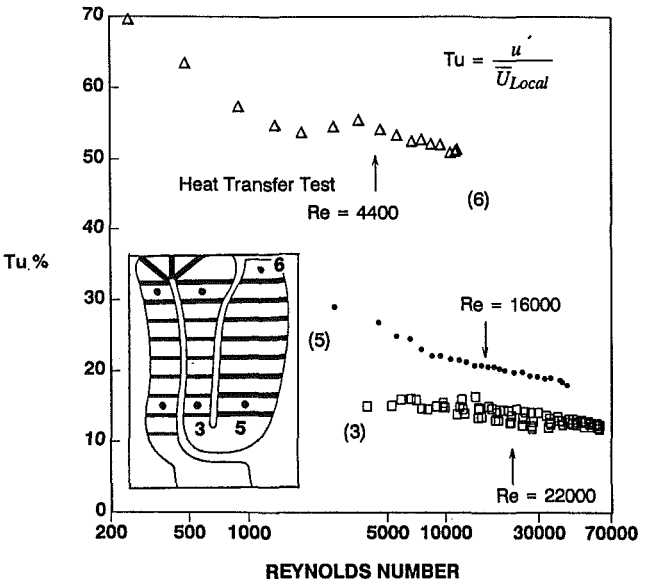

Fig. 10 Midchannel axial turbulence intensity at location 3, 5, and 6 versus Reynolds numbers

180-deg turn of the serpentine circuit, shows a much higher turbulence intensity level than the first two locations, 1 and 2, and suggests an explanation for the higher heat transfer coefficients downstream of the turbulated turn in Fig. 4(*b*).

The midchannel turbulence intensities measured at Locations 3, 5, and 6 are shown in Fig. 10 as a function of the local flow Reynolds numbers. At Location 3, the level is almost identical to station 2, which is at the exit of the first outflow channel and the decrease again is about 25 percent from 0.16 to 0.12 as the Reynolds numbers increase from 4000 to 63,000. The decrease is less pronounced than the one observed at Location 4, which was at the inlet of the midchord passage after the first 180-deg turn. The turbulence intensities measured at location 5 decrease about 40 percent from 0.29 to 0.18 as the Reynolds numbers increase from 2750 to 42,050. While the decrease in the turbulence intensity with the Reynolds numbers is stronger at locations downstream of 180-deg turns (Locations 4 and 5), the turbulence level downstream of the turbulated tip turn (Station 4) is more than 50 percent higher than the

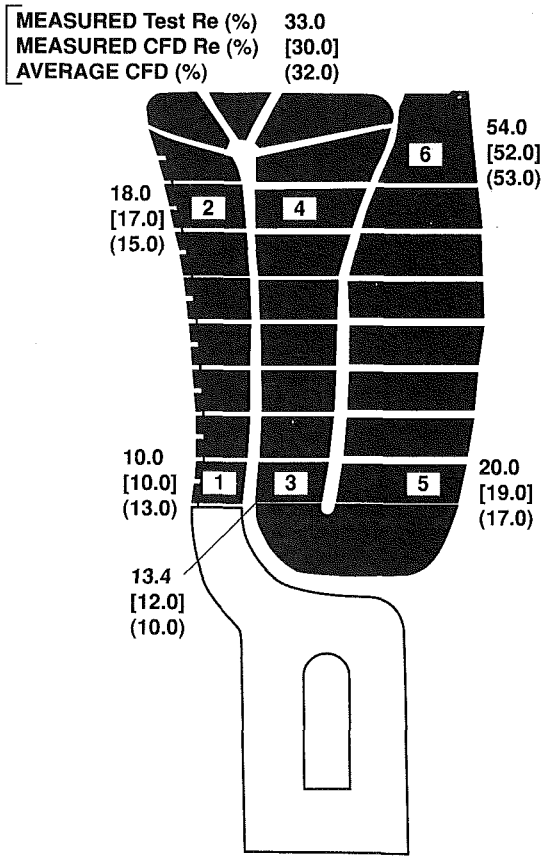

Fig. 11 Comparison of the midchannel measured average axial turbulence intensities (*Tu*) at the heat transfer test and CFD Reynolds number, and CFD analysis

unturbulated root turn (Station 5). The turbulence intensities at Location 6, the trailing edge tip whose air is significantly depleted out the trailing edge holes, decreases from 0.7 to 0.5 as the Reynolds numbers increased a fivefold order of magnitude. Figure 11 and Table 1 summarize the axial turbulence intensities measured at the six separate locations for the heat transfer test flow rate and Reynolds number. These are also compared with the CFD values to be discussed in Section 4.3.

The trailing edge tip high turbulence intensities at Station 6 shown in Table 1 and Fig. 11, with axial average velocities of less than 3 m/s at design Reynolds number of 4400, tend to illustrate why the heat transfer enhancement factors in Fig. 5(*c*) remain high at the trailing edge tip. It is hypothesized that the high percent turbulence intensity is generated at Station 6 not only by the high turbulator rib blockage at the very low channel aspect ratio (0.144), but by the propagation of high turbulence from the trailing edge root turn (19 percent) in conjunction with a 4:1 root-to-tip decrease in trailing edge channel axial velocity. These three factors in combination could potentially contribute to the observed high turbulence measured.

4.3 Comparison With CFD Analysis. Since the k–ϵ model for turbulence used in the CFD code does not directly evaluate the axial turbulence intensities, the equivalent value of the axial turbulent intensities is calculated from the CFD midchannel turbulent kinetic energy (k) by the assumption of isotropic turbulence (Marinaccio, 1991a) where

$$Tu = \text{Axial Turbulence Intensity} = \frac{(2/3k)^{1/2}}{U_{\text{Local}}} \times 100 \text{ percent}$$

The comparison of the measured midchannel axial turbulence intensities at the six specific locations with those calculated by

Table 1 Comparison of axial turbulence intensities

Location	Measured Test Re (%)	Measured CFD Re (%)	CFD Range (%)	CFD Avg. (%)
1	10.0	10.0		
			12.5-13.5	13.0
2	18.0	17.0		
			10.5-19.5	15.0
4	33.0	30.0	29.5-34.5	32.0
3	13.4	12.0	6.5-13.5	10.0
5	20.0	19.0	14.5-19.5	17.0
6	54.0	52.0	27.5-78.5	53.0

CFD, with a turbulence intensity of 5 percent at the inlet of the test section, is presented in Table 1. The comparison is made at the test and at the CFD calculated flow Reynolds numbers. The same information is also shown in Fig. 11. The differences in the measured turbulence intensities between the test and calculated CFD Reynolds numbers are relatively small.

The CFD turbulence intensity results from Marinaccio (1991b) show significant variations in the turbulence intensities in the plane of the measurements. Since the measurements were performed with a hot wire having a small diameter and a width of around 3 mm, this finite dimension provided data on the turbulence intensities averaged over a finite area. The comparison in Table 1 is made with the turbulence intensity ranges and the average evaluated from the CFD analysis.

The comparisons show that the measured and calculated values agree in magnitude and in trends. The turbulence intensities at the exit sections of the 180-deg turns are higher than at the inlet sections. Both Locations 4 and 5 show higher axial turbulence intensities than Locations 3 and 2. The turbulence intensity at Location 6 has the highest value. Measurements show a value of 0.52 while the CFD analysis averages around 0.53. These high-intensity percentages at the trailing edge tip suggest a sustaining velocity turbulence from the root 180-deg turn and turbulators, coupled with a substantial decrease in channel average velocity after the inlet flow is depleted to the trailing edge slots.

5 Summary and Conclusions

Turbulated passage convex surface detailed heat transfer coefficients using the liquid crystal technique, and inlet and exit midchannel axial turbulence intensities were measured in a 10X plexiglass model of a three-pass serpentine turbine blade cooling flow circuit at design Reynolds number.

Enhancement factors of measured average heat transfer coefficients between ribs above smooth pipe fully developed coefficients show that the relatively short passage lengths after the turns appear to maintain the flows in a continuously developing mode when correlated and compared against single-channel fully developed comparable data.

The high measured turbulence intensities of over 50 percent at the exit bleed flow tip region of the trailing edge passage suggest the reason for the relatively high heat transfer coefficients measured even at low Reynolds numbers. The turbulent intensity measurements reasonably confirm the CFD analysis distributions and support the explanation for the much higher heat transfer coefficients measured in the 10X model trailing edge tip in a disappearing flow region. These observed phenomena tend to explain the lack of turbine blade temperature distress in the trailing edge cavity low-flow tip region.

The higher turbulence intensities in the exit regions of the 180-deg turns relative to the turbulence intensities measured in the inlet of the turns, again, point to the apparent reason for the higher measured heat transfer enhancements, even at lower exit than inlet Reynolds numbers.

The 10X model stationary heat transfer and turbulence intensity data, compared with the CFD 1X rotating blade model,

indicate that the level and trends in the three-pass serpentine passage with 180-deg turns are in reasonable agreement. The sample levels of the axial midchannel turbulence intensities at the channel inlet and exit locations are close to the average values of the midchannel CFD analysis.

References

Boyle, R. J., 1984, "Heat Transfer in Serpentine Passages With Turbulence Promoters," ASME Paper No. 84-HT-24.

Burggraf, F., 1970, "Experimental Heat Transfer and Pressure Drop With Two-Dimensional Turbulence Promoter Applied to Two Opposite Walls of a Square Tube," *Augmentation of Convective Heat and Mass Transfer*, ASME, New York, pp. 70–79.

Chyu, M. K., 1991, "Regional Heat Transfer in Two-Pass and Three-Pass Passages With 180-degree Sharp Turns," ASME *Journal of Heat Transfer*, Vol. 113, pp. 63–70.

Fodemski, T. R., 1988, "The Simulation of Flow and Heat Transfer in Channels With Ribbed Surfaces," *Transport Phenomena in Turbulent Flow*, Hemisphere Publishing Corp., Washington, DC.

Han, J. C., Glicksman, L. R., and Rohsenow, W. M., 1978, "An Investigation of Heat Transfer and Friction for Rib-Roughened Surfaces," *Int. J. Heat Mass Transfer*, Vol. 21, pp. 1143–1156.

Han, J. C., and Lei, C. K., 1983, "Heat Transfer and Friction in Square Ducts With Two Opposite Rib-Roughened Walls," ASME Paper No. 83-HT-26.

Han, J. C., 1984, "Heat Transfer and Friction in Channels With Two Opposite Rib-Roughened Walls," ASME *Journal of Heat Transfer*, Vol. 106, pp. 774–781.

Han, J. C., Park, J. S., and Lei, C. K., 1985, "Heat Transfer Enhancement in Channels With Turbulence Promoters," ASME *Journal of Engineering for Gas Turbines and Power*, Vol. 107, pp. 628–635.

Han, J. C., and Park, J. S., 1986, "Local Heat Transfer Augmentation in Channels With Two Opposite Ribbed Surfaces," *Heat Transfer 1986*, Hemisphere Publishing Co., pp. 2885–2890.

Han, J. C., and Park, J. S., 1988, "Developing Heat Transfer in Rectangular Channels With Rib Turbulators," *Int. J. Heat Mass Transfer*, Vol. 31, No. 1, pp. 183–195.

Han, J. C., Chandra, P. R., and Lau, S. C., 1988, "Local Heat/Mass Transfer Distribution Around Sharp 180 Degree Turns in Two-Pass Smooth and Rib-Roughened Channels," ASME *Journal of Heat Transfer*, Vol. 110, pp. 91–98.

Han, J. C., 1988, "Heat Transfer and Friction Characteristics in Rectangular Channels With Rib Turbulators," ASME *Journal of Heat Transfer*, Vol. 110, pp. 321–328.

Kline, S. J., and McClintock, F. A., 1953, "Describing Uncertainties in Single-Sample Experiments," *Mech. Eng'g.*, Vol. 75(1), pp. 3–8.

Koch, R., 1960, "Pressure Loss and Heat Transfer for Turbulent Flow," AEC-tr-3875, p. 32.

Kostic, M., and Hartnett, J. P., 1986, "Heat Transfer to Water Flowing Turbulently Through a Rectangular Duct With Asymmetric Heating," *Int. J. Heat Mass Transfer*, Vol. 29(8), pp. 1283–1291.

Krishnamoorthy, V., and Sukhatme, S. P., 1989, "The Effect of Free-Stream Turbulence on Gas Turbine Blade Heat Transfer," ASME JOURNAL OF TURBOMACHINERY, Vol. 111, pp. 497–501.

Lau, S. C., Han, J. C., and Batten, T., 1989, "Heat Transfer, Pressure Drop, and Mass Flow Rate in Pin Fin Channels With Long and Short Trailing Edge Ejection Holes," ASME JOURNAL OF TURBOMACHINERY, Vol. 111, pp. 116–123.

Marinaccio, T., 1989, "Three Dimensional Flow Analysis of the Cooling Passages of a Turbine Blade: Analysis Summary," ADAPCO, Report No. 06-35-003.

Marinaccio, T., and Hur, N., 1990a, "Three Dimensional Flow Analysis of the Cooling Flow in a Turbine Blade: Mesh Density Sensitivity Study," ADAPCO Report 06-42-001.

Marinaccio, T., and Hur, N., 1990b, "Three Dimensional Flow Analysis of the Cooling Passages of a Turbine Blade: Additional Results," ADAPCO, Report No. 06-35-004.

Marinaccio, T., 1990, personal communication, letter to N. Abuaf.

Marinaccio, T., 1991a, "Additional Turbulence Intensity Information," personal communication to D. Kercher, Jan. 8 and 11.

Marinaccio, T., 1991b, "Comparison Between Leading Edge Coarse and Fine Mesh Average Heat Transfer Coefficients," ADAPCO letter 06-35-007 to D. Kercher.

Metzger, D. E., Fan, C. S., and Pennington, J. W., 1983, "Heat Transfer and Flow Characteristics of Very Rough Transverse Ribbed Surfaces With and Without Pin Fins," *Proceedings ASME-JSME Thermal Engineering Joint Conference*, Vol. 1, pp. 429–436.

Metzger, D. E., Plevich, C. W., and Fan, C. S., 1984, "Pressure Loss Through Sharp 180 deg Turns in Smooth Rectangular Channels," ASME *Journal of Engineering for Gas Turbines and Power*, Vol. 106, pp. 677–681.

Metzger, D. E., and Sahm, M. K., 1986, "Heat Transfer Around Sharp 180-deg Turns in Smooth Rectangular Channels," ASME *Journal of Heat Transfer*, Vol. 108, pp. 500–506.

Metzger, D. E., Fan, C. S., and Plevich, C. W., 1988, "Effects of Transverse Rib Roughness on Heat Transfer and Pressure Losses in Rectangular Ducts With Sharp 180 Degree Turns," Paper AIAA-88-0166.

Moffat, R. J., and Maciejewski, P. K., 1985, "Heat Transfer With Very High Free-Stream Turbulence," *NASA Turbine Engine Hot Section Technology*, NASA Lewis Research Center, pp. 203–215.

Simonich, J. C., and Moffat, R. J., 1982, "New Technique for Mapping Heat Transfer Coefficient Contours," *Rev. Sci. Instruments*, Vol. 53, No. 5, pp. 678–683.

Sparrow, E. M., Lloyd, J. R., and Hixon, C. W., 1966, "Experiments on Turbulent Heat Transfer in an Asymmetrically Heated Rectangular Duct," ASME *Journal of Heat Transfer*, Vol. 88, pp. 170–174.

Taslim, M. E., and Spring, S. D., 1987, "Friction Factors and Heat Transfer Coefficients in Turbulated Passages of Different Aspect Ratios. Part I. Experimental Results," Paper No. AIAA-87-2009.

Taslim, M. E., and Spring, S. D., 1988, "Experimental Heat Transfer and Friction Factors in Turbulated Cooling Passages of Different Aspect Ratios Where Turbulators are Staggered," Paper No. AIAA-88-3014.

Taslim, M. E., Rahman, A., and Spring, S. D., 1991, "An Experimental Investigation of Heat Transfer Coefficients in a Spanwise Rotating Channel With Two Opposite Rib-Roughened Walls," ASME JOURNAL OF TURBOMACHINERY, Vol. 113, pp. 75–82.

Taslim, M. E., and Spring, S. D., 1991, "An Experimental Investigation Into the Effects Turbulator Profile and Spacing Have on Heat Transfer Coefficients and Friction Factors in Small Cooled Turbine Airfoils," Paper No. AIAA-91-2033.

Turbine Engine Hot Section Technology (HOST), 1987, *NASA Conference Publication 2493*, Oct.

Wagner, J. H., Johnson, B. V., Graziani, R. A., and Yeh, F. C., 1992, "Heat Transfer in Rotating Serpentine Passages With Trips Normal to the Flow," ASME JOURNAL OF TURBOMACHINERY, Vol. 114, pp. 847–857.

Zerkle, R. D., and Lounsbury, R. J., 1989, "Freestream Turbulence Effect on Turbine Airfoil Heat Transfer," *J. Propulsion*, Vol. 5, No. 1, pp. 82–88.